ADVANCES IN EXPERIMENTAL MEDICINE AND BIOLOGY

Volume 662

OXYGEN TRANSPORT TO TISSUE XXXI

Edited by
Eiji Takahashi
and
Duane F. Bruley

Springer

Oxygen Transport to Tissue XXXI

For other titles published in this series, go to
http://www.springer.com/series/5584

Advances in Experimental Medicine and Biology

Editorial Board:

NATHAN BACK, *State University of New York at Buffalo*

IRUN R. COHEN, *The Weizmann Institute of Science*

ABEL LAJTHA, *N.S. Kline Institute for Psychiatric Research*

JOHN D. LAMBRIS, *University of Pennsylvania*

RODOLFO PAOLETTI, *University of Milan*

Eiji Takahashi · Duane F. Bruley
Editors

Oxygen Transport to Tissue XXXI

Springer

Editors
Eiji Takahashi
Department of Physiology
Yamagata University School of Medicine
Yamagata
990-9585 Japan
eiji@med.id.yamagata-u.ac.jp

Duane F. Bruley
Synthesizer, Inc.
2773 Westminster Road
Ellicott City, MD 21043
USA
bruley@umbc2.umbc.edu

ISSN 0065-2598
ISBN 978-1-4419-1239-8 e-ISBN 978-1-4419-1241-1
DOI 10.1007/978-1-4419-1241-1
Springer New York Dordrecht Heidelberg London

Library of Congress Control Number: 2009938210

© Springer Science+Business Media, LLC 2010
All rights reserved. This work may not be translated or copied in whole or in part without the written permission of the publisher (Springer Science+Business Media, LLC, 233 Spring Street, New York, NY 10013, USA), except for brief excerpts in connection with reviews or scholarly analysis. Use in connection with any form of information storage and retrieval, electronic adaptation, computer software, or by similar or dissimilar methodology now known or hereafter developed is forbidden. The use in this publication of trade names, trademarks, service marks, and similar terms, even if they are not identified as such, is not to be taken as an expression of opinion as to whether or not they are subject to proprietary rights.
While the advice and information in this book are believed to be true and accurate at the date of going to press, neither the authors nor the editors nor the publisher can accept any legal responsibility for any errors or omissions that may be made. The publisher makes no warranty, express or implied, with respect to the material contained herein.

Printed on acid-free paper

Springer is part of Springer Science+Business Media (www.springer.com)

International Society on Oxygen Transport to Tissue (ISOTT)

ISOTT2008

Officers

President	Eiji Takahashi (Japan)
Past-President	Per Liss (Sweden)
President-Elect (2009)	Joseph C. LaManna (USA)
Secretary	Oliver Thews (Germany)
Trasurer	Peter E. Keipert (USA)
Chairperson, Knisely Award Committee	Duane F. Bruley (USA)

Executive Committee

Arthur Fournell (Germany)	Fahmeed Hyder (USA)
Paul Okunieff (USA)	Akitoshi Seiyama (Japan)
Sabine Van Huffel (Belgium)	William Welch (USA)
Martin Wolf (Switzerland)	Christopher B. Wolff (UK)

Local Committee

Mamoru Tamura	
Ichiro Kuwahira	Hirosuke Kobayashi
Shunsaku Koga	Yoko Hoshi
Kaoru Sakatani	Akitoshi Seiyama
Masataka Kinjo	Katsuyuki Yamamoto

Awardees

Melvin H. Knisely Award	Kazuto Masamoto (Japan)
Dietrich W. Lübbers Award	Joke Vanderhaegen (Belgium)
Britton Chance Award	Jianting Wang (USA)
Duane F. Bruley Award	Sebastiano Cicco (Italy)

Oxygen Transport to Tissue XXXI

Editorial Board

Principal Editor	Eiji Takahashi (Japan)
Co-editors	Yoko Hoshi (Japan)
	Akitoshi Seiyama (Japan)
Scientific Editor	David K. Harrison (UK)
Editor In Chief	Duane F. Bruley (USA)
Language Editor	Laraine Visser-Isles (The Netherlands)
Technical Editor	Eileen Harrison

Panel of Reviewers

Ryon M Bateman, Keio University School of Medicine, Tokyo, Japan
Emma Bowers, Freeman Hospital, Newcastle upon Tyne, UK
Giuseppe Cicco, University of Bari, Italy
Chris E Cooper, University of Essex, Colchester, UK
Dominique De Smet, Katholieke Universiteit Leuven, Belgium
Clare E Elwell, University College London, UK
Simon Faithfull, Fidelis Consulting, San Diego,USA
Norberto C Gonzalez, University of Kansas Medical Center, Kansas City, USA
Takafumi, Hamaoka, National Institute of Fitness and Sports, Kagoshima, Japan
Peter Hansell, Uppsala University, Sweden
David K Harrison, University Hospital of North Durham, UK
Yoko Hoshi, Tokyo Institute of Psychiatry, Japan
Kyung A Kang, University of Louisville, USA
Peter E Keipert, Sangart Inc., San Diego, USA
Ichiro Kuwahira, Tokai University Tokyo Hospital, Japan
Joseph C LaManna, Case Western Reserve University School of Medicine, Cleveland, USA
Terence Leung, University College London, UK
Arnulf G Mayer, University of Mainz, Germany
Kevin K McCully, University of Georgia, Athens, USA
Fredrik Palm, Uppsala University, Sweden
Gerhard Pichler, Medical University of Graz, Austria
Roland Pittman, Virginia Commonwealth University, Richmond, USA
David C Poole, Kansas State University, Manhattan, USA
Kaoru Sakatani, Nihon University School of Medicine, Tokyo, Japan
John W Severinghaus, University of California San Francisco, USA
Masahiro Shibata, Shibaura Institute of Technology, Saitama, Japan
Ilias Tachtsidis, University College London, UK
Eiji Takahashi, Yamagata University, Japan
Sabine Van Huffel, Katholieke Universiteit Leuven, Belgium
Peter W Vaupel, University of Mainz, Germany
Heidrun Wabnitz, Physikalisch-Technische Bundesanstalt, Berlin, Germany
David F Wilson, University of Pennsylvania, Philadelphia, USA

Preface

The International Society on Oxygen Transport to Tissue (ISOTT, *www.isott.info*) is an interdisciplinary society comprising about 250 members worldwide. Its purpose is to further the understanding of all aspects of the processes involved in the transport of oxygen from the air to its ultimate consumption in the cells of the various organs of the body. The annual meeting brings together scientists, engineers, clinicians and mathematicians in a unique international forum for the exchange of information and knowledge, the updating of participants on latest developments and techniques, and the discussion of controversial issues within the field of oxygen transport to tissue. Founded in 1973, the society has been the leading platform for the presentation of many of the technological and conceptual developments within the field both at the meetings themselves and in the proceedings of the society. These have been published first by Plenum Publishing (1973), then by Kluwer Academic/Plenum Publishers and presently by Springer Publishing, all in the *Advances In Experimental Medicine and Biology Series*.

The 36th Annual ISOTT conference was held in Sapporo, Japan during August 3–7, 2008. It was the second occasion that the ISOTT meeting was held in Japan; the first one was held in the same place in 1987 organized by Professor Masaji Mochizuki. The meeting consisted of one special lecture by the Honorary President Professor Mamoru Tamura, 8 invited lectures, 7 organized sessions (31 presentations altogether), a specially planned Asians session (4 presentations), 20 general oral presentations, and 64 poster presentations. In addition, we had an opportunity to hold a satellite symposium in the same venue titled "Oxygen Transport and Medicine" (4 presentations) chaired by Professor Makoto Suematsu, Keio University School of Medicine. We welcomed 131 full registrants (with 15 accompanying persons) and 38 one-day-ticket holders. In addition to promoting enthusiastic in-depth discussions in the conference, at after-hours, we offered special occasions so that the participants could relax and feel ISOTT's traditional familiar atmosphere. One example is the Summer Ski Jump demonstrations performed by Mr. Kazuyoshi Funaki, the Gold Medalist in 1998's Winter Olympic Games in Nagano, Japan.

This volume is the fruit of Sapporo ISOTT meeting. All the manuscripts have been carefully reviewed and revised according to the reviewer's recommendation.

I wish to thank all the reviewers for their time and effort so that the volume attains high scientific quality.

Lastly, I, on behalf of the organizing committee, cordially thank the supports from

Japan Society for the Promotion of Science
The Federation of Pharmaceutical Manufacturers' Associations of JAPAN (FPMAJ)
The Akiyama Foundation
Inoue Foundation for Science
Iwatani Naoji Foundation
The Kajima Foundation
The Kao Foundation for Arts and Sciences
The MIKIYA Science And Technology Foundation
RAKUZAN-KAI
Terumo Life Science Foundation
The Uehara Memorial Foundation

Yamagata, Japan

Eiji Takahashi, Ph.D.
President, ISOTT2008

Contents

Part I Physiology and Pathophysiology of O_2 Transport

Unfinished Physiology 3
John W. Severinghaus

Cell Respiration Under Hypoxia: Facts and Artefacts in Mitochondrial Oxygen Kinetics 7
Francesca M. Scandurra and Erich Gnaiger

Alveolar Hypoxia-Induced Systemic Inflammation: What Low PO_2 Does and Does Not Do 27
Norberto C. Gonzalez and John G. Wood

The Influence of Oxygen Supply, Hemorheology and Microcirculation in the Heart and Vascular Systems 33
Giuseppe Cicco and Sebastiano Cicco

Could Dilated Cardiomyopathy Alter the Peripheral Microcirculation and Blood Rheology? 41
Giuseppe Cicco, Valeria Fanelli, Sebastiano Cicco, Massimo Iacoviello, and Stefano Favale

The Role of Glyoxalase System in Renal Hypoxia 49
Reiko Inagi, Takanori Kumagai, Toshiro Fujita, and Masaomi Nangaku

Intracortical Microcirculatory Change Induced by Anesthesia in Rat Somatosensory Cortex 57
Kazuto Masamoto, Takayuki Obata, and Iwao Kanno

Macrophages That Survive Hyperoxia Exposure Have Higher Superoxide Dismutase Activities in Their Mitochondria 63
Kenichi Kokubo, Saki Soeda, Toshihiro Shinbo, Minoru Hirose, Noriyuki Fuku, Yutaka Nishigaki, Masashi Tanaka, and Hirosuke Kobayashi

Diet-Induced Ketosis Improves Cognitive Performance in Aged Rats 71
Kui Xu, Xiaoyan Sun, Bernadette O. Eroku, Constantinos P. Tsipis, Michelle A. Puchowicz, and Joseph C. LaManna

Fenofibrate, a Peroxisome Proliferator-Activated Receptor α Agonist, Improves Hepatic Microcirculatory Patency and Oxygen Availability in a High-Fat-Diet-Induced Fatty Liver in Mice 77
Kazunari Kondo, Tadao Sugioka, Kosuke Tsukada, Michiyoshi Aizawa, Masayuki Takizawa, Kenji Shimizu, Masaya Morimoto, Makoto Suematsu, and Nobuhito Goda

Renal Vasoconstriction in Rats Causes a Decrease in Capillary Density and an Increase in Alkaline Phosphatase Expression in Cardiac Capillary Nets 83
Tomiyasu Koyama and Akira Taka

The Effects of Cilostazol on Tissue Oxygenation upon an Ischemic-reperfusion Injury in the Mouse Cerebrum 89
Takayuki Morikawa, Katsuji Hattori, Mayumi Kajimura, and Makoto Suematsu

Effect of Transient Forebrain Ischemia on Flavoprotein Autofluorescence and the Somatosensory Evoked Potential in the Rat 95
Takahiro Igarashi, Kaoru Sakatani, Tatsuya Hoshino, Norio Fujiwara, Yoshihiro Murata, Tsuneo Kano, Jun Kojima, Takamitsu Yamamoto, and Yoichi Katayama

Assessing a Shift of Glucose Biotransformation by LC-MS/MS-based Metabolome Analysis in Carbon Monoxide-Exposed Cells 101
Naoharu Takano, Takehiro Yamamoto, Takeshi Adachi, and Makoto Suematsu

T-state Stabilization of Hemoglobin by Nitric Oxide to Form α-Nitrosyl Heme Causes Constitutive Release of ATP from Human Erythrocytes . . . 109
Tomotaka Akatsu, Kosuke Tsukada, Takako Hishiki, Kazuhiro Suga-numa, Minoru Tanabe, Motohide Shimazu, Yuko Kitagawa, Ayako Yachie-Kinoshita, and Makoto Suematsu

Age-Related Changes in the Trachea in Healthy Adults 115
Hiroaki Sakai, Yasutaka Nakano, Shigeo Muro, Toyohiro Hirai, Yasutaka Takubo, Yoshitaka Oku, Hiroshi Hamakawa, Ayuko Takahashi, Toshihiko Sato, Fengshi Chen, Hisashi Sahara, Takuji Fujinaga, Kiyoshi Sato, Makoto Sonobe, Tsuyoshi Shoji, Ryo Miyahara, Kenichi Okubo, Toru Bando, Toshiki Hirata, Hiroshi Date, and Michiaki Mishima

Polycythemia and Changes in Erythropoietin Concentration in Rats Exposed to Intermittent Hypoxia 121
Makoto Ishii, Tokuzen Iwamoto, Asuka Nagai, Gen Sasao, Masayuki Iwasaki, and Ichiro Kuwahira

A Case of HAPE on K2 and Literature Review 127
Gen Sasao, Asuka Nagai, Tokuzen Iwamoto, Toshio Ichiwata, and Ichiro Kuwahira

Synchronization Between Cardiac and Respiratory Rhythms in Healthy Subjects and Patients 133
Masaki Shimane, Yutaka Tomita, Toshihiro Shinbo, Kenichi Kokubo, Minoru Hirose, Ryuji Hataishi, Hisashi Mitsufuji, Masaru Kubota, Noriyuki Masuda, and Hirosuke Kobayashi

Part II In Vivo Measurement of O_2

Time-Resolved Near-Infrared Spectroscopy and Imaging of the Adult Human Brain 143
Heidrun Wabnitz, Michael Moeller, Adam Liebert, Hellmuth Obrig, Jens Steinbrink, and Rainer Macdonald

Clinical Electron Paramagnetic Resonance (EPR) Oximetry Using India Ink 149
Benjamin B. Williams, Nadeem Khan, Bassem Zaki, Alan Hartford, Marc S. Ernstoff, and Harold M. Swartz

Measurement of Oxygen in the Microcirculation Using Phosphorescence Quenching Microscopy 157
Roland N. Pittman, Aleksander S. Golub, and Helena Carvalho

Optimization of the Coherence Measurement Computed by Means of the Welch Averaged Periodogram Method for Assessment of Impaired Cerebral Autoregulation 163
D. De Smet, J. Vanderhaegen, G. Naulaers, and S. Van Huffel

A Hybrid Multi-Distance Phase and Broadband Spatially Resolved Spectrometer and Algorithm for Resolving Absolute Concentrations of Chromophores in the Near-Infrared Light Spectrum 169
Ilias Tachtsidis, Lei Gao, Terence S. Leung, Matthias Kohl-Bareis, Chris E. Cooper, and Clare E. Elwell

Comparison of Local Adipose Tissue Content and SRS-Derived NIRS Muscle Oxygenation Measurements in 90 Individuals 177
Chris E. Cooper, Stacey-Marie Penfold, Clare E. Elwell, and Caroline Angus

Muscle Oxygen Saturation Measured Using "Cyclic NIR Signals" During Exercise 183
Terence S. Leung, Anna Wittekind, Tiziano Binzoni, Ralph Beneke, Chris E. Cooper, and Clare E. Elwell

Determination of Oxygen Dosage Effects on Cytochrome Oxidase after Anoxia in Brain 191
Fred Kriedt, Christopher Kriedt, Chase Patterson, and Keith Van Meter

A Mathematical Model for Analyses of Muscle Oxygenation Measurements Using NIR Spectroscopy 199
Khai Jun Kek, Nobuki Kudo, and Katsuyuki Yamamoto

Mapping of Optical Pathlength of Human Adult Head at Multi-Wavelengths in Near Infrared Spectroscopy 205
Akihisa Katagiri, Ippeita Dan, Daisuke Tuzuki, Masako Okamoto, Noriaki Yokose, Kouji Igarashi, Tatsuya Hoshino, Tokuo Fujiwara, Youichi Katayama, Yui Yamaguchi, and Kaoru Sakatani

Changes of Evoked Cerebral Blood Oxygenation and Optical Pathlength in the Frontal Lobe During Language Tasks: A Study by Multi-Channel, Time-Resolved Near-Infrared Spectroscopy and Functional MRI 213
Yoshihiro Murata, Kaoru Sakatani, Tatsuya Hoshino, Norio Fujiwara, Yoichi Katayama, Daisuke Yamashita, Takeshi Yamanaka, Motoki Oda, and Yutaka Yamashita

The Partial Coherence Method for Assessment of Impaired Cerebral Autoregulation using Near-infrared Spectroscopy: Potential and Limitations 219
D. De Smet, J. Jacobs, L. Ameye, J. Vanderhaegen, G. Naulaers, P. Lemmers, F. van Bel, M. Wolf, and S. Van Huffel

Active Muscle Oxygenation Dynamics Measured During High-Intensity Exercise by Using Two Near-Infrared Spectroscopy Methods 225
Tadashi Saitoh, Anna Ooue, Narihiko Kondo, Kyuichi Niizeki, and Shunsaku Koga

Theoretical and Experimental Investigation of the Influence of Frontal Sinus on the Sensitivity of the NIRS Signal in the Adult Head 231
Eiji Okada, Daisuke Yamamoto, Naoya Kiryu, Akihisa Katagiri, Noriaki Yokose, Takashi Awano, Kouji Igarashi, Sin Nakamura, Tatsuya Hoshino, Yoshihiro Murata, Tsuneo Kano, Kaoru Sakatani, and Yoichi Katayama

Functional Optical Topography Analysis Using Statistical Parametric Mapping (SPM) Methodology with and without Physiological Confounds 237
Ilias Tachtsidis, Peck H. Koh, Charlotte Stubbs, and Clare E. Elwell

Comparison of Somatosensory Evoked Potentials and Cerebral Blood Oxygenation Changes in the Sensorimotor Cortex During Activation in the Rat 245
Yuko Kondo, Kaoru Sakatani, Takahiro Igarashi, Tatsuya Hoshino, Yoshihiro Murata, Emiri Tejima, Tsuneo Kano, and Yoichi Katayama

Individual Differences in Blood Volume and Oxygenation in the Brain during a Cognitive Task based on Time-Resolved Spectroscopic Measurements 251
Tadashi Niioka, Soichiro Ohnuki, and Yoshifumi Miyazaki

Cerebral Oxygenation in the Frontal Lobe Cortex during Incremental Exercise Tests: The Regional Changes Influenced by Volitional Exhaustion 257
Mikio Hiura, Tetsuya Mizuno, and Tsukasa Fujimoto

Implantable Resonators – A Technique for Repeated Measurement of Oxygen at Multiple Deep Sites with In Vivo EPR 265
Hongbin Li, Huagang Hou, Artur Sucheta, Benjamin B. Williams, Jean P. Lariviere, Md. Nadeem Khan, Piotr N. Lesniewski, Bernard Gallez, and Harold M. Swartz

Use of Visible Spectrophotometry to Assess Tissue Oxygenation in the Colostomy Stoma 273
Daya B. Singh, Iain Bain, and David K. Harrison

Automatic Detection of Motion Artifacts in Infant Functional Optical Topography Studies 279
Anna Blasi, Derrick Phillips, Sarah Lloyd-Fox, Peck Hui Koh, and Clare E. Elwell

Modelling of Mitochondrial Oxygen Consumption and NIRS Detection of Cytochrome Oxidase Redox State 285
Murad Banaji, Alfred Mallet, Clare E. Elwell, Peter Nicholls, Ilias Tachtsidis, Martin Smith, and Chris E. Cooper

Forced Oscillation Technique as a Non-Invasive Assessment for Lung Transplant Recipients 293
Hiroshi Hamakawa, Hiroaki Sakai, Ayuko Takahashi, Jintian Zhang, Toshihiro Okamoto, Naoki Satoda, Akihiro Aoyama, Fengshi Chen, Takuji Fujinaga, Tsuyoshi Shoji, Toru Bando, Michiaki Mishima, Hiromi Wada, and Hiroshi Date

Part III Exercise and O_2 Transport

Muscle Microcirculatory O_2 Exchange in Health and Disease 301
David C. Poole and Timothy I. Musch

Arteriolar Vasomotor Control and Contractile Performance During Fatiguing Tetanic Contractions in Rat Skeletal Muscle: Role of Sympathetic System 309
Tadakatsu Inagaki, Takashi Sonobe, David C. Poole, and Yutaka Kano

The Influence of Passive Stretch on Muscle Oxygen Saturation 317
Kevin K. McCully

NIRS Measurement of O_2 Dynamics in Contracting Blood and Buffer Perfused Hindlimb Muscle 323
Kazumi Masuda, Hisashi Takakura, Yasuro Furuichi, Satoshi Iwase, and Thomas Jue

Muscle Reoxygenation Difference Between Superficial and Deep Regions of the Muscles During Static Knee Extension 329
Chihoko Ueda and Atsuko Kagaya

Arterial Oxygen Desaturation Response to Repeated Bouts of Sprint Exercise in Healthy Young Women 335
Shimpei Kuniyoshi, Yumiko Endoh, Minoru Kobayashi, and Hiroshi Endoh

The Effect of Endurance Training on Resting Oxygen Stores in Muscle Evaluated by Near Infrared Continuous Wave Spectroscopy 341
Takayuki Sako

Cerebrovascular Response During Heavy Upper Body Exercise: Effect of Mode of Ventilation on Blood Flow Velocity in the Middle Cerebral Artery 347
K. Sato, A. Hirasawa, N. Tsunoda, Y. Taniguchi, and T. Sadamoto

Unchanged Muscle Deoxygenation Heterogeneity During Bicycle Exercise After 6 Weeks of Endurance Training 353
Ryotaro Kime, Masatsugu Niwayama, Masako Fujioka, Kiyoshi Shiroishi, Takuya Osawa, Kousuke Shimomura, Takuya Osada, Norio Murase, and Toshihito Katsumura

Comparison of Muscle O_2 Dynamics at Different Sites of the Forearm Flexor Muscles During Incremental Handgrip Exercise 359
Masako Fujioka, Ryotaro Kime, Shunsaku Koga, Takuya Osawa, Kousuke Shimomura, Takuya Osada, Norio Murase, and Toshihito Katsumura

Blood Flow and Arterial Vessel Diameter Change During Graded Handgrip Exercise in Dominant and Non-dominant Forearms of Tennis Players 365
Atsuko Kagaya, Fumiko Ohmori, Shizuyo Okuyama, Yoshiho Muraoka, and Kohei Sato

Changes in Perfusion Related to Muscle Length Affect the Pressor Response to Isometric Muscle Contraction 371
Masaki Mizuno, Ken Tokizawa, and Isao Muraoka

Decreased Muscle Oxygenation and Increased Arterial Blood Flow in the Non-Exercising Limb During Leg Exercise 379
Kiyoshi Shiroishi, Ryotaro Kime, Takuya Osada, Norio Murase, Kousuke Shimomura, and Toshihito Katsumura

Effects of Acute Hypoxia on the Inflection Point of Muscle Oxygenation 385
Takuya Osawa, Ryotaro Kime, Toshihito Katsumura, and Masayoshi Yamamoto

Part IV O_2 Microenvironment in Cancer

No Sustained Improvement in Tumor Oxygenation After Localized Mild Hyperthermia. 393
Debra K. Kelleher and Peter Vaupel

HIF-Mediated Hypoxic Response is Missing in Severely Hypoxic Uterine Leiomyomas 399
Arnulf Mayer, Michael Hoeckel, Angelika von Wallbrunn, Lars-Christian Horn, Alexander Wree, and Peter Vaupel

FRET-Like Fluorophore-Nanoparticle Complex for Highly Specific Cancer Localization 407
Jianting Wang, Michael H. Nantz, Samuel Achilefu, and Kyung A. Kang

Design of Novel Hypoxia-Targeting IDO Hybrid Inhibitors Conjugated with an Unsubstituted L-TRP as an IDO Affinity Moiety 415
Hitomi Nakashima, Kazuhiro Ikkyu, Kouichiro Nakashima, Keiichiro Sano, Yoshihiro Uto, Eiji Nakata, Hideko Nagasawa, Hiroshi Sugimoto, Yoshitsugu Shiro, Yoshinori Nakagawa, and Hitoshi Hori

Phosphorescence-Assisted Microvascular O_2 Measurements Reveal Alterations of Oxygen Demand in Human Metastatic Colon Cancer in the Liver of Superimmunodeficient NOG Mice 423
Kan Handa, Mitsuyo Ohmura, Chiyoko Nishime, Takako Hishiki, Yoshiko Nagahata, Kenji Kawai, Hiroshi Suemizu, Masato Nakamura, Masatoshi Wakui, Yuko Kitagawa, Makoto Suematsu, and Kosuke Tsukada

Part V Clinical Aspects of O_2 Transport

Hemoglobin-Vesicle, a Cellular Artificial Oxygen Carrier that Fulfils the Physiological Roles of the Red Blood Cell Structure 433
Hiromi Sakai, Keitaro Sou, Hirohisa Horinouchi, Koichi Kobayashi, and Eishun Tsuchida

Safer Surgery Using Zymogen Protein C Concentrate 439
Duane F. Bruley, Simon C. Mears, and Michael B. Streiff

Cerebral and Peripheral Tissue Oxygenation in Children Supported on ECMO for Cardio-Respiratory Failure 447
Maria D. Papademetriou, Ilias Tachtsidis, Terence S. Leung, Martin J. Elliott, Aparna Hoskote, and Clare E. Elwell

Effects of Acupuncture on Autonomic Nervous Function and Prefrontal Cortex Activity 455
Kaoru Sakatani, Takeshi Kitagawa, Naoki Aoyama, and Mitsuyoshi Sasaki

The Effect of Glycaemia on the Cerebral Oxygenation in Very Low Birthweight Infants as Measured by Near-Infrared Spectroscopy 461
Joke Vanderhaegen, Sophie Vanhaesebrouck, Christine Vanhole, Paul Casaer, and Gunnar Naulaers

A Novel Approach to Evaluate the Vessel Function Determined by Near Infrared Spectroscopy 467
Hajime Miura and Nao Okumura

Effects of Aging on Activity of the Prefrontal Cortex and Autonomic Nervous System during Mental Stress Task 473
Kaoru Sakatani, Masahiro Tanida, and Masako Katsuyama

Activity in the Premotor Area Related to Bite Force Control – A Functional Near-Infrared Spectroscopy Study. 479
Tomotaka Takeda, Mami Shibusawa, Osamu Sudal, Kazunori Nakajima, Keiichi Ishigami, and Kaoru Sakatani

Functional Near-Infrared Spectroscopy Study on Primary Motor and Somatosensory Cortex Response to Biting and Finger Clenching 485
Mami Shibusawa, Tomotaka Takeda, Kazunori Nakajima, Handa Jun, Shinichi Sekiguchi, Keiichi Ishigami, and Kaoru Sakatani

Changes in Cerebral Blood Oxygenation and Hemodynamics After Endovascular Treatment of Vascular Malformation Measured by Time-Resolved Spectroscopy 491
Tatsuya Hoshino, Kaoru Sakatani, Noriaki Yokose, Takashi Awano, Sin Nakamura, Yoshihiro Murata, Tsun eo Kano, and Yoichi Katayama

Development of a New Rehabilitation System Based on a Brain-Computer Interface Using Near-Infrared Spectroscopy 497
Takafumi Nagaoka, Kaoru Sakatani, Takayuki Awano, Noriaki Yokose, Tatsuya Hoshino, Yoshihiro Murata, Yoichi Katayama, Akihiro Ishikawa, and Hideo Eda

Bedside Assessment of Cerebral Vasospasms After Subarachnoid Hemorrhage by Near Infrared Time-Resolved Spectroscopy 505
Noriaki Yokose, Kaoru Sakatani, Yoshihiro Murata, Takashi Awano, Takahiro Igarashi, Sin Nakamura, Tatsuya Hoshino, Tsuneo Kano, Atsuo Yoshino, Yoichi Katayama, Etsuko Ohmae, Toshihiko Suzuki, Motoki Oda, and Yutaka Yamashita

Development of an Artificial Vital Sign Generator for Pulse Oximeter 513
Tomoyasu Ichimura and Hiroshi Endoh

EC-IC Bypass Function in Moyamoya Disease and Non-Moyamoya Ischemic Stroke Evaluated by Intraoperative Indocyanine Green Fluorescence Angiography 519
Takayuki Awano, Kaoru Sakatani, Noriaki Yokose, Tatsuya Hoshino, Norio Fujiwara, Shin Nakamura, Yoshihiro Murata, Tsuneo Kano, Yoichi Katayama, Takahiro Shikayama, and Mitsuharu Miwa

Effects of Revascularisation on Evoked Cerebral Blood Oxygenation Responses in Stroke Patients 525
Shin Nakamura, Kaoru Sakatani, Tsuneo Kano, Tetsuya Hoshino, Norio Fujiwara, Yoshihiro Murata, and Yoichi Katayama

Effects of Oral Single-Dose Administration of Sarpogrelate Hydrochloride on Saturation O_2 of Calf Muscle During Plantar Flexion Exercise 531
Masahiro Horiuchi, Koichi Okita, Shingo Takada, Masashi Omokawa, Tadashi Suga, Noriteru Morita, Kagami Hirabayashi, Takashi Yokota, Shintaro Kinugawa, and Hiroyuki Tsutsui

Oxidative Capacity of the Skeletal Muscle and Lactic Acid Kinetics During Exercise in Healthy Subjects and Patients with COPD 537
Toshio Ichiwata, Gen Sasao, Tokuro Abe, Kiyokazu Kikuchi, Kenya Koyama, Hiroki Fujiwara, Asuka Nagai, Ichiro Kuwahira, and Koshu Nagao

Index 545

Contributors

Tokuro Abe Department of Respiratory Medicine, Dokkyo Medical University Koshigaya Hospital, 2-1-50 Minamikoshigaya, Koshigaya-shi, Saitama, 343-8555, Japan

Samuel Achilefu Department of Radiology, Washington University School of Medicine, St. Louis, MO 63110, USA

Takeshi Adachi Department of Biochemistry & Integrative Medical Biology, School of Medicine, Keio University, Tokyo, 160-8582, Japan

Michiyoshi Aizawa Department of Biochemistry and Integrative Medical Biology, Keio University School of Medicine, Tokyo, 160-8582, Japan

Tomotaka Akatsu Departments of Surgery, School of Medicine, Keio University, Tokyo, Japan

L. Ameye Department of Electrical Engineering (ESAT), SCD Division, Katholieke Universiteit Leuven, Belgium

Caroline Angus Department of Biological Sciences, Centre for Sports and Exercise Science, University of Essex, Wivenhoe Park, Colchester, Essex, CO4 3SQ, UK

Akihiro Aoyama Department of Thoracic Surgery, Kyoto University, 54 Shogoin Kawahara-Cho, Sakyo-Ku, Kyoto, 606-8507, Japan

Naoki Aoyama Division of Optical Brain Engineering, Department of Neurological Surgery, Nihon University School of Medicine, Tokyo, Japan

Takayuki Awano Division of Neurosurgery, Department of Neurological Surgery, Nihon University School of Medicine, Tokyo, Japan

Iain Bain General Surgery, University Hospital of North Durham, Durham, DH1 5TW, UK

Murad Banaji Department of Biological Sciences, University of Essex, Colchester, CO4 3SQ, UK

Toru Bando Departments of Organ Preservation Technology, Graduate School of Medicine, Institute for Frontier Medical Sciences, Kyoto University, Kyoto, 606-8507, Japan

Ralph Beneke Department of Biological Sciences, University of Essex, Colchester Essex, UK

Tiziano Binzoni Département de l'Imagerie et des Sciences de l'Information Médicale, University Hospital, and Département des Neurosciences Fondamentales, Uni. of Geneva, Switzerland

Anna Blasi Biomedical Optics Research Laboratory, Department of Medical Physics and Bioengineering, University College London, Gower Street, London, WC1E 6BT, UK

Duane F. Bruley Synthesizer, Inc., 2773 Westminster Road, Ellicott City, MD 21043, USA

Helena Carvalho Department of Physiology and Biophysics, Virginia Commonwealth University, Richmond, Virginia 23298, USA

Paul Casaer Neonatal Intensive Care Unit, University Hospitals Gasthuisberg, Katholieke Universiteit Leuven, Leuven, Belgium

Fengshi Chen Departments of Organ Preservation Technology, Graduate School of Medicine, Institute for Frontier Medical Sciences, Kyoto University, Kyoto, 606-8507, Japan

Giuseppe Cicco C.E.M.O.T. – Interdepartmental Center of Research on Hemorheology, Microcirculation, Oxygen Transport and Non Invasive Optical Technologies, Università degli studi di Bari "Aldo Moro", Policlinico, Piazza G. Cesare, 11 70124 Bari, Italy

Sebastiano Cicco C.E.M.O.T. – Interdepartmental Center of Research on Hemorheology, Microcirculation, Oxygen Transport and Non Invasive Optical Technologies, Università degli studi di Bari "Aldo Moro", Policlinico, Piazza G. Cesare, 11 70124 Bari, Italy

Chris E. Cooper Department of Biological Sciences, Centre for Sports and Exercise Science, University of Essex, Wivenhoe Park, Colchester, Essex, CO4 3SQ, UK

Ippeita Dan National Food Research Institute, Tsukuba, Japan

Hiroshi Date Department of Thoracic Surgery, Kyoto University, 54 Shogoin Kawahara-Cho, Sakyo-Ku, Kyoto, 606-8507, Japan

D. De Smet Department of Electrical Engineering (ESAT), SCD Division, Katholieke Universiteit Leuven, Belgium

Hideo Eda Graduate School for the Creation of New Photonics Industries, Hamamatsu, Japan

Martin J. Elliott Great Ormond Street Hospital for Children, London, WC1N 3JH, UK

Clare E. Elwell Biomedical Optics Research Laboratory, Department of Medical Physics and Bioengineering, University College London, Gower Street, London, WC1E 6BT, UK

Hiroshi Endoh Department of Health and Physical Education, University of the Ryukyus Graduate School of Education, Nishihara, Okinawa, 903-0213, Japan

Yumiko Endoh Department of Clinical Nursing, Yamagata University School of Medicine, Yamagata, 990-9585, Japan

Marc S. Ernstoff Dartmouth Hitchcock Medical Center, Norris Cotton Cancer Center, Lebanon, NH, USA

Bernadette O. Eroku Department of Anatomy, Case Western Reserve University, 10900 Euclid Avenue, Cleveland, OH 44106, USA

Valeria Fanelli Institute of Cardiology, DETO, Università degli studi di Bari "Aldo Moro", Policlinico, p.zza G. Cesare, 11, 70124, Bari, Italy

Stefano Favale Institute of Cardiology, DETO, Università degli studi di Bari "Aldo Moro", Policlinico, p.zza G. Cesare, 11, 70124, Bari, Italy

Tsukasa Fujimoto Department of Neurosurgery, Showa University School of Medicine Fujigaoka Hospital, Yokohama, Japan

Takuji Fujinaga Departments of Organ Preservation Technology, Graduate School of Medicine, Institute for Frontier Medical Sciences, Kyoto University, Kyoto, 606-8507, Japan

Masako Fujioka Department of Sports Medicine for Health Promotion, Tokyo Medical University, Tokyo, 160-8402, Japan

Toshiro Fujita Division of Nephrology and Endocrinology, University of Tokyo School of Medicine, Tokyo, Japan

Hiroki Fujiwara Department of Respiratory Medicine, Dokkyo Medical University Koshigaya Hospital 2-1-50 Minamikoshigaya, Koshigaya-shi, Saitama, 343-8555, Japan

Norio Fujiwara Division of Neurosurgery, Department of Neurological Surgery, Nihon University School of Medicine,30-1, Oyaguchi-Kamimachi, Itabashi-ku, Tokyo, 173-8610, Japan

Tokuo Fujiwara Division of Neurological Surgery, Department of Neurological Surgery, Nihon University School of Medicine, Tokyo, Japan

Noriyuki Fuku Department of Genomics for Longevity and Health, Tokyo Metropolitan Institute of Gerontology, Tokyo, 173-0015, Japan

Yasuro Furuichi The graduate School of Education, Kanazawa University, Kanazawa, 920-1192, Japan

Bernard Gallez EPR Center for Viable Systems, Department of Radiology, Dartmouth Medical School, 703 Vail, Hanover, NH 03755, USA

Lei Gao Biomedical Optics Research Laboratory, Department of Medical Physics and Bioengineering, University College London, Gower Street, London, WC1E 6BT, UK

Erich Gnaiger Medical University of Innsbruck, Department of General and Transplant Surgery, D. Swarovski Research Laboratory, Innsbruck, Austria; and OROBOROS INSTRUMENTS, Innsbruck, Austria

Nobuhito Goda Department of Life Science and Medical Bio-Science, Waseda University School of Advanced Science and Engineering, Tokyo, 162-8480, Japan; Core Research for Evolutional Science and Technology, Japan Science and Technology Agency, Kawaguchi, Saitama, 332-0012, Japan

Aleksander S. Golub Department of Physiology and Biophysics, Virginia Commonwealth University, Richmond, Virginia 23298, USA

Norberto C. Gonzalez Department of Molecular and Integrative Physiology, University of Kansas Medical Center, Kansas City, KS 66160, USA

Hiroshi Hamakawa Departments of Organ Preservation Technology, Department of Thoracic Surgery, Graduate School of Medicine, Institute for Frontier Medical Sciences, Kyoto University, Kyoto, 606-8507, Japan

Kan Handa Department of Surgery, School of Medicine, Keio University, Tokyo, 160-8582, Japan

David K. Harrison Department of Medical Physics and General Surgery, University Hospital of North Durham, Durham, DH1 5TW, UK

Alan Hartford Dartmouth Hitchcock Medical Center, Norris Cotton Cancer Center, Lebanon, NH, USA

Ryuji Hataishi Department of Medicine, Kitasato University, Kanagawa, 228-8555, Japan

Katsuji Hattori Department of Biochemistry and Integrative Medical Biology, Keio University School of Medicine, Tokyo, 160-8582, Japan

Kagami Hirabayashi Department of Cardiovascular Medicine, Hokkaido University of Education, Sapporo, Japan

Toyohiro Hirai Departments of Respiratory Medicine, Institute for Frontier Medical Sciences, Kyoto University, Kyoto, 606-8507, Japan

A. Hirasawa Research Institute of Physical Fitness, Japan Women's College of Physical Education, Tokyo, 157-8565, Japan

Toshiki Hirata Departments of Thoracic Surgery, Institute for Frontier Medical Sciences, Kyoto University, Kyoto, 606-8507, Japan

Minoru Hirose Department of Medical Engineering and Technology, School of Allied Health Sciences, Kitasato University, Kanagawa, 228-8555, Japan

Takako Hishiki Department of Biochemistry and Integrative Medical Biology, School of Medicine, Keio University, Tokyo, 160-8582, Japan

Mikio Hiura Faculty of Humanity and Environment, Hosei University, Tokyo, Japan; Department of Neurosurgery, Showa University School of Medicine Fujigaoka Hospital, Yokohama, Japan

Michael Hoeckel Department of Gynecology and Obstetrics, University Medical Center, Leipzig, Germany

Hitoshi Hori Department of Life System, Institute of Technology and Science, Graduate School, The University of Tokushima, Tokushima, 770-8506, Japan

Hirohisa Horinouchi Department of Surgery, School of Medicine, Keio University, Tokyo, Japan

Masahiro Horiuchi Department of Human Care Studies, Hokkaido University of Education, Sapporo, Japan

Lars-Christian Horn Department of Pathology, University Medical Center, Leipzig, Germany

Tatsuya Hoshino Division of Neurological Surgery, Department of Neurological Surgery, Nihon University School of Medicine, Tokyo, Japan

Tetsuya Hoshino Department of Neurosurgery, Nihon University School of Medicine, Tokyo, Japan

Aparna Hoskote Great Ormond Street Hospital for Children, London, WC1N 3JH, UK

Huagang Hou EPR Center for Viable Systems, Department of Radiology, Dartmouth Medical School, 703 Vail, Hanover, NH 03755, USA

S. Van Huffel Department of Electrical Engineering (ESAT), SCD Division, Katholieke Universiteit Leuven, Belgium

Massimo Iacoviello Institute of Cardiology, DETO, Università degli studi di Bari "Aldo Moro", Policlinico, p.zza G. Cesare, 11, 70124, Bari, Italy

Tomoyasu Ichimura Department of Electronic Control Engineering, Oyama National College of Technology, Tochigi, 323-0806, Japan

Toshio Ichiwata Department of Respiratory Medicine, Dokkyo Medical University Koshigaya Hospital, Koshigaya, Saitama, 343-8555, Japan

Kouji Igarashi Division of Neurological Surgery, Department of Neurological Surgery, Nihon University School of Medicine, Tokyo, Japan

Takahiro Igarashi Division of Neurosurgery, Department of Neurological Surgery, Nihon University School of Medicine, Tokyo, 173-8610, Japan

Kazuhiro Ikkyu Department of Life System, Institute of Technology and Science, Graduate School, The University of Tokushima, Tokushima, 770-8506, Japan

Tadakatsu Inagaki Departments of Applied Physics and Chemistry, University of Electro-Communications, Chohu, Tokyo, Japan

Reiko Inagi Division of Nephrology and Endocrinology, University of Tokyo School of Medicine, 7-3-1 Hongo, Bunkyo-ku, Tokyo, 113-8655, Japan

Keiichi Ishigami Department of Sports Dentistry, Tokyo Dental College, Nihon University School of Medicine, Tokyo, Japan

Makoto Ishii Department of Medicine, Tokai University School of Medicine, Isehara, Kanagawa, 259-1193, Japan

Akihiro Ishikawa R&D Department, Medical Systems Division, Shimadzu Corporation, Kyoto, Japan

Tokuzen Iwamoto Department of Medicine, Tokai University Tokyo Hospital, Tokyo, 151-0053, Japan

Masayuki Iwasaki Department of General Thoracic Surgery, Tokai University School of Medicine, Isehara, Kanagawa, 259-1193, Japan

Satoshi Iwase Department of Physiology, Aichi Medical University, Nagakute, 480-1195, Japan

J. Jacobs Department of Electrical Engineering (ESAT), SCD Division, Katholieke Universiteit Leuven, Belgium

Thomas Jue Department of Biochemistry and Molecular Medicine, University of California Davis, Davis 95616-8635, USA

Handa Jun Department of Sports Dentistry, Tokyo Dental College, Nihon University School of Medicine, Tokyo, Japan

Atsuko Kagaya Research Institute of Physical Fitness, Japan Women's College of Physical Education, Tokyo, 57-8565, Japan

Mayumi Kajimura Department of Biochemistry and Integrative Medical Biology, Keio University School of Medicine, Tokyo, 160-8582, Japan

Kyung A. Kang Department of Chemical Engineering, University of Louisville, Louisville, KY 40292, USA

Iwao Kanno Molecular Imaging Center, National Institute of Radiological Sciences, Chiba, 263-8555, Japan

Tsuneo Kano Division of Neurosurgery, Department of Neurological Surgery, Nihon University School of Medicine, Tokyo, 173-8610, Japan

Yutaka Kano Departments of Applied Physics and Chemistry, University of Electro-Communications, Chohu, Tokyo, Japan

Akihisa Katagiri Division of Neurological Surgery, Department of Neurological Surgery, Nihon University School of Medicine, Tokyo, Japan

Yoichi Katayama Division of Neurosurgery, Department of Neurological Surgery; Division of Applied System Neuroscience, Department of Advanced Medical Science, Nihon University School of Medicine, Tokyo, 173-8610, Japan

Toshihito Katsumura Department of Sports Medicine for Health Promotion, Faculty of Medicine, Tokyo Medical University, Tokyo, 160-8402, Japan

Masako Katsuyama Shiseido Functional Food Research & Development Center, Shiseido, Yokohama, Tokyo, Japan

Kenji Kawai Central Institutes for Experimental Animals, Kanagawa, 216-0001, Japan

Khai Jun Kek Graduate School of Information Science and Technology, Hokkaido University, Sapporo, 060-0814, Japan

Debra K. Kelleher Institute of Physiology and Pathophysiology, University of Mainz, 55099 Mainz, Germany

Nadeem Khan EPR Center for Viable Systems, Department of Radiology, Dartmouth Medical School, 703 Vail, Hanover, NH 03755, USA

Kiyokazu Kikuchi Department of Respiratory Medicine, Dokkyo Medical University Koshigaya Hospital, Saitama, 343-8555, Japan

Ryotaro Kime Department of Sports Medicine for Health Promotion, Faculty of Medicine, Tokyo Medical University, Tokyo, 160-8402, Japan

Shintaro Kinugawa Department of Cardiovascular Medicine, Hokkaido University of Education, Sapporo, Japan

Naoya Kiryu Department of Electronics and Electrical Engineering, Keio University, Yokohama, Japan

Takeshi Kitagawa Division of Optical Brain Engineering, Department of Neurological Surgery, Nihon University School of Medicine, Tokyo, Japan

Yuko Kitagawa Department of Surgery, School of Medicine, Keio University, Tokyo, 160-8582, Japan

Hirosuke Kobayashi Department of Medical Engineering and Technology, School of Allied Health Sciences, Kitasato University, Kanagawa, 228-8555, Japan

Koichi Kobayashi Department of Surgery, School of Medicine, Keio University, Tokyo, Japan

Minoru Kobayashi Department of Health and Physical Education, University of the Ryukyus Graduate School of Education, Okinawa, 903-0213, Japan

Shunsaku Koga Applied Physiology Laboratory, Kobe Design University, Kobe, 651-2103, Japan

Peck H. Koh Biomedical Optics Research Laboratory, Department of Medical Physics and Bioengineering, University College London, Gower Street, London, WC1E 6BT, UK

Matthias Kohl-Bareis University of Applied Sciences Koblenz, RheinAhrCampus, Remagen, Germany

Jun Kojima Division of Neurosurgery, Department of Neurological Surgery, Nihon University School of Medicine, Tokyo, 173-8610, Japan

Kenichi Kokubo Department of Medical Engineering and Technology, School of Allied Health Sciences, Kitasato University, Kanagawa, 228-8555, Japan

Kazunari Kondo Department of Biochemistry and Integrative Medical Biology, Keio University School of Medicine, Tokyo, 160-8582, Japan

Narihiko Kondo Laboratory for Applied Human Physiology, Graduate School of Human Development and Environment, Kobe University, Kobe, 657-8501, Japan

Yuko Kondo Division of Neurological Surgery, Department of Neurological Surgery, Nihon University School of Medicine, Tokyo, Japan

Kenya Koyama Department of Respiratory Medicine, Dokkyo Medical University Koshigaya Hospital, Koshigaya, Saitama, 343-8555, Japan

Tomiyasu Koyama Hokkaido University, Sapporo, Japan

Christopher Kriedt Baromedical Research Institute, New Orleans, LA, USA

Fred Kriedt Baromedical Research Institute, New Orleans, LA, USA

Masaru Kubota Department of Medicine, Kitasato University, Kanagawa, 228-8555, Japan

Nobuki Kudo Graduate School of Information Science and Technology, Hokkaido University, Sapporo, 060-0814, Japan

Takanori Kumagai Division of Nephrology and Endocrinology, University of Tokyo School of Medicine, Tokyo, Japan

Shimpei Kuniyoshi Department of Health and Physical Education, University of the Ryukyus Graduate School of Education, Okinawa, 903-0213, Japan

Ichiro Kuwahira Department of Medicine, Tokai University School of Medicine, Isehara, Kanagawa, 259-1193, Japan; Department of Medicine, Tokai University Tokyo Hospital, Tokyo, 151-0053, Japan

Joseph C. LaManna Department of Anatomy, Case Western Reserve University, 10900 Euclid Avenue, Cleveland, OH 44106, USA

Jean P. Lariviere EPR Center for Viable Systems, Department of Radiology, Dartmouth Medical School, 703 Vail, Hanover, NH 03755, USA

P. Lemmers Department of Neonatology, Wilhelmina Children's Hospital, Utrecht, Netherlands

Piotr N. Lesniewski EPR Center for Viable Systems, Department of Radiology, Dartmouth Medical School, 703 Vail, Hanover, NH 03755, USA

Terence S. Leung Biomedical Optics Research Laboratory, Department of Medical Physics and Bioengineering, University College London, London, UK

Hongbin Li EPR Center for Viable Systems, Department of Radiology, Dartmouth Medical School, 703 Vail, Hanover, NH 03755, USA

Adam Liebert Institute of Biocybernetics and Biomedical Engineering, 02-109 Warsaw, Poland

Sarah Lloyd-Fox Centre for Brain and Cognitive Development, Henry Wellcome Building, Birkbeck, University of London, Malet Street, London, WC1E 7HX, UK

Rainer Macdonald Physikalisch-Technische Bundesanstalt, 10587 Berlin, Germany

Alfred Mallet Department of Medical Physics and Bioengineering, University College London, Gower St., London, WC1E 6BT, UK

Kazuto Masamoto Molecular Imaging Center, National Institute of Radiological Sciences, Chiba, 263-8555, Japan

Kazumi Masuda Faculty of Human Sciences, Kanazawa University, Kanazawa, 920-1192, Japan

Noriyuki Masuda Department of Medicine, Kitasato University, Kanagawa, 228-8555, Japan

Arnulf Mayer Institute of Physiology and Pathophysiology, University Medical Center, Mainz, Germany

Kevin K. McCully Department of Kinesiology, University of Georgia, 330 River Road, Athens, GA 30602, USA

Simon C. Mears Department of Orthopaedic Surgery, Johns Hopkins University, 4940 Eastern Ave., Baltimore, MD 21224, USA

Keith Van Meter Baromedical Research Institute, New Orleans, LA, USA

Michiaki Mishima Department of Respiratory Medicine, Kyoto University, Kyoto, 606-8507, Japan

Hisashi Mitsufuji Department of Medicine, Kitasato University, Kanagawa, 228-8555, Japan

Hajime Miura Laboratory for Applied Physiology, Faculty of Integrated Arts and Sciences, University of Tokushima, Tokushima, Japan

Mitsuharu Miwa Hamamatsu Photonics, Central Research Laboratory, Hamamatsu, Japan

Ryo Miyahara Departments of Thoracic Surgery, Institute for Frontier Medical Sciences, Kyoto University, Kyoto, 606-8507, Japan

Yoshifumi Miyazaki Center for Environment, Health and Field Sciences, Chiba University, Kashiwa, 277-0882, Japan

Masaki Mizuno Department of Cardiovascular Dynamics, National Cardiovascular Center Research Institute, 5-7-1 Fujishirodai, Suita, 565-8565, Japan

Tetsuya Mizuno College of Liberal Arts and Science, Tokyo Medical and Dental University, Ichikawa, Japan

Michael Moeller Hochschule für Technik und Wirtschaft des Saarlandes, 66117 Saarbruecken, Germany

Takayuki Morikawa Department of Biochemistry and Integrative Medical Biology, Keio University School of Medicine, Tokyo, 160-8582, Japan

Masaya Morimoto ASKA Pharmaceutical Co., Ltd., Tokyo, 108-8532, Japan

Noriteru Morita Department of Sports Education, Hokkaido University of Education, Sapporo, Japan

Isao Muraoka Faculty of Sport Sciences, Waseda University, Tokorozawa, 359-1192, Japan

Yoshiho Muraoka Faculty of Humanities and Social Sciences, Meisei University, Tokyo, 191-8506, Japan

Norio Murase Department of Sports Medicine for Health Promotion, Faculty of Medicine, Tokyo Medical University, Tokyo, 160-8402, Japan

Yoshihiro Murata Division of Neurosurgery, Department of Neurological Surgery, Nihon University School of Medicine, Tokyo, Japan

Shigeo Muro Departments of Respiratory Medicine, Institute for Frontier Medical Sciences, Kyoto University, Kyoto, 606-8507, Japan

Timothy I. Musch Departments of Kinesiology, Anatomy and Physiology, Kansas State University, Manhattan, Kansas 66506, USA

Yoshiko Nagahata Department of Biochemistry and Integrative Medical Biology, School of Medicine, Keio University, Tokyo, 160-8582, Japan

Asuka Nagai Department of Medicine, Tokai University School of Medicine, Isehara, Kanagawa, 259-1193, Japan; Department of Medicine, Tokai University Tokyo Hospital, Tokyo, 151-0053, Japan

Koshu Nagao Department of Respiratory Medicine, Dokkyo Medical University Koshigaya Hospital, Koshigaya-shi, Saitama, 343-8555, Japan

Takafumi Nagaoka Division of Neurosurgery, Department of Neurological Surgery, Nihon University School of Medicine, Tokyo, Japan

Hideko Nagasawa Laboratory of Pharmaceutical Chemistry, Gifu Pharmaceutical University, Gifu, 502-8585, Japan

Yoshinori Nakagawa Morita Pharmaceutical Ind. Ltd, Fukuyama, Hiroshima, 721-0923, Japan

Kazunori Nakajima Department of Sports Dentistry, Tokyo Dental College, Nihon University School of Medicine, Tokyo, Japan

Masato Nakamura Central Institutes for Experimental Animals, Kanagawa, 216-0001, Japan; Department of Pathology and Regenerative Medicine, Tokai University School of Medicine, Kanagawa, 259-1193, Japan

Shin Nakamura Department of Neurosurgery, Nihon University School of Medicine, Tokyo, Japan

Sin Nakamura Division of Neurological Surgery, Department of Neurological Surgery, Nihon University School of Medicine, Tokyo, Japan

Yasutaka Nakano Division of Respiratory Medicine, Department of Medicine, Shiga University of Medical Science, Otsu, 520-2192, Japan

Hitomi Nakashima Department of Life System, Institute of Technology and Science, Graduate School, The University of Tokushima, Tokushima, 770-8506, Japan

Kouichiro Nakashima Department of Life System, Institute of Technology and Science, Graduate School, The University of Tokushima, Tokushima, 770-8506, Japan

Eiji Nakata Department of Life System, Institute of Technology and Science, Graduate School, The University of Tokushima, Tokushima, 770-8506, Japan

Masaomi Nangaku Division of Nephrology and Endocrinology, University of Tokyo School of Medicine, Tokyo, Japan

Michael H. Nantz Department of Chemistry, University of Louisville, Louisville, KY 40292, USA

G. Naulaers Department of Neonatology, University Hospital Gasthuisberg, Katholieke Universiteit Leuven, Belgium

Gunnar Naulaers Neonatal Intensive Care Unit, University Hospitals Gasthuisberg, Katholieke Universiteit Leuven, Leuven, Belgium

Peter Nicholls Department of Biological Sciences, University of Essex, Colchester, CO4 3SQ, UK

Tadashi Niioka Graduate School of Environmental Earth Science, Hokkaido University, Sapporo, 060-0810, Japan

Kyuichi Niizeki Department of Bio-System Engineering, Graduate School of Science and Engineering, Yamagata University, Yonezawa, 992-0038, Japan

Yutaka Nishigaki Department of Genomics for Longevity and Health, Tokyo Metropolitan Institute of Gerontology, Tokyo, 173-0015, Japan

Chiyoko Nishime Department of Biochemistry and Integrative Medical Biology, School of Medicine, Keio University, Tokyo, 160-8582, Japan; Central Institutes for Experimental Animals, Kanagawa, 216-0001, Japan

Masatsugu Niwayama Department of Electrical and Electronic Engineering, Faculty of Engineering, Shizuoka University, Shizuoka, 432-8561, Japan

Takayuki Obata Molecular Imaging Center, National Institute of Radiological Sciences, Chiba, 263-8555, Japan

Hellmuth Obrig Department of Neurology, Charité - Universitaetsmedizin Berlin, 10098 Berlin, Germany

Motoki Oda Central Laboratory, Department of Neurological Surgery, Nihon University School of Medicine, Tokyo, Japan

Motoki Oda Central Laboratory, Hamamatsu Photonics K.K., Shizuoka, Japan

Etsuko Ohmae Central Laboratory, Hamamatsu Photonics K.K., Shizuoka, Japan

Fumiko Ohmori Research Institute of Physical Fitness, Japan Women's College of Physical Education, Tokyo, 57-8565, Japan

Mitsuyo Ohmura Department of Biochemistry and Integrative Medical Biology, School of Medicine, Keio University, Tokyo, 160-8582, Japan

Soichiro Ohnuki Graduate School of Environmental Earth Science, Hokkaido University, Sapporo, 060-0810, Japan

Eiji Okada Department of Electronics and Electrical Engineering, Keio University, Yokohama, Japan

Masako Okamoto National Food Research Institute, Tsukuba, Japan

Toshihiro Okamoto Department of Thoracic Surgery, Kyoto University, Kyoto, 606-8507, Japan

Koichi Okita Department of Wellness Planning, Hokkaido University of Education, Sapporo, Japan

Yoshitaka Oku Department of Physiology, Hyogo college of Medicine, Nishinomiya, 663-8501, Japan

Kenichi Okubo Departments of Thoracic Surgery, Institute for Frontier Medical Sciences, Kyoto University, Kyoto, 606-8507, Japan

Nao Okumura Laboratory for Applied Physiology, Faculty of Integrated Arts and Sciences, University of Tokushima, Tokushima, Japan

Shizuyo Okuyama Institute of Physical Education, Keio University, Kanagawa, 223-8521, Japan

Masashi Omokawa Department of Wellness Planning, Hokkaido University of Education, Sapporo, Japan

Anna Ooue Laboratory for Applied Human Physiology, Graduate School of Human Development and Environment, Kobe University, Kobe, 657-8501, Japan

Takuya Osada Department of Sports Medicine for Health Promotion, Faculty of Medicine, Tokyo Medical University, Tokyo, 160-8402, Japan

Takuya Osawa Department of Sports Medicine for Health Promotion, Faculty of Medicine, Tokyo Medical University, Tokyo, 160-8402, Japan

Maria D. Papademetriou Biomedical Optics Research Laboratory, Department of Medical Physics and Bioengineering, University College London, Gower Street, London, WC1E 6BT, UK

Chase Patterson Baromedical Research Institute, New Orleans, LA, US

Stacey-Marie Penfold Centre for Sports and Exercise Science, Department of Biological Sciences, University of Essex, Wivenhoe Park, Colchester, Essex, CO4 3SQ, UK

Derrick Phillips Biomedical Optics Research Laboratory, Department of Medical Physics and Bioengineering, University College London, Gower Street, London, WC1E 6BT, UK

Roland N. Pittman Department of Physiology and Biophysics, Virginia Commonwealth University, Richmond, Virginia 23298, USA

David C. Poole Departments of Anatomy, Physiology and Kinesiology, Kansas State University, Manhattan, Kansas 66506, USA; School of Sports and Health Sciences, University of Exeter, Exeter, Devon, UK

Michelle A. Puchowicz Department of Anatomy, Case Western Reserve University, 10900 Euclid Avenue, Cleveland, OH 44106, USA

T. Sadamoto Research Institute of Physical Fitness, Japan Women's College of Physical Education, Tokyo, 157–8565, Japan

Hisashi Sahara Departments of Thoracic Surgery, Institute for Frontier Medical Sciences, Kyoto University, Kyoto, 606-8507, Japan

Tadashi Saitoh Department of Bio-System Engineering, Graduate School of Science and Engineering, Yamagata University, Yonezawa, 992-0038, Japan

Hiroaki Sakai Departments of Thoracic Surgery, Institute for Frontier Medical Sciences, Kyoto University, Kyoto, 606-8507, Japan

Hiromi Sakai Research Institute for Science and Engineering, Waseda University, Tokyo, Japan

Kaoru Sakatani Division of Optical Brain Engineering, Department of Neurological Surgery; Division of Applied System Neuroscience, Department of Advanced Medical Science, Nihon University School of Medicine, Tokyo, 173-8610, Japan

Takayuki Sako Department of Food and Nutrition, Japan Women's University, Tokyo, 112-8681, Japan

Keiichiro Sano Department of Life System, Institute of Technology and Science, Graduate School, The University of Tokushima, Tokushima, 770-8506, Japan

Mitsuyoshi Sasaki Department of Neurophysiology, Tokyo Medical University, Tokyo, Japan

Gen Sasao Department of Medicine, Tokai University Tokyo Hospital, Tokyo, 151-0053, Japan

K. Sato Research Institute of Physical Fitness, Japan Women's College of Physical Education, Tokyo, 157-8565, Japan

Kiyoshi Sato Departments of Thoracic Surgery, Institute for Frontier Medical Sciences, Kyoto University, Kyoto, 606-8507, Japan

Kohei Sato Research Institute of Physical Fitness, Japan Women's College of Physical Education, Tokyo, 157-8565, Japan

Toshihiko Sato Department of Bioartificial organs, Institute for Frontier Medical Sciences, Kyoto University, Kyoto, 606-8507, Japan

Naoki Satoda Department of Thoracic Surgery, Kyoto University, Kyoto, 606-8507, Japan

Francesca M. Scandurra Medical University of Innsbruck, Department of General and Transplant Surgery, D. Swarovski Research Laboratory, Innsbruck, Austria; OROBOROS INSTRUMENTS, Innsbruck, Austria

Shinichi Sekiguchi Division of Optical Brain Engineering, Department of Neurosurgery, Nihon University School of Medicine, Tokyo, Japan

John W. Severinghaus UCSF, San Francisco, CA, USA

Mami Shibusawa Department of Sports Dentistry, Tokyo Dental College, Nihon University School of Medicine, Tokyo, Japan

Takahiro Shikayama Hamamatsu Photonics, Central Research Laboratory, Hamamatsu, Japan

Masaki Shimane Department of Respiratory Medicine, Kitasato University Kitasato Institute Medical Center Hospital, Saitama, 364-8501, Japan

Motohide Shimazu Departments of Surgery, School of Medicine, Keio University, Tokyo, Japan

Kenji Shimizu ASKA Pharmaceutical Co., Ltd., Tokyo, 108-8532, Japan

Kousuke Shimomura Department of Sports Medicine for Health Promotion, Faculty of Medicine, Tokyo Medical University, Tokyo, 160-8402, Japan

Toshihiro Shinbo Department of Medical Engineering and Technology, School of Allied Health Sciences, Kitasato University, Kanagawa, 228-8555, Japan

Yoshitsugu Shiro Biometal Science Laboratory, RIKEN SPring-8 Center, Harima Institute, Hyogo, 679-5148, Japan

Kiyoshi Shiroishi Department of Judotherapy and Sports Medicine, Faculty of Health Science, Ryotokuji University, Chiba, 279-8567, Japan; Department of Sports Medicine for Health Promotion, Tokyo Medical University, Tokyo, 160-8402, Japan

Tsuyoshi Shoji Department of Thoracic Surgery, Kyoto University, Kyoto, 606-8507, Japan

Daya B. Singh Department of Medical Physics, University Hospital of North Durham, Durham, DH1 5TW, UK

Martin Smith Department of Neuroanaesthesia and Neurocritical care, The National Hospital for Neurology and Neurosurgery, Queen Square, London, WC1N 3BG, UK

Saki Soeda Department of Medical Engineering and Technology, School of Allied Health Sciences, Kitasato University, Kanagawa, 228-8555, Japan

Makoto Sonobe Departments of Thoracic Surgery, Institute for Frontier Medical Sciences, Kyoto University, Kyoto, 606-8507, Japan

Takashi Sonobe Departments of Applied Physics and Chemistry, University of Electro-Communications, Chohu, Tokyo, Japan

Keitaro Sou Research Institute for Science and Engineering, Waseda University, Tokyo, Japan

Jens Steinbrink Department of Neurology, Charité - Universitaetsmedizin Berlin, 10098 Berlin, Germany

Michael B. Streiff Division of Hematology, Department of Medicine, Johns Hopkins, 720 Rutland Avenue/ Ross 1025, Baltimore, MD 21205-2196, USA

Charlotte Stubbs Biomedical Optics Research Laboratory, Department of Medical Physics and Bioengineering, University College London, Gower Street, London, WC1E 6BT, UK

Artur Sucheta EPR Center for Viable Systems, Department of Radiology, Dartmouth Medical School, 703 Vail, Hanover, NH 03755, USA

Osamu Suda Department of Sports Dentistry, Tokyo Dental College; Nihon University School of Medicine, Tokyo, Japan

Makoto Suematsu Department of Biochemistry and Integrative Medical Biology, School of Medicine, Keio University, Tokyo, 160-8582, Japan

Hiroshi Suemizu Central Institutes for Experimental Animals, Kanagawa, 216-0001, Japan

Tadashi Suga Department of Cardiovascular Medicine, Hokkaido University of Education, Sapporo, Japan

Kazuhiro Suga-numa Departments of Surgery, School of Medicine, Keio University, Tokyo, Japan

Hiroshi Sugimoto Biometal Science Laboratory, RIKEN SPring-8 Center, Harima Institute, Hyogo, 679-5148, Japan

Tadao Sugioka Department of Biochemistry and Integrative Medical Biology, Keio University School of Medicine, Tokyo, 160-8582, Japan

Xiaoyan Sun Department of Anatomy, Case Western Reserve University, 10900 Euclid Avenue, Cleveland, OH 44106, USA

Toshihiko Suzuki Central Laboratory, Hamamatsu Photonics K.K., Shizuoka, Japan

Harold M. Swartz EPR Center for Viable Systems, Department of Radiology, Dartmouth Medical School, 703 Vail, Hanover, NH 03755, USA

Ilias Tachtsidis Biomedical Optics Research Laboratory, Department of Medical Physics and Bioengineering, University College London, Gower Street, London, WC1E 6BT, UK

Akira Taka Sapporo-Aoba School of Holistic Medicine, Sapporo, Japan

Shingo Takada Department of Wellness Planning, Hokkaido University of Education, Sapporo, Japan

Ayuko Takahashi Departments of Organ Preservation Technology, Graduate School of Medicine, Institute for Frontier Medical Sciences, Kyoto University, Kyoto, 606-8507, Japan

Hisashi Takakura The Graduate School of Natural Science and Technology, Kanazawa University, Kanazawa, 920-1192, Japan

Naoharu Takano Department of Biochemistry & Integrative Medical Biology, School of Medicine, Keio University, Tokyo, Japan

Tomotaka Takeda Department of Sports Dentistry, Tokyo Dental College; Nihon University School of Medicine, Tokyo, Japan

Masayuki Takizawa ASKA Pharmaceutical Co., Ltd., Tokyo, 108-8532, Japan

Yasutaka Takubo Hamamatsu Rosai Hospital, Hamamatsu, 430-8525, Japan

Minoru Tanabe Departments of Surgery, School of Medicine, Keio University, Tokyo, Japan

Masashi Tanaka Department of Genomics for Longevity and Health, Tokyo Metropolitan Institute of Gerontology, Tokyo, 173-0015, Japan

Masahiro Tanida Shiseido Innovative Science Research & Development Center, Shiseido, Yokohama, Tokyo, Japan

Y. Taniguchi Research Institute of Physical Fitness, Japan Women's College of Physical Education, Tokyo, 157-8565, Japan

Emiri Tejima Division of Neurological Surgery, Department of Neurological Surgery, Nihon University School of Medicine, Tokyo, Japan

Ken Tokizawa Faculty of Human Sciences, Waseda University, Tokorozawa, 359-1192, Japan

Yutaka Tomita Department of Biosciences and Informatics, Keio University, Kanagawa, 223-8522, Japan

Constantinos P. Tsipis Department of Anatomy, Case Western Reserve University, 10900 Euclid Avenue, Cleveland, OH 44106, USA

Eishun Tsuchida Research Institute for Science and Engineering, Waseda University, Tokyo, Japan

Kosuke Tsukada Department of Biochemistry and Integrative Medical Biology, School of Medicine, Keio University, Tokyo, 160-8582, Japan

N. Tsunoda Research Institute of Physical Fitness, Japan Women's College of Physical Education, Tokyo, 157-8565, Japan

Hiroyuki Tsutsui Department of Cardiovascular Medicine, Hokkaido University of Education, Sapporo, Japan

Daisuke Tuzuki National Food Research Institute, Tsukuba, Japan

Chihoko Ueda Research Institute of Physical Fitness, Japan Women's College of Physical Education, Tokyo, 157-8565, Japan

Yoshihiro Uto Department of Life System, Institute of Technology and Science, Graduate School, The University of Tokushima, Tokushima, 770-8506, Japan

F. van Bel Department of Neonatology, Wilhelmina Children's Hospital, Utrecht, Netherlands

S. Van Huffel Department of Electrical Engineering (ESAT), SCD Division, Katholieke Universiteit Leuven, Belgium

J. Vanderhaegen Department of Neonatology, University Hospital Gasthuisberg, Katholieke Universiteit Leuven, Belgium

Joke Vanderhaegen UZ Gasthuisberg, Herestraat 49, B-3000 Leuven, Belgium

Sophie Vanhaesebrouck Neonatal Intensive Care Unit, University Hospitals Gasthuisberg, Katholieke Universiteit Leuven, Leuven, Belgium

Christine Vanhole Neonatal Intensive Care Unit, University Hospitals Gasthuisberg, Katholieke Universiteit Leuven, Leuven, Belgium

Peter Vaupel Institute of Physiology and Pathophysiology, University Medical Center, Mainz, Germany

Angelika von Wallbrunn Institute of Physiology and Pathophysiology, University Medical Center, Mainz, Germany

Heidrun Wabnitz Physikalisch-Technische Bundesanstalt, 10587 Berlin, Germany

Hiromi Wada Department of Thoracic Surgery, Kyoto University, Kyoto, 606-8507, Japan

Masatoshi Wakui Department of Biochemistry and Integrative Medical Biology, School of Medicine, Keio University, Tokyo, 160-8582, Japan; Central Institutes for Experimental Animals, Kanagawa, 216-0001, Japan

Jianting Wang Department of Chemical Engineering, University of Louisville, Louisville, KY 40292, USA

Benjamin B. Williams EPR Center for Viable Systems, Department of Radiology, Dartmouth Medical School, 703 Vail, Hanover, NH 03755, USA

Anna Wittekind Department of Biological Sciences, University of Essex, Colchester Essex, UK

M. Wolf Clinic of Neonatology, University Hospital Zurich, Switzerland

John G. Wood Department of Molecular and Integrative Physiology, University of Kansas Medical Center, Kansas City, KS 66160, USA

Alexander Wree Institute of Physiology and Pathophysiology, University Medical Center, Mainz, Germany

Kui Xu Department of Anatomy, Case Western Reserve University, 10900 Euclid Avenue, Cleveland, OH 44106, USA

Ayako Yachie-Kinoshita Departments of Biochemistry and Integrative Medical Biology, Keio University, Tokyo, Japan

Yui Yamaguchi National Food Research Institute, Tsukuba, Japan

Daisuke Yamamoto Department of Electronics and Electrical Engineering, Keio University, Yokohama, Japan

Katsuyuki Yamamoto Graduate School of Information Science and Technology, Hokkaido University, Sapporo, 060-0814, Japan

Masayoshi Yamamoto Research Center for Training Science and Applied Physiology, National Institute of Fitness and Sports in Kanoya, Kagoshima, 891-2393, Japan

Takamitsu Yamamoto Division of Neurosurgery, Department of Neurological Surgery; Division of Applied System Neuroscience, Department of Advanced Medical Science, Nihon University School of Medicine, Tokyo, 173-8610, Japan

Takehiro Yamamoto Department of Biochemistry & Integrative Medical Biology, School of Medicine, Keio University, Tokyo, Japan

Takeshi Yamanaka Central Laboratory, Department of Neurological Surgery, Nihon University School of Medicine, Tokyo, Japan

Daisuke Yamashita Central Laboratory, Department of Neurological Surgery, Nihon University School of Medicine, Tokyo, Japan

Yutaka Yamashita Central Laboratory, Department of Neurological Surgery, Nihon University School of Medicine, Tokyo, Japan

Yutaka Yamashita Central Laboratory, Hamamatsu Photonics K.K., Shizuoka, Japan

Noriaki Yokose Division of Neurological Surgery, Department of Neurological Surgery, Nihon University School of Medicine, Tokyo, Japan

Takashi Yokota Department of Cardiovascular Medicine, Hokkaido University of Education, Sapporo, Japan

Atsuo Yoshino Division of Neurological Surgery, Department of Neurological Surgery, Nihon University School of Medicine, Tokyo, Japan

Bassem Zaki Dartmouth Hitchcock Medical Center, Norris Cotton Cancer Center, Lebanon, NH, USA

Jintian Zhang Department of Thoracic Surgery, Kyoto University, Kyoto, 606-8507, Japan

Part I
Physiology and Pathophysiology of O_2 Transport

Unfinished Physiology

John W. Severinghaus

Abstract The following was an invited pre-dinner commentary to the standing group waiting for supper, light heartedly suggesting several still unsettled physiologic problems in need of study.

1 Introduction

Professor Ichiro Kuwahira wrote in June asking me to briefly inspire you young investigators before dinner. I can only inspire air and have no talent for giving useful advice. The Danish mathematician – philosopher – poet Piet Hein wrote short poems he called "GROOKS":

> "Shun advice at any price. That's what I call good advice."

If I had 20–30 min I could describe two physiologic unsettled questions that need some young investigators to tackle. But we are hungry and standing, so I'll just pose the questions. Details after dinner when we can all sit down somewhere.

1. How does the law of mass action work for the electron-oxygen reaction at cytochrome aa_3? (Fig. 1)
2. What makes brain capillary flow stop and go at about 6–10 times per min, and what is the neuro-chemistry involved? (Fig. 2)

And remember another GROOK.

> "When technology is master we shall reach disaster faster."

Good luck and bon appetite!

J.W. Severinghaus (✉)
UCSF, San Francisco, CA, USA
e-mail: jwseps@comcast.net

E. Takahashi, D.F. Bruley (eds.), *Oxygen Transport to Tissue XXXI*,
Advances in Experimental Medicine and Biology 662,
DOI 10.1007/978-1-4419-1241-1_1, © Springer Science+Business Media, LLC 2010

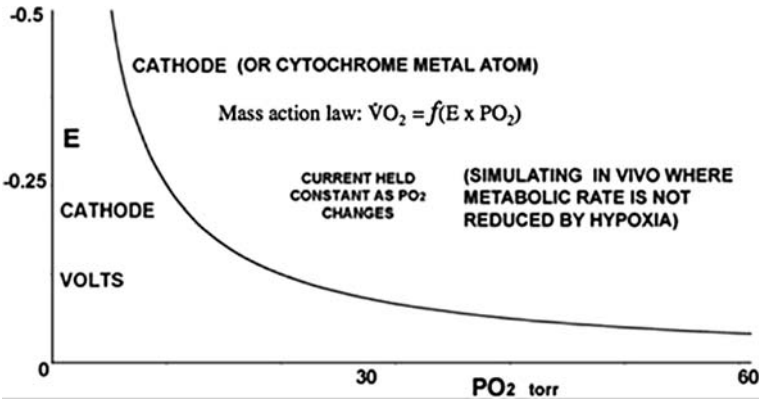

Fig. 1 Polarographic simulation of brain cytochrome aa_3 copper electron-O_2 physical chemistry in progressive hypoxia. To maintain a constant polarographic electrode current (VO_2) as PO_2 falls, cathode negative potential must be increased hyperbolically. Brain metabolic rate does not fall in moderate hypoxia (>30 torr PaO_2) until mitochondrial PO_2 falls from its normal level of about 15 torr to below 1 torr (Chance). A widespread misinterpretation of Chance's finding has led to assumptions that mitochondrial PO_2 is normally less than 1 torr. The mass law, when applied at constant metabolic rate, insures a hyperbolic relation of copper potential and local PO_2. In vivo, during redox reduction by arterial hypoxia, cytochrome aa_3 copper (negative) potential is increased by increased substrate concentrations in the citric acid cycle (at constant flux). A common source of confusion is the biochemical view of redox reduction as positive rather than negative

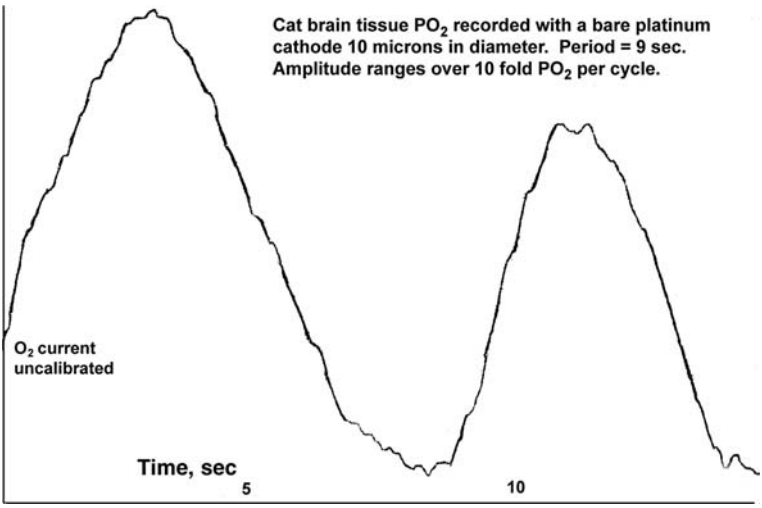

Fig. 2 PO_2 cycles in cat brain with a 10 μm implanted oxygen electrode [1]. Adjacent tissue within about 1 mm is usually synchronous, but not so at greater distances, This is due to digital opening and closing of precapillary sphincters at 6–12/min, is exaggerated at low PCO_2 and abolished in hypoxia. What is the mechanism?

References

1. Ozanne GM, Vilnis V, Severinghaus JW (1975) Implications of O_2 wave shapes and synchrony for regulation of cerebral microcirculation. In: Blood Flow and Metabolism of the Brain. Edited by Harper M, et al., Churchill Livingstone, Edinburgh, pp. 9.3–9.7 (Proc 7th Int Congr CBF).

Cell Respiration Under Hypoxia: Facts and Artefacts in Mitochondrial Oxygen Kinetics

Francesca M. Scandurra and Erich Gnaiger

Abstract When oxygen supply to tissues is limiting, mitochondrial respiration and ATP production are compromised. To assess the bioenergetic consequences under normoxia and hypoxia, quantitative evaluation of mitochondrial oxygen kinetics is required. Using high-resolution respirometry, the "apparent K_m" for oxygen or p_{50} of respiration in 32D cells was determined at 0.05 ± 0.01 kPa (0.4 mmHg, 0.5 μM, 0.25% air saturation). Close agreement with p_{50} of isolated mitochondria indicates that intracellular gradients are small in small cells at routine activity. At intracellular $p_{O_2} < 2$ kPa (15 mmHg, 10% air saturation) in various tissues under normoxia, respiration is limited by >2% with a p_{50} of 0.05 kPa. Over-estimation of p_{50} at 0.4 kPa (3 mmHg) would imply significant (>17%) oxygen limitation of respiration under intracellular normoxia. Based on a critical review, we conclude that p_{50} ranges from 0.01 to 0.10 kPa in mitochondria and small cells in the absence of inhibitors of cytochrome *c* oxidase, whereas experimental artefacts explain the controversial >200-fold range of p_{50} in the literature on mitochondrial oxygen kinetics.

1 Introduction

Intracellular oxygen levels in the microenvironment of mitochondria are the result of a dynamic balance between oxygen transport to tissues through the respiratory cascade [1] and oxygen utilization by the mitochondrial respiratory electron transport system [2]. At any physiological steady state, a metabolic perturbation of oxygen demand leads to a shift of intracellular oxygen concentration (decrease after stimulation or increase after arrest), unless effective control of oxygen supply exerts a compensatory effect to maintain intracellular oxygen levels within a regulated range. Conversely, an environmental

E. Gnaiger (✉)
D. Swarovski Research Laboratory, Department of General and Transplant Surgery, Medical University of Innsbruck, Innsbruck, Austria; OROBOROS INSTRUMENTS, Innsbruck, Austria
e-mail: erich.gnaiger@i-med.ac.at

E. Takahashi, D.F. Bruley (eds.), *Oxygen Transport to Tissue XXXI*, Advances in Experimental Medicine and Biology 662,
DOI 10.1007/978-1-4419-1241-1_2, © Springer Science+Business Media, LLC 2010

perturbation from normoxic to hypoxic or hyperoxic levels modifies the variables of oxygen transport and the metabolic capacity for oxygen consumption is compromised if mitochondrial oxygen pressures are changed below the level of kinetic saturation. Three elements, therefore, are responsible for controlling cellular oxygenation: the environmental oxygen level, oxygen transport and respiratory metabolism.

This review is focused on cellular and mitochondrial respiration, under the control of extracellular or mitochondrial oxygen pressure (Section 2). In Section 3, we summarize our experience gained by application of high-resolution respirometry to the study of isolated mitochondria and intact cells under conditions of varying oxygen concentrations. Extending the comprehensive review on mitochondrial oxygen kinetics published in 1995 [3], we discuss in Section 4 possible explanations for discrepancies on the p_{50} of mitochondrial respiration, i.e. the partial pressure at which respiration rate is 50% of flux at kinetic oxygen saturation. There is a >200-fold range of mitochondrial p_{50} reported in the literature. Whereas instrumental and methodological artefacts are responsible for the major part of this large range, a 10-fold variation of p_{50} is due to turnover of cytochrome *c* oxidase (between the minimum of respiration compensating for leak and fully ADP-stimulated respiration) and variation between different mitochondrial sources and various small cells. In Section 5, we relate the p_{50} of mitochondrial respiration to intracellular oxygen regimes under normoxia and hypoxia, discussing the theoretical consequences of the actual p_{50} of mitochondrial respiration under physiological conditions, for energy homeostasis and mitochondrial excess capacities, oxygen sensing and signalling responses to hypoxia. In particular, comparison of the p_{50} in isolated mitochondria and intact cells supports the direct measurement of high intracellular oxygen gradients in cardiomyocytes [4, 5], in contrast to the comparatively negligible intracellular oxygen gradients in small cells [6].

2 Mitochondrial and Cellular Oxygen Kinetics

2.1 Isolated Mitochondria

Mitochondrial respiration is a hyperbolic function of oxygen partial pressure, p_{O_2},

$$j_{O_2} = \frac{p_{O_2}}{p_{50} + p_{O_2}} \tag{1}$$

where j_{O_2} is the rate expressed relative to the maximum pathway flux, J_{max}, observed at kinetic oxygen saturation in a defined metabolic state. Characteristic metabolic states of isolated mitochondria, incubated with selected substrate combinations (e.g. pyruvate, malate, glutamate, succinate), are (i) *OXPHOS* (State 3 [7]; maximally ADP-stimulated oxidative phosphorylation; but see [8]), and (ii) *LEAK* (State 4 [7]; minimum oxygen flux required to compensate for proton leak,

slip and cation cycling, without providing ADP or by inhibiting phosphorylation; for discussion see [9]). J_{max}, therefore, is a complex function of coupling and electron supply through the mitochondrial electron transport system to cytochrome *c* oxidase. Similarly, the maximum reaction velocity of an enzyme, V_{max}, varies as a function of the concentrations of other substrates and enzyme concentration, [E]. The enzyme turnover, $V_{max}/[E]$, or pathway flux, J_{max}, exert an influence on the apparent Michaelis-Menten constant, K_m', or p_{50}. The p_{50} of mitochondrial respiration, therefore, depends on the metabolic state. If catalytic efficiency, V_{max}/K_m', is constant, then K_m' and p_{50} increase in direct proportion to enzyme turnover [10]. In addition to substrate and ADP supply [11], coupling of electron transport to phosphorylation modifies the p_{50} of cellular and mitochondrial respiration [2, 12, 13]. Since the present review is focussed on mitochondrial physiology, we will not consider uncoupled states which provide a measure of the capacity of the electron transport system, *ETS*.

2.2 Intact Cells

In the *ROUTINE* state, cell respiration is controlled by physiological aerobic ATP demand at routine steady-state ADP levels, which result from the dynamic balance of ATP production (aerobic and glycolytic) and cellular ATP utilization. After inhibition of electron transport, e.g. by 0.5 μM myxothiazol, residual oxygen consumption (*ROX*) is observed which is subtracted from total oxygen consumption to obtain mitochondrial *ROUTINE* respiration. As shown by the inhibitory effect of oligomycin, which inhibits ATP synthase and induces a *LEAK* respiratory state, *ROUTINE* respiration is about two to four times higher than *LEAK* respiration, and is thus significantly less than *OXPHOS* capacity, which may be six to ten times the *LEAK* respiration, as expressed by the respiratory control ratio [14, 15].

In addition to the enzymatically catalyzed oxygen consumption, the oxygen dependence of cell respiration is controlled by oxygen gradients related to oxygen transport from the extracellular medium to the mitochondria. The oxygen pressure difference, Δp_{cell}, between the extracellular medium and the average mitochondrion is a function of cell size, cell shape, mitochondrial distribution and oxygen flux. At half-maximum oxygen flux, oxygen gradients are 50% of their maximum at unlimited flux, and maximum $\Delta p_{cell} = 2 \cdot \Delta p_{50}$ can be calculated as the p_{50} difference of respiration in intact cells and isolated mitochondria, at comparable metabolic states [6],

$$\Delta p_{50} = p_{50,cell} - p_{50,mito} \tag{2}$$

For comparison of mitochondria and cells, respiration is expressed as oxygen flux per mitochondrial protein, J_{O_2} [pmol·s^{-1}·mg^{-1}], or relative to a mitochondrial marker such as aa_3 content or citrate synthase activity. Cell respiration is frequently expressed as oxygen flow per number of cells, I_{O_2} [pmol·s^{-1}·10^{-6}], which is an extensive quantity and varies with cell size and

mitochondrial content [16]. High oxygen flow in large and active cells, such as cardiomyocytes, results in proportionally high Δp_{50} [6].

3 Oxygen Kinetics and High-Resolution Respirometry

3.1 Nanomolar Resolution of Oxygen Concentration

Measurement of mitochondrial oxygen kinetics presents an experimental challenge [3, 17, 18], considering the demands set on oxygen monitoring with high sensitivity and high time resolution. High-resolution respirometry (HRR) was developed for routine measurement of low volume-specific oxygen flux and low, sub-micro molar oxygen concentration [3]. The instrumental and methodological basis of HRR (Oxygraph-2 k; OROBOROS INSTRUMENTS, Austria; www.oroboros.at) has been discussed in detail [11]. Since 2001, HRR was improved further in a second generation of instruments (Oxygraph-2 k) with reduced signal noise (Fig. 1; compare Fig. 3) as achieved by higher temperature stability, improved stirring and advanced electronics and mechanical design. The HRR features most important for oxygen kinetics are summarized briefly: (1) The experimental chamber and sealings are made of inert materials which do not store and release dissolved oxygen (no Perspex, no Teflon coated stirrers). (2) Unstirred layers are minimized by effective stirring, and gas-aqueous phase

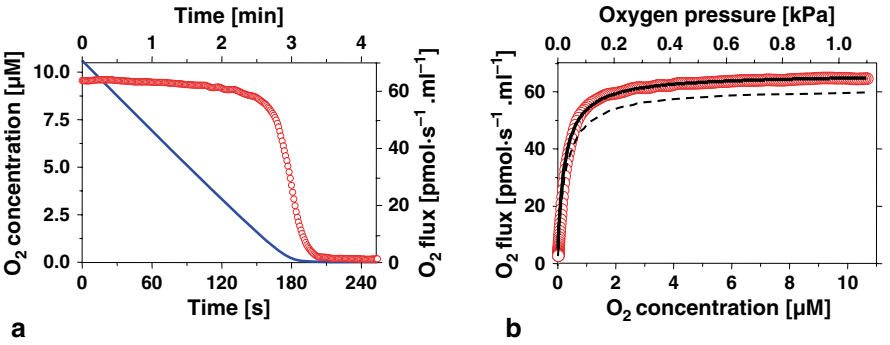

Fig. 1 Oxygen kinetics of respiration of 32D cells in a closed chamber (2 ml mitochondrial respiration medium MiR05; OROBOROS Oxygraph-2 k; $5{\cdot}10^6$ cells·ml^{-1}, 37°C). **a**. Oxygen concentration (*continuous line*) and volume-specific oxygen flux (*circles*) as a function of time during the aerobic-anoxic transition. The oxygen signal was corrected for the time constant ($\tau = 2.8$ s) of the O_2 sensor. Oxygen flux was corrected for instrumental background. **b**. Hyperbolic fit (*continuous line*) in the low-oxygen range of oxygen flux (*circles*) as a function of oxygen concentration or oxygen pressure (oxygen solubility 9.71 µM/kPa). Maximum flux, $J_{V,\max}$, was 66 pmol·s^{-1}·ml^{-1}. Corresponding to the low maximum flow, $I_{\max}$, of 13 pmol·s^{-1}·ml^{-1} in the endogenous *ROUTINE* state, the p_{50} was 0.028 kPa (0.21 mmHg; 0.27 µM). After re-oxygenation and dilution of the cells by a factor of 0.94–4.7·10^6 cells·ml^{-1} (due to injections of aerobic respiration medium; not shown), respiratory flow (per cell) returned to the initial value, and the p_{50} was 0.022 kPa in a second aerobic-anoxic transition (dashed line, showing the lower volume-specific flux at the lower cell density)

boundaries are avoided to exclude uncontrolled oxygen gradients. (3) Polarographic oxygen sensors (POS) with a large cathode, inserted into the precisely thermostated O2k-chamber (±0.001°C) yield a linear signal with low noise over a 500,000-fold dynamic range. Noise decreases with declining oxygen pressure, which eliminates the requirement for smoothing in the low-oxygen range and ensures high time resolution. (4) Accurate oxygen calibrations are obtained at air saturation and zero oxygen concentration, with correction for signal drift in the nanomolar concentration range. (5) High digital resolution (2 nM) and data recording at intervals of one second are a basis for deconvolution of the oxygen signal with the calibrated first-order exponential time constant of the POS, and for calculating oxygen flux, J_{V,O_2} [pmol·s^{-1}·ml^{-1}], as the time derivative of oxygen concentration. (6) Errors of oxygen flux are minimized by on-line correction for instrumental background, calibrated by measurement of residual oxygen back-diffusion into the system and oxygen consumption by the POS over the entire experimental oxygen range. (7) Concentrations of mitochondria or cells are varied in a range compatible with instrumental sensitivity, time resolution and steady-state enzyme kinetics. In this range, measurement of p_{50} must be independent of sample concentration or transition time. (8) Before aerobic-anoxic transitions, oxygen flux must be sufficiently stable to exclude time effects superimposed over oxygen dependence of respiration. In addition, reversibility and stability of respiration are evaluated after re-oxygenation, which is particularly important in prolonged experiments with steady-state oxygen levels. (9) By selecting oxygen pressures <1.1 kPa for hyperbolic analysis [3], oxygen levels >10 times the p_{50} are covered, without extending to non-physiological high oxygen pressures. (10) Non-linear hyperbolic fits of the flux/oxygen pressure relation are tested by evaluation of residuals rather than linearity of double-reciprocal plots [19].

3.2 High-Resolution Oxygen Kinetics: Effects of Cell Density and Cell Activity

Mouse parental promyeloid 32D cells [20] are small cells grown in suspension in RPMI 1640 (PAA Laboratories Pasching, Austria). Figure 1a shows typical traces of oxygen concentration and oxygen flux during an aerobic-anoxic transition. Flux was a hyperbolic function of oxygen concentration with a p_{50} of 0.028 and 0.022 kPa in the first and second transition, at I_{max} of 13 pmol·s^{-1}·10^{-6} (Fig. 1b). Oxygen flow of intact 32D cells varied between cultures, with identical or occasionally very low activities of cells incubated in mitochondrial respiration medium MiR05 (compared to cell culture medium RPMI; Fig. 2a). The "intracellular" mitochondrial respiration medium is not physiological, but is frequently used in respiratory studies with cells, when plasma membrane permeabilization is effected as part of the titration protocol in the Oxygraph-2 k chamber [16]. The lowest values of oxygen flow in MiR05 are representative of an inactive respiratory state, as shown by comparison with oligomycin-inhibited respiration of cells measured in RPMI (Fig. 2a). In Fig. 2b, p_{50} values from the same experiments are plotted against volume-

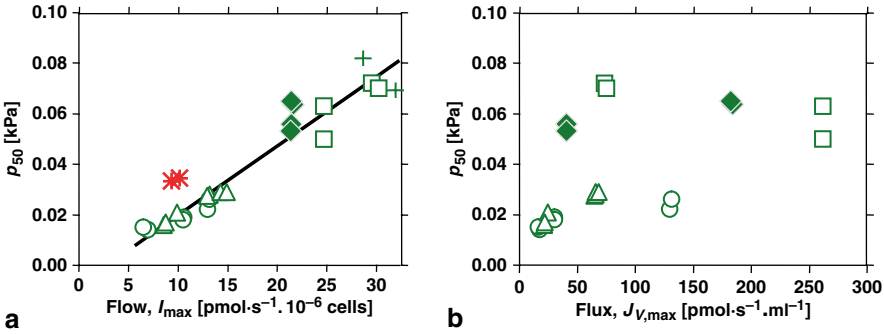

Fig. 2 Oxygen kinetics of respiration of 32D cells incubated in cell culture medium RPMI (*full symbols*) or mitochondrial respiration medium MiR05 (*open symbols*). **a**. Dependence of p_{50} on oxygen flow (per 10^6 cells). * and + indicate averages from two parallel determinations of *ROUTINE* and *LEAK* respiration, respectively, with 32D-vRAF cells. **b**. Independence of p_{50} on oxygen flux (per ml of cell suspension), in paired experiments at two dilutions of cell concentration [x10^6 cells/ml]: 2.5 and 5.0 (*triangles*); 2.9 and 10.0 (*circles*); 2.5 and 10.6 (*squares*); 1.9 and 8.5 (*diamonds*). Each symbol indicates a single aerobic-anoxic transition

specific *ROUTINE* oxygen flux, which was varied from 16 to 260 pmol·s^{-1}·ml^{-1} by incubation of each cell culture at two different cell concentrations in the range of $2 \cdot 10^6$–$11 \cdot 10^6$ cells/ml. Cell density exerts its effect not only on volume-specific flux, $J_{V,max}$, but may also modulate cell-specific oxygen flow, I_{max} (for HUVEC, see [12]). As reported previously [12, 13, 18], variation of mitochondrial or cell density provides an essential test for instrumental time resolution and kinetic consistency of p_{50} values.

Variation of oxygen flow (per cell; Fig. 2a) in paired experiments with the same cell culture (Fig. 2b) was due to different levels of activity in the *ROUTINE* state. The corresponding range in turnover of cytochrome *c* oxidase explains the linear dependence of p_{50} on cell respiration (Fig. 2a). Variation of cell size and mitochondrial content provides an alternative mechanism for variation of respiratory activity per cell [16]. At constant mitochondrial p_{50} (constant turnover of cytochrome *c* oxidase), however, cellular p_{50} would not vary with oxygen flow per cell, except if intracellular gradients and Δp_{50} (Eq. 2) increase with cell size in different cultures.

The linear increase of p_{50} as a function of oxygen flow (per cell; Fig. 2a) indicates varying enzyme turnover at constant mitochondrial content per cell, which was further supported by the constant citrate synthase activity per cell (data not shown). Additional support for our interpretation in terms of variation of mitochondrial activity stems from independent control experiments with 32D-vRAF cells suspended in RPMI and pharmacological intervention with respiratory activity. When *ROUTINE* respiration was inhibited by oligomycin (2 µg/ml), the p_{50} declined proportional to the reduced *LEAK* respiratory flow. These results are comparable to the decrease of p_{50} in isolated mitochondria from the active *OXPHOS* state to the passive *LEAK* state ([2, 13, 21]; Table 1).

Table 1 p_{50} of mitochondrial respiration in different metabolic states of coupled respiration (*LEAK*: resting, not ADP-activated; *OXPHOS*: active, ADP-activated; *ROUTINE*: under physiological control of activation in intact cells). Respiratory flux at kinetic oxygen saturation, J_{max}, is expressed in pmol/(s·unit x); if unit x is cell number, then J_{max} becomes I_{max}. J_{Vmax} is flux per volume of incubation medium. **A**: p_{50} in isolated mitochondria (mt) and small cells. **B**: Results in closed systems with J_{Vmax} above 500 pmol·s^{-1}·ml^{-1} [13], and in closed and open systems with apparent problems of oxygen heterogeneity. **C**: p_{50} based on intracellular p_{O_2} reported by myoglobin in large muscle cells and tissues

Model [1,2]	T (°C)	J_{max} (pmol/(s·x))	Unit [3]X	Density (x/ml)	J_{Vmax} (pmol/(s·ml))	p_{50} (kPa)	Exp.[4]	Ref.
A.								
LEAK								
Beef HMmt	25	–	–	–	52	0.005	C	1965 [10]
RLmt, GS	25	–	–	–	42	0.004	C	1965 [10]
Pigeon HMmt, GS	25	–	–	–	19	0.002	C	1965 [10]
RHMmt, GM	25	465	Nmol *c*	0.2	93	0.032	C	1990 [18]
RHMmt, GMS	25	1170	Nmol *c*	0.2	234	0.048	C	1990 [18]
RLmt, S(Rot)	25	210	mg P_{mt}	0.6	126	0.025	C_{HRR}	1994 [31]
RSMmt, GM	37	–	–	–	170	0.025	C_{HRR}	1995 [3]
RLmt, S(Rot)	37	210	mg P_{mt}	0.6	126	0.025	C_{HRR}	1995 [3]
RLmt, S(Rot)	25	170	mg P_{mt}	0.5	85	0.028	C_{HRR}	1997 [32]
RHMmt, PM	25	190	mg P_{mt}	0.5	95	0.023	C_{HRR}	1997 [32]
RHMmt, PM	30	590	mg P_{mt}	0.12	71	0.016	C_{HRR}	1998 [2]
RLmt, S(Rot)	30	280	mg P_{mt}	0.5	140	0.02	C_{HRR}	1998 [2]
RLmt, S(Rot)	25	210	mg P_{mt}	0.58	122	0.024	C_{HRR}	2000 [27]
Artemia Emt, S(Rot)	25	223	mg P_{mt}	0.26	58	0.057	C_{HRR}	2000 [27]
Frog SMmt, PM	20	82.6	mg P_{mt}	1	83	0.024	C_{HRR}	2000 [28]
Frog SMmt, PM	3	20	mg P_{mt}	1	20	0.005	C_{HRR}	2000 [28]
32D-vRaf, RPMI, Omy	37	10	10^6 cells	$6 \cdot 10^6$	60	0.034	C_{HRR}	Fig. 2
Pigeon HMmt, GS	25	530	mg P_{mt}	0.2	106	0.008	O	1974 [21]
RLmt, S(Rot)	25	210	mg P_{mt}	0.21	42	0.02	O_{HRR}	2000 [11]
OXPHOS								
RLmt, S	26	–	mg P_{mt}	0.2	–	0.015	C	1970 [51]
Beef Amt, S	26	–	mg P_{mt}	0.2	–	0.024	C	1970 [51]

Table 1 (continued)

Model [1,2]	T (°C)	J_{max} (pmol/(s·x))	Unit [3]X	Density (x/ml)	J_{Vmax} (pmol/(s·ml))	p_{50} (kPa)	Exp.[4]	Ref.
Yeast mt, PM	25	–	mg P_{mt}	0.2	–	0.04	C	1970 [51]
RHMmt	30	4500	mg P_{mt}	0.1	450	0.035	C_{HRR}	1998 [2]
RLmt, S(Rot)	30	1240	mg P_{mt}	0.3	372	0.057	C_{HRR}	1998 [2]
Frog SMmt, PM	20	420	mg P_{mt}	1	420	0.052	C_{HRR}	2000 [28]
Frog SMmt, PM	3	89	mg P_{mt}	1	89	0.015	C_{HRR}	2000 [28]
RLmt, PM	–	110	mg P_{mt}	6	660	0.05	O	1971 [52]
Pigeon HMmt, GS	25	2900	mg P_{mt}	0.2	580	0.08	O	1974 [21]
ROUTINE								
Yeast, ethanol	25	–	–	–	–	0.035	C	1965 [10]
CHP-404	–	79	mg W_d	5	395	0.110	C	1989 [53]
IMR-5	–	68	mg W_d	5	340	0.103	C	1989 [53]
HUVEC, EGM	37	45	10^6 cells	2	90	0.063	C_{HRR}	1994 [54]
HUVEC, M199	37	20	10^6 cells	2	40	0.094	C_{HRR}	1994 [54]
HUVEC, EGM	37	40	10^6 cells	2	125	0.075	C_{HRR}	1996 [12]
Platelets	37	0.1	10^6 cells	1500	149	0.082	C	1999 [48]
Fibroblast	37	49.6	10^6 cells	1.5	74	0.082	C_{HRR}	2002 [24]
Fibroblast	37	60.5	mg P_c	0.7	42	0.039	C_{HRR}	2004 [25]
32D-vRAF, RPMI	37	30	10^6 cells	6	180	0.076	C_{HRR}	Fig. 2
32D cells; RPMI	37	18	10^6 cells	10	180	0.051	C_{HRR}	Fig. 2
Rat coronary EC	37	65	mg P_c	–	–	0.110	O	1990 [55]
Sunflower leaves	22	60	cm^2	–	–	0.041	O	2007 [26]
Aspen leaves	22	100	cm^2	–	–	0.059	O	2007 [26]
B.								
LEAK								
RLmt, GS	25	670	mg P_{mt}	1.0	670	0.060	C	1988 [56]
RHMmt, GMS	25	1158	nmol *c*	0.8	926	0.051	C	1990 [18]
RLmt, S(Rot)	37	333	mg P_{mt}	1.0	–	0.333	O_{GAP}	2007 [38]

Table 1 (continued)

Model [1,2]	T (°C)	J_{max} (pmol/(s·x))	Unit [3]X	Density (x/ml)	J_{Vmax} (pmol/(s·ml))	p_{50} (kPa)	Exp.[4]	Ref.
OXPHOS								
RLmt, S(Rot)	25	1780	mg P_{mt}	0.5	890	0.157	C_{HRR}	1997 [32]
RHMmt, PM	25	1550	mg P_{mt}	0.5	775	0.135	C_{HRR}	1997 [32]
RSMmt, GM	25	1500	mg P_{mt}	10	15000	0.005	O_{GAP}	1982 [37]
RLmt, S(Rot)	37	–	mg P_{mt}	1	–	0.258	O_{GAP}	2003 [39]
RLmt, S(Rot)	37	1833	mg P_{mt}	1	1833	0.278	O_{GAP}	2007 [38]
ROUTINE								
Jurkat cells	37	19.2	10^6 cells	26	500	0.245	C	2003 [34]
HUVEC, L-NMMA	37	–	10^6 cells	31	~1000	0.436	C	2004 [33]
RAW 246.7, L-NMMA	37	18	10^6 cells	52	937	0.309	C	2004 [33]
BAEC	37	10	10^6 cells	2	20	0.153	C_u	2006 [35]
BAEC	37	10	10^6 cells	3	31	0.247	C_u	2006 [35]
BAEC	37	16	10^6 cells	5	78	0.340	C_u	2006 [35]
BAEC	37	159	10^6 cells	8	1276	0.631	C_u	2008 [57]
BAEC, stress	37	73	10^6 cells	8	580	0.340	C_u	2008 [57]
C.								
RH myocytes	30	91	mg P_c	0.3	27	0.015	O_{GAP}	1985 [43]
Perfused RH	25	160	mg W_d	–	–	0.070	P	1995 [40]
Human SM	37	–	–	–	–	0.2	P	1999 [41]
Mouse SM	37	6.86	mg W_w	–	–	0.16	P	2003 [42]

(1) Mitochondria (mt): 32D (32D-vRaf), murine promyeloid cells (over-expressing the *v*-Raf gene); *Artemia* E, *Artemia franciscana* embryo; Amt, adrenocortical mt; BAEC, bovine aortic endothelial cells; BAEC stress, after shear stress; CHP-404, neuroblastoma cell line; EC, endothelial cells; HM, heart muscle; HUVEC, human umbilical vein endothelial cells; IMR-5, neuroblastoma cell line; Jurkat cells, human leukocytes; RAW 246.7, murine monocytic cell line; RH, rat heart; RHM, rat heart muscle; RL, rat liver; RSM, rat skeletal muscle; SM, skeletal muscle.
(2) Substrates, inhibitors and media: *c*, cytochrome *c*; EGM, endothelial growth medium; G, glutamate; L-NMMA, N^G-monomethyl-L-arginine monoacetate; M, malate; M199, growth medium; Omy, oligomycin; P, pyruvate; Rot, rotenone; RPMI, growth medium; S, succinate.
(3) Unit [mg]: P_c, cell protein; P_{mt}; mitochondrial protein; W_d, dry weight; W_w, wet weight.
(4) Experimental system: C, closed; C_{HRR}, closed high-resolution respirometry; C_u, closed unstirred; O, open; O_{GAP}, open with the gas-aqueous phase system of [37]; O_{HRR}, open high-resolution respirometry; P, perfused organ including measurement in vivo.

A linear dependence of the K_m' of cytochrome *c* oxidase on enzyme turnover [10] was shown conclusively in the bacterial enzyme [22, 23].

Respiratory flow in the *ROUTINE* state of 32D cells in RPMI averaged 18.4 ± 3.7 pmol·s^{-1}·10^{-6} ($N = 39$; compare [15]), and the corresponding p_{50} was 0.051 ± 0.012 kPa (= 0.38 mmHg; $c_{50} = 0.48$ µM; Table 1). The 32D cell volume is 0.0009 ± 0.0001 mm^3 (0.9 pL), determined in a CASY1 TT system (Schärfe System, Reutlingen, Germany). These cells are comparable to human umbilical vein endothelial cells (HUVEC) in terms of cell volume, *ROUTINE* respiration, electron transport capacity after uncoupling and p_{50} [12, 15].

We have not determined the oxygen kinetics of mitochondria isolated from 32D cells, but may compare the cellular p_{50} with results on mitochondria isolated from rat liver and rat heart, which is 0.016 and 0.020 kPa in the passive *LEAK* state and 0.035 and 0.057 kPa in the active *OXPHOS* state with substrates for Complex I or succinate + rotenone for Complex II ([2, 13]; Fig. 3a, b). Since the substrate combination for Complex I + II exerts an additive effect and stimulates *OXPHOS* capacity to a higher level of cytochrome *c* oxidase turnover [9], the p_{50} in the active *OXPHOS* state of Complex I- or Complex

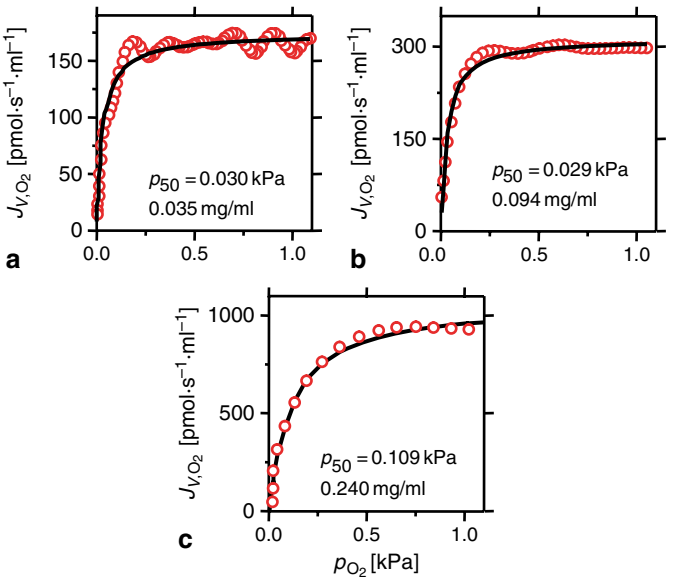

Fig. 3 Oxygen flux per volume of incubation medium, J_{V,O_2} [pmol·s^{-1}·ml^{-1}], as a function of oxygen pressure, p_{O_2}, in the low-oxygen range <1.1 kPa, in active heart mitochondria (*OXPHOS*, 1 mM ADP, 1 mM ATP, 2 mM pyruvate, 5 mM malate; 30°C), at different mitochondrial protein concentrations [mg/ml]. Protein-specific flux at kinetic oxygen saturation, J_{max}, is 4.5 nmol·s^{-1}·mg^{-1} independent of protein concentration. Similarly, the p_{50} is independent of protein concentration (**a** and **b**), whereas the increase of p_{50} (**c**) is an experimental artefact at protein concentrations >0.15 mg/ml, corresponding to volume-specific J_{max} >500 pmol·s^{-1}·ml^{-1}. From [13]

II-respiration is quite comparable to turnover conditions in the *ROUTINE* state. Taken together, these data indicate that the small intracellular oxygen gradients (Eq. 2) in 32D cells are close to the limit of detection. Similar conclusions are drawn [6] from the oxygen kinetics of HUVEC (*ROUTINE* $I_{O_2} = 30–50$ pmol·s^{-1}·10^{-6} and $p_{50} = 0.05–0.08$ kPa [12]) and human fibroblasts (*ROUTINE* $I_{O_2} = 50$ pmol·s^{-1}·10^{-6} and $p_{50} = 0.04–0.08$ kPa [24, 25], where oxygen flow, I_{O_2}, is given per number of cells).

4 Discussion

4.1 Comparative Mitochondrial Physiology and p_{50} of Mitochondrial Respiration

Extending previous reviews on oxygen kinetics of mitochondrial respiration [3, 6], Table 1A and Fig. 4 summarize p_{50} and respiration in isolated, coupled mitochondria incubated with physiological substrates and in intact small cells. With a focus on mitochondrial physiology, no data are included on (i) uncoupled respiration [3, 12, 13, 18]; (ii) the isolated step of cytochrome *c* oxidase with artificial substrates, and (iii) large cells (hepatocytes, cardiomyocytes) where oxygen gradients are significant [4, 6]. In addition to rat liver, rat heart and various mammalian cell types, a large variety of mitochondrial sources has been tested, including plants [26], brine shrimp embryos (*Artemia* [27]), and frog skeletal muscle [28]. Considering this broad spectrum of comparative mitochondrial physiology and respiratory states from *LEAK* to *ROUTINE* and *OXPHOS*, the range of p_{50} from 0.01 to 0.11 kPa (0.08–0.75 mmHg) is remarkably consistent, and independent of measurement in closed or open chambers if methodological criteria are met as summarized above (Section 3.1; [3]).

Close agreement of p_{50} for small cells and isolated mitochondria suggests that Δp_{50} (Eq. 2) is in the order of 0.01–0.03 kPa (Table 1A). A 10- to 20-fold higher Δp_{cell} has been reported by delayed fluorescence of endogenous protoporphyrin in small cells [29], which is not supported by a model of oxygen diffusion [18].

Comparison of results reported for identical experimental models (e.g. isolated rat liver mitochondria or HUVEC; Table 1A, B) suggests that discrepancies of p_{50} are primarily related to methodological issues. The scatter of reported p_{50} values increased dramatically since 2003 (Fig. 4). Consideration of fundamental instrumental and experimental criteria helps to discriminate between physiological variability and experimental bias (Fig. 3). In several cases, separation of facts and artefacts on oxygen kinetics is impossible without extending the studies in question by methodological tests, particularly variation of mitochondrial or cell density (Fig. 2; [12, 13]).

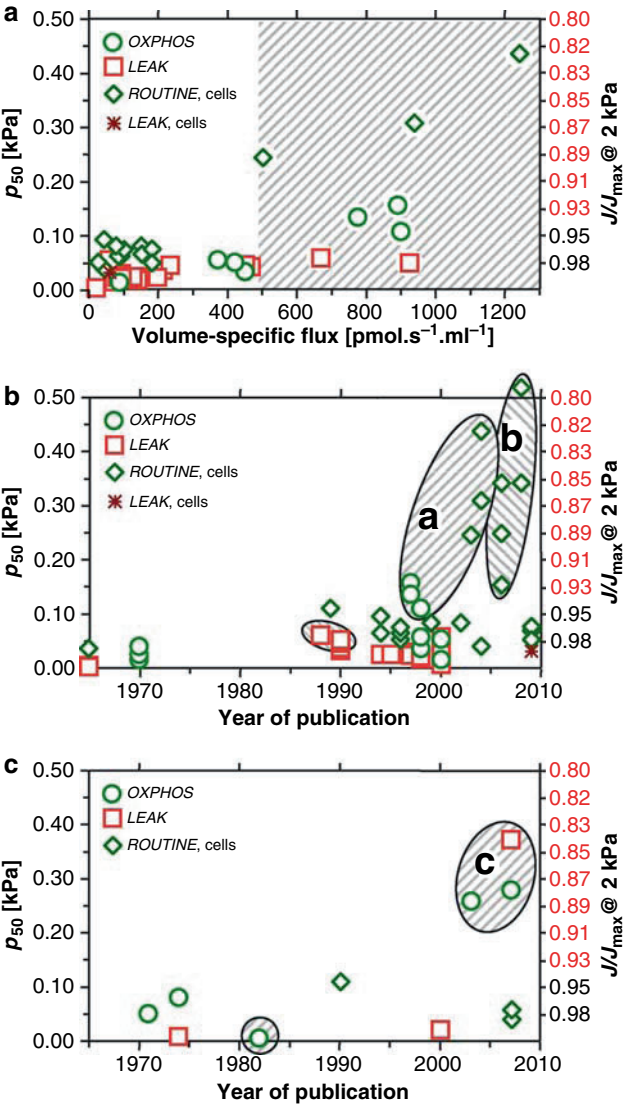

Fig. 4 p_{50} for respiration of isolated, coupled mitochondria and intact small cells. **a**: p_{50} measured in closed, well stirred respirometry chambers with aerobic-anoxic transitions as a function of volume-specific oxygen flux. The critical range >500 pmol·s^{-1}·ml^{-1} is hatched. **b**: Closed systems; hatched areas (**a**) high volume-specific flux, correspondingly fast aerobic-anoxic transitions and insufficient time resolution (Fig. 3c), and (**b**) EPR oxymetry without stirring. **c**: Open systems; hatched areas (**c**) indicate results obtained with an identical GAP instrument including a gas phase. Experimental details and references in Table 1

4.2 Methodological Limitations of Closed Systems

The basis of oxygen kinetic measurements in closed respirometry systems [30] is the measurement of oxygen flux in aerobic-anoxic transitions (Fig. 1). To compensate for low instrumental resolution, high mitochondrial concentrations (>0.2 mg mitochondrial protein/ml) have been used to achieve accurate measurement of oxygen flux. Under these conditions, rapid aerobic-anoxic transitions present a potential problem as pointed out by Britton Chance more than 40 years ago: "It is probable that the enzyme concentrations were so high under our experimental conditions that the enzyme passed too rapidly through the first order region for an accurate measurement of the K_m value" [10]. Direct experimental evidence for the magnitude of such inaccuracies was provided by using a large range of mitochondrial densities for measurement of oxygen kinetics [13]. Volume-specific oxygen flux is shown as a function of oxygen pressure at increasing protein concentrations of isolated rat heart mitochondria (Fig. 3). The p_{50} is 0.035 kPa in the active *OXPHOS* state, as measured at protein concentrations ranging from 0.02 to 0.12 mg/ml (Fig. 3a,b). At higher mitochondrial concentrations, volume-specific fluxes >500 $\text{pmol}\cdot\text{s}^{-1}\cdot\text{ml}^{-1}$ result in artificially high p_{50} values (Fig. 3c).

Correction of the oxygen signal for the exponential time constant of the POS [3] is important but insufficient at high flux when the aerobic-anoxic transition time is too short (Fig. 4a). At densities of 0.2–0.5 mg/ml (25°C) of rat liver and heart mitochondria in the passive *LEAK* state, volume-specific fluxes are in the range of 50–100 $\text{pmol}\cdot\text{s}^{-1}\cdot\text{ml}^{-1}$, which are optimum for oxygen kinetics and result in a reproducible p_{50} of 0.02 kPa [3, 27, 31, 32] (Table 1A). In contrast, even high-resolution respirometry cannot resolve short transition times <30–40 s from 10 μM to zero oxygen at high volume-specific flux >500 $\text{pmol}\cdot\text{s}^{-1}\cdot\text{ml}^{-1}$ in closed chambers, which explains the erroneously high p_{50} of 0.15 kPa for rat liver and heart mitochondria [32] respiring in the active *OXPHOS* state (Table 1B; Fig. 4a).

Varying human umbilical vein endothelial cell (HUVEC) density in a three-fold range from $0.6\cdot10^6$ to $2.0\cdot10^6$ cells/ml, maximum oxygen flow and p_{50} of *ROUTINE* respiration vary by a factor of 1.4, from 35 to 49 $\text{pmol}\cdot\text{s}^{-1}\cdot10^{-6}$ and from 0.052 to 0.075 kPa, respectively, in endothelial growth medium without inhibitor [12]. In contrast, a 6-fold higher p_{50} of 0.44 kPa was reported for HUVEC in the presence of L-NMMA (NOS inhibitor) with $31\cdot10^6$ cells/ml and corresponding high volume-specific flux [33]. Instruments with high O_2 back-diffusion [33, 34] are particularly sensitive to artefacts of rapid aerobic-anoxic transitions (Fig. 4a).

In electron paramagnetic resonance (EPR) oxymetry, small numbers of cells can be studied in micro chambers of 50 μl volume [35]. Without sufficient stirring, oxygen gradients develop in diffusion zones around cells [35], comparable to the diffusion zone towards the POS membrane [36]. Although diffusion conditions across unstirred POS are simpler to model in comparison to

suspended cells, corrections are inherently inaccurate and the only satisfactory solution for measurement of dissolved oxygen is obtained by vigorous stirring, as in HRR. Taking oxygen diffusion in unstirred EPR oxymetry into consideration reduces the estimate of p_{50} for respiration of endothelial cells two-fold [35], but the corrected p_{50} values remain highly sensitive to cell density ($2 \cdot 10^6$–$5 \cdot 10^6$ cells/ml; Table 1B). The minimum oxygen pressure, $p^{\#}$, at which cessation of respiration in EPR oxymetry indicates equilibrium to be established within mitochondria, is at 0.05 kPa [35] (in the range of p_{50} from HRR), whereas the thermodynamic equilibrium p_{O_2} is 0.0003 kPa for coupled mitochondrial oxygen reduction [3]. Perhaps oxygen diffusion through the tube sealing clay contributes to the high $p^{\#}$ in capillaries used for EPR oxymetry. The sensitivity (>2-fold) of $p^{\#}$ on diffusion corrections indicates that it is not a thermodynamic equilibrium property, since diffusion gradients are dissipated in the approach to equilibrium. Further uncertainties may result from high noise of flux and lack of temperature control in EPR oxymetry. The diffusion model applied for correction in EPR oxymetry assumes that the diffusion zone increases as a steady function of time [35], whereas experimental validation – using the POS as a test system – suggests that a steady-state is reached after a short period of a few minutes. Wall effects are not considered, nor potential effects of cell aggregation in the confinement of a 50 µl capillary [35]. Taken together, these difficulties may explain the high apparent p_{50} derived from EPR oxymetry (Fig. 4b).

4.3 Variation of p_{50} in Open Systems

Using a steady-state approach with oxygen transfer from the gas to aqueous phase (GAP), Sugano et al. [21] report a p_{50} of 0.08 kPa in active pigeon heart mitochondria at a protein concentration of 0.2 mg/ml (Table 1A). At 10 mg/ml, however, Cole et al. [37] obtained a p_{50} of 0.005 kPa in active rat skeletal muscle mitochondria. Using the identical instrumental GAP respirometry system, a p_{50} of 0.37 kPa was reported for rat liver mitochondria in the passive *LEAK* state [38], 75 times higher than in ADP-stimulated rat skeletal muscle mitochondria [37] (Fig. 4c). In contrast to the well established direct proportionality between p_{50} and turnover of cytochrome *c* oxidase [10–13, 22, 26, 28], the p_{50} obtained by GAP respirometry was paradoxically higher in the quiescent *LEAK* state compared to the active *OXPHOS* state [38]. GAP respirometry, therefore, yields inconsistent results on mitochondrial oxygen kinetics (Fig. 4c). Under conditions of very high flux [37], oxygen gradients between the gas and aqueous phases and towards the oxygen sensor at the bottom of the chamber may explain differences between the mitochondrial response to oxygen pressure in the heterogeneous system and the much lower p_{50} reported by the POS in GAP respirometry. This does not explain, however, why the reported p_{50} increases as the volume specific flux declines in this GAP respirometric system (Table 1B).

In addition, previous claims that the p_{50} may be lower in closed than open systems [39] are rejected with reference to the literature summarized over the past 40 years in general and to discrepancies of GAP respirometry in particular (Fig. 4, Table 1).

4.4 Variation of p_{50} In Vivo

Living cells provide an in vivo model that can be studied *in vitro*, both in closed measuring systems or open systems at steady state. The p_{50} of mitochondrial respiration in vivo varies as a function of metabolic state (turnover of cytochrome *c* oxidase), as observed in living cells (Fig. 2). The ^{1}H nuclear magnetic resonance signal of deoxymyoglobin provides an elegant means of monitoring intracellular oxygen saturation in vivo, reducing Δp_{50} (Eq. 2) to the effects of intracellular oxygen gradients. Using this approach in perfused rat heart [40], maximally active human skeletal muscle [41] and mouse skeletal muscle at rest or stimulated by uncoupling [42], p_{50} values of mitochondrial respiration range from 0.07 to 0.2 kPa (Table 1C), whereas the p_{50} in resting rat cardiomyocytes is 0.015 based on intracellular p_{O_2} derived from spectrophotometric myoglobin saturation measurements [43]. The dependence of cellular or tissue respiration on average myoglobin saturation does not accurately reflect the p_{50} of mitochondrial respiration. Direct comparison would require modelling of the distribution of mitochondria [44] over the range of local oxygen pressures as determined by intracellular oxygen gradients [4], and particularly evaluation of anoxic core regions [5] and their effect on the overall response of tissue or cell respiration under these heterogeneous oxygen conditions. A mitochondrial p_{50} of 0.067 has been derived from a model of brain oxygen supply [45].

5 Conclusions

The p_{50} of mitochondrial respiration in the range of 0.02–0.05 kPa (0.15–0.4 mmHg) indicates close matching of the affinity of cytochrome *c* oxidase to the demands imposed on enzyme function in the low-oxygen environment within cells. 86% myoglobin saturation (2 kPa O_2) in normoxic resting mouse skeletal muscle [42] supports full (99%) respiratory capacity of mitochondria in the *LEAK* state (Table 1A). At maximum aerobic exercise in human muscle, however, myoglobin saturation is 50% ($p_{O_2} = 0.3$–0.4 kPa) [41, 46], which implies an oxygen limitation to 0.9 of maximum mitochondrial capacity, assuming homogenous oxygen distribution. Short-term performance at the extreme of maximum aerobic muscle power induces physiological, intracellular hypoxia at environmental normoxia, if we consider oxygen limitation by $>5\%$ as a criterion of defining bioenergetic hypoxia.

In contrast, with a p_{50} as high as 0.4 kPa (3 mmHg; Table 1B), mitochondrial activity would be limited to 0.44 of respiratory capacity at 50% myoglobin saturation. Even at an intracellular oxygen pressure of 4–5 kPa in liver [47], respiration rate would reach only 0.9 of capacity. Such high p_{50} values of mitochondrial respiration are experimental artefacts resulting from high volume-specific flux in closed chambers (Fig. 4a) and of diffusion limitation in unstirred systems (Fig. 4b). Internally inconsistent results on p_{50} from open GAP respirometry indicate a methodological problem which remains unresolved (Fig. 4c). Several recent studies on the inhibition of cytochrome *c* oxidase by NO report erroneously high p_{50} in the absence of inhibitor [33, 34, 39]. A critical evaluation is required whether or not these methodological deficiencies extend into the higher oxygen range where NO inhibits cytochrome *c* oxidase, a compensatory shift may occur of cytochrome redox states [33, 48] and mitochondrial ROS production may be affected.

At half-maximum aerobic power, myoglobin saturation in skeletal muscle is increased to 70% ($p_{O_2} = 0.9$ kPa [46]), corresponding to oxygen limitation of 5% with a p_{50} of 0.05 kPa. An intracellular p_{O_2} of 1–2 kPa at modest routine activity, therefore, is the normoxic mitochondrial microenvironment in skeletal muscle, and the high affinity of mitochondrial respiration for oxygen prevents significant oxygen limitation under these conditions. On the other hand, a p_{50} of 0.02–0.05 kPa is not excessively low and thus provides the potential for mitochondria to function as a bioenergetic oxygen sensor and playing a role in oxygen signalling and adaptation to hypoxia [49, 50].

Acknowledgments We thank Prof. Dr. Jakob Troppmair for providing the 32D and 32D-vRAF cell lines.

References

1. Weibel ER, Taylor CR, Hoppeler H (1991) The concept of symmorphosis: a testable hypothesis of structure-function relationship. Proc Natl Acad Sci USA 88:10357–10361.
2. Gnaiger E, Lassnig B, Kuznetsov AV et al. (1998) Mitochondrial oxygen affinity, respiratory flux control and excess capacity of cytochrome *c* oxidase. J Exp Biol 201:1129–1139.
3. Gnaiger E, Steinlechner-Maran R, Méndez G et al. (1995) Control of mitochondrial and cellular respiration by oxygen. J Bioenerg Biomembr 27:583–596.
4. Takahashi E, Endoh H, Doi K (2000) Visualization of myoglobin-facilitated mitochondrial O_2 delivery in a single isolated cardiomyocyte. Biophys J 78:3252–3259.
5. Takahashi E (2008) Anoxic cell core can promote necrotic cell death in cardiomyocytes at physiological extracellular PO_2. Am J Physiol Heart Circ Physiol 294:H2507–H2515.
6. Gnaiger E (2003) Oxygen conformance of cellular respiration. A perspective of mitochondrial physiology. Adv Exp Med Biol 543:39–55.
7. Chance B, Williams GR (1955) Respiratory enzymes in oxidative phosphorylation. III. The steady state. J Biol Chem 217:409–427.
8. Puchowicz MA, Varnes ME, Cohen BH et al. (2004) Oxidative phosphorylation analysis: assessing the integrated functional activity of human skeletal muscle mitochondria-case studies. Mitochondrion 4:377–385.

9. Gnaiger E, ed (2007) Mitochondrial pathways and respiratory control. OROBOROS MiPNet Publications, Innsbruck.
10. Chance B (1965) Reaction of oxygen with the respiratory chain in cells and tissues. J Gen Physiol 49:163–195.
11. Gnaiger E (2001) Bioenergetics at low oxygen: dependence of respiration and phosphorylation on oxygen and adenosine diphosphate supply. Respir Physiol 128:277–297.
12. Steinlechner-Maran R, Eberl T, Kunc M et al. (1996) Oxygen dependence of respiration in coupled and uncoupled endothelial cells. Am J Physiol 271:C2053–C2061.
13. Gnaiger E, Lassnig B, Kuznetsov AV, Margreiter R (1998) Mitochondrial respiration in the low oxygen environment of the cell. Effect of ADP on oxygen kinetics. Biochim Biophys Acta 1365:249–254.
14. Hütter E, Renner K, Pfister G, Stöckl P et al. (2004) Senescence-associated changes in respiration and oxidative phosphorylation in primary human fibroblasts. Biochem J 380:919–928.
15. Gnaiger E (2008) Polarographic oxygen sensors, the oxygraph, and high-resolution respirometry to assess mitochondrial function. In: Dykens JA, Will Y (ed) Mitochondrial dysfunction in drug-induced toxicity. Wiley, New York.
16. Renner K, Amberger A, Konwalinka G et al. (2003) Changes of mitochondrial respiration, mitochondrial content and cell size after induction of apoptosis in leukemia cells. Biochim Biophys Acta 1642:115–123.
17. Schindler FJ (1967) Determination of oxygen affinity. Methods Enzymol 10:629–634.
18. Rumsey WL, Schlosser C, Nuutinen EM et al. (1990) Cellular energetics and the oxygen dependence of respiration in cardiac myocytes isolated from adult rat. J Biol Chem 265:15392–15402.
19. Cornish-Bowden A (1995) Fundamentals of enzyme kinetics. Portland Press, London.
20. Troppmair J, Rapp UR (2003) Raf and the road to cell survival: a tale of bad spells, ring bearers and detours. Biochem Pharmacol 66:1341–1345.
21. Sugano T, Oshino N, Chance B (1974) Mitochondrial functions under hypoxic conditions. The steady states of cytochrome *c* reduction and of energy metabolism. Biochim Biophys Acta 347:340–358.
22. Verkhovsky MI, Morgan JE, Puustinen A, Wikström M (1996) Kinetic trapping of oxygen in cell respiration. Nature 380:268–270.
23. Riistama S, Puustinen A, García-Horsman A et al. (1996) Channelling of dioxygen into the respiratory enzyme. Biochim Biophys Acta 1275:1–4.
24. Hütter E, Renner K, Jansen-Dürr P, Gnaiger E (2002) Biphasic oxygen kinetics of cellular respiration and linear oxygen dependence of antimycin A inhibited oxygen consumption. Mol Biol Rep 29:83–87.
25. Pecina P, Gnaiger E, Zeman J et al. (2004) Decreased affinity for oxygen of cytochrome-*c* oxidase in Leigh syndrome caused by SURF1 mutations. Am J Physiol Cell Physiol 287:C1384–C1388.
26. Laisk A, Oja V, Eichelmann H (2007) Kinetics of leaf oxygen uptake represent in planta activities of respiratory electron transport and terminal oxidases. Physiol Plant 131:1–9.
27. Gnaiger E, Mendez G, Hand SC (2000) High phosphorylation efficiency and depression of uncoupled respiration in mitochondria under hypoxia. Proc Natl Acad Sci USA 97:11080–11085.
28. St-Pierre J, Tattersall GJ, Boutilier RG (2000) Metabolic depression and enhanced O_2 affinity of mitochondria in hypoxic hypometabolism. Am J Physiol Regul Integr Comp Physiol 279:R1205–R1214.
29. Mik EG, Stap J, Sinaasappel M et al. (2006) Mitochondrial PO_2 measured by delayed fluorescence of endogenous protoporphyrin IX. Nature Methods 3:939–945.
30. Longmuir IS (1957) Respiration rate of rat-liver cells at low oxygen concentrations. Biochem J 65:378–382.

31. Mendez G, Gnaiger E (1994) How does oxygen pressure control oxygen flux in isolated mitochondria? A methodological approach by high-resolution respirometry and digital data analysis. In Gnaiger E, Gellerich FN, Wyss M (ed) What is controlling life? Modern Trends BioThermoKinetics, Innsbruck University Press, Innsbruck.
32. Costa LE, Mendez G, Boveris A (1997) Oxygen dependence of mitochondrial function measured by high-resolution respirometry in long-term hypoxic rats. Am J Physiol 273:C852–C858.
33. Palacios-Callender M, Quintero M, Hollis VS et al. (2004) Endogenous NO regulates superoxide production at low oxygen concentrations by modifying the redox state of cytochrome *c* oxidase. Proc Natl Acad Sci USA 101:7630–7635.
34. Hollis VS, Palacios-Callender M, Springett RJ et al. (2003) Monitoring cytochrome redox changes in the mitochondria of intact cells using multi-wavelength visible light spectroscopy. Biochim Biophys Acta 1607:191–202.
35. Presley T, Kuppusamy P, Zweier JL, Ilangovan G (2006) Electron paramagnetic resonance oximetry as a quantitative method to measure cellular respiration: a consideration of oxygen diffusion interference. Biophys J 91:4623–4631.
36. Gnaiger E, Forstner H (1983) Polarographic Oxygen Sensors. Aquatic and Physiological Applications. Springer, Berlin.
37. Cole RC, Sukanek PC, Wittenberg JB, Wittenberg BA (1982) Mitochondrial function in the presence of myoglobin. J Appl Physiol 53:1116–1124.
38. Hoffman DL, Salter JD, Brookes PS (2007) Response of mitochondrial reactive oxygen species generation to steady-state oxygen tension: implications for hypoxic cell signaling. Am J Physiol Heart Circ Physiol 292:H101–H108.
39. Brookes PS, Kraus DW, Shiva S et al. (2003) Control of mitochondrial respiration by $NO^{\bullet}$, effects of low oxygen and respiratory state. J Biol Chem 278:31603–31609.
40. Kreutzer U, Jue T (1995) Critical intracellular O_2 in myocardium as determined by 1H nuclear magnetic resonance signal of myoglobin. Am J Physiol 268:H1675–H1681.
41. Richardson RS, Leigh JS, Wagner PD, Noyszewski EA (1999) Cellular PO_2 as a determinant of maximal mitochondrial O_2 consumption in trained human skeletal muscle. J Appl Physiol 87:325–331.
42. Marcinek DJ, Ciesielski WA, Conley KE, Schenkman KA (2003) Oxygen regulation and limitation to cellular respiration in mouse skeletal muscle in vivo. Am J Physiol Heart Circ Physiol 285:H1900–H1908.
43. Wittenberg BA, Wittenberg JB (1985) Oxygen pressure gradients in isolated cardiac myocytes. J Biol Chem 260:6548–6554.
44. Benard G, Rossignol R (2008) Ultrastructure of the mitochondrion and its bearing on function and bioenergetics. Antiox Redox Signaling 10:1313–1342.
45. Gjedde A, Johannsen P, Cold GE, Ostergaard L (2005) Cerebral metabolic response to low blood flow: possible role of cytochrome oxidase inhibition. J Cereb Blood Flow Metab 25:1183–1196.
46. Molé PA, Chung Y, Tran TK et al. (1999) Myoglobin desaturation with exercise intensity in human gastrocnemius muscle. Am J Physiol 277:R173–R180.
47. Mik EG, Johannes T, Zuurbier CJ et al. (2008) In vivo mitochondrial oxygen tension measured by a delayed fluorescence lifetime technique. Biophys J 95:3977–3990.
48. Arthur PG, Ngo C-T, Moretta P, Guppy M (1999) Lack of oxygen sensing by mitochondria in platelets. Eur J Biochem 266:215–219.
49. Kwast KE, Burke PV, Staahl BT, Poyton RO (1999) Oxygen sensing in yeast: evidence for the involvement of the respiratory chain in regulating the transcription of a subset of hypoxic genes. Proc Natl Acad Sci USA 96:5446–5451.
50. Fukuda R, Zhang H, Kim J-W et al. (2007) HIF-1 regulates cytochrome oxidase subunits to optimize efficiency of respiration in hypoxic cells. Cell 129:111–122.
51. Barzu O, Satre M (1970) Determination of oxygen affinity of respiratory systems using oxyhemoglobin as oxygen donor. Anal Biochem 36:428–433.

52. Degn H, Wohlrab H (1971) Measurement of steady-state values of respiration rate and oxidation levels of respiratory pigments at low oxygen tensions. A new technique. Biochim Biophys Acta 245:347–355.
53. Robiolio M, Rumsey WL, Wilson DF (1989) Oxygen diffusion and mitochondrial respiration in neuroblastoma cells. Am J Physiol 256:C1207–C1213.
54. Steinlechner R, Eberl T, Margreiter R, Gnaiger E (1994) Oxygen dependence of cellular respiration in endothelial cells: a sensitive toxicological test. In Gnaiger E, Gellerich FN, Wyss M (ed) What is controlling life? 50 years after Erwin Schrödinger's What is Life? Innsbruck University Press, Innsbruck.
55. Mertens S, Noll T, Spahr R et al. (1990) Energetic response of coronary endothelial cells to hypoxia. Am J Physiol 258:H689–H694.
56. Wilson DF, Rumsey WL, Green TJ, Vanderkooi J (1988) The oxygen dependence of mitochondrial oxidative phosphorylation measured by a new optical method for measuring oxygen concentration. J Biol Chem 263:2712–2718.
57. Jones CI, Han Z, Presley T et al. (2008) Endothelial cell respiration is affected by the oxygen tension during shear exposure: role of mitochondrial peroxynitrite. Am J Physiol Cell Physiol 295:C180–C191.

Alveolar Hypoxia-Induced Systemic Inflammation: What Low PO_2 Does and Does Not Do

Norberto C. Gonzalez and John G. Wood

Abstract Reduction of alveolar PO_2 (alveolar hypoxia, AH) may occur in pulmonary diseases such as chronic obstructive pulmonary disease (COPD), or in healthy individuals ascending to altitude. Altitude illnesses may develop in non-acclimatized persons who ascend rapidly. The mechanisms underlying these illnesses are not well understood, and systemic inflammation has been suggested as a possible contributor. Similarly, there is evidence of systemic inflammation in the systemic alterations present in COPD patients, although its role as a causative factor is not clear.

We have observed that AH, induced by breathing 10% O_2 produces a rapid (minutes) and widespread micro vascular inflammation in rats and mice. This inflammation has been observed directly in the mesenteric, skeletal muscle, and pial microcirculations. The inflammation is characterized by mast cell degranulation, generation of reactive O_2 species, reduced nitric oxide levels, increased leukocyte-endothelial adherence in post-capillary venules, and extravasation of albumin. Activated mast cells stimulate the renin-angiotensin system (RAS) which leads to the inflammatory response via activation of NADPH oxidase. If the animals remain in hypoxia for several days, the inflammation resolves and exposure to lower PO_2 does not elicit further inflammation, suggesting that the vascular endothelium has "acclimatized" to hypoxia.

Recent experiments in cremaster microcirculation suggest that the initial trigger of the inflammation is not the reduced tissue PO_2, but rather an intermediary re-leased by alveolar macrophages into the circulation. The putative intermediary ac-tivates mast cells, which, in turn, stimulate the local renin-angiotensin system and induce inflammation.

N.C. Gonzalez (✉)
Department of Molecular and Integrative Physiology, University of Kansas Medical Center, Kansas City, KS 66160, USA
e-mail: ngonzale@kumc.edu

E. Takahashi, D.F. Bruley (eds.), *Oxygen Transport to Tissue XXXI*, Advances in Experimental Medicine and Biology 662,
DOI 10.1007/978-1-4419-1241-1_3, © Springer Science+Business Media, LLC 2010

1 Introduction

Reduction of alveolar PO_2 is commonly encountered in pulmonary disease and in healthy subjects exposed to altitude. Rapid ascent may trigger illnesses such as acute mountain sickness, high altitude pulmonary edema or high altitude cerebral edema [1]. The pathogenesis of these diseases is unknown; while inflammation is present, it is unclear whether it is a cause or an epiphenomenon of the disease. Altitude exposure is accompanied by increased levels of inflammatory markers [2–5] and leukocytosis [6], increased superoxide generation and CD18 expression by granulocytes, and enhanced inflammatory response of neutrophiles [7, 8]. Anti-inflammatory drugs such as dexamethasone are useful therapeutic agents [1]. Either acclimatization [9] or hypoxic preconditioning [6] prevent or attenuate these changes. These findings suggest that inflammation may play a role, either in the genesis or the development of altitude illness. These conditions are becoming increasingly common owing to the large number of individuals worldwide who reach altitudes higher than 2,500 m within a few hours for recreational, work, or military purposes [1].

Pulmonary diseases such as COPD may present systemic effects, including weight loss, skeletal muscle dysfunction, and cardiovascular and nervous system abnormalities [10]. While the systemic hypoxemia commonly present in COPD may influence these effects, it has been suggested that systemic inflammation may also contribute to the genesis or development of these systemic abnormalities [11]. As with diseases of altitude, the role of inflammation in COPD is still unclear.

We have shown that reduction of inspired PO_2 initiates a rapid and widespread inflammation in mesentery [9], skeletal muscle [12, 13] and pial microcirculations [14] of rats. The inflammation features increased levels of reactive O_2 species (ROS) [15], mast cell degranulation [12, 13, 16], local renin-angiotensin system (RAS) activation [17], leukocyte-endothelial adhesive interactions [15, 18], and albumin extravasation [18]. If hypoxia is maintained for several days, the inflammation resolves and more severe hypoxia is not accompanied by inflammation, suggesting that the vascular endothelium has "acclimatized" to prolonged hypoxia [9].

Recent observations support the hypothesis that the systemic inflammation of alveolar hypoxia is not triggered by the reduction of systemic PO_2, but by a mediator released into the circulation from alveolar macrophages. This paper will review the evidence that led us to formulate this hypothesis.

2 Dissociation Between Cremaster Microvascular PO_2 Values and Cremaster Inflammation

The first observation suggesting that local hypoxia was not the trigger of systemic inflammation was the dissociation observed between cremaster microvascular PO_2 (PmO_2) – estimated from the phosphorescence decay method [19],

and cremaster inflammation [12, 13]. Selective reduction of cremaster PmO_2 (local ischemia or selective cremaster hypoxia induced by equilibrating the cremaster with 95% N_2, 5% CO_2) in rats breathing room air did not produce leukocyte endothelial adherence (LEA) or mast cell degranulation (MCD). On the other hand, lowering alveolar (and systemic) PO_2 produced cremaster LEA and MCD, even when the cremaster PmO_2 was higher than normal. Accordingly, cremaster LEA and MCD occur only when alveolar PO_2 is reduced, independent of the value of cremaster PmO_2. One possible explanation for this phenomenon, among other alternatives, is that the inflammation is triggered by a substance released from a distant site.

3 Plasma from Hypoxic Rats Produces Inflammation in Normoxic Cremaster

We reasoned that if the putative mediator is carried by the circulation, plasma obtained from hypoxic rats should produce inflammation in normoxic tissues. Blood obtained from conscious rats breathing 10% O_2 was centrifuged and plasma separated allowing plasma PO_2 equilibration with room air [20]. Application of plasma onto the surface of normoxic cremaster elicited a rapid increase in LEA and substantial MCD. These responses are similar to those observed in various vascular beds during alveolar hypoxia [9, 12, 16]. The inflammation is specific of plasma from hypoxic donors, since it was not elicited by application of plasma from normoxic rats. The inflammatory agent is not generated by blood cells, since no inflammation developed in response to plasma separated after hypoxic in vitro equilibration. The inflammation of hypoxic plasma is not due to agents released by activated leukocytes or mast cells in the systemic microcirculation of the donor, since plasma obtained from hypoxic donors pretreated with cromolyn still elicited inflammation. Cromolyn blocks LEA and MCD in the hypoxic donor [20]. The combined data of these studies strongly support the idea that the inflammation of alveolar hypoxia is triggered by an agent(s) released from a distant site and transported by the circulation.

4 Alveolar Macrophages Are Necessary for the Inflammation of Alveolar Hypoxia

Several reasons suggest the lungs as the site of origin for the agent(s) responsible for triggering the inflammation of alveolar hypoxia. First, inflammation occurs only when the alveolar PO_2 is reduced, independent of systemic tissue PO_2; second, the lung receives the entire cardiac output so substances released by the lung rapidly reach the systemic circulation. Alveolar macrophages (AMØ) are ideally positioned to sense changes in alveolar PO_2. Additionally, AMØ store a number of substances which could trigger inflammation. While most known

effects of AMØ activation occur within the lung, examples of systemic inflammation secondary to AMØ activation have been documented [21, 22].

AMØ were depleted by tracheal instillation of disodium clodronate-containing liposomes [7]. This technique results in temporary depletion of AMØ [23]; in our hands, the number of AMØ recovered from each rat by broncho-alveolar lavage (BAL) decreased from a normal of $6.7 \pm 0.3 \times 10^6$ to $0.45 \pm 0.07 \times 10^6$ four days after treatment. Alveolar hypoxia (10% O_2 breathing) in AMØ-depleted rats failed to increase LEA, MCD, or albumin extravasation. This was not due to inability of the AMØ- depleted rats to mount an inflammatory response to Angiotensin II (Ang II) or mast cell secretagogues. Plasma obtained from hypoxic, AMØ-depleted donors did not produce increased LEA or MCD in normoxic cremaster; furthermore, supernatant of primary cultures of AMØ exposed to hypoxia produced inflammation in the normoxic cremaster [18].

5 Activation of Mast Cells by the AMØ-Generated Intermediary Stimulates the Local Renin-Angiotensin System (RAS)

The RAS plays a role in the inflammation of alveolar hypoxia: Ang II receptor blockade or Ang I-converting enzyme (ACE) inhibition attenuate LEA, MCD and increased vascular permeability of alveolar hypoxia [17]. The inflammatory effects of plasma from hypoxic rats [17] and of supernatant of hypoxic AMØ are also attenuated by blockade of the RAS [24]. The activation of the RAS in these cases is secondary to mast cell degranulation. Several lines of evidence support this: 1. Topical Ang II induces LEA but not MCD; 2. Ang II-induced LEA is not blocked by cromolyn, while this agent blocks the inflammatory responses to plasma from hypoxic rats and from supernatant from hypoxic AMØ; 3: The inflammation induced by the mast cell secretagogue C4880 is blocked by RAS blockade [24]. These findings indicate that the effects of Ang II in the leukocyte-endothelial interface are downstream from mast cell activation, and that MCD leads to generation of Ang II. The mechanism by which this occurs is not clear, mast cells of some species contain an angiotensin I converting chymase; also renin is contained in cardiac mast cells of several species.

The data summarized here indicate that the inflammation of alveolar hypoxia is initiated by a substance released into the circulation by AMØ stimulated by the reduced alveolar PO_2. This substance activates perivascular mast cells which, in turn, activate the local RAS and initiate the inflammatory response. The identity of the mediator is still unclear; the data suggest that it is a mast cell secretagogue either stored or rapidly assembled by AMØ. Identification of this substance and development of means to antagonize its effects may provide a useful tool for improving our understanding of the strategies employed by intact organisms to adapt to reduced alveolar PO_2.

Acknowledgments Supported by National Institutes of Health, USA, grant HL39443

References

1. Basnyat B, Murdoch BR (2003) High altitude illnesses. Lancet 361:1967–1974.
2. Hartmann C, Tschopp M, Fischer R, Bidlingmaier C, Riepl R, Tschopp K, Hartmann H, Endres S, Toepfer M (2000) High altitude increases circulating interleukin-6, interleukin-1 receptor antagonist and C-reactive protein. Cytokine 12:246–252.
3. Klausen T, Olsen NV, Poulsen TD, Richalet JP, Pedersen BK (1997) Hypoxemia increases serum interleukin-6 in humans. Eur J Appl Physiol Occup Physiol 76:480–482.
4. Kokker M, Kharazmi A, Galbo H, Bygberg I, Pedersen BK (1993) Influence of in vivo hypobaric hypoxia on function of lymphocytes, neurocytes, natural killer cells and cytokines. J Appl Physiol 74:1100–1106.
5. Møller P, Loft S, Lundby C, Olsen NV (2001) Acute hypoxia and hypoxic exercise induce DNA strand breaks and oxidative DNA damage in humans. FASEB J 15:1181–1186.
6. Beidleman BA, Muza SR, Fluke CS, Cymerman A, Staab JE, Sawka MN, Lewis SF, Skrinar GS (2006) White blood cell and hormonal responses to 4300 m altitude before and after intermittent altitude exposure. Cli Sci 111:163–169.
7. Choukèr A, Demetz F, Martignoni A, Smith L, Setzer F, Bauer A, Hölzl J, Peter K, Christ F, Thiel M (2005) Strenuous physical exercise inhibits granulocyte activation induced at high altitude. J Appl Physiol 98:640–647.
8. Tamura DY, Moore EM, Partrick DA, Johnson JL, Offner PJ, Silliman CC (2002) Acute hypoxemia in humans enhances the neutrophil inflammatory response. Shock 17:269–273.
9. Wood JG, Johnson JS, Mattioli LF, Gonzalez NC (1999a) Systemic hypoxia promotes leukocyte-endothelial adherence via reactive oxidant generation. J Appl Physiol 87:1734–1740.
10. Agustí AG (2005) Systemic effects of chronic obstructive pulmonary disease. Proc Am Thorac Soc 2:367–370; discussion 371–2.
11. Gan WQ, Man SF, Senthilselvan A, Sin DD (2004) Association between chronic obstructive pulmonary disease and systemic inflammation: a systematic review and a meta-analysis. Thorax 59:574–580.
12. Dix R, Orth T, Allen J, Wood JG, Gonzalez NC (2003) Activation of mast cells by systemic hypoxia, but not by local hypoxia, mediates increased leukocyte-endothelial adherence in cremaster venules. J Appl Physiol 95:2495–2502.
13. Shah S, Allen J, Wood JG, Gonzalez NC (2003) Dissociation between microvascular PO_2 and hypoxia-induced microvascular inflammation. J Appl Physiol 94:2323–2329.
14. Mc Donald JT, Gonzalez NC, Wood JG (2003) Mast cell degranulation promotes the cerebral microvascular inflammatory response to hypoxia. (Abstract) FASEB J 17:A1282 (Abstract).
15. Wood JG, Mattioli LF, Gonzalez NC (1999b) Hypoxia causes leukocyte adherence to mesenteric venules in non-acclimatized rats but not after acclimatization. J Appl Physiol 86:873–881.
16. Steiner DR, Gonzalez NC, Wood JG (2003) Mast cells mediate the microvascular inflammatory response to hypoxia. J Appl Physiol 94:325–334.
17. Gonzalez NC, Allen J, Schmidt EJ, Casillan AJ, Orth T, Wood JG (2007b) Role of the renin-angiotensin system in the systemic microvascular inflammation of alveolar hypoxia. Am J Physiol Heart Circ Physiol 292:H2285–H2294.
18. Wood JG, Johnson JS, Mattioli LF, Gonzalez NC (2000) Systemic hypoxia increases leukocyte emigration and vascular permeability in conscious rats. J Appl Physiol 89:1561–1568.
19. Rumsey WL, Vandrkooi JM, Wilson DF (1988) Imaging of Phosphorescence: a novel method for measuring O_2 distribution in perfused tissue. Science 241:1649–1651.
20. Orth T, Allen J, Wood JG , Gonzalez NC (2005) Plasma from conscious hypoxic rats stimulates leukocyte-endothelial interactions in normoxic cremaster venules. J Appl Physiol 99:290–297.

21. Ishii H, Hayashi H, Hogg JC, Fujii T, Goto Y, Sakamoto N, Mukae H, Vincent R, Van Eeden S (2005) Alveolar macrophage-epithelial cell interaction following exposure to atmospheric particles induces the release of mediators involved in monocyte mobilization and recruitment. Resp Res 5:87–98.
22. Van Eeden DF, Tan WC, Suwa T, Mukae H, Terashima T, Fuji T, Qui D, Vincent R, Hogg JC (2001) Cytokines involved in the systemic inflammatory response induced by particulate matter air pollutants. Am J Respir Crit Care Med 164:826–830.
23. Van Rooijen N, Sanders A (1994). Liposome mediated depletion of macrophages: mechanism of action, preparation of liposomes and application. J Immunol Methods 174:83–93.
24. Gonzalez NC, Allen JA, Blanco VG, Schmidt EJ, van Rooijen N, Wood JW (2007a) Alveolar macrophages are necessary for the systemic inflammation of acute alveolar hypoxia. J Appl Physiol 103:1386–1394.

The Influence of Oxygen Supply, Hemorheology and Microcirculation in the Heart and Vascular Systems

Giuseppe Cicco and Sebastiano Cicco

Abstract The microcirculation is an important system, containing resistance arterioles, capillaries and venules, whose main function is to transport oxygen and nutrients to the tissues. Endothelial cells are the main cell types of the microcirculation; their homeostasis is modulated by constant shear stress. Altered hemorheology induces a change in the production of vasodilator and vasoconstrictor agents. The most important pattern inducing endothelium dysfunction is an increase in oxidative stress, which decreases the amount of nitric oxide and favors microvascular phlogosis. In this review we will consider the main scientific reports about the cardiovascular risk factors such as smoking, hypercholesterolemia, hyperviscosity, hypertension, diabetes, stress and increased homocysteine levels, all having as common etiopathogenetic factor alterations in microcirculation and in tissue oxygenation. We also focus on their influence on endothelial cells, inducing endothelial changes and dysfunction related to altered oxygen supply and linked to increased oxidative stress. Also important are endothelial stem cells, that are able to repair vascular endothelial damage, especially in cardiovascular patients, with or without endothelial dysfunction. Under these circumstances the numbers of these stem cells are altered, which means there is a decrease in regeneration capability (post ischaemia modified albumin, etc.). This could be an important negative prognostic factor. Microcirculation and tissue oxygenation are very important factors strongly linked to hemorheology, especially in cardiovascular patients, and their alterations could cause impairment, or initiate cardiovascular pathologies.

G. Cicco (✉)
C.E.M.O.T. – Interdepartmental Center of Research on Hemorheology, Microcirculation, Oxygen Transport and Non Invasive Optical Technologies, Università degli studi di Bari "Aldo Moro", Policlinico, Piazza G. Cesare, 11 70124 Bari, Italy
e-mail: gcicco.emo@tiscali.it

E. Takahashi, D.F. Bruley (eds.), *Oxygen Transport to Tissue XXXI*, Advances in Experimental Medicine and Biology 662,
DOI 10.1007/978-1-4419-1241-1_4, © Springer Science+Business Media, LLC 2010

1 Microcirculation Anatomy

Organs are not isolated islands in our body. They are all connected by a "big sea" and together compose the continent that we call the body. That "sea" is blood and the channels in which it flows is the circulation. To take what they need for their "life", organs need a microcirculation, which could be considered as an organ itself, being composed of the smallest blood vessels all over the body including resistance arterioles, capillaries and venules. Its most important function is the transport of oxygen to peripheral parts of the body and the removal of the CO_2 produced.

All mechanisms that regulate blood flow into the microcirculation are designed to ensure this transport function. In the intima the endothelial cell layer regulates coagulation, fibrinolysis and vasomotion. In the endothelial tunica there are muscular cells that modulate vascular contractility; in the adventitia tunica the connective tissue, nerves and capillaries provide mechanical shielding, innervation and nutrition to vessel walls respectively [1].

2 Endothelial Physiology

The main cell types of microcirculation are the endothelial cells, which form the inner lining of all blood vessels. A constant shear stress modulates vascular endothelium homeostasis, increased shear stress leading to a change in the secretion of vasodilator and vasoconstrictor agents. Increased oxidative stress is a major pathogenetic mechanism of endothelial dysfunction, causing decreased nitric oxide (NO) bioavailability and microvascular inflammation [2].

The endothelium contributes to the local balance between pro- and anti-inflammatory mediators, hemostatic balance, as well as vascular permeability and cell proliferation. Normal endothelium cells show vasodilator, anticoagulant and anti-adhesive properties, and release vasodilators (nitric oxide, prostacyclin) and vasoconstrictors (endothelin 1, thromboxane A2). NO is synthesized from the amino acid L-arginine in a reaction catalyzed by a family of enzymes called NO synthases (NOSs) requiring tetrahydrobiopterin (BH4) as co-factor; this leads to relaxation of smooth muscle cells by increasing intracellular cyclic guanosine-monophosphate levels [3, 4] (Fig. 1).

The endothelium modulates fibrinolysis, coagulation, vascular tone, leukocyte adhesion, platelet aggregation, vascular permeability, cell proliferation, and myocardial contractility. All these mediators are important for the living micro-circulatory homeostasis. Also produced are phlogosis mediators (interleukins), procoagulants (thromboxane A_2), anticoagulants (antithrombin – AT-III, heparin, plasminogen activator – PAF), vasodilators (NO), and vasoconstrictors (TXA_2, Endothelin ET-1) [5].

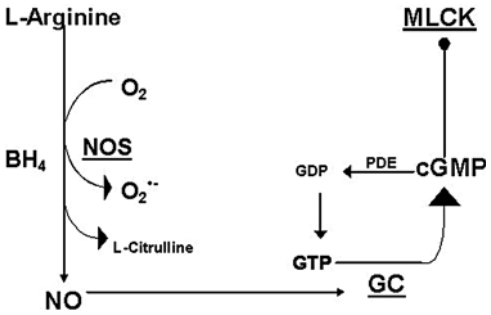

Fig. 1 NOS produces NO starting from L-Arginine and oxygen. NO stimulates the guanylyl cyclise (GC) function that increases cGMP production, which inhibits the Myosin Light Chain Kinase (MLCK) with the final result of relaxation of smooth muscle cells. Enzymes are *underlined*

3 Hemorheology and the Microcirculation

Interesting is the capability of the red cell (RBC) to pass through narrow capillaries. The diameter of arterioles is about 3.5 μm while the diameter of RBC is about 7 μm; RBC transit and oxygen transport to the cells is only possible due to RBCs being able to deform themselves.

The first experiments in hemorheology were performed in 1675 by Antoni von Leewenhoek (The Netherlands), who was the first to study the shape of RBCs with his newly developed microscope [6]. From these early experiments hemorheology has continued to develop and finally led to development of the Laser Assisted Optical Rotational Red Cell Analyzer (LORCA). This is a computerized instrument, served by a dedicated software, and able to detect RBC deformability (Elongation Index, EI) evaluated at different shear stresses from 0.3 to 30 Pascals (Pa), as well as RBC aggregability [7–9].

Shear stress influences the release of mediators by the endothelium, but also influences the possibility of RBCs to gain entrance into the smallest capillaries. Studying how RBCs deform themselves, using LORCA, enables us to understand potential problems with peripheral perfusion. Changes in RBC rheological properties are due to many factors, such as genetic defects, alterations in RBC metabolism, oxidative damage, micro-enviromental influences on RBC etc.; LORCA is able to investigate these.

Many types of changes can influence blood composition, such as alterations in hematocrit, increased number of leukocytes, and damage to plasma composition [10]. These changes can lead to altered aggregation, which can also result from changes in plasma composition, alterations in RBC deformability, and alterations in the surface properties of the RBCs.

4 Vessels and Oxidative Stress

Reactive Oxygen Species (ROS) and their derived Reactive Nitrogen Species (RNS) are synthesized in all vascular cells. It has been shown that an increase in ROS and RNS production induces damage such as hyper- cholesterolemia, diabetes, and hypertension [11, 12]. The most important species for the cardiovascular system is the superoxide anion (O_2^-). When this anion links itself with nitric oxide it produces the peroxinitrite ($ONOO^-$), which is the most toxic to cells.

Oxidative stress is physiologically present in our cells, but the scavenger system balances their production, to protect cells. In the presence of exogenous stimuli like smoking, diabetes, hypertension, hypercholesterolemia or stress, in combination with the physiological increase in oxidative stress due to age, scavengers are not able to protect cells, resulting in a net production of ROS and RNS. These anions react with lipoproteins, which starts an endothelial phlogosis, that damages endothelium, leading to atherosclerosis. One of the main effects of atherosclerosis is vascular remodelling, that increases the risk of a possible major event, such as infarction, aneurism or stroke. This is the reason why cardiologists consider smoking, hypercholesterolemia, hypertension and diabetes as major risk factors in infarct pathogenesis, and try to prevent infarction by reducing these risk factors [11–16].

Very important is the rarefaction and the desertification detected with capillaroscopy in some areas in vascular patients, especially hypertensives and cardiac patients. Karch et al. analyzing patients suffering from cardiac disease, showed that there were differences between the groups of hearts analyzed: the infarcted heart had the worst scenario compared with both controls and dilated hearts, with an increase in heart capillaries distance, an increase in cell diameter and a decrease in capillary density [17].

5 Microcirculation and the Heart

Capillary density (evaluated using computerized videocapillaroscopy) and spatial arrangement of capillaries are determinants in maintaining the balance between myocardial oxygen demand and supply. These indices may be seriously altered in patients with heart failure caused by idiopathic dilated cardiomyopathy, ischemic cardiomyopathy, or inflammatory cardiomyopathy. Cardiac remodelling includes changes in both the myocytes and the extracellular matrix. Dilated cardiomyopathy and ischemic cardiomyopathy are associated with apoptosis, myocyte hypertrophy, and increased interstitial fibrosis, ultimately leading to decreased capillary density, and thus to increased diffusion distances and impaired oxygen delivery to capillaries from myocytes.

Endothelial activation is the main cause of the vessel wall light phlogosis that ends in endothelial dysfunction. This dysfunction is not only related to

cardiovascular risk; tissue ischemia and a reduction of shear stress increase the oxidative stress. This, combined with the increase in cytosolic calcium (due to the ATP-K^+ channel block with the consequent depolarization and Ca^{2+} channel opening) this increases NO and $ONOO^-$ production with an alteration in the secretion of vasoconstrictors, an increase of the membrane oxidation, cell proliferation and leukocyte adhesion.

All the above mechanisms result in an increase of the risk of coagulation and of the possibility that platelets could clot on plaque. When this happens, the event that could increase damage to cells is ischemia. An obstructive thrombus is like a major accident on a motorway at rush hour. Due to the decreased arterial flow, blood can not arrive at the peripheral cells; these try to survive for some time before dying with tissue hypoxia, which occurs just before necrosis. The attempt to survive needs a metabolic switch from aerobic to anaerobic metabolism, causing a consequent increase in glycolisis producing enough energy to give ATP to the cell that dies after six hours. If revascularization can be achieved in time, functional failure of the stunned myocardium is reversible. However, if cells suffer more than they could repair the damage, they die with necrosis in contractile bands with the mitochondrial calcium phosphate (if the reperfusion is done within 40 min) or without. Thus, the heart could dilate its chambers with the consequent ventricular aneurism. In the case of non- reflow coagulative necrosis results.

Cells try to compensate for ischemic damage by producing pro-angiogenetic molecules like VEGF and FGF. These molecules stimulate the neoangiogenesis; but this mechanism is not useful in the heart. Revascularization is scarce in the heart and it happens only at the peripheral infarcted area close to the still functioning capillaries.

Garmy-Susini et al. showed that endothelial stem cells from bone marrow were able to repair vascular endothelial damage in systemic circulation [18]. Especially in cardiovascular patients with or without endothelial dysfunction, the number of these stem cells is decreased and this means that there is a decreased regeneration capability (post-infarction, decreased neoangiogenesis). This could also be an important negative prognostic factor. Thus, the use of endothelial stem cells injected directly into the infarcted area is the new clinical perspective.

6 Microcirculation and Pathology

When considering the role of microcirculation and its most important variables (vessels, haematocrit, blood viscosity), a current definition of the ischemic syndrome, could be that the resistance microvessels are not able to compensate for the effects of a decrease in perfusion pressure following stenosis and/or change in systemic blood pressure, with resulting impairment of the supply of nutrients and oxygen and the removal of catabolites. Besides

this physiopathologic role, the microcirculation, where exchange between vessels and tissues occurs has a very important role in inducing complications (i.e. renal damage, cardiac or cerebral damage) during hyper-tension, diabetes, vasculitis, immunological inflammatory syndromes; hyperviscosity syndromes, and cardiovascular risk factors such as hypercholesterolemia, age, smoking, etc [19].

Finally the microcirculation has an important etiopathogenetic role in venous ulcers, in vascular vertigo, in sepsis, in a good acceptance of organ transplantation, in cancer neoangiogenesis and in other pathologies. The study of the microcirculation and its hemorheology is a very large area of investigation with many clinical implications and fields of research. Due to its ability to alter oxygen supply and delivery in various tissues, the microcirculation is strongly linked to blood perfusion and tissue exchange.

References

1. Forconi S, Gori T, Lisi M (2006) Microcircolo; aspetti morfologici e funzionali; in Microangiologia 1:1–5.
2. Crimi E et al. (2007) Microcirculation and oxidative stress. Free Radic Res (41)12:1364–1375.
3. Galley HF, Webster NR (2004) Physiology of endothelium. Br J Anaesth 93(1):105–1113.
4. Casentino F, Luscher TF (1998) Tetrahydrobiopterin and endothelial function. Eur Heart J 19(Suppl G):G3–G8.
5. Gori T (2006) La disfunzione endoteliale; in Microangiologia 1:1–6.
6. Mokken CF (1996) *Clinical and Experimental Studies on Hemorheology*, *Elinkwisk bv. Ed.*, Historical aspects of hemorheology, Utrecht, The Netherlands.
7. Hardeman MR, Goedhart PT, Dobbe JGG, Lettinga KR (1994) Laser assisted optical rotational red cell analyzer (LORCA). Clin Hemorheol 14:605–618.
8. Hardeman MR, Goedhart PT, Shut NT (1994) Laser assisted optical rotational red cell analyzer (LORCA) II. Clin Hemorheol 14:619–630.
9. Cicco G (2006) Hemorheological in clinical and experimental practice. *Oxygen Transport to Tissue XXVII, Springer Edr*. NY AEMB 578:1–9.
10. Baskurt O (2007) Mechanisms of blood rheology alterations. O Baskurt, M Hardeman, M Rampling, H Meiselman, (eds) *Handbook of Hemorheology and Hemodynamics*, IOS Press, Amsterdam, The Netherlands.
11. Beckman JS, Koppenol WH (1996) Nitric Oxide, superoxide and peroxynitrite: the good, the bad and the ugly. Am J Physiol 271(5 Pt 1):C1424–C1437.
12. Munzel T, Daiber A, Ullrich V, Mulsch A (2005) Vascular consequences of endothelial nitric oxide synthase uncoupling for the activity and expression of the soluble guanylyl cyclise and cGMP-dependent protein kinase. Arteriosler Thromb Vasc Biol 25(8):1551–1557.
13. Fester BE, Tsao PS, Rockson SG (2003) Endothelial dysfunction: clinical strategies for treating oxidative stress. Am J Physiol 143(2):218–226.
14. Heitzer T, Schlinzing T, Krohn K, Meinrtz T, Munzel T (2001) Endothelial dysfunction, oxidative stress and risk of cardiovascular event in patients with coronary artery disease. Am J Cardiol 104(22):2673–2678.
15. Samuni A, Krishna CM, Mitchell JB, Collins CR, Russo A (1990) Superoxide reaction with nitroxides; Free Radic Res Commun 9(3–6):241–249.

16. Nakazono K, Watanabe N, Matsuno K, Sasaki J, Sato T, Inoue M (1991) Does superoxide underline the pathogenesis of hypertension? Proc Natl Acad Sci USA 88(22):10045–10048.
17. Karch R, Neumann F, Ullrich R et al (2005) The spatial pattern of coronary capillaries in patients with dilated, ischemic and inflammatory cardiomyopathy. Cardiovasc Pathol 14:135–144.
18. Garmy-Susini B, Varner JA (2005) Circulating endothelial progenitor cells. Br J Cancer 93:855–858.
19. Cicco G (2007) Hemorheological aspects in the microvasculature of several pathologies. *Oxygen Transport to Tissue XXVIII, Springer Edr*. NY AEMB 599:7–15.

Could Dilated Cardiomyopathy Alter the Peripheral Microcirculation and Blood Rheology?

Giuseppe Cicco, Valeria Fanelli, Sebastiano Cicco, Massimo Iacoviello, and Stefano Favale

Abstract Our aim was to perform a preliminary study of blood flow in the peripheral microcirculation in patients with heart failure. Cardiac patients were investigated to establish possible microcirculatory changes due to this pathology. We evaluated 16 patients (non-smokers, dislipidemic with hypercholesterolemia), receiving oral treatment and in NYHA class 2.3 ± 0.5. A dilated cardiomyopathy (DCM) group was evaluated before cardiac resynchronization therapy (CRT) obtained by biventricular intra-cardiac defibrillator (ICD) implantation, and again 3 months after its implantation. We measured the ejection fraction (EF), peripheral blood flow (using laser Doppler) at the left wrist on the volar side, capillary morphology (using computerized videocapillaroscopy) on the nail bed of the 4th finger of the left hand, rheological status (using the LORCA), as well as hematocrit, hemoglobin concentration, red blood cell (RBC) surface acetylcholinesterase (AchE), and homocysteine. Our data show that in the DCM vs. control group, peripheral flow did not depend only on the heart: throughout the study, blood flow did not change significantly compared to controls and was increased after CRT. There was no decrease in aggregation time. The blood flow did not alter RBC deformability or RBC surface AchE. Due to the lower oxygenation and to a non-significant increase in the number of capillaries after CRT, DCM patients are at higher cardiovascular risk than healthy subjects.

1 Introduction

The heart is the "primum movens" of the blood. And its work is necessary to push the red blood cells (RBC) into vessels and microvessels. Pathology of the heart might influence this mechanism at the source of motion.

G. Cicco (✉)
C.E.M.O.T. – Interdepartmental Center of Research on Hemorheology, Microcirculation, Oxygen Transport and Non Invasive Optical Technologies, Università degli studi di Bari "Aldo Moro", Policlinico, Piazza G. Cesare, 11 70124 Bari, Italy
e-mail: gcicco.emo@tiscali.it

E. Takahashi, D.F. Bruley (eds.), *Oxygen Transport to Tissue XXXI*, Advances in Experimental Medicine and Biology 662,
DOI 10.1007/978-1-4419-1241-1_5, © Springer Science+Business Media, LLC 2010

To investigate blood rheology and microcirculation an important point is to consider how blood can arrive in the microvasculature; in fact, if the source of motion does not work well, the microcirculation might also suffer.

As Turchetti et al. [1] have shown, cardiological pathologies also interfere with blood rheology, with a decrease in blood deformability. Starting from these considerations, we wanted to explore the microcirculatory situation in patients suffering heart pathology.

The possibility that heart failure could also interfere with the RBC structure idea needs to be thoroughly investigated because a combination of heart pathology and changes in RBC could be dangerous for the patient. Impairment between blood demand and heart work could also interfere with oxygen demand and supply, and this could aggravate the peripheral oxygenation and metabolism. Finally lower blood flow could aggravate a bad peripheral situation; this hypothesis also needs to be investigated.

For our initial investigation we chose patients with dilated cardiomyopathy (DCM). These patients suffer from an organ pathology that is not related to microvessel status as is, for example, infarction. In fact patients with DCM have heart dysfunction due to a variety of causes (e.g. idiopathic, alcoholism, etc) not related to vessel status.

2 Material and Methods

Criteria for entry into the study were an ejection fraction (EF) of $<35\%$ and the absence of previous myocardial infarction. Of the 126 patients with DCM evaluated using echo–color–Doppler since 2006, only 16 patients (14 males) fitted the criteria. They were aged 58 ± 11 years, had a low mean EF ($26 \pm 4\%$) and were in NYHA class 2.3 ± 0.5. They were non-smokers, with low cholesterolemia due to pharmacological therapy (statins, 40 mg per day) they had received before their first examination and confirmed by us (Table 1). They needed to have cardiac resynchronization therapy (CRT) to extend their life, and to improve the EF, which was obtained by implantation of a biventricular intracardiac defibrillator (ICD). These patients were examined before ICD implantation and again 3 months later. Medical therapy included: ACE inhibitors, β-blockers, sartans and oral anticoagulants following INR values.

These 16 patients were compared with 10 healthy controls (6 males), non-smokers, with no vascular and cardiac pathologies, with no work limitations, and taking no medication (Table 1).

To investigate blood flow we used a laser Doppler (Periflux 5010/5020, Periflux combined system, Perimed, Sweden); the laser Doppler pole was placed on the skin of the volar face of the left wrist. Transcutaneous tissue oxygen partial pressure ($TcpO_2$) was also evaluated using a Combi sensor placed on the skin of the left forearm at the medium third of its volar face (Periflux 5040, Periflux combined system, Perimed, Sweden). Blood flow and $TcpO_2$ were

Table 1 Data on groups studied

		DCM		
		Before CRT	After CRT	Controls
Number		16 (14 M)		10 (6 M)
Age		53 ± 11		38 ± 11
Smokers		No		No
Mean arterial pressure	(mmHg ± SD)	101.8 ± 4.7	90.7 ± 9.2	88.2 ± 17.4
Ejection fraction	(%±SD)	26 ± 4	40 ± 10	
NYHA class		2.3 ± 0.5		
Hb	(mg/dl ± SD)	14.4 ± 1.5	13.8 ± 1.2	14.1 ± 1.4
Hematocrit	(% ± SD)	40.6 ± 4.0	40.3 ± 3.3	41.2 ± 2.6
LDL	(mg/dl ± SD)	101.6 ± 39.6	105.2 ± 42.2	100.7 ± 6.9
HDL	(mg/dl ± SD)	42.6 ± 7.6	41.5 ± 8.9	43.4 ± 2.4
Homocysteine	(ng/dl ± SD)	11.8 ± 5.9	11.3 ± 3.2	9.5 ± 2.2

measured many times. We waited 10 min in order to calibrate and establish the values. After this we measured the basal value (T_0) for 60 s. For the organ pathology under study it was important to establish change in blood flow and $TcpO_2$ during muscle work; therefore, we evaluated blood flow during hand motion for 30 s (T_1) and blood flow after motion for 15 s (T_2), tracking the values after 5 s from the end of the hand motion ($T_{1\text{-}2}$). We repeated the same measurements at the second examination, but then we also evaluated blood flow and $TcpO_2$ response when warming-up the skin temperature with the Periflux 5010/5020 probe. We evaluated blood flow and $TcpO_2$ for 120 s while skin temperature was at 44°C (T_3) and blood flow after heating for 90 s (T_4) with 210 s between T_3 and T_4 (Table 2).

Table 2 Overview of the periflux time steps (in seconds)

600	**60**	**30**	**30**	**5**	**15**	**65**	**120**	**210**	**90**
Calibr.	Basal (T_0)		Hand motion (T_1)		After motion (T_2)		Skin temp 44°C (T_3)		After heat (T_4)

To evaluate microvessel morphology at both visits we used computerized videocapillaroscopy (Videocap, Mitsubishi, Japan) at both visits was performed on the nail bed of the fourth finger of the left hand (taking 5 pictures) and we established an average value for each patient for the number of capillaries, and of tortuosity and ectasia. Both the capillaroscopy and Periflux measurements were done in a temperature-controlled room (24°C).

Rheological, changes were detected using the LORCA system (Mechatronics, NL) at both examination times. Using this instrument we evaluated RBC deformability expressed as the Elongation Index (EI_{30Pa}) at 30 Pa shear stress.

This was done using a 125 μl EDTA blood sample in 3 ml PVP (polyvinyl pyrrolidone). We also evaluated RBC aggregability as the half-time (t½ in seconds) needed to form clots in the LORCA cup. To evaluate the RBC surface, using on the Li-heparin blood sample, we determined the surface acetylcholine esterase (AchEs) concentration as the absorption difference between the first and the sixth evaluation on the single sample at both examination times.

As laboratory routine we evaluated hemoglobin (Hb) concentration, hematocrit and LDL and HDL concentration (Table 1). We also evaluated the serum fibrinogen and homocysteine levels. All statistical analyses were done with Student's *t*-tests; significance was considered at p-values less than 0.05.

3 Results

In the DCM group the ejection fraction (EF) after CRT was significantly increased (25.85 ± 4% before RCT vs. 40 ± 10% after the treatment; $p < 0.001$).

We also found an increase in basal values of the blood flow (T_0) after CRT in basal values (T_0) (before 15 ± 5 vs. after 21 ± 3 Perfusion Units (PU), $p < 0.009$). Also, during hand motion (T_1) there was a significant increase in blood flow values (before 55 ± 23 vs. after 86 ± 47 PU; $p < 0.02$), whereas there was no significant difference when comparing blood flow after hand motion (T_2) before and after CRT. Instead, before and after CRT, basal flow (T_0) and after motion (T_2) the values of the DCM group were not significantly changed if compared to the control group, while the DCM hand motion values (T_1) compared to controls were significantly decreased at the first examination (DCM before CRT 55 ± 23 vs. controls 110 ± 37 PU; $p < 0.001$). These values (T_1) were not significantly decreased at the second examination (DCM after CRT 86 ± 47 vs. controls 110 ± 37 PU). Due to the patients critical physical condition at the first examination it was not possible to collect data on blood flow influenced by heat (44°C) at that time. Therefore, we compared the blood flow response after heat stress compared to the blood flow value after motion. We found an increase due to heat (DCM after CRT T_2 18.6 ± 8.9 vs. DCM after CRT T_4 41.7 ± 28.2 PU; $p < 0.004$). Comparing values after heat stress (T_4) between the DCM group and controls there was no significant difference (DCM T_4 41.7 ± 28.2 vs. control T_4 58.7 ± 15.9 PU; n. s.). Regarding oxygenation ($TcpO_2$) there was no significant difference (p = n.s.) before and after CRT (T_0 Before 74 ± 15 vs. After 72 ± 19 mmHg; T_1 Before 75 ± 13 vs. After 74 ± 17 mmHg; T_2 Before 76 ± 13 vs. After 74 ± 16 mmHg). Instead, comparing values of the DMC group to the controls there was a significant decrease in $TcpO_2$ in DCM before and after CRT compared to controls, at basal $TcpO_2$ (DCM Before CRT 74 ± 15 vs. controls 99 ± 16 mmHg, $p < 0.001$; DCM after CRT 72 ± 19 vs. controls 99 ± 16 mmHg, $p < 0.002$), during motion (DCM before CRT 75 ± 13 vs. controls 98 ± 14 mmHg, $p < 0.003$; DCM after CRT 74 ± 17 vs. controls 98 ± 14 mmHg,

$p < 0.001$) and after motion (DCM after CRT 76 ± 13 vs. controls 98 ± 15 mmHg, $p < 0.001$; DCM After CRT 74 ± 16 vs. controls 98 ± 15 mmHg, $p < 0.002$).Investigating the morphology of the microvessels with computerized videocapillaroscopy we found a significant decrease in the number of capillaries compared to controls both before and after CRT (DCM before CRT 9.6 ± 2 vs. controls 11.56 ± 2, $p < 0.02$; DCM after CRT 9.6 ± 2.2 vs. controls 11.56 ± 2, $p < 0.02$). Capillary morphology was significantly changed. In fact the number of ectasi and tortuosities were significantly increased when comparing values before and after CRT values to the controls (ectasia: DCM before CRT 6.4 ± 1.9 vs. controls 1.1 ± 0.5, $p < 0.001$; DCM after CRT 6.5 ± 2.1 vs. controls 1.1 ± 0.5, $p < 0.0009$; Tortuosities: DCM before CRT 8.4 ± 2.3 vs. controls 3.0 ± 1.3, $p < 0.001$; DCM after CRT 8.5 ± 2.2 vs. controls 3.0 ± 1.3, $p < 0.002$).

Laboratory data showed no significant change when comparing the values before and after CRT (hematocrit: DCM before CRT 14.4 ± 1.5 vs. after CRT 13.8 ± 1.2 mg/dl; hemoglobin: DCM before CRT 40.6 ± 4.0 vs. after CRT 40.3 ± 3.3%).

RBC surface AchEs, homocysteine and RBC deformability (EI_{30}) and RBC aggregability (t ½) also showed no significant change when comparing the data on DCM before vs. after CRT and comparing the DCM values with controls. Only fibrinogen was significantly decreased (before 335 ± 63 vs. after 277 ± 45 mg/dl; $p < 0.006$) after therapy; we assume this result is due to the medical therapy that patients had received during the 3 months between the two examination times.

4 Discussion

Our aim was to explore the relationship between the heart and peripheral microcirculation. In recent years studies on heart pathology have mainly focused on organ status and few researchers have explored heart microcirculation alone: many being predominantly interested in the pharmacological response. The main difficulty is related to the location of the heart, therefore in vivo studies must evaluate indirect parameters such as the VO_2 peak in the mask during cycloergometry. Using this parameter Baravelli et al. [2] evaluated dilated cardiomyopathy. Studing NYHA class II-III patients (as we did), they noted that the peak VO_2 associated with the ECG T-wave evaluation could be used as a prognostic factor of heart function in the prediction of heart failure. They demonstrated that cardiac events were more likely to occur in patients that have an altered T-wave combined with a decreased peak.

On the other hand, the peripheral microcirculation could also suffer due to the DCM status, and this might aggravate peripheral pathologies. In fact an ischemic status could initiate damage (such as stroke, diabetic damage to the retina or legs, tumors, etc.). In the present study, we noted a reduction in transcutaneous tissue oxygenation ($TcpO_2$) compared to controls, suggesting

that these patients have a difficult O_2 exchange in the micro-vasculature in all situations, also after CRT. In fact there is a reduction in peripheral oxygenation that does not increase with an increase of the EF. Kronenberg et al. [3], using positron emission tomography, determined the carbon-11-acetate in myocardium, and stressed that cardiac mitochondria suffer from an altered metabolism. They hypothesized that the suffering mitochondria could be smaller or inefficient. This situation could also interfere with the vascular metabolism and could modify the vasa vasorum morphology.

Following the above hypothesis Karch et al. [4] analyzed different pathological hearts after biopsy or autopsy. They demonstrated that the coronary microcirculation was changed: the microvessels analyzed were smaller in diameter, had an increased distance between them, and there was an altered architecture. This information is important, because it presents another problem to be investigated i.e. what is the state of the peripheral microvessel morphology and architecture? To explore this, we used videocapillaroscopy. Analyzing a standard area we analyze of the fourth finger of the left hand, and, to reduce possible interpersonal variability we averaged the values of the images to reduce possible interpersonal variability. We also showed that in patients with a DCM there was vascular remodelling-vessels in DCM were winding and with ectasia, reduced in number and often they were not well perfused with blood.

An important function of the heart is to push blood into vessels. Heart failure reduces the amount of blood that every contraction pushes into the aorta: thus it is possible that reduced $TcpO_2$ might be due to the reduced blood flow at the end of the capillaries. Laser Doppler data do not confirm this, but demonstrated that the response to muscle stress is lower in patients that have not received CRT. However, blood flow was significantly increased after CRT in DCM patients at basal time (T_0). The values at this point were not significantly different from controls, while the data show that blood flow values are significantly decreased in T_1, while the ejection recovery decreased the difference versus controls.

The $TcpO_2$ values do not normalize after 3 months of CRT. In the DCM groups, at the first examination it was not possible to do the heat stress test due to the patients' critical status. At the second examination we performed the test to gain insight into the neurological response during heart pathology. This test revealed a good and maintained, as in controls; this underlines that neurological flow maintenance is well preserved. RBCs, on the other hand, did not show modifications: we did not find any significant alterations compared to controls in the tested parameters (as elongation, aggregation, hemoglobin concentration, hematocrit and AchEs). This suggests again that reduced $TcpO_2$ is a consequence of a reduced VO_2 peak that, combined with the reduced blood flow could present its bill during muscle activity. At the end, the peripheral microcirculation continues to suffer from the heart pathology, also after CRT [5–11].

5 Conclusion

Our data show that heart failure puts the microvasculature in a bad situation: it must support blood flow while suffering from reduced flow itself. CRT and the medical therapy we provided to patients were unsuccessful in increasing the $TcpO_2$ by increasing blood flow. In fact an increase of the EF and of blood flow does not correspond with an increase in oxygenation. This might be due to the altered microvascular morphology that we revealed. RBCs do not suffer from the low $TcpO_2$ and maintain their plasticity, an important characteristic necessary for transit of the capillary lumen, but this is insufficient in the presence of low oxygenation or the presence of longer microcirculatory pathways bringing nutrients to cells.

References

1. V. Turchetti, L. Boschi, G. Donati, L. Tribalzini, S. Forconi, Impact of hemorheological and endothelial factors on microcirculation. Oxygen Transport to Tissue XXVI Springer NY, Adv Exp Med Biol 578, 107–112 (2006).
2. M. Baravelli, C. Fantoni, S. Rogiani et al. Combined prognostic value of peak O_2 uptake and microvolt level T-wave alternant in patients with idiopathic dilated cardiomyopathy. Int J Cardiol, Elsevier 121, 23–29 (2007).
3. M. Kronenberg, G. Cohen, M. Leonen et al. Myocardial oxidative metabolic supply demand relationships in patients with nonischemic dilated cardiomyopathy. J Nucl Cardiol 13(4), 544–553 (2006).
4. R. Karch, F. Neumann, R. Ullrich et al. The spatial pattern of coronary capillaries in patients with dilated, ischemic and inflammatory cardiomyopathy. Cardiovasc Pathol 14, 135–144 (2005).
5. K. Lyabakh, I. Mankovskaya, Role of differences in microcirculatory blood flow velocity in optimizing parameters of skeletal muscle oxygen model. Oxygen Transport to Tissue XXVII, Springer NY Adv Exp Med Biol 578, 81–86 (2006).
6. K. Sato, T. Komaru, H. Shioiri et al. Hypertcholesterolemia impairs transduction of vasodilator signals derived from ischemic myocardium: myocardium-microvessel crosstalk. Arterioscler Thromb Vasc Biol 24, 2034–2039 (2004).
7. A. Salvetti, S. Taddei, L'endotelio, fisiopatologia e valore clinico; Monografie di Cardiologia (2002).
8. E. Crimi et al., Microcirculation and oxidative stress. Free Radic Res 41(12), 1364–1375 (2007).
9. G. Cicco, Hemorheological aspects in the microvasculature of several pathologies. Oxygen Transport to Tissue XXVIII, Springer NY Adv Exp Med Biol 599, 7–15 (2007).
10. S. Forconi, T. Gori, M. Lisi, Microangiologia, (2006).
11. O. Baskurt, M. Hardeman, M. Rampling, H. Meiselman, Handbook of hemorheology and hemodynamics, IOS Press, Amsterdam, The Netherlands (2007).

The Role of Glyoxalase System in Renal Hypoxia

Reiko Inagi, Takanori Kumagai, Toshiro Fujita, and Masaomi Nangaku

Abstract Methylglyoxal (MG), a highly reactive α-oxoaldehyde generated by oxidation of carbohydrate and glycolysis, binds to proteins and forms advanced glycation end products (AGE). MG and MG adducts have been implicated in oxidative stress-related diseases, therefore, MG detoxifying system such as the glyoxalase system (glyoxalase I) also contributes to progression of these diseases. Recent papers have emphasized the pathophysiological effects of MG and the glyoxalase system in acute hypoxic injury, which is associated with acute oxidative stress. We investigated the kinetics of MG level and glyoxalase I activity in renal acute hypoxic injury induced by ischemia-reperfusion (I/R). I/R induced tubulointerstitial injury and the histological changes were associated with a significant decrease in renal glyoxalase I activity and an increase in MG level in the damaged tubular cells. Of note, rats over expressing human glyoxalase I showed amelioration of I/R-induced histological and functional damages and it was associated with a decrease in MG level in the lesion resulting in reduction of oxidative stress and tubular cell apoptosis. In conclusion, glyoxalase I has renoprotective effects in renal hypoxia such as I/R injury via a reduction in cytotoxic MG level in tubular cells.

1 Hypoxia in the Kidney

Cells convert biochemical energy from nutrients into adenosine triphosphate (ATP). Organisms that use oxygen as a final electron acceptor in respiration are described as aerobic. Aerobic metabolism is approximately 19 times more efficient than anaerobic metabolism. Therefore, under hypoxic conditions, cells suffer from ATP deficiency. Furthermore, hypoxic conditions are associated with oxidative stress. While previous studies demonstrated oxidative

R. Inagi (✉)
Division of Nephrology and Endocrinology, University of Tokyo School of Medicine,
7-3-1 Hongo, Bunkyo-ku, Tokyo, 113-8655, Japan
e-mail: inagi-npr@umin.ac.jp

E. Takahashi, D.F. Bruley (eds.), *Oxygen Transport to Tissue XXXI*,
Advances in Experimental Medicine and Biology 662,
DOI 10.1007/978-1-4419-1241-1_6, © Springer Science+Business Media, LLC 2010

stress as excessive production of reactive oxygen species (ROS) under hyperoxic conditions, the current consensus is that oxidative stress is observed whenever oxygen homeostasis is disrupted and can be demonstrated both in hyper- and hypoxia.

A decrease in oxygen tension plays a major role in a variety of kidney diseases. Acute hypoxia causes acute kidney failure, which has remained a significant health concern with high mortality rates. The most common cause of human acute renal failure is ischemia due to hypotension or sepsis. Also in kidney trans-plantation, ischemia-reperfusion (I/R) injury is the significant problem. Recent papers have emphasized the pathological effects of hypoxia not only in acute renal failure but also in chronic kidney diseases: chronic hypoxia in diabetic nephropa-thy, hypertension, and chronic glomerulonephritis is a final common pathway to end-stage renal disease [1]. This background indicates the clinical importance of renal hypoxic injury.

The cellular response to hypoxia is centered on hypoxia-inducible factor, HIF. This factor is composed of two subunits, an oxygen-sensitive HIF-α subunit and a constitutively expressed HIF-β subunit. Intracellular accumulation of HIF induces the coordinated expression of a number of adaptive genes against hypoxic insult, such as the genes related to glucose metabolism, hematopoiesis, and angiogenesis. Three isoforms of HIF-α subunits have been identified, HIF-1α, HIF-2α, and HIF-3α. HIF-1 is ubiquitously distributed and shows protective effects to tubulointerstitial damage induced by I/R or hyperglycemia [2, 3]. HIF-2α is involved in the regulation of erythropoietin as well as oxidative stress in the renal endothelium and interstitium [4]. Little is known about HIF-3, but it is likely that HIF-3 serves as an inhibitory role because HIF-3 lacks activation domains [5].

2 Role of Methylglyoxal (MG), a Precursor of Protein Glycation, in Hypoxic Injury

Hypoxia is associated with oxidative stress as described above. Under the oxidative stress, proteins are posttranslationally modified by phosphorylation, carbonylation, or glycation in an enzyme dependent or independent manner. These posttranslational protein modifications contribute to the development of the various manifestations of oxidative stress-related diseases. In fact, phosphorylation induced by oxidative stress causes intracellular signaling resulting in cell death in-cluding apoptosis, cell proliferation, and inflammation. Protein carbonylation or glycation leads to their conformational modification and thereby induces loss of their original physiological activities and/or gain of pathogenic functions, one of which accelerates the vicious cycle of oxidative stress and hypoxia.

In glycation, methylglyoxal (MG) is one of the major precursors to form advanced glycation endproducts (AGE) as unfavorable byproducts of various

metabolic pathways. MG is generated from the oxidation of carbohydrates or gly-colysis, and increased oxidative stress is associated with conditions of increased MG. MG serves as a highly reactive carbonyl compound, binding not only to pro-teins but also to DNA with subsequent modification of these molecules to form AGE, which exert multiple and diverse pathological effects through the binding to receptor for AGE, RAGE. Furthermore, MG itself is cytotoxic and pro-apoptotic. MG selectively inhibits mitochondrial respiration and glycolysis in the cells [6, 7]. In relation to this, MG has been shown to inactivate membrane ATPases and glyceraldehyde-3-phosphate dehydrogenase, a key enzyme of the glycolytic pathway [8]. MG induces apoptosis via c-Jun N-terminal kinase (JNK) activation or through activation of protein kinase Cδ [9, 10]. Co-treatment with concentrations of MG and glucose comparable to those seen in the blood circulation of diabetes causes cell apoptosis or necrosis with an increase in the ROS content in cultured human endothelial cells [11].

MG has been implicated with various diseases related to oxidative stress including diabetes mellitus, diabetic complications such as vascular and renal diseases, chronic renal failure, neuronal disease, hypertension, and aging. Recent studies demonstrate that MG and MG-arginine adducts are accumulated in the heart and brain damaged by I/R, respectively, suggesting the diverse pathogenic contribution of MG not only in the chronic diseases but also in the acute diseases including hypoxia [12, 13]. In diabetes, hyperglycemic condition triggers MG production due to the change of glucose metabolism and/or hyperglycemia-mediated oxidative stress. However, the precise mechanism of MG and MG adducts accumulation under hypoxic condition is not defined.

3 Glyoxalase System for Detoxification of MG and its Pathophysiology

Cells are endowed with the system that efficiently metabolizes and detoxifies MG, i.e. the glyoxalase system. The glyoxalase system is composed of two enzymes: glyoxalase I, which metabolizes MG to S-D-lactoylglutathione, and glyoxalase II, which converts S-D-lactoylglutathione to D-lactate [14]. The glyoxalase system is ubiquitously expressed and is well conserved in many species, suggesting the biological importance of this system. Glyoxalase I prevents the accumulation of not only MG but also other reactive α-oxoaldehydes including glyoxal, therefore, it is a key enzyme in the glycation defense system. The glyoxalase I activity requires the cofactor, reduced glutathione (GSH), indicating that the glycation defense activity is regulated not only by transcriptional status but also by redox status.

The glyoxalase system, especially glyoxalase I, plays an important role in the regulation of the MG level in the body. Therefore, a decrease in glyoxalase I, which enhances MG production and MG adducts accumulation, might be one

of the risk factors of MG-related disease progression. Increasing evidence suggests the pathophysiological significance of glyoxalase I in diabetes mellitus, diabetic complications such as retinopathy and nephropathy, Alzheimer disease, anxiety, tumor, and aging. We previously demonstrated that one 69-year-old female patient who had been on hemodialysis for three years and had suffered from recurrent cardiovascular complications despite the absence of significant risk factors showed the deficiency of glyoxalase I activity with high levels of glycated proteins accumulation in plasma [15].

Many investigations indicate the protective role of glyoxalase I as a MG detoxifying enzyme in hyperglycemic condition. Proteomic analysis of glomeruli obtained from type 2 diabetic mice showed increased expression of glyoxalase I. However, renal cortical glyoxalase I activity was decreased in these mice because of a decrease in its cofactor, GSH [16]. Thus, it is likely that the increased expression of glyoxalase I may represent an insufficient adaptive response to increased MG formation in diabetic kidneys. These results were consistent with another paper demonstrating that glyoxalase I overexpression in endothelial cells ameliorated MG formation, along with intracellular AGE accumulation, thereby prevented increased macromolecular endocytosis under hyperglycemic conditions [17].

Relationship between glyoxalase I and aging was emphasized by the re-cent study demonstrating that C. elegans overexpressing glyoxalase I decreased MG modifications of mitochondrial proteins and mitochondrial ROS production with subsequent prolongation of lifespan [18].

In solid tumors, malignant cells suffer from stress conditions, such as glucose starvation and hypoxia. Glyoxalase I is often elevated in drug- and apoptosis-resistant cancers, demonstrating the adaptive effects of glyoxalase I as a detoxifying enzyme in tumor cell survival [19].

4 Renoprotective Effect of Glyoxalase I in Hypoxic Injury

MG and the glyoxalase system have been implicated in oxidative stress-related diseases as described above. However, their pathogenic contribution to kidney suffering from oxidative stress via acute hypoxia remains elusive. While many previous reports emphasized a pathogenic role of MG mainly in chronic disorders, recent studies suggested the involvement of MG in acute diseases such as I/R injury. MG content is increased in the I/R heart associated with the accumulation of AGE, Nϵ-carboxymethyl lysine (CML) [13]. In I/R injury of the brain, MG-arginine adducts, argpyrimidine, is detected after 24 h reoxygenation [12].

To evaluate the pathological effects of MG and glyoxalase I in acute renal injury due to hypoxia, we investigated a role of the glyoxalase system in this injury. We examined the kinetics of glyoxalase I activity in a rat renal I/R model and found that I/R significantly induced a decrease in renal glyoxalase I activity

without any changes in its mRNA or protein level and in a manner independent of GHS level. The decreased glyoxalase I activity was associated with an increase in its substrate, MG: MG level estimated by MG-lysine adducts (Nϵ-carboxyethyl lysine, CEL) accumulation was significantly increased in the tubulointerstitial lesion [20]. Our preliminary data demonstrated that renal I/R causes the lowering of gly-oxalase I activity resulting in MG accumulation in the tubular lesion. It strongly suggests a contribution of glyoxalase I in development of the I/R injury.

MG is not only an AGE precursor leading to the vicious cycle of oxidative stress and glycation but also cytotoxic and pro-apoptotic [9, 10]. Therefore, from a theoretical point of view, glyoxalase I might be a key factor for detoxifying MG and protecting organs against I/R injury. To test this hypothesis, we established transgenic rats overexpressing glyoxalase I in the kidney [21]. We observed that the rats overexpressing glyoxalase I were resistant against I/R injury at pathological and functional level in the kidney [20]. In particular, I/R-induced decrease in glyoxalase I was prevented by glyoxalase I overexpression and it was associated with reduction of an increased MG level by I/R. The pathological improvement included a significant reduction of lipid peroxidation and tubular cell apoptosis.

HIF is a master gene switch of adaptive responses against hypoxia. Recent studies showed that HIF function is impaired by ROS-induced modification of HIF-α subunit by MG in cultured fibroblasts. HIF-α subunit modification by MG reduced heterodimer formation and HIF-α binding to all relevant promoters [22]. Glyoxalase I overexpression prevented these MG-modified HIF. Thus, in addition to the cytotoxic and pro-apoptotic effects by MG, MG can aggravate tissue injury in ischemic injury via impairment of a defensive mechanism in ischemia. The glyoxalase system is expected to restore the defense against hypoxia.

5 Conclusion

Recent accumulating reports have demonstrated that MG and the glyoxalase system contribute to the development of acute hypoxic injury. Our studies also support their pathophysiological effects in I/R-injured kidney: glyoxalase I activity is lowered by I/R and thereby leads to an increase in MG level in the damaged tubular cells and augments the disease manifestations mediated by cytotoxic MG including exacerbation of oxidative stress and apoptosis. Overexpression of glyoxalase I reduces I/R-induced renal MG accumulation and improves the renal damage, giving an important insight into understanding the pathophysiology of acute hypoxic injury.

Acknowledgments This work was supported by Grants-in-Aid for Scientific Research from Japan Society for the Promotion of Science (19590939 to RI and 19390228 to MN).

References

1. Nangaku M (2006) Chronic hypoxia and tubulointerstitial injury: a final common pathway to end-stage renal failure. J Am Soc Nephrol 17:17–25.
2. Matsumoto M, Makino Y, Tanaka T et al. (2003) Induction of renoprotective gene expression by cobalt ameliorates ischemic injury of the kidney in rats. J Am Soc Nephrol 14:1825–1832.
3. Ohtomo S, Nangaku M, Izuhara Y et al. (2008) Cobalt ameliorates renal injury in an obese, hypertensive type 2 diabetes rat model. Nephrol Dial Transplant 23:1166–1172.
4. Kojima I, Tanaka T, Inagi R et al. (2007) Protective role of hypoxia-inducible factor-2alpha against ischemic damage and oxidative stress in the kidney. J Am Soc Nephrol 18:1218–1226.
5. Makino Y, Cao R, Svensson K et al. (2001) Inhibitory PAS domain protein is a negative regulator of hypoxia-inducible gene expression. Nature 414:550–554.
6. Biswas S, Ray M, Misra S et al. (1997) Selective inhibition of mitochondrial respiration and glycolysis in human leukaemic leucocytes by methylglyoxal. Biochem J 323:343–348.
7. de Arriba SG, Stuchbury G, Yarin J et al. (2007) Methylglyoxal impairs glucose metabolism and leads to energy depletion in neuronal cells. Neurobiol Aging 28:1044–1050.
8. Halder J, Ray M, Ray S (1993) Inhibition of glycolysis and mitochondrial respiration of Ehrlich ascites carcinoma cells by methylglyoxal. Int J Can-cer 54:443–449.
9. Chan WH, Wu HJ, Shiao NH (2007) Apoptotic signaling in methylglyoxal-treated human osteoblasts involves oxidative stress, c-Jun N-terminal kinase, caspase-3, and p21-activated kinase 2. J Cell Biochem 100:1056–1069.
10. Godbout JP, Pesavento J, Hartman ME et al. (2002) Methylglyoxal enhances cisplatin-induced cytotoxicity by activating protein kinase C delta. J Biol Chem 277:2554–2561.
11. Chan WH, Wu HJ (2008) Methylglyoxal and high glucose co-treatment induces apoptosis or necrosis in human umbilical vein endothelial cells. J Cell Biochem 103:1144–1157.
12. Oya T, Hattori N, Mizuno Y et al. (1999) Methylglyoxal modification of protein. Chemical and immunochemical characterization of methylglyoxal-arginine adducts. J Biol Chem 274:18492–18502.
13. Bucciarelli LG, Kaneko M, Ananthakrishnan R et al. (2006) Receptor for advanced-glycation end products: key modulator of myocardial ischemic injury. Circulation 113:1226–34.
14. Thornalley PJ (2003) Glyoxalase I–structure, function and a critical role in the enzymatic defence against glycation. Biochem Soc Trans 31:1343–1348 Review.
15. Miyata T, van Ypersele de Strihou C, Imasawa T et al. (2001) Glyoxalase I deficiency is associated with an unusual level of advanced glycation end products in a hemodialysis patient. Kidney Int 60:2351–1359.
16. Barati MT, Merchant ML, Kain AB et al. (2007) Proteomic analysis defines altered cellular redox pathways and advanced glycation end-product metabolism in glomeruli of db/db diabetic mice. Am J Physiol Renal Physiol 293:F1157–F1165.
17. Shinohara M, Thornalley PJ, Giardino I et al. (1998) Overexpression of glyoxalase-I in bovine endothelial cells inhibits intracellular advanced glycation endproduct formation and prevents hyperglycemia-induced increases in macromolecular endocytosis. J Clin Invest 101:1142–1147.
18. Morcos M, Du X, Pfisterer F et al. (2008) Glyoxalase-1 prevents mitochondrial protein modification and enhances lifespan in Caenorhabditis elegans. Aging Cell 7:260–269.
19. Creighton DJ, Zheng ZB, Holewinski R et al. (2003) Glyoxalase I inhibitors in cancer chemotherapy. Biochem Soc Trans 31:1378–1382 Review.
20. Kumagai T, Nangaku M, Kojima I et al. (2008) Glyoxlase I overexpression ameliorates renal ischemia-reperfusion injury in rats. Am J Physiol Renal Physiol 296(4):F912–F921.

21. Inagi R, Miyata T, Ueda Y et al. (2002) Efficient in vitro lowering of carbonyl stress by the glyoxalase system in conventional glucose peritoneal dialysis fluid. Kidney Int 62:679–87.
22. Ceradini DJ, Yao D, Grogan RH et al. (2008) Decreasing intracellular superoxide corrects defective ischemia-induced new vessel formation in diabetic mice. J Biol Chem 283:10930–10938.

Intracortical Microcirculatory Change Induced by Anesthesia in Rat Somatosensory Cortex

Kazuto Masamoto, Takayuki Obata, and Iwao Kanno

Abstract The present study aimed to characterize microcirculatory responses to anesthesia in brain tissue. With multi-photon excitation fluorescence microscopy, intra-cortical capillary dimension and red blood cell (RBC) flow were successfully visualized up to a depth of ~0.6 mm from the cortical surface in rats anesthetized with either isoflurane or α-chloralose. We observed that the diameter of the major cerebral artery was ~100 μm under isoflurane, but ~75 μm under α-chloralose. The capillary diameter was observed to be larger under α-chloralose than isoflurane: 5.1 ± 1.2 μm vs. 4.8 ± 1.1 μm, respectively. A significant difference in the mean RBC speed measured in single capillaries was observed: 0.4 ± 0.4 mm/s under α-chloralose vs. 1.5 ± 0.4 mm/s under isoflurane. In agreement with these observations, arterio-venous transit-time and laser-Doppler flowmetry consistently showed a significant reduction of the RBC and plasma blood speed under α-chloralose relative to isoflurane. These findings may indicate that local blood flow regulatory mechanisms exist at the capillary level for the balance of oxygen supply and demand induced by anesthesia in the brain tissue.

1 Introduction

A variety of brain tissue oxygen levels have been observed in animals under general anesthesia [1]. The direct and indirect effects of anesthesia involve the degree of anesthetic action on cerebral metabolic rate of oxygen (CMR_{O2}) and cerebral blood flow (CBF).

In a previous study, we found that rodents treated with inhalation anesthetics (e.g., isoflurane) or intravenous anesthetics (e.g., α-chloralose) that are widely used for brain activation studies, showed quite different behaviors for

K. Masamoto (✉)
Molecular Imaging Center, National Institute of Radiological Sciences, Chiba, 263-8555, Japan
e-mail: masamoto@nirs.go.jp

E. Takahashi, D.F. Bruley (eds.), *Oxygen Transport to Tissue XXXI*, Advances in Experimental Medicine and Biology 662,
DOI 10.1007/978-1-4419-1241-1_7, © Springer Science+Business Media, LLC 2010

the activation-induced cortical hemodynamics [2]. Since hemodynamic-based brain imaging techniques rely on the microcirculatory responses to local neural activity, the effects of anesthesia on the brain microcirculation are critically important for interpretation of the imaging signals. However, the effects of anesthesia on the brain microcirculation, such as vessel dimension and red blood cell (RBC) flow remain unaddressed.

In the present study, we directly measured intracortical capillary dimension and RBC flow in the cerebral cortex of rats anesthetized with either volatile isoflurane or injectable α-chloralose. A biocompatible fluorescent dye was intravenously injected for visualization of blood plasma and cortical microvasculature was three-dimensionally visualized with in vivo multi-photon excitation fluorescent microscopy up to a depth of 0.6 mm from the cortical surface. Intraluminal vascular dimension and fluorescently labeled RBC speed were then measured.

2 Materials and Methods

All animal protocols were approved by the NIRS Animal Experiment Committee. The animals (250–350 g Sprague-Dawley rats, $N = 9$) were initially anesthetized with 4–5% isoflurane and maintained with 2% during surgical procedures. The animal was mechanically ventilated and physiologic parameters (e.g., end-tidal CO_2, anesthetic gas concentration, respiratory rate, heart rate, and mean arterial blood pressure) were monitored throughout all experiments. Arterial blood gas was periodically measured, and respiratory rate and minute ventilation volume were adjusted as needed. Rectal temperature was maintained at $37.0 \pm 0.2^{\circ}C$.

A portion of the left skull (3 mm by 3 mm) over the somatosensory area was removed. The opened area was filled with physiologic saline solution. For experiments, the anesthesia level was first maintained with isoflurane (~1.4%) and then switched to α-chloralose (45 mg/kg/h, i.v.), as previously reported [2]. For visualization of the cortical vasculature, a bolus of Qdot® 605 (1 μM in buffered solution, Invitrogen) was intravenously injected (0.2–0.4 ml). The cortical vasculature was then visualized with multi-photon excitation fluorescent microscope (TCS SP5, Leica Microsystems) with an excitation wavelength of 900 nm (Mai-Tai, Ti:Sapphire laser, Spectra-Physics). The objective lens was a 20× water-immersion lens (0.5 NA, Leica Microsystems). The 512 pixel by 512 pixel images covered a cortical area of 456 μm by 456 μm with a pixel resolution of 0.89 μm. To obtain the three-dimensional structure, contiguous images were captured up to a depth of 0.6 mm from the cortical surface with a step size of 0.01 mm in the z-direction. The region of interest was selected with care to avoid areas having vessels of a relatively large size at the cortical surface. A final image was taken to cover an area of 912 μm by 912 μm in the x-y plane by scanning four adjacent regions. For display purposes, a maximum-intensity projection was constructed from contiguous images obtained in the z-direction.

Based on their pulsation and branching geometry, arterial and venous networks were distinguished at the cortical surface, and then tracked into the parenchyma tissue. To measure capillary diameter, a maximum intensity projection was created from every 0.1-mm thickness in the z-direction and then the width in the image was calculated. A single capillary was defined as the single vessel having cross-sectional thickness less than 8 μm and for which both edges continued to two new vessels as a branching.

The RBC speed was measured by tracking a FITC-labeled RBC through a single capillary. Time-lapse images were obtained at a rate of 14–167 frames per second, depending on the number of lines to be scanned in each single frame. The scanning area was set to cover the whole structure of the single-capillary shape (i.e., 64–256 lines). Similarly, the speed of blood plasma was evaluated by tracking 0.1-μm diameter fluorescent beads that were intravenously injected. For the measurement of mean arterio-venous transit time, a bolus injection (0.1 ml) of fluorescently labeled RBCs or fluorescent beads was performed via the femoral vein. The time-lapse image was obtained with a 5× objective lens at a rate of seven frames per second. Statistical significance was determined with a *t*-test ($P < 0.05$).

3 Results

There was no detectable difference in the measured physiologic parameters (arterial blood gas and blood pressure) between isoflurane and α-chloralose conditions (Table 1). We observed that the diameter of the principal artery at the cortical surface was ∼100 μm under isoflurane, but ∼75 μm under α-chloralose. The results showed that the principal artery shrank significantly after induction with α-chloralose. However, the intracortical capillary diameter was slightly larger under α-chloralose (5.1 ± 1.2 μm, $n = 1682$ vessels) compared to the isoflurane condition (4.8 ± 1.1 μm, $n = 1746$ vessels). A statistically significant difference was observed between two conditions. These results indicate that the upstream and downstream vessels react differently depending on the anesthetics.

Table 1 Blood gas conditions, mean arterial blood pressure (BP), and mean capillary diameter (Dc) observed under isoflurane (Iso) and α-chloralose (Acl) conditions (Mean ± SD, $N = 9$). *$P < 0.05$ (Iso vs. Acl)

	*p*H	pCO_2 (mmHg)	pO_2 (mmHg)	BP (mmHg)	Dc (μm)
Iso	7.43 ± 0.03	37 ± 3	128 ± 18	94 ± 11	4.8 ± 1.1
Acl	7.44 ± 0.02	36 ± 2	123 ± 16	115 ± 15	5.1 ± 1.2*

The mean RBC speed in a single capillary was significantly lower under α-chloralose relative to the isoflurane condition: 0.4 ± 0.4 mm/s under α-chloralose vs. 1.5 ± 0.4 mm/s under isoflurane. Under α-chloralose, some RBCs were found

to be very slow (<0.01 mm/s), whereas most RBCs measured under isoflurane had a relatively high speed (0.4–3.0 mm/s).

As expected, the arterio-venous transit-time of the labeled RBCs was significantly longer under α-chloralose (2.8 ± 1.7 s at peak-to-peak) as compared to the isoflurane condition (1.0 ± 0.9 s). Similar results were observed for the transit time of blood plasma: 1.8 ± 1.3 s under α-chloralose and 1.2 ± 0.7 s under isoflurane. These results indicated that the both RBC and plasma blood speed were significantly lower under α-chloralose relative to isoflurane conditions.

4 Discussion

It has been previously shown by other groups that the baseline CBF under α-chloralose was 30–50% lower than under isoflurane in rat somatosensory cortex, i.e. 70–90 mL/100 g/min under α-chloralose [3, 4] vs. 130–150 mL/100 g/min under isoflurane [5, 6]. In a previous study, we found the baseline CBF measured with laser-Doppler flowmetry was 31% lower under α-chloralose compared with isoflurane [2]. Our measurements of the arterial dimension are in good agreement with these literature data, indicating that the tone in the upstream resistance vessels has a significant role in the regulatory mechanism of the baseline CBF induced by anesthesia. However, we also found that the effect of the anesthesia on the intracortical capillary diameter was opposite to the arterial response. Namely, a larger capillary diameter was observed under α-chloralose as compared to the isoflurane condition. This might indicate that the upstream arteries and intracortical microvessels have separate or independent mechanisms for the regulation of local CBF.

Our results for the mean RBC speed consistently showed that the speed was significantly lower under α-chloralose relative to the isoflurane condition. The results are consistent with previous CBF data. However, the measured RBC speed under isoflurane was relatively high. Kleinfeld et al. (1998) reported that the intra-cortical RBC speed was 0.77 mm/s in rats anesthetized with urethane [7]. The ranges of RBC speed in capillaries were reported as 0.3–3.2 mm/s [8]. In the present study, we showed that the variable speed of RBCs could be due to a local regulatory mechanism rather than upstream arterial regulation. Since the capillary volume and speed of RBCs critically affect oxygen transfer processes from nearby blood vessels to the energy consuming tissue site, it is worthwhile to compare the tissue oxygen level between both anesthesia conditions. Our group has reported that the mean tissue oxygen level in rat somatosensory cortex was 29 mmHg under α-chloralose and 33 mmHg under isoflurane [9, 10]. Another study with electron paramagnetic resonance oximetry showed that the mean tissue oxygen level at normoxic conditions was 13 mmHg under a cocktail of α-chloralose and urethane and 38 mmHg under isoflurane [11]. The data from those studies were in good agreement with the CBF data; higher CBF produces higher tissue oxygen and vice versa. The anesthesia may also affect the tissue oxygen metabolic rate in a different manner, and thus a possible scenario

where the effect of anesthesia on the energy metabolism becomes a dominant factor leading to the observed difference in tissue oxygen level cannot be ruled out. However, it should be noted that endothelial cells have the ability to control their dimension by sensing the nearby blood oxygenation level [12], which may play a role in adjusting local oxygen demand and supply via regulation of capillary volume and RBC speed. Further studies are needed to elucidate the full regulatory mechanism for the local regulation of the microvascular dimensions and RBC traffic.

Acknowledgments This work was partially supported by KAKENHI (#19800065).

References

1. Ndubuizu, O., LaManna, J. C., 2007, Brain tissue oxygen concentration measurements, Antioxid Redox Signal. 9:1207–1219.
2. Masamoto, K., Kim, T., Fukuda, M., Wang, P., Kim, S. G., 2007, Relationship between neural, vascular, and BOLD signals in isoflurane-anesthetized rat somatosensory cortex, Cereb Cortex. 17:942–950.
3. Ueki, M., Linn, F., Hossmann, K. A., 1988, Functional activation of cerebral blood flow and metabolism before and after global ischemia of rat brain, J Cereb Blood Flow Metab. 8:486–494.
4. Lee, S. P., Duong, T. Q., Yang, G., Iadecola, C., Kim, S. G., 2001, Relative changes of cerebral arterial and venous blood volumes during increased cerebral blood flow: implications for BOLD fMRI, Magn Reson Med. 45:791–800.
5. Maekawa, T., Tommasino, C., Shapiro, H. M., Keifer-Goodman, J., Kohlenberger, R. W., 1986, Local cerebral blood flow and glucose utilization during isoflurane anesthesia in the rat, Anesthesiology. 65:144–151.
6. Lenz, C., Frietsch, T., Futterer, C., Rebel, A., van Ackern, K., Kuschinsky, W., Waschke, K. F., 1999, Local coupling of cerebral blood flow to cerebral glucose metabolism during inhalational anesthesia in rats: desflurane versus isoflurane, Anesthesiology. 91:1720–1723.
7. Kleinfeld, D., Mitra, P. P., Helmchen, F., Denk, W., 1998, Fluctuations and stimulus-induced changes in blood flow observed in individual capillaries in layers 2 through 4 of rat neocortex, Proc Natl Acad Sci U S A. 95:15741–15746.
8. Hudetz, A. G., 1997, Blood flow in the cerebral capillary network: a review emphasizing observations with intravital microscopy, Microcirculation. 4:233–252.
9. Masamoto, K., Kershaw, J., Ureshi, M., Takizawa, N., Kobayashi, H., Tanishita, K., Kanno, I., 2007, Apparent diffusion time of oxygen from blood to tissue in rat cerebral cortex: implication for tissue oxygen dynamics during brain functions, J Appl Physiol. 103:1352–1358.
10. Masamoto, K., Vazquez, A., Wang, P., Kim, S. G., 2008, Trial-by-trial relationship between neural activity, oxygen consumption, and blood flow responses, Neuroimage. 40:442–450.
11. Hou, H., Grinberg, O. Y., Taie, S., Leichtweis, S., Miyake, M., Grinberg, S., Xie, H., Csete, M., Swartz, H. M., 2003, Electron paramagnetic resonance assessment of brain tissue oxygen tension in anesthetized rats, Anesth Analg. 96:1467–1472.
12. Inoue, K., Tomita, M., Fukuuchi, Y., Tanahashi, N., Kobari, M., Takao, M., Takeda, H., Yokoyama, M., 2003, Dynamic observation of oxygenation-induced contraction of and transient fiber-network formation-disassembly in cultured human brain microvascular endothelial cells, J Cereb Blood Flow Metab. 23:821–828.

Macrophages That Survive Hyperoxia Exposure Have Higher Superoxide Dismutase Activities in Their Mitochondria

Kenichi Kokubo, Saki Soeda, Toshihiro Shinbo, Minoru Hirose, Noriyuki Fuku, Yutaka Nishigaki, Masashi Tanaka, and Hirosuke Kobayashi

Abstract Prolonged exposure to hyperoxia, which is routinely used in patients with severe respiratory failure, leads to the generation of excessive reactive oxygen species, resulting in lung injury. In the present study, we focused on macrophages and their survival, superoxide dismutase (SOD) activity in mitochondria (Mn-SOD activity), and mitochondrial DNA (mtDNA) mutation after exposure to hyperoxia. Macrophages were cultured under two different conditions: normoxia and intermittent hyperoxia. The number of cells exposed to intermittent hyperoxia for 3 weeks significantly decreased, compared with the number of cells exposed to normoxia. The Mn-SOD activity of the cells that survived intermittent hyperoxia exposure was significantly higher than that of the cells exposed to normoxia. Direct sequencing and a PCR-RFLP assay did not provide any evidence of mutation in the cells that survived intermittent hyperoxia exposure. In conclusion, an increase in the antioxidative activity of mitochondria is important for the survival of macrophages exposed to hyperoxia, and the increased activity level possibly enhances protective effects against mtDNA mutations in surviving cells.

1 Introduction

Prolonged exposure to hyperoxia, which is routinely used in patients with severe respiratory failure, leads to the generation of excessive reactive oxygen species (ROS) in the lungs, resulting in lung injury [1]. In the present study, we focused on macrophages, since alveolar macrophages are exposed to hyperoxia and their functions are important in host defense. We investigated their survival, the superoxide dismutase (SOD) activity in mitochondria (Mn-SOD activity), and mitochondrial DNA (mtDNA) mutation after exposure to hyperoxia.

K. Kokubo (✉)
Department of Medical Engineering and Technology, School of Allied Health Sciences, Kitasato University, Kanagawa, 228-8555, Japan
e-mail: kokubo@kitasato-u.ac.jp

E. Takahashi, D.F. Bruley (eds.), *Oxygen Transport to Tissue XXXI*, Advances in Experimental Medicine and Biology 662,
DOI 10.1007/978-1-4419-1241-1_8, © Springer Science+Business Media, LLC 2010

The major function of mitochondria is to produce energy to support cellular activities through the oxidative phosphorylation pathway [2]. During this process, ROS are generated. Since mtDNA is an easy target for oxidative DNA damage by ROS, the mutation rate of mtDNA is considered to be at least ten times higher than that of nuclear DNA [3, 4]. Therefore, the survival of macrophages exposed to hyperoxia might be related to their SOD activity and its protective effects against mtDNA mutation.

The aim of this study was to determine whether the Mn-SOD activity of surviving cells was altered and whether mtDNA mutations occurred after exposure to hyperoxia. To this end, we measured the changes in the number of cells and the Mn-SOD activities of cells exposed to hyperoxia and then analyzed mtDNA mutations in these cells using direct sequencing and a PCR-RFLP assay.

2 Materials and Methods

2.1 Macrophages Culture

We used macrophages that differentiated from a human monocyte cell line (THP-1, ATCC) after the cell line was cultured with phorbol myristate acetate for 2 days. The haplogroup of the mitochondria in the cells was classified as F1b1a. The cells were cultured in RPMI 1640 medium (Sigma) supplemented with 10% (v/v) fetal bovine serum (CELLect^{TM}; MP Biomedicals), 100 units/mL of penicillin, and 100 μg/mL of streptomycin (GIBCO^{TM}; Invitrogen) at 37°C in a humidified 5% CO_2 atmosphere. The macrophages were cultured under two different conditions: normoxia (21% O_2 + 5% CO_2, for 3 weeks) and intermittent hyperoxia (three repeats of 90% O_2 + 5% CO_2 for 4 days and 21% O_2 + 5% CO_2 for 3 days; i.e., 3 weeks in total). Intermittent hyperoxia was applied in the present study because cells that were continuously exposed to hyperoxia all died within 2 weeks. Intermittent hyperoxia enabled a long-term experiment to be conducted, with the normoxia phases allowing the mitochondria to recover, grow, and possibly accumulate mutated mtDNA.

2.2 Cell Counting and SOD Activity Assay

We measured the changes in the number of cells and Mn-SOD activity, which reflects the antioxidative activity in mitochondria. The number of cells was determined using a counting chamber. Mn-SOD activity was measured using the SOD assay kit (Dojindo Laboratories) and KCN (final concentration: 40 μM) as an inhibitor of Cu/Zn-SOD [5].

2.3 Isolation and Amplification of DNA

Total DNA was extracted from the cells using the QIAamp Blood Mini Kit (QIAGEN). The entire mitochondrial genome was amplified as six fragments (3000–3400 bp) by the first PCR and 60 overlapping segments (600–1000 bp) by the second PCR. The primer pairs and their nucleotide sequences were described previously [6]. The primer pairs were designed to cover the entire mtDNA including an overlapped region that enabled us to confirm the sequences near the 3′- and 5′-ends of the PCR products using two fragments. The conditions for the first and second PCR were the same: 94°C for 5 min; 15 s at 94°C, 15 s at 60°C, 3 min at 72°C; and a final extension for 10 min at 72°C. The amplified fragments were analyzed using electrophoresis on a 1% agarose gel and visualized by staining with ethidium bromide. These second PCR products were purified using MultiScreen-PCR Plates (Millipore). The quality of the DNA templates was examined using electrophoresis on a 1.2% agarose gel after staining with ethidium bromide using a Ready-To-Run Separation Unit (Amersham Pharmacia Biotech).

2.4 Sequence Analysis of Mitochondrial DNA

We analyzed the mutations in the mtDNA of the cells using direct sequencing after the cells had been exposed to intermittent hyperoxia or normoxia for 3 weeks. Sequence reactions were performed using a BigDye terminator cycle sequencing FS ready reaction kit (Applied Biosystems). After excess dye terminators had been removed with MultiScreen-HV plates (Millipore) packed with Sephadex G50 superfine (Pharmacia), the purified DNA samples were precipitated with ethanol, dried, and suspended in the template suppression reagent or formamide (Applied Biosystems). The dissolved DNA samples were heated for 2 min at 95°C for denaturation, then immediately cooled on ice. The sequences were analyzed with automated DNA sequencers 377 and 310 using the Sequencing Analysis Program version 4.1 (Applied Biosystems).

2.5 PCR-RFLP Assay

We analyzed three suspected mutation sites in cells exposed to normoxia using a PCR-RFLP assay. These sites showed different direct sequencing results for the overlapping segment of the two different fragments in cells exposed to normoxia (see the Results section). Firstly, PCR was performed using 5 ng of the cDNA as a template and PCR buffer, dNTP mix, forward and reverse primers (5′-AAACCCT CGTTCCACAGAAG-3′ (forward primer) and 5′-TGATT-GAGATGGGGGCTA GT-3′ (reverse primer) for mt.4732, 5′-GTTCTTTCA TGGGGAAGCAG-3′ (forward primer) and 5′-GTGGCTTTGGAGTTG

CAGTT-3′ (reverse primer) for mt.16129, and 5′-CTGTTCTTTC ATGGG-GAAGC-3′ (forward primer) and 5′- TAGTTGAGGGTTGATTGCTG-3′ (reverse primer) for mt. mt.16189), and rTaq DNA polymerase (Toyobo). The reaction conditions were as follows: 94°C for 5 min; 15 s at 94°C, 15 s at 58–60°C (59.9°C for mt.4732, 59.3°C for mt.16129, 58°C for mt.16189), 3 min at 72°C for 40 cycles; and a final extension for 10 min at 72°C. The amplified fragments were analyzed using electrophoresis on a 1% agarose gel and visualized by staining with ethidium bromide. Then, restriction enzyme was added to each fragment solution. We used Sca I [10 U/μL]

(Roche), BsrG I [10 U/μL] (Daiichi Pure Chemicals), or Mnl I [2 U/μL] (Daiichi Pure Chemicals), incubated with the PCR products at 37°C for 1 h to cut the sequences of AGTACT, TGTACA, and CCTC, respectively. Electrophoresis on a 3% agarose gel was performed to detect the fragment size after digestion with the restriction enzyme.

2.6 Statistical Analysis

All data are given as the mean ± SD. Statistically significant differences were determined using a Wilcoxon matched-pair signed-rank test (cell counting assay) or a Student *t*-test (SOD assay). A probability value (p-value) of less than 0.05 was considered statistically significant.

3 Results

The number of cells exposed to intermittent hyperoxia for more than a week significantly decreased, compared with the number of cells exposed to normoxia (Fig. 1a). The Mn-SOD activity per 100 cells increased with time and was significantly higher in the cells exposed to intermittent hyperoxia than in the

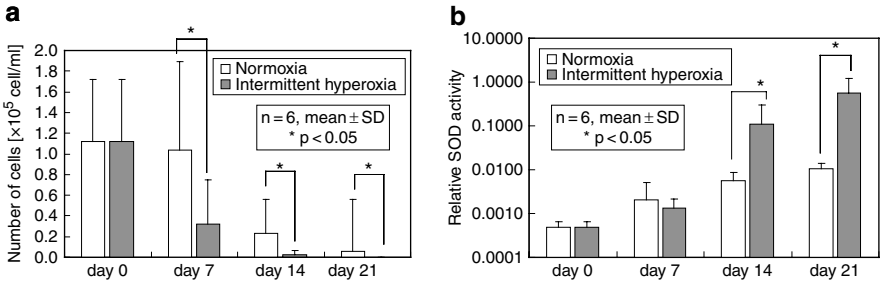

Fig. 1 (**a**) Changes in the number of cells exposed to normoxia or intermittent hyperoxia. (**b**) Relative SOD activity per 100 macrophages. Relative SOD activity was defined based on a value at which 100 cells eliminated all the available superoxide

cells exposed to normoxia (Fig. 1b). The Mn-SOD activity of the surviving cells was about half of the total SOD activity (data not shown).

Using direct sequencing, six sites (nucleotide position: mt.4732, mt.16129, mt.16189, mt.16232, mt.16249, mt.16362) in the mtDNA were identified as suspected sites of mutation located in one coding region and five non-coding regions of the D-loop in mtDNA (Fig. 2). These six suspected sites were located in the overlapped region of the alternative fragments in the second PCR amplification. At these sites, a heteroplasmic sequence was observed in the cells exposed to normoxia. For example, sequence chromatogram showed overlapped peaks of A and G, suggestive of heteroplasmy, at nucleotide position 4732 in the fragment 16. Analysis of the neighboring second PCR product (fragment 17), however, showed only a peak of C at the same site, suggestive of homoplasmy. To confirm this result, Three of the six sites, including the one in a coding region (mt.4732), were amplified by one-step direct amplification from DNA isolated from the cells and were further verified using a PCR-RFLP assay for these potentially heteroplasmic sites. The PCR products were almost completely digested by the restriction enzyme or were completely undigested (Fig. 2), meaning that these three sites were not heteroplasmic and were not mutation sites. We confirmed that complete digestion was attained using another cDNA with the same recognition sites as a positive control (data not shown).

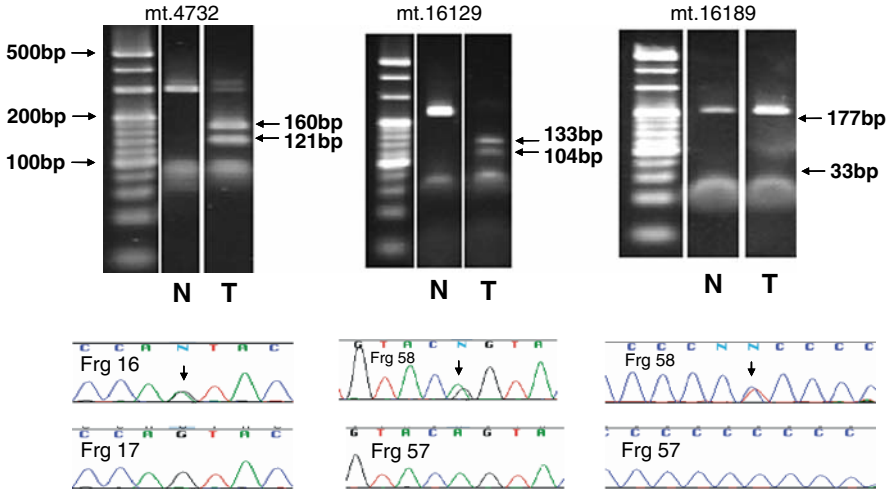

Fig. 2 Gel electrophoresis of PCR-RFLP products and gene sequences measured using direct sequencing of cells exposed to normoxia. N: PCR products without treatment, T: PCR products treated with restriction enzyme. The PCR products, including mt.4732 and mt.16129, were almost completely digested by the restriction enzyme, while mt.16189 was completely undigested (no bands observed at 177 and 33 bp), meaning that these three sites were not heteroplasmic, although a heteroplasmic sequence was suggested by the alternative fragments in the direct sequencing of the other DNA fragments amplified with another pair of primers

4 Discussion

In the present study, we found that hyperoxia induced the cell death of macrophages and that the macrophages that survived intermittent hyperoxia exposure had higher Mn-SOD activities and no mutations in their mtDNA. The survival of the macrophages exposed to intermittent hyperoxia was related to their SOD activities and possibly to their protective effects against mtDNA mutations induced by oxidative DNA damage. Cells that were exposed to hyperoxia but could not increase their SOD activity sufficiently might have been killed by the resulting oxidative DNA damage.

Because of the lack of protective histone proteins and a limited DNA repair mechanism, mtDNA is more susceptible to oxidative DNA damage [3, 4] than nuclear DNA. In the present study, the Cu/Zn-SOD activity of the surviving cells, which reflects the SOD activity in the cytosol, increased as well as the Mn-SOD activity (data not shown), suggesting that the nuclear DNA was also protected from the oxidative stress. Therefore, the possibility of oxidative damage to the nuclear DNA in the surviving macrophages after hyperoxia exposure was considered to be relatively low. Our results implied that antioxidative activities in the cytosol and mitochondria are important and can enhance the survival of macrophages exposed to hyperoxia.

A PCR-RFLP assay was considered to be a more reliable assay to detect mutations than direct sequencing, showing no heteroplasmic sequences, indicating that the three sites were not mutation sites. Although not all of the suspected mutation sites were verified using a PCR-RFLP assay because of the limited availability of appropriate restriction enzymes, the three suspected mutation sites that were not examined were located in non-coding regions, which would have produced innocent mutations even if they had occurred. Thus, no mutations in coding regions occurred in the surviving cells, and any cells with fatal mutations likely died after the hyperoxic insult.

In conclusion, the increase in antioxidative activity in mitochondria is important for the survival of macrophages exposed to hyperoxia, and this increase possibly enhances protective effects against mtDNA mutation in surviving cells.

Acknowledgments This work was supported by a Grant-in-Aid for Research Project (No. 2007-1009) from Kitasato University School of Allied Health Sciences to H. K.

References

1. Zaher TE, Miller EJ, Morrow DM et al. (2007) Hyperoxia-induced signal transduction pathways in pulmonary epithelial cells. Free Radic Biol Med 42:897–908.
2. Attardi G, Schatz G (1988) Biogenesis of mitochondria. Annu Rev Cell Biol 4:289–333.
3. Wallace DC, Shoffner JM, Trounce I et al. (1995) Mitochondrial DNA mutations in human degenerative diseases and aging. Biochim Biophys Acta 1271:141–151.

4. Copeland WC, Wachsman JT, Johnson FM et al. (2002) Mitochondrial DNA alterations in cancer. Cancer Invest 20:557–569.
5. Oyanagui Y (1984) Reevaluation of assay methods and establishment of kit for superoxide dismutase activity. Anal Biochem 142:290–296.
6. Tanaka M, Hayakawa M, Ozawa T (1996) Automated sequencing of mitochondrial DNA. Methods Enzymol 264:407–421.

Diet-Induced Ketosis Improves Cognitive Performance in Aged Rats

Kui Xu, Xiaoyan Sun, Bernadette O. Eroku, Constantinos P. Tsipis, Michelle A. Puchowicz, and Joseph C. LaManna

Abstract Aging is associated with increased susceptibility to hypoxic/ischemic insult and declines in behavioral function which may be due to attenuated adaptive/defense responses. We investigated if diet-induced ketosis would improve behavioral performance in the aged rats. Fischer 344 rats (3- and 22-month-old) were fed standard (STD) or ketogenic (KG) diet for 3 weeks and then exposed to hypobaric hypoxia. Cognitive function was measured using the T-maze and object recognition tests. Motor function was measured using the inclined-screen test. Results showed that KG diet significantly increased blood ketone levels in both young and old rats. In the aged rats, the KG diet improved cognitive performance under normoxic and hypoxic conditions; while motor performance remained unchanged. Capillary density and HIF-1α levels were elevated in the aged ketotic group independent of hypoxic challenge. These data suggest that diet-induced ketosis may be beneficial in the treatment of neurodegenerative conditions.

1 Introduction

The brain, unlike other organs, is normally completely dependent on glucose, but is capable of using ketones as an alternate energy source, as occurs with prolonged starvation or chronic feeding of a high fat-low carbohydrate (ketogenic, KG) diet. The aging population is subject to increased rates of morbidity and mortality as a result of ischemic and hypoxic events related to stroke and neurodegenerative disease. There are many physiological factors that play a role in recovery and survival. These include those related to stabilization of energy metabolism, the ability to defend against oxidative stress and maintain vascular integrity and density [1]. We have previously shown that diet-induced ketosis increased cortical capillary density [2] and reduced CMRglu in the young rats [3], and was neuroprotective against focal ischemic insult [4]. One

J.C. LaManna (✉)
Department of Anatomy, Case Western Reserve University, 10900 Euclid Avenue, Cleveland, OH 44106, USA
e-mail: jcl4@case.edu

E. Takahashi, D.F. Bruley (eds.), *Oxygen Transport to Tissue XXXI*, Advances in Experimental Medicine and Biology 662,
DOI 10.1007/978-1-4419-1241-1_9, © Springer Science+Business Media, LLC 2010

mechanism related to ketotic-induced neuroprotection may be through the upregulation of hypoxic inducible factor-1alpha (HIF-1α) [4, 5]. Aging is associated with increased susceptibility to ischemic/hypoxic insult [6] and cognitive decline [7]. In this study, we investigated if diet-induced ketosis improves behavioral performance in the aged rats. Capillary density and HIF-1αresponses were determined in the young and aged rats fed a STD or KG diet under normoxic and hypoxic conditions.

2 Methods and Materials

2.1 Animal Preparation and Hypoxic Exposure

Male Fischer 344 rats (young: 3-month-old, and aged: 22-month-old) were purchased and allowed to acclimatize in the animal facility at Case Western Reserve University for 1 week before being studied. Rats were fasted overnight before being assigned to two groups fed with either STD or KG diets [2] for 3 weeks. Body weights and ketotic markers such as plasma levels of BHB were measured twice a week. Hypoxic rats were kept in hypobaric chambers for up to 3 weeks at a constant pressure of 0.5 ATM (380 mmHg, equivalent to 10% normobaric oxygen) except for a maximum of 3 h daily when the pressure is returned to atmospheric for cage cleaning, water, food and weighing and behavioral tests. The normoxic control rats were housed in the same room to ensure identical ambient conditions [8].

2.2 Behavioral Tests

(1) Object recognition test: This test is based on the natural tendency of rodents to investigate a novel object instead of a familiar one as well as their innate tendency to re-start exploring when they were presented with a novel environment. The number of times and length of time inspecting the objects over the different trials was calculated. (2) T-maze test: This test is used for general cognitive function and it is based on the innate preference of animals to explore an arm that has not been previously explored (spontaneous alternations). The number of arms entered as well as the sequence of entries was recorded and the alternation rate was calculated. (3) Inclined screen test (60 and 90°): This is to test balance, muscle strength and coordination. Latency to climb to the top of the screen and/or latency to fall was recorded, and overall score was calculated.

2.3 Immunoreactivity of HIF-1α and GlUT-1

HIF-1α protein content was analyzed in cortical tissue lysates by Western blot analysis [2]. Capillary density (number/mm^2) in cortical regions was assessed by immunohistochemical staining with GLUT-1 [2, 9].

2.4 Statistical Analysis

Quantitative data are expressed as mean ± SD. Statistical analyses were performed using SPSS V13.0 for windows. The comparison between any two groups was analyzed with a *t*-test. Significance was considered at the level of $p < 0.05$.

3 Results

3.1 Physiological Variables

During the 3-week diet period, the body weight gain was 12–20% in the aged and young, respectively. Hematocrits were similar between the two diet groups (47 ± 2, $n = 6$) in the young. However, hematocrit was elevated in the KG-diet aged group (57 ± 4, $n = 12$) prior to hypoxic exposure. After 3-week hypoxia, hematocrit (%) reached about 70 in both diet groups young and old. Ketosis as measured by blood ketone levels (mM) ranged 0.8–2.8 following 3 weeks of KG diet in young and old and remained unchanged during hypoxic exposure.

3.2 Behavioral Performance

Cognitive function was assesses by a T-maze test and an object recognition test. In the T-maze test, a high alternation rate and quick decision on choosing which arm to enter are indicatives of sustained cognition as the animals must remember which arm was entered last to not re-enter it. In the young rats, the STD and KG rats had similar alternation rate (~53%) and time on choosing arms (~ 30 s). Compared to the young rats, the STD-diet aged rats had lower alternation rate and longer time to choose arms; however, the KG-diet aged group had similar performance compared to the young. In the aged rat, the KG-diet group had a significantly higher alternation rate (%, 63 ± 21 vs. 37 ± 21, $n = 7$ each) and significantly shorter time on choosing arms (seconds, 28 ± 15 vs. 48 ± 7, $n = 7$ each) than that of the STD-diet group. In the object recognition test, the percent of new object exploration is higher with good cognitive function. Under normoxic conditions, on either diet, the younger rats had significantly higher new object exploration (Fig. 1) compared to the aged rats. Yet, in the aged rats, the new object exploration was significantly increased in the KG-diet group compared to the STD-diet group under normoxic condition (Fig. 1) and at 1 day hypoxia (%, 80 ± 17 vs. 55 ± 29, $n = 7$ each).

The motor function was assessed by an inclined screen test (60 and 90°). Latency to climb to the top and/or latency to fall was recorded, and overall score was calculated using a scoring system as following: 2 = climb to the top; 1 = fail to climb to the top but stay on the screen; 0 = fall. Under normoxic

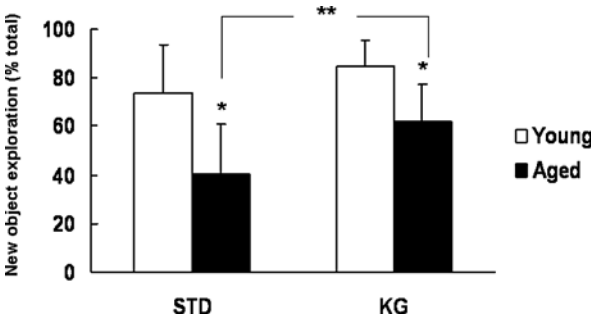

Fig. 1 Object recognition test. New object exploration (%) = (exploration time on new object/total exploration time) × 100. Values are mean ± SD, in the young, STD: $n = 4$, KG: $n = 3$; in the aged, $n = 7$ each. * indicates significant difference compared to the young with same diet (*t*-test, $p < 0.05$); ** indicates significant difference between STD and KG diet groups (*t*-test, $p < 0.05$)

conditions, the aged rats had significantly lower scores (2.0 ± 1.4 and 2.6 ± 1.8, STD and KG groups respectively, $n = 11$ each) for 60-degree incline compared to the young rats with the same diet (4.5 ± 1.3 and 5.0 ± 1.0, STD and KG groups, respectively, $n = 4$ each). Similar trends were found in the 90-degree incline test, with lower scores in each group. There was no significant difference between the KG-diet group and the STD diet group in any age group under normoxic or hypoxic conditions.

3.3 Detection of HIF-1α Protein in Brain Cortex

Levels of HIF-1α in brain cortex were detected using Western blot analysis (Fig. 2). The data show an upregulation of HIF-1with ketosis in the young and old brain under normoxic conditions (STD vs. KG), similar to what we have previously reported in the young adult [4].

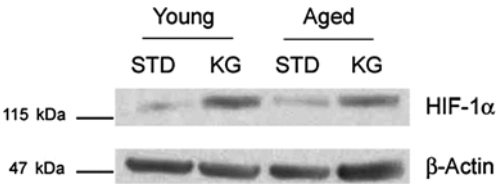

Fig. 2 Western blot analysis showing HIF-1α expression in STD and KG rat brain cortex in both young and aged groups

3.4 Capillary Density: GLUT-1 Immunoreactivity

Increase in capillary counts as measured by GLUT-1 immunoreactivity in coronal-cortical sections of aged rat brain after 3 weeks of feeding diets (STD and KG diets. Following hypoxic exposure, capillary density increased 40% in

the aged and 60% in the young fed STD diet compared to normoxia. In the KG-diet aged group the capillary density increased similar to what was observed with hypoxic exposure. There was no additive effect of hypoxia with KG diet.

4 Discussion

The key findings derived from this study are that there are quantifiable declines in cognitive and motor skills with aging in the Fisher 344 rat model, and that at least the cognitive deficits can be overcome through dietary intervention. These studies also show that a KG diet can be tolerated in both young and aged Fischer rats, consistent with what we have previously reported [2]. Moderate ketosis was observed following 3-wk feeding of the KG diet in both age groups. Cognitive function was improved with ketosis in the aged rat under normoxic conditions and when challenged by environmental hypoxia. The data also show that brain capillary density was lower and its responsiveness to hypoxia was attenuated compared to young rats. In the aged rats, ketosis induced angiogenesis and increased capillary density equivalent to that observed after hypoxic exposure in young rats. We speculate that the KG diet revitalized the neurovascular unit in the older rats helping to support cognitive function. Thus, diet-induced ketosis may improve adaptation process to hypoxia through elevated HIF-1α and increased capillary density.

References

1. Prins ML (2008) Cerebral metabolic adaptation and ketone metabolism after brain injury. J Cereb Blood Flow Metab 28(1):1–16.
2. Puchowicz MA, Xu K, Sun X, Ivy A, Emancipator D, LaManna JC (2007) Diet-induced ketosis increases capillary density without altered blood flow in rat brain. Am J Physiol Endocrinol Metab 292(6):E1607–E1615.
3. Koppaka SS, Puchowicz, MA LaManna JC, Gatica JE (2008) Effect of alternate energy substrates on mammalian brain metabolism during ischemic events. Adv Exp Med Biol 614:361–370.
4. Puchowicz MA, Zechel JL, Valerio J, Emancipator DS, Xu K, Pundik S, LaManna JC, Lust WD (2008) Neuroprotection in diet-induced ketotic rat brain after focal ischemia. J Cereb Blood Flow Metab 28(20):1907–1916.
5. Chavez JC, LaManna JC (2002) Activation of hypoxia-inducible factor-1 in the rat cerebral cortex after transient global ischemia: potential role of insulin-like growth factor-1. J Neurosci 22(20):8922–8931.
6. Xu K, Sun X, Puchowicz MA, LaManna JC (2007) Increased sensitivity to transient global ischemia in aging rat brain. Adv Exp Med Biol 599:199–206.
7. Schulz D, Kouri C, Huston JP (2007) Behavior on the water maze platform: relationship to learning and open field exploration in aged and adult rats. Br Res Bull 74(4):206–215.
8. Xu K, Puchowicz MA, LaManna JC (2004) Renormalization of regional brain blood flow during prolonged mild hypoxic exposure in rats. Br Res 1027(1–2):188–191.
9. Pichiule P, LaManna JC (2002) Angiopoietin-2 and rat brain capillary remodeling during adaptation and deadaptation to prolonged mild hypoxia. J Appl Physiol 93(3):1131–1139.

Fenofibrate, a Peroxisome Proliferator-Activated Receptor α Agonist, Improves Hepatic Microcirculatory Patency and Oxygen Availability in a High-Fat-Diet-Induced Fatty Liver in Mice

Kazunari Kondo, Tadao Sugioka, Kosuke Tsukada, Michiyoshi Aizawa, Masayuki Takizawa, Kenji Shimizu, Masaya Morimoto, Makoto Suematsu, and Nobuhito Goda

Abstract Nonalcoholic fatty liver disease (NAFLD) is a common disease of chronic liver diseases. Peroxisome proliferator-activated receptor α (PPARα) has been implicated to play important roles in the development of the disease. Beyond its effects on lipid metabolisms, PPARα activation in the vascular system has emerged as an attractive therapeutic potential for NAFLD, although its actions in the microcirculatory system are not fully understood. In this study, we investigated the effects of fenofibrate, a PPARα synthetic agonist, on hepatic microcirculation in a high-fat diet (HFD)-induced fatty liver in mice. In vivo imaging analysis revealed the adverse effects of HFD on hepatic vasculature with narrowing of hepatic sinusoids and hepatic microcirculatory perfusion. Oxygen tension was significantly decreased in portal venules, while NADH autofluorescence in hepatocytes was greatly elevated. Fenofibrate treatment remarkably improved microvascular patency, tissue oxygenation and redox states in the affected liver. These results suggest beneficial roles of PPARα activated by fenofibrate on the regulation of both lipid metabolisms and microvascular environments of oxygen metabolism in HFD-induced fatty liver.

1 Introduction

Nonalcoholic fatty liver disease (NAFLD) represents a large spectrum of chronic liver disease ranging from simple hepatic steatosis to nonalcoholic steatohepatitis and cirrhosis. NAFLD is strongly associated with obesity,

N. Goda (✉)
Department of Life Science and Medical Bio-Science, Waseda University School of Advanced Science and Engineering, Tokyo, 162-8480, Japan; Core Research for Evolutional Science and Technology, Japan Science and Technology Agency, Kawaguchi, Saitama, 332-0012, Japan
e-mail: goda@waseda.jp

E. Takahashi, D.F. Bruley (eds.), *Oxygen Transport to Tissue XXXI*,
Advances in Experimental Medicine and Biology 662,
DOI 10.1007/978-1-4419-1241-1_10, © Springer Science+Business Media, LLC 2010

type II diabetes and hypertriglyceridemia [5]. Insulin resistance appears to be a primary factor for the development of NAFLD, as it is associated with increased lipolysis and reduced utilization of fatty acids in adipose tissues, leading to enhanced influx of fatty acids to the liver and accumulation of fatty acids as triglyceride (TG) in hepatocytes. These metabolic alterations evoke not only functional defects in the affected hepatocytes, but also distortion of hepatic microcirculation with a marked reduction in sinusoidal spaces and a decrease in the number of functional sinusoids. Such microvascular changes would limit oxygen supply for hepatocytes to oxidize fatty acids, accelerating progression to severer fatty liver diseases.

Peroxisome proliferator-activated receptor α (PPARα) is activated by binding with ligands including fibrate drugs [3]. A growing body of evidence suggests that PPARα is implicated in the pathogenesis and treatment of NAFLD [5]. A high-fat diet (HFD) feeding in mice has been reported to enhance deposit of TG in the liver in conjunction with reduced activity of PPARα. Loss of PPARα in mice has shown to cause severer hepatic steatosis in response to a high-fat diet feeding [2]. Thus, PPARα plays critical roles in the prevention of fat accumulation in the liver by stimulating fatty acid oxidation, for which microvascular blood supply should be ensured to meet the oxygen demands of hepatocytes. However, little is known about the roles of PPARα in the regulation of hepatic microcirculation and tissue oxygenation. To determine the effects of fenofibrate on hepatic microcirculation and tissue oxygenation in NAFLD, we investigated changes in sizes of sinusoids, blood oxygen tension and hepatic NADH autofluorescence in HFD-induced fatty liver in mice. Our present study demonstrated that treatment with fenofibrate remarkably improved microvascular patency, tissue oxygenation and redox states in the liver of HFD-fed mice. These results suggest beneficial roles of PPARα activated by fenofibrate on the regulation of both lipid metabolisms and microvascular environments of oxygen metabolism in the HFD-induced fatty liver.

2 Materials and Methods

Male C57BL/6 mice (5-week-old, Japan CLEA, Tokyo, Japan) were fed a control chow (CE-2, Japan CLEA) or a high-fat diet (HFD, D12327; 20% protein, 40% carbohydrate, and 40% fat, Research Diets Inc., New Brunswick, NJ) for 8 weeks. One experimental group treated with HFD was administered orally fenofibrate (Laboratoires Fournier S.A., Dijon, France) once a day at the dose of 30 mg/kg body weight/day for the last 3 weeks. As controls, mice fed control or HFD chow received 0.5% of carboxymethylcellulose (10 ml/kg body weight/day, Wako Pure Chemical Industries, Japan). Plasma and hepatic TG obtained from over-night fasted mice at the end of experiments were determined by automatic analyzer (TBA-120FR, Toshiba Medical Systems, Inc., Tokyo). For histochemical analysis, frozen sections with 10 μm-thickness from mice at

the end of experiments were stained with hematoxylin and eosin (HE, Wako Pure Chemical Industries). For intravital fluorescence microscopical analysis, surface of left lateral liver lobe was observed with an inverted intravital microscopy (Eclipse TE2000-U, Nikon Inc, Tokyo, Japan) assisted by a charge coupled device camera (JK-TU52H, Toshiba Inc, Tokyo, Japan). After a trans-illuminational image of the liver was captured, size of the sinusoids was measured at 10 points per sinusoid of five randomly selected sinusoids which were located at regular intervals between portal and central venule. After eliminating intrinsic vitamin A autofluorescence in fat-storing Ito cells, NADH autofluorescence was recorded in five randomly selected lobuli at 30 s after re-exposing to epi-illumination and was densitometrically assessed by computer-assisted gray level determination (Win ROOF Version 5.5, Tech Jam, Inc, Osaka, Japan). Oxygen tension in portal and central venule was measured by injecting Pd-meso-tetra-(4-carboxyphenyl)-porphyrin (Pd-TCPP, Porphyrin Products Inc., Logan, UT, 30 mg/kg body weight) intravenously, as described in detail previously [8]. All experiments were approved by the Animal Care and Utilization Committee of Keio University School of Medicine. Statistical analyses were carried out by Student's *t*-test for all experiments. P values less than 0.05 were considered significant.

3 Results

HFD feeding displayed a significant elevation of TG in plasma compared to control chow (67.7 ± 13.2 vs. 34.9 ± 2.6 mg/dl). In mice treated with both HFD and fenofibrate, these values were reduced notably to the levels observed in mice fed control chow (26.1 ± 3.9 mg/dl). Histochemical analysis revealed that HFD feeding elicited accumulation of various sizes of fat droplets predominantly around portal venules, whereas treatment with fenofibrate greatly prevented these fat infiltrations (Fig. 1). Consistent with these findings, the amounts of hepatic TG were significantly higher in HFD-fed mice than those in the control chow-fed group (338.7 ± 37.1 vs. 266.0 ± 43.0 μg/mg protein),

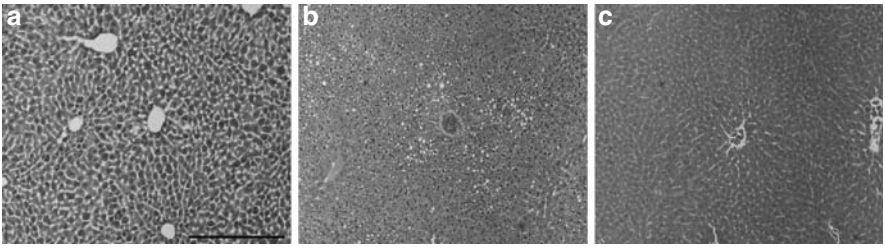

Fig. 1 Fenofibrate treatment reduces fat deposition in mice fed HFD. Shown are representative HE stained sections collected from mice fed control chow (**a**), HFD (**b**) or HFD plus fenofibrate (**c**). Bar, 300 μm

whereas this induction was completely abolished by fenofibrate treatment (178.0 ± 22.7 μg/mg protein).

To determine the impacts of HFD feeding on hepatic microcirculation, in vivo microscopic analysis was performed. In response to a HFD feeding, hepatic sinusoidal perfusion was notably reduced with blood flow being sluggish in some sinusoids, presumably by hepatocytes swollen with accumulated lipids, which narrow the lumen of sinusoids and damage sinusoidal linings. The mean sizes of hepatic sinusoids significantly decreased by 33% in HFD-fed mice compared to control chow-fed mice (Fig. 2a). These morphological alterations were completely abolished by treatment with fenofibrate. Oxygen tension in portal venule was notably lower in HFD-fed mice than that in control mice, whereas fenofibrate treatment partially but significantly restored microvascular oxygen levels (Fig. 2b). To further determine whether fenofibrate improves tissue oxygenation in the affected liver, we measured NADH autofluorescence intensity upon UV epi-illumination. A substantial increase in NADH fluorescence intensity in hepatocytes around both portal and central venules was observed upon HFD exposure (Fig. 2c). Fenofibrate completely abolished these alterations and further decreased the fluorescence intensity below the values of control chow-fed mice.

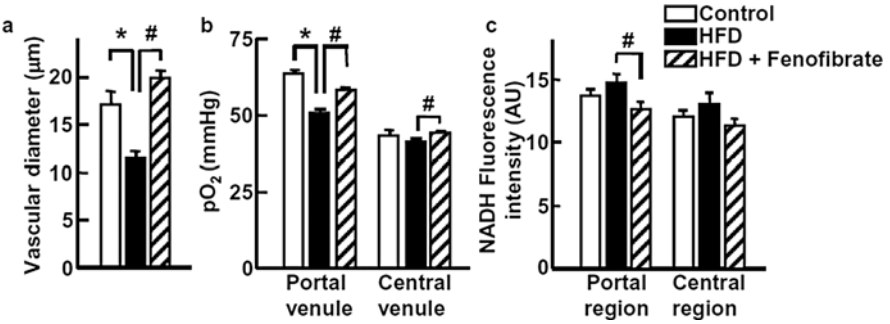

Fig. 2 Fenofibrate treatment improves hepatic microcirculation and oxygenation in mice fed HFD. Changes in size of sinusoids (**a**), oxygen tension (**b**) and NADH fluorescence (**c**) were investigated by using intravital microscopy. Data are expressed as mean ± S.E. of 5 mice per treatment group. $^{*}P < 0.05$ HFD vs. control. $^{\#}P < 0.05$ HFD + fenofibrate vs. HFD

4 Discussion

In the present study, we have shown that fenofibrate, a synthetic PPARα agonist, reduces HFD-induced deposition of TG in the liver and corrects systemic lipid abnormalities. Beyond the effects on lipid metabolism, fenofibrate not only increased the size of sinusoidal vessels, but also restored tissue oxygenation and redox state in the affected liver.

PPARα has been reported to control lipid metabolism in metabolically active organs such as liver by regulating expression of genes involved in mitochondrial and peroxisomal fatty acid oxidation [3, 6]. PPARα activation also increases lipoprotein lipase activity and uptake of fatty acids by peripheral tissues. Considering these biological functions of PPARα, our results showing improvement of hepatic and systemic lipid abnormalities by fenofibrate are most likely explained by the direct effects of PPARα activation in the body. These metabolic alterations lead to morphological changes in hepatocytes with a reduction of both sizes and numbers of fat droplets in cytoplasm. Consequently, physical oppression of sinusoids by fat-swollen hepatocytes is released, and sinusoidal vasodilation occurs [7]. In fact, these microvascular changes were observed in HFD-fed mice treated with fenofibrate, and were associated with an increase in blood flow in hepatic sinusoids. Although the recovery of hepatic sinusoidal perfusion most likely results from morphological changes in hepatic microvasculature by lipid-lowering effects of fenofibrate, direct effects of the drug on hepatic microcirculation can be considered to be involved. Fenofibrate has been reported to show vasoprotective effects by either stimulating production of nitric oxide (NO) [4] or inhibiting endothelin-1 (ET-1) production [1]. Since these vasoactive molecules can regulate vascular tone at the sinusoidal levels, improvement of hepatic microcirculation by the treatment of fenofibrate can be accounted for, at least in part, by eNOS activation and/or ET-1 inhibition. Further investigations are needed to determine the extent to which fenofibrate improves hepatic microcirculation through acting directly on vascular beds in the diet-induced fatty liver.

HFD feeding evoked a decrease and an increase in oxygen tension in portal venule and NADH autofluorescence of hepatocytes in the liver, respectively. In addition, we observed that the difference in oxygen tension between portal and central venule was greatly attenuated in HFD-treated liver, suggesting oxygen extraction (utilization) by the liver was impaired by the diet. On the other hand, treatment of HFD-fed mice with fenofibrate greatly reversed levels of both oxygen tension and NADH. Although hepatic sinusoids seem to be crucial sites responsible for fenofibrate treatment, our present results showing a great reduction of oxygen tension in portal venule may indicate that proximal portal veins or venules rather than sinusoids also are target points of fenofibrate to regulate oxygen supply and availability in liver microcirculation. Considering that both oxygen and NADH serve as important regulators to determine the balance between fatty acid oxidation and TG synthesis in the liver, the adequate tissue oxygenation with increased PPARα-target gene expressions are a prerequisite for hepatocytes to oxidize fatty acids effectively, leading to prevention and treatment of hepatic steatosis.

In conclusion, fenofibrate regulates both lipid metabolism and vascular functions in liver in a coordinated manner, and shows a promising therapeutic potential for NAFLD.

Acknowledgments This work was supported by Japan Society for the Promotion of Science Grant-in-Aid for Creative Scientific Research 17GS0419 and by CREST, JST.

References

1. Irukayama-Tomobe Y, Miyauchi T, Sakai S et al. (2004) Endothelin-1-induced cardiac hypertrophy is inhibited by activation of peroxisome proliferator-activated receptor-alpha partly via blockade of c-Jun NH2-terminal kinase pathway. Circulation 109(7):904–910.
2. Lee SS, Pineau T, Drago J et al. (1995) Targeted disruption of the alpha isoform of the peroxisome proliferator-activated receptor gene in mice results in abolishment of the pleiotropic effects of peroxisome proliferators. Mol Cell Biol 15:3012–3022.
3. Lefebvre P, Chinetti G, Fruchart JC et al. (2006) Sorting out the roles of PPAR alpha in energy metabolism and vascular homeostasis. J Clin Invest 116(3):571–580.
4. Murakami H, Murakami R, Kambe F et al. (2006) Fenofibrate activates AMPK and increases eNOS phosphorylation in HUVEC. Biochem Biophys Res Commun 341(4):973–978.
5. Postic C, Girard J (2008) Contribution of de novo fatty acid synthesis to hepatic steatosis and insulin resistance: lessons from genetically engineered mice. J Clin Invest 118(3):829–838.
6. Reddy JK, Rao MS (2006) Lipid metabolism and liver inflammation. II. Fatty liver disease and fatty acid oxidation. Am J Physiol Gastrointest Liver Physiol 290(5):G852–G858.
7. Seifalian AM, Piasecki C, Agarwal A et al. (1999) The effect of graded steatosis on flow in the hepatic parenchymal microcirculation. Transplantation 68(6):780–784.
8. Tsukada K, Sekizuka E, Oshio C et al. (2004) Red blood cell velocity and oxygen tension measurement in cerebral microvessels by double-wavelength photoexcitation. J Appl Physiol 96(4):1561–1568.

Renal Vasoconstriction in Rats Causes a Decrease in Capillary Density and an Increase in Alkaline Phosphatase Expression in Cardiac Capillary Nets

Tomiyasu Koyama and Akira Taka

Abstract In the rat, experimental renal vasoconstriction induced by the use of a Goldblatt clamp caused arterial hypertension, cardiomyocyte hypertrophy and an increased capillary to cardiomyocyte ratio, the latter indicating the formation of new cardiac capillaries. Total capillary density decreased, but capillary portions expressing alkaline phosphatase increased. This suggested a greater arterialization of capillaries which would increase the flow of arterial blood to the myocardial capillary nets. However, the observed increase in the area of the capillary domains means the extra arterialization was not sufficient to compensate for the lengthening of the oxygen diffusion pathway caused by the hypertrophy. Since the effects of renal vasoconstriction were not seen in rats treated with an inhibitor of angiotensin converting enzyme (ACE) it is suggested they are induced by angiotensin II via activation of the renin-angiotensin system (RAS).

1 Introduction

Hyper-reninemic and/or hyperaldosteronemic cardiac hypertrophies are often considered in the treatment of hypertensive patients [1, 2]. However, few experimental studies have been made on the effects of the hypertrophy on myocardial microvessels. Batra et al. [3, 4] induced hypertrophy by aortic constriction in rats on the postnatal 5th day when they are growing rapidly and functional compensation may readily occur. Six weeks later a significant increase in the capillary domain area was observed in the arteriolar capillary portion but there were no significant changes in the capillary domain area of the venular capillary portion. Since renal hypertension in humans occurs more often in adults than in the young, we tried to study the effects in rats which were subjected to renal vasoconstriction in early adulthood. We have hitherto

T. Koyama (✉)
Hokkaido University, Sapporo, Japan
e-mail: tomkoyamajp@yahoo.co.jp

E. Takahashi, D.F. Bruley (eds.), *Oxygen Transport to Tissue XXXI*,
Advances in Experimental Medicine and Biology 662,
DOI 10.1007/978-1-4419-1241-1_11, © Springer Science+Business Media, LLC 2010

made several studies in the stroke-prone spontaneously hypertensive rats (SHRSP) [5]. However, since SHRSP are reported to have genetic deficits not directly related to kidney [6–9], in the present experiment we studied normotensive Wistar rats made hypertensive by renal vasoconstriction. The direct activation of renin angiotensin system by the reduction in renal blood flow may be more effective in causing changes in myocardial microvessels than the mere mechanical overload on the heart. Moreover, in aortic constriction a redistribution of blood flow to the coronary artery may occur from organs other than the kidney; this may partially reduce the remodelling effects on the microvessel network.

2 Methods

Vasoconstriction was produced with a silver clip applied to the left renal artery [10]. The clips, 3.0 mm long with a gap of 0.22 mm, were made from silver ribbon 0.2 mm thick and 1.5 mm wide. Ten six-week old male Wistar rats (body weight 182 $\pm$ 12 g) were anesthetized with sodium pentobarbitone (50 mg/kg; i.p.). The left renal artery was exposed through an abdominal incision and constricted with a clip; the abdominal wall was then closed. Arterial blood pressure was measured from the tail with a balloon-cuff manometer (Natsume tail manometer Model KN-0090, Tokyo). Four weeks after surgery arterial blood pressure was above 160 mmHg in eight of the rats. These hypertensive rats were divided randomly into two groups of four. One group (RVC-water) was supplied ad libitum with water alone; the other group (RVC-delap) was supplied ad libitum with water containing the angiotensin converting enzyme (ACE) inhibitor, delapril [11], at a dose of 500 mg/l. As sham-operated controls (sham-op) five rats of the same age were exposed to a similar surgical procedure except that the clip was simply placed round the renal artery but not closed.

Eleven weeks after the groups had been set up (and 15 weeks after surgery), body weight (BW) and systolic arterial blood pressure (BP) were measured. The rats were then instantaneously guillotined. The heart was removed, the right ventricle dissected, the left ventricle (LVW) weighed and then quickly frozen in liquid nitrogen. Kidneys were also removed and the weights of the right (RKW) and left (LKW) kidneys recorded. Four frozen transverse sections of the left ventricle were cut at the level of the maximal heart diameter, stained for alkaline phosphatase (ALP), the enzyme marker for the arteriolar capillary portion, and for dipeptidylpeptidaseIV (DPPIV), the enzyme marker for the venular capillary portion as previously described [12, 4, 13]. Capillaries and cardiomyocytes were counted in transverse subendocardial sections as previously described [4, 13]. The capillary domain area was determined as described by Hoofd et al. [14]. Capillary to myocyte ratio (C:M) was calculated as an index of the vascularity [15]. Data are given as mean $\pm$ S.D. Significance was checked by Student's unpaired *t*-test or Mann-Whitney test and considered significant at $P < 0.05$.

The study conformed with the Hokkaido University institutional guide for the care and use of laboratory animals.

3 Results

Table 1 shows some physical parameters of the rats after 15 weeks of renal vasoconstriction, with drug treatment during the final 11 weeks. Compared with the sham-op and RVC-delap groups, the RVC-water group had a lower BW, a higher LVW and a higher systolic blood pressure. BW, LVW and BP in the RVC-delap group showed no significant differences from the sham-op group except for a significant decrease in the weight of the left kidney.

The capillary domain area, CDA [14], represents the cross-sectional area of the tissue cylinder supplied by an individual capillary portion. CDAs for arteriolar, intermediate and venular capillary portions are listed in Table 2. CDAs of all capillary portions in the RVC-water group were significantly larger than those in sham-op and RVC-delap groups.

Table 3 shows that the cross-sectional area of cardiomyocytes in the RVC-water group was significantly larger than that in the sham-op and RVC-delap groups.

Table 1 Physical parameters after 15 weeks of renal artery vasoconstriction

Rat group	BW (g)	LVW (mg)	RKW (mg)	LKW (mg)	BP (mmHg)
Sham-op	613 ± 23	1191 ± 130	2738 ± 63	2693 ± 118	122 ± 3
RVC-water	$474 \pm 84^{\dagger}$	$1707 \pm 185^{*}$	2728 ± 218	$1623 \pm 246^{*}$	$220 \pm 45^{*}$
RVC-delap	553 ± 54	1090 ± 48	2613 ± 489	$1148 \pm 235^{*}$	132 ± 15

$\dagger\ p < 0.05$, $*p < 0.02$ vs. Sham-op group (Student's unpaired *t*-test)

Table 2 Capillary domain areas, CDA (μm^2), obtained for arteriolar, intermediate and venular capillary portions in the three groups

Rat group	Arteriolar	Intermediate	Venular
Sham-op	678 ± 206	589 ± 161	559 ± 147
RVC-water	$757 \pm 233^{**}$	$684 \pm 184^{**}$	$638 \pm 153^{**}$
RVC-delap	622 ± 202	572 ± 182	562 ± 183

$** p < 0.01$ vs. Sham-op (Student's unpaired *t*-test)

Table 3 Cardiomyocyte area (μm^2) in three groups

Sham-op	RVC-water	RVC-delap
453 ± 196	$1108 \pm 491^{***}$	438 ± 201

$*** p < 0.001$ vs. Sham-op and RVC-delap (Mann-Whitney test)

Table 4 Capillary density expressed as number/mm^2 (upper values) and the number of arteriolar, intermediate and venular portions as a percentage of total capillaries (lower values) in the three groups

Rat group	Arteriolar	Intermediate	Venular	Total
Sham-op	219 ± 107	369 ± 135	1279 ± 264	1867 ± 150
	12.0 ± 6.4%	19.8 ± 7.5%	68.2 ± 11.7%	
RVC-water	328 ± 91	519 ± 220	701 ± 168*	1548 ± 212**
	21.2 ± 4.8%**	33.1 ± 9.0%**	45.0 ± 10.6%**	
RVC-delap	357 ± 116	553 ± 134	1221 ± 357	2175 ± 351
	16.8 ± 6.2%	26.3 ± 7.0%	56.1 ± 10.2%	

*$p < 0.02$; ** $p < 0.01$ vs. Sham-op (Student's unpaired t-test)

The capillary density, i.e. the total number of capillaries per mm^2 of transverse cross-sectional area of the subendocardial layer was significantly smaller in the RVC-water group than in sham-op and RVC-delap groups (Table 4). Compared with the sham-op rats, the RVC-water group showed an insignificant increase in the density of arteriolar and intermediate capillary portions but a significant increase in their percentages. The increase in the totals for arteriolar and intermediate capillary portions in the RVC-water group, compared with those in the sham-op group, was significant ($p < 0.05$). Both the density and percentage of the venular capillary portions, were, however, lower in the RVC-water group than in the sham-op and RVC-delap groups.

The ratio of the number of capillaries to cardiomyocytes (C:M) was significantly higher in the RVC-water group than in the other two groups.

4 Discussion

The significant increase in the cross-sectional area of the cardiomyocytes shows that the hypertension caused by renal constriction led to cardiac hypertrophy. The high value for C:M ratio was similar to that found in the stroke-prone spontaneously hypertensive rats [5]. Since, in the current experiments, the degree of hypertrophy was more marked than was the capillary proliferation, the CDA increased for all three capillary portions. Thus renal vasoconstriction increased the diffusion path distance for oxygen supply for all the capillary portions.

The present finding that the CDA was larger in the ALP-sensitive capillary portions in the RCV-water group than in other groups was consistent with the result reported in the aorta constriction study by Batra et al. [4]. However, in contrast to the present results, they found no significant changes in CDA nor in the DPPIV-sensitive capillary portions or the total. The total capillary density showed no changes. The present renal vasoconstriction caused profound effects on the micro vessel networks in cardiac tissues, since CDA increased also in the intermediate and DPPIV-sensitive capillary portions or the total capillary density.

A striking effect of renal vasoconstriction in the present study was the increase in the arteriolar (ALP-sensitive) capillary portions accompanied by a decrease in the venular (DPPIV-sensitive) portions. The differential changes in the capillary portions seem to be a response of the network to stress induced by hypertrophy. Circulatory stress promotes arterialization of capillaries [16] and could be a factor in the decreased percentage of venular portions. The increase in the arteriolar inflow to the capillary networks would partially improve the oxygen supply to cardiac cells. Such a compensatory control system seemed to be activated in rat hearts subjected to the changes by renal vasoconstriction. None of these effects were found in the group treated with the angiotensin converting enzyme inhibitor, suggesting the involvement of angiotensin II in the hypertrophic changes induced by renal vascular constriction.

The increase in ALP-sensitive and the decrease in DPPIV-sensitive capillary portions may seem to contradict the previous finding that in ischemia/reperfusion stress [17, 18] the proliferating cell nuclear antigen appeared mainly on the DPPIV-sensitive capillaries. The reason for this apparently discrepant result may be that the hypertensive stress to which the new capillaries are subjected in this experiment favours the development of ALP-containing arteriolar rather than DPPIV-containing venular portions. Shear stress is said to induce ALP expression [19]. In an in vitro experiment where endothelial cells were cocultured with pericytes, which are typical of arterioles and arteriolar capillary portions there was increased ALP expression [20]. The phenotype of the capillary endothelial cells may have changed and so expresses ALP. Confirmation of this speculation however, remains for a future study.

The difference in the effects seen in this study compared with those reported by Batra et al. [4], following aortic constriction may be attributable to two factors. First, vasoconstriction at 6 weeks of age may have a more serious effect on oxygen transport to cardiac tissues than vasoconstriction at 5 days after the birth. Second, with renal vasoconstriction there is no compensatory redistribution of blood flow from other organs to the left renal artery. In contrast, aortic vasoconstriction allows a redistribution resulting in increased inflow to the kidney and coronary artery from other organs. Thus, it is not surprising that renal vasoconstriction may cause more profound effects on the kidney than does aortic constriction. It remains to be established unequivocally if it is RAS, not hypertension itself, that causes the changes in the cardiac vasculature.

References

1. Raizada V, Skipper B, Luo W, Griffith J (2007) Intracardiac and intrarenal renin-angiotensin systems: mechanisms of cardiovascular and renal effects. J Investig Med 55:341–359.
2. Sanchez R, Fischer P, Cuniberti L, Masnatta LD, Ramirez AJ (2007) Vascular oxidative stress is associated with insulin resistance in hyperreninemic nonmodulating essential hypertension. J Hypertens 25:2434–2440.
3. Batra S, Rakusan K (1991) Geometry of capillary networks in hypertrophied rat heart. Microvasc Res 41:29–40.

4. Batra S, Rakusan K (1992) Capillary network geometry during postnatal growth in rat hearts. Am J Physiol 262:H636–H640.
5. Xie Z, Gao M, et al. (1998) Rearrangement of the ventricular capillary network in stroke-prone spontaneously hypertensive rats (SHRSP) following a late start of treatment with angiotensin converting enzyme-blocker, Temocapril. Jap Heart J 39:699–706.
6. Volpe M, Iaccarino G, Vecchione C et al. (1996) Association and cosegregation of stroke with impaired endothelium-dependent vasorelaxation in stroke prone, spontaneously hypertensive rats. J Clin Invest 98:256–261.
7. Yamori Y, Murakami S, Nara Y, Ikeda K (1995) Stroke-prone SHR and arteriolipidosis-prone SHR as models for atherosclerosis: their mechanisms and application for nutritional and pharmacological studies. Clin Exp Pharmacol Physiol Suppl 22(1):S244–S245.
8. De Lange RP, Burr K, Clark Js, Negrin CD, Brosnan MJ, St Clair DM, Dominiczak AF, Shaw DJ (2001) Mapping and sequencing rat dishevelled-1: a candidate gene for cerebral ischaemic insult in a rat model of stroke. Neurogenetics 3:99–106.
9. Ueno K, Togashi H, Matsumoto M, Ohashi S, Saito H, Yoshioka M (2002) Alpha4beta2 nicotinic acetylcholine receptor activation ameliorates impairment of spontaneous alteration behavior in stroke-prone spontaneously hypertensive rats, an animal model of attention deficit hyperactivity disorder. J Pharmacol Exp Ther 302:95–100.
10. Leenen FHH, Jong WD (1971) A solid clip for induction of predictable levels of renal hypertension in the rat. J Appl Physiol 31:142–144.
11. Inada Y, Terashita Z et al. (1986) Inhibition of angiotensin converting enzyme by CV-3317, a nonsulfhydril compound. Jpn J Pharmacol 42:99–108.
12. Lojda Z (1977) Studies on glycyl-proline naphthylamidase. Histochemistry 54:299–309.
13. Koyama T, Xie Z, Gao M, Suzuki J, Batra S (1998) Adaptive changes in the capillary network in the left ventricle of rat heart. Jpn J Physiol 48:229–241.
14. Hoofd L, Turek Z, Kubat K, Ringanalda BEM, Kazda S (1985) Variability of intercapillary distance estimated on histological sections of rat heart. In: Oxygen Transport to Tissues VIII, eds Kreuzer F, Cain SM, Goldstick TK, Plenum Publ Co, New York & London. pp. 239–247.
15. Milkiewicz M, Pugh CW, Eggington S (2004) Inhibition of endogenous HIF inactivation induces angiogenesis in ischaemic skeletal muscles of mice. J Physiol 560:21–26..
16. Price RJ, Owens GK, Skalak TC (1977) Immunohistochemical identification of arteriolar development using markers of smooth muscle differentiation – Evidence that capillary arterialization proceeds from terminal arterioles. Circ Res 14:53–65 .
17. Koyama T, Xie Z, Suzuki J (2002) Coronary ischemia/reperfusion increases proliferating cell nuclear antigen in vascular endothelial cells in rat hearts. Angiogenesis 5:119–124.
18. Koyama T, Xie Z, Suzuki J, Abe K (2003) Expression of proliferating cell nuclear antigen in rat hearts subjected to transient ischemia followed by reperfusion. In: Oxygen Transport to Tissues XXIV, eds Dunn J & Swartz HM, Kluwer Acad/Plenum Publ: 587–591.
19. Sterpetti AV, Cucina A, Morena AR, et al. (1993) Shear stress increases the release of interleukin-1 and interleukin-6 by aortic endothelial cells. Surgery 114:911–914.
20. Linder H, Behrends U, Misumi Y, Kremmer E, Eissner G, Schultz-Hector S (1998) Loss of myocardial capillary endothelial-cell alkaline phosphatase (ALP) activity in pimary endothelial cell culture. Cell Tissue Res 291:497–505.

The Effects of Cilostazol on Tissue Oxygenation upon an Ischemic-reperfusion Injury in the Mouse Cerebrum

Takayuki Morikawa, Katsuji Hattori, Mayumi Kajimura, and Makoto Suematsu

Abstract Although cilostazol, an inhibitor of cyclic nucleotide phosphodiesterase 3 (PDE3), is known to exert a potent antiplatelet function by raising intracellular cAMP concentration, its effect on cerebral microcirculation upon an ischemic insult is not clearly understood. To examine effects of cilostazol on the global ischemic injury in the brain, we first measured the plasma leakage using modified Miles assay after mice had been subjected to 60 min of a bilateral common carotid artery (BCCA) occlusion followed by reperfusion for 4 h. Oral treatment with cilostazol (30 mg/kg) significantly increased plasma leakage. This result led us to examine if the treatment with cilostazol recruits more capillaries leading to an increase in surface area for exchange and oxygen transport to tissues. To do so, we simultaneously measured degrees of tissue hypoxia and vessel perfusion. Pimonidazol was injected intraperitoneally 1 h before sacrifice and capillary patency was assessed by fluorescein isothiocyanate-labeled Lycopersicon esculentum lectin bound to the endothelial surface. Treatment with cilostazol markedly increased the capillary patency which was accompanied by a reduction in the hypoxic area. Although the treatment with cilostazol caused an increase in the flux of plasma proteins across endothelial barrier that may imply an adverse role after a BCCA occlusion, this increase in protein leakage was attributable to the increased surface area for exchange which in turn brought about a reduction in tissue hypoxia. Taken together cilostazol appears to produce a protective effect against the ischemic-reperfusion injury.

1 Introduction

Cilostazol exerts a potent antiplatelet function by inhibiting cyclic nucleotide phosphodiesterase 3 (PDE3), resulting in raising intracellular cAMP concentration. Besides inhibiting platelet aggregation, this PDE3 inhibitor is known to possess

T. Morikawa (✉)
Department of Biochemistry and Integrative Medical Biology, Keio University School of Medicine, Tokyo, 160-8582, Japan
e-mail: mi081031@sc.itc.keio.ac.jp

E. Takahashi, D.F. Bruley (eds.), *Oxygen Transport to Tissue XXXI*, Advances in Experimental Medicine and Biology 662,
DOI 10.1007/978-1-4419-1241-1_12, © Springer Science+Business Media, LLC 2010

multiple pharmacological effects including a vasodilatory action on resistance vessels [1] and anti-inflammatory effect on the endothelium [2]. It has been approved by the Japanese health authorities as an antiplatelet agent for the treatment of chronic cerebral infarction since 2001. In recent clinical trials using a double-blind method, a long-term administration of cilostazol has shown effectiveness in preventing the recurrence of lacunar infarction [3, 4]. Since lacunar infarction is a small infarction involving occlusion of small penetrating arterioles, it is necessary to test its effect on the microvasculature. We, therefore, conducted a study to understand the mechanism whereby cilostazol elicits a protective effect on the cerebral microcirculation. To do so, we examined if administration of cilostazol changes plasma leakage and oxygen transport across exchange vessels upon ischemic insult.

2 Materials and Methods

2.1 Animal Preparation

Experiments were performed in adult male C57BL/6 mice weighing 19–23 g (aged 8–10 weeks). The animals were anesthetized with an intraperitoneal injection of α-chloralose (60 mg/kg) and urethane (600 mg/kg) and a femoral vein was cannulated with a polyethylene catheter. Forebrain ischemia was induced by ligation of bilateral common carotid arteries (BCCA) with 5-0 silk sutures for 60 min. Exposure of the BCCA without occlusion was used to produce sham control animals. Animals were killed at variable time points according to the experimental protocols. Cilostazol (30 mg/kg, Otsuka Pharmaceutical) was suspended in 0.5% carboxymethylcellulose solution at a volume of 10 ml/kg. The control groups received the same volume of the corresponding vehicle solution. The drugs were administered orally at 4h prior to the reperfusion.

2.2 Measurement of Plasma Leakage

Plasma leakage was measured by modified Miles assay as described previously [5]. Briefly, Evans blue (30 mg/kg in 100 μl of PBS) was injected intravenously after removing the ligature on BCCA. At this concentration 98% of the dye should be bound to the plasma protein; thus it can serve as a plasma marker. Four hours after reperfusion, the vasculature was perfused transcardially with 50 mmol/L citrate buffer (pH3.5) for 2 min. The brain was removed, the dye was extracted from tissues with 1 ml of formamide overnight at 55°C, and its amount was determined by spectrophotometry.

2.3 Evaluation of Capillary Patency

To evaluate capillary patency, we labeled plasma with dichlorotriazinylamino fluorescein (DTAF; Sigma-Aldrich) as described previously [6]. DTAF conjugated with bovine serum albumin was injected into a saphenous vein. Thirty seconds after completion of the injection, each mouse was decapitated and the brain was fixed in 80% ethanol for 24 h. Coronal brain slices, 50 μm in thickness, were prepared with a vibratome and examined under a fluorescence microscope. Photographs were taken at the level of bregma and at 3 mm caudal from bregma. Each photograph was analyzed to calculate an index for capillary patency that is defined as % of the perfused area divided by the total cross-sectional area.

2.4 Evaluation of Hypoxia and Vessel Perfusion

To assess hypoxic region, Hypoxyprobe-1 (60 mg/kg, Chemicon) was injected intraperitoneally 1 h before sacrifice. To mark vessel perfusion, mice were injected via a femoral vein with FITC labeled Lycopersicon esculentum lectin (4 mg/kg, Vector Laboratories) and lectin was circulated for 1 min. Brain tissues were processed for histochemical analysis [7]. Tissues were stained for anti-Hypoxyprobe-1 and for lectin bound to the endothelial cell surface. Furthermore, endothelial cells were visualized by anti-CD31 antibody.

2.5 Image Analysis

The collected images were processed by the digital imaging software (MetaMorph 6.1, Universal Imaging Corporation). Subsequently, the pixel-based data were converted into gray levels. To determine cross-sectional area of the perfused vessels, a certain grayscale value was applied as a cutoff point and grayscale values above the cutoff were treated as the area being perfused.

3 Results

First, we examined whether cilostazol modulates permeability properties of blood brain barrier (BBB) upon ischemic insult. To do so, we compared the flux of plasma protein across BBB using modified Miles assay. Ischemic insult induced by BCCA occlusion elevated leakage of plasma from the vasculature (Fig. 1a, black bar). We initially predicted that treatment of this PDE3 inhibitor could reduce plasma leakage by tightening the BBB through raising intracellular cAMP concentration in the endothelium. On the contrary, the plasma leakage in the cilostazol-treated group (Fig. 1a, gray bar) was greater than that

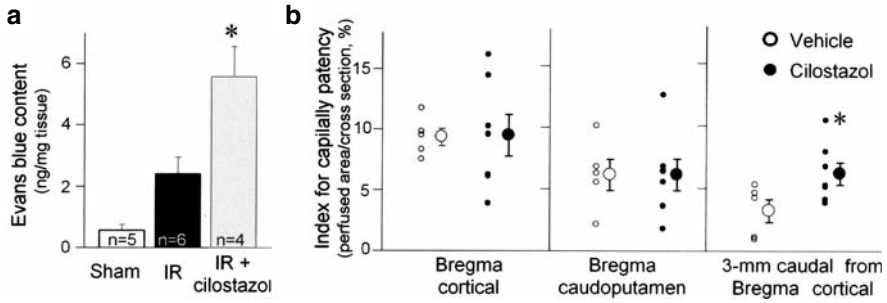

Fig. 1 Effects of the cilostazol treatment on plasma leakage and on capillary patency upon ischemic insult. **a**. Spectrophotometric measurement of amount of extravasated Evans blue in the brain 4 h after ischemic reperfusion (IR). Baseline leakage (*white bar*) was elevated after IR (*black bar*). Treatment with cilostazol (*gray bar*) caused a further elevation. **b**. Quantification of capillary patency in the three different sections of the brain. *Significantly greater leakage in treated group than in corresponding untreated group, $P < 0.05$

in the non-treated group. This finding led us to examine the possibility that cilostazol recruits more capillaries being perfused leading to an increase in the surface area for exchange of hydrophilic solutes during ischemic reperfusion. No difference in capillary patency was found in the sections at bregma. By contrast, in the cortical area at 3-mm caudal from bregma, cilostazol caused a significant increase in capillary patency (Fig. 1b).

To investigate whether this increase in capillary patency brings about optimizing tissue oxygenation, hypoxic areas were compared. As shown in Fig. 2a, a

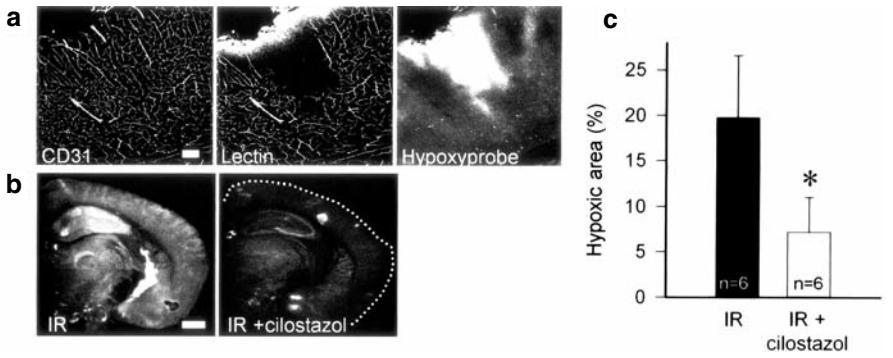

Fig. 2 Effects of the cilostazol treatment on oxygenation of the tissue upon ischemic insult. **a**. Hypoxia was found in the region of non-perfused area. This coronal section was stained for CD31 (*left*), L. esculentum lectin (*middle*) and hypoxyprobe (*right*) to mark vasculature, perfused vessels, and tissue hypoxia, respectively. Scale bar = 100 μm. **b**. Comparison of hypoxic area with and without the treatment of cilostazol. These sections were cut at 3-mm caudal from bregma. Scale bar = 2 mm. **c**. Quantification of hypoxic area. The treatment of cilostazol upon IR reduced hypoxic area. *, $P < 0.05$

non-perfused region appeared to show extensive hypoxia as indicated by a mirror image of lectin-negative and hypoxyprobe stainings. Histologic assessment showed significantly less extensive hypoxia in cilostazol-treated group than that in control (Fig. 2b, c), indicating more functional capillaries were being perfused when treated with cilostazol during ischemic insult. There was a correlation between the degree of capillary patency and the extent of tissue being hypoxic.

4 Discussion

In this study, we investigated the mechanisms of actions of cilostazol in an acute model of cerebral infarction. Main findings are: (i) that treatment with cilostazol increases protein flux across microvessels in the brain upon ischemia; and (ii) that it enhances oxygen transport to the brain parenchyma which is linked with an increase in the functional capillary density during ischemia.

From the point of view of transcapillary solute exchange, increased flux of plasma protein seen in the cilostazol treated animal can be accounted for by multiple factors. They are: (i) the surface area of exchange vessels; (ii) the endothelial permeability; (iii) the difference in the solute concentration across the exchange surface; (iv) the convective transport; and (v) the rate of delivery of the solute dissolved in the blood [8]. Although we are unable to demonstrate a causal relation between the increased plasma leakage and each factor listed above, the data showing an increase in capillary patency enables us to conclude that cilostazol causes protein flux to increase by recruiting more surface area for the exchange upon ischemic injury in the brain.

Previous studies indicate that cilostazol can elicit protective effects on the cerebral injury in ischemic stroke [3, 4]. Based on our result that cilostazol causes a reduction in hypoxic area after ischemia, it can be speculated that the treatment of this kind increases the oxygen delivery to the tissue. Considering the fact that reactive oxygen species are generated from oxygen, outcomes after increasing oxygen delivery might be two-fold and caution must be taken when we interpret current results.

In summary, cilostazol has a broad spectrum of pharmacological effects that may work together to improve tissue perfusion upon ischemic insult. Further studies are required to elucidate the mechanisms of this phenomenon.

Acknowledgments Supported by Japan Society for the Promotion of Science, Grant-in-Aid for Scientific Research 19500329, Health Labour Sciences Research Grant, Research on Advanced Medical Technology from the Ministry of Health Labour and Welfare (to M. K.), and Grant-in-Aid for Creative Scientific Research from the Ministry of Education, Culture, Sports, Science and Technology in Japan (to M.S.).

References

1. Yashiro Y, Ohhashi T. Effects of cilostazol, a selective cyclic AMP phosphodiesterase inhibitor on isolated rabbit spinal arterioles. Jpn J Physiol 2002;52:471–477.
2. Torii H, Kubota H, Ishihara H, Suzuki M. Cilostazol inhibits the redistribution of the actin cytoskeleton and junctional proteins on the blood-brain barrier under hypoxia/reoxygenation. Pharmacol Res 2007;55:104–110.
3. Gotoh F, Tohgi H, Hirai S, Terashi A, Fukuuchi Y, Otomo E et al. Cilostazol Stroke Prevention Study: A placebo-controlled double-blind trial for secondary prevention of cerebral infarction. J Stroke Cerebrovasc Dis 2000;9:147–157.
4. Huang Y, Cheng Y, Wu J, Li Y, Xu E, Hong Z et al. Cilostazol as an alternative to aspirin after ischaemic stroke: a randomised, double-blind, pilot study. Lancet Neurol 2008;7:494–499.
5. Thurston G, Suri C, Smith K, McClain J, Sato TN, Yancopoulos GD et al. Leakage-resistant blood vessels in mice transgenically overexpressing angiopoietin-1. Science 1999;286:2511–2514.
6. Kitagawa K, Matsumoto M, Mabuchi T, Yagita Y, Ohtsuki T, Hori M et al. Deficiency of intercellular adhesion molecule 1 attenuates microcirculatory disturbance and infarction size in focal cerebral ischemia. J Cereb Blood Flow Metab 1998;18:1336–1345.
7. Inai T, Mancuso M, Hashizume H, Baffert F, Haskell A, Baluk P et al. Inhibition of vascular endothelial growth factor (VEGF) signaling in cancer causes loss of endothelial fenestrations, regression of tumor vessels, and appearance of basement membrane ghosts. Am J Pathol 2004;165:35–52.
8. Michel CC, Curry FE. Microvascular permeability. Physiol Rev 1999;79:703–761.

Effect of Transient Forebrain Ischemia on Flavoprotein Autofluorescence and the Somatosensory Evoked Potential in the Rat

Takahiro Igarashi, Kaoru Sakatani, Tatsuya Hoshino, Norio Fujiwara, Yoshihiro Murata, Tsuneo Kano, Jun Kojima, Takamitsu Yamamoto, and Yoichi Katayama

Abstract In order to evaluate the effect of cerebral ischemia on the flavoprotein fluorescence (FPF), we compared the changes in the FPF and somatosensory evoked potential (SEP) during transient cerebral ischemia in the rat. We measured the FPF and SEP simultaneously via a cranial window made over the right sensorimotor cortex during the left median nerve stimulation in F344 rats. We compared change in FPF and SEP during cerebral ischemia for 60 min. The rCBF were rapidly recovered after reperfusion. However, the recovery rates of the FPF were significantly faster than those of the SEP after reperfusion. These findings indicate that activity-dependent changes of the FPF do not necessarily correlate with the electrical activity after transient cerebral ischemia.

1 Introduction

Recently, it has been demonstrated that the autofluorescence of flavoproteins is applicable for brain functional imaging in rats [7]. Flavoproteins are involved in the electron transfer system of mitochondria. Neuronal activity increases the intracellular Ca^{2+}, which converts the flavoprotein from the reduced form to the oxidized form. The oxidized flavoprotein emits green autofluorescence upon excitation with blue light. Studies on flavoprotein fluorescence (FPF) imaging have demonstrated that changes in the FPF in response to sensory stimulation are much faster and more localized compared to those in the cerebral vascular responses [7]. Furthermore, measurement of the FPF is more stable than that of the NADH fluorescence response [6]. FPF has been applied to functional imaging in the sensorimotor cortex [7], cerebellar cortex [6], auditory cortex [9], and visual cortex [10, 4] in rodents and cats.

K. Sakatani (✉)
Division of Optical Brain Engineering, Department of Neurological Surgery; Division of Applied System Neuroscience, Department of Advanced Medical Science, Nihon University School of Medicine, Tokyo, 173-8610, Japan
e-mail: sakatani@med.nihon-u.ac.jp

E. Takahashi, D.F. Bruley (eds.), *Oxygen Transport to Tissue XXXI*, Advances in Experimental Medicine and Biology 662,
DOI 10.1007/978-1-4419-1241-1_13, © Springer Science+Business Media, LLC 2010

However, it is not yet clear how cerebral ischemia affects the fluorescence; previous functional studies using the FPF have been conducted under normal circulatory conditions [7, 6, 9]. This issue is important for application of the FPF to research on functional reorganization after neuronal injury such as ischemic stroke. In the present study, we evaluated the effect of transient cerebral ischemia on the activity-dependent changes of FPF in the rat. We compared the changes of the FPF and somatosensory evoked potential (SEP) induced by transient cerebral ischemia.

2 Methods

2.1 Experimental Protocol

We employed adult male Fischer 344 rats (250 and 300 g, $n = 10$) anesthetized with 1.5% halothane. The right femoral artery was cannulated for recording of the arterial blood pressure and sampling of blood gases. The bilateral common carotid arteries were exposed, and closed with a tourniquet for transient forebrain ischemia. The rats then were fixed in a stereotaxic frame, and the right parieto-temporal bone was thinned (5 × 5 mm) over the sensorimotor cortex. Transient forebrain ischemia was induced by occlusion of the bilateral common carotid arteries for 60 min. The rectal temperature was maintained at about 37°C with an automatic heating pad. The arterial blood pressure (110 ± 8 mmHg, mean ± SD) remained stable throughout the experiments. The present animal experiments were performed carefully in accordance with the guiding principles for the care and use of laboratory animals approved by Nihon University School of Medicine.

2.2 Measurements of Flavoprotein Fluorescence

We recorded images of the green autofluorescence (barrier filter bandwidth, 500–550 nm) excited with blue light (excitation filter bandwidth, 450–490 nm) employing a cooled CCD camera system (AQUACOSMOS, Hamamatsu Photonics, Hamamatsu, Japan). The method of Britton Chance was referred to for measurement of the ratio of autofluorescence [3]. The left median nerve was stimulated with bipolar needle electrodes. The autofluorescence images (Fig. 1a) were analyzed by a pixel-by-pixel division to detect intrinsic signals, and the time course of the autofluorescence intensity was estimated (Fig. 1b). The autofluorescence responses reached a peak at 0.8–1.0 s after the stimulus onset, while the hemodynamic responses reached a peak at 2.0–2.5 s after the stimulus onset.

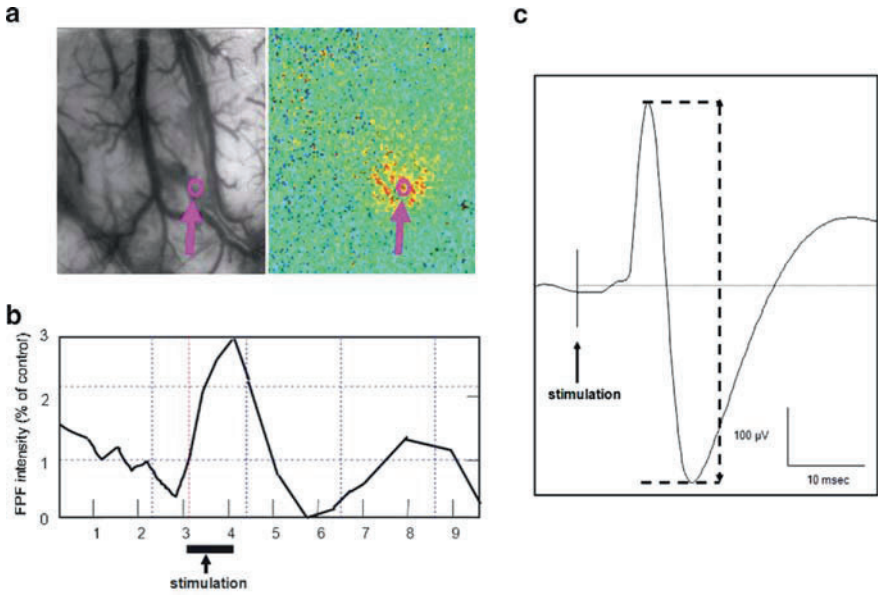

Fig. 1 **a**: Anatomical image of the recording area (*left*) and pseudo-color image of FPF changes during activation (*right*). **b**: Time course of the FPF intensity (*pink circle* in **a**) during activation. The ordinate indicates % change of FPF intensity. The thick horizontal bar indicates the period of electrical stimulation (1 s). **c**: Typical example of the SEP. The peak-to-peak amplitude was measured (*dotted lines*).

2.3 Measurements of SEP

We recorded the SEP with a Ag/AgCl ball electrode positioned at the forelimb area in the right sensorimotor cortex during left median nerve stimulation. A reference electrode was attached to the surrounding muscles and the ground lead was inserted in the right hind limb. The electrical stimulation was provided by a stimulator (SYNAX 2100, NEC), and 50 responses were averaged with a bandpass filter (10–1000 Hz). The amplitudes were measured peak-to-peak using the primary cortical response (Fig. 1c).

2.4 Data Analysis

Changes in SEP amplitude and FPF intensity were expressed as percentages of the responses under non-ischemic conditions (i.e. % SEP amplitude and % FPF intensity). Changes in regional cerebral blood flow (rCBF) caused by transient cerebral ischemia were measured with a laser-Doppler flowmeter (OMEGA-FLO FLO-N1, Omegawave). Changes in rCBF were expressed as a percentage of the non-ischemic baseline (i.e. % rCBF). Statistical analysis was performed

by means of an unpaired Student's *t*-test for comparisons involving the two ischemia models.

3 Results

Initially, we evaluated the frequency responses and intensity responses of the FPF and SEP under non-ischemic conditions ($n = 5$). Maximal SEP amplitude was observed at 0.5 Hz, and decreased with increase of the stimulus frequency. In contrast, the intensity of the FPF increased in association with increase of the stimulus frequency, and attained maximal intensity at 50 Hz (Fig. 2a). The FPF intensities and SEP amplitudes reached plateau levels at a stimulus intensity of over 4 mA (Fig. 2b). Based on these findings, we carried out ischemia-reperfusion experiments using supramaximal stimulation.

Occlusion of the bilateral common carotid arteries decreased the rCBF to $15.8 \pm 3.8\%$ of the controls. After reperfusion, the rCBF gradually recovered to $85.2 \pm 15.1\%$ of the controls at 90 min after reperfusion.

Figure 3a compares the changes in SEP and FPF during transient forebrain ischemia. The SEP and FPF disappeared rapidly after occlusion of the bilateral common carotid arteries. After reperfusion, the SEP and FPF gradually recovered; however, the recovery rates of the FPF were significantly faster than those of the SEP at 15 min ($p < 0.05$) and 30 min ($p < 0.01$) after reperfusion (Fig. 3b).

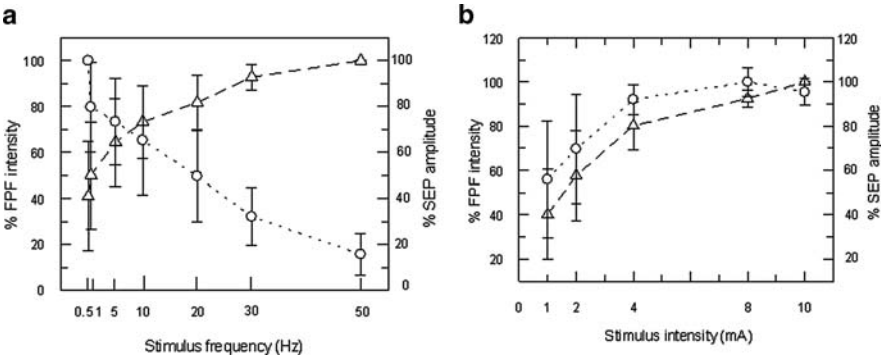

Fig. 2 **a**: Frequency responses of the FPF intensity and SEP amplitude. The ordinates indicate % changes of the maximal responses of the FPF intensity (*left*) and SEP amplitude (*right*), while the abscissa indicates the stimulus frequency (Hz). Open circles (○, n = 5) indicate the mean value of the % SEP amplitude; open triangles (△, n = 5) indicate the mean value of the % FPF intensity. **b**: Stimulus intensity responses of the FPF intensity and SEP amplitude. The ordinates indicate % changes of the maximal responses of the FPF intensity (*left*) and SEP amplitude (*right*), while the abscissa indicates the stimulus intensity (mA)

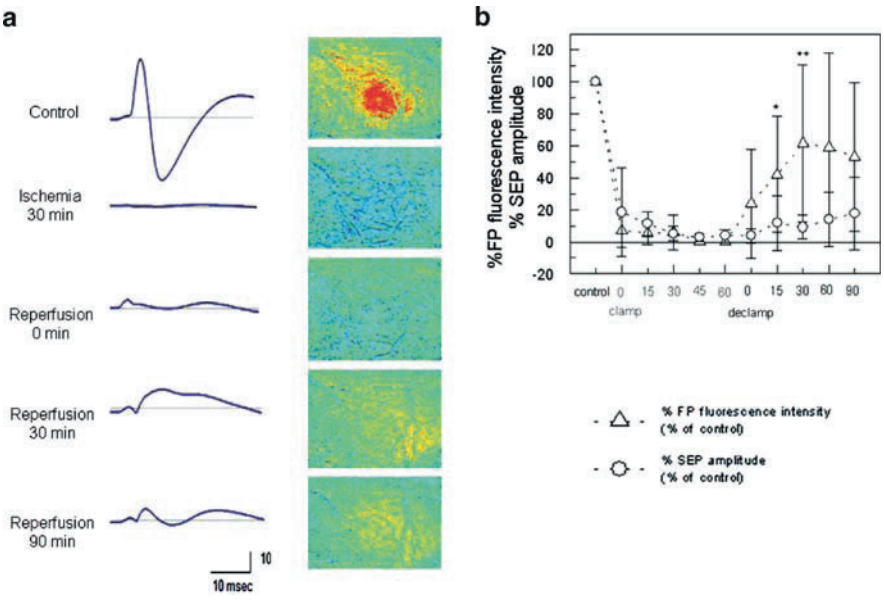

Fig. 3 **a**: Changes of SEP amplitude and FPF intensity during cerebral ischemia and after reperfusion in the 60-min ischemia model. **b**: There were significant differences in recovery rate between the SEP amplitude and FPF intensity at 15 and 30 min after reperfusion (*$p <$ 0.05, **$p < 0.01$)

4 Discussion

The present study demonstrated that the recovery rate of the SEP amplitude was significantly slower than that of the FPF after transient forebrain ischemia for 60 min. These findings indicate that transient cerebral ischemia affects the relation between activity-dependent changes of the FPF and the electrical activity.

Although the physiological mechanism of the dissociation in recovery rates between the FPF and SEP is not yet clear, FPF signal from astrocytes may play a role in the higher recovery rate of the FPF after reperfusion. Several reports have proposed that astrocytes play an important role in the active control of neuronal activity and synaptic neurotransmission [1, 5]. Astrocytes respond to neuronal activity with an increase of their internal Ca^{2+}, which triggers the release of chemical transmitters from the astrocytes themselves and, in turn, causes feedback regulation of the neuronal activity and synaptic strength. Such activity of astrocytes during neuronal activity could induce oxidation of flavoprotein in the electron transfer system, leading to emission of autofluorescence similar to that of neurons. Indeed, it has been demonstrated that the autofluorescence intensity was significantly decreased by the blocking of glial activity [2]. It should be noted that astrocytes are relatively resistant to ischemia as

compared to neurons [8]. These observations suggest that the FPF signal from astrocytes might be involved in the greater recovery of the FPF response after reperfusion in the 60-min ischemia model.

Conclusion: The present findings indicate that activity-dependent changes of the FPF do not necessarily correlate with the electrical activity after transient cerebral ischemia. The following mechanisms are suggested for the dissociation in recovery rates of the FPF and SEP after reperfusion. First, the FPF signal from astrocytes may contribute to the higher recovery rate of the FPF. Second, there are differences in ischemic tolerance between the cortical layers which generate FPF and SEP signals; the second and third layers which generate the FPF are more resistant to ischemia than the fourth layer which generates the SEP.

References

1. Araque A, Parpura V, Sanzgiri RP et al. (1998) Glutamate-dependent astrocyte modulation of synaptic transmission between cultured hippocampal neurons. Eur J Neurosci 10:2129–2142.
2. Buchheim K, Wessel O, Siegmund H et al. (2005) Processes and components participating in the generation of intrinsic optical signal changes in vitro. Eur J Neurosci 22:125–132.
3. Chance B, Legallais V (1963) A spectrofluorometer for recording of intracellular oxidation-reduction states. IEEE Trans Biomed Eng 10:40–47.
4. Husson TR, Mallik AK, Zhang JX et al. (2007) Functional imaging of primary visual cortex using flavoprotein autofluorescence. J Neurosci 27:8665–8675
5. Koizumi S, Saito Y, Nakazawa K et al. (2002) Spatial and temporal aspects of Ca^{2+} signaling mediated by P2Y receptors in cultured rat hippocampal astrocytes. Life Sci 72:431–442.
6. Reinert KC, Dunbar RL, Gao W et al. (2004) Flavoprotein autofluorescence imaging of neuronal activation in the cerebellar cortex in vivo. J Neurophysiol 92:199–211.
7. Shibuki K, Hishida R, Murakami H et al. (2003) Dynamic imaging of somatosensory cortical activity in the rat visualized by flavoprotein autofluorescence. J Physiol 549:919–927.
8. Siesjö BK (1988) Mechanisms of ischemic brain damage. Crit Care Med 16:954–963.
9. Takahashi K, Hishida R, Kubota Y et al. (2006) Transcranial fluorescence imaging of auditory cortical plasticity regulated by acoustic environments in mice. Eur J Neurosci 23:1365–1376.
10. Tohmi M, Kitaura H, Komagata S et al (2006) Enduring critical period plasticity visualized by transcranial flavoprotein imaging in mouse primary visual cortex. J Neurosci 26:11775–11785.

Assessing a Shift of Glucose Biotransformation by LC-MS/MS-based Metabolome Analysis in Carbon Monoxide-Exposed Cells

Naoharu Takano, Takehiro Yamamoto, Takeshi Adachi, and Makoto Suematsu

Abstract Carbon monoxide (CO) is the stress-inducible gas generated by heme oxygenase (HO). Although the HO/CO system appears to contribute to cell protection and tissue repair under stress conditions, its mode of actions remains largely unknown. We hypothesized that CO might alter the cellular energetic conditions and thereby modulate oxygen metabolism. To examine this hypothesis, we attempted to establish a method to follow the global flux of ^{13}C-glucose in the cells using metabolomic approaches with liquid chromatography-mass spectrometry (LC-MS/MS). The human monoblastic leukemia cell line U937 was exposed to the CO-releasing molecule (CORM). The CO exposure attenuated the conversion of the mass-labeled glucose to its downstream metabolites, while significantly stimulating its conversion to those for pentose phosphate pathway, suggesting roles of stress-inducible CO in a shift of glucose biotransformation.

1 Introduction

Within the cells, glucose is mainly catalyzed through glycolysis and pentose phosphate pathway. Such a utilization of glucose is necessary for cellular adaptation against stressors. For examples, hypoxia induces a transcriptional factor, hypoxia inducible factor-1 (HIF-1), which induces GLUT-1, GAPDH, PDK-1, and LDH [1], and promotes anaerobic glycolysis to adapt hypoxia. Since hypoxia causes an induction of heme oxygenase [2, 3], the CO-producing enzyme, it is not unreasonable to hypothesize that the gas might also change the biotransformation of glucose. To measure the global picture of glucose utilization, we have herein established the flux analysis with ^{13}C-labeled glucose using

M. Suematsu (✉)
Department of Biochemistry & Integrative Medical Biology, School of Medicine, Keio University, Tokyo, 160-8582, Japan
e-mail: msuem@sc.itc.keio.ac.jp

E. Takahashi, D.F. Bruley (eds.), *Oxygen Transport to Tissue XXXI*, Advances in Experimental Medicine and Biology 662,
DOI 10.1007/978-1-4419-1241-1_14, © Springer Science+Business Media, LLC 2010

LC-MS/MS. Using this methodology, we aimed to examine the effects of CO on glucose utilization through the fluxome analysis.

2 Materials and Methods

2.1 Materials and Extraction of Metabolites

DHAP, 2-deoxy-G6P, Gal1P, GA3P, 3PG, and 6PG were purchased from Sigma. Fru1, 6P2, Ribo5P, and Xylu5P were purchased from Fluka. Fru6P, Glu1P, Glu6P, Pyr, PEP, were purchased from Wako. Lac was purchased from Tokyo Kasei Kogyo. Sed7P was purchased from GLYCOTEAM GmbH. CORM (Tricarbonyldichlororuthenium(II) dimer) and ruthenium (III) chloride (Ru) were purchased from Aldrich. U937 cells were cultured with RPMI-1640 medium supplemented with 10% FBS, penicillin and streptomycin, and grown in a CO_2 incubator. U937 cells were plated at 5×10^6 cells/10 cm dish and cultured around 14 h. Then the cells were treated with 100 μM CORM or Ru as a control for 30 min. After the CORM or Ru treatment, medium was exchanged to glucose-free RPMI-1640 supplemented with 10% FBS, penicillin and streptomycin, and added $^{13}C_6$-glucose at 2000 mg/L. After the addition of $^{13}C_6$-glucose containing medium, cells were left for 5 min in the CO_2 incubator and immediately centrifuged to collect them at 1,500 rpm for 2 min. Then cells were washed with PBS(–) once. Collected cells were immediately frozen in liquid N_2 and stored at –80°C until extraction. 400 μl methanol containing internal standard (IS) (2-deoxy-glucose-6P: 0.3 μM) were added to harvested cells and voltexed. Then, 200 μL water was added and mixed for 30 min. After the addition of 400 μL chloroform and voltexed, centrifuged at 14,000×*g* for 30 min. Supernatant were filtrated with 5 kDa cut-off filter and dried with Speed-Vac. Dried samples were stored at –80°C till LC-MS/MS analysis.

2.2 LC-MS/MS

LC-MS/MS analysis was performed as previously reported with some modifications [4, 5]. Chromatographic separations were carried out on Synergi Hydro-RP (C18) column (150 × 2.0 mm, 4 μm, 80 Å, phenomenex). The chromato-graphic system was an Agilent 1100 series binary HPLC system (Agilent Technologies). Separations were performed under gradient conditions as described in Table 1. Column temperature was set to 40°C. Mobile phases consisted of 15 mM acetic acid/10 mM tributylamine/H_2O (A) and 100% Methanol (B).

Mass spectrometry analysis was carried out on Applied Biosystems/API 3000 equipped with a TurboIon spray source. The MS was operated in the negative ion and multiple reactions monitoring (MRM) mode. Single analyte standard dissolved in a 10 mM acetic acid was infused at a flow rate of 5 μL/min

Table 1 Gradient profile

Period	Step	Total time (min)	Flow rate (μL/min)	A(%)	B(%)
1	0	10.0	200	99	1
1	1	10.0	200	99	1
1	2	25.0	200	80	20
2	3	30.0	200	80	20
2	4	30.1	200	65	35
2	5	35.0	200	65	35
2	6	40.0	200	40	60
2	7	45.0	200	40	60
2	8	45.1	200	10	90
2	9	55.0	200	10	90

Column was equilibrated in step 0 for 10 min and MRM scan was separated in 2 periods at step 3

for tuning compound dependent MS parameters. These parameters were as follows: ionspray voltage −4000 V, nebulizer gas (NEB) 14, curtain gas (GUS) 14, auxiliary gas temperature (TEM) 400, and collision gas (CAD) 4. MS parameters for each metabolite are given in Table 2. Extracted metabolites were diluted with 50 μL of H_2O and the injected volume was 10 μL. Standard samples (1 μM) and extracted metabolites from cultured cells were measured by LC-MS/MS and detected peaks were compared. Areas of each metabolite were calculated and divided by IS peak area.

3 Results

3.1 Measurement of ^{13}C-Labeled Metabolites by LC-MS/MS

To assess the effect of carbon monoxide on glucose metabolism, we tried to establish a method for measuring the global flux of $^{13}C_6$-labeled glucose by modifying the method previously reported by Luo et al. [4, 5]. First, we measured standard samples and confirmed the detection of each metabolite. Detected peaks of each standard are shown in Fig. 1. Sed7P, Ribo5P, Ribu5P, Xylu5P, Glu6P, Fru6P, Glu1P, Gal1P, GA3P, DHAP, Pyr, Lac and 2-deoxy-G6P were detected in period 1 and 6PG, Fru1, 6P2, 3PG, and PEP were detected in period 2. MS scan for Glu1P/Gal1P and Glu6P/Fru6P detected all other metabolites but in lower sensitivity (Fig. 1d). Next, we confirmed the detection of ^{13}C-labeled metabolites. We measured the cells cultured without $^{13}C_6$-glucose as a negative control and confirmed that they did not give peaks of ^{13}C-labeled metabolites (data not shown). Then, we measured the cells cultured with $^{13}C_6$-glucose and checked the overlap of signals derived from ^{13}C-labeled metabolites and non-labeled metabolites (Fig. 1). With these results, we confirmed that metabolites derived from $^{13}C_6$-glucose were measured correctly.

Table 2 MS parameters

Compound	Q1(12C)	Q1(13C)	Q3(12C)	Q3(12C)	DP	FP	EP	CE	CXP
Glu1P/Gal1P	258.744	264.744	78.95	78.95	−41	−300	−10	−40	−5
Glu6P/Fru6P	258.745	264.744	97.15	97.15	−36	−36	−10	−24	−5
GA3P/DHAP	168.751	171.75	97.15	97.15	−41	−330	−10	−14	−5
Pyr	86.852	89.8	43.25	45.3	−31	−330	−10	−12	−1
Lac	88.826	91.8	43.25	45.3	−26	−240	−10	−18	−1
Rbio5P/Ribu5P/Xylu5P	228.714	233.714	97.15	97.15	−31	−230	−10	−18	−5
Sed7P	288.817	295.817	97.15	97.15	−41	−330	−10	−28	−5
2-deoxy-G6P	242.85		97.15		−86	−250	−10	−22	−5
Fru1,6P2	338.4	344.4	97.15	97.15	−36	−260	−10	−30	−7
3PG	184.782	187.782	97.15	97.15	−31	−260	−10	−22	−5
PEP	166.758	169.758	79.05	79.05	−21	−220	−10	−16	−1
6PG	274.826	280.826	97.15	97.15	−21	−230	−10	−24	−5

Abbreviations: Glu1P: glucose-1-phosphate; Gal1P: galactose-1-phosphate; Glu6P: glucose-6-phosphate; Fru6P: frucotse-6-phosphate; GA3P: glyceraldehyde-3-phosphate; DHAP: dihydroxy-acetone-phosphate; Pyr: pyruvate; Lac: lactate; Ribo5P: ribose-5-phosphate; Ribu5P: ribulose-5-phosphate; Xylu5P: xylulose-5-phosphate; Sed7P: sedheptulose-7-phosphate; 2-deoxy-G6P: 2-deoxy-glucose-6-phosphate; Fru1,6P2: fructose-1,6-bisphosphate; 3PG: 3-phospho-glycerate; PEP: phosphoenolpyruvate; 6PG: 6-phospho-gluconate.

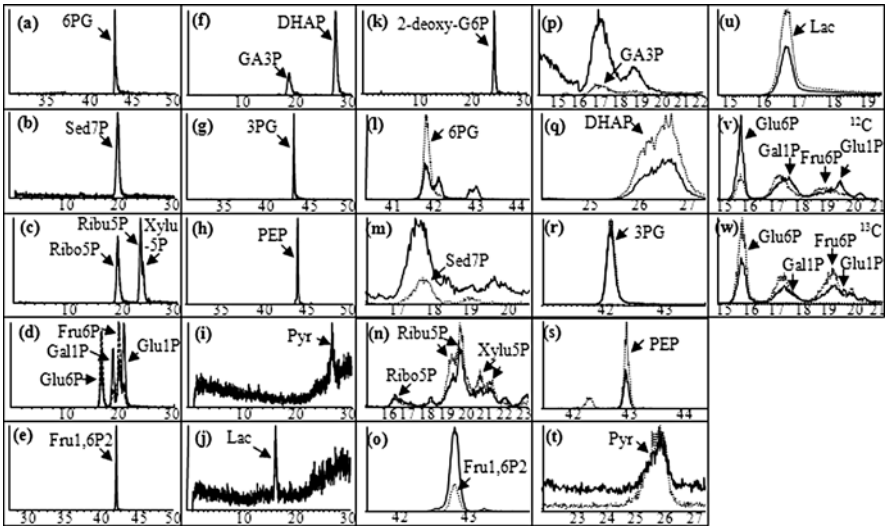

Fig. 1 Chromatograms of standard samples (**a–k**) and metabolites in extracted samples (**l–w**). Each chromatogram shows the result of LS-MS/MS analysis of 1 μM standard samples (**a–k**). Retention times are shown at the bottom of each chromatogram. Arrows (**a–k**) indicate peaks of detected standard samples. (**d**) Solid line indicates MS scan of Gal1P/Glu1P and dashed line indicates MS scan of Glu6P/Fru6P. Solid lines indicate [^{12}C] metabolites and dashed lines indicate [^{13}C] metabolites (**l–u**). Solid line indicates MS scan of Gal1P/Glu1P and dashed line indicates MS scan of Glu6P/Fru6P (v, w). [^{12}C] metabolites and [^{13}C] metabolites are shown in (v) and (w), respectively. Arrows indicate detected [^{13}C] labeled in each metabolite (**l–w**)

3.2 Effect of CO on Glucose Metabolism

To assess the effect of CO on glucose metabolism, we measured and compared the global flux of $^{13}C_6$-glucose between CORM treated and Ru treated U937 cells (Fig. 2). This result shows that the amount of 6PG, Xylu5P was significantly increased and Sed7P and Ribu5P were modestly increased by CORM treatment, they were located on PPP. On the other hand, GA3P and 3PG were significantly decreased and PEP was modestly decreased by CORM treatment, they were located on the glycolytic pathway. These results indicate that CO suppressed flux to the glycolytic pathway, and increased flux to PPP.

4 Discussion

CO is produced by HO in response to a variety of stress, and is known to contribute to cell protection [2, 3]. In this report, we showed that CO worked as a putative metabolic regulator for glucose biotransformation, although the mechanisms remain unknown. Because activation of PPP produces NADPH by G6PD [6], CO might regulate redox conditions within cells, functioning

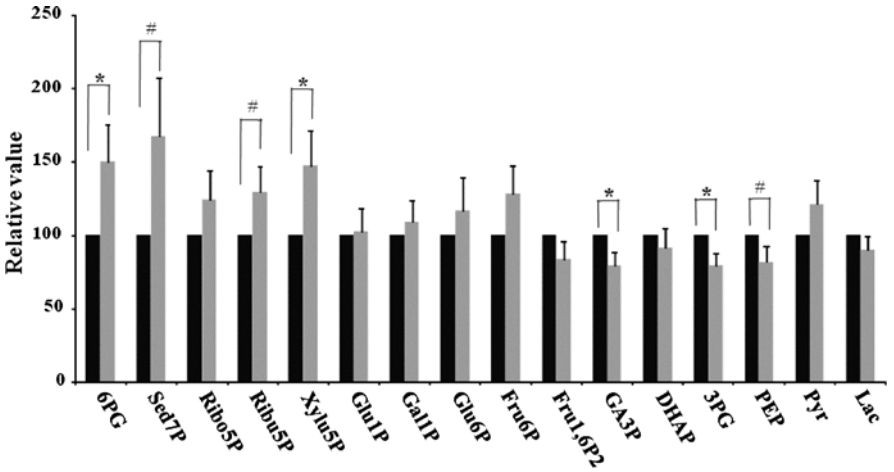

Fig. 2 Measurement of each [^{13}C] metabolite in Ru (*black bars*) or CORM (*gray bars*) treated U937 cells. Each value was calculated as relative value when the amount of each metabolite in Ru-treated cells was defined as 100. Bars indicate means ± S.E , $*P < 0.05$, $\#P < 0.07$, $n = 7$

against stresses. On the other hand, CO appears to suppress glycolysis. Since the cells were viable under the current experimental conditions, alternative mechanisms for cellular energetic to maintain ATP in the CO-exposed cells should be further examined. Collectively, the current study provided a useful method to follow the fate of glucose in different types of cells including not only those of mammals but of microorganisms which are exposed to varied stress conditions.

Acknowledgments This study is supported in part by Grant-in-Aid for Creative Scientific Research from MEXT, Grant-in-Aid for Young Scientists (B) from MEXT, Health and Labor Science Research Grant on Advanced Medical Technology from MHLW, and Scientific Frontier Research Grant from MEXT.

References

1. Airley RE, and Mobasheri A. Hypoxic regulation of glucose transport, anaerobic metabolism and angiogenesis in cancer: novel pathways and targets for anticancer therapeutics. Chemotherapy. 53(4), 233–256 (2007).
2. Suematsu M, and Ishimura Y. The heme oxygenase-carbon monoxide system: a regulator of hepatobiliary function. Hepatology. 31(1), 3–6 (2000).
3. Kyokane T, Norimizu S, Taniai H, Yamaguchi T, Takeoka S, Tsuchida E, Naito M, Nimura Y, Ishimura Y, and Suematsu M. Carbon monoxide from heme catabolism protects against hepatobiliary dysfunction in endotoxin-treated rat liver. Gastroenterology.120(5), 1227–1240 (2001).
4. Luo B, Groenke K, Takors R, Wandrey C, and Oldiges M. Simultaneous determination of multiple intracellular metabolites in glycolysis, pentose phosphate pathway and

tricarboxylic acid cycle by liquid chromatography-mass spectrometry. J. Chromato. A. 1147, 153–164 (2007).
5. Tian J, Bryk R, Itoh M, Suematsu M, and Nathan C. Variant tricarboxylic acid cycle in My-cobacterium tuberculosis: identification of alpha-ketoglutarate decarboxylase. Proc Natl Acad Sci USA. 102(30), 10670–10675 (2005).
6. Ho HY, Cheng ML, and Chiu DT. Glucose-6-phosphate dehydrogenase – from oxidative stress to cellular functions and degenerative diseases. Redox Rep. 12(3), 109–118 (2007).

T-state Stabilization of Hemoglobin by Nitric Oxide to Form α-Nitrosyl Heme Causes Constitutive Release of ATP from Human Erythrocytes

Tomotaka Akatsu, Kosuke Tsukada, Takako Hishiki, Kazuhiro Suga-numa, Minoru Tanabe, Motohide Shimazu, Yuko Kitagawa, Ayako Yachie-Kinoshita, and Makoto Suematsu

Abstract Upon hypoxia, erythrocytes utilize hemoglobin (Hb) to trigger activation of glycolysis through its interaction with band 3. This process contributes to maintenance of ATP, a portion of which is released extracellularly to trigger endothelium-dependent vasorelaxation. However, whether the ATP release results either from metabolic activation of the cells secondarily or from direct regulation of the gating through Hb allostery remains unknown. This study aimed to examine if stabilization of T-state Hb could induce steady-state and hypoxia-induced alterations in glycolysis and the ATP release from erythrocytes. Treatment of deoxygenated erythrocytes with a nitric oxide (NO) donor generated α-NO Hb that is stabilized T-state allostery. Under these circumstances, the release of ATP was significantly elevated even under normoxia and not further enhanced upon hypoxia. These events did not coincide with activation of glycolysis of the cells, so far as judged by the fact that intracellular ATP was significantly decreased by the NO treatment. Collectively, the present study suggests that hypoxia-induced ATP release is triggered through mechanisms involving R-T transition of Hb, and the gating process might occur irrespective of hypoxia-responsive regulation of glycolysis.

1 Introduction

Erythrocytes (RBCs) can sense alterations in local concentrations of gases using Hb. A decrease of partial oxygen tension (PO_2) and an increase in partial carbon dioxide tension (PCO_2) are known to stabilize Hb in the T state, facilitating the release of O_2 from Hb in the peripheral tissue. There is a growing body of evidence that RBCs respond to hypoxia to release a portion of intracellular ATP to the extracellular space, activating vascular relaxation to support oxygen supply to ischemic regions [1, 2]. Extracellular ATP activates the

T. Akatsu (✉)
Departments of Surgery, School of Medicine, Keio University, Tokyo, Japan
e-mail: gi026001@yahoo.co.jp

E. Takahashi, D.F. Bruley (eds.), *Oxygen Transport to Tissue XXXI*,
Advances in Experimental Medicine and Biology 662,
DOI 10.1007/978-1-4419-1241-1_15, © Springer Science+Business Media, LLC 2010

purinergic receptor on the vascular endothelial cells to trigger calcium ion (Ca^{2+}) influx and release of vasorelaxing signals such as NO and prostaglandin I_2 to the vascular smooth muscle cells, thereby eliciting vasorelaxation [3]. Several lines of experimental evidence have been provided to support the hypothesis that alterations in Hb allostery serve as a mechanism by which ATP is released to the extracellular space [4, 5]. Band 3, the anion exchanger type 1, accounts for approximately 25% of the total erythrocyte membrane protein, and its cytoplasmic domain has a greater affinity for the T-state Hb rather than for the R-state one [4, 6, 7]. CO exposure to the cells that stabilizes R-state Hb or treatment with DIDS that blocks function of band 3 attenuated the hypoxia-induced ATP release, suggesting that the interaction between Hb and band 3 plays a crucial role [4–6]. On the other hand, recent studies have revealed that hypoxia induces translocation of glycolytic enzymes from band 3 on the cell membrane and accelerates glucose oxidation to maintain ATP [4, 7]. These results led us to inquire whether the ATP release results either from metabolic activation of the cells secondarily or from direct regulation of the gating through Hb allostery. To this end, we attempted to examine effects of T-state stabilization of Hb on energy metabolism and the ATP release under normoxia and hypoxia.

2 Materials and Methods

RBCs were isolated from heparinized peripheral blood samples collected from healthy male volunteers. The samples were centrifuged at $600 \times g$ for 5 min at 4°C, and the plasma and buffy coat were removed by aspiration. The packed cells were resuspended and washed three times at 4°C in Tris-buffered solution (in mM; 140.5 NaCl, 4.7 KCl, 2.0 CaCl2, 1.2 MgSO4, 21 Tris, 5.5 glucose, with 10 g/L human albumin, final pH adjusted to 7.4). In some experiments, Hb was stabilized in the R state by CO. In brief, after Hb was fully deoxygenated by gentle purge with purified argon gas for 30 min at 4°C, the suspension was purged with CO for 30 min at 4°C. A portion of the sample was hemolyzed to determine the percentage of CO saturation by measuring light absorption spectra for CO-Hb, deoxygenated Hb, and oxygenated Hb. The actual percentage of CO saturation was $93 \pm 3\%$ (mean $\pm$ SE, $n = 4$). In other experiments, Hb was stabilized in the T state by pretreating the cells with an NO donor, FK 409 at a half molar concentration to that of Hb, as described elsewhere [8]. A portion of the sample was characterized by electron spin resonance spectrometry.

RBC suspension (Hct, 2.6%) was incubated at 37°C for 1 min in normoxic and hypoxic solutions. The reactions were completed by immersion in ice-cold water, and they were centrifuged at $600 \times g$ for 5 min at 4°C to collect the supernatant. The final PO_2 was determined in the supernatants using a fiber-optic oxygen sensor (OxyMicro, WPI Inc., FL, USA). The concentrations of ATP in the supernatants were measured by a luciferin-luciferase assay using a commercially available kit (Molecular Probes, Inc., OR, USA). The amount of free Hb in the supernatants was determined to examine the presence of

hemolysis caused by the cell preparation processes by measuring light absorbances at specific peaks of Hb derivatives between 400 and 450 nm (415 nm for oxyHb and 419 nm for CO-Hb) in a portion of the supernatants for ATP measurement. The rate of hemolysis was less than 0.025% in all experiments, suggesting that the current procedures for the cell preparation did not induce notable hemolysis. The actual amount of ATP release was defined by the following formula: (extracellular ATP) – (ATP derived from hemolysis). The mean intracellular ATP concentration under normoxia was 1.6 mM, and the amount of Hb derived from RBCs at 2.6% Hct was 1.6 μg/10^6 RBCs. Based on these data, the amount of ATP released by the hemolysis was calculated by the following formula: 1.6 mM × [free Hb (μg/10^{10} RBCs)]/[1.6 μg/10^6 RBCs)].

RBC suspension (Hct, 2.0%) was incubated at 37°C for 1 min in normoxic and hypoxic solutions. The reactions were completed by immersion in ice-cold water, and they were centrifuged at 600×*g* for 5 min at 4°C to collect the cells. Intracellular ATP and glycolytic products were measured by metabolome analyses with capillary electrophoresis mass spectrometry (CE-MS) according to the previously described methods [7].

3 Results

3.1 Hb Allostery Serves as a Trigger for ATP Release from Erythrocytes

As seen in Fig. 1a, the amounts of ATP released from the cells were increased 3 fold at 1 min after exposure to hypoxia. On the other hand, CO treatment

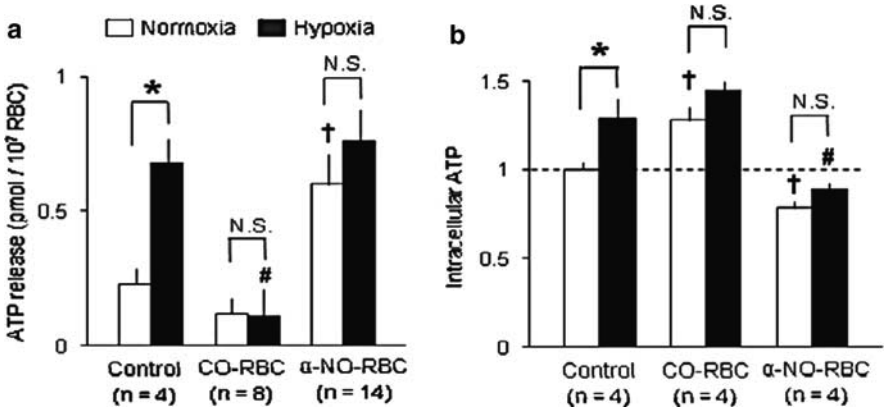

Fig. 1 **a** ATP release. **b** Intracellular ATP. The data are normalized to basal concentration in control group under normoxia. Means ± SE are shown. $^*P < 0.05$; $^\dagger P < 0.05$ (compared to data of control group upon normoxia); $^\#P < 0.05$ (compared to data of control group upon hypoxia). The PO_2 values for hypoxic groups: 16 ± 1 mmHg (mean ± SE) in RBC, 15 ± 2 mmHg in CO-RBC, and 16 ± 1 mmHg in α-NO-RBC, respectively

attenuated the hypoxia-induced ATP release almost completely. In contrast, T-state stabilization of Hb by pretreatment with NO resulted in the activation of ATP release even in the absence of hypoxia. These results suggest that the R-T transition of Hb plays a crucial role in triggering hypoxia-induced release of ATP from the cells.

3.2 T-state Stabilization of Hb by NO did not Increase Intracellular ATP in Erythrocytes

The amounts of ATP in control RBCs were increased by 29% at 1 min after exposure to hypoxia (Fig. 1b). We inquired if the α-NO treatment of Hb could activate glycolysis to increase the release of ATP. As seen in Fig. 1b, treatment with CO increased the basal level of ATP, while that with NO inversely suppressed it. In both groups, exposure of the cells to hypoxia did not cause any significant elevation of intracellular ATP levels. These results suggest that activation of the ATP release from α-NO-RBC (Fig. 1a) is unlikely to result from the glycolytic acceleration. Such a notion was well supported by results from metabolome analysis (Table 1). Under hypoxia, the control RBC increased intracellular lactate contents, while neither CO nor NO induced it, suggesting that the NO treatment did not accelerate glycolysis. To note is the difference in 2,3-bisphosphoglycerate (2,3-BPG) contents among groups. Treatment with CO but not with α-NO significantly increased both basal and hypoxia-stimulated contents of 2,3-BPG; This event appeared to result from R-state stabilization of Hb by the gas through inhibition of the metabolite binding to its allosteric site [7].

Table 1 Intracellular glycolytic metabolites. The data (%) are normalized to methionine sulfone, which is an internal standard that was added at 100 μM to protein-free samples for metabolome analysis collected from RBC lysates. Data indicate mean ± SE of 4 separate experiments. G6P: glucose 6-phosphate; F-1,6BP: fructose 1,6-bisphophate; 2,3-BPG: 2,3-bisphosphoglycerate; 3PG: 3-phosphoglycerate. $^{*}P < 0.05$; $^{\dagger}P < 0.05$ (compared to data of control group upon normoxia); $^{\#}P < 0.05$ (compared to data of control group upon hypoxia)

	Control		CO-RBC		α-NO-RBC	
	Normoxia	Hypoxia	Normoxia	Hypoxia	Normoxia	Hypoxia
G6P	16.5 ± 1.6	11.5 ± 0.3*	18.8 ± 0.3	20.5 ± 0.5$^{\#}$	2.9 ± 0.6†	2.7 ± 0.5$^{\#}$
F-1,6BP	4.8 ± 0.3	4.3 ± 0.4	9.7 ± 0.9†	12.7 ± 0.4*$^{\#}$	7.7 ± 0.5†	7.8 ± 0.5$^{\#}$
2,3-BPG	84.5 ± 5.3	100.3 ± 4.1*	166.8 ± 2.6†	224.7 ± 6.1*$^{\#}$	85.4 ± 6.2	91.4 ± 2.6
3PG	5.0 ± 0.4	3.8 ± 0.1*	7.8 ± 1.0†	7.4 ± 0.5$^{\#}$	5.9 ± 0.6	5.8 ± 0.6$^{\#}$
Lactate	22.6 ± 1.3	39.5 ± 0.8*	20.9 ± 1.5	22.4 ± 1.0$^{\#}$	20.5 ± 0.8	22.7 ± 0.7$^{\#}$

4 Discussion

Treatment of deoxygenated RBCs with the NO donor generated α-NO Hb that is stabilized in the T-state allostery. Under these circumstances, ATP release was activated even under normoxia but not further enhanced upon hypoxia. These events did not coincide with glycolytic activation of the cells, so far as judged by the results from metabolome analysis. Collectively, the current study suggests that hypoxia-responsive ATP release is triggered through mechanisms involving R-T transition of Hb, and the gating process might occur independently of hypoxia-responsive regulation of glycolysis. Previous study indicated that shear stress enhances endothelial ATP production and thereby activates NO-dependent vasodilatory mechanism [3]. RBCs in the ischemic regions could serve as an alternative resource of extracellular ATP to guarantee microvascular patency through its vasorelaxing action. Collectively with recent observation suggesting roles of cytochrome *c* oxidase in tissue-associated apparatus for hypoxic vasodilation [9], further investigation is necessary to unveil whole pictures of adaptive mechanisms against hypoxic insults.

Acknowledgments This work was supported by Grant-in-Aid for Creative Scientific Research 17GS0419 from MEXT Japan.

References

1. S. Locovei, L. Bao, G. Dahl. Pannexin 1 in erythrocytes: function without a gap. Proc. Natl. Acad. Sci. U. S. A. 103, 7655–7659 (2006).
2. M. L. Ellsworth, T. Forrester, C. G. Ellis, H. H. Dietrich. The erythrocyte as a regulator of vascular tone. Am. J. Physiol. Heart Circ. Physiol. 269, 2155–2161 (1995).
3. K. Yamamoto, T. Sokabe, T. Matsumoto, K. Yoshimura, M. Shibata, N. Ohura, T. Fukuda, T. Sato, K. Sekine, S. Kato, M. Isshiki, T. Fujita, M. Kobayashi, K. Kawamura, H. Masuda, A. Kamiya, J. Ando. Impaired flow-dependent control of vascular tone and remodeling in P2X4-deficient mice. Nat. Med. 12, 133–137 (2006).
4. J. E. Jagger, R. M. Bateman, M. L. Ellsworth, C. G. Ellis. Role of erythrocyte in regulating local O_2 delivery mediated by hemoglobin oxygenation. Am. J. Physiol. Heart Circ. Physiol. 280, 2833–2839 (2001).
5. J. Gonzalez-Alonso, D. B. Olsen, B. Saltin. Erythrocyte and the regulation of human skeletal muscle blood flow and oxygen delivery: role of circulating ATP. Circ. Res. 91, 1046–1055 (2002).
6. G. R. Bergfeld, T. Forrester. Release of ATP from human erythrocytes in response to a brief period of hypoxia and hypercapnia. Cardiovasc. Res. 26, 40–47 (1992).
7. A. Kinoshita, K. Tsukada, T. Soga, T. Hishiki, Y. Ueno, Y. Nakayama, M. Tomita, M. Suematsu. Roles of hemoglobin allostery in hypoxia-induced metabolic alterations in erythrocytes: simulation and its verification by metabolome analysis. J. Biol. Chem. 282, 10731–10741 (2007).
8. K. Suganuma, K. Tsukada, M. Kashiba, A. Tsuneshige, T. Furukawa, T. Kubota, N. Goda, M. Kitajima, T. Yonetani, M. Suematsu. Erythrocytes with T-state-stabilized

hemoglobin as a therapeutic tool for postischemic liver dysfunction. Antioxid. Redox. Signal. 8, 1847–1855 (2006).
9. M. Palacios-Callender, V. Hollis, M. Mitchison, N. Frakich, D. Unitt, S. Moncada. Cytochrome *c* oxidase regulates endogenous nitric oxide availability in respiring cells: A possible explanation for hypoxic vasodilatation. Proc. Natl. Acad. Sci. U. S. A. 104, 18508–18513 (2007).

Age-Related Changes in the Trachea in Healthy Adults

Hiroaki Sakai, Yasutaka Nakano, Shigeo Muro, Toyohiro Hirai, Yasutaka Takubo, Yoshitaka Oku, Hiroshi Hamakawa, Ayuko Takahashi, Toshihiko Sato, Fengshi Chen, Hisashi Sahara, Takuji Fujinaga, Kiyoshi Sato, Makoto Sonobe, Tsuyoshi Shoji, Ryo Miyahara, Kenichi Okubo, Toru Bando, Toshiki Hirata, Hiroshi Date, and Michiaki Mishima

Abstract To investigate age-related changes in the shape of trachea, normal male volunteers ($n = 83$, mean $\pm$ SD: 47.7 $\pm$ 20.2 years old) underwent inspiratory CT scans at full inspiration and lung function tests. Subjects who showed VC $< 80\%$ predicted or FEV1 $< 80\%$ predicted on lung function tests were excluded. The CT data, which is located at 2.0 cm above the aortic arch, were transferred to a personal computer. The tracheal area (St) and two parameters, Tracheal index (Ti) and Circularity (Ci) indicating the shape of the trachea, were automatically calculated. Ti was defined the ratio of the coronal to the sagittal diameter of the trachea, and the Ci ($Ci = 4\pi S/L2$, S: tracheal area, L: tracheal perimeter) was used to indicate the roundness of the trachea. A Ci value of less than 1 indicated the distortion of the roundness. Both St and St/BSA (body surface area) showed a significant correlation with age ($r = 0.37$, $r = 0.52$; $p = 0.0006$, $p < 0.0001$). Ti was not correlated with age ($r = -0.20$; $p = 0.0697$), whereas Ci was significantly correlated with age ($r = -0.32$; $p = 0.00364$). There were measurable age related changes of the trachea both in the area and the shape. Aging results in the increased tracheal area and a distortion of the roundness.

1 Introduction

The automated method for the analysis of the digital computed tomography (CT) images has been developed recently [1–5]. Using CT images, we can evaluate the airway size and configuration on its transection plane in vivo [6], and can examine in detail compared to plain chest roentgenogram. For example, we have reported that the trachea was distorted in COPD patients [7]. Hoffmann et al. showed the change in the tracheal cross-sectional area in children from 0 to 20 years old by CT image [8]. However, to our knowledge,

H. Sakai (✉)
Departments of Thoracic Surgery, Institute for Frontier Medical Sciences, Kyoto University, Kyoto, 606-8507, Japan
e-mail: hsakai@kuhp.kyoto-u.ac.jp

E. Takahashi, D.F. Bruley (eds.), *Oxygen Transport to Tissue XXXI*, Advances in Experimental Medicine and Biology 662,
DOI 10.1007/978-1-4419-1241-1_16, © Springer Science+Business Media, LLC 2010

there was no report about the age-related changes of the tracheal configuration evaluated by CT in healthy adults. In this study, we used an automated method for the analysis of the tracheal lumen on its size and configuration, and investigated age-related changes of those parameters.

2 Methods

This study included eighty-three healthy normal subjects ranging from 21 to 83 years old who were specially recruited for this study. They had no history of asthma or serious previous chest disease. Approval for the study was obtained from the Ethics Committee of Kyoto University, and written informed consent was obtained from each subject prior to the study. Pulmonary function was tested with a Chestac-65 V (Chest MI, Tokyo, Japan) on the same day that CT scans were performed. Vital capacity (VC), forced expiratory flow in one second (FEV1), residual volume (RV) by helium dilution method, and carbon monoxide diffusing capacity (DLCO) by the single breath method were measured. Subjects who showed VC $< 80\%$ predicted or FEV1 $< 80\%$ predicted on lung function tests were excluded. CT scans were performed with the subject in the supine position using the high-resolution scanner, X-Vigor (Toshiba, Tokyo, Japan), with the following settings: 2 mm slice thickness, scanning time 1.0 s, electrical voltage 120 kV, electrical current 200 mA, and a field of view (FOV) 32 cm [9, 3, 4]. Standard reconstruction algorithm for the lung field (FC85) was adopted. During the scan, subjects were requested to hold his breath after deep inspiration. Contrast medium was not used. Each CT image was composed of 512×512 matrix data of Hounsfield Unit (HU). The CT data were transferred to a personal computer, and were analyzed using custom software. The software automatically detected lung fields [1, 5], and trachea [7]. Tracheal size was analyzed on the CT image at 2 cm above the upper margin of the aortic arch. When the tracheal lumen was detected, the area, the sagittal length (Lsag) and the coronal length (Lcor) of the tracheal lumen were automatically measured. The short radius (SR) was defined as the minimal distance from the centroid of the tracheal lumen to the internal surface of the tracheal wall, and the long radius (LR) was defined as the maximum distance. The tracheal index (Ti) was defined as the ratio of Lcor/Lsag for the index of tracheal deformity [10, 11]. We also calculated another index to evaluate the roundness of the trachea; circularity (Ci) as 4πStr/a square of internal perimeter [7]. In general, if the figure is the circle, circularity is one. When the figure is distorted from circle, the circularity decreases. Therefore, circularity is the parameter for the roundness. All data were expressed mean $\pm$ SD. Linear regression analysis was used to determine the correlation between age and the results of the parameter for tracheal configuration, Fischer's Z transform test was used for to evaluate a significant correlation with age. A p value $p < 0.05$ was considered to be statistically significant.

3 Results

Table 1 shows the results of the size and parameters for configuration of the trachea. Table 2 shows the correlation coefficients between age and the parameters of the trachea. Both area of trachea (Str) and Str/BSA (body surface area) showed a significant correlation with age ($r = 0.34$, $p = 0.0069$; $r = 0.50$, $p < 0.0001$). However, Ti was not correlated with age, whereas both Ci and Lsag were significantly correlated with age ($r = -0.27$, $p = 0.0037$; $r = 0.42$, $p < 0.0001$).

Table 1 The parameters for the tracheal size and configuration in normal subjects

		Mean value	SD	Minimum	Maximum
Ci		0.87	0.03	0.75	0.91
Ti		0.91	0.11	0.59	1.34
Lsag	(mm)	20.2	2.5	16.4	28.5
Lcor	(mm)	18.2	2.01	14.6	26.3
Str	(mm^2)	287.4	56	188.7	520.8
Str/BSA		166.9	35.5	110.1	302.9

Ci: Circularity, Ti: Tracheal Index (Lcor/Lsag), Lsag: sagittal length, Lcor: coronal length, Str: area of trachea, BSA: Body Surface Area

Table 2 Correlation coefficients of parameters for tracheal configuration versus age in normal subjects

	Correlation coefficient	p value
Ci	−0.32	0.00364*
Ti	−0.2	0.0697
Lsag	0.41	<.0001*
Lcor	0.21	0.0629
Str	0.37	0.0006*
Str/BSA	0.52	<.0001*

Ci: Circularity, Ti: Tracheal Index (Lcor/Lsag), Lsag: sagittal length, Lcor: coronal length, Str: area of trachea, BSA: body surface area *: $p < 0.05$ (Fisher's Z transform)

4 Discussion

The results of this study showed that there were measurable age-related changes in the trachea both in the area and the shape. Significant information concerning tracheal cross-section has been observed from the diameter on frontal or lateral chest radiographs [12]. However, variations in the shape of the trachea and locations not tangential to the x-ray beam can complicate such analysis. Tsao and Shich [6] reported that Lsag of the trachea had a significant positive linear correlation with lateral chest diameter, and Trigaux et al. [13] showed that the Ti was significantly correlated with the functional residual capacity and

with the sternum-spine distance. In this study, we used CT to more accurately evaluate the size and the shape of the trachea. Although Ti measured by CT failed to show significant relationship with RV/TLC, Ci, Str/BSA and Lsag correlated significantly with RV/TLC. More importantly, Ci, Lsag, Str, Str/BSA correlated with age.

Rains et al. showed that there was a progressive increase in the tensile stiffness of tracheal cartilage with age. James et al. [14] .and Moreno et al. [15, 16] have shown that the degree of shortening of maximally contracted airway smooth muscle is influenced by the integrity of airway cartilage. The increased cartilage stiffness with increasing age could increase resting smooth muscle tension and decrease the potential for smooth muscle shortening by causing an increased after load. And since the shape of the trachea might be influenced by both sides of the lung, it is reasonable to get the result that the sagittal length of the trachea is increasing.

We also found that the measurements of the trachea correlated with FEV1. Airway cartilage is mechanically important in resisting airway collapse during maximal expiratory flow maneuvers and cough. The wave-speed theory of maximal expiratory flow limitation predicts that maximal expiratory flow from the lung is determined not only by the driving pressure and the resistance of airways upstream from the flow-limiting segment but also by the cross-sectional area and compliance of the airway at the flow-limiting site [17]. Studies both in humans [18, 19] and in experimental animals [20] show that the flow-limiting sites within the tracheobronchial tree are located predominantly in central cartilaginous airways during most of the forced expiratory vital capacity. Because cartilage makes up such an important structural component of the airway wall in central airways, it is reasonable to assume that its mechanical properties are important in determining their pressure-area behavior. Caldwell and Fry [21] and McCormack et al. [22] have shown that softening of tracheal cartilage by the intravenous injection of papain in the rabbit results in a significant reduction in maximal expiratory flow from the lung. In the present study we have found a significant negative correlation between age and PFR ($r = 0.637$, $P = 0.00037$). The Ti was originally defined as the ratio of Lcor, measured on the lateral view of a plain roentgenogram, to Lsag, measured on the posteroanterior view [10]. On plain roentgenograms, however, the length on the image is not the same as the real value because the image is enlarged in accordance with the distance between the subject and the film. Therefore, we used the CT image to make a precise evaluation of the trachea. On CT images, the axis of the trachea, however, is not always parallel to the sagittal plane nor to the horizontal plane. The plane of the CT image may not be vertical to the long axis of the trachea, and we may overestimate the deformity of the trachea on CT images. Therefore, we calculated the centroid of the trachea, using two CT images (2 and 4 cm above the top of the aortic arch) and determined the long axis of the trachea. Then, we calculated the angle of deviation between the long axis of the trachea to the vertical axis of the CT plane as previously reported [7].

The importance of this study is that the shape of the trachea is gradually distorted and increased in size by aging. When we consider the aging the residual volume is increasing with age, and this effect is more sensitive to the airway size. From the physiological view point increase in the size of the trachea with age is an acceptable result for the decrease in the flow-limitation with age. We concluded that there were measurable age-related changes in the trachea both in the area and the shape. Aging may result in the increased tracheal area and a distortion of the roundness.

Acknowledgments The authors thank Arnab Majumdar of the Department of Physics, Boston University for helpful advice and manuscript editing.

References

1. Sakai N et al.: An automated method to assess the distribution of low attenuation areas on chest CT scans in chronic pulmonary emphysema patients. Chest 1994; 106:1319–1325.
2. Nakano Y et al.: Comparison of low attenuation areas on CT between inner and outer segments of the lung in COPD patients: Incidence and contribution to lung function. Thorax 1999; 54:384–389.
3. Mishima M et al.: Optimized scanning conditions of HRCT in the follow-up of pulmonary emphysema. J Comput Assist Tomogr 1999; 23:380–384.
4. Mishima M et al.: Complexity of terminal airspace geometry assessed by lung computed tomography in normal subjects and patients with chronic obstructive pulmonary disease. Proc Natl Acad Sci USA 1999; 96:8829–8834.
5. Dechman G et al.: Assessment of acute pleural effusion in dogs by computed tomography. J Appl Physiol 1994; 76:1993–1998.
6. Tsao TC and Shieh WB: Intrathoracic tracheal dimensions and shape changes in chronic obstructive pulmonary disease. Taiwan I Hsueh Hui Tsa Chih 1994; 93:30–34.
7. Muro S et al.: Distorted trachea in patients with chronic obstructive pulmonary disease. Respiration 2000; 67:638–644.
8. Eoffmann EL et al.: Tracheal cross-sectional area in children: CT determination. Radiology 1983; 149:137–140.
9. Nishimura K et al.: Comparison of different computed tomography scanning methods for quantifying emphysema. J Thorac Imaging 1998; 13:193–198.
10. Greene R et al.: 'Saber-sheath' trachea: Relation to chronic obstructive pulmonary disease. Am J Roentgenol 1978; 130:441–445.
11. Greene R et al.: 'Saber-Sheath' trachea: A clinical and functional study of marked coronal narrowing of the intrathoracic trachea. Radiology 1975; 115:258–265.
12. Mishima M et al.: Standardization of low attenuation area versus total lung area in chest X-ray CT as an indicator of chronic pulmonary emphysema. Front Med Biol Eng 1997; 8:79–86.
13. Trigaux JP et al.: CT of saber-sheath trachea. Correlation with clinical, chest radiographic and functional findings. Acta Radiol 1994; 35:247–250.
14. James AL et al.: Quantitative measurement of smooth muscle shortening in isolated pig trachea. J Appl Pysiol 1987; 63:1360–1365.
15. Moreno RH et al.: Isovolumetric and isobaric rabbit tracheal contraction in vitro. J Appl Physiol 1987; 62: 82–90.
16. Moreno RH et al.: Intravenous papain-induced cartilage softening decreases preload of tracheal smooth muscle. Appl Physiol 1989; 66:1694–1698.

17. Dawson SV et al.: Wave-speed limitation on expiratory flow-a unifying concept. J Appl Physiol 1977; 43:498–515.
18. Fraser, RG et al.: Measurement of caliber of the human bronchi in 3 phases of respiration by tine bronchography. J Can Assoc Radiol 1961; 31:102–110.
19. Fraser, RG et al.: Bronchial dynamics in health and obstructive airway disease: Physiology and roentgenology. In: Frontiers of Chest Radiology, edited by M. Simon, E. J. Potchen and N. LeMay. New York: Grume & Stratton, 1969, pp. 76–101.
20. Mink S et al.: Mechanism of increased maximum expiratory flow during HeO, breathing in dogs. J Appl Physiol 1979; 47:490–502.
21. Caldwell EJ et al.: Pulmonary mechanics in the rabbit. J Appl Physiol 1969; 27:280–285.
22. Mccormack GS et al.: Lung mechanics in papain treated rabbits, J Appl Physiol 1986; 60:242–246.
23. Kory RC et al.: The veterans administration-army cooperative study of pulmonary function. I. Clinical spirometry in normal men. Am J Med 1961; 30:243–258.

Polycythemia and Changes in Erythropoietin Concentration in Rats Exposed to Intermittent Hypoxia

Makoto Ishii, Tokuzen Iwamoto, Asuka Nagai, Gen Sasao, Masayuki Iwasaki, and Ichiro Kuwahira

Abstract It is not clear whether blood hemoglobin concentration ([Hb]) increases with an increase in the exposure period of intermittent hypoxia (IHx) and reaches a constant level. Furthermore, it is not known whether plasma erythropoietin concentration ([EPO]) also increases with an increase in the exposure period. Using a rat model, first, we evaluated changes in [EPO] every hour after single exposure of 10% O_2 for 120 min in order to determine a peak level of [EPO]. Second, we evaluated the effect of IHx of 10% O_2, 120 min/day for 0 (control), 1, 2, 3, 4, 6 and 8 weeks on [Hb], arterial blood pressure (BP), heart rate (HR), arterial blood gases (ABGs) and [EPO]. [EPO] increased after cessation of the single hypoxic exposure, reached a peak at 1 h, and decreased gradually to the control levels within 18 h. IHx of 10% O_2, 120 min/day, produced a time-dependent increase in [Hb], and [Hb] reached a constant level after the exposure for 6 weeks. BP increased after the exposure for 4 weeks and remained elevated. There was no significant difference in HR and ABGs. [EPO] increased significantly and remained elevated at the same level for 1–3 weeks, however, the peak level of [EPO] declined markedly after [Hb] reached a constant level.

1 Introduction

Conditions such as obstructive sleep apnea syndrome (OSAS) are characterized by intermittent hypoxia (IHx). Arterial O_2 pressure (Pao_2) is reduced, but its reduction and duration varies considerably depending on the severity of the disease. Accordingly, not all patients develop polycythemia. Using a rat model, we have previously shown that there is a threshold to elicit polycythemia and

I. Kuwahira (✉)
Department of Medicine, Tokai University School of Medicine, Isehara, Kanagawa, 259-1193, Japan; Department of Medicine, Tokai University Tokyo Hospital, Tokyo, 151-0053, Japan
e-mail: kuwahira@tok.u-tokai.ac.jp

E. Takahashi, D.F. Bruley (eds.), *Oxygen Transport to Tissue XXXI*, Advances in Experimental Medicine and Biology 662,
DOI 10.1007/978-1-4419-1241-1_17, © Springer Science+Business Media, LLC 2010

that repetitive exposure to 10% O_2 for 120 min/day produces polycythemia [1]. However, it is not clear whether blood hemoglobin concentration ([Hb]) increases with an increase in the hypoxic exposure period and reaches a constant level during IHx. Furthermore, it is not known whether plasma erythropoietin concentration ([EPO]) also increases with an increase in the exposure period of IHx. In the present study, we evaluated effects of IHx of 10% O_2, 120 min/day on [Hb] and [EPO] in the rat.

2 Methods

2.1 Production of Intermittent Hypoxia

Male Sprague-Dawley rats were housed in an environmental Plexiglas chamber (30 × 30 × 30 cm), two rats in each, at a temperature of 23 ± 1(SE)°C, at a 12:12-h light-dark photoperiod. With the use of a timed solenoid valve, the gas flushing the chamber was automatically switched from compressed air to a mixture of 10% O_2 in N_2 and back to compressed air at a rate of 30 L/min. The O_2 concentration in the chamber was monitored by an O_2 analyzer (Beckman MO-11). The rats assigned to the IHx groups were exposed to 10% O_2 for 120 min/day for the desired exposure period in the chamber (see below). The experimental protocol had been reviewed by the Ethics Committee for Animal Experiments of our university.

2.2 Experimental Protocol and Statistics

First, we evaluated changes in [EPO] every hour after single exposure of 10% O_2 for 120 min in order to determine a peak level of [EPO]. Nine groups of male Sprague-Dawley (S-D) rats, 5 rats in each (weight 335 ± 4 g), were studied for the 0, 1, 2, 3, 4, 5, 6, 8 and 18 h after cessation of the hypoxic exposure. A PE-50 catheter was inserted 10–20 mm into the middle caudal artery under halothane anesthesia for withdrawal of blood samples. [EPO] was determined by radioimmunoassay (RIA).

Second, additional male S-D rats were divided into the following 7 experimental groups depending on the length (weeks) of hypoxic exposure – a 0-week (0-W, normoxic controls), a 1-week (1-W), a 2-week (2-W), a 3-week (3-W), a 4-week (4-W), a 6-week (6-W), and a 8-week (8-W) IHx groups, 6 rats in each (weight 347 ± 3 g). In each IHx group, the rats were exposed to 10% O_2, 120 min/day (1:00–3:00 P.M.) in the IHx chamber described above.

At the end of the desired exposure length to IHx, a PE-50 catheter was inserted 10–20 mm into the middle caudal artery under halothane anesthesia for monitoring blood pressure (BP) and heart rate (HR) and for withdrawal of blood samples. After completion of surgery, the rat was transferred to an

accommodation box described before [2] and allowed to recover fully from anesthesia and surgery for 3 h. BP and HR were monitored continuously, using a pressure transducer (Statham P23Gb) and a chart recorder. When stable BP and HR were attained, arterial blood samples were obtained under normoxia. Arterial blood gases (ABGs) were analyzed by means of a pH/blood-gas analyzer (Instrumentation Laboratory Model 1304). [Hb] was measured with a Radiometer OSM3 hemoximeter. [EPO] was determined by RIA. At the end of the experiment, the rat was anesthetized with halothane and killed by an overdose of pentobarbital sodium.

All results are means ± SE. Comparisons of the data among the different length (weeks) of hypoxic exposure were carried out by the following procedure. First, the Kruskal-Wallis rank test was used to determine whether a difference among the data was detected. If a difference was detected, the Mann-Whitney U-test was used to compare the data. A P value less than 0.05 was considered to indicate statistically significant differences.

3 Results

Figure 1 shows changes in [Hb] in the IHx group. IHx of 10% O_2, 120 min/day, induced polycythemia in 1 week and produced a time-dependent increase in [Hb] from 13.7 ± 0.1 (0 week) to 17.4 ± 0.4 g/dl (6 weeks). There was no significant difference in [Hb] between 6 and 8 weeks, indicating that [Hb] reached a constant level after the exposure for 6 weeks. Fig. 2 shows changes in [EPO] after single exposure of 10% O_2 for 120 min. [EPO] increased markedly after cessation of the single hypoxic exposure, reached a peak at 1 h, and decreased gradually to the control levels within 18 h. Figure 3 shows changes in [EPO] in the IHx group. [EPO] increased significantly and remained elevated at almost the same level for 1–3 weeks (107.3 ± 10.0 ∼ 109.5 ± 9.4 mU/ml), but declined to 63.2 ± 3.5 (6 weeks) and 44.9 ± 5.4 mU/ml (8 weeks) even though

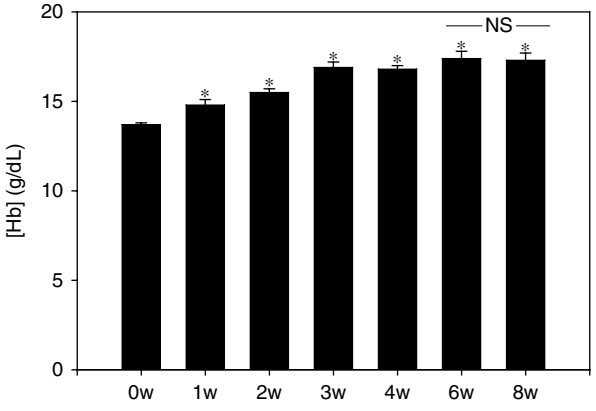

Fig. 1 Changes in [Hb] in the IHx group (*$P < 0.05$)

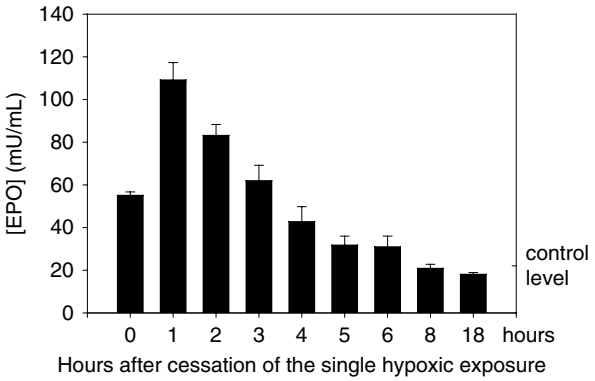

Fig. 2 Changes in [EPO] after single exposure of 10% O_2 in N_2 for 120 min

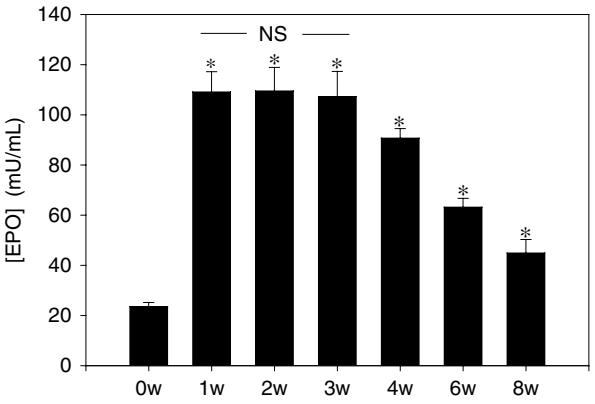

Fig. 3 Changes in [EPO] in the IHx group ($*P < 0.05$)

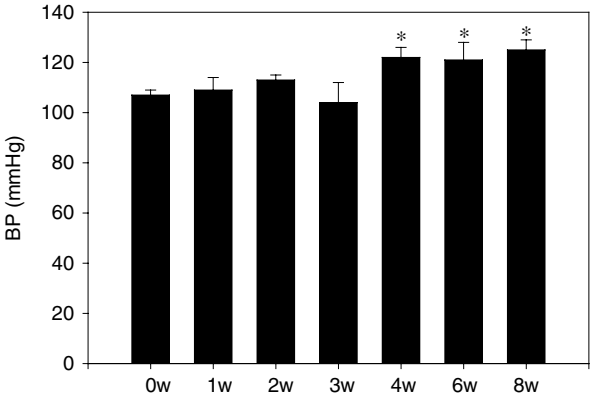

Fig. 4 Changes in BP in the IHx group ($*P < 0.05$)

the IHx exposure was continued. As shown in Fig. 4, BP increased significantly after the exposure for 4 weeks and remained elevated. There was no significant difference in HR and ABGs among all experimental groups.

4 Discussion

The results of the present study indicate that [Hb] increases with an increase in the hypoxic exposure period and reaches a constant level depending on the severity of hypoxia. It has been reported that repetitive exposure to 10% O_2 for 60 min/day for up to 5 weeks does not produce polycythemia [3, 4]. These results suggest that the intermittent hypoxia threshold for polycythemia might exist between 60 and 120 min/day in this level of hypoxia. Clinical conditions associated with IHx such as OSAS, often present permanent polycythemia. In these cases, the number of daily hypoxic episodes, and the total duration of hypoxia might reach the threshold to elicit permanent polycythemia. The magnitude of the increase in [Hb] may depend on the severity of the disease.

The IHx exposure is associated with a significant increase in [EPO]. [EPO] reaches a peak at 1 h after the daily hypoxic exposure, and decreases gradually to the control levels within 18 h. Cahan et al. examined the relationship between the duration of hypoxic exposure and EPO production in the rat [5]. They demonstrated that 1 h of hypobaric hypoxic exposure (0.5 atm, equivalent to 10% O_2) resulted in increased EPO levels 1 h after termination of hypoxia. Eckardt et al. found that [EPO] was significantly elevated 84 min after termination of hypoxic exposure in 4400 m for 5.5 h in humans [6]. Recently, it has been reported that EPO release in humans is increased as a result of 120 min of acute normobaric hypoxia, equivalent to 3100 m [7]. The results of the present study are in good agreement with these observations, although the duration and severity of hypoxia are variable between experiments. It has been also reported that mRNA for EPO is increased in rat kidneys after 1 h of acute hypoxia [8].

The peak level of [EPO] is markedly reduced after [Hb] reaches a constant level even though the IHx exposure is continued. The results suggest a marked reduction in EPO production in kidneys despite continued IHx. Although there might be a negative feedback control in EPO formation, mechanisms mediating the decline of [EPO] could not be determined from the present study.

An increase in [Hb] results in hypertension. The cause of hypertension is probably a combination of an increased sympathetic activity during IHx as well as increased blood viscosity derived from polycythemia. It has been reported that repetitive episodic hypoxia causes elevations of systemic blood pressure in rats [9]. It has been also demonstrated that the increased blood viscosity due to polycythemia is only partially responsible for the systemic hypertension [10]. In the present study, hypertension occurred after 4 weeks of IHx, although a significant increase in [Hb] was induced at 1 week of IHx. An increased sympathetic activity during IHx may play an important role on the systemic

hypertension. In summary, the results of the present study indicate that [Hb] increases with an increase in IHx and reaches a constant level. IHx is associated with an increase in [EPO]. However, the peak level of [EPO] is markedly reduced after [Hb] reaches a constant level despite continued IHx.

Acknowledgments The skillful technical assistance of Katsuko Naito, Yoko Takahari, and Yoshiko Shinozaki is gratefully acknowledged. This study was supported, in part, by the Ministry of Education, Science, Sports and Culture, Japan, Grant-in-Aid for Exploratory Research (No. 20659133, 2008).

References

1. Iwamoto T, Kamiya U, Ishii M, Urano T, Kuwahira I (2005) The threshold of the intermittent hypoxic exposure period to elicit polycythemia in rats. Tokai J Exp Clin Med 30:157–161.
2. Kuwahira I, Gonzalez NC, Heisler N, Piiper J (1993) Regional blood flow in conscious resting rats determined by microsphere distribution. J Appl Physiol 74:203–210.
3. Kuwahira I, Kamiya U, Iwamoto T, Moue Y, Urano T, Ohta Y, Gonzalez NC (1999) Splenic contraction-induced reversible increase in hemoglobin concentration in intermittent hypoxia. J Appl Physiol 86:181–187.
4. Kuwahira I, Kamiya U, Iwamoto T, Ishii M, Moue Y, Ohta Y, Gonzalez NC (2000) Alpha2-Adrenergic-receptor response in reversible increase in hemoglobin concentration in intermit-tent hypoxia. Pathophysiology 7:165–169.
5. Cahan C, Hoekje PL, Goldwasser E, Decker MJ, Strohl KP (1990) Assessing the characteristic between length of hypoxic exposure and serum erythropoietin levels. Am J Physiol 258:R1016–R1021.
6. Eckardt K-U, Boutellier U, Kurtz A, Schopen M, Koller EA, Bauer C (1989) Rate of erythropoietin formation in humans in response to acute hypobaric hypoxia. J Appl Physiol 66:1785–1792.
7. Mackenzie RWA, Watt PW, Maxwell NS (2008) Acute normobaric hypoxia stimulates erythropoietin release. High Alt Med Biol 9:28–37.
8. Schuster SJ, Wilson JH, Erslev AJ, Caro J (1987) Physiologic regulation and tissue localization of renal erythropoietin messenger RNA. Blood 70:316–381.
9. Fletcher EC, Lesske J, Qian W, Miller CC 3rd, Unger T (1992) Repetitive episodic hypoxia causes diurnal elevations of systemic blood pressure in rats. Hypertension 19:555–561.
10. Gonzalez NC, Erwing LP, Painter CF III, Clancy RL, Wagner PD (1994) Effect of hematocrit on systemic O_2 transport in hypoxic and normoxic exercise in rats. J Appl Physiol 77:1341–1348.

A Case of HAPE on K2 and Literature Review

Gen Sasao, Asuka Nagai, Tokuzen Iwamoto, Toshio Ichiwata, and Ichiro Kuwahira

Abstract HAPE (High Altitude Pulmonary Edema) is a serious and fatal disease in mountains. Early diagnosis and immediate descent are important for successful treatment. One of the authors (GS), who was healthy and a well trained climber, participated in the expedition to K2 (8611 m) in 2006 and developed HAPE. Under the severe environmental condition, it was difficult to evaluate his condition in its early stage. The earliest symptoms were nonspecific for HAPE as reported in many papers. Neither had he suffered from HAPE on the previous expeditions. These facts probably delayed the diagnosis in spite of its typical onset. This is a rare case report by a medical doctor who suffered from HAPE. The present case may remind the climbers of the difficulties in diagnosing HAPE on a mountain.

1 Introduction

HAPE (High Altitude Pulmonary Edema) is a serious disease for all climbers in high altitude. Because of lack of specific symptoms in its early stage, it is sometimes difficult to notice its onset and climbers may lose their chance to descend safely. The Tokai University K2 Expedition succeeded in reaching the summit of K2 (8611 m) in Pakistan on Aug 1, 2006. One of the authors (GS) participated in the expedition as a deputy leader and developed HAPE although he had never suffered from HAPE before, even over 7000 m. This report describes his experience. This is a rare case report by a medical doctor who suffered from and survived HAPE.

I. Kuwahira (✉)
Department of Medicine, Tokai University School of Medicine, Isehara, Kanagawa, 259-1193, Japan; Department of Medicine, Tokai University Tokyo Hospital, Tokyo, 151-0053, Japan
e-mail: kuwahira@tok.u-tokai.ac.jp

E. Takahashi, D.F. Bruley (eds.), *Oxygen Transport to Tissue XXXI*, Advances in Experimental Medicine and Biology 662,
DOI 10.1007/978-1-4419-1241-1_18, © Springer Science+Business Media, LLC 2010

2 Case

The patient, a 34 y/o medical doctor, was healthy and a well trained climber. He participated in the Tokai University K2 Expedition as a deputy leader from June 7 to August 25, 2006. In his daily life, he took alcoholic beverages occasionally and smoked 10 cigarettes per day for 10 years, but he quit smoking 6 months before the present expedition. Previously he had once reached the east summit of Kula Kangri (7381 m) in Tibet in 2001 without adverse health effects. In order to increase exercise performance, he had run 10–20 km, 3 times a week for 6 months prior to the present expedition. The profile of his climbing and changes in SpO_2 and AMS score (Lake Louise score, AMS self assessment) during the expedition are summarized in Fig. 1. Those were determined everyday in the morning during the expedition. SpO_2 was measured by the pulseoximeter, PULSOXC (Minolta Co. Ltd., Japan).

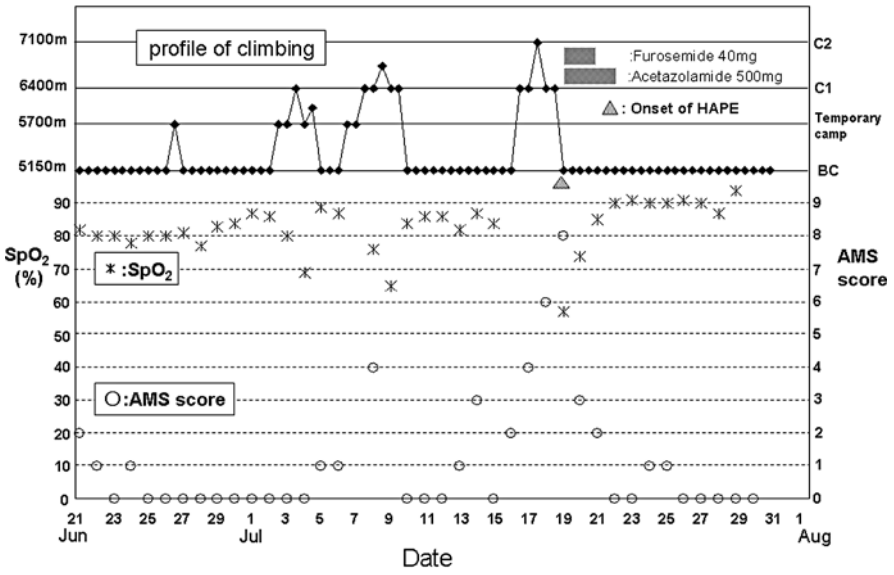

Fig. 1 Profile of climbing and changes in SpO_2 and AMS score during the expedition

After a 7 day trek from Askole (3000 m), which leads to the Baltoro Glacier, he reached the BC (Base Camp, 5150 m) on June 21. At BC, together with other members of the expedition, he participated in daily climbs. On June 26, his SpO_2 was 80% and AMS score was 0 at BC. On July 3, at the temporary camp (5700 m), his SpO_2 was 80% and AMS score was 0. He was in good condition at BC and the temporary camp. When he spent the first night at C1 (6400 m) on July 7, he did not sleep well. On July 8 in the morning at C1, he had a slight

headache and felt dizzy. His SpO_2 was 76% and AMS score was 4. But he pushed himself because many climbers sometimes have such symptoms in high altitude. As he climbed up, he gradually improved and could move the same as his companion up to the altitude of 6900 m. He came down to C1 safely during that day and ascribed his headache and dizziness to lack of sleep. On July 9, in the morning at C1, his SpO_2 was 65% (AMS score was not recorded) and he descended to BC without any serious problems.

After a few days rest, on July 16, he again ascended to C1 to open their route. On July 17, he again felt dizzy in the morning at C1. His AMS score was 4 (SpO_2 was not recorded). He left for C2 (7100 m) because he recognized that his condition was not severe AMS and self-limiting. But this time, during his climbing, he gradually noticed a marked decrease in exercise performance, dyspnea on exhaustion and a persistent dry cough. He reached C2 in the afternoon but soon he started to return. His symptoms continued to be worse. He complained of severe malaise, appetite loss, somnolence and headache when he returned to C1 in the evening. A companion noted his facial edema. He realized that descent was indispensable for his recovery. On July 18, he and his companion started the journey to BC. As he descended, his exercise performance and shortness of breath became worse, although they were relieved quickly by short resting. Taking a short rest every 10 m, he arrived at BC around 5 P.M. Their journey lasted twice as long as usual. He did not eat dinner and rested in his tent at 8 P.M. A few hours later, he awoke with abrupt onset of severe dyspnea, productive cough with serous and frothy sputum, chest oppression and orthopnea. Self-auscultation with a stethoscope revealed coarse crackles over the whole lung. Having diagnosed HAPE, he started to take furosemide (Lasix® 40 mg/day) and acetazolamide (Diamox® 500 mg/day), and rested in the sitting position. He did not use supplemental oxygen. The symptoms remained unabated through the night. On July 19, his AMS score was 8 and SpO_2 was 57% in the morning at BC. However, there was a slight relief in his symptoms. On July 20, his condition had improved markedly. On July 22, his symptoms had essentially disappeared. His SpO_2 was 90% and AMS score was 0. He discontinued the medication. Since then, he has been in very good health without signs of HAPE.

3 Discussion

HAPE is the most common cause of death from high altitude illness [1]. Younger persons and women seem more susceptible than men [2, 3]. Individual susceptibility, previous history of HAPE, rate of ascent, altitude reached, cold, physical exertion, and use of sleeping medications are all factors implicated in its occurrence [1, 4]. Symptoms of AMS often noted before the onset of HAPE include headache, loss of appetite, malaise, decreased exercise performance, slow recovery from exercise, fatigue, weakness and dyspnea on exertion. Signs

of impending pulmonary dysfunction in HAPE are persistent dry cough, orthopnea, dyspnea at rest, cyanosis and substernal pain. In HAPE, a productive cough often has traces of blood in the edema fluid. Cerebral signs and symptoms are common [5, 6]. The condition typically worsens at night. The clinical transition from AMS to HACE or to HAPE is often difficult to ascertain. For the successful treatment, early diagnosing is important. Hackett et al. reported that decreased exercise performance and persistent dry cough should raise suspicion of HAPE [5]. The best treatment is immediate descent. Delaying may be fatal unless oxygen is available [3].

In the present case, he acclimatized well at BC and the temporary camp. On July 17, just before leaving C1 for C2, his AMS score was 4 (headache 1, fatigue/weak 1 and sleeping difficulty 2), as shown in Fig. 2. But he pushed himself to further ascent and his symptoms became worse during his climbing. On the next day, at night he abruptly developed HAPE after he climbed down to BC. Considering the clinical course, it is possible that he was not acclimatized enough for the altitude of C1. His further exhaustion might trigger the onset of HAPE at BC. This may be a typical case. Hackett et al. reported that reports of victims dying during descent are probably related to the additional exertion offsetting the benefit of lower altitude [5]. He should have noticed and stopped climbing earlier.

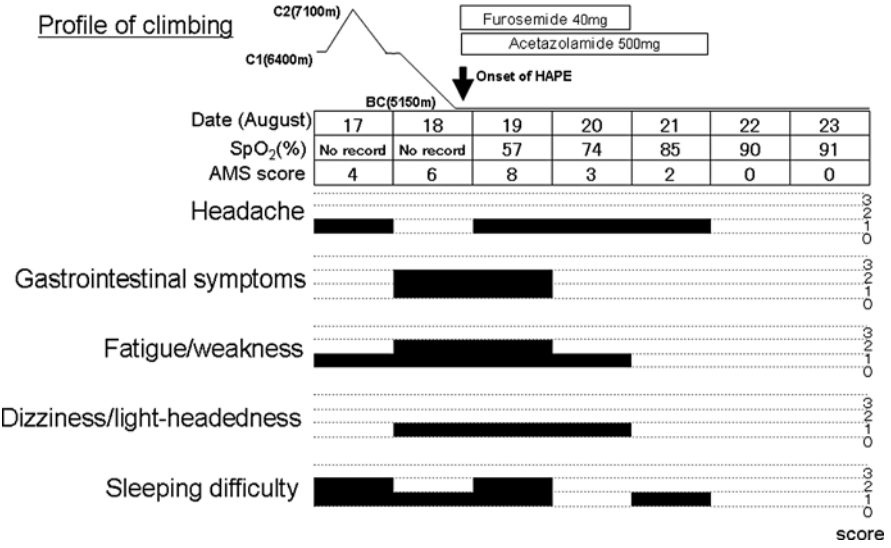

Fig. 2 Changes of SpO_2 and AMS score during the patient's HAPE

But there are some reasons why he delayed diagnosing HAPE. One is his climbing carrier over 7000 m. It is true that people who have had one episode of HAPE are likely to have another. Bartsch et al. reported that persons with prior

episode of HAPE may have a risk of recurrence as high as 60% if they abruptly ascend to an altitude of 4559 m [7]. But in this case, he was too dependent on his carrier. And some of the early symptoms, which are needed to understand the health condition, were difficult to be evaluated in the severe environmental condition like high camp. For instance, sleeping difficulty is important in scoring AMS. But, on the other hand, it is also common at altitude in people who do not have AMS [8]. Moreover, the prevailing conditions in high camp, such as marked incline of the terrain, rugged and hard floor, and cold, also could disturb his sleeping in this case. Cyanosis is difficult to detect in climbers' lips and face which are severely sunburned. The nail bed is pale because of cold. Audible crackles in the chest should be an important and sometimes the earliest sign of HAPE [9]. But it was hard to do auscultation precisely. The noise of a jacket rubbing or outside strong wind can easily disturb it. Dry cough and decreased performance should raise suspicion of HAPE [5]. But, cough is also common at high altitude and not particularly associated with AMS [1]. Recent work suggests that altitude hypoxia actually lowers the cough threshold, as measured with an inhaled citric acid stimulus [10]. Therefore, the clinical transition from AMS to HAPE is often difficult to ascertain.

Descent and oxygen supply are essential for treatment of HAPE [3]. But he did not use the supplemental oxygen in order to save it for other members. Although he improved gradually, he should have been treated with oxygen in addition to medication. Diuretics are not recommended presently [3], although it was once used [11].

4 Conclusion

In conclusion, to our best knowledge, this is not the first [12], but a rare case report in which a medical doctor developed and survived from HAPE. Climbers sometimes seem to push themselves hard and try to overcome the hardships in mountains even though they are not in good condition. The present case reminds us of the difficulties in evaluating our health condition on a mountain. Climbers should recognize that they may suffer from HAPE even without previous experience, and they also should be careful for the subsequent onset of HAPE when they have AMS.

Acknowledgments We would like to thank all those who contributed to the original work. These include climbers, scientists and other supporters who made the project possible.

References

1. Hackett PH, Roach RC (2001) High-Altitude Medicine. In: Auerbach PS (ed.) Wildernes Medicine 4th edn. Mosby, St. Louis.
2. Sophocles AM, Bachman J (1983) High-altitude pulmonary edema among visitors to Summit County, Colorado. J Fam Pract 17: 1015.

3. West JB, Schoene RB, Milledge JS (2007) High altitude pulmonary edema. In: High Altitude Medicine and Physiology 4th edn. Hodder Arnold, London.
4. Reeves JT et al. (1993) Seasonal variation in barometric pressure and temperature in Summit County: effect on altitude illness. In: Sutton JR, Houston CS, Coates G, (eds). Hypoxia and Molecular Medicine. Queen City Press, Vermont.
5. Hackett PH, Roach RC (2001) Review Articles. Current concepts high-altitude illness. N Engl J Med 345(2): 107–114.
6. Hultgren HN, Honigman B, Theis K, Nicholas D (1996) High-altitude pulmonary edema at a ski resort. West J Med 164:222–227.
7. Bartsch P, Maggiorini M, Ritter M, Noti C, Vock P, Oelz O (1991) Prevention of high altitude pulmonary edema by nifedipine. N Engl J Med 325:1284–1289.
8. West JB, Schoene RB, Milledge JS (2007) Sleep. In: High Altitude Medicine and Physiology 4th edn. Hodder Arnold, London.
9. Maggiorini M. (2006) High altitude-induced pulmonary oedema. Cardiovasc Res 72: 41–50.
10. Mason NP et al. (1999) Cough frequency and cough receptor sensitivity to citric acid challenge during a simulated ascent to extreme altitude. Eur Respir J 13:508.
11. Singh I, Kapila CC, Khanna PK, Nanda RB and Rao BDP (1965) High-altitude pulmonary oedema. Lancet 1: 229–234.
12. Wilkenson JA (2001) A personal account of high-altitude pulmonary edema. Wilderness Environ Med 12(1): 69–69.

Synchronization Between Cardiac and Respiratory Rhythms in Healthy Subjects and Patients

Masaki Shimane, Yutaka Tomita, Toshihiro Shinbo, Kenichi Kokubo, Minoru Hirose, Ryuji Hataishi, Hisashi Mitsufuji, Masaru Kubota, Noriyuki Masuda, and Hirosuke Kobayashi

Abstract Synchronization between cardiac and respiratory rhythms may be important for oxygen transport to tissues. The aim of this study was to investigate the synchronization between cardiac and respiratory rhythms. We evaluated the rhythms in 12 healthy males and 24 patients. The incidence rates of heart beats were obtained in each time interval relative to the initiation time point of inspiration. A simple index of timing variability of heart beats was defined. When the variability is large, the link between cardiac and respiratory rhythms was considered to be strong. The variability value of patients with disorder in the autonomic nervous system was larger than that of healthy subjects ($p < 0.05$). The variability of patients on controlled ventilation was lower than that of healthy subjects ($p < 0.01$), whereas the value on cardiac pacemaker did not differ from healthy subjects. In conclusion, the synchronization between cardiac and respiratory rhythms was confirmed, and it is suggested that the synchronization is enhanced when feed-back signals from respiratory movement to respiratory center were decreased.

1 Introduction

Rhythmic phenomena in biological systems often show coordinate regulation that may lead to synchronization among rhythms. In some instances rhythms may be entrained by other strong rhythms, and respiration is an important factor in the rhythm modulation of the cardiovascular system, which is known as respiratory sinus arrhythmia [1]. On the other hand, the cardiovascular system also affects the rhythm control of respiration, *via* right ventricular strain [2], *via* pulmonary J receptor [3], and *via* aortic and carotid bodies [4]. Evidence of these mutual coordinate regulations between the respiratory and

H. Kobayashi (✉)
Department of Medical Engineering and Technology, School of Allied Health Sciences, Kitasato University, Kanagawa, 228-8555, Japan
e-mail: hiro@kitasato-u.ac.jp

E. Takahashi, D.F. Bruley (eds.), *Oxygen Transport to Tissue XXXI*, Advances in Experimental Medicine and Biology 662,
DOI 10.1007/978-1-4419-1241-1_19, © Springer Science+Business Media, LLC 2010

cardiovascular systems has been accumulating during the past two decades (reviewed by Daly [5]). Although the synchronization between cardiac and respiratory rhythms has been reported [6–11], the synchronization has not yet been investigated in detail, particularly in patients. The aim of this study was to investigate the synchronization between cardiac and respiratory rhythms in healthy subjects and patients with several kinds of disease.

2 Methods

Twelve healthy male subjects, ranging from 21 to 71 years old, and 24 patients, 15 males and 9 females, ranging from 37 to 83 years old, were studied. The lung function of healthy subjects was %VC at 96 ± 21% (mean ± SD) and FEV_1% at 77 ± 11%. The patients consisted of 8 patients with chronic obstructive pulmonary disease (COPD) with %VC at 94 ± 29% and FEV_1% at 41 ± 13%, 5 with fibrosing lung disease (FLD) with %VC at 43 ± 12% and FEV_1% at 93 ± 8%, 5 with disorders of the autonomic nervous system (ANS) (1 with Shy-Drager syndrome, 1 with multiple sclerosis, 2 with olivo-ponto-cerebellar atrophy, 1 with severe orthostatic hypotension), 3 on ventilator therapy (1 with heart failure, 1 with COPD, 1 with FLD) and 3 with sick sinus syndrome on cardiac pacemaker.

The subjects breathed through a face mask (Survivor Blue, Hans Rudolph, Kansas city, M.O.) installed with a hot-wire flowmeter (ATD280, Minato Medical Science, Osaka, Japan). Electrocardiogram (ECG) was monitored using surface electrodes on the chest. The subjects breathed for 40 min in a quiet room. The continuous signals of mouth-flow and ECG were fed to a computer via a 12-bit AD converter with 100 Hz (10 ms) sampling rate. The signal from the pneumotachograph indicated that there were no superimposed cardiogenic oscillatory waves. Initial unsteady data were discarded. In 5 healthy subjects, we employed an elastic load of 1.8 kgw/cm^2 by restricting the chest wall movement using a chest band, and abdominal wall was restricted with a corset, or employed an inspiratory resistance of 10 cmH_2O/l/min by adding a flow resistance tube (TV241T, Nihon Koden, Tokyo, Japan) to the inspiratory port of a two-way non-rebreathing valve (1500 series, Hans-Rudolf, Kansas City, M.O.). The dead space was 25 ml. This investigation was performed in accordance with Declaration of Helsinki.

The starting points of inspiration (tr_1, tr_2, etc.; Fig. 1a) and R waves (th_1, th_2, etc.; Fig. 1b) were identified. Using these time series data, we obtained plots for the incidence rate of cardiac beats relative to the start of inspiration as follows. The incidence of the R waves within a given time window (± Δ s) at a given delay time (t s) after or before the start of inspiration (marked as "hit" in Fig. 1c) was identified, and then the incidence rate of R waves was calculated by the number of "hits" divided by the number of breaths. The delay time from the start of inspiration (t) was varied, ranging from – half the mean respiration interval to + half the mean respiration interval (Fig. 1d). We deleted the range over ±2SD

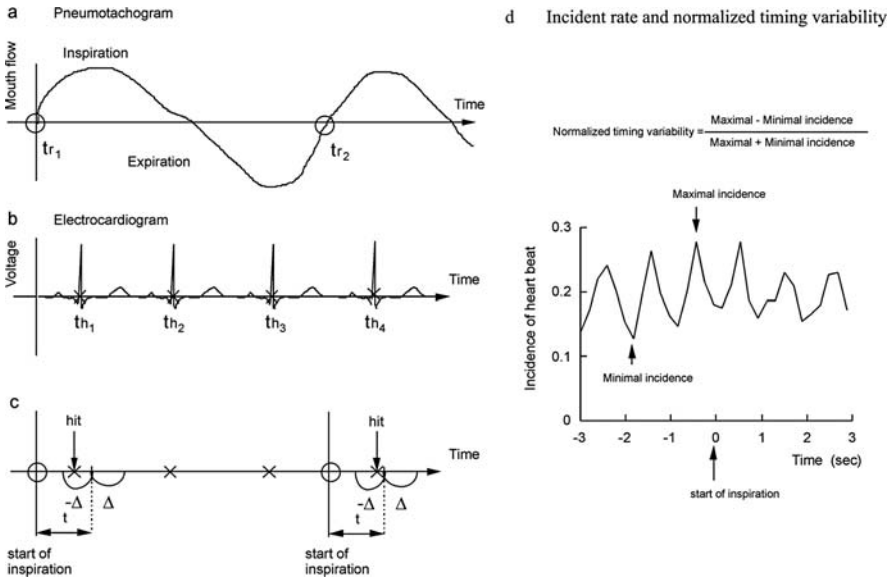

Fig. 1 Data analysis. The start of inspiration (tr_1, tr_2, etc.; **a**) and R waves (th_1, th_2, etc.; **b**) were identified. The incidence of R waves within a given time window ($\pm \Delta$ s) at a delay time (t s) from the start of inspiration was identified (marked as "hit" in **c**), and then the incidence rate of R waves relative to the start of inspiration was calculated (**d**). Then the normalized timing variability was obtained

of mean respiration interval on both sides to avoid the effects of breathing fluctuation. The time window of each subject, $\pm \Delta$, was set as mean R-R interval multiplied by 0.1. This constant multiplier was chosen, since the plots of the incidence rate with 0.02 or 0.3 did not substantially differ, but was more stable with 0.1.

A simple index of timing variability of heart beats was defined as the difference between the maximum and the minimum values of the heart-beat incidence rate, and was normalized as (maximal – minimal incidence rate)/(maximal + minimal incidence rate), thereby ranging from 0 to 1 (Fig. 1d). If the timing of heart beat was completely independent of breathing and was observed for a long time, the incidence rate profile becomes even throughout breathing, the normalized timing variability becoming zero (no synchronization). If the timing of heart beat was completely synchronized with breathing, the maximal incidence rate becomes one, the minimal being zero between the peaks, thereby the normalized timing variability being one (full synchronization). In a preliminary study the normalized timing variability value became stable as the number of respirations exceeded 200, and was evaluated by 500 breaths.

Probability histograms of heart-beat and breathing intervals were also obtained to investigate the relationship between heart beat and breathing intervals.

The normalized timing variability values were expressed as means ± SEM and other values were expressed as means ± SD. An unpaired Wilcoxon analysis was employed to compare the normalized timing variability of each patient group with that of healthy subjects, and analysis of variance was employed to test the difference in the normalized timing variability values of healthy subjects between loaded and unloaded conditions. $P < 0.05$ was considered as significant.

3 Results

In 12 healthy subjects the normalized timing variability was 0.28 ± 0.03 (mean ± SEM: larger than 0, $p < 0.001$), and was independent of age which ranged from 21 to 71 years old ($r = 0.03$, *n.s.*). The normalized timing variability of 8 COPD patients at 0.26 ± 0.03 and of 5 patients with FLD at 0.33 ± 0.07 did not differ from healthy subjects. In 5 patients with ANS disorders, it was 0.55 ± 0.10, and was larger than that of healthy subjects ($p < 0.05$). In 3 patients on controlled ventilation it was 0.12 ± 0.01, and was lower than healthy subjects ($p < 0.01$), but that of 3 patients on cardiac pacemaker at 0.27 ± 0.05 did not differ from healthy subjects. In 5 healthy subjects, the normalized timing variability was 0.29 ± 0.04 at rest without load, and increased to 0.56 ± 0.12 with elastic load ($p < 0.05$), while the value with resistive load at 0.31 ± 0.03 did not differ from that without load (Fig. 2).

In all subjects, probability histograms of time intervals of heart beats had a single peak (Fig. 3a–c), while the probability histograms of breathing intervals in subjects with larger normalized timing variability had one-to-several peaks at integer multiples of the mean interval of heart beats (Fig. 3a, b). Patients on

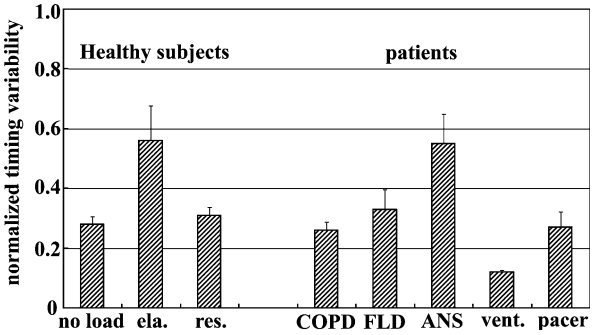

Fig. 2 Normalized timing variability in healthy subjects and patients. no load: without load; ela.: elastic load, res.: resistive load; COPD: chronic obstructive pulmonary em-physema; FLD: fibrosing lung disease;ANS:autonomic nerv-ous system disorder; vent.: on ventilator; pacer: on pace-maker. *: $P < 0.05$; **: $P < 0.01$ compared to healthy subjects with no load ($n = 5$ vs. ela. or res., $n = 12$ vs. patient groups)

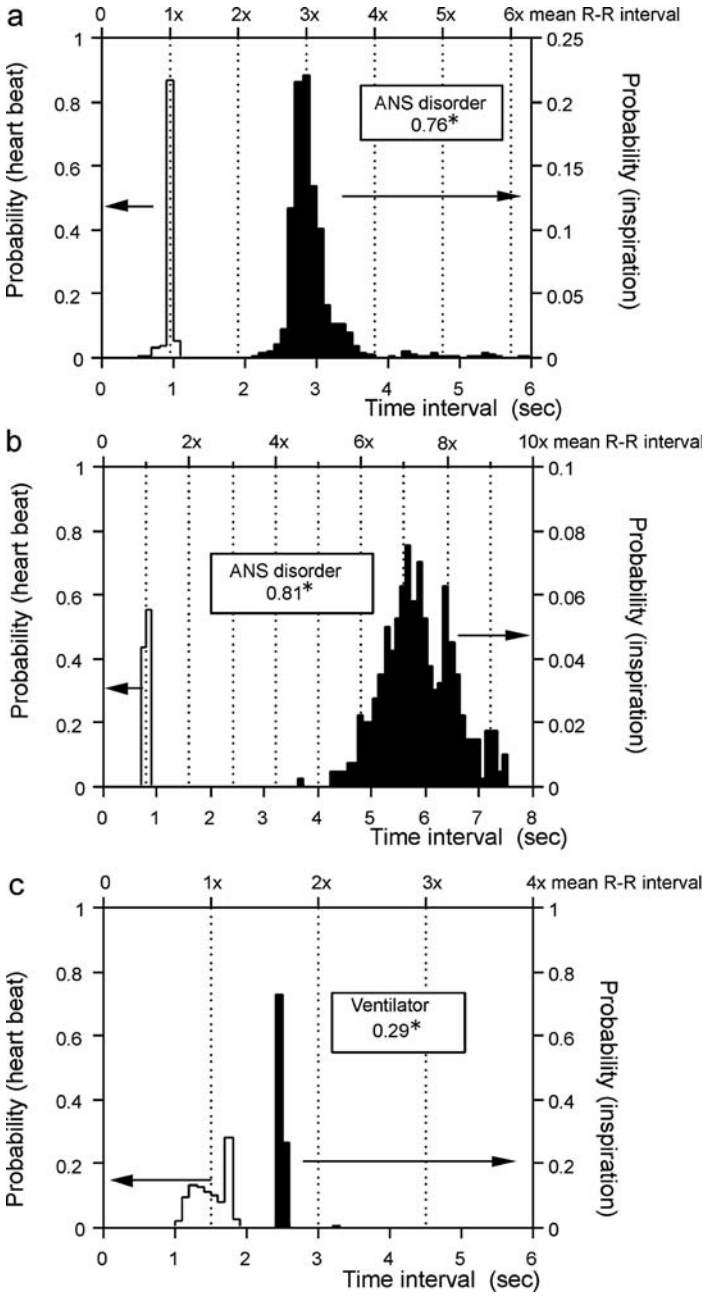

Fig. 3 Probability histogram of heart beats and breathing. The probability histogram of heart-beat intervals had a single peak in all subjects, while the probability histogram of breathing intervals had one (**a**: a patient with ANS disorder) to several (**b**: a patient with

controlled ventilation (Fig. 3c) had a single peak for breathing intervals, which did not locate at integer multiples of the mean interval of heart beats.

4 Discussion

Hinderling [12] and Hinderling and Bucher [13] investigated the mutual synchronization of cardiac and respiratory rhythms, by artificially inducing cardiac rhythm by a pacemaker or by employing voluntary hyper- or hypoventilation in humans, and found that pacemaker regulation synchronized respiration rate, while voluntary ventilation failed to synchronize heart rate. We have also confirmed that in patients on controlled ventilation the average normalized timing variability was significantly lower than that of healthy subjects, while the average normalized timing variability of patients on cardiac pacemaker regulation did not differ from that of healthy subjects. In contrast to the single-peaked probability histogram of heart beat intervals, the histogram of breathing intervals had one-to-several peaks at integer multiples of the mean interval of heart beats, particularly in the patients with larger normalized timing variability, a finding that also indicated that respiratory rhythm was entrained by the heart rhythm in these cases.

It is likely that cardiac rhythm is influenced by respiratory movement, whereas the respiratory rhythm is influenced and entrained by cardiac rhythm, but is also influenced by a feed-back control of respiration, such as the Hering-Breuer reflex. During quiet breathing with restricted thoracic movement, when the reflex is not activated, respiratory rhythm is considered to be mainly synchronized by cardiac rhythm. However, under conditions that enhance the feed-back signals of respiratory movement, the synchronization of respiratory rhythm to cardiac rhythm would be disturbed. Patients with disorders of the ANS are likely to have defective feed-back control by respiratory movement, while the afferent signals originated from cardiac beats will be transmitted to the central nervous system via several afferent routes, thereby increasing the normalized timing variability.

The physiological significance of the synchronization between respiratory and cardiac rhythm is not obvious. However, since respiratory movement influences the circulation with the change in venous return and blood pressure due to pleural pressure oscillation, it could be speculated that the rhythm synchronization would improve the energy cost for the circulation. It has

Fig. 3 (continued) ANS disorder) peaks at integer multiples of the mean interval of heart beats in the subjects with high normalized timing variability values. A patient on controlled ventilation (**c**) had a single peak in the probability histogram of breathing intervals, which did not locate at integer multiples of mean interval of heart beats.*: normalized timing variability

been shown that respiratory sinus arrhythmia benefits the pulmonary gas exchange and may improve the energy efficiency of pulmonary circulation by "saving heartbeats" [14, 15].

Another possible physiological significance could be that the possible entrainment of respiratory rhythm to cardiac rhythm might assure the safety of generation of respiratory rhythm. Cardiac rhythm is mainly generated locally in the sinus node. If the sinus node fails, another slower pacemaker in the AV node and/or ventricular branches will assure control of heart rhythm. In contrast, if the rhythm generating system in brain stem is disturbed or damaged, there are no secondary regulatory centers that may assure the control of breathing. The cardiac rhythm is generated in the sinus node even during the apnea for a while, and the respiratory center may incorporate the afferent signal(s) of cardiac rhythm to generate and restart a new respiratory rhythm. This hypothesis should be further investigated.

In conclusion, the synchronization between cardiac and respiratory rhythms was confirmed, and it is likely that the synchronization is enhanced in the situation that feed-back signals from respiratory movement to respiratory center were decreased.

Acknowledgments We would like to thank Tateo Ogura, Department of Medicine, Kitasato Univ. Hospital, Shuji Ariga and Takanori Hirata, Department of Engineering, Keio University, for their excellent technical assistance, and Naosada Takizawa, Information Science Center, Kitasato Univ. for his technical advice in this study.

References

1. Hirsch JA, Bishop B (1981) Respiratory sinus arrhythmia in humans: how breathing pattern modulates heart rate. *Am. J. Physiol.* 241 (*Heart Circ. Physiol.* 10): H620–H629.
2. Jones PW, Huszczuk A, Wasserman K et al. (1982) Cardiac output as a controller of ventilation through changes in right ventricular load. *J. Appl. Physiol.* 53, 218–224.
3. Anand A, Paintal AS (1980) Reflex effects following selective stimulation of J receptors in the cat. *J. Physiol.* 299, 553–572.
4. Lahiri S, Delaney RG (1975) Stimulus interaction in the responses of the carotid body chemoreceptor single afferent fibers. *Respir. Physiol.* 24, 249–266.
5. De Burgh Daly M (1986) Interactions between respiration and circulation. In: Handbook of Physiology, Section 3: The Respiratory System, Vol. II: Control of Breathing, Part 2. American Physiological Society, Bethesda, pp. 529–594.
6. Bucher K (1963) Das Herz als Schrittmacher für die Atmung. *Z. naturwiss.-med. Grundlagenforsch.* 1, 318–331.
7. Engel P, Hildebrandt G, Scholz HG et al. (1967) Die Messung der Phasenkoppelung zwischen Herzschlag und Atmung beim Menschen mit einem neuen Koinzidenzmeßgerät. *Pflügers Arch. ges. Physiol.* 298, 258–270.
8. Hildebrandt G, Daumann F (1965) Die Koordination von Puls- und Atemrhythmus bei Arbeit. *Int. Z. angew. Physiol.* 21, 27–48.
9. Hinderling PC, Bucher K (1965) Synchronismen zwinschen Kreislauf und Atmung am Menschen. *Helv. Physiol. Acta.* 23, 374–381.
10. Kenner T, Pessenhofer H, Schwaberger G et al. (1976) Method for the analysis of the entrainment between heart rate and ventilation rate. *Pflügers Arch.* 363, 263–265.

11. Peβenhofer H, Kenner T (1975) Zur Methodik der Kontinuierlichen Bestimmung der Phasenbeziehung zwinschen Herzschlag und Atmung. *Pflügers Arch*. 355, 77–83.
12. Hinderling P (1967) Weitere Charakterisierung von Synchronismen zwinschen Kreislauf und Atmung. *Helv. Physiol. Acta*. 25, 24–31.
13. Hinderling PC, Bucher K (1968) Synchronismen zwinschen Kreislauf und Atmung. *Helv. Physiol. Acta*. 26, 171–176.
14. Hayano J, Yasuma F, Okada A, Mukai S, Fujinami T (1996) Respiratory sinus arrhythmia. A phenomenon improving pulmonary gas exchange and circulatory efficiency. *Circulation* 94, 842–847.

Part II
In Vivo Measurement of O_2

Time-Resolved Near-Infrared Spectroscopy and Imaging of the Adult Human Brain

Heidrun Wabnitz, Michael Moeller, Adam Liebert, Hellmuth Obrig, Jens Steinbrink, and Rainer Macdonald

Abstract Near-infrared spectroscopy (NIRS) of the human brain is aiming at the non-invasive determination of concentration changes of oxy- and deoxy-hemoglobin in the cortex. However, it usually relies on the assumption of spatially homogeneous absorption changes. To overcome this limitation we performed instrumental and methodological developments of time-resolved NIRS with the aim to achieve depth resolution. We present our recently developed time-domain near-infrared brain imager based on picosecond diode lasers and time-correlated single photon counting (TCSPC) which can be used at the bedside. To achieve depth localization of absorption changes we analysed statistical moments (integral, mean time of flight and variance) of measured time-of-flight distributions of diffusely reflected photons. In particular, variance has a selective sensitivity to deep absorptions changes and provides a suitable representation of cerebral signals. The separation of cerebral and extracerebral changes of hemoglobin concentrations is demonstrated for a motor stimulation experiment.

1 Introduction

Near-infrared spectroscopy (NIRS) based on continuous (cw) light has become a widely used tool to study hemodynamic processes in brain and muscle. It measures changes of light intensity at several wavelengths to determine absorption changes from which, in particular, changes of concentrations of oxy- and deoxyhemoglobin (HbO_2, Hb) are derived. Data analysis relies on the modified Beer-Lambert law (MBLL) [1] assuming spatially homogeneous absorption changes. However, in functional activation studies of the human brain, the cerebral activation is often accompanied by systemic effects leading to absorption changes in extracerebral tissues as well. The cw NIRS method is sensitive to

H. Wabnitz (✉)
Physikalisch-Technische Bundesanstalt, 10587 Berlin, Germany
e-mail: heidrun.wabnitz@ptb.de

E. Takahashi, D.F. Bruley (eds.), *Oxygen Transport to Tissue XXXI*,
Advances in Experimental Medicine and Biology 662,
DOI 10.1007/978-1-4419-1241-1_20, © Springer Science+Business Media, LLC 2010

both deep and superficial changes but cannot distinguish between them. This fact also impairs bolus tracking measurements based on intravenous injection of an optical contrast agent aiming at the assessment of cerebral perfusion [2, 3]. The intensity changes due to the passage of the dye bolus in the brain are always superimposed by those from the time-dependent dye concentration in superficial tissues.

These limitations of the cw NIRS method can be overcome by recording the time of flight of each individual photon between source and detector. Photons arriving after short times of flight ("early photons") on average penetrate less deeply into the tissue than photons with long times of flight ("late photons"). Thus the analysis of the shape of measured time-of-flight distributions of diffusely reflected photons can provide depth localization of absorption changes. To this end various methods have been developed, i.e. evaluation of changes (i) in the full temporal profile by using the concept of time-dependent mean partial pathlengths [4], or by fitting time-resolved reflectance and applying the microscopic Lambert-Beer law [5], (ii) in the intensity of various time windows [6, 7], or (iii) in the moments of the distribution of times of flight of photons [2, 8].

Multi-channel instruments for time-domain brain imaging that combine time resolution with topographic mapping or with optical tomography have been developed by several groups [5, 6, 9–12]. They are being applied in various functional stimulation experiments as well as in the assessment of cerebral perfusion by indocyanine green bolus tracking [2].

2 Time-Domain Optical Brain Imager

A multi-channel instrument was developed for mapping of time-resolved diffuse reflectance of the head. A picosecond diode laser system Sepia (PicoQuant, Germany) is operated with three laser heads emitting at the wavelengths 687, 803, and 826 nm. The output of each laser head may be attenuated or blocked and is coupled into an optical fiber. The three laser pulse trains are interlaced within the repetition period (about 23 ns) by suitable delays which allows for parallel, quasi-simultaneous recording at all three wavelengths.

Four parallel detection channels are based on a multi-board TCSPC system (SPC-134, Becker&Hickl, Germany) and detection modules containing fast photomultipliers R7400U-02 (Hamamatsu Photonics, Japan), high voltage power supplies, preamplifiers as well as dedicated relay optics and mechanical shutters.

Mapping of a larger area of the head is achieved by addressing up to 9 source positions by a 1×9 multimode fiber switch (piezosystem jena, Germany). The nine source fibers are arranged on an optode holder pad together with four detection fiber bundles of 4 mm diameter (Loptek Glasfasertechnik, Germany). The 16 nearest-neighbor source-detector pairs (separation $d = 3$ cm) form a 4×4 grid of "pixels".

Time-of-flight (TOF) distributions are recorded in the four detection channels in parallel, with a collection time of, e.g., 100 ms in a continuous sequence. To achieve high signal-to-noise ratios the TCSPC count rate is adjusted to values between 2 and 3 MHz, if possible. In this way, the TOF distribution for each wavelength contains $\sim 10^5$ photon counts per 100 ms. A complete map is acquired within $\sim$1 s. The trigger pulses for data acquisition as well as for fiber switching are obtained from a programmable counter/timer board (PCI-6601, National Instruments, USA). All laser and detector modules are controlled by individual microcontrollers. A LabVIEW user interface provides automated control of data acquisition as well as of all module functions together with real-time display.

The modular design of the instrument allows for an easy change between different configurations and applications. The device is compact and portable and can be operated at the bedside in a clinical setting. The technical approval regarding safety requirements for use in clinical studies has been obtained. For a more detailed description of the instrument see [11].

3 Data Analysis

For quantitative reconstruction of depth-resolved absorption changes we previously developed two approaches. We started (i) from changes in the full TOF profile [4] and (ii) from changes in moments of the TOF distribution at several source -detector separations [8]. In both cases the observed signal changes were linearly related to the underlying changes in the depth-dependent absorption coefficient via sensitivity functions. These were obtained from forward Monte-Carlo simulations with a layered tissue model and assumed background optical properties (scattering and absorption coefficients). A prerequisite to achieve a reliable quantification of the depth-resolved absorption changes is the knowledge of these background optical properties of the various tissue types. However, these properties are not exactly known in vivo and probably exhibit substantial interindividual variability.

An alternative to such reconstruction approaches is the attempt to find quantities that exhibit a selective sensitivity to deep (cerebral) absorption changes. This approach allows one to distinguish between cerebral and extracerebral changes and to analyze their time course without the need of quantitative reconstruction. In particular, the analysis of statistical moments of measured TOF distributions $N(t)$, i.e. integral N_{tot} (equivalent to a cw NIRS measurement), mean time of flight $<t>$ (first moment) and variance V (second centralized moment), turned out to be advantageous. Figure 1 shows the spatial sensitivity profiles of N_{tot} and V. They were obtained from a perturbation approach based on the diffusion approximation for the propagation of photon density [13]. For this simulation the reduced scattering coefficient, absorption coefficient and the refractive index were taken as $\mu_s' = 10\,\mathrm{cm}^{-1}$, $\mu_a = 0.1\,\mathrm{cm}^{-1}$

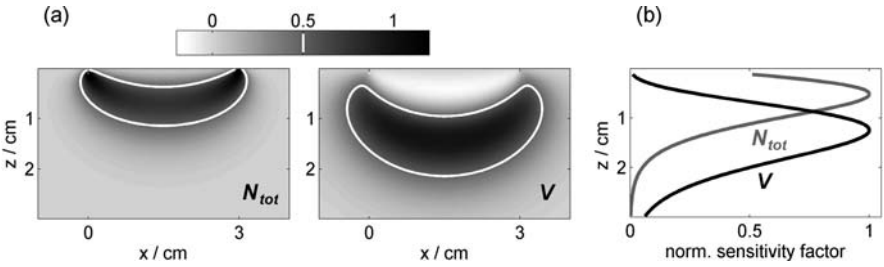

Fig. 1 Normalized two-dimensional (**a**) and depth-dependent (**b**) sensitivities to small absorption changes for integral N_{tot} and variance V of time-of-flight distributions for a semi-infinite medium. Source at $(x, y, z) = (0, 0, -0.1\,\mathrm{cm})$, detector at $(x, y, z) = (3\,\mathrm{cm}, 0, 0)$. In (**a**) the 50% levels are highlighted by a white contour

and $n = 1.33$, respectively. Figure 1a shows the two-dimensional (x, z) sensitivities of N_{tot} and V to a point-like absorber after integration over y, Fig. 1b the resulting z-dependent sensitivities after additional integration over x. The integral N_{tot} is sensitive to both deep and superficial changes with a higher sensitivity to the latter, whereas V is almost exclusively sensitive to deep changes since late photons contribute with large weight according to $(t-\langle t\rangle)^2$. Therefore variance is expected to suitably represent cerebral signals.

4 Application to Functional Stimulation of the Brain

The effect of depth selectivity is exemplarily shown for a motor stimulation experiment on a healthy volunteer. The optode holder pad was centered over the left motor cortex. The subject performed 23 blocks of 20 s right (contralateral) hand movement (compression of a soft ball) interrupted by 20 s of rest. The 4×4-panel maps (not shown) of the wavelength-dependent averaged responses of ΔN_{tot} and ΔV to the stimulation were clearly different. In the central region both quantities showed a rather similar behavior, whereas in several locations outside this region the behavior differed significantly. In Fig. 2 the results for three selected source-detector pairs (A in the central region, B and C outside) are displayed in terms of normalized changes of oxy- and deoxyhemoglobin. For this plot we assumed ΔN_{tot} and ΔV to be proportional to $\Delta\mu_a$ with sensitivity factors S_{Ntot} and S_V, respectively, each being independent of position as well as of wavelength. For the wavelength pair used (687, 826 nm) the latter assumption is not unrealistic. For a homogeneous medium, S_{Ntot} is related to the differential pathlength factor (DPF) [1] which can be derived from the time-resolved measurement via $DPF = v\langle t\rangle/d$ where v is the velocity of light in tissue ($n = 1.4$). As average over all 16 "pixels" of the map, DPF was found to be 7.0 at 687 nm and 6.6 at 826 nm. Taking the actual wavelength-dependent DPF values for each source-detector pair into account, the time courses do not change remarkably in comparison to those displayed in Fig. 2a.

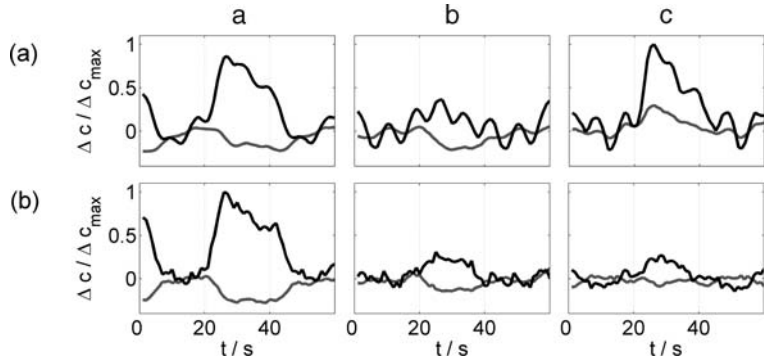

Fig. 2 Responses to motor stimulation (from 20 to 40 s) for several positions on the head for oxy- (*black*) and deoxyhemoglobin (*grey*) as derived from integral (**a**) and variance (**b**) of measured time-of-flight distributions. All traces in (**a**) and in (**b**), respectively, were normalized to the maximum value for oxyhemoglobin and smoothed with a 5 s sliding average

In case A the time courses of ΔN_{tot} and ΔV are largely similar. This fact indicates a dominant cerebral activation, since changes in integral ΔN_{tot} are influenced by both systemic (superficial) and cerebral (deep) responses whereas changes in variance ΔV are governed by cerebral absorption changes. In the other two cases the cerebral activation as derived from ΔV is much weaker. Substantial and heterogeneous superficial effects are present. The ΔN_{tot} signals at both locations B and C show a distinct low-frequency oscillation of about 0.125 Hz in the oxyhemoglobin traces which is not visible in the variance signal. Such systemic oscillation is most likely connected to "Mayer waves", for a recent discussion see [14]. Moreover, in the ΔN_{tot} signal at location C another superficial effect becomes obvious. The signal is comparably large, but exhibits a different behavior compared to case A. In particular, both HbO_2 and Hb show an increase during stimulation. The "triangular" superficial component is possibly due to a stimulus-related change in heart rate or blood pressure, or a coupling artifact. On the contrary, the relatively small (cerebral) signal in ΔV shows the expected stimulus-related increase in HbO_2 and decrease in Hb concentrations.

5 Conclusions

Depth localization of absorption changes in the adult head has been achieved by time-resolved NIRS together with appropriate methods of data analysis. This approach is suitable to separate cortical signal contributions from those of superficial tissues. It may lead to a deeper understanding of cw NIRS signals and in some cases to their reevaluation. The development of methods for obtaining realistic estimates of the actual background optical properties of the various tissue types of the head remains an important task.

Acknowledgments The work was supported by the German Federal Ministry of Economics and Labour (BMWA VI A2-12/03) and the German Federal Ministry of Education and Research (BMBF 01 GO 0208, Berlin Neuroimaging Center).

References

1. Delpy DT, Cope M, van der Zee P et al. (1988) Estimation of optical pathlength through tissue from direct time of flight measurement. Phys Med Biol 33:1433–1442.
2. Liebert A, Wabnitz H, Steinbrink J et al. (2005) Bed-side assessment of cerebral perfusion in stroke patients based on optical monitoring of a dye bolus by time-resolved diffuse reflectance. Neuroimage 24:426–435.
3. Leung TS, Tachtsidis I, Tisdall M et al. (2007) Theoretical investigation of measuring cerebral blood flow in the adult human head using bolus Indocyanine Green injection and near-infrared spectroscopy. Appl Opt 46(10):1604–1614.
4. Steinbrink J, Wabnitz H, Obrig H et al. (2001) Determining changes in NIR absorption using a layered model of the human head. Phys Med Biol 46:879–896.
5. Contini D, Torricelli A, Pifferi A et al. (2006) A multi-channel time-resolved system for functional near infrared spectroscopy. Opt Express 14:5418–5432.
6. Selb J, Stott JJ, Franceschini MA et al. (2005) Improved sensitivity to cerebral hemodynamics during brain activation with a time-gated optical system: analytical model and experimental validation. J Biomed Opt 10:11013.
7. Montcel B, Chabrier R, Poulet P (2005) Detection of cortical activation with time-resolved diffuse optical methods. Appl Opt 44:1942–1947.
8. Liebert A, Wabnitz H, Steinbrink J et al. (2004) Time-resolved multi-distance NIR spectroscopy of the adult head: intra- and extra-cerebral absorption changes from moments of distributions of times of flight of photons. Appl Opt 43:3037–3047.
9. Eda H, Oda I, Ito Y et al. (1999) Multichannel time-resolved optical tomographic imaging system. Rev Sci Instrum 70:3595–3602.
10. Schmidt FEW, Fry ME, Hillman EMC et al. (2000) A 32-channel time-resolved instrument for medical optical tomography. Rev Sci Instrum 71:256–265.
11. Wabnitz H, Moeller M, Liebert A et al. (2005) A time-domain NIR brain imager applied in functional stimulation experiments. In: Licha K, Cubeddu R (eds) Photon Migration and Diffuse-Light Imaging II, Proc. OSA-SPIE Biomed Opt 5859:58590H.
12. Kacprzak M, Liebert A, Sawosz P et al. (2007) Time-resolved optical imager for assessment of cerebral oxygenation. J Biomed Opt 12:034019.
13. Carraresi S, Shatir TS, Martelli F et al. (2001) Accuracy of a perturbation model to predict the effect of scattering and absorbing inhomogeneities on photon migration. Appl Opt 40:4622–4632.
14. Peng T, Ainslie PN, Cotter JD et al. (2008) The effects of age on the spontaneous low-frequency oscillations in cerebral and systemic cardiovascular dynamics. Physiol Meas 29:1055–1069.

Clinical Electron Paramagnetic Resonance (EPR) Oximetry Using India Ink

Benjamin B. Williams, Nadeem Khan, Bassem Zaki, Alan Hartford, Marc S. Ernstoff, and Harold M. Swartz

Abstract Electron paramagnetic resonance (EPR) oximetry can be used to provide direct absolute measurements of pO_2 in living tissue using India ink as an O_2 reporter. In vivo measurements are made using low frequency (1.2 GHz) EPR spectroscopy and surface loop resonators, which enable measurements to be made at superficial sites through a non-invasive (after placing the ink in the tissues) and repeatable measurement procedure. Ongoing EPR oximetry studies in human subjects include measurement of subcutaneous pO_2 in the feet of healthy volunteers to develop procedures that could be used in the treatment of peripheral vascular disease and oximetry in tumors during courses of radiation and chemotherapy, to follow pO_2 so oxygen-dependent therapies can be optimized. In each case, we aim to provide quantitative measurements of tissue pO_2 which will aid physicians in the characterization of disease status and the effects of therapeutic measures, so that treatments can be applied with optimal effectiveness by taking into account the oxygen-dependent aspects of the therapy. The overall goal is to enhance clinical outcomes. Oximetry measurements of subcutaneous tissue on dorsal and plantar foot surfaces have been made in 9 volunteers, with measurements ongoing for each and the longest set of measurements carried out successfully over the last 5 years. Tumor oximetry measurements have been performed in tumor tissues of 10 patients during courses of radiation and chemotherapy. Tumor types include melanoma, basal cell, soft tissue sarcoma, and lymphoma, and measurement sites have ranged from the feet to the scalp. These studies demonstrate the feasibility of EPR oximetry in a clinical setting and the potential for more widespread use in the treatment of these and other oxygen-dependent diseases.

B.B. Williams (✉)
EPR Center for Viable Systems, Department of Radiology, Dartmouth Medical School, 703 Vail, Hanover, NH 03755, USA
e-mail: ben.williams@dartmouth.edu

E. Takahashi, D.F. Bruley (eds.), *Oxygen Transport to Tissue XXXI*, Advances in Experimental Medicine and Biology 662,
DOI 10.1007/978-1-4419-1241-1_21, © Springer Science+Business Media, LLC 2010

1 Introduction

In vivo electron paramagnetic resonance (EPR) is a magnetic resonance technique that can be used for functional spectroscopy or imaging of living systems, reporting such parameters as partial pressure of oxygen, free radical concentration, microviscosity, and redox status [1]. EPR measures the absorption of energy, at radio- or microwave frequencies, by unpaired electrons present within the sample and the recorded absorption spectrum contains information about the magnetic environment. As most free radicals present in biological systems are short-lived and present in low concentrations, for most in vivo EPR measurements an exogenous molecular probe is either injected or implanted and acts as a reporter of the physiologic parameter of interest. Many such probes exist, including water soluble molecules [2] and particulate materials [3], with specific sensitivities to particular biologic parameters.

The ability of in vivo EPR techniques to provide repeated non-invasive measurements of tissue oxygenation is of particular interest due to the critical importance of O_2 in normal physiology and disease and the lack of other clinically applicable means to perform such measurements. While the EPR methods do require the intravascular injection of a water soluble probe or prior local implantation of a particulate probe in the tissue of interest, there is no locally invasive procedure needed at the time of measurement. The particulate probes typically are introduced into tissues using a small gauge needle (21–25 gauge), often several days prior to measurement, in order to minimize trauma and allow for healing and incorporation of the material into the tissue prior to pO_2 measurement. An advantage of the particulate approach is that once the probes have been introduced, they may be used to make repeated measurements at the same location without the need to introduce additional material or wait for introduced material to be cleared. This characteristic is particularly useful for the monitoring of tissue oxygenation during the development of disease or in response to therapy, as needed for the optimal treatment of solid tumor cancers and peripheral vascular disease.

We carry out EPR oximetry in human subjects using India ink as the EPR-sensitive oxygen reporter [4, 5]. India ink has a long history of clinical use as an anatomic marker for surgery and radiotherapy and, fortuitously, the suspended carbon black contains stable radical species at sufficient concentrations with EPR spectra that are highly sensitive to the presence of oxygen. The presence of molecular oxygen leads to a decrease in the EPR relaxation time of these radicals, and an associated oxygen dependent broadening of the observed absorption spectrum. This broadening can be directly and quantitatively related to the tissue pO_2 and described by use of an established monotonic calibration curve. India ink and other EPR oximetry particulate probes are highly sensitive to changes occurring at low levels of oxygen, making them very well suited to the study of ischemic diseases and tissue hypoxia.

2 Materials and Methods

The ongoing clinical EPR oximetry measurements are performed using an India ink formulated as a suspension of Printex-U carbon black (200 mG/mL) in a 0.9% saline solution with carboxy methyl cellulose as a suspending agent [6]. For these studies 20–50 μL of ink was injected directly into the tissue of interest using a 21 gauge needle. Occasionally, this injection was preceded by the application of local lidocaine anesthesia. For measurements in normal subcutaneous tissue, the ink was injected approximately 2 mm below the surface of the skin; for measurements in tumors, the depth varied depending on the specific anatomy with a range of 2–10 mm below the surface of the skin. At least one day was allowed for healing and incorporation of the ink into the tissue prior to oxygen measurement.

All of the measurements were made using a low frequency (1.2 GHz) clinical EPR spectrometer specifically designed for human applications [7, 8]. The spectrometer is equipped with a number of ancillary patient positioning devices, including an insertable bed which facilitates measurements of subjects in a lying position and an adjustable chair which is used for foot measurements. Throughout all measurements, the surface temperature of the subject is monitored using a thermocouple and a warm air supply is adjusted to maintain a temperature of 37°C.

The parameters used for EPR data acquisition varied in accordance with the properties of the observed signal. In general, parameters were chosen to avoid instrumental distortion of the EPR spectral shape. Spectra were individually recorded, averaged, analyzed using non-linear least squares spectral fitting, and the fitted linewidth was converted to pO_2 using the previously determined oxygen calibration.

3 Results

The response of tumors to cytotoxic therapies, especially ionizing radiation, is critically dependent on pO_2 [9]. In vitro studies indicate that cells in hypoxic environments are approximately 3-times less sensitive to radiation than cells that are well oxygenated. Accordingly, tumor hypoxia is a major limiting factor in the application of radiation therapy and its efficacy. It is also important to recognize that tumor pO_2 is not static, especially during the course of treatment when changes in O_2 consumption, interstitial pressure, and perfusion are expected. If available, direct knowledge of tumor pO_2 could be used to optimize treatment on an individual basis through the application of drugs or procedures that increase tumor oxygenation and/or the optimizations of both temporal and spatial patterns of irradiation to maximize the therapeutic ratio.

Building off of instrumental and methodological developments and previous successes in animal model systems, we are now pursuing the development of

EPR oximetry in a clinical setting to meet this need and demonstrate the feasibility of these measurements within the clinical setting. We have performed measurements on tumors in 10 subjects, including 7 with melanoma lesions and metastases, and others with basal cell, soft-tissue sarcoma, and lymphoma tumors. For several subjects, measurements in more than one tumor, or more than one site, have been possible. The distribution of measurement sites is shown in Fig. 1a, which illustrates the capability of making measurements with the current in vivo EPR spectrometer at a wide variety of locations, from head to toe.

We have previously described the ability of the EPR measurements to measure baseline levels of tumor pO_2 and the response to the inspiration of 100% O_2 [10, 11]. In both of these instances, including melanoma and lymphoma tumors, baseline pO_2 values were observed to be quite low (13 and 4 mmHg, respectively) and the application of inhaled oxygen led to dramatic increases in tumor pO_2. Similar measurements have been made with additional subjects, and serial measurements during the course of radiation treatment have been performed. One such set of serial measurement was performed at 2 sites within separate metastatic melanoma tumors during a course of radiation treatment where a total of 36 Gy was applied using 6 Gy $\times$ 6 doses (Fig. 1b). The tumors were located in the upper right scalp and on the right side of the neck just below the ear. Similar pO_2 levels were observed at each site immediately before and after each fraction, but differences were observed between the sites and during the course of treatment. In the tumor located in the neck, consistently low, nearly anoxic, values were recorded with a small upward trend as the therapy progressed. In the scalp, considerably higher values of pO_2 were observed, ranging from approximately 3–10 mmHg.

It is especially important to note that in vivo EPR oximetry has been used successfully in the clinical setting to make repeated non-invasive direct measurements of tumor pO_2. We have observed that the tumor pO_2 values have varied among the patients studied and over the courses of treatment and that different responses of tumor pO_2 to increased fractions of inhaled oxygen are observed. Based on the measurements to date, we believe that it is feasible that in vivo EPR oximetry could be used to monitor tumor pO_2 in the clinical setting and guide the optimal application of strategies to enhance tumor oxygenation at the time of treatment.

Peripheral Vascular Disease (PVD) is a major cause of morbidity and mortality in diabetics, where a local low tissue pO_2 due to poor perfusion can lead to the development of chronic wounds, which often necessitates amputation. The direct measurement of tissue pO_2 would facilitate the rational development of treatments for PVD and could be applied on individual bases to monitor the development of the disease and guide the application of interventions. The development of in vivo EPR oximetry of subcutaneous tissue aimed at assessment of PVD has begun with measurements in healthy subjects to develop the necessary procedures and to observe the short- and long-term oxygen dynamics present in a controlled population. We have made

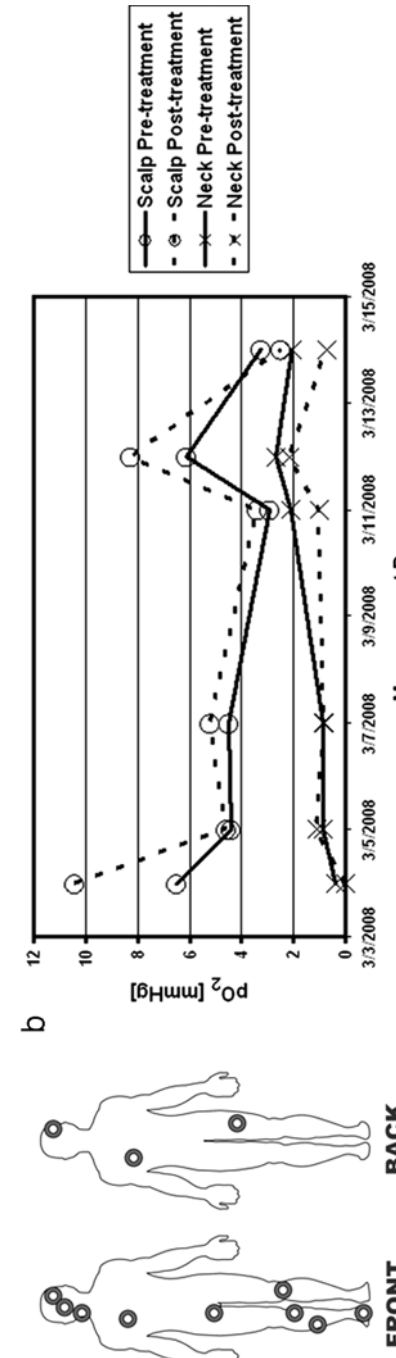

Fig. 1 (**a**) Tumor pO_2 has been measured for 10 volunteers with different tumor locations from head to toe. (**b**) Tumor pO_2 was monitored in melanoma metastases at two sites, in the scalp and neck, during the course of radiation treatment. Spectra were recorded immediately before and after each fraction while the patient inspired room air. These results indicate hypoxic environments that vary on a day-to-day basis, but show little acute response in pO_2 due to radiation

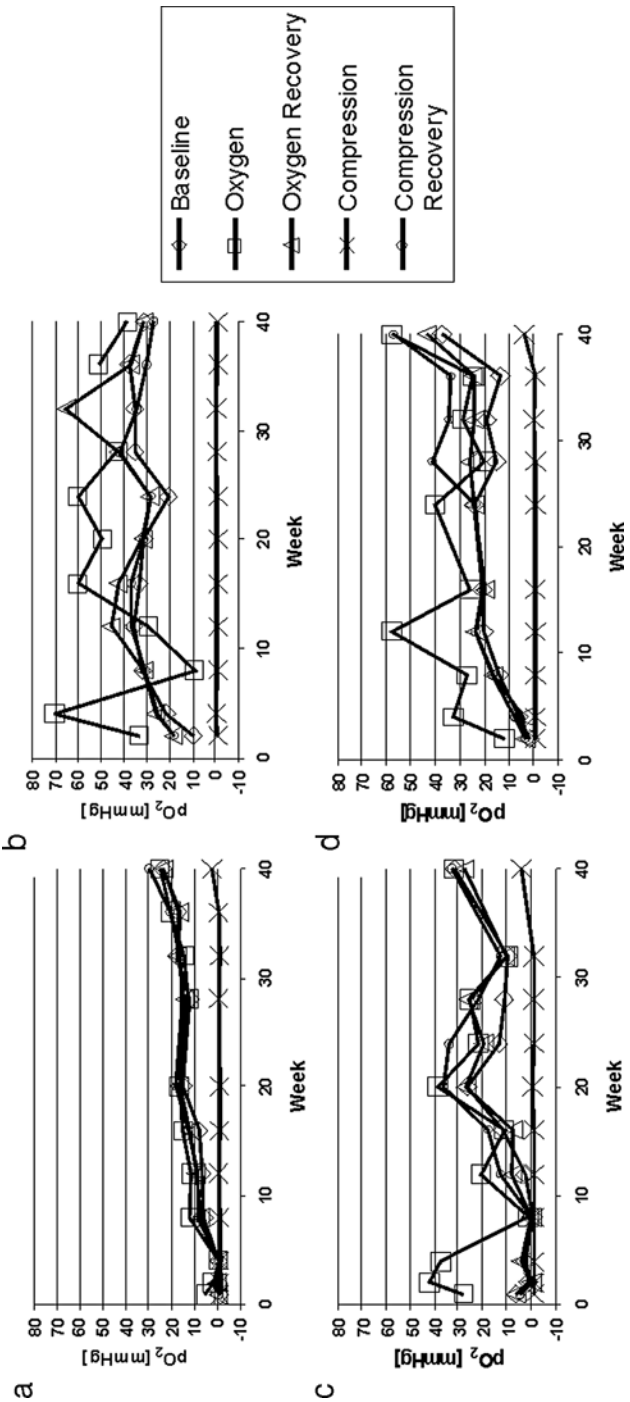

Fig. 2 Tissue pO_2 in the dorsal surface is shown for baseline, inspired O_2, recovery following O_2, compression, and compression recovery periods. For all subjects (**a**–**d**) the baseline O_2 values rise gradually in the weeks after ink injection. Baseline and recovery values are consistent, compression results in anoxia, and O_2 generally leads to increased tissue pO_2

measurements at 14 sites in 9 healthy volunteers, dating back to Oct. 2002. The earliest studies have been described previously [4, 8, 10, 11]. In the current studies, measurements of pO_2 are being performed on a monthly basis at both the dorsal and plantar surfaces of the foot under baseline conditions, as well as with inhalation of increased oxygen and temporary interruption of perfusion of the tissue. Consistent with prior measurements, we have observed that there appears to be a period of decreased pO_2 in the weeks following injection, with a gradual increase back to values near 20–30 mmHg. The nature of this apparent decrease is a matter of ongoing investigation. In all studies, we have consistently observed narrowing of the EPR signal following interruption of perfusion, consistent with consumption driving tissue pO_2 to near anoxic values. Similarly, we see general, but less consistent, increases in tissue pO_2 following the administration of inhaled O_2. Following each of these interventions, we generally observe tissue pO_2 returning to the baseline levels. These patterns of oxygenation are demonstrated in the data included in Fig. 2, which describes measurements in the dorsal surfaces of the feet of 4 of the most recent research subjects.

4 Conclusions

We have demonstrated that in vivo EPR oximetry can provide repeated, direct measurements of absolute pO_2 of tumors and other tissues in human subjects and that the measurement procedure is compatible with clinical practice. In tumors, where pO_2 is a key factor in the efficacy of radiation therapy, preliminary measurements showed that increased pO_2 following inspiration of O_2 varies among patients and tumor pO_2 changes during the course of radiation therapy. Measurements in subcutaneous foot tissue were performed to develop procedures that could be used to assess pO_2 in the treatment of PVD and chronic wound care. These measurements have demonstrated the response of tissue pO_2 to the delivery of O_2 and ability to perform measurements at the same site over long durations for disease monitoring.

Acknowledgments This work was supported by National Institutes of Health awards P01-EB2180, R21-CA121593, and R21-DK072112 and used the facilities of The EPR Center for the Study of Viable Systems (P41 EB002032). Pilot funding for additional clinical development of EPR was awarded by the Friends of Norris Cotton Cancer Center.

References

1. Swartz, H.M. and H.J. Halpern (1998). EPR studies of living animals and related model systems (*in vivo* EPR). In: Berliner LJ (ed) Spin Labeling, Biol. Magn. Reson. 14. Kluwer Academic/Plenum Publishers, New York.
2. Halpern, H.J. (2004). Stable soluble paramagnetic compounds. In: Berliner LJ (ed) *In vivo* EPR (ESR) Theory and Applications, Biol. Magn. Reson. 18. Kluwer Academic/Plenum Publishers, New York.

3. Dunn, J.F. and H.M. Swartz (2003) *In vivo* electron paramagnetic resonance oximetry with particulate materials. Methods 30(2): 159–166.
4. Khan, N., H. Hou, P. Hein et al. (2005). Black magic and EPR oximetry: from lab to initial clinical trials. In: Okunieff P (ed) Oxygen Transport to Tissue. Plenum Publishers, New York.
5. Swartz, H.M., K.J. Liu, F. Goda et al. (1994) India ink: a potential clinically applicable EPR oximetry probe. Magn Reson Med 31(2): 229–232.
6. Charlier, N., N. Beghein and B. Gallez (2004) Development and evaluation of biocompatible inks for the local measurement of oxygen using *in vivo* EPR. NMR Biomed 17(5): 303–310.
7. Salikhov, I., T. Walczak, P. Lesniewski et al. (2005) EPR spectrometer for clinical applications. Magn Reson Med 54(5): 1317–1320.
8. Swartz, H.M., N. Khan, J. Buckey et al. (2004) Clinical applications of EPR: overview and perspectives. NMR Biomed 17(5): 335–351.
9. Hall, E.J. (2000). Radiobiology for the Radiologist. Lippincott Williams & Wilkins, Philadelphia.
10. Khan, N., B.B. Williams, H. Hou et al. (2007) Repetitive tissue pO_2 measurements by electron paramagnetic resonance oximetry: current status and future potential for experimental and clinical studies. Antioxid Redox Signal 9(8): 1169–1182.
11. Khan, N., B.B. Williams and H.M. Swartz (2006) Clinical applications of *In vivo* EPR: Rationale and initial results. Appl Magn Reson 30: 185–199.

Measurement of Oxygen in the Microcirculation Using Phosphorescence Quenching Microscopy

Roland N. Pittman, Aleksander S. Golub, and Helena Carvalho

Abstract According to the classical concept of Krogh, O_2 is delivered to the tissues solely by capillaries and intra-capillary resistance to O_2 diffusion is negligible. Over the past three decades longitudinal PO_2 and SO_2 gradients in arterioles have been observed with a transmural PO_2 gradient in small arterioles of only 1–2 mmHg. Application of phosphorescence quenching microscopy to measurements of PO_2 in arterioles of the rat mesentery by Tsai et al. (1998) found a large transmural PO_2 in these arterioles. That led to the provocative conclusion that the arteriolar wall is the major sink for O_2 in the microcirculation. Our studies indicate that many of these results can be explained by photoactivated O_2 consumption following phosphor excitation, combined with a large excitation area and high frequency of flash excitation. We have developed the basic principles for phosphorescence quenching microscopy including the need to use a small excitation area, a low excitation frequency and a scanning excitation for stationary samples.

1 Introduction

The transport of O_2 to tissue is the most important function of the microcirculation. The pioneering work of August Krogh included anatomical, biophysical and physiological studies that resulted in a mathematical model of O_2 transport that bears his name. He concluded that only a small O_2 tension (PO_2) gradient was needed to supply an adequate amount of O_2 from the capillary blood to the tissue.

Over 50 years passed before the first systematic measurements of PO_2 in microvascular networks was carried out [1]. These studies resulted in the discovery of longitudinal gradients of PO_2 in arterioles. Following the

R.N. Pittman (✉)
Department of Physiology and Biophysics, Virginia Commonwealth University, Richmond, Virginia 23298, USA
e-mail: pittman@vcu.edu

E. Takahashi, D.F. Bruley (eds.), *Oxygen Transport to Tissue XXXI*, Advances in Experimental Medicine and Biology 662,
DOI 10.1007/978-1-4419-1241-1_22, © Springer Science+Business Media, LLC 2010

development of a photometric method to measure hemoglobin O_2 saturation (SO_2), simultaneous measurement of PO_2 and SO_2 confirmed a longitudinal gradient and showed that the paired values of PO_2 and SO_2 were consistent with the O_2 dissociation curve. These measurements have been confirmed in a variety of tissues and species over the past thirty years [2].

The estimation of O_2 diffusion from arteriolar segments using mass balance of convective O_2 flow led to the conclusion that about two-thirds of the O_2 loss in tissues with low blood flow and metabolic rate occurs in the arterioles. Comparison of the experimental results with a computational model revealed that there was an order of magnitude discrepancy between predicted and observed O_2 loss from arterioles [2]. The answer to the question "What is the destination for the 'lost' O_2?" has several choices: (1) consumption by adjacent cells, (2) diffusion to and uptake by nearby microvessels, and (3) consumption by the microvessel wall [3].

2 Phosphorescence Quenching Microscopy

A new tool for measuring PO_2, based on the ability of O_2 to quench the phosphorescence of excited phosphor molecules, was developed by Wilson and colleagues [4]. To apply this technique in the microcirculation, an adequate signal-to-noise ratio (S/N) is needed to obtain accurate PO_2 values from fitting the phosphorescence decay curve and it is necessary to use a higher phosphor concentration and excitation light intensity than is required for macro-scale applications [5].

Application of phosphorescence quenching microscopy (PQM) to measurements of PO_2 in arterioles of the rat mesentery led to a provocative conclusion regarding the fate of O_2 that diffused from these microvessels. A larger than expected transmural PO_2 was found in these arterioles [3], contrary to the previous report of a transmural gradient of only 1–2 mmHg [1]. This finding implied that the arteriolar wall consumes O_2 at a rate of more than 100 times higher than expected. One can estimate the maximum O_2 consumption of the wall, M_{mt}, based on its mitochondrial content. A compilation of O_2 consumption data for vascular tissue [6] revealed that all published values were smaller than M_{mt}. However, the calculated value of wall O_2 consumption by [3] was 10 times larger than M_{mt}, making it inconsistent with previous reports.

A potential source of error to account for the apparent high O_2 consumption of the arteriolar wall lies with the implementation of PQM. When the phosphor is excited, it can decay back to the ground state by emitting light (phosphorescence) or by transferring energy to O_2 (collisional quenching), thereby creating singlet O_2. Singlet O_2 can react with nearby organic molecules, thereby consuming O_2. One can minimize this artifact by reducing the excitation flash energy density and phosphor concentration. For typical values of these two variables, each pulse results in a reduction of PO_2 at the measurement site of

about 0.3 mmHg per flash [5]. This value is higher than that reported by [3]; however, it was later pointed out that their value was initially underestimated by a factor of about 15 [5].

Another important factor that determines the effect of the flash excitation on the decrement in PO_2 is the size of the excitation region. Following an excitation pulse, there is a small decrease in PO_2 (about 0.3 mmHg) and it returns to the pre-excitation level after a sufficient time has passed for O_2 to diffuse into the region. If enough O_2 can diffuse into the excitation region before the next flash occurs, then the PO_2 can be restored to its initial value. If the next flash occurs before the O_2 has been replenished at the site, then PO_2 will fall. It is important to recognize that there is a physical constraint between excitation spot size (L) and flash frequency (F), such that the time between successive flashes ($T_{flash} = 1/F$) should be longer than the characteristic time it takes for diffusion to replenish the consumed O_2 ($T_{diff} \approx L^2/2D$, where L is one-half the side of the square excitation region and D is the diffusion coefficient of O_2, 1.04×10^{-5} cm^2/s). A critical value is the ratio T_{diff}/T_{flash}; if this ratio is $>>1$, then there will be insufficient time to replenish O_2 between flashes and PO_2 at the measurement site will fall. An example of our use of PQM applied to capillary measurements had $L = 0.45$ μm and flash frequency = 100 Hz, yielding $T_{diff} = 105$ μs and $T_{flash} = 10$ ms, for a ratio of 0.011 [7]. The corresponding parameters used by [3] were $L = 70$ μm and flash frequency = 30 Hz, yielding $T_{diff} = 2.5$ s and $T_{flash} = 33$ ms, for a ratio of 77. Thus, one would expect a considerable fall in PO_2 using the parameters reported by [3].

It is important to avoid multiple excitations of the same volume containing the phosphor probe. This led us to analyze the performance of two prototypical instruments used for measurements of PO_2 in PQM [5]. We have labeled these two configurations as Large Excitation Area (LEA) and Small Excitation Area (SEA) instruments (see Fig. 1). The LEA instrument, similar to that used by [3],

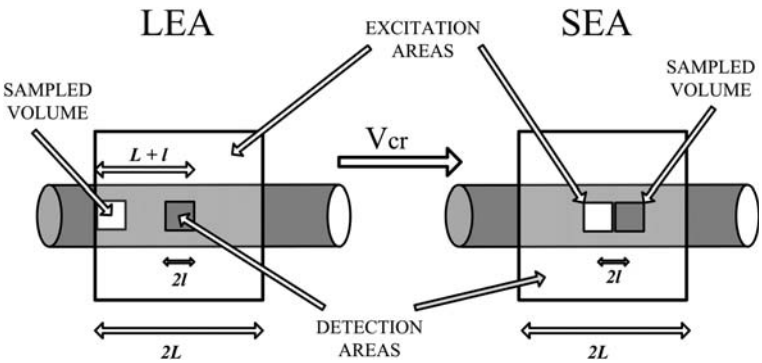

Fig. 1 Estimation of the critical velocity, V_{cr} , for LEA and SEA instruments. In a LEA instrument, at V_{cr} the sampled volume covers the distance ($L + l$) from flash to flash. In a SEA instrument that volume must move out of the excitation area a distance *2 l* during this time. For any flash rate, V_{cr} for a SEA instrument is much lower than that for a LEA instrument

has a large excitation area (L^2) and a small detection area (l^2), whereas the SEA instrument, similar to that used by [5], has a small excitation area (l^2) and a large detection area (L^2). While it is obvious that a potential artifact of O_2 consumption by PQM exists for a stationary medium, this problem also exists in a moving fluid and leads to the concept of critical velocity. In order to avoid multiple excitations, and hence depression of PO_2 in a moving medium (e.g., flowing blood or lymph), it is necessary for the fluid to move faster than a critical velocity, V_{cr}. The value of the V_{cr} for the two different configurations is given by $V_{cr}(\text{LEA}) = (L + l)\text{F}$ and $V_{cr}(\text{SEA}) = 2l\text{F}$, since in the SEA instrument only the size of the excitation area determines V_{cr}. If the velocity of the medium is less than V_{cr}, then multiple excitations of the sampled volume will occur and lead to artifactual results [5].

The criteria for reliable microcirculatory PO_2 measurements using PQM are a low excitation light intensity, low phosphor concentration, low flash frequency, small excitation region and large detection region [5]. The data acquisition and data analysis features incorporated into the instrument in Fig. 2 have been described previously and include use of a short light pulse xenon lamp or short laser pulses for excitation, gating of the excitation pulse to exclude any early non-phosphorescent signal from analysis, recording individual decay curves before averaging, exponential analysis of heterogeneous decays, automatic analysis of multiple decays, small excitation spot and low flash rate in flowing blood and a scanning approach for PO_2 measurements in stationary media (see Fig. 2).

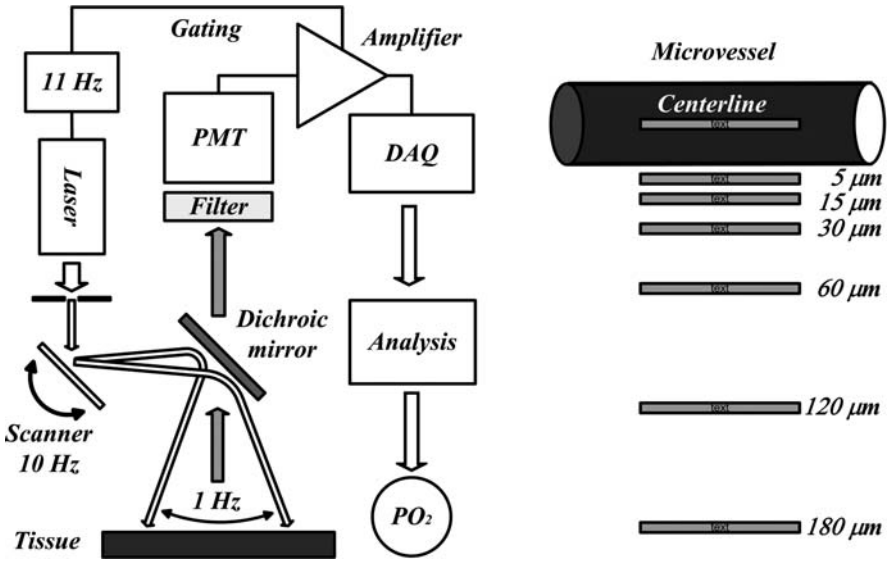

Fig. 2 Principle of scanning phosphorescence PO_2 measurements in a stationary tissue (*left*). One scan cycle produces 11 discrete phosphorescent decays along the scan strip (5 × 57 μm), oriented parallel to the vessel. Measurements are made at different distances from the inner vessel wall, leaving at least 60 μm of a vascular tissue beyond the last site (*right*)

3 Applications of PQM

Two major findings using PQM are described here as examples of studies that can be performed with the SEA instrumentation: (1) the first measurements of Erythrocyte Associated Transients (EATs) of PO_2 in capillaries and (2) the observation of only a small (1–2 mmHg) transmural PO_2 gradient in arterioles and only a small PO_2 gradient in the interstitial fluid.

For almost 60 years following the publication of the Krogh Cylinder Model in 1919 the intra-luminal component of resistance to O_2 transport was neglected. Hellums [8] calculated the fraction of intravascular resistance to O_2 transport in capillaries and concluded that it was far from negligible, accounting for about 50% of the total resistance. This resistance is contributed primarily by the low solubility of O_2 in the plasma, and it increases when the width of the plasma gap increases. Hellums predicted that this intra-luminal resistance to O_2 transport in capillaries should manifest itself as EATs of PO_2 in capillaries, that is, fluctuations in PO_2 as RBCs and plasma gaps alternately pass an observation point along a capillary. Although EATs were first predicted in 1977, they were only observed recently when PQM was refined to provide sufficient spatial (1 μm) and temporal (10 ms) resolution to measure the fluctuations in PO_2 [7]. EATs reflect the particulate nature of blood and the low solubility of O_2 in the plasma gaps, indicating a significant resistance to O_2 transport in the blood. EATs can limit the O_2 supply to tissue and provide two roles for capillary hematocrit in determining O_2 transport: (1) a decrease of convective O_2 delivery into capillaries; and (2) an increase in the EAT-related diffusion resistance for O_2 transport.

We have made recent measurements to map PO_2 profiles in and near arterioles in the rat mesentery [9, 10]. The results of the PO_2 profiles are shown in Fig. 3 Our results are in contrast to the large transmural and tissue PO_2 gradients reported by [3] in numerous publications since 1998. It appears that these results can be explained by photo-activated O_2 consumption following

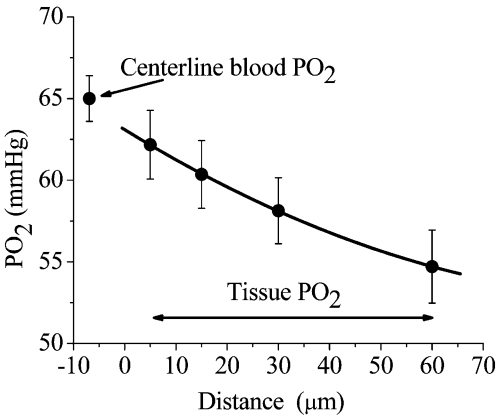

Fig. 3 PO_2 in 78 arterioles and peri-arteriolar tissue (84 profiles) in rat mesentery (mean ± SE). The blood PO_2 was close to the parabolic PO_2 profile in connective tissue extrapolated to the blood/wall interface, indicating a small O_2 consumption by the vessel wall

phosphor excitation, as explained above, combined with an excitation area and frequency of flash excitation that are too large. We have reported similar measurements in arterioles of the hamster cheek pouch [11], where the transmural PO_2 gradient was found to be small (about 1 mmHg) and the intraluminal PO_2 gradient was found to be larger (about 5 mmHg), consistent with a net diffusive flux of O_2 from the arterioles. These are but a few key examples of how PQM has proven to be a robust and reliable method for measuring O_2 levels in the microcirculation.

Acknowledgments Supported by grant AHA-0655449U from the American Heart Association, Mid-Atlantic Affiliate and grants HL18292 and HL079087 from the NHLBI.

References

1. Duling BR, Berne RM (1970) Longitudinal gradients in periarteriolar oxygen tension. A possible mechanism for the participation of oxygen in local regulation of blood flow. Circ Res 27:669–678.
2. Pittman RN (2005) Oxygen transport and exchange in the microcirculation. Microcirculation 12:59–70.
3. Tsai AG, Friesenecker B, Mazzoni MC, Kerger H, Buerk DG, Johnson PC, Intaglietta M (1998) Microvascular and tissue oxygen gradients in the rat mesentery. Proc Natl Acad Sci USA 95:6590–6595.
4. Vanderkooi JM, Maniara G, Green TJ, Wilson DF (1987) An optical method for measurement of dioxygen concentration based upon quenching of phosphorescence. J Biol Chem 262:5476–5482.
5. Golub AS, Pittman RN (2008) PO_2 measurements in the microcirculation using phosphorescence quenching microscopy at high magnification. Am J Physiol Heart Circ Physiol 294:H2905–H2916.
6. Vadapalli AR, Pittman RN, Popel AS (2000) Estimating oxygen transport resistance of the microvascular wall. Am J Physiol Heart Circ Physiol 279:657–671.
7. Golub AS, Pittman RN (2005) Erythrocyte-associated transients in PO_2 revealed in capillaries of rat mesentery. Am J Physiol Heart Circ Physiol 288:H2735–H2743.
8. Hellums JD (1977) The resistance to oxygen transport in the capillaries relative to that in the surrounding tissue. Microvasc Res 13:131–136.
9. Golub AS, Barker MC, Pittman RN (2007) PO_2 profiles near arterioles and tissue oxygen consumption in the rat mesentery. Am J Physiol Heart Circ Physiol 293:H1097–H1106.
10. Golub AS, Barker MC, Pittman RN (2008) Microvascular oxygen tension in the rat mesentery. Am J Physiol Heart Circ Physiol 294:H21–H28.
11. Carvalho H, Pittman RN (2008) Longitudinal and radial gradients of PO_2 in the hamster cheek pouch microcirculation. Microcirculation 15:215–224.

Optimization of the Coherence Measurement Computed by Means of the Welch Averaged Periodogram Method for Assessment of Impaired Cerebral Autoregulation

D. De Smet, J. Vanderhaegen, G. Naulaers, and S. Van Huffel

Abstract The coherence method (COH) has been widely used to study the concordance between continuously measured signals intervening in the assessment of cerebral autoregulation in neonates. Several research groups have applied this method to mean arterial blood pressure (MABP) combined with cerebral signals such as the intravascular oxygenation (HbD), cerebral tissue oxygenation (TOI), and regional oxygen saturation (rSO_2) measured by near-infrared spectroscopy (NIRS). All groups contributed in a particular way to the fine-tuning of the application of COH with the Welch averaged periodogram (WAP) method. We have made a comparative study of all published results coupled with an optimization of the use of the WAP method within COH. We have also proposed a pre-processing algorithm to remove signal artefacts, and defined a new critical score value (*CSV*) for COH to distinguish infants with impaired autoregulation from those without.

1 Introduction

Tsuji et al. [1] were the first to use continuously measured NIRS signals to study impaired cerebral autoregulation in neonates over non-successive 30 min epochs. They looked at the concordance between HbD and MABP – reflecting impaired autoregulation – by means of the COH method. If COH was >0.5 the infant was considered to have poor autoregulation. Morren et al. [2] introduced the use of an overlapping sliding window approach dividing the long duration signal into smaller 30 min epochs prior to analysis. They also attempted to maximize the *SNR* of the WAP method. Finally Soul et al. [3] introduced the use of the *CSV* as defined by Taylor et al. [4] applied to the case of impaired autoregulation.

S.Van Huffel (✉)
Department of Electrical Engineering (ESAT), SCD Division, Katholieke Universiteit, Leuven, Belgium
e-mail: sabine.vanhuffel@diversiteit.kuleuven.be

E. Takahashi, D.F. Bruley (eds.), *Oxygen Transport to Tissue XXXI*, Advances in Experimental Medicine and Biology 662,
DOI 10.1007/978-1-4419-1241-1_23, © Springer Science+Business Media, LLC 2010

In this study, we looked at the influences on COH of the signal sample frequency, the parameters intervening in the WAP method, and the frequency band of interest. Furthermore, we developed a new method to fix the *CSV*, based on the calibration of the mean COH score on the mean absolute-valued correlation coefficient (COR) score, which allows us to use the value 0.5 as the threshold above which a patient is said to have impaired autoregulation. Finally we developed a pre-processing algorithm to remove signal artefacts.

2 Datasets

All mathematics were developed for and applied on preterm infants from the University Hospital Zurich (Switzerland), the University Medical Centre Utrecht (The Netherlands), and the University Hospital Leuven (Belgium). SaO_2 was measured continuously by pulse oximetry, and MABP by an indwelling arterial catheter. Transcranial NIRS signals HbD (measured by the Critikon Cerebral Oxygenation Monitor 2001), rSO_2 (INVOS4100, Somanetics), and TOI (NIRO300, Hamamatsu) were measured for non-invasive monitoring of cerebral oxygenation. All signals were measured simultaneously in the first days of life, and recorded at the frequency of 0.333 Hz (periodicity = 3 s).

3 Methods

The first constraints concern the signal sample frequency (f_s) and the frequency band of interest. Urlesberger et al. [5] and later von Siebenthal et al. [6] showed that the measured NIRS signals could have a cyclic duration of as little as 10 s. Because of the use of the fast Fourier transform (FFT), the *Nyquist theorem of digital sampling* means the sampling frequency must be at least twice the smallest signal intrinsic frequency, i.e. at least 0.2 Hz ($f_s \geq 0.2$ Hz). von Siebenthal et al. [6] also showed that MABP fluctuates with a periodicity of 60–150 s (cut-off frequency $f_{\text{cut}} \geq 0.0067$ Hz). MABP being the most influential signal of all those considered, we studied impaired autoregulation in the periodicity band 25–300 s [3].

The continuously recorded signals were divided into epochs of a shorter duration beforehand, allowing us to have a continuous assessment of impaired autoregulation [2]. For this reason we called them calculation epochs (*C-epochs*), of duration *TC* (min). The WAP method computes an averaged frequency spectrum of the signal on each of these C-epochs. The average is performed on the basis of N smaller overlapping epochs into which each C-epoch is divided. We called these smaller epochs *H-epochs* as they apply a highpass (time-domain) filtering on the signals. The duration of a H-epoch

(*TH*, min) should be at least one cycle of the signal periodicity ($TH \geq 2.5$ min). To ensure the last H-epoch contained in a C-epoch is not cropped (which would mean that the signal is again highpass filtered), we could demonstrate:

$$N = \frac{TC - TH_{\text{Over}}}{TH - TH_{\text{Over}}} \tag{1}$$

where TH_{Over} (min) is the overlap width between two successive H-epochs. As it was not certain we included an integer number of signal cycles in each H-window, we applied a *Hanning window* to each H-epoch to avoid the leakage phenomenon when using the FFT. Notice that no Hanning windowing was applied to the C-epochs, as it generated an artefact in the low frequencies of the COH spectrum. Carter et al. [7] showed the H-epochs should be half-overlapped in the case of the application of Hanning windowing ($TH_{\text{Over}} = TH/2$). On the other hand, we found that the higher the value of N (the higher the *SNR*), the lower the amplitude of COH. Thus, by choosing a different N, we obtained different COH values. Eq. 1 became:

$$TC = \frac{TH(N+1)}{2} \tag{2}$$

The duration of the C-epochs in which the full-length signals are originally divided may – ideally seen – not be chosen. We also found that the ratio TH/TC should be in the range of 0.5 or smaller ($TH \leq TC/2$) otherwise there is no sense in applying the WAP method as the H-epoch duration tends to the C-epoch one.

In 1998, Taylor et al. [4] found that the amplitude of COH was influenced by the parameters intervening in the WAP method. To distinguish patients demonstrating a concordance between the two signals investigated from those with no concordance, they set up a new *CSV* definition computed from *TC*, *TH*, and a *F*-hypothesis test. However this definition did not take into account the influence of TH_{Over} intervening in Eq. 1. Therefore we have proposed a new methodology: adapt N until the mean COH – on all infants from the same medical centre – equals the mean absolute-valued (for comparability with COH) COR, the *CSV* of COR being per definition 0.5. Making N variable changes only the *SNR* of the frequency spectrum and does not affect the signals. The sole free parameter in Eq. 2 is *TH*, in that it fulfils some conditions. We chose *TH* to be equal to 5 min in accordance with the work of Soul et al. Table 1 presents the summary of the parameter values used by all working groups, to which we added those of Wong et al. [8].

Finally, we have also developed a pre-processing stage to remove measurement artefacts induced by medical interferences and by the conversion between analogue and digital data. Each artefact point in a signal was simultaneously

Table 1 The following is a summary of all parameters intervening in the Welch averaged periodogram method applied by Tsuji et al. (2000), Morren et al. (2001), Soul et al. (2007), and Wong et al. (2008)

	Tsuji et al.	Morren et al.	Soul et al.	Wong et al.
f_s	2 Hz (0.2 Hz)	6 Hz (0.2 Hz)	2 Hz (0.4 Hz)	1 Hz
f_{cut}	0.01 Hz	0.01 Hz	0.04 Hz	0.02 Hz
TH	–	12 min	5 min	10 min
TH_{Over}	–	11 min 55 s	2.5 min	7.5 min
N	–	217	3	5
TC	30	30	10	20
TH/TC	–	0.4	0.5	0.5
TC_{Over}	–	10	0	0
CSV	0.5	0.5	0.77	0.5

deleted in all other signals, as done by Soul et al. for artefacts lasting more than 1.5 s. The steps of the algorithm we developed are:

1. Remove artefact-like repetitive points included in the recordings.
2. Keep the signals in normal physiological ranges, particularly SaO_2 in the range 80–100%.
3. Divide the signals in non overlapping 10-min epochs, from each of which we kept only the portions belonging to interval $[median - IQR, median + IQR]$.
4. As this is not enough to detect some extra peak artefacts of longer duration contained in MABP and SaO_2 (the two most influential signals), centre and absolute-value MABP (and afterwards SaO_2) (result 1), and on the other side differentiate, square, and reduce it (result 2) with the aim of emphasizing the signal extremes. Result 1 gives an average peak amplitude, and result 2 acts as a ponderation coefficient with value close to 1 at peak abscises. Finally, multiply together the obtained signals, which indicates which signal points may be deleted.

4 Results

There are about 55% repetitive points for the INVOS, 45% for the Critikon, and 15% for the NIRO spectrometers. They were all removed prior to application of pre-processing steps 2 to 4 which themselves delete about 60% of the data. Steps 2 to 4 are very effective: values of COH and COR are significantly higher than without pre-processing. Fig. 1 illustrates an example of pre-processed data. The optimized values of TC (N) for the Zurich, Leuven, and Utrecht data are 10 min (3), 12.5 min (4), and 15 min (5). The CSV computation of Taylor et al. [4] generates high values (around 0.7) in the case of measured NIRS signals, only affordable with a low N, i.e. a low SNR.

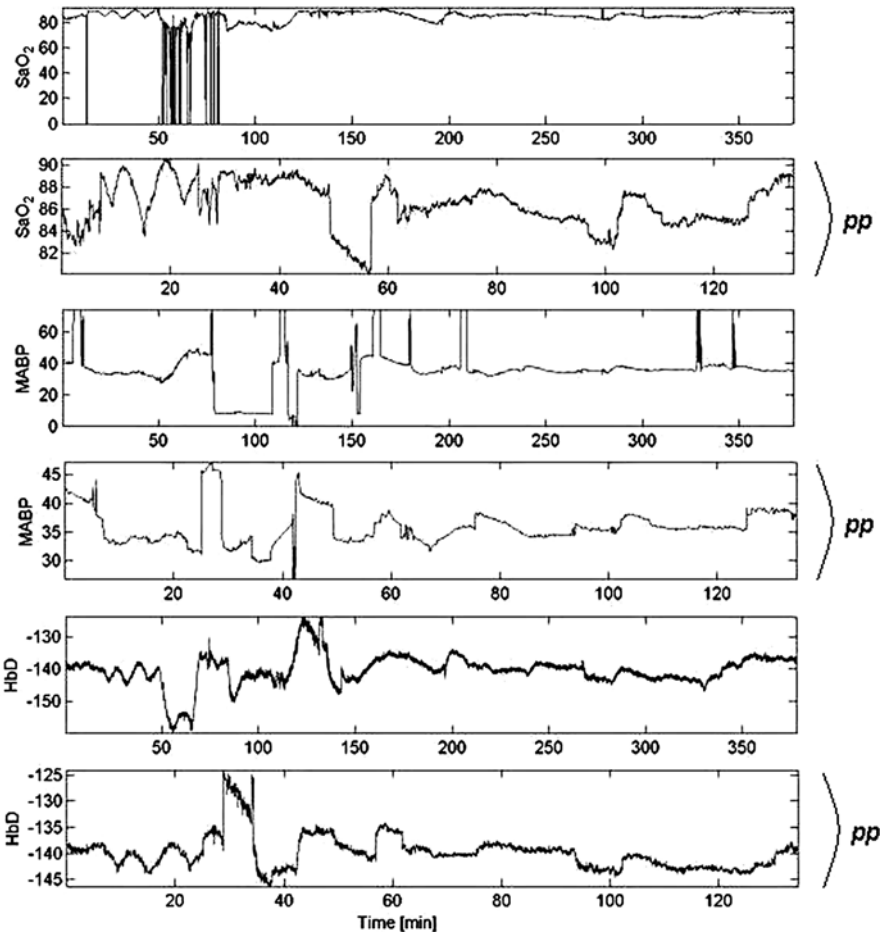

Fig. 1 Illustration of the efficiency of the preprocessing algorithm applied to SaO_2, MABP, and HbD/rSO_2/TOI. The figure shows original and preprocessed (*pp*) signals measured in the University Hospital Zurich (Switzerland) by the Critikon Cerebral Oxygenation Monitor 2001. Most of the artefacts due to medical interferences and patient handling were removed. Although efficient, the preprocessing makes the signals very short and damages their frequency content

5 Discussion

The repetitive points in the data prior to analysis may be due to the conversion from analogue to digital data, to the spectrometer resolution and some simply to the sometimes constant nature of the signals. This step in the pre-processing of the data, however, is not needed as we discovered that the repetitive points are equally distributed all along the recording. The pre-processing otherwise has a bad influence on the frequency content of the signals. We should

complementarily set up an *intelligent interpolation* for artefacts lasting more than 1.5 s otherwise we break the signal periodicities. The pre-processing also makes the recording much shorter in duration, with the risk that it becomes impossible to analyse by means of a sliding-window approach.

With regard to the WAP method, the FFT assumes the signals to be periodic: we assume this periodicity in line with the works of von Siebenthal et al. [6] and Urlesberger et al. [5]. The decrease in the coherence amplitude with increasing N should thus actually not occur, because between one H-epoch and another the extremes in the frequency spectrum of COH should occur at the same frequencies.

Finally, working with a *CSV* of COH equal to 0.5 suggests a relation between two signals based on 50% shared variance, which can be defended. But this *CSV* should ideally be determined empirically from the patient clinical characteristics and outcomes, or statistically in the way done by Taylor et al. [4]. With the *CSV* fixation we have proposed, the amplitude of COH is in the range of COR which allows comparability of these two complementary methods. The *CSV* definition of Taylor et al. [4] generates high values in the case of detection of impaired cerebral autoregulation, but could perhaps be used in other applications (e.g. for cardiologic data).

Acknowledgments The research was supported by: Research Council KUL: GOA AMBioRICS, CoE EF/05/006, by FWO projects G.0519.06 (Non-invasive brain oxygenation), and G.0341.07 (Data fusion), by Belgian Federal Science Policy Office IUAP P5/22. We thank particularly Prof. Frank van Bel and Dr. Petra Lemmers from the University Medical Centre Utrecht (The Netherlands), and PD Dr. Martin Wolf from the University Hospital Zurich (Switzerland) for having let us use their signal recordings.

References

1. Tsuji M, Saul J, du Plessis A et al. (2000) Cerebral intravascular oxygenation correlates with mean arterial pressure in critically ill premature infants. Pediatr Rev 106(4):625–632.
2. Morren G, Lemmerling P, Van Huffel S et al. (2001) Detection of autoregulation in the brain of premature infants using a novel subspace-based technique. Proc of 23rd Intern IEEE-EMBS Conf 2:2064–2067.
3. Soul J, Hammer P, Tsuji M et al. (2007) Fluctuating pressure-passivity is common in the cerebral circulation of sick premature infants. Pediatr Res 61(4):467–473.
4. Taylor J, Carr D, Myers C et al. (1998) Humans mechanisms underlying very-low-frequency RR-interval oscillations in humans. Circulation 98:547–555.
5. Urlesberger B, Trip K, Ruchti J et al. (1998) Quantification of cyclical fluctuations in cerebral blood volume in healthy infants. Neuropediatrics 29(4):208–211.
6. von Siebenthal K, Beran J, Wolf M et al. (1999) Cyclical fluctuations in blood pressure, heart rate and cerebral blood volume in preterm infants. Brain & Dev 21:529–534.
7. Carter D, Knapp C, Nuttall A (1973) Estimation of the magnitude-squared coherence function via overlapped fast Fourier transform processing. IEEE Trans Audio Electroacoust 21(4):337–344.
8. Wong F, Leung T, Austin T et al. (2008) Impaired autoregulation in preterm infants identified by using spatially resolved spectroscopy. Pediatrics 121:604–611.

A Hybrid Multi-Distance Phase and Broadband Spatially Resolved Spectrometer and Algorithm for Resolving Absolute Concentrations of Chromophores in the Near-Infrared Light Spectrum

Ilias Tachtsidis, Lei Gao, Terence S. Leung, Matthias Kohl-Bareis, Chris E. Cooper, and Clare E. Elwell

Abstract For resolving absolute concentration of tissue chromophores in the human adult brain with near-infrared spectroscopy it is necessary to calculate the light scattering and absorption, at multiple wavelengths with some depth resolution. To achieve this we propose an instrumentation configuration that combines multi-distance frequency and broadband spectrometers to quantify chromophores in turbid media by using a hybrid spatially resolved algorithm. Preliminary results in solid phantoms as well as liquid dynamic homogeneous and inhomogeneous phantoms and in-vivo muscle measurements showed encouraging results.

1 Introduction

Reflectance near-infrared spectroscopy (NIRS) is a technique for characterizing turbid media that has become widely used in medical diagnostics. In particular the in-vivo determination of the optical properties of the human muscle, breast and brain is of the utmost importance.

Typically in biological tissue, the near infrared absorbers and major intrinsic chromophores which need to be quantified are hemoglobin, cytochrome-*c*-oxidase and water. Many researchers rely on a small number of discrete wavelengths to recover the concentrations of these constituents from non-invasive in-vivo measurements, usually above and below the isosbestic wavelength of oxygenated (HbO_2) and deoxygenated (HHb) hemoglobin (near 800 nm). Recovery of all intrinsic chromophores in tissue is a somewhat ill-posed problem; the measurements are often hampered by errors due to poor signal-to-noise ratio, wide range of possible chromophores concentrations, difficulties in and requirement for instrument calibration, poor depth resolution and inhomogeneous structure of the tissue

I. Tachtsidis (✉)
Biomedical Optics Research Laboratory, Department of Medical Physics and Bioengineering, University College London, Gower Street, London, WC1E 6BT, UK
e-mail: iliastac@medphys.ucl.ac.uk

E. Takahashi, D.F. Bruley (eds.), *Oxygen Transport to Tissue XXXI*, Advances in Experimental Medicine and Biology 662,
DOI 10.1007/978-1-4419-1241-1_24, © Springer Science+Business Media, LLC 2010

being investigated. To help overcome these problems it can be useful to use multi-spectral and multi-distance measurements of NIR light attenuation to resolve absorption and scattering.

This paper reports on a novel approach to calculate absolute concentrations of chromophores in turbid media such as biological tissue by fusing multi-distance frequency resolved and multi-distance broadband near-infrared spectroscopy with a hybrid spatially resolved algorithm.

2 Methods

2.1 The Instrument

The instrumentation configuration consisted of two spectrometers (Fig. 1). The first is a four wavelength (690, 750, 790, 850 nm) multi-distance frequency domain (110 MHz) spectrometer (MDFD), which is a modification of the commercially available OxiplexTSTM from ISS Inc (Champaign, IL, USA). This instrument allows for the determination of the average value (dc), amplitude (ac) and phase (Φ) of the modulated intensity at two different source-detector distances (3 and 3.5 cm) at each wavelength. This multi-distance method affords the quantitative assessment of the absorption (μ_a) and reduced scattering (μ_s') coefficients by using the paired ac and Φ data [1].

The second instrument is a multi-distance broadband spectrometer (MDBBS). It consists of a white light source that utilizes a 50 W halogen bulb and a short pass filter to minimize temperature effects. The spectrograph is based on a configuration of lenses (rather than mirrors), and is comprised of a

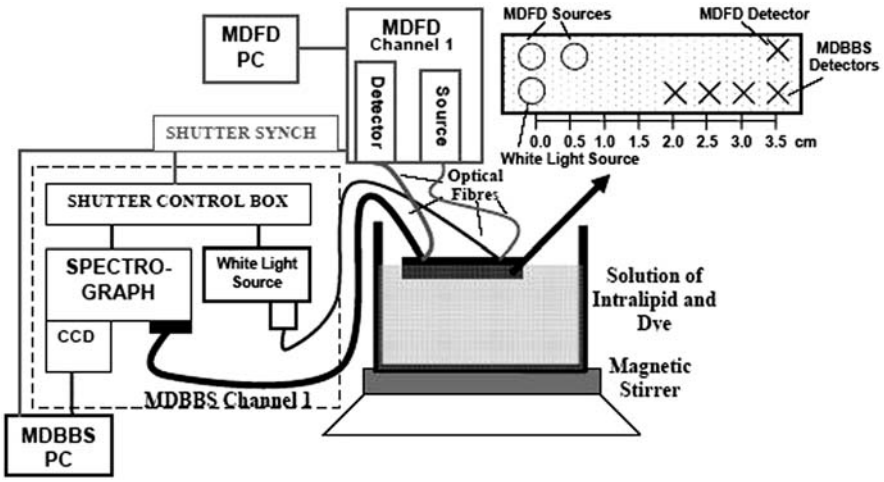

Fig. 1 Instrumentation diagram and experimental set up for dynamic homogeneous phantom studies also showing the configuration of the optodes from both systems

50 × 50 mm grating with 300 grooves per mm that is blazed at 1000 nm (to optimize the reflection in NIR). The light spectrum is detected by a CCD camera (PIXIS:512f, Princeton Instruments), with chip dimensions of 12.3 × 12.3 mm that corresponds to 512 × 512 pixels with a pixel size of 24 × 24 μm. In order to use most of CCD chip the current design involves four detector fibres with different diameters, where the diameter of the furthest detector (3.5 cm) is 3 mm, the diameter for the second detector (3 cm) is 2 and 1 mm for the two closest detectors (2.5 and 2 cm). In addition to that the geometry of the fibre bundles on the distal end was changed from round to approximate oval in order to decrease the area blocked by the slit. The optical bandwidth of the MDBBS is 564 nm (504–1068 nm) and the mean wavelength resolution is 4 nm. The MDBBS is an upgrade of an early design of a Lens Imaging Spectrograph (or LImS) developed earlier [2].

The two instruments measure sequentially with the frequency domain system providing the synchronization trigger. The measurement cycle consists of an MDBBS measurement followed by an MDFD measurement, resulting in a minimum sampling rate of 1 Hz and a maximum sampling rate of 0.25 Hz.

2.2 The Algorithm

The MDBBS measures light attenuation at several wavelengths ($A_{(\lambda n)}$) at four distances. From these measurements we calculate the slope of light attenuation versus distance, ρ ($\partial A_{(\lambda n)}/\partial\rho$). Using the MDFD derived values of scattering for the four wavelengths and assuming scattering is following a power function versus wavelength we can derive estimates of $\mu_s'{}_{(\lambda n)}$ at all other wavelengths. One then can calculate absorption ($\mu_{a(\lambda n)}{}^{SRS}$) from the spatially resolved spectroscopy (SRS) methodology using Eq. (1) [3]. To obtain the absolute broadband hybrid absorption ($\mu_{a(\lambda n)}{}^{Hybrid}$) we use the MDFD derived $\mu_{a(MDFD)}$ for the four wavelengths to scale the $\mu_{a(\lambda n)}{}^{SRS}$ by minimizing the mean squared difference between them.

$$\mu_{a(\lambda n)}^{SRS} = \frac{1}{3 \cdot \mu'_{s(\lambda n)}} \cdot \left(\ln 10 \cdot \frac{\partial A_{(\lambda n)}}{\partial \rho} - \frac{2}{\rho} \right)^2 \tag{1}$$

where $\mu_{a(\lambda n)}{}^{SRS}$ is the absorption, $\mu_s'{}_{(\lambda n)}$ is the reduced scattering, ($\partial A_{(\lambda n)}/\partial\rho$) is the slope of light attenuation versus optode distance and ρ is the mean optode distance.

3 Results

3.1 Solid Homogeneous Phantoms

The instrumentation and methodology was first tested on homogeneous solid phantoms (Block A and B) with known absorption and scattering properties (Table 1).

Table 1 Comparison of absorption and scattering between real and measured values for Block A and Block B (the percentage values inside the parenthesis show the error)

Wavelengths (nm)						
Block A	Real μ_a (cm^{-1})	Real μ_s' (cm^{-1})	$\mu_{a\,(MDFD)}$ (cm^{-1})	$\mu_{s\,(MDFD)}'$ (cm^{-1})	μ_a^{Hybrid} (cm^{-1})	$\mu_s'^{\,Hybrid}$ (cm^{-1})
690	0.115	10.9	0.112 (−3%)	10.8 (−1%)	0.109 (−5%)	10.9 (0%)
750	0.112	10.2	0.110 (−2%)	10.1 (−1%)	0.111 (−1%)	10.3 (1%)
790	0.109	9.9	0.107 (−2%)	9.7 (−2%)	0.109 (0%)	10.0 (1%)
850	0.106	9.5	0.106 (0%)	9.6 (2%)	0.104 (−2%)	9.5 (0%)
Block B						
690	0.146	5.1	0.146 (0%)	5.1 (0%)	0.143 (−2%)	5.0 (−1%)
750	0.144	4.7	0.144 (0%)	4.7 (−1%)	0.144 (0%)	4.7 (0%)
790	0.143	4.5	0.143 (0%)	4.5 (0%)	0.143 (0%)	4.5 (1%)
850	0.142	4.3	0.139 (−2%)	4.3 (0%)	0.141 (−1%)	4.3 (0%)

3.2 Dynamic Homogeneous and Inhomogeneous Phantoms

To further test the accuracy of the hybrid instrument and algorithm, measurements were performed in dynamic liquid phantoms. First a diluted absorbing dye (ADS842MC) was dissolved in steps of 3, 7.5 and 15 ml in a small tank containing 2850 ml of deionized water mixed with 150 ml of aqueous scattering suspension (Intralipid-20%). Measurements were done (see Fig. 2a) with the optodes of the hybrid system slightly submerged below the surface of the solution. Second a small tank with an outside wall made of epoxy resin with thickness of 5 mm and fixed absorption coefficient of 0.35 cm^{-1} and reduced scattering 14.5 cm^{-1} (at 780 nm). Measurements were done (see Fig. 2b) with the optodes of the hybrid system attached to the outside of the wall and a diluted ADS842MC was dissolved in steps of 1.5, 3.75 and 7.5 ml in 1425 ml in deionized water mixed with 75 ml of aqueous scattering suspension (Intralipid-20%).

Using the specific extinction coefficients of the dye (fitting from 680 to 900 nm) and the measured absorption coefficient, the absolute concentration of the dye was calculated and compared with the theoretical expected values. The mean error and standard deviation (SD) between the measured and the expected concentrations of the dye for the homogeneous phantom was 56.4% (83.4%) for the MDFD system and 8.2% (10.2%) for the hybrid system; for the inhomogeneous phantom the errors were 35.6% (40.5%) for the MDFD system and 24.4% (8.2%) for the hybrid system. In both cases the hybrid instrument outperformed the MDFD.

3.3 In-Vivo Muscle

The optodes of the hybrid instrument were placed on the forearm muscle of three young volunteers (mean age 24) (see Fig. 3)

Using the absorption coefficients measured as described above we fitted the specific extinction coefficient of HbO_2 and HHb and calculated the concentrations of these chromophores and from this the tissue oxygen saturation (StO_2) (Table 2)

4 Discussion

The central novelty and innovation of this methodology is that by using the MDFD derived μ_a and μ_s' values we can convert the MDBBS slope measurements of attenuation to measurements of absolute μ_a across the NIR wavelength range. Broadband μ_a will allow a more accurate quantification of chromophores such as cytochrome-*c*-oxidase with less cross talk from HbO_2 and HHb [4]. We have tested the instrumentation and methodology in solid phantoms, homogeneous and inhomogeneous dynamic liquid phantoms and human muscle. The results were encouraging and this technology will soon be used for studies in human adult volunteers and patients undergoing neurocritical care.

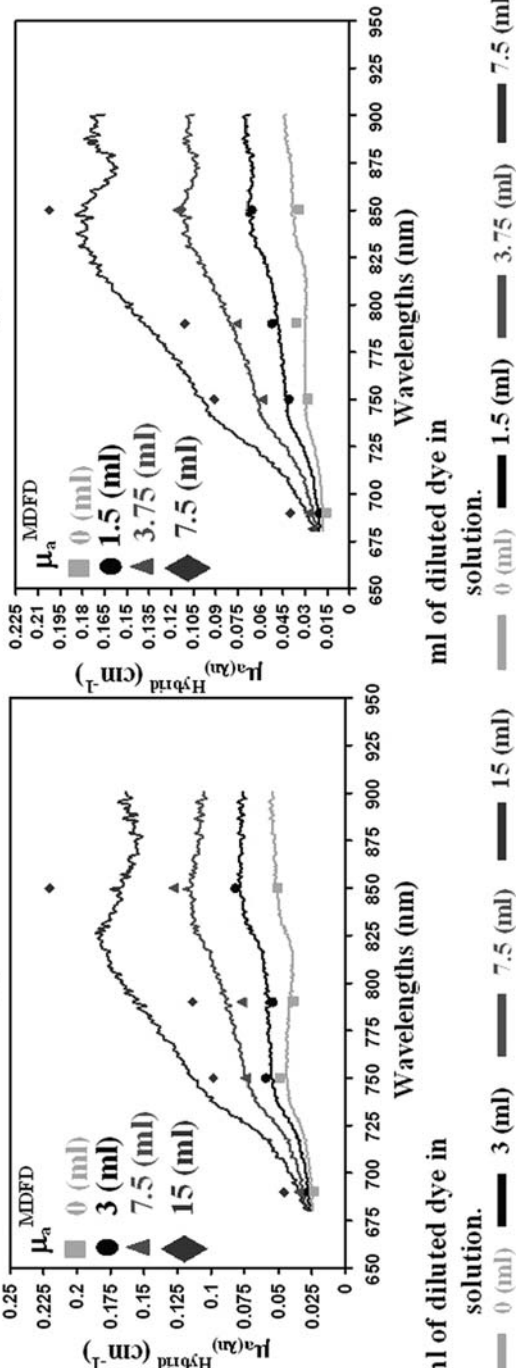

Fig. 2 Measurements of absorption coefficient with the MDFD and hybrid instrument in the (**a**) homogeneous liquid phantom and (**b**) inhomogeneous liquid phantom

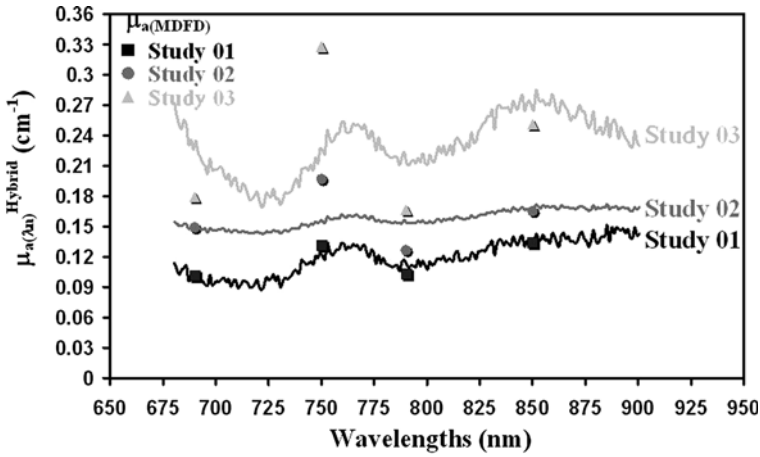

Fig. 3 Absolute broadband absorption from in-vivo muscle measurements in three volunteers during rest

Table 2 Absolute concentrations of oxy- and deoxy- hemoglobin, total hemoglobin (HbT = HbO_2 + HHb) and tissue oxygen saturation (StO_2 = HbO_2/HbT)

		HbO_2(μM)	HHb(μM)	HbT (μM)	StO_2 (%)
Study 01	MDFD	28.1	17.4	45.5	61.8
(Female)	Hybrid	30.3	18	48.3	62.7
Study 02	MDFD	32.3	28.6	60.9	53
(Female)	Hybrid	35.4	28.1	63.5	55.8
Study 03	MDFD	58.9	37.6	96.5	61
(Male)	Hybrid	60.2	38.5	98.7	60.9

Acknowledgments The authors would like to thank the EPSRC (EP/D060982/1) for the financial support of this work.

References

1. Hueber DM, Franceschini MA, Ma HY et al. (2001) Non-invasive and quantitative near-infrared hemoglobin spectrometry in the piglet brain during hypoxic stress, using a frequency-domain multi-distance instrument. Phys Med Biol 46:41–62
2. Soschinski J, Geraskin D, Milosavljevic B et al. (2007) Cerebral oxygenation monitoring during cardiac bypass surgery in babies with broad band spatially resolved spectroscopy. Adv Med Eng 114
3. Suzuki S, Takasaki S, Ozaki T et al. (1999) A tissue oxygenation monitor using NIR spatially resolved spectroscopy. Proc SPIE 3597:582–592.
4. Matcher SJ, Elwell CE, Cooper CE et al. (1995) Performance comparison of several published tissue near-infrared spectroscopy algorithms. Anal Biochem 227(1):54–68.

Comparison of Local Adipose Tissue Content and SRS-Derived NIRS Muscle Oxygenation Measurements in 90 Individuals

Chris E. Cooper, Stacey-Marie Penfold, Clare E. Elwell, and Caroline Angus

Abstract Adipose content in the region over the vastus lateralis muscle was measured in a young (21.1 ± 3.1 years old, mean ± SD) population of males ($n = 62$) and females ($n = 28$). Three techniques were used: skinfold thickness, ultrasound and near infrared spectroscopy. All techniques closely correlated with each other and all showed a significantly larger adipose content in females and a limited overlap with the range of values in males. Spatially resolved near infrared spectroscopy (SRS-NIRS) was then used to measure the tissue oxygenation index (TOI) at the same site. A source-detector separation of 4 cm was used to allow for significant light penetration into muscle tissue. TOI at rest was significantly higher in the female (65.3 ± 7.0, mean ± SD) than the male (61.9 ± 5.1, mean ± SD) group. There was a strong positive correlation between adipose content and TOI in male subjects. However, no correlation was seen in the female group. The possible optical and physiological explanations for these results are discussed.

1 Introduction

Near infrared spectroscopy (NIRS) attempts to measure muscle oxygenation and haemodynamics face a significant challenge from the widely varying thickness of the adipose tissue layer. Differential spectroscopy methods attempt to overcome this by assuming that adipose tissue is inert during a physiological challenge [1]. However, this approach is not available to methods that attempt to measure absolute concentrations of muscle chromophores at rest, using the diffusion equation e.g. Hamamatsu NIRO-200 (spatially resolved), ISS OxiplexTS (phase resolved) and Hamamatsu TRS-10 (time resolved). In these cases the most relevant work has focused on experimental [2] and theoretical [3] calculations that seek to optimize the source:detector separation for maximal

C.E. Cooper (✉)
Department of Biological Sciences, Centre for Sports and Exercise Science, University of Essex, Wivenhoe Park, Colchester, Essex, CO4 3SQ, UK
e-mail: ccooper@essex.ac.uk

E. Takahashi, D.F. Bruley (eds.), *Oxygen Transport to Tissue XXXI*,
Advances in Experimental Medicine and Biology 662,
DOI 10.1007/978-1-4419-1241-1_25, © Springer Science+Business Media, LLC 2010

sensitivity to the muscle tissue. However, multi-layer simulations have recently been used to correct the measured absolute values of muscle oxygen saturation for the varying adipose layer [4].

The purpose of this study was to determine, in a large population, the range in local adipose content and its effect on quantifying absolute tissue oxygen saturation. We chose to test spatially resolved spectroscopy (SRS) measurements of tissue oxygen saturation [5] as used in a range of systems commercialized by Hamamatsu Photonics, ASTEM Co.Ltd, Artinis Medical and many in-house NIR spectrometers.

2 Methods

Ninety subjects (62 males and 28 females) of a variety of ethnic backgrounds volunteered to participate in this study, all of whom are students at the University of Essex and were considered healthy at the time of testing. Subjects were aged between 18 and 40 years the majority being between 18 and 25 years. The study was approved by the University of Essex Ethical Committee. All subjects were required to complete an informed consent form prior to participation and were able to withdraw at any time without reason.

Subject age was 21.1 $\pm$ 3.1 years (mean $\pm$ SD). There was no significant difference between age for males and females. The height and weight of the male subjects was 1.79 $\pm$ 0.06 m and 78.2 $\pm$ 11.1 kg. This was significantly different ($p < 0.01$) from that of the females (1.63 m $\pm$ 0.06 and 62.0 $\pm$ 8.0 kg).

All measurements were made on the dominant leg above the lateral quadriceps (vastus lateralis) muscle, calculated as one third of the distance between the greater trochanter and the lateral femoral condoyle. Ultrasound (Aloka SSD-900, Tokyo, Japan) was used to measure the thickness of the subcutaneous adipose tissue layer. Skinfold measurements were made following standard procedures using Harpenden calipers. NIRS measurements of body fat were performed with a Futrex 6100 (Futrex Inc.). This device uses multi-site measurements in NIR absorbance at 810, 932, 944 and 976 nm to quantify the lipid absorbance and hence generate a percentage total body fat content. However, for measurement at a single site this index will be representative of the local NIR absorbing lipid. Measurements of tissue oxygenation (TOI) were made with a NIRO200 (Hamamatsu Photonics) at 4 cm optode separation. Pearson's product-moment correlation was used to determine the relationship between the different adipose tissue measurements and TOI, with significance set to $p < 0.05$.

3 Results

Table 1 shows the values for the different measurements of adipose content in the 90 individuals. All measurements of adipose content in the quadriceps correlated significantly with each other for all subjects and for male subjects. For female subjects all measurements correlated with the exception of the NIRS

Table 1 Comparison of different measurements between subject groups (mean ± SD)

Method	Total	Male	Female
Ultrasound adipose thickness (mm)	2.9 ± 2.1	2.0 ± 1.4	5.0 ± 1.8
Skinfold (mm)	14.0 ± 7.7	10.7 ± 5.2	21.5 ± 7.2
% Body fat (NIRS)	18.7 ± 6.9	15.2 ± 4.8	26.5 ± 3.6
Tissue Oxygenation Index (NIRS)	62.9 ± 5.9	61.9 ± 5.1	65.3 ± 7.0

and ultrasound. All methods showed significantly lower values for males than females and there was only a limited overlap between the two genders. An example of this is shown in Table 2, which lists the % body fat as measured by NIRS in the male and female subjects.

Table 2 NIRS-measured % Body fat for male ($n = 62$) and female ($n = 28$) subjects

% Body fat	Males	Females
5.0–9.9	6	0
10.0–14.9	31	0
15.0–19.9	13	0
20.0–24.9	9	9
25.0–29.9	3	15
30.0–34.9	0	4

Mean TOI was also significantly lower in males than females. Figure 1 shows the NIR measurements of body fat plotted against TOI. All measurements of adipose content showed a significant positive correlation with TOI for (a) all subjects and (b) male subjects but no such correlation was seen in (c) the female subjects. However, the small number of subjects with similar body fat values (Table 2) make direct male:female comparisons difficult. For the largest overlap group ($n = 9$), the NIRS measured body fat was 21.7 ± 1.2 (male) and 22.7 ± 1.8 (female); TOI was 60.8 ± 6.1 (male) and 65.8 ± 7.3 (female). The male:female TOI comparison for this, admittedly small, group was not significantly different.

4 Discussion

This study shows that methods of measuring tissue oxygen saturation in muscle are affected by the adipose layer of the individual. In particular spatially resolved spectroscopy (SRS) show a positive correlation amongst male subjects between local adipose content and tissue oxygenation. Female subjects, with higher adipose content and tissue oxygenation, show no such correlation.

It has previously been assumed [4] that variations in muscle oxygenation changes as a function of adipose content are an optical artifact i.e. if suitable allowances are made for the differences in the optical path [2] measurements can

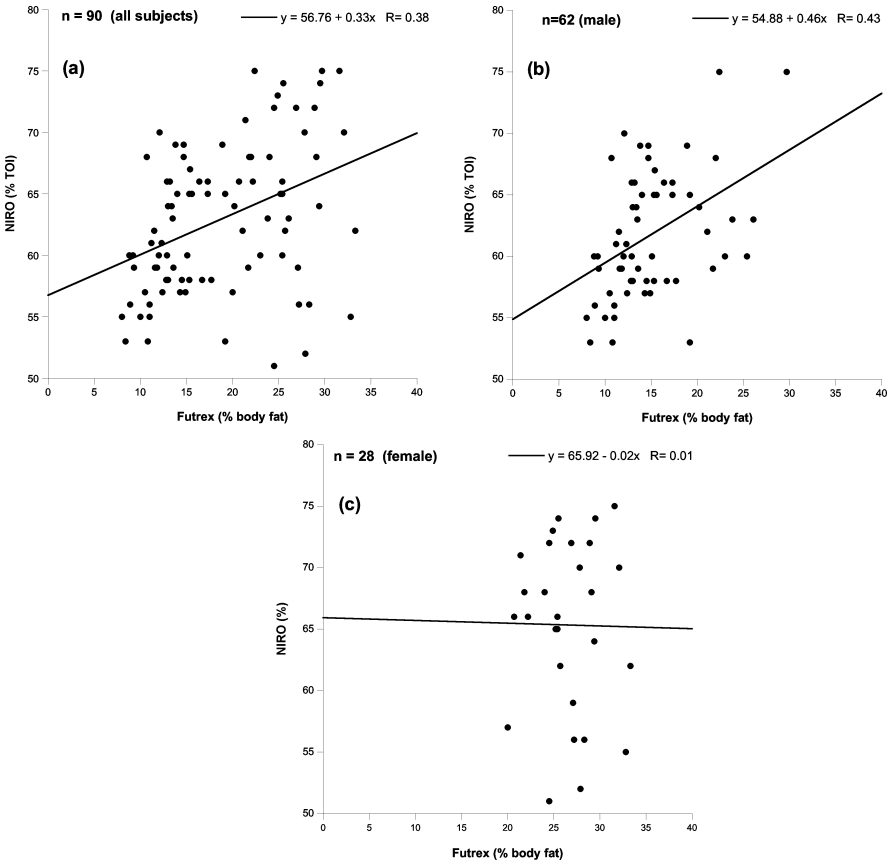

Fig. 1 Correlation of NIRS measurements of body fat and tissue oxygenation for all subjects (**a**), male subjects (**b**) and female subjects (**c**)

be "corrected". Indeed incorporating two layer models into absolute tissue oxygen saturation measurements does cause large changes in the measured value [6, 7]. However, subjects with differing adipose content may have different physiology and it is unclear what differences, if any, in skin, lipid and muscle oxygen metabolism exist between subjects with different levels of adipose content. Changes in adipose content may therefore cause, or correlate, with a physiological change in muscle tissue oxygen saturation. It is possible that a decreased adipose content predisposes to a decreased tissue oxygen saturation; physiology may act instead of, or more likely in tandem with, optics to produce the observed correlations.

In our study we see significant gender differences in resting TOI. Gender differences have been seen previously in arterial [8] and muscle [9] oxygen saturation. Females have smaller muscle mass, lower capillary density, lower hemoglobin content and lower oxidative potential than males. This leads to a

lower arteriovenous oxygen content difference, during peak exercise [10]. Similar physiological differences at rest could explain why TOI was higher in the female group.

We show here, in agreement with the original work by Conway [11] and other more recent studies [6], that local NIRS measurements of adipose content correlate with other established techniques. This means that a single optical device will be able to measure simultaneously the extent of the adipose layer and the oxygen saturation of the muscle beneath. In principle, therefore the same device can measure muscle oxygen saturation and correct for any optical artifacts due to surface layers. However, whilst there is clearly much to be gained from minimizing the optical effects of tissue heterogeneity in muscle measurements, we caution against assuming that resting tissue oxygen saturation is a constant. It is clear that more needs to be done to clarify these issues; in the context of this study more male and female subjects need to be studied in the regions where adipose content overlaps to determine if gender differences contribute to this variability.

Acknowledgments The authors would like to thank the EPSRC (EP/F006551/1) for financial support and Prof. Di Newham and Dr. Lynsey Duffell (King's College London) for the loan of the ultrasound machine.

References

1. Quaresima V, Lepanto R, Ferrari M (2003) The use of near infrared spectroscopy in sports medicine. J Sports Med Phys Fitness 43:1–13.
2. van Beekvelt MC, Borghuis MS, van Engelen BG et al. (2001) Adipose tissue thickness affects in vivo quantitative near-IR spectroscopy in human skeletal muscle. Clin Sci (Lond) 101:21–28.
3. Feng W, Haishu D, Fenghua T et al. (2001) Influence of overlying tissue and probe geometry on the sensitivity of a near-infrared tissue oximeter. Physiol Meas 22:201–208.
4. Geraskin D, Platen P, Franke J et al. (2007) Algorithms for muscle oxygenation monitoring corrected for adipose tissue thickness. Advances in Medical Engineering 114:384–388.
5. Suzuki S, Takasaki S, Ozaki T et al. (1999) A tissue oxygenation monitor using NIR spatially resolved spectroscopy. Proc SPIE 3597:582–592.
6. Geraskin D, Boeth H, Kohl-Bareis M (2007) Spectroscopic measurement of adipose tissue thickness and comparison with ultrasound imaging. Proc SPIE 6628:art. no. 66281H.
7. Hunter RJ, Patterson MS, Farrell TJ et al. (2002) Haemoglobin oxygenation of a two-layer tissue-simulating phantom from time-resolved reflectance: effect of top layer thickness. Phys Med Biol 47:193–208.
8. Ricart A, Pages T, Viscor G et al. (2008) Sex-linked differences in pulse oxymetry. Br J Sports Med 42:620–621.
9. Reybrouck T, Fagard R (1999) Gender differences in the oxygen transport system during maximal exercise in hypertensive subjects. Chest 115:788–792.
10. Sugisaki M, Misawa A, Ikai A et al. (2001) Sex differences in the hemoglobin oxygenation state of the resting healthy human masseter muscle. J Orofac Pain 15:320–328.
11. Conway JM, Norris KH, Bodwell CE (1984) A new approach for the estimation of body composition: infrared interactance. Am J Clin Nutr 40:1123–1130.

Muscle Oxygen Saturation Measured Using "Cyclic NIR Signals" During Exercise

Terence S. Leung, Anna Wittekind, Tiziano Binzoni, Ralph Beneke, Chris E. Cooper, and Clare E. Elwell

Abstract A new approach to measure muscle oxygen saturation (SmO_2) using near infrared spectroscopy (NIRS) has been proposed in this paper. This approach exploits the cyclic NIRS signals seen during exercise which are often regarded as "movement artefacts". This new measure, which we term the "cyclic SmO_2", has the potential to be less affected by the myoglobin which is traditionally believed to be indistinguishable from haemoglobin using NIRS techniques. The cyclic SmO_2 also has fewer assumptions than the conventional SmO_2 measured using time, phase and spatially resolved spectroscopy methods. In a cycling exercise study, NIRS measurements were made over the Vastus lateralis muscle of 11 subjects. In a light exercise protocol, the group mean of the conventional SmO_2 was $51.7 \pm 4.3\%$ and that of the cyclic SmO_2 was $56.0 \pm 3.9\%$. It was immediately followed by a hard exercise protocol and the group mean of the conventional SmO_2 was reduced to $42.6 \pm 6.1\%$ and that of the cyclic SmO_2 to $48.5 \pm 5.6\%$. The reduction agrees with the general expectation. The cyclic SmO_2 is a promising new measure of muscle oxygenation.

1 Introduction

Near infrared spectroscopy (NIRS) has been widely used in measuring muscle oxygenation [1, 2]. It is well known that NIRS signals are prone to movement artefacts which are especially prominent during exercise. They are often considered as noise and filtered out during data analysis. In this paper, we show that there is evidence to suggest that these movement artefacts or cyclic NIRS signals, as we prefer to call them, contain physiological information about the oxygenation of the muscle. Many commercial NIRS monitors today exploit the diffusion equation to derive muscle oxygen saturation (SmO_2), or more

T.S. Leung (✉)
Biomedical Optics Research Laboratory, Department of Medical Physics and Bioengineering, University College London, London, UK
e-mail: tsl@medphys.ucl.ac.uk

E. Takahashi, D.F. Bruley (eds.), *Oxygen Transport to Tissue XXXI*, Advances in Experimental Medicine and Biology 662,
DOI 10.1007/978-1-4419-1241-1_26, © Springer Science+Business Media, LLC 2010

generally tissue oxygen saturation from optical measurements. In this approach, the diffusion equation is solved based on a particular geometry, for example a homogenous semi-infinite half-space geometry, and a particular set of optical measurements. Examples of this type of monitors include Hamamatsu NIRO-200 (spatially resolved), ISS OxiplexTS (phase resolved) and Hamamatsu TRS-10 (time resolved) [2]. Based on the theoretical solution, an algorithm can be designed to calculate the absorption coefficients, μ_a from optical measurements. The μ_a measured at multiple wavelengths can eventually be converted into oxygen saturation via Beer Lambert law. However, these models assume a homogenous medium which is inevitably different from the reality and affects the accuracy. An obvious example in the muscle application is that a fat layer often exists between the surface mounted optical probe and muscle, making the medium an inhomogeneous one. As a result, reflected light is attenuated not only due to absorption in the muscle but also in the skin and the fat layer.

This paper introduces a new approach to measure SmO_2 during exercise which is not based on the diffusion equation but exploits the Beer Lambert law. The technique therefore does not require the assumption of a particular geometry or homogeneity of the medium. Instead, its principle is based on the assumption that the muscle is squeezed of blood during contraction, and refilled during relaxation. This newly defined measure is known as cyclic SmO_2. Unlike the conventional SmO_2, the cyclic SmO_2 is also expected to be less influenced by myoglobin.

2 Methods

2.1 Experiments

Eleven trained male subjects with (mean $\pm$ std) age of 32 $\pm$ 11 years, body mass of 77 $\pm$ 9 kg, and height of 177 $\pm$ 6 cm, participated in the study which was approved by the University of Essex research ethics committee. The peak aerobic power (PAP) was first determined using an incremental cycling protocol. A commercial NIR monitor (NIRO-200, Hamamatsu Photonics KK), which has a sampling frequency of 6 Hz and three wavelengths, i.e. 780, 813 and 853 nm, was used in the study. The optical source and detector were attached to the Vastus lateralis muscle of the subject. Subjects were asked to cycle a mechanically braked cycle ergometer fitted with power cranks at (i) 60 revolutions per minutes (rpm) at 40% of the PAP for 5 min (light exercise), and immediately afterwards at (ii) 80 rpm at 110% of the PAP for 1 min (hard exercise). Three NIRS signals were measured with the NIRS monitor, namely, changes in oxy- and deoxy-haemoglobin concentrations ($\Delta[HbO_2]$ and Δ[HHb]) and tissue oxygenation index (TOI, used as the conventional SmO_2 here).

2.2 Data Analysis

The attenuation can be described by

$$A_\lambda = \{\varepsilon_{HHb,\lambda}[HHb] + \varepsilon_{HHo_2,\lambda}[Hbo_2] + \varepsilon_{Mb,\lambda}[Mb] + \varepsilon_{Mbo_2,\lambda}[Mbo_2]\}l + \mu^{bk}_{a,\lambda} + \mu'_{s,\lambda} \quad (1)$$

where A_λ is the attenuation at wavelength λ, $\varepsilon_{HHb,\lambda}$, $\varepsilon_{HbO_2,\lambda}$, $\varepsilon_{Mb,\lambda}$ and $\varepsilon_{MbO_2,\lambda}$ are the specific extinction coefficients for deoxy- (HHb), oxy-haemoglobin (HbO_2), deoxy- (Mb) and oxy-myoglobin (MbO_2), [HHb], [HbO_2], [Mb] and [MbO_2] are their concentrations, l is the optical path length, μ is the absorption coefficient accounting for all background absorbers such as water and melanin, and μ is the reduced scattering coefficient. It should be noted that the correction factors for the wavelength dependence of path length are embedded within the specific extinction coefficients [3]. In order to reduce the effects of changes in μ which could be significant during exercise, the difference of A_λ between two wavelengths is calculated,

$$\begin{aligned} A_{\lambda 1-\lambda 2} &= A_{\lambda 1} - A_{\lambda 2} \\ &= \{\varepsilon_{HHb,\lambda 1-\lambda 2}[HHb] + \varepsilon_{Hbo_2,\lambda 1-\lambda 2}[Hbo] \\ &\quad + \varepsilon_{Mb,\lambda 1-\lambda 2}[Mb] + \varepsilon_{Mbo_2,\lambda 1-\lambda 2}[Mbo_2]\}l + \mu^{bk}_{a,\lambda 1-\lambda 2} + \mu'_{s,\lambda 1}. \end{aligned} \quad (2)$$

In the calf muscle, μ decreases steadily by 0.8% per 10 nm between 760 and 900 nm [4]. Therefore, $\mu'_{s,\lambda 1}$ is expected to be small when λ_1 and λ_2 are reasonably close to each other. This approach has the same rationale as the dual wavelength photometry previously described in the literature [5]. Figure 1 depicts an example of the $A_{780\text{-}}$ signals obtained from a subject during exercise. It can be seen that the cyclic signal resembles a sinusoid and the amplitude of the sinusoid can be considered as the difference between the peak (point X in the figure) and mean (point Y) values which can also be written as:

$$\Delta A_{\lambda 1-\lambda 2} \approx \{\varepsilon_{HHb,\lambda 1-\lambda 2}\Delta[HHb] + \varepsilon_{Hbo_2,\lambda 1-\lambda 2}\Delta[Hbo_2] \quad (3)$$

It is assumed that both the background absorption and the amount of myoglobin do not change significantly during exercise. Therefore both terms are expected to be small and can be neglected from equation (3). To estimate the amplitude of the cyclic signal, the discrete Fourier transform (DFT) has been used. Both the fundamental and the first harmonic are often present in the amplitude spectrum. $\Delta A_{\lambda 1}$ is then estimated as the total area (bandwidth = 0.5 Hz) under the two spectral peaks. In this work, both $\Delta A_{780\text{-}}$ and $\Delta A_{853\text{-}}$ have been calculated, and then converted into Δ[HHb] and Δ[HbO_2] by using multilinear regression based on equation (3). Both Δ[HHb] and Δ[HbO_2] here can be considered as the amplitudes of the cyclic signals. The cyclic SmO_2 is defined as: cyclic SmO_2 = Δ[HbO_2]/(Δ[HbO_2] + Δ[HHb]).

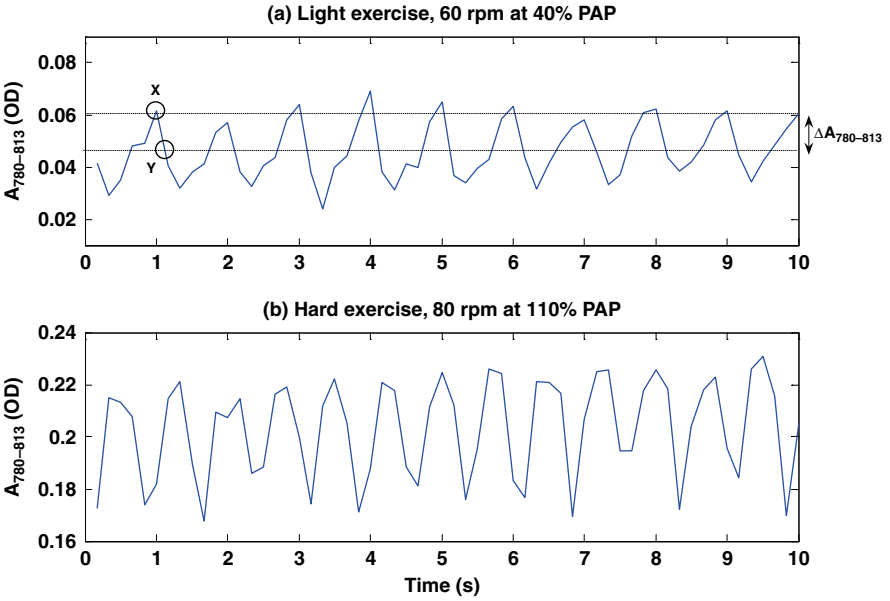

Fig. 1 An example of the cyclic optical signals $A_{780–813}$ in one subject during (**a**) light exercise, and (**b**) hard exercise. The scattering is greatly reduced in the $A_{780–813}$ signal and the signal's absolute amplitude contains mainly two parts, namely the constant (DC) and the varying (AC) parts. Absorption due to background absorbers and myoglobin are expected to be the same during exercise and are therefore regarded as the DC part. The AC part (the cyclic signal) predominantly accounts for the absorption changes caused by a portion of blood shifting in and out of the muscle during exercise. The amplitude of the AC part, i.e. $\Delta A_{780–813}$, is relatively free from the effects of scattering and other constant absorbers (the DC part)

Two sections of data were analysed for each subject, i.e. 30 s of data during the light (started from 3 min into the exercise) and hard (started from 25 s into the exercise) exercises respectively. For each section of data, the mean conventional SmO_2 and one cyclic SmO_2 were calculated. To derive the cyclic SmO_2, the size of the DFT was 60 samples (= 10 s) and a Hanning window of the same size was used with 50% (5 s) overlap. For 30 s of data, four amplitude spectra were obtained which were averaged to one smoothed spectrum from which the cyclic SmO_2 was calculated as described earlier.

A larger size for the DFT and the averaging of spectra would both ensure a more robust cyclic SmO_2 over time, but would also lead to a poorer time resolution. In using the parameters described above, only one value of cyclic SmO_2 can be calculated for 30 s worth of data. To illustrate how the cyclic SmO_2 compared with conventional SmO_2 in a finer time resolution, a different set of parameters were used to calculate the cyclic SmO_2 in one subject, i.e. the size of DFT = 12 samples (2 s) with 50% (1 s) overlap and no spectra averaging. Figure 2 shows both TOI and cyclic SmO_2 in transition from light to hard exercise.

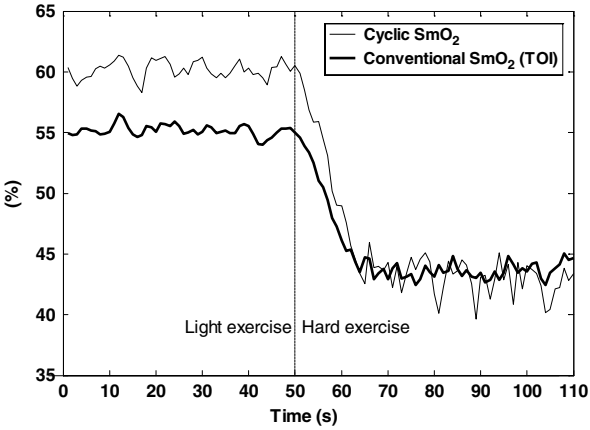

Fig. 2 Conventional (TOI) and cyclic SmO_2 in transition from light to hard exercise in one subject. DFT size = 12 samples: mean cyclic SmO_2 for the light exercise (time 0 – 30 s) = 60.2% and that for the hard exercise (time 80 – 110 s) = 43.0%. For comparison, DFT size = 30 samples: cyclic SmO_2 for the light exercise = 59.3% and that for the hard exercise = 42.3%

3 Results

Figure 3 depicts the conventional and cyclic SmO_2 during light and hard exercise in 11 subjects. In all subjects, both the conventional and cyclic SmO_2 are higher during light exercise than during hard exercise. This is indeed expected from a physiological point of view because in muscle undergoing a more intense exercise regime the oxygen consumption increase is greater than any compensatory change in muscle blood flow. As less oxygen remains in the

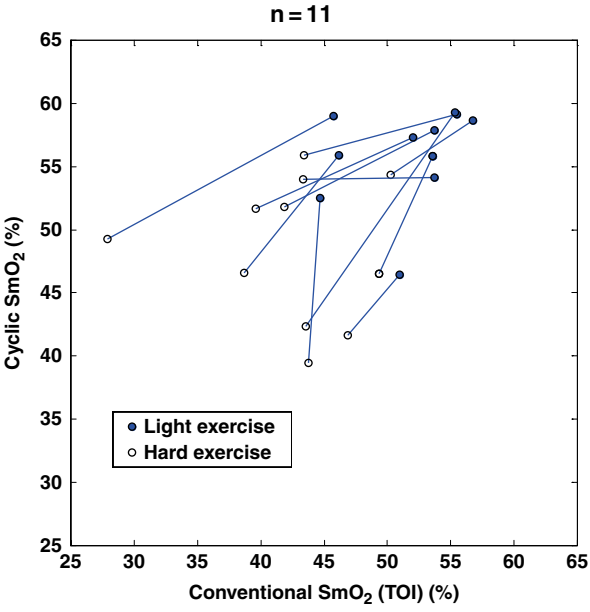

Fig. 3 Conventional (TOI) and cyclic SmO_2 for all 11 subjects during light and hard exercise

Table 1 Group mean and standard deviation of the conventional (TOI) and cyclic SmO_2 during light and hard exercise in 11 subjects

	Light exercise	Hard exercise
Conventional SmO_2/TOI (%)	51.7 ± 4.3	42.6 ± 6.1
Cyclic SmO_2 (%)	56.0 ± 3.9	48.5 ± 5.6

muscle, a lower SmO_2 is expected. Table 1 shows the group mean and standard deviation of the conventional and cyclic SmO_2 during light and hard exercise. The cyclic SmO_2 has higher means and smaller standard deviations in both light and hard exercise.

4 Discussion

The measurement of cyclic SmO_2 requires the generation of cyclic NIRS signals from the exercising muscle. Previous research showed that muscle blood flow in both the artery and vein is decreased during muscle contraction, and increased during muscle relaxation due to changes in intramuscular pressure, a mechanism known as the "skeletal muscle pump" [6, 7]. The main assumption in our technique is that the cyclic NIRS signal $\Delta A_{\lambda 1\text{-}\lambda 2}$ is predominantly caused by absorption changes due to a portion of blood shifting in and out of the muscle during exercise. This portion of shifting blood can be considered as the net change of blood volume caused by contraction and relaxation during muscle exercise. It is expected that the venous blood accounts for a larger proportion of the shifting blood because the venous compartment has a lower pressure therefore allowing a larger blood volume change. As a result, the cyclic SmO_2 should be more biased towards venous oxygen saturation. We also assume that the thickness of the fat layer does not change significantly during exercise and that the blood vessels inside the fat are not "squeezed" or redistributed. Exercising muscle would undergo both anatomical and blood flow changes, both of which cause scattering changes. To reduce the effect of scattering changes during exercise, the dual wavelength photometry algorithm was introduced in this work. Myoglobin and haemoglobin have very similar absorption spectra and they are often considered indistinguishable using NIRS [1, 2]. The cyclic SmO_2 is able to minimize the effect of myoglobin because the amount of myoglobin in the probed muscle is expected to remain constant during the exercise and the algorithm of the cyclic SmO_2 is capable of subtracting off the effect of any constant absorbers. However, the accuracy of the cyclic SmO_2 is still to be affected by the wavelength dependency of path lengths which is a factor applicable to all NIRS problems in general [4].

Acknowledgments The authors would like to thank Hamamatsu Photonics KK. and the EPSRC (EP/F006551/1) for their financial support of this work.

References

1. Quaresima V, Lepanto R, Ferrari M (2003) The use of near infrared spectroscopy in sports medicine. J Sports Med Phys Fitness **43**: 1–13.
2. Wolf M, Ferrari M, Quaresima V (2007) Progress of near-infrared spectroscopy and topography for brain and muscle clinical applications. J Biomed Opt **12**(6): 062104.
3. Essenpreis M, Elwell CE, Cope M, et al. (1993) Spectral dependence of temporal point spread functions in human tissues. Appl Opt **32**(4): 418–425.
4. Matcher SJ, Cope M, Delpy DT (1997) In vivo measurements of the wavelength dependence of tissue-scattering coefficients between 760 and 900 nm measured with time-resolved spectroscopy. Appl Opt **36**(1), 386–396.
5. Hoshi Y, Hazeki O, Kakihana Y, Tamura M (1997) Redox behaviour of cytochrome oxidase in the rat brain measured by NIRS. J Appl Physiol **83**(6):1842–1848.
6. Lutjemeier BJ, Miura A, Scheuermann BW, et al. (2005) Muscle contraction-blood flow interactions during upright knee extension exercise in humans. J Appl Physiol **98**: 1575–1583.
7. Dobson JL, Gladden LB (2003) Effect of thythmic titanic skeletal muscle contractions on peak muscle perfusion. J Appl Physiol **94**: 11–19.

Determination of Oxygen Dosage Effects on Cytochrome Oxidase after Anoxia in Brain

Fred Kriedt, Christopher Kriedt, Chase Patterson, and Keith Van Meter

Abstract Recent evidence reports that high doses of O_2 administered via hyperbaric oxygen therapy (HBOT) improve the return of spontaneous circulation (ROSC), and the outcome of damage to the heart following a 25 min normothermic cardiac arrest. However, excessive O_2 during HBOT can be toxic. Near infrared absorbance spectroscopy (NIRS) measures and determines when cytochrome oxidase (aa_3), the O_2 end user, changes from reduced to oxidized, signifying adequate dosage. Present NIRS monitoring methods do not account for change in scattering expected in severe anoxia. Given this limitation, we simultaneously measured changes in intensity and scattering that occurred over time after 830 nm light traveled 4.25 cm through brain tissue during both normoxia and anoxia. Results indicated increased intensity and scattering during anoxia with correlation between the two, demonstrating that scattering does not remain constant and is associated with intensity. With this additional insight in concurrent scattering and intensity change during anoxia, we believe improvements can be made to our aa_3 measuring technique resulting in a method to ascertain adequate O_2 dosage during HBOT.

1 Introduction

A recent publication reported that use of HBOT during resuscitation results in ROSC after 25 min of normothermic arrest [1]. These results are possible because HBOT raises atmospheric pressure, increasing O_2 solubility in plasma and providing a higher O_2 content at the mitochondrial site of O_2 utilization. Because such high O_2 dosages are necessary after cardiac arrest and excessive oxygen is toxic, beneficial, but not excessive dosages are necessary for clinical therapy. Currently, no method exists to measure nontoxic, beneficial O_2 dosage.

F. Kriedt (✉)
Baromedical Research Institute, New Orleans, LA, USA
e-mail: fkriedt1@cox.net

E. Takahashi, D.F. Bruley (eds.), *Oxygen Transport to Tissue XXXI*,
Advances in Experimental Medicine and Biology 662,
DOI 10.1007/978-1-4419-1241-1_27, © Springer Science+Business Media, LLC 2010

Jobsis first discovered a NIRS technique to measure adequate O_2 dosage [2]. He used relative transparency of tissue and Beer's equation to interrogate brain tissue metabolism non-invasively. NIRS monitors three chromophores: oxygenated hemoglobin (HbO_2), deoxygenated hemoglobin (Hb), and aa_3. Neither Hb nor HbO_2 are helpful to determine nontoxic dosages of O_2. Monitoring the redox of aa_3 appears to be a useful indicator of brain tissue O_2 dosage. Lack of O_2 causes aa_3 reduction (i.e. buildup of electrons); however, when adequate O_2 has removed the excessive electron population, aa_3 becomes oxidized. A reliable aa_3 signal marking a change from reduced to oxidized would determine adequate O_2 dosage during HBOT resuscitation.

In 1988, Jobsis advised that the NIRS technology was ready for measuring equipment to be produced [3]. This publication reported that the halfwidth of the aa_3 spectrum measured in mitochondrial and bloodless *in situ* rat heads (i.e. scattering media) was 75% of the measured halfwidth in purified aa_3 (i.e. non scattering media). Although halfwidth reduction was observed Jobsis did not elaborate on this phenomenon. He and others produced algorithms for aa_3 signal extraction based on Beer's equation, but assumed scattering to be constant. Our laboratory became interested in using NIRS for HBOT, but found in vivo aa_3 measurements problematic and controversial. Problems included the following: a weak aa_3 signal, the use of Beer's equation in a scattering media, and Hb signal contamination [4]. In 2002, we proposed a method for aa_3 signal extraction using a Fortier filtering technique (FFT), which did not require Beer's equation [5]. We observed that the spectral peak half width was reduced as anoxia progressed. If the aa_3 spectrum was also changing, it would cause errors in the FFT.

Kawauchi reported simultaneous measurements in scattering and intensity during anoxia, which was correlated to reduction of aa_3 in vivo [6] and later attributed the change in scatter to mitochondrial shrinkage and dendrite swelling [7]. These publications led our team to hypothesize that FFT may have been confounded by a changing aa_3 spectrum due to scatter. To examine these effects, we used a scatter model in swine, which was compared to a phantom experiment. Concurrent observation of change in intensity and scatter at 830 nm could lead to the elucidation of how it might affect our FFT extraction and allow adequate O_2 dosage measurements.

2 Materials and Methods

Six pigs (30 ± 2 kg) were anesthetized continuously throughout the experiment with Telazol/Xylazine in accordance with our Institutional Animal Care and Use Committee approved protocol. The animals were intubated and provided with 100% O_2. The scalp was removed and a template attached to the skull with 3 bone screws to maintain a precise distance between optodes for each animal. The template's 12 mm diameter input optode was positioned on the midline of the skull 20 mm rostral to the bregma, providing a guide to precisely locate a

5 mm hole, which was drilled through the skull, 40 mm rostral to bregma and 9 mm left of midline. The dura was punctured and a collection optode placed 20 mm below dural tissue.

After assessing for a normal and stable condition, 100 control spectra were taken while the animal was breathing 100% O_2. Breathing gas was changed to 100% N_2 immediately after control spectra were completed. Recording continued with 200 experimental spectra while the animal's condition progressed from normoxia to anoxia, and finally death. Spectra identification numbers were noted when mean arterial pressure (η) fell below 50 mmHg (see Figs. 1a and 2) and when cardiac arrest occurred (i.e. beginning of phase III). After death, a 65 mm diameter portion of the skull was trephinized (centered at the template) for use in the phantom experiments.

A phantom experiment measured identical conditions in various concentrations of whole milk and water. Light was directed to traverse the same distance through the scattering media as in vivo. A series of 20 spectra were taken at each concentration and repeated six times to insure repeatability. The effect of absorbance was measured by adding India ink to 100% whole milk, (i.e. 4 increments of 1–4 μL) ($n = 6$) while the mixture was magnetically stirred.

A stabilized 250 W Quartz Tungsten Halogen lamp with an additional intensity stabilizer provided stable light within 1%. The light was then directed through an 830 nm filter (20 nm halfwidth), resulting in a steady state spectral pulse (SSSP or S^3P) centered at 830 nm with a measured power of 50 mW. The S^3P was directed into the skull, dura and brain and collected with a custom fiber optics probe and processed with a liquid N_2 CCD spectrophotometer (integration time 29 s with 1 s interval) and stored on a personal computer.

Spectra were extracted from the data at the beginning of each 5 min interval and processed using Grams32 AI software. For intensity measurements the peak of the spectra was considered the intensity value. Normalized forward scattering (NFS) measurements were determined. Each spectrum was normalized to evaluate area change by multiplying by 60,000/intensity measurement (see above) to raise the peak to a fixed value of 60,000 data units while maintaining identical geometrical proportions. Integration provided area under the spectra which represented any broadening or narrowing effects by scattering on the original S^3P entering the brain. The intensity and measured area (i.e. NFS) of all control measurements were averaged, representing the 100% normalized value. All other measurements were divided by this value to give their relative normalized values.

3 Results and Discussion

Our swine model data accompanied with phantom NFS and intensity data show at 830 nm, scattering does not remain constant and correlates with normalized intensity during the normoxia to anoxia transition. The concurrent

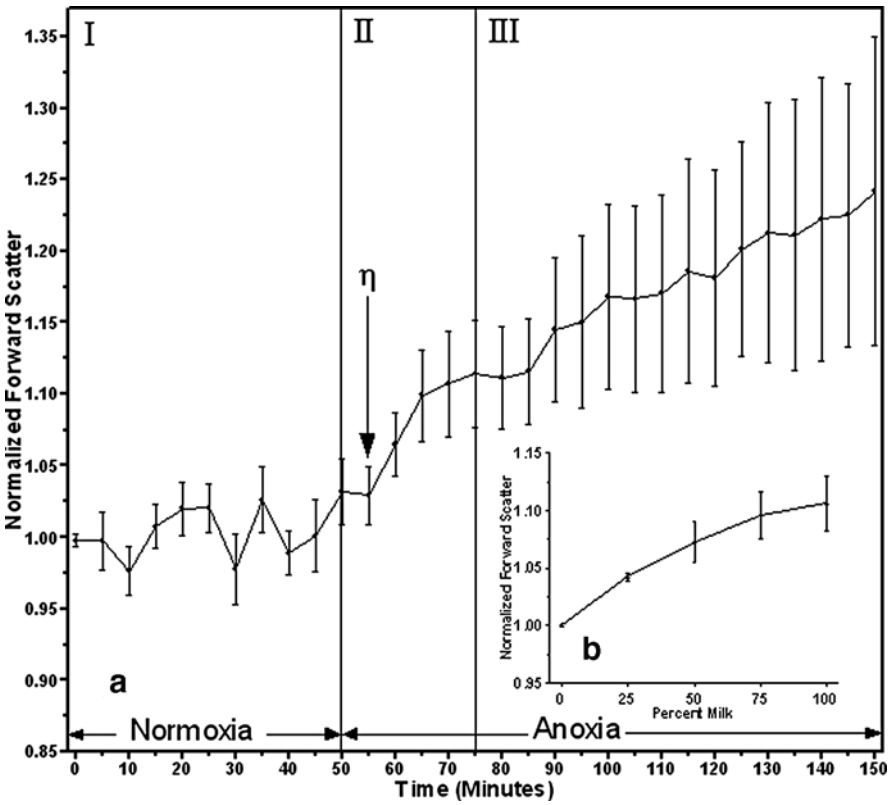

Fig. 1 (**a**) Change in NFS (1/change area under a normalized S^3P) ($n = 6$) in vivo is plotted against time while a steady state (1%) spectral pulse (830 nm filtered light × 20 nm halfwidth) has traversed 4.25 ± .09 cm through brain tissue. The time course on the x-axis (in 5 min increments) is divided into three phases: Phase I – Normoxia (control period while breathing 100% O_2). Note: O_2 was substituted for air to compensate for probe insertion brain trauma; Phase II – Anoxia (experimental period while breathing 100% N_2 (condition moved from normoxia to anoxia and finally cardiac arrest)); and Phase III – Post Cardiac Arrest (breathing 100% N_2). The data were normalized by determining the average scattering values during the 50 min control period and dividing all measured scattering values by this calculated average. Repeated measures ANOVA indicated that normoxia measurements were significantly different from anoxia ($p < 0.001$). Label (η) is the time point in phase II when MAP fell below 50 mmHg. (b) Phantom data for NFS ($n = 6$) demonstrate that increased NFS (1/change area under a normalized S^3P) occurs when the concentration of scattering media is increased from water to 100% whole milk

changes in NFS and normalized intensity as S^3P traveled 4.25 ± 0.09 cm through the brain (from dura to collection optode) are shown in Figs. 1a and 2. Figure 1b shows the results of phantom NFS measurements and the effect of increasing concentration of scatter media. Notice a 0.1 change in NFS when transitioning from clear water to milk, but a 0.25 NFS change in vivo

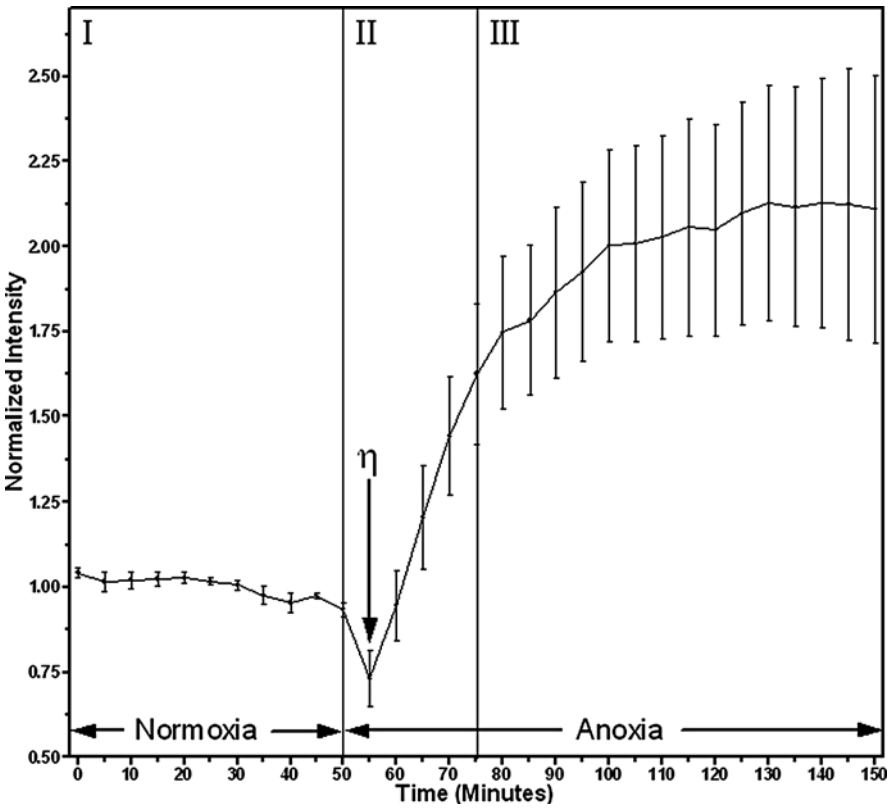

Fig. 2 Change in intensity ($n = 6$) is plotted against time while a steady state (1%) spectral pulse (830 nm filtered light × 20 nm halfwidth) has traversed 4.25 ± .09 cm through brain tissue in vivo. See Fig. 1a for time scale details and normalization process. Repeated measure ANOVA indicated that normoxia measurements were significantly different from anoxia ($p < 0.001$). Label (η) is the time point in phase II when MAP fell below 50 mmHg

when shifting from normoxia to anoxia (Fig. 1a), implying a large change in scatter. Phantom absorbance studies indicated no effect on NFS as intensity dropped from 100 to 10% by stepwise increasing absorption media. Our method to measure NFS is novel but uses a narrowing effect on peak halfwidth reported by Jobsis [4], which we believe is caused by increasing scatter. To ensure that results were not caused by artifact due to our novel method of measuring NFS, we preformed a correlation analysis comparing normoxia and anoxia (Fig. 3)

In Fig. 1a, forward scattering over Phase I is constant but oscillates about the mean value. In Fig. 2, intensity over Phase I decreases approximately 0.125. This decrease is likely due to tissue recovery (i.e. aa_3 oxidation) in the neighborhood of the collection optode trauma. In Fig. 1a at the beginning of phase II, scatter reverses from increasing to decreasing, but at 55 min again reverses to a

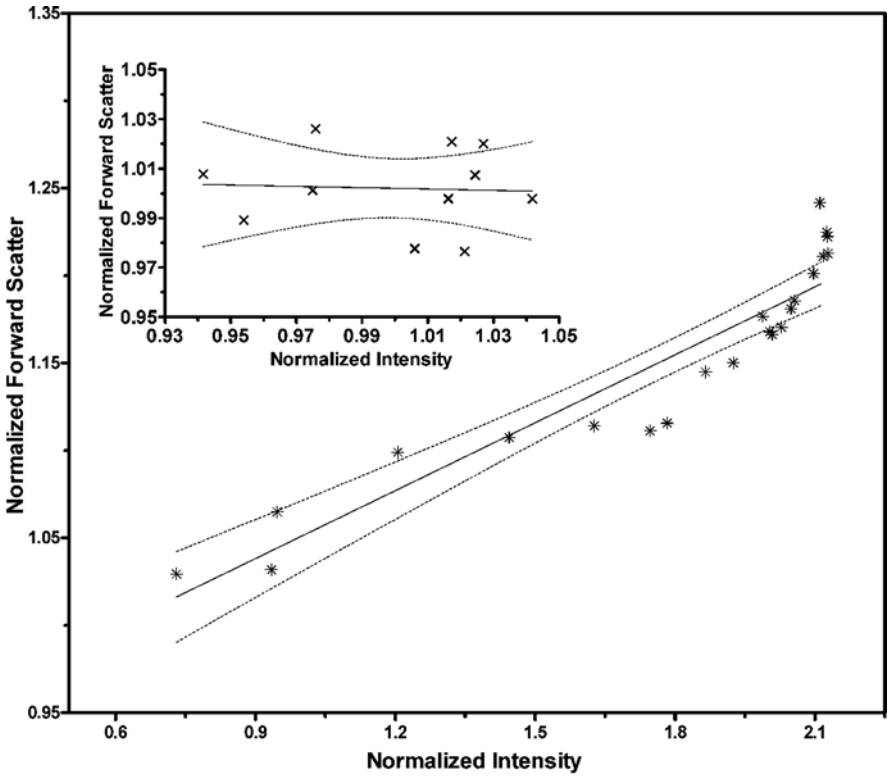

Fig. 3 Correlation of normalized intensity and measured change of normalized forward scatter (NFS) in (**a**) anoxic animals (breathing N_2) was significant ($r^2 = 0.92$, $p < 0.0001$). Both NFS and intensity increased. However, (**b**) normoxic animals (breathing O_2) showed no correlation

rapid increasing rate, and at 65 min continues to rise at a slower rate. In Fig. 2, during Phase II, intensity rapidly decreases; we believe this is due to increased blood volume during initial hypoxia, but at 55 min reverses to a rapidly increasing value due to the reduction of aa_3. In both scatter and intensity the bidirectional change is centered at the time point when MAP (η) falls below 50 mmHg. In Figs. 1b and 2 during Phase III, scatter continues to increase, but less rapidly, and intensity continues to increase until 120 min, then remains constant.

Kawauchi [7] reported tridirectional changes in scattering in rats during anoxia. Many investigators have reported bi and tridirectional changes in intensity using tissue slices during hypoxic episodes. We agree with their assessment that change in scattering is probably due to mitochondrial shrinkage and cellular swelling [8].

There is no question that HBOT resuscitation requires a method to ascertain adequate but not excessive dosage, and monitoring aa_3 by NIRS has potential. With the evidence that change in scatter is affecting the aa_3 spectrum, we believe we can improve our FFT signal extraction method, allowing a precise determination of aa_3 conversion from reduced to oxidized signaling adequate O_2 dosage.

References

1. Van Meter K, Sheps S, Kriedt F et al. (2008) Hyperbaric oxygen improves rate of return of spontaneous circulation after prolonged normothermic porcine cardiopulmonary arrest. Resus 78(2):200–214.
2. Jobsis F (1977) Noninvasive, infrared monitoring of cerebral and myocardial oxygen sufficiency and circulatory parameters. Science 198:1264–1267.
3. Jobsis F, Paintadosi C, Sylvia A et al. (1988) Near infrared monitoring of cerebral oxygen sufficiency. Neurol Res 10(1):7–17 .
4. Springett R, Newman J, Cope M et al. (2000) Oxygen dependency and precision of cytochrome oxidase signal from full spectral NIRS of the piglet brain. Am J Physiol Heart Circ Physiol 279:H2202–H2209.
5. Kriedt F, Walker C, Swanson H et al. (2002) Application of Fortier filtering techniques for determining redox change in cerebral cortical cytochrome oxidase. EMBS/BMES Conference. Proceedings of the Second Joint 3(23–26):2257–2258.
6. Kawauchi S, Sato S, Ooigawa H et al. (2007) Correlation between light scattering and reduction level of cytochrome oxidase in perfused brains of rats. IFMBE Proceedings 14(2):1281-1283.
7. Kawauchi S, Sato S, Ooigawa H et al. (2008) Simultaneous measurement of light absorption due to reduction of cytochrome oxidase and light scattering in rat brains during loss of tissue viability. Appl Opt 47(22):4164–4176.
8. Aitken P, Fayuk D, Somjen G et al. (1999) Use of intrinsic optical signals to monitor physiological changes in brain tissue slices. Methods 18:91–103.

A Mathematical Model for Analyses of Muscle Oxygenation Measurements Using NIR Spectroscopy

Khai Jun Kek, Nobuki Kudo, and Katsuyuki Yamamoto

Abstract Near-infrared spectroscopy (NIRS) enables noninvasive measurement of muscle oxygenation. However, since NIRS does not enable direct measurement of muscle metabolism, it is necessary to analyze the dynamic changes in metabolism during exercise using other methods in order to understand the relationship between NIRS measurements and muscle metabolism. A model of muscle metabolism that is composed of aerobic and anaerobic metabolic systems and O_2 transport to tissue system was developed. Using the model, the temporal profiles of muscle oxygenation during exercise with different intensities (20, 40 and 70% maximum voluntary contraction), measured using NIRS in a single subject, were sufficiently reproduced. In addition, analyses of simulation results of (i) aerobic and anaerobic metabolic systems and (ii) O_2 consumption were performed, and the intensity-dependent differences in the temporal responses during exercise and recovery periods were estimated. The initial results show the usefulness of the model for simulating the kinetics of NIRS measurement data and for systematic interpretation of the relationship between NIRS data and muscle metabolism.

1 Introduction

Near-infrared spectroscopy (NIRS) is a useful technique for noninvasive measurement of muscle oxygenation. However, analyses of changes in muscle metabolism based only on experimental observations using NIRS are difficult. In recent years, various models have been constructed for the detailed study of metabolic pathways [1–3]. Results of those studies have shown that the models can be used to investigate dynamic changes in physiological events for which measurements using conventional instruments are difficult. However,

K.J. Kek (✉)
Graduate School of Information Science and Technology, Hokkaido University, Sapporo, 060-0814, Japan
e-mail: kek@bme.ist.hokudai.ac.jp

E. Takahashi, D.F. Bruley (eds.), *Oxygen Transport to Tissue XXXI*, Advances in Experimental Medicine and Biology 662,
DOI 10.1007/978-1-4419-1241-1_28, © Springer Science+Business Media, LLC 2010

macroscopic interpretation of the principal system that contributes to the changes in metabolic pathways is difficult because these models are complex. Previously, we developed a simple model to investigate the relationship between NIRS measurements and muscle metabolism [4]. Using this model, analyses of simulated temporal profiles of (i) aerobic and anaerobic metabolic systems and (ii) O_2 consumption during continuous and intermittent exercises were performed, and differences in response to the variation in exercise protocol were observed. In this study, we used our model to analyze the changes in muscle metabolism in response to variation in exercise intensity.

2 Materials and Methods

A five-component model (consisting of phosphocreatine breakdown, glycolysis, oxidative phosphorylation, and venous and tissue components) of muscle metabolism [4, 5] was constructed. For modeling purposes, only first- and second-order kinetics equations are used and the kinetics of enzymes is ignored. The following equation was derived:

$$dATP(t)/dt = \dot{q}_{\mathrm{ATP,\,PCr}} + \dot{q}_{\mathrm{ATP,\,Gl}} + \dot{q}_{\mathrm{ATP,\,aerobic}} - \dot{q}_{\mathrm{total}}, \tag{1}$$

where $\dot{q}_{\mathrm{total}}$ represents the total ATP consumption rate. The ATP production rate consists of three components: $\dot{q}_{\mathrm{ATP,\,PCr}}$, $\dot{q}_{\mathrm{ATP,\,Gl}}$ and $\dot{q}_{\mathrm{ATP,\,aerobic}}$, where the subscripts "PCr", "Gl" and "aerobic" mean phosphocreatine breakdown, glycolysis, and aerobic oxidative phosphorylation, respectively. The diffusion of O_2 from capillaries (blood) into muscle cells (tissue) is represented by:

$$dC_{\mathrm{v}}/dt = \dot{Q} \cdot (C_{\mathrm{a}} - C_{\mathrm{v}}) - G \cdot (P_{\mathrm{v}}(t) - P_{\mathrm{t}}(t)), \tag{2}$$

$$dC_{\mathrm{t}}/dt = G \cdot (P_{\mathrm{v}}(t) - P_{\mathrm{t}}(t)) - \kappa \dot{q}_{\mathrm{ATP,\,aerobic}}, \tag{3}$$

where C_{v} and C_{t} represent O_2 concentration in venous and tissue components, respectively; C_{a} is a constant that represents O_2 concentration in the arterial blood; $\dot{Q}$ is blood flow rate; G is a constant that determines the rate of O_2 diffusion between the venous and tissue components; κ is a unit conversion coefficient between the ATP production rate and oxygen consumption rate in the aerobic metabolic system; and $P_{\mathrm{v}}(t)$ and $P_{\mathrm{t}}(t)$ represent the partial pressure of O_2 in venous and tissue components, respectively. The dissociation curves of hemoglobin (Hb) and myoglobin (Mb) were used for conversion between Hb and Mb concentrations and $P_{\mathrm{v}}(t)$ and $P_{\mathrm{t}}(t)$. The equations were numerically solved with Mathematica® 4.0. Inputs to the model, which were initial constants and exercise-dependent $\dot{Q}$, $\dot{q}_{\mathrm{total}}$ and total Hb concentration, were determined from reported values in the literature [4, 5] and our in vivo measurements [6].

The accuracy of the model was validated by comparing the results of simulation to those obtained by in vivo measurement in a single subject using NIRS [6]. A healthy male subject (age: 24 years, height: 168 cm, weight: 60 kg) participated in the measurement. Informed consent was obtained from the subject prior to measurement. The subject performed 30-s continuous isometric knee extension exercises at 20, 40 and 70% maximum voluntary contraction (MVC). Measurements were carried out using an instrument based on spatially resolved spectroscopy (NIR_{SRS}) [6]. A probe was placed on the skin surface over the belly of the rectus femoris of the right leg for measurement of oxy- and deoxygenated Hb and Mb concentrations ([oxy-(Hb + Mb)] and [deoxy-(Hb + Mb)]). The concentration of Hb also includes that of Mb because the absorption spectra of these two chromophores are similar.

3 Results

As shown in Fig. 1a, the blood flow rate $\dot{Q}$, a model input, was varied to simulate the exercise intensity-dependent changes ("low" intensity exercise ≡ 20% MVC; "medium" ≡40% MVC and "high" ≡ 70% MVC). $\dot{Q}$ was equivalent to: (i) the rest value during "low" and (ii) 50 and 0% of the rest value during "medium" and "high", respectively. After the end of exercise, $\dot{Q}$ was increased to a value four-time greater than the rest value and then decreased exponentially to the baseline value. As shown in Fig. 1b, the ATP consumption rate during exercise ATP_{exerc}, another model input, was increased step-wise to values four-,

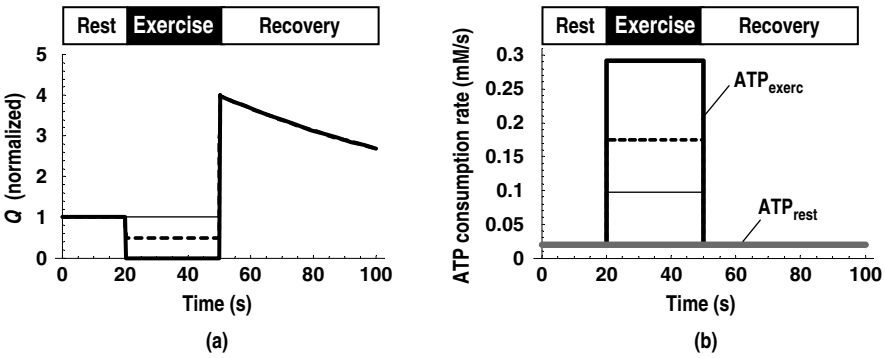

Fig. 1 Model inputs that vary with exercise. (**a**) $\dot{Q}$ (blood flow rate) and (**b**) ATP consumption rate during rest, 30-s exercise at different intensities (low, medium and high) and recovery. (**a**) The values of $\dot{Q}$ were normalized using the value at rest (0 s). (b) $ATP_{exerc} = \chi \cdot ATP_{rest}$, where χ is an arbitrary coefficient that is equivalent to the exercise intensity that was used during in vivo measurements. The exercise started at 20 s. *Thin* lines: "low" intensity exercise ≡ 20% maximum voluntary contraction (MVC); *broken* lines: "medium" ≡ 40% MVC; *thick* lines: "high" ≡ 70% MVC

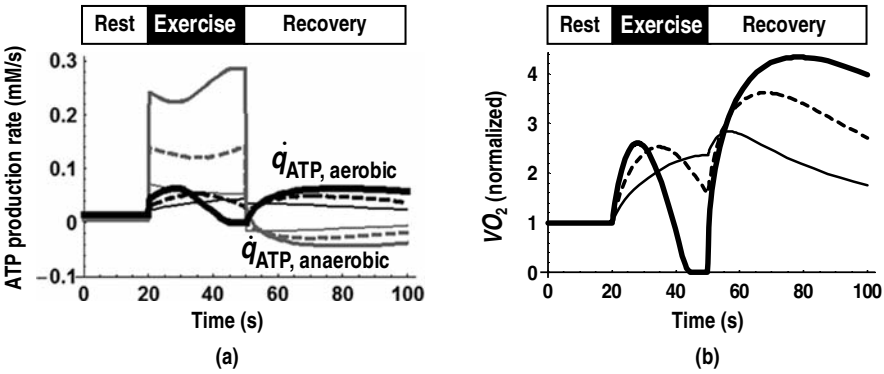

Fig. 2 Example of model outputs: simulated temporal changes in (**a**) ATP production rate in the aerobic metabolic system $\dot{q}_{ATP,\ aerobic}$ (*thick*, *broken* and *thin black* lines) and the anaerobic metabolic system $\dot{q}_{ATP,\ anaerobic}$ (*thick*, *broken* and *thin grey* lines) and (**b**) O_2 consumption $\dot{V}o_2$ during rest, 30-s exercise and recovery. (**a**) $\dot{q}_{ATP,\ anaerobic} = \dot{q}_{ATP,\ PCr} + \dot{q}_{ATP,\ Gl}$, where $\dot{q}_{ATP,\ PCr}$ is the rate of phosphocreatine (PCr) breakdown and $\dot{q}_{ATP,\ Gl}$ is the rate of glycolysis (Gl). (**b**) The values of $\dot{V}o_2$ were normalized using the value at rest (0 s). The exercise started at 20 s. *Thin* lines: "low" intensity exercise ≡20% maximum voluntary contraction (MVC); *broken* lines: "medium" ≡ 40% MVC; *thick lines*: "high" ≡ 70% MVC

eight- and 14-times greater than the rest value for "low", "medium" and "high", respectively. Some examples of model outputs are shown in Figs. 2 and 3.

As shown in Fig. 2a, the energy needed during "high" was supplied mostly by $\dot{q}_{ATP,\ anaerobic}\left(= \dot{q}_{ATP,\ PCr} + \dot{q}_{ATP,\ Gl}\right)$, and that during "medium" and "low" was supplied by both $\dot{q}_{ATP,\ aerobic}$ and $\dot{q}_{ATP,\ anaerobic}$ operating synergistically. As shown in Fig. 2b, O_2 consumption $\dot{V}o_2$ reached peak values 10–30 s after the start of exercise, depending on the intensity of exercise. $\dot{V}o_2$ of "high" reached a plateau of zero at about 25 s after the start of exercise, indicating that the energy needed at this stage of exercise was mainly supplied by $\dot{q}_{ATP,\ anaerobic}$. During recovery, the $\dot{V}o_2$ values of "high" were larger than those of "medium" and "low" due to significant O_2 debt.

Separate traces of Hb and Mb are shown in Fig. 3a,b, respectively. The ratio of [total-(Hb)] ([oxy-(Hb)] + [deoxy-(Hb)]) to [total-(Mb)] ([oxy-(Mb)] + [deoxy-(Mb)]) is assumed to be 4–1. The simulated temporal changes in [oxy-(Hb + Mb)] and [deoxy-(Hb + Mb)] are shown in Fig. 3c,d, respectively. Typical temporal changes in [oxy-(Hb + Mb)] and [deoxy-(Hb + Mb)] in the rectus femoris are shown in Fig. 4a,b, respectively. The values of [oxy-(Hb + Mb)] decreased to values ranging from 0.7 to 0.2-times smaller than the rest value, whereas the values of [deoxy-(Hb + Mb)] increased to values 1.4–1.8-times greater than the rest value, depending on the intensity of exercise. As shown in Fig. 3c,d, the characteristic changes in [oxy-(Hb + Mb)] and [deoxy-(Hb + Mb)] in response to variation in exercise intensity were sufficiently reproduced by simulation.

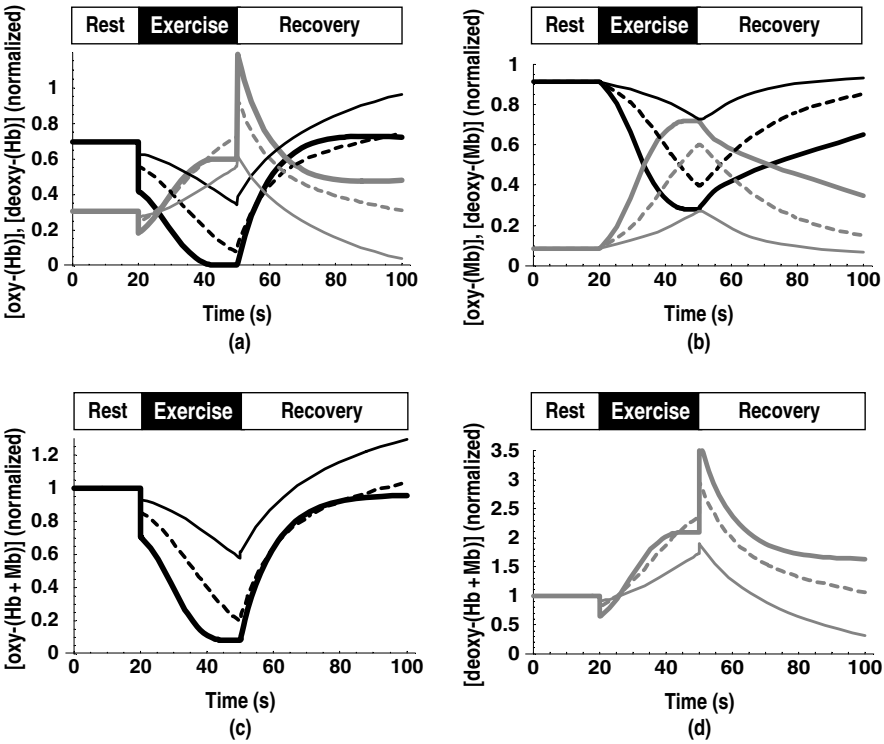

Fig. 3 Example of model outputs: temporal changes in molar concentrations of (**a**) oxy- and deoxygenated hemoglobin ([oxy-(Hb)] and [deoxy-(Hb)]) and (**b**) oxy- and deoxygenated myoglobin ([oxy-(Mb)] and [deoxy-(Mb)]) during rest, 30-s exercise and recovery. Black lines: (**a**) [oxy-(Hb)] and (**b**) [oxy-(Mb)]. *Grey* lines: (**a**) [deoxy-(Hb)] and (**b**) [deoxy-(Mb)]. The values of (**a**) and (**b**) were normalized using [total-(Hb)] ([oxy-(Hb)] + [deoxy-(Hb)]) and [total-(Mb)] ([oxy-(Mb)] + [deoxy-(Mb)]) at rest (0 s), respectively. The ratio of [total-(Hb)] to [total-(Mb)] was assumed to be 4 to 1. Temporal changes in (**c**) oxygenated Hb and Mb [oxy-(Hb + Mb)] and (**d**) deoxygenated Hb and Mb [deoxy-(Hb + Mb)], which were normalized using [oxy-(Hb + Mb)] and [deoxy-(Hb + Mb)] at rest (0 s), respectively. The exercise started at 20 s. *Thin* lines: "low" intensity exercise ≡ 20% maximum voluntary contraction (MVC); *broken* lines: "medium" ≡ 40% MVC; *thick* lines: "high" ≡ 70% MVC

4 Discussion and Conclusions

The distinct feature of our model is that a minimum number of equations offer a good macroscopic view of the metabolic changes in muscle. As shown in Figs. 2–4, the results show the causal relationship between muscle metabolism $\left(\dot{q}_{\mathrm{ATP,\ aerobic}}, \dot{q}_{\mathrm{ATP,\ anaerobic}} \text{ and } \dot{V}o_2\right)$ and NIRS measurements. In spite of the highly simplified properties of the equations and the small number of mechanisms modeled, the simulated profiles of [oxy-(Hb + Mb)] and [deoxy-(Hb + Mb)] (Fig. 3) agreed well with those obtained in vivo using $\mathrm{NIR_{SRS}}$ (Fig. 4).

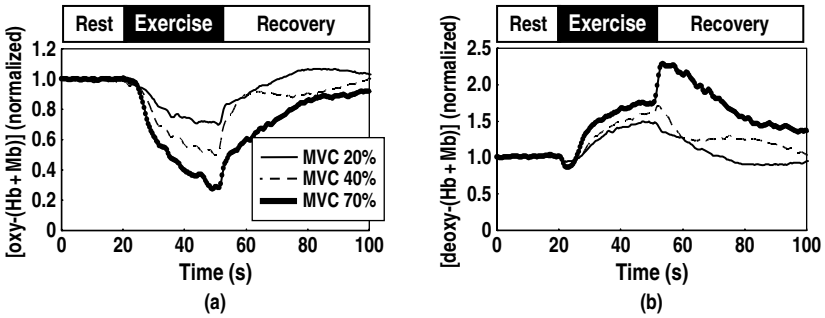

Fig. 4 In vivo measurements in a single subject: temporal changes in (**a**) oxygenated hemoglobin (Hb) and myoglobin (Mb) concentrations [oxy-(Hb + Mb)] and (**b**) deoxygenated Hb and Mb concentrations [deoxy-(Hb + Mb)] in the rectus femoris during isometric knee extension exercise for 30 s at 20, 40, and 70% maximum voluntary contraction (MVC). The measurements were made using an instrument based on spatially resolved spectroscopy. The exercise started at 20 s. The values of [oxy-(Hb + Mb)] and [deoxy-(Hb + Mb)] were normalized using the value at rest (0 s)

The results suggest that the model is a useful tool for simulation of the kinetics of NIRS measurements for systematic interpretation of the relationship between NIRS measurement data and muscle metabolism.

Acknowledgments This study was supported by a research fellowship and a Grant-in-aid for Scientific Research from the Japan Society for the Promotion of Science. We thank Hokkaido Red Cross Blood Center for providing blood for performance tests of the instrument.

References

1. Chiari L, Avanzolini G et al. (1997) A comprehensive simulator of the human respiratory system: validation with experimental and simulated data. Ann Biomed Eng **25**:985–999.
2. Korzeniewski B, Zoladz JA (2001). A model of oxidative phosphorylation in mammalian skeletal muscle. Biophys Chem **92**:17–34.
3. Lambeth MJ, Kushmerick MJ (2002) A computational model for glycogenolysis in skeletal muscle. Ann Biomed Eng **30**:808–827.
4. Kek KJ, Miyakawa T et al. (2006) Simulation of exercise-dependent difference in metabolism with a mathematical model for analyses of measurements using near-infrared spectroscopy. Conf Proc IEEE Eng Med Biol Soc **1**:5101–5104.
5. http://bmisys.bme.ist.hokudai.ac.jp/bim/research.html
6. Kek KJ, Kibe R et al. (2008) Optical imaging instrument for muscle oxygenation based on spatially resolved spectroscopy. Opt Express **16**:18173–18187.

Mapping of Optical Pathlength of Human Adult Head at Multi-Wavelengths in Near Infrared Spectroscopy

Akihisa Katagiri, Ippeita Dan, Daisuke Tuzuki, Masako Okamoto, Noriaki Yokose, Kouji Igarashi, Tatsuya Hoshino, Tokuo Fujiwara, Youichi Katayama, Yui Yamaguchi, and Kaoru Sakatani

Abstract Measurement of multichannel continuous-wave near-infrared spectroscopy (CW-NIRS) is dependent on the modified Beer-Lambert law, which includes optical pathlength (PL) as an essential parameter. PLs are known to differ across different head regions and different individuals, but the distribution of PLs for the whole head has not been evaluated so far. Thus, using time-resolved near-infrared spectroscopy (TR-NIRS), we measured the optical characteristics including PL, scattering coefficients (μ'_s), and absorption coefficients (μ_a) at three wavelengths (760, 800, 830 nm). Then, we constructed maps of these parameters on the subjects' head surface. While the PLs in nearby channels are similar, they differ depending on the regions of the head. The PLs in the region above the Sylvian fissure tended to be shorter than those in the other regions at all of the wavelengths. The difference in the distribution of PLs may be attributed to differences in tissue absorption and scattering properties. The current study suggests the importance of considering PL differences in interpreting functional data obtained by CW-NIRS.

1 Introduction

Multichannel continuous-wave near-infrared spectroscopy (CW-NIRS), also known as functional NIRS (fNIRS), or Optical topography (OT), is an emerging neuroimaging technique that allows the noninvasive monitoring of hemodynamic changes associated with human brain activity [1]. CW-NIRS has several advantages with respect to other neuroimaging methods: it is more tolerant of physical movements, allows more freedom in choice of experimental settings and is less expensive. Thus, CW-NIRS has been applied in various

K. Sakatani (✉)
Division of Optical Brain Engineering, Department of Neurological Surgery; Division of Applied System Neuroscience, Department of Advanced Medical Science, Nihon University School of Medicine, Tokyo, 173-8610, Japan
e-mail: sakatani@med.nihon-u.ac.jp

E. Takahashi, D.F. Bruley (eds.), *Oxygen Transport to Tissue XXXI*, Advances in Experimental Medicine and Biology 662,
DOI 10.1007/978-1-4419-1241-1_29, © Springer Science+Business Media, LLC 2010

diagnostic settings, including pre-surgery language dominance determination [2], preoperative planning of tumor removal [3], determining epileptic foci [4], monitoring rehabilitation [5], psychiatric diagnosis [6], pediatric diagnosis [7] and postoperative cerebral oxygenation monitoring [8].

Despite these merits, CW-NIRS measurement still has a technical drawback in that it measures absorbance without reference to optical pathlength (PL). Lack of this variable makes it impossible to calculate absolute, rather than relative changes of hemoglobin concentration when using the modified Beer Lambert law [9]. A recent study examining PL in foreheads, somatosensory motor and occipital regions revealed that PL varied among the regions of head and subjects [10], suggesting that the analysis can not be extended to the comparison between data from different channels. Also, data integration between different channels, which is necessary for topographic map reconstruction, is difficult to validate. This limits the potential of CW-NIRS measurement.

Thus, as a step toward solving the optical PL issue in CW-NIRS, we created a whole-head optical PL map by measuring PL at various regions of an adult head using time-resolved near-infrared spectroscopy (TR-NIRS). Using this, we assess the regional difference of the optical PL across different cortical regions, and discuss the feasibility of data integration among different channels.

2 Method

2.1 TR-NIRS System

We used a TR-NIRS system (TRS-10, Hamamatsu Photonics K.K., Japan) [11] to measure optical PL at three different wavelengths (760, 800, 830 nm) in normal adult subjects ($n = 8$). Detailed description of the apparatus and mechanism of the measurement is as previously described [12]. Briefly, the light source of the system emits a 5 MHz of light pulses at the three wavelengths from semiconductor lasers (Picosecond Light Pulser, Hamamatsu Photonics K.K., Japan). The light is guided through an illuminating optical fiber and emitted onto the scalp, traveling through the head and brain tissue. Some fraction of the light reaches a detecting optical fiber placed on the scalp 3 cm away from the illuminating optical fiber, and is guided into a photomultiplier tube (PMT, H6279-MOD, Hamamatsu Photonics K.K., Japan) to generate an electric signal. This signal is processed by constant fraction discriminators, time-to-amplitude converters, A/D converters and histogram memories. The mean PL was calculated from the observed temporal profiles of the light intensity [13]. Also, by fitting the observed temporal profiles to the photon diffusion equation [14], using a non-linear least square fitting method, we calculated the reduced scattering (μ'_s) and absorption coefficients (μ_a) at the three wavelengths.

2.2 Data Analysis

The midpoint between illuminating and detecting optical fibers defined a channel, the point where the optical properties of the underlying tissue was monitored. In a pilot study, we confirmed that the directional anisotropy of the channel placement was negligible. We selected approximately 80 evenly distributed scalp positions and marked them on a flexible mesh cap according to the 10–20 system of EEG placement [15]. We sequentially placed the channels at the scalp positions and performed TRS measurements. After each TRS measurement, the location of the fiber placement was measured by a 3D-magnetic digitizer (FASTRAK, Polhemus, Colchester, VT), and these locations were translated to segmented magnetic resonance images of each subject. In this way, we constructed a PL distribution map on the scalp. For all surface positions on the scalps of the subjects, the optical PLs were interpolated at a $1 \times 1 \times 1$ mm resolution, from the measuring points using a nearest neighbor method. For creating the PL distribution map on the cortical surface, each head surface position was projected onto the cortical surface as previously described [16].

3 Results

The spatial distribution of the optical PLs, μ_a and μ'_s for a subject is shown in Fig. 1. We used the optical properties measured at the international 10–20 positions (20 positions; summarized in Table 1) to perform statistical analysis. To assess laterality effects, zenith positions (Fz, Cz and Pz) were excluded. The remaining positions were divided into eight pairs of laterally symmetrical positions. A $2 \times 3 \times 8$ (laterality $\times$ pathlengths $\times$ positions) ANOVA was performed on the values for PL, μ_a and μ'_s. For PL, there was no significant main effect ($P < 0.05$) of laterality ($F_{(1,7)} = 0.4$) whereas significant main effects for pathlength ($F_{(2,14)} = 121.2$) and position ($F_{(7,49)} = 20.6$) were observed.. A significant interaction between pathlength and position ($F_{(14,98)} = 6.2$) was also detected. An ad-hoc multiple comparison revealed the following relation: $PL_{760} = PL_{800} > PL_{830}$ ($P < 0.05$, Bonferroni-corrected). Generally, differences in optical PLs among neighboring channels were rather small, but some global tendencies were observed. The PLs were the shortest in the peri-Sylvian regions located at the border between frontal and temporal regions. The regions above the temporal lobe also exhibited relatively short PLs. The longest PL was observed in the medial frontal and occipital regions. Frontal and parietal regions exhibited moderate PLs. These overall tendencies were observed at all of the wavelengths.

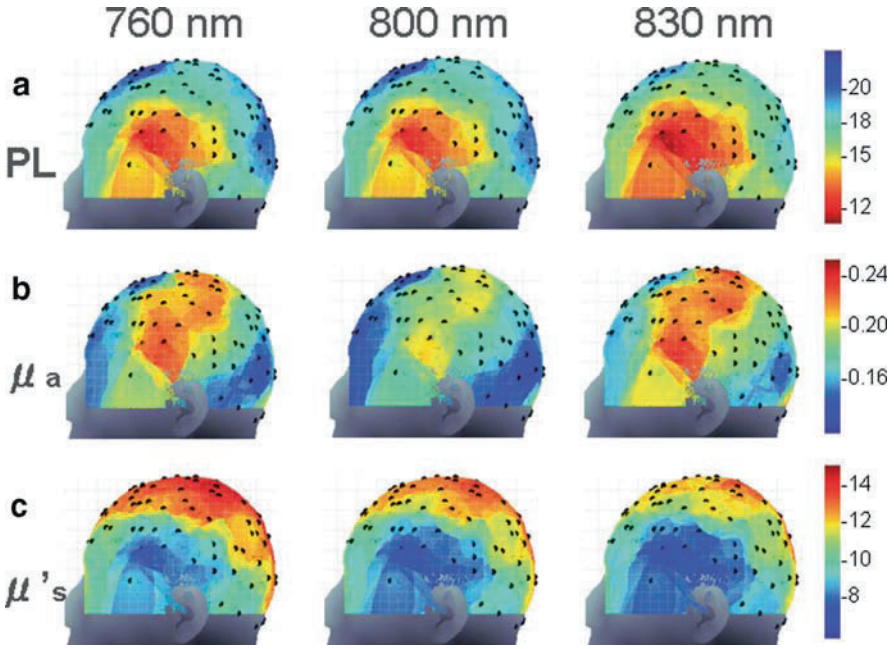

Fig. 1 **a**: Distribution of optical pathlength (PL) in a unit of cm on a scalp at 760, 800, and 830 nm. **b**: Distribution of scattering coefficients (μ_a) in a unit of cm^{-1} on a scalp at 760, 800, and 830 nm. **c**: Distribution of absorption coefficients (μ'_s) in a unit of cm^{-1} on a scalp at 760, 800, and 830 nm

While ANOVA revealed no significant main effect of laterality for μ_a ($F_{(1,7)} = 0.3$), there were significant main effects for pathlength ($F_{(2,14)} = 35.8$) and position ($F_{(7,49)} = 9.5$). Significant interaction between pathlength and position ($F_{(14,98)} = 10.3$) was also detected. Use of an ad-hoc multiple comparison revealed the following relation: $\mu_{a830} = \mu_{a760} > \mu_{a800}$ on most positions except for F4, O2, P3, P7, and P8 exhibiting $\mu_{a830} > \mu_{a760} > \mu_{a800}$ relation ($P < 0.05$, Bonferroni-corrected). Generally, μ_a was larger in the region above the central sulcus.

For μ'_s, ANOVA revealed no significant main effect of laterality ($F_{(1,7)} = 0.3$), whereas significant main effects for pathlength ($F_{(2,14)} = 29.1$) and position ($F_{(7,49)} = 6.3$) were detected. Significant interaction between pathlength and position ($F_{(14,98)} = 2.2$) was also detected, with ad-hoc multiple comparison revealing the relation: $\mu'_{s760} = \mu'_{s800} > \mu'_{s830}$ at most positions except for Fp1, F7, and P7 exhibiting only $\mu'_{s760} > \mu'_{s800}$ relation, and F8 exhibiting $\mu'_{s760} > \mu'_{s830}$ relation ($P < 0.05$, Bonferroni-corrected). Generally, μ'_s was larger in the regions above the inter-hemispheral fissure.

Table 1 Distribution of optical parameters. All values are presented as mean ± standard deviation

	Optical PL (cm)			μ_a (cm^{-1})			μ'_s (cm^{-1})		
	760 nm	800 nm	830 nm	760 nm	800 nm	830 nm	760 nm	800 nm	830 nm
Fp1	22.1 ± 4.4	22.2 ± 4.7	21.1 ± 4.7	0.15 ± 0.03	0.14 ± 0.03	0.16 ± 0.03	14.9 ± 6.9	14.4 ± 7.0	14.5 ± 7.4
Fp2	23.1 ± 3.9	23.0 ± 3.8	21.7 ± 3.7	0.16 ± 0.04	0.15 ± 0.03	0.16 ± 0.04	15.7 ± 6.7	14.9 ± 6.3	14.7 ± 6.9
F3	21.0 ± 4.6	21.1 ± 4.8	19.9 ± 4.6	0.17 ± 0.05	0.16 ± 0.05	0.18 ± 0.06	15.0 ± 7.4	14.2 ± 7.0	14.2 ± 7.3
F4	22.3 ± 3.5	22.5 ± 3.5	21.0 ± 3.4	0.17 ± 0.05	0.16 ± 0.04	0.18 ± 0.05	16.7 ± 8.9	15.9 ± 8.4	15.6 ± 8.9
F7	16.1 ± 2.0	16.4 ± 2.5	15.6 ± 2.3	0.23 ± 0.07	0.21 ± 0.06	0.23 ± 0.07	11.5 ± 4.8	10.7 ± 4.2	10.9 ± 4.6
F8	17.6 ± 3.0	17.8 ± 2.7	16.9 ± 2.6	0.24 ± 0.11	0.21 ± 0.10	0.24 ± 0.11	14.9 ± 11.6	13.5 ± 10.2	13.5 ± 11.0
Fz	24.4 ± 3.2	24.0 ± 3.1	22.8 ± 3.2	0.16 ± 0.04	0.16 ± 0.05	0.17 ± 0.05	17.9 ± 8.2	17.2 ± 8.1	17.1 ± 8.6
T7	17.7 ± 3.7	17.8 ± 3.7	17.1 ± 3.7	0.19 ± 0.03	0.17 ± 0.03	0.19 ± 0.03	11.4 ± 4.3	10.7 ± 4.2	10.8 ± 4.4
T8	17.8 ± 3.0	17.8 ± 3.0	16.9 ± 2.9	0.19 ± 0.06	0.17 ± 0.06	0.19 ± 0.06	11.9 ± 7.0	11.1 ± 6.6	11.0 ± 7.0
C3	21.0 ± 2.4	21.0 ± 2.3	19.9 ± 2.2	0.21 ± 0.05	0.19 ± 0.05	0.21 ± 0.05	16.7 ± 6.7	15.7 ± 6.2	15.7 ± 6.6
C4	20.8 ± 4.0	20.8 ± 3.8	19.7 ± 3.7	0.20 ± 0.04	0.18 ± 0.04	0.21 ± 0.05	16.2 ± 8.5	15.3 ± 8.3	15.1 ± 9.0
Cz	21.9 ± 4.3	21.7 ± 4.2	20.9 ± 4.0	0.22 ± 0.07	0.21 ± 0.07	0.23 ± 0.08	18.8 ± 10.7	17.9 ± 10.4	18.1 ± 10.6
P3	23.8 ± 4.8	23.7 ± 4.5	22.5 ± 4.4	0.16 ± 0.04	0.15 ± 0.04	0.17 ± 0.04	16.2 ± 5.0	15.5 ± 4.8	15.5 ± 5.1
P4	23.3 ± 4.4	23.3 ± 4.3	21.9 ± 4.3	0.16 ± 0.03	0.15 ± 0.03	0.16 ± 0.03	16.1 ± 6.8	15.4 ± 6.4	15.0 ± 6.9
P7	22.4 ± 5.0	22.2 ± 4.9	21.2 ± 4.8	0.14 ± 0.03	0.13 ± 0.03	0.15 ± 0.03	13.7 ± 5.6	13.0 ± 5.3	13.0 ± 5.5
P8	22.5 ± 3.8	22.3 ± 3.6	21.2 ± 3.5	0.15 ± 0.04	0.15 ± 0.04	0.16 ± 0.04	15.0 ± 6.6	14.3 ± 6.4	14.2 ± 6.7
Pz	22.7± 3.5	22.4 ± 3.6	21.4 ± 3.4	0.17 ± 0.04	0.17 ± 0.04	0.19 ± 0.05	16.4 ± 5.9	15.6 ± 5.6	15.8 ± 5.8
O1	22.7 ± 5.9	22.8 ± 5.6	21.6 ± 5.5	0.14 ± 0.02	0.13 ± 0.02	0.14 ± 0.02	13.9 ± 5.9	13.3 ± 5.6	13.1 ± 5.8
O2	24.1 ± 4.2	24.0 ± 4.1	22.8 ± 4.0	0.15 ± 0.03	0.14 ± 0.03	0.16 ± 0.04	16.6 ± 7.6	15.9 ± 7.2	15.7 ± 7.7
Oz	24.4 ± 4.5	24.1 ± 4.4	23.1 ± 4.4	0.14 ± 0.03	0.13 ± 0.03	0.15 ± 0.03	15.5 ± 5.7	14.8 ± 5.5	14.9 ± 5.6

4 Discussion

The current study extends the former study by Zhao et al. assessing optical PL distribution in the forehead, Somatosensory motor and occipital regions [10]. We broadened the region of interest to the whole head and demonstrated that optical PL varies among scalp locations, with those above the peri-Sylvian regions being the shortest and those in medial frontal and occipital regions being the longest. The inhomogenous nature of the optical PLs may be attributed to inhomogenous distribution of absorbent and tissue structures. The former is well represented by the distribution of μ_a. The observation that μ_a was smallest at 800 nm, which is the equiabsorbance point for oxygenated and deoxygenated Hbs, suggests that Hb concentration is a dominant factor in determining μ_a. Large μ_a in the region around the central sulcus likely signify a higher Hb concentration in this region, probably due to the bridging veins around the superior sagittal sinus and the Sylvian veins. In addition, the effects of the temporal muscle would play a part. On the other hand, μ'_s is expected to reflect differences in tissue properties; however, the medially-oriented larger distribution of μ'_s suggests a contribution of skull thickness. Since the current analysis did not involve elaborate segmentation of the tissues, we cannot specify which component was the most influential, and further study will be necessary to clarify the detailed aspects of tissue contribution. In addition, there was no laterality in the optical parameters tested. This finding may provide experimental support for the interhemispheric comparison of cortical activation on symmetrical regions often practiced in various CW-NIRS studies (e.g., language dominance assessment [2]).

In this study, we have presented the PL distribution on the subject's own MRI and left inter-subject integration as a future topic of study. Our intention here was to simply perform spatial normalization of the data to the standard stereotaxic brain space using transformation based on gross matching of cortical structures. However, we noted the substantial effects of non-cortical structure on PL distribution, probably due to temporal muscles and Sylvian veins. In this case, spatial normalization of the data solely based on cortical structure may be misleading, and scalp-based normalization would be more appropriate. Since there is no such method established for this, we are currently developing one.

5 Conclusion

We constructed a whole-head map for optical PL distribution. While the PLs in local vicinities are similar, they differ according to locations on the head. The difference in the distribution of PLs may be further attributed to differences in tissue absorption and scattering properties. The current study suggests the importance of considering PL differences in interpreting functional data obtained by CW-NIRS.

Acknowledgments This work was in part supported by Hamamatsu Photonics K.K. (Hamamatsu, Japan), the Program for Promotion of Basic Research Activities for Innovative Bioscience, Health and Labor Sciences Research Grants, Research on Psychiatric and Neurological Diseases and Mental Health, and grant-in-aids from the Ministry of Education, Culture, Sport, Science, and Technology, Japan (18700625 awarded to MO and 18390404 to ID).We thank Dr. Lester Clowney for proofreading the manuscript.

References

1. Obrig, H., Villringer, A. 2003. Beyond the visible-imaging the human brain with light. *J. Cereb. Blood Flow Metab*. **23**. 1–18 .
2. Watanabe, E., Maki, A., Kawaguchi, F., Takashiro, K., Yamashita, Y., Koizumi, H., Mayanagi, Y. 1998. Non-invasive assessment of language dominance with near-infrared spectroscopic mapping. *Neurosci. Lett*. **30**. 49–52.
3. Fujiwara, N., Sakatani, K., Katayama, Y., Murata, Y., Hoshino, T., Fukaya, C., Yamamoto, T. 2004. Evoked-cerebral blood oxygenation changes in false-negative activations in BOLD contrast functional MRI of patients with brain tumors. *Neuroimage* **21**. 1464–1471.
4. Watanabe, E., Maki, A., Kawaguchi, Y., Yamashita, Y., Koizumi, H., Mayanagi, Y. 2000. Noninvasive cerebral blood volume measurement during seizures using multichannel near infrared spectroscopic topography. *J. Biomed. Opt*. **5**. 287–290 .
5. Miyai, I., Tanabe, H.C., Sase, I., Eda, H., Oda, I., Konishi, I., Tsunazawa, Y., Suzuki, T., Yanagida, T., Kubota, K. 2001. Cortical mapping of gait in humans: a near-infrared spectroscopic topography study. *Neuroimage* **14**. 1186–1192.
6. Suto, T., Fukuda, M., Ito, M., Uehara, T., Mikuni, M. 2004. Multichannel near-infrared spectroscopy in depression and schizophrenia: cognitive brain activation study. *Biol. Psychiatry*. **55**. 501–511.
7. Isobe, K., Kusaka, T., Nagano, K., Okubo, K., Yasuda, S., Kondo, M., Itoh, S., Onishi, S. 2001. Functional imaging of the brain in sedated newborn infants using near infrared topography during passive knee movement. *Neuroci. Lett*. **299**. 221–224.
8. Murata, Y., Katayama, Y., Sakatani, K., Fukaya, C., Kano, T. 2003. Evaluation of extracranial-intracranial arterial bypass function by using near-infrared spectroscopy. *J. Neurosurg*. **99**. 304–310 .
9. Cope, M., Delpy, D.T., Reynolds, E.O., Wray, S., Wyatt, J., van der Zee, P. 1988. Methods of quantitating cerebral near infrared spectroscopy data. *Adv. Exp. Med. Biol*. **222**. 183–189 .
10. Zhao, H., Tanikawa, Y., Gao, F., Onodera, Y., Sassaroli, A., Tanaka, K., Yamada, Y. 2002. Maps of optical differential pathlength factor of human adult forehead, somatosensory motor and occipital regions at multi-wavelengths in NIR. *Phys. Med. Biol*. **47.** 2075–2093.
11. Oda, M., Nakano, T., Suzuki, A., Shimizu, K., Hirano, I., Shimomura, F., Ohmae, E., Suzuki, T., Yamashita, Y. 2000. Nearinfrared time resolved spectroscopy system for tissue oxygenation monitor. *SPIE* **4160**. 204–210.
12. Sakatani, K., Yamashita, D., Yamanaka, T., Oda, M., Yamashita, Y., Hoshino, T., Fujiwara, N., Murata, Y., Katayama, Y. 2006. Changes of cerebral blood oxygenation and optical pathlength during activation and deactivation in the prefrontal cortex measured by time-resolved near infrared spectroscopy. *Life Sci*. **78.** 2734–2741.
13. Zhang, H., Miwa, M., Urakami, T., Yamashita, Y., Tsuchiya, Y. 1998. Simple subtraction method for determining the mean path length traveled by photons in turbid media. *Jpn. J. Appl. Phys*. **37**. 700–704.

14. Patterson, M.S., Chance, B., Wilson, B.C. 1989. Time resolved reflectance and transmittance for the noninvasive measurement of tissue optical properties. *Appl. Opt*. **28.** 2331–2336.
15. Jurcak, V., Tsuzuki, D., Dan, I. 2007. 10/20, 10/10, and 10/5 systems revisited: their validity as relative head-surface-based positioning systems. *Neuroimage* **34.** 1600–1611.
16. Okamoto, M., Dan, I. 2005. Automated cortical projection of head-surface locations for transcranial functional brain mapping. *Neuroimage* **26.** 18–28.

Changes of Evoked Cerebral Blood Oxygenation and Optical Pathlength in the Frontal Lobe During Language Tasks: A Study by Multi-Channel, Time-Resolved Near-Infrared Spectroscopy and Functional MRI

Yoshihiro Murata, Kaoru Sakatani, Tatsuya Hoshino, Norio Fujiwara, Yoichi Katayama, Daisuke Yamashita, Takeshi Yamanaka, Motoki Oda, and Yutaka Yamashita

Abstract To determine the alterations in optical characteristics and cerebral blood oxygenation (CBO) in the frontal lobe during language tasks, we evaluated the changes in mean optical pathlength (MOP) and CBO induced by a verbal fluency task (VFT) in the right and left frontal lobes in normal adults ($n = 9$, mean age $= 29.6 \pm 4.8$ years). We employed a newly developed 8-channel time-resolved near-infrared spectroscopy (TRS) instrument. The results demonstrated differences in MOP in the fronto-temporal areas with subject and wavelength; however, there was no significant difference between the right and left sides ($p > 0.05$). Also, the VFT did not affect the MOP significantly as compared to that before the tasks ($p > 0.05$). In all of the recording regions, the VFT caused increases in concentration of oxyhemoglobin and total hemoglobin associated with a decrease in deoxyhemoglobin concentration, indicating that these cortical areas were activated by the VFT. However, the mean concentration changes of oxyhemoglobin and total hemoglobin on the left side were larger than those on the right side. In addition, functional MRI demonstrated that the inferior frontal gyrus on the left side was activated in the subjects who exhibited increases in oxyhemoglobin concentration in these areas. These results suggest that TRS may be useful to study language function and to assess hemispheric dominance for language.

Y. Murata (✉)
Division of Neurosurgery, Department of Neurological Surgery, Nihon University School of Medicine, Tokyo, Japan
e-mail: ymcooper@med.nihon-u.ac.jp

E. Takahashi, D.F. Bruley (eds.), *Oxygen Transport to Tissue XXXI*, Advances in Experimental Medicine and Biology 662,
DOI 10.1007/978-1-4419-1241-1_30, © Springer Science+Business Media, LLC 2010

1 Introduction

Near-infrared spectroscopy (NIRS) is a non-invasive method for investigation of functional activation in the human cerebral cortex [1]. BOLD-fMRI is also useful to image activated areas in brain. BOLD-fMRI does not provide precise information about evoked cerebral blood oxygenation (CBO) changes during activation.

In the present study, employing newly developed multichannel TRS, we evaluated the evoked CBO changes in the bilateral frontal-temporal area, including Broca's area, during a language task. In order to determine language dominance, we compared the evoked CBO changes in the left and right measurement sites. The results were compared with activation maps of BOLD-fMRI. In addition, we examined whether the MOP affects the determination of language dominance by measurements of evoked CBO changes.

2 Method

We investigated 10 normal adult subjects (9 men and 1 woman; mean age, 28 ± 0.05 years [mean $\pm$ SD]). We employed a verbal fluency task (VFT), which entails naming as many animals or fruits as possible, as the language task; the VFT is a well-established neuropsychological test of frontal lobe function [2]. An 8-channel TRS system was used [3]. Four channels on each side were mounted on a thermoplastic shell, which were placed over the inferior frontal gyrus (including Broca's area) on both sides. The location of the channels was adjusted by MRI (Fig 1a). The evoked CBO changes were compared with the results of BOLD imaging obtained by means of 1.5 T MRI (Symphony, Siemens, Germany).

3 Results

In all subjects, the VFT significantly altered the CBO in all measurement sites. The VFT caused increases of oxyhemoglobin (O_2Hb) and total Hb (tHb) associated with a decrease of deoxyhemoglobin (HHb). These evoked CBO

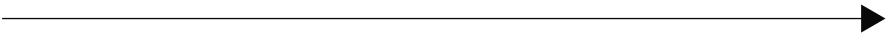

Fig. 1 (continued) (**a**): Eight channel probes were placed over the bilateral fronto-temporal area including inferior frontal gyrus based on surface anatomical imaging by MRI. The probes were named as follows; R1 (*right* side superior probe), R2 (*right* side anterior probe), R3 (*right* side inferior probe), R4 (*right* side posterior probe), L1 (*left* side superior probe), L2 (*left* side anterior probe), L3 (*left* side inferior probe), L4 (*left* side posterior probe). (**b**): Typical example of the CBO changes in the *right* and *left* fronto-temporal areas during the course of the experiments. The ordinates indicate the concentration changes of O_2Hb (*red* lines), HHb (*blue* lines), and tHb (*green* lines) in μM. The thick bars below the NIRS parameter changes indicate the periods of the tasks. The VFT caused increases of O_2Hb and tHb associated with a decrease of HHb

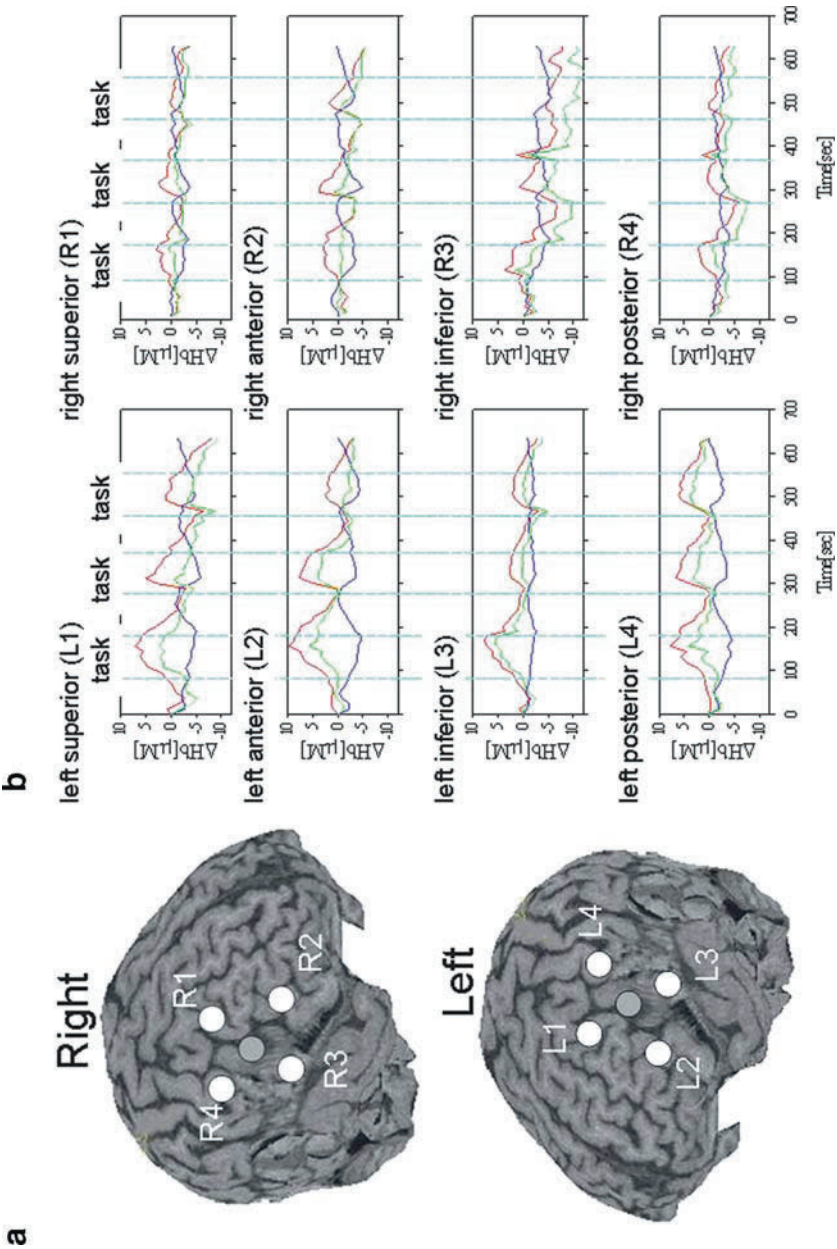

Fig. 1 (a) (continued)

changes returned to the control level during the recovery phase. Figure 1b shows a typical example of the CBO changes. The mean concentration changes of O_2Hb and tHb on the left side of all measurement sites were larger than those on the right side, and the difference between the left and right sides was significant for O_2Hb, though not for tHb (Fig. 2). The results demonstrated differences in MOP in the fronto-temporal areas with subject and wavelength; however, there was no significant difference between the right and left sides in each measurement site ($p > 0.05$). Also, the VFT did not affect the MOP significantly as compared to that before the tasks ($p > 0.05$). The BOLD-fMRI results demonstrated that the fronto-temporal area, particularly around the inferior frontal gyrus on the left side, was activated in the subjects (Fig. 3)

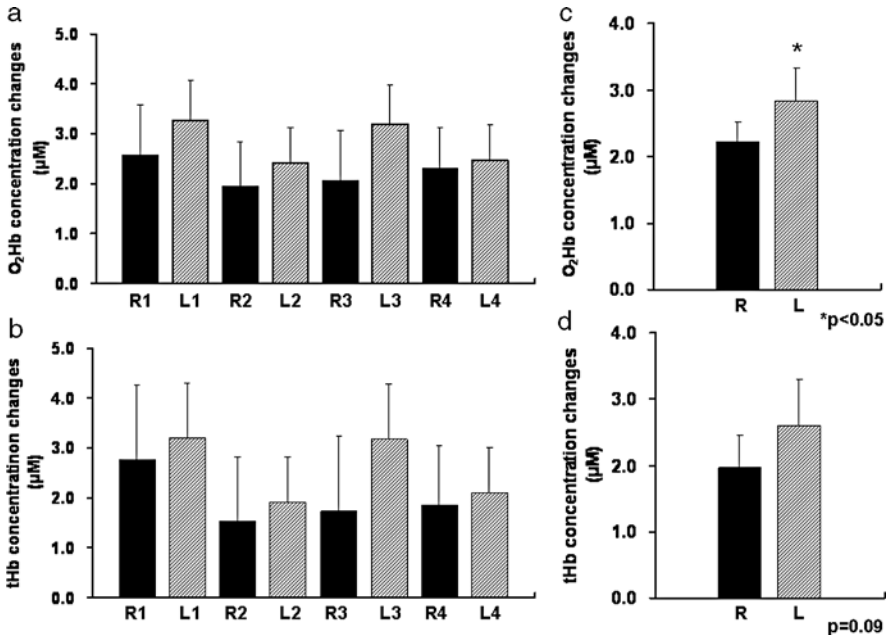

Fig. 2 Bar graphs indicate the average of O_2Hb (**a**) and tHb (**b**) concentration changes during the task detected by each probe (i.e. R1-4, L1-4). Both O_2Hb and tHb were significantly increased during the task. Additionally, the average of O_2Hb and tHb changes on the *left* side were larger than those in the *right* side, however, the differences were not significant at each measurement site. Bar graphs (**c**) and (**d**) show comparisons between the mean O_2Hb and tHb concentration changes in all measurement sites on the *left* side and those on the *right* side. O_2Hb and tHb changes on the *left* side were lager than those on the *right* side. The difference between the *left* and *right* sides in O_2Hb was significant ($p < 0.05$), whereas that in tHb was not significant ($p = 0.09$)

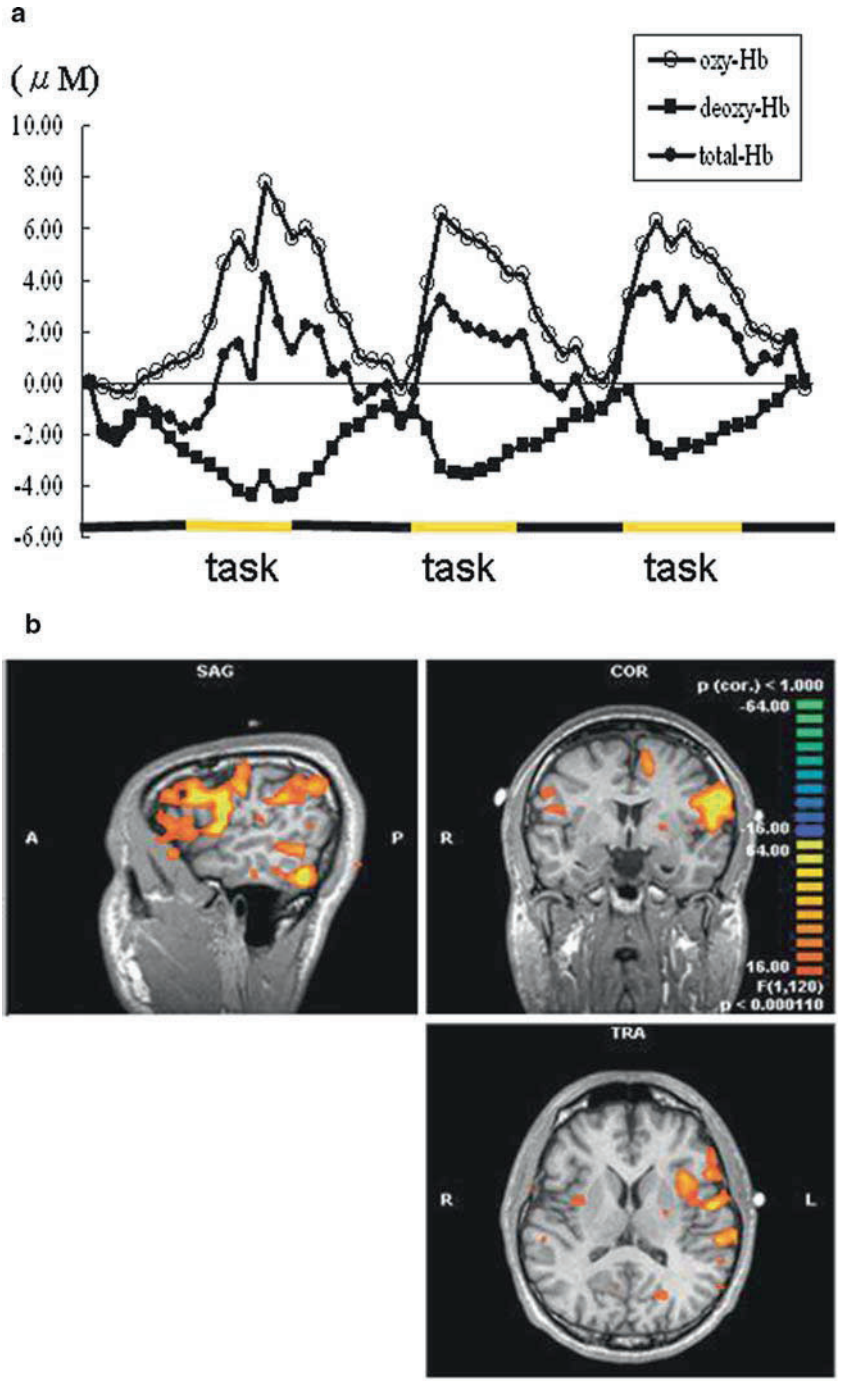

Fig. 3 (continued)

4 Discussion

The present time-resolved NIRS allowed measurements of the MOP changes during tasks with a sampling time of 1 s. We observed no significant difference in MOP at each wavelength during the tasks, although there were small fluctuations of the MOP (SD $<$ 0.2 cm). This implies that the task-induced hemodynamic changes in the fronto-temporal area did not significantly affect the light scattering in the brain tissue, although the absorption was affected by the Hb concentration changes. The increase in O_2Hb indicates that rCBF rises in the activated area, while the decrease in HHb is caused by a large increase of rCBF, which exceeds the increase in oxygen consumption during activation [4]. BOLD-fMRI revealed activation in the left inferior temporal gyrus during the language task in this study. Additionally, the mean concentrations of O_2Hb and tHb on the left side were larger than those on the right side in TRS measurement. It was considered that the CBO change evaluated by TRS measurement is compatible with the result of BOLD-fMRI. However, there is a possibility that systemic changes (such as blood pressure and so on) may influence the difference between left and right in NIRS measurement [5]. The findings in this study suggest that TRS may be useful to study language function and to assess hemispheric dominance for language.

Acknowledgments This work was supported by Grants-in-Aid from the Ministry of Education, Culture, Sports, Sciences and Technology of Japan (A12307029, A15209047, C15591553, and a grant for the promotion of industry-university collaboration at Nihon University) by Hamamatsu Photonics K.K. (Hamamatsu, Japan).

References

1. Villringer A, Planck J, Stodieck S et al. (1994) Noninvasive assessment of cerebral hemodynamics and tissue oxygenation during activation of brain cell function in human adults using near infrared spectroscopy. Adv Exp Med Biol 345:559–565.
2. Lezak MD (1995) Neuropsychological Assessment, Third edition, Oxford University Press, New York.
3. Ueda Y, Yamanaka T, Yamashita D, et al. (2005) Reflectance diffuse optical tomography: its application to human brain mapping. Jpn J Appl Phys 44:L1203–L1206.
4. Fox PT Raichle ME (1986) Focal physiological uncoupling of cerebral blood flow and oxidative metabolism during somatosensory stimulation in human subjects. Proc Natl Acad Sci USA 83:1140–1144.
5. Tachtsidis I, Leung TS, Devoto L, Delpy DT, Elwell CE (2008) Measurement of frontal lobe functional activation and related systemic effects: a near-infrared spectroscopy investigation. Adv Exp Med Biol 614: 397–403.

Fig. 3 (continued) (**a**): CBO changes during the task detected by the L2 (*left* side anterior) probe of TRS is shown. Increases of O_2Hb and tHb associated with a decrease of HHb were observed. *Yellow* and *black* bars indicate task and rest, respectively. (**b**): BOLD-fMRI revealed robust activation in the fronto-temporal language area

The Partial Coherence Method for Assessment of Impaired Cerebral Autoregulation using Near-infrared Spectroscopy: Potential and Limitations

D. De Smet, J. Jacobs, L. Ameye, J. Vanderhaegen, G. Naulaers, P. Lemmers, F. van Bel, M. Wolf, and S. Van Huffel

Abstract The most important forms of brain injury in premature infants are partly caused by disturbances in cerebral autoregulation. As changes in cerebral intravascular oxygenation (HbD), regional cerebral oxygen saturation (rSO_2), and cerebral tissue oxygenation (TOI) reflect changes in cerebral blood flow (CBF), impaired autoregulation can be measured by studying the concordance between HbD/rSO_2/TOI and the mean arterial blood pressure (MABP), assuming no changes in oxygen consumption, arterial oxygen saturation (SaO_2), and in blood volume. We investigated the performance of the partial coherence (PCOH) method, and compared it with the coherence method (COH). The PCOH method allows the elimination of the influence of SaO_2 on HbD/rSO_2/TOI in a linear way. We started from long-term recordings measured in the first days of life simultaneously in 30 infants from three medical centres. We then compared the COH and PCOH results with patient clinical characteristics and outcomes, and concluded that PCOH might be a better method for assessing impaired autoregulation.

1 Introduction

In this study in preterm infants, NIRS is used to measure cerebral autoregulation over long periods, reflecting *static autoregulation*. The use of NIRS for this purpose was described by Tsuji et al. [1]. Changes in HbD, rSO_2, or TOI reflect changes in CBF and the correlation between MABP and HbD/rSO_2/TOI is a reflection of autoregulation. A good correlation was found between autoregulation and outcome, i.e. frequency of severe intraventricular bleeds. rSO_2 and TOI are both absolute values, they are less prone to movement artefacts than HbD, and easier to measure in clinical practice.

S.Van Huffel (✉)
Department of Electrical Engineering (ESAT), SCD Division, Katholieke Universiteit Leuven, Belgium
e-mail: sabine.vanhuffel@diversiteit.kuleuven.be

E. Takahashi, D.F. Bruley (eds.), *Oxygen Transport to Tissue XXXI*,
Advances in Experimental Medicine and Biology 662,
DOI 10.1007/978-1-4419-1241-1_31, © Springer Science+Business Media, LLC 2010

We studied the concordance between HbD/rSO_2/TOI and MABP by means of the coherence (COH, measuring the degree of linear dependence between the frequency spectra of two signals), and partial coherence (PCOH) [2] coefficients. The latter allows the elimination of the linear influence of one signal on another one. This means that, in contrast to COH, PCOH can also be applied in periods of fluctuating SaO_2 thereby improving the automation and the use of the method. We developed and investigated four PCOH algorithms fixing the physiological interactions between SaO_2, MABP, and HbD/rSO_2/TOI. We studied the PCOH properties, in particular during periods of fluctuating SaO_2. For this purpose we used parameters that synthesize patient level of autoregulation: the mean score (*mCOH* and *mPCOH*) [1], the pressure-passive index (*PPI*) [3] and the critical percentage of the recording time (*CPRT*) [4]. Finally, we compared these parameters with the infant clinical characteristics and outcomes: infant post menstrual age (PMA, in weeks), birth weight (BW, in g), Bayley's psychomotor (PDI) and mental (MDI) developmental indices after 9, 18, and 24 months (for the Leuven, Zurich, and Utrecht data respectively), Griffith developmental index (combination of a mental and psychomotor test) after 24 months, and APGAR score at birth and 5 min after birth.

2 Datasets

Thirty premature infants with need for intensive care were monitored, of whom 10 were from the University Hospital Zurich (Switzerland), 10 from the University Medical Centre Utrecht (The Netherlands), and 10 from the University Hospital Leuven (Belgium). SaO_2 was measured continuously by pulse oximetry, and MABP by an indwelling arterial catheter. Transcranial NIRS signals HbD (measured by the Critikon Cerebral Oxygenation Monitor 2001), rSO_2 (INVOS4100, Somanetics Corp.), and TOI (NIRO300, Hamamatsu) were measured for non-invasive monitoring of cerebral oxygenation. The signals were measured simultaneously in the first days of life. For the Zurich data, the babies were characterized by a mean PMA of 28 1/7 weeks (*std* = 2 1/7) and a mean BW of 1198 g (*std* = 439). For the Utrecht data, the babies were characterized by a mean PMA of 29 2/7 weeks (*std* = 1 2/7) and a mean BW of 1130.67 g (*std* = 311.36). For the Leuven data, the babies were characterized by a mean PMA of 28 5/7 weeks (*std* = 3 2/7) and a mean BW of 1125 g (*std* = 503.76). HbD, rSO_2, and TOI were recorded digitally on a personal computer at a sampling frequency of 1.677, 1, and 10 Hz for the Zurich, Utrecht, and Leuven data respectively. Afterwards the signals from all datasets were down-sampled to the smallest frequency multiple of the recording frequencies i.e. 0.333 Hz (periodicity: 3 s) to ensure comparability. A pre-processing algorithm was applied to the recordings of all centres to remove signal artefacts. Each artefact point was simply deleted from the recording for each signal [3]. Among the pre-processing operations, we kept all variables within normal ranges, in particular SaO_2 in the range 80–100%.

3 Methods

Since the possible concordance between MABP and the NIRS signals varies with time, we computed COH and PCOH over successive half-overlapping epochs of duration 10, 15, and 12.5 min for the Zurich, Utrecht, and Leuven data respectively. The average of COH and PCOH over the frequency band 0.0033–0.04 Hz (corresponding to phenomena of duration in the range 25–300 s) [3] was used as score for the considered epoch. The epoch durations were computed from the calibration of the mean COH (for all patients of each centre) on the mean absolute-valued correlation coefficient (COR), to be sure that the score value of 0.5 could be considered as critical (it suggests a relation between the signals based on 50% shared variance) [5]. If *mCOH* or *mPCOH* was higher than this critical score value (*CSV*), the infant was said to have an impaired cerebral autoregulation. We built the PCOH algorithms from the supposed physiological models fixing the interactions between the measured signals as follows:

- $SaO_2 = i(SaO_2) + f(MABP)$
- $MABP = i(MABP) + f(SaO_2)$
- $NIRS = i(NIRS) + f(MABP) + f(SaO_2)$

where $i(\ldots)$ represents the independent part of the signal, $f(\ldots)$ stands for *is a function of*, and *NIRS* represents HbD, rSO_2, or TOI. The algorithms are:

- PCOH1 = $COH(MABP–SaO_2, NIRS–SaO_2)$
- PCOH2 = $COH(MABP, NIRS–SaO_2)$
- PCOH3 = $COH(MABP–i(SaO_2), NIRS–i(SaO_2))$
- PCOH4 = $COH(MABP, NIRS–i(SaO_2))$

where $COH(\ldots, \ldots)$ is the coherence computed between both signals. For all patients we studied the performances of PCOH compared to COH on a global basis, but we also looked in detail at epochs with fluctuating SaO_2 and compared the results when using extra raw (non pre-processed) data.

4 Results

When considering all patients, we saw a trend of higher *mPCOH*s as compared to *mCOH*. In addition the *CPRT*s and *PPI*s of PCOH were generally higher as compared to the *CPRT* and *PPI*s of COH. PCOH3 shows a higher *mPCOH*, *CPRT, and PPI* than the other PCOH algorithms, and than PCOH2 which shows the lowest values. For more details we refer to Tables 1, 2 and 3. We also considered patients for whom the oxygen fraction of the inspired air has been intentionally modified. We particularly concentrated on epochs with a high variance in SaO_2. In these epochs, mean scores were significantly higher with PCOH3 as the highest. More details are given in Table 4 and Fig. 1

Table 1 Mean score, standard deviation (*std*), critical percentage of the recording time (*CPRT*), and pressure-passive index (*PPI*) with confidence level $\alpha = 0.1$ of the Leuven data. The numbers below are averages on the ten infants from Leuven

Leuven	COH	PCOH1	PCOH2	PCOH3	PCOH4
Mean	0.39	0.41	0.41	0.44	0.42
Std	0.09	0.1	0.09	0.12	0.1
CPRT	14%	20%	14%	27%	22%
PPI10	10.64%	12.40%	11.60%	18.35%	17.02%

Table 2 Mean score, standard deviation, *CPRT*, and *PPI10* of the Utrecht data. The numbers below are averages on the ten infants from Utrecht

Utrecht	COH	PCOH1	PCOH2	PCOH3	PCOH4
Mean	0.35	0.34	0.33	0.39	0.36
Std	0.09	0.09	0.09	0.1	0.09
CPRT	13%	11%	8%	22%	17%
PPI10	20.80%	19.30%	15.10%	28.16%	21.45%

Table 3 Mean score, standard deviation, *CPRT*, and *PPI10* of the Zurich data. The numbers below are averages on the ten infants from Zurich

Zurich	COH	PCOH1	PCOH2	PCOH3	PCOH4
Mean	0.57	0.61	0.57	0.63	0.63
Std	0.09	0.1	0.09	0.12	0.12
CPRT	72%	75%	70%	80%	71%
PPI10	17.02%	34.02%	19.27%	40.06%	29.04%

Table 4 Local analysis: the oxygen fraction inhibited by the infant has, in some Zurich patients, intentionally been modified to create locally a high variance in SaO_2. The table contains the overall score means of such a patient, and the means related to the epoch of high SaO_2 variance (20–40 min). Please see also Fig. 1

Zurich	*mCOH*	*mPCOH1*	*mPCOH2*	*mPCOH3*	*mPCOH4*	$stdSaO_2$
Overall	0.55	0.52	0.52	0.61	0.57	1.2
20–40	0.64	0.51	0.61	0.75	0.73	2.51

mPCOH3 detects a few more patients with impaired autoregulation than do *mCOH* and the other *mPCOHs*. The *CPRT* and *PPI10* (with confidence level $\alpha = 0.1$) detects many more patients with impaired autoregulation than *mCOH* and *mPCOHs*, and approximately twice as many patients as *PPI5* ($\alpha = 0.05$).

Patients with *mCOH* and *mPCOHs* > 0.5 have a slightly lower mean PMA and BW than the overall average. High PCOH values ($m > 0.5$, $CPRT > 0$, $PPI > 0$) are better indicators of poor clinical outcome than COH (MDI < 84, PDI < 84, Apgar < 7). *CPRT* and *PPI10* are better indicators of poor clinical outcome than mean score values.

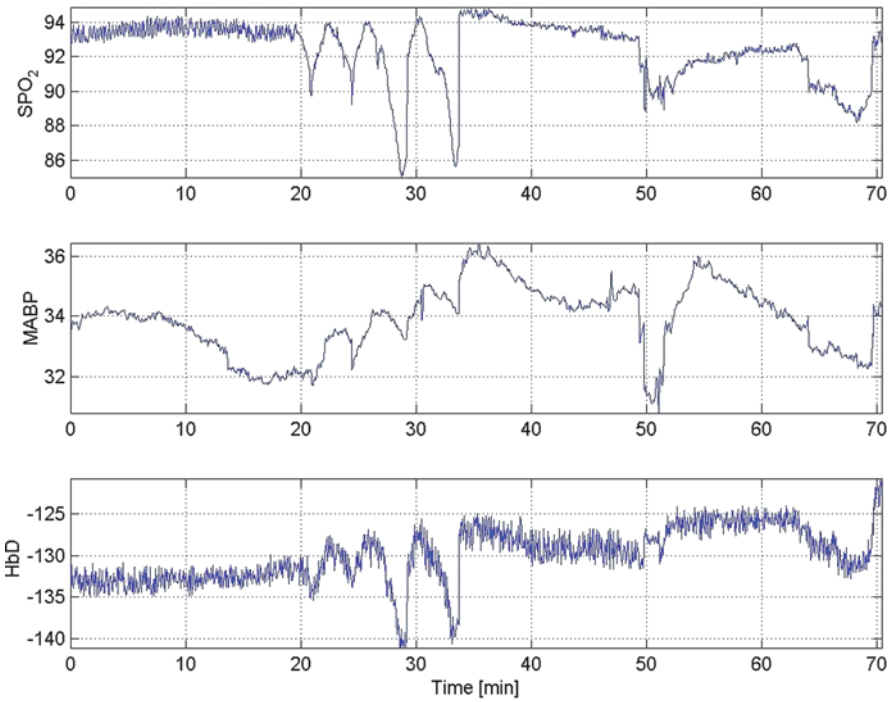

Fig. 1 Local analysis: the oxygen fraction inhibited by the infant has, in some Zurich patients, intentionally been modified to create locally a high variance in SaO_2. Please see also Table 4

5 Discussion

It is important to remember that COH and PCOH are measurements of impaired cerebral autoregulation, and that the considered clinical patient characteristics suggest possible brain damage. An evident correlation between impaired autoregulation and brain damage in neonates has been described in the literature and this is what we assume in this study. We looked for the method that best fits the occurrences of brain damage. Our results indicate that (1) the PCOH score is more accurate in detecting infants with brain malfunctions as compared to the COH method; (2) PCOH3 has the highest accuracy in detecting impaired autoregulation.

In particular, the *CPRT* and *PPI10* – computed from the COH and PCOH scores – detect more than 50% of all infants with poor clinical outcomes. These observations indicate rather that PCOH highlights more cases of impaired autoregulation as compared to COH, and does not necessarily mean that PCOH indicates a better fit between patients with impaired autoregulation and patients with poor clinical outcome. However, we should remark that in this study the patient characteristics and outcomes are not available for all

patients whereas further statistical analysis on larger multicentre datasets are needed

We expected the PCOH4 model to be more realistic than the PCOH3 method, because SaO_2 was seen to have an influence on MABP only in those recordings with changes in SaO_2 which were deliberately provoked by modifying the inspired oxygen fraction. Nevertheless, this could not be confirmed by our results. Furthermore, a lack of concordance with patient neurological outcomes could also be explained by the fact that COH (and consequently PCOH) only measures the linear and stationary concordance between MABP and the NIRS-measured signals, or by the fact that PCOH assumes a linear dependency between the considered signals.

In conclusion, as HbD/rSO_2/TOI are often considered as surrogate for CBF, impaired autoregulation can be assessed by quantifying the concordance between these signals and MABP. As it is able to eliminate the influence of other signals such as SaO_2, the partial coherence method was shown to perform better than the classical coherence method.

Acknowledgments The research was supported by: Research Council KUL: GOA AMBioRICS, CoE EF/05/006, by FWO projects G.0519.06 (Non-invasive brain oxygenation), and G.0341.07 (Data fusion), by Belgian Federal Science Policy Office IUAP P5/22.

References

1. Tsuji M, Saul J, du Plessis A et al. (2000) Cerebrl intravascular oxygenation correlates with mean arterial pressure in critically ill premature infants. Pediatr Rev 106(4):625–632.
2. Leuridan J, Rost B (1985) Multiple input estimation of frequency response functions: diagnostic techniques for the excitation. ASME 85-DET-107.
3. Soul J, Hammer P, Tsuji M et al. (2007) Fluctuating pressure-passivity is common in the cerebral circulation of sick premature infants. Pediatr Res 61(4):467–473.
4. De Smet D, Vanderhaegen J, Naulaers G et al. (2008) New measurements for assessment of impaired cerebral autoregulation using near-infrared spectroscopy. Proceedings of the 2007 ISOTT conference, Uppsala (Sweden), to be published in 2008.
5. de Boer R, Karemaker J, Strackee J (1985) Relationships between short-term blood-pressure fluctuations and heart-rate variability in resting subjects, I: a spectral analysis approach. Med Biol Eng Comput 23:352–358.

Active Muscle Oxygenation Dynamics Measured During High-Intensity Exercise by Using Two Near-Infrared Spectroscopy Methods

Tadashi Saitoh, Anna Ooue, Narihiko Kondo, Kyuichi Niizeki, and Shunsaku Koga

Abstract Near-infrared spectroscopy is a noninvasive optical technique used to monitor tissue oxygenation. Generally, the modified Beer-Lambert's law (MBL) using continuous-wave light has been used to measure active muscle oxygenation during exercise; however, it cannot measure absolute changes in the oxy- (oxy-[Hb + Mb]), deoxy- (deoxy-[Hb + Mb]), and total hemoglobin/myoglobin concentrations (total-[Hb + Mb]) because the pathlength and scattering coefficient are not measured. In contrast, the time-resolved spectroscopy (TRS) using a ultra short pulsed laser can be used to determine absolute changes in the concentration, although the temporal resolution is inferior to that in MBL. This study evaluated the absolute changes in active muscle oxygenation and the optical mean pathlength and scattering and absorption coefficient during high-intensity exercise by using the TRS system. In addition, the difference between the changes determined using TRS and MBL measurements was assessed. When the TRS and MBL measurements obtained during high-intensity exercise were compared, the total-[Hb + Mb] and oxy-[Hb + Mb] dynamics differed markedly during high-intensity exercise, while the deoxy-[Hb + Mb] dynamics and kinetics did not differ.

1 Introduction

Near-infrared spectroscopy (NIRS), which is the spectrum measurement method based on the absorption of light in the near-infrared radiation wave length region that is generally from 0.7 to 2.5 μm, is widely used as a noninvasive measurement method of oxygenation in biological tissues, which are an optical scatterer [8, 10]. The modified Beer-Lambert law (MBL) system that is a continuous wave NIRS system and assumes that scattering and mean optical

T. Saitoh (✉)
Department of Bio-System Engineering, Graduate School of Science and Engineering, Yamagata University, Yonezawa, 992-0038, Japan
e-mail: saitoh-t@yz.yamagata-u.ac.jp

E. Takahashi, D.F. Bruley (eds.), *Oxygen Transport to Tissue XXXI*, Advances in Experimental Medicine and Biology 662,
DOI 10.1007/978-1-4419-1241-1_32, © Springer Science+Business Media, LLC 2010

pathlength are constant [2, 8] estimates simultaneously the relative changes in the concentrations of oxyhemoglobin/myoglobin (oxy-[Hb + Mb]) and deoxyhemoglobin/myoglobin (deoxy-[Hb + Mb]) but not absolute changes in the concentrations of oxy- and deoxy-[Hb + Mb]. On the other hand, although temporal resolution is inferior to that in the MBL system, the time-resolved spectroscopy (TRS) system that is the ultra short pulse NIRS system can estimate the absolute values of oxy- and deoxy-[Hb + Mb] because the mean optical pathlength is measured from the center of gravity of the temporal response characteristic and scattering and absorption coefficient are estimated using the optical diffusion equation [9].

Several interesting studies showing dynamic changes in the active muscle oxygenation measured using NIRS have been reported [1, 4–7]. Most of these studies have also used the MBL system for estimating tissue oxygenation [1, 5–7]. However, it is possible that a contraction of active skeletal muscle and an environmental change in the cellular tissue by exercise influence the mean optical pathlength and scattering and absorption coefficient during exercise, particularly high-intensity exercise. If the mean optical pathlength and/or scattering and absorption coefficient change at the work-rate transition or during exercise, it may influence the estimation of tissue oxygenation by NIRS. This influence can be elucidated by TRS measurement which can estimate the mean optical pathlength and scattering and absorption coefficient. In this study, we aimed to evaluate the mean optical pathlength and scattering and absorption coefficient by using the TRS system and investigate the difference between MBL measurement and TRS measurement during high-intensity exercise.

2 Methods

Seven healthy men (mean ± SD: age, 22.7 ± 4.7 years; height, 168.4 ± 7.0 cm; body mass, 56.7 ± 6.3 kg) who exercise regularly participated in this study, which was approved by the Human Subjects Committee of Kobe Design University. All exercise tests were performed on an electronically braked cycle ergometer in a sitting position. In each subject's first visit to the laboratory, a ramp incremental cycling exercise test was performed to determine his individual peak of pulmonary oxygen uptake (pVO_2) for each exercise mode. In the second visit to the laboratory after 3 days from the first visit, each subject performed a high-intensity cycling exercise test. The protocol consisted of 1 min rest and 4 min of unloaded exercise, followed by 6 min of heavy exercise (work-rate of 80% peak pVO_2 intensity).

Throughout the experiment, gas exchange and heart rate (HR) measurements were performed similar to those described previously [7]. Muscle oxygenation profiles of the quadriceps vastus lateralis muscle were evaluated by the MBL (NIRO-200, Hamamatsu Photonics KK, Japan) and TRS systems

(TRS-20, Hamamatsu Photonics KK). In both systems, the distal probes were set on an optically dense plastic board, thus ensuring that the position of the probes, with a distance of 3 cm from each other, was fixed and invariant. The probes of NIRO-200 were attached to the vastus lateralis of the left leg and the probes of TRS-20 were attached to the vastus lateralis of the right leg by using double-sided tape and surgical tape. The NIRS data were collected continuously throughout the experiment. The relative and absolute changes in the concentrations of total hemoglobin/myoglobin (total-[Hb + Mb]) were calculated from oxy-$[Hb + Mb]_{MBL}$ + deoxy-$[Hb + Mb]_{MBL}$ and oxy-$[Hb + Mb]_{TRS}$ + deoxy-$[Hb + Mb]_{TRS}$, respectively.

To evaluate the adjustment deoxy- and total-[Hb + Mb] kinetics prior to the slow component, each data was respectively fitted using a nonlinear least squares regression technique and a single exponential function of form:

$$Y(t) = BL + Amp \cdot [1 - e^{-(t-TD)/\tau}]$$

where $Y(t)$ represents each response at a given time t; BL represents the baseline data before starting the heavy exercise; and Amp, TD, and τ represent the amplitude, time delay, and time constant of the primary component, respectively. For the deoxy-[Hb + Mb] kinetics, the analyses were conducted on data from 30-s baseline cycling to the first 60 s following the increase in work-rate. For the total-[Hb + Mb] kinetics, the analyses were conducted on data from 30-s baseline cycling to the first 180 s following the increase in work-rate.

The amplitude of deoxy- and total-[Hb + Mb] in the slow component was evaluated for each data from 3 to 6 min after the onset of the high-intensity exercise.

Significant statistical differences between the MBL and TRS measurements were analyzed by a paired t-test. Statistical significance was accepted at $P < 0.05$.

3 Results

All the subjects participated in daily exercise, and the subjects' peak pVO_2 was 3069.5 ± 551.4 ml/min and peak pVO_2/body mass was 53.8 ± 4.2 ml/(min·kg). At rest, the subjects' pVO_2, $pVCO_2$, and HR were 299.6 ± 44.1 ml/min, 247.5 ± 45.0 ml/min, and 70.0 ± 13.4 beats/min, respectively.

The dynamics of oxy-, deoxy-, and total-[Hb + Mb] measured using the MBL and TRS systems during the exercise test are shown in Fig. 1, after the initial value in the relative changes evaluated by the MBL measurement was replaced with the value by the TRS measurement. The oxy-[Hb + Mb] decreased rapidly at the start of high-intensity exercise, and the oxy-$[Hb + Mb]_{MBL}$ then increased gradually, while the oxy-$[Hb + Mb]_{TRS}$ remained constant. The deoxy-[Hb + Mb] increased exponentially at the start of high-intensity exercise and then had gradual slow component (Table 1). After the start of high-intensity exercise, the total-$[Hb + Mb]_{TRS}$ increased exponentially, while

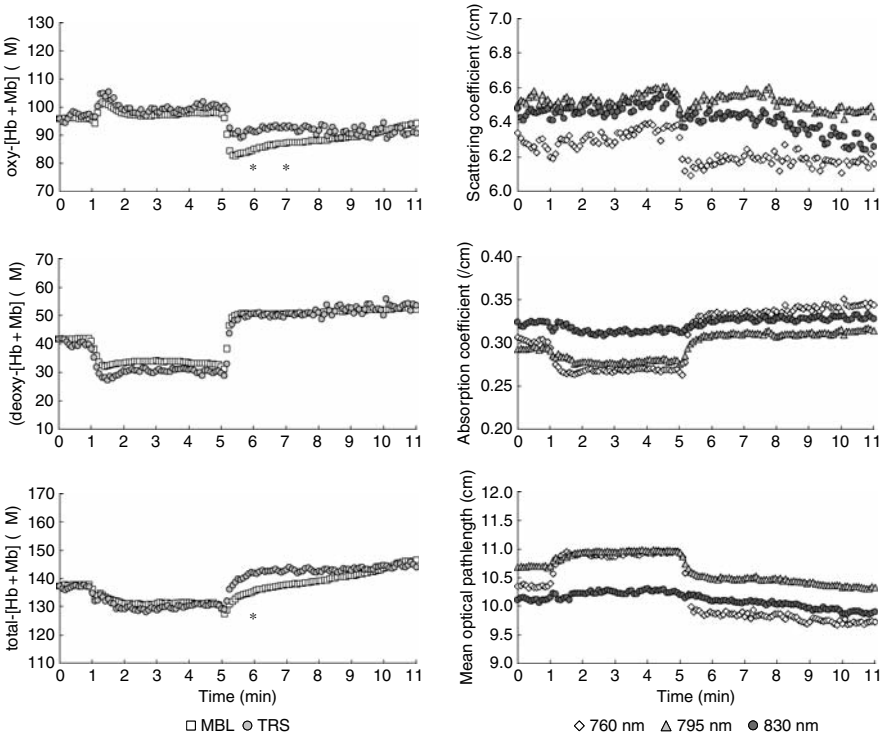

Fig. 1 Oxy-, deoxy-, and total-[Hb + Mb] responses (*left*) and scattering and absorption coefficient and mean optical pathlength (*right*) during the experiment. ∗ significant different between the MBL and TRS measurement ($P < 0.05$)

the total-$[Hb + Mb]_{MBL}$ kept increasing progressively until the end of high-intensity exercise. In the kinetics of deoxy-[Hb + Mb] response, the difference between the MBL and TRS measurement was not significant (Table 1). In the kinetics of total-[Hb + Mb] response, the time constant and amplitude in the slow component of MBL measurement were significantly greater than those of TRS measurement (Table 1; $P < 0.05$)

The mean optical pathlength and scattering and absorption coefficient are shown in Fig. 1. The scattering coefficients of the 3 wavelengths lasers rapidly

Table 1 Kinetic parameters of deoxy- and total-[Hb + Mb] measured using the MBL and TRS systems

	deoxy-[Hb + Mb]		Total-[Hb + Mb]	
	MBL	TRS	MBL	TRS
Amp (μM)	17.6 ± 7.2	19.6 ± 7.7	8.8 ± 4.2	12.5 ± 6.1
TD (s)	8.0 ± 1.5	9.5 ± 2.8	14.8 ± 13.4	6.4 ± 3.5
τ (s)	5.0 ± 1.4	4.9 ± 1.9	54.2 ± 36.3	18.8 ± 12.4 ∗
SC (μM)	1.5 ± 1.2	2.8 ± 3.0	6.9 ± 4.8	2.0 ± 2.0 ∗

∗: significant difference between the MBL and TRS measurements ($P < 0.05$).

decreased after the start of high-intensity exercise. The absorption coefficients of 760- and 795-nm wavelength laser increased exponentially at the start of high-intensity exercise. The absorption coefficient of 830-nm wavelength laser was almost constant until the end of high-intensity exercise. The mean optical pathlengths of the 3 wavelengths lasers showed a pattern completely reverse of that of absorption coefficients.

4 Discussion

In the present study, we first showed simultaneous changes in the mean optical pathlength and scattering and absorption coefficient during high-intensity exercise. In addition, the difference between the 2 muscle oxygenation response that were simultaneously evaluated by the MBL and TRS systems during high-intensity exercise was investigated.

During high-intensity exercise, the scattering coefficients tended to be a little low; the mean optical pathlengths tended to be a little short; and the absorption coefficients tended to be a little high when compared with baseline exercise. These results might suggest that some factors of optical absorption were increased because of the environmental change in the tissue by high-intensity exercise; as a result, it might influence the evaluation of oxy-[Hb + Mb] during high-intensity exercise, particularly immediately after the start of high-intensity exercise.

In a previous study using the MBL system [1, 5], although total-[Hb + Mb] after the start of high-intensity exercise tended to increase progressively as the MBL measurement in the present study, the result of the present study using the TRS system suggests that the total-[Hb + Mb] comparatively rapidly increased, and then achieved a steady state.

Since the total-[Hb + Mb] is the concentration of total hemoglobin and myoglobin per unit volume, there is a possibility that the rapid increase in total-[Hb + Mb] indicate the rapid distribution of capillary blood flow to the active muscle. Ferreira et al. [3] reported the following equation:

$$\text{capillary blood flow} \approx \text{pVO}_2(\text{primary component})/\text{deoxy} - [\text{Hb} + \text{Mb}]$$

However, the kinetics of total-[Hb + Mb] × deoxy-[Hb + Mb] did not coincide with the kinetics of pVO_2 in the primary component in this study (data not shown). Therefore, there is a possibility that the total-[Hb + Mb] response is not approximate to the capillary blood flow response. Further studies are required to clarify this issue.

In conclusion, the present study showed changes in the optical characteristics and dynamics of active muscle oxygenation measured using the MBL and TRS systems simultaneously during high-intensity exercise. It was suggested that the evaluation of active muscle oxygenation was influenced by the changes in

optical characteristics. It was also confirmed that the kinetics of deoxy-[Hb + Mb] response was not significantly different between the MBL and TRS measurements. Furthermore, it was clarified that total-$[Hb + Mb]_{TRS}$ showed a faster exponential increase compared with MBL, and then achieved a steady state for a while.

References

1. DeLorey DS, Kowalchuk JM, Paterson DH (2005) Adaptation of pulmonary O_2 uptake kinetics and muscle deoxygenation at the onset of heavy-intensity exercise in young and older adults. J Appl Physiol 98: 1697–1704.
2. Delpy DT, Cope M, van der Zee P et al. (1988) Estimation of optical pathlength through tissue from direct time of flight measurement. Phys Med Biol 33: 1433–1442.
3. Ferreira LF, Harper AJ, Townsend DK et al. (2005) Kinetics of estimated human muscle capillary blood flow during recovery from exercise. Exp Physiol 90: 715–726.
4. Ferreira LF, Lutjemeier BJ, Townsend DK et al. (2005) Dynamics of skeletal muscle oxygenation during sequential bouts of moderate exercise. Exp Physiol 90: 393–401.
5. Jones AM, Berger NJA, Wilkerson DP et al. (2006) Effects of "priming" exercise on pulmonary O_2 uptake and muscle deoxygenation kinetics during heavy-intensity cycle exercise in the supine and upright positions. J Appl Physiol 101: 1432–1441.
6. Kime R, Im J, Moser D et al. (2005) Reduced heterogeneity of muscle deoxygenation during heavy bicycle exercise. Med Sci Sports Exerc 37: 412–417.
7. Koga S, Poole DC, Ferreira LF et al. (2007) Spatial heterogeneity of quadriceps muscle deoxygenation kinetics during cycle exercise. J Appl Physiol 103: 2049–2056.
8. Owen-Reece H, Smith M, Elwell CE et al. (1999) Near infrared spectroscopy. Br J Anaesth 82: 418–426.
9. Patterson MS, Chance B, Wilson BC (1989) Time resolved reflectance and transmittance for the non-invasive measurement of tissue optical properties. Appl Op 28: 2331–2336.
10. Wray S, Cope M, Delpy DT et al. (1988) Characterization of the near infrared absorption spectra of cytochrome aa3 and haemoglobin for the non-invasive monitoring of cerebral oxygenation. Biochim Biophys Acta 933: 184–192.

Theoretical and Experimental Investigation of the Influence of Frontal Sinus on the Sensitivity of the NIRS Signal in the Adult Head

Eiji Okada, Daisuke Yamamoto, Naoya Kiryu, Akihisa Katagiri, Noriaki Yokose, Takashi Awano, Kouji Igarashi, Sin Nakamura, Tatsuya Hoshino, Yoshihiro Murata, Tsuneo Kano, Kaoru Sakatani, and Yoichi Katayama

Abstract The sensitivity of the near-infrared spectroscopy signal to the brain activation depends on the thickness and structure of the superficial tissues. The influence of the frontal sinus, which is void region in the skull, on the sensitivity to the brain activation is investigated by the time-resolved experiments and the theoretical modelling of the light propagation in the head. In the time-resolved experiments, the mean-time of flight for the forehead scarcely depends upon the existence of the frontal sinus when probe spacing was shorter than 30 mm. The partial optical path length in the brain, which indicates the sensitivity of the near-infrared spectroscopy signal to the brain activation, in a simplified head model is predicted by Monte Carlo simulation. The influence of the frontal sinus on the sensitivity of the signal depends on the thickness of the skull and the depth of the frontal sinus.

1 Introduction

In near infrared spectroscopy (NIRS) and imaging of brain activation, the source and detection probes are attached onto the scalp, requiring the light to pass through the superficial layers such as scalp, skull, and subarachnoid space filled with cerebrospinal fluid (CSF) both before and after passing through the brain tissue. The heterogeneity of the tissue in the head, especially the low-scattering subarachnoid space has been previously shown to have a strong effect on light propagation in the brain i.e. the sensitivity of the NIRS signal [1]. The frontal sinus in the skull is a non-absorption and non-scattering (void) region. The existence of the frontal sinus is likely to affect the light propagation in the brain. In this study, the mean optical path length in the head and the partial optical path length in the brain are obtained by the time-resolved experiment

E. Okada (✉)
Department of Electronics and Electrical Engineering, Keio University, Yokohama, Japan
e-mail: okada@elec.keio.ac.jp

E. Takahashi, D.F. Bruley (eds.), *Oxygen Transport to Tissue XXXI*, Advances in Experimental Medicine and Biology 662,
DOI 10.1007/978-1-4419-1241-1_33, © Springer Science+Business Media, LLC 2010

and Monte Carlo simulation to investigate the influence of the frontal sinus on the sensitivity of the NIRS signal to the brain activity.

2 Methods

2.1 Time-Resolved Experiments

The temporal point spread functions (TPSFs) of the forehead of two volunteers were measured by the time-resolved experiment system (TRS-20, Hamamatsu). Figure 1 shows the probe positions of the time-resolved experiments for a volunteer. Each number in the figure indicates the midpoint of the source and detector probes. The probes were attached on the scalp with and without the frontal sinus below. The probe spacing was varied from 22.5 to 37.5 mm. The mean optical path length in the head was calculated from the TPSF.

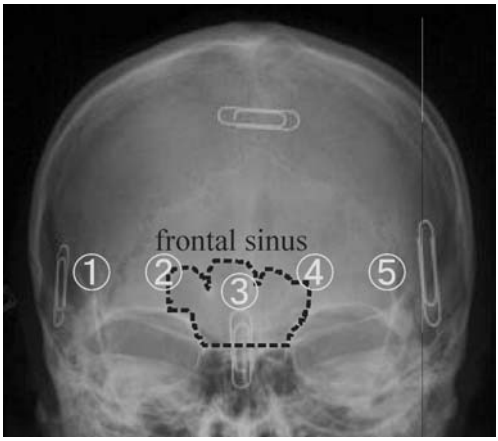

Fig. 1 Probe positions for the time-resolved experiment. The numbers indicate the midpoints of the source and detector probes. The broken line indicates the frontal sinus

2.2 Modelling of the Light Propagation in the Head Model

The light propagation in the simplified head model was calculated to analyse the influence of the frontal sinus on the mean optical path length in the head and on the partial optical path length in the brain. The mean optical path length in the head can be obtained from the TPSF measured by the time-resolved experiment whereas the partial optical path length in the brain cannot be directly obtained from the experimental results. The cross-section of the head model is shown in Fig. 2. The head model consisted of the scalp, skull, subarachnoid space, grey matter and white matter. The optical properties (transport scattering coefficient μ_s' and absorption coefficient μ_a) of each layer for 780-nm wavelength shown in Table 1 were chosen from the reported data [2–5].

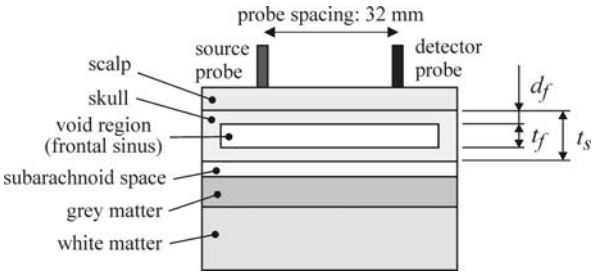

Fig. 2 An adult head model with a void region mimicking the frontal sinus for the estimation of mean optical path length in the head and partial optical path length in the brain

Table 1 The thickness and the optical properties of the head models

Tissue type	Thickness [mm]	μ_s' [mm^{-1}]	μ_a [mm^{-1}]
Scalp	3	1.0	0.02
Skull	7 ~ 21	0.8	0.016
Subarachnoid space	2	0.319	0.0044
Grey matter	4	2.26	0.036
White matter	20	9.25	0.016

The void rectangular region was placed in the skull to mimic the frontal sinus. The depth of the void region d_f, thickness of the skull t_s and void region t_f were varied to evaluate the influence of the frontal sinus on the light propagation in the brain. Reflection and refraction caused by the refractive index mismatch was considered only at the boundary between the scalp and the air. The light propagation in the head model was predicted by Monte Carlo simulation to obtain the mean optical path length in the head and the partial optical path length in the brain for the probe spacing of 32 mm.

3 Results and Discussion

The measured TPSFs of a volunteer for the probe spacing of 37.5 mm at positions 3 and 5 are shown in Fig. 1 and the input pulses are shown in Fig. 3(a). The wavelength of the pulsed laser was 760 nm. The mean time of flight for the forehead with the frontal sinus below (position 3) is shorter than that without the frontal sinus (position 5). The mean optical path length calculated from the TPSFs as a function of probe spacing at each position is shown in Fig. 3(b). The mean-time of flight scarcely depends upon the existence of the frontal sinus when probe spacing was shorter than 30 mm. The mean optical path length for the forehead with the frontal sinus (position 2 and 3) was shorter than that without the frontal sinus when probe spacing was 37.5 mm. The influence of the frontal sinus on the TPSFs of other volunteer was not significant. The influence of the frontal sinus on the light propagation in the head differs among individuals.

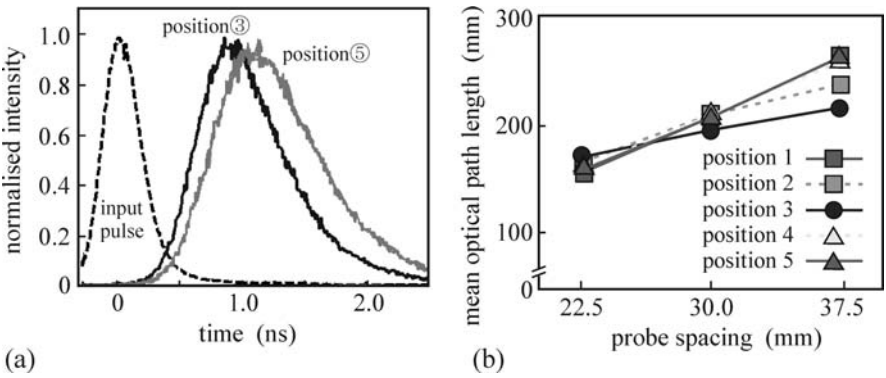

Fig. 3 (**a**) The TPSFs of human forehead measured by the time-resolved experiments. (**b**) The mean optical path length calculated from the TPSFs

The mean optical path length and the partial optical path length in the brain for the head models with and without a void region mimicking the frontal sinus as a function of skull thickness are shown in Fig. 4(a). The void region was located at an intermediate depth into the skull and the thickness of the void region was a third of the skull thickness. The mean optical path length in the head with the frontal sinus is shorter than that without the frontal sinus when the thickness of the skull is 7 or 14 mm as shown in Fig. 4(a). The frontal sinus does not affect the mean optical path length in the head model with a 21-mm thick skull. The partial optical path length in the brain, which is the sensitivity of the NIRS signal to the brain activation, decreases with an increase in skull thickness. The partial optical path length is decreased by the influence of the frontal sinus when the skull thickness of the model was 7 mm whereas the partial optical path length is slightly increased when the skull thickness was 14 or 21 mm.

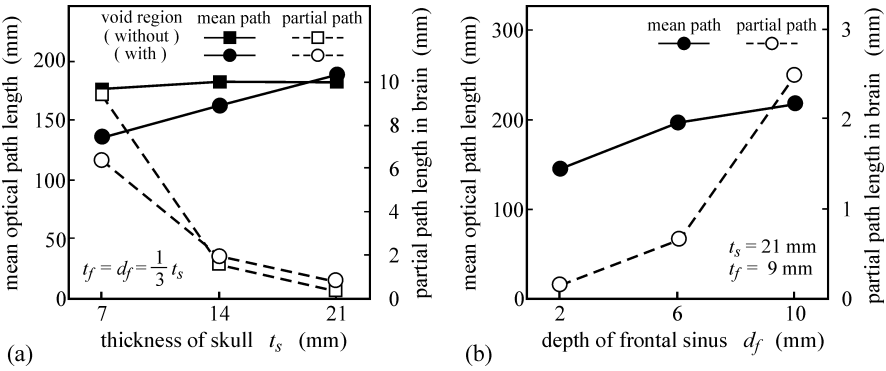

Fig. 4 Effect of skull thickness on the mean optical path length in the head and the partial optical path length in the brain

The influence of the depth of the frontal sinus on the light propagation in the head is shown in Fig. 4(b). The depth of the void region, d_f, was altered but the thickness of the skull and of the void region were held constant at 21 and 9 mm, respectively. In the case where the void region is placed in the shallow region ($d_f = 2$ mm), the light tends to propagate in the shallow region of the skull. Both the mean optical path length in the head and partial optical path length in the brain are decreased by the influence of the frontal sinus. In the case where the void region is placed in the deep region ($d_f = 10$ mm), the light tends to propagate in the deeper region of the skull. The partial path length in the brain is increased by the influence of the frontal sinus whereas the mean optical path length in the head is scarcely changed by the influence of the frontal sinus. The penetration depth, which relates with the sensitivity of the NIRS signal to the brain activation, increases with an increase in the depth of the frontal sinus. The influence of the frontal sinus on the partial optical path length in the brain is more significant than that on the mean optical path length in the head.

4 Conclusions

The mean optical path length of the forehead and the partial optical path length in the brain are obtained by the time-resolved experiments and the modelling of the light propagation in the head to investigate the influence of the frontal sinus on the sensitivity of the NIRS signal to the brain activation. The theoretical analysis reveals that influence of the frontal sinus on the light propagation in the head depends on the thickness of the skull and the depth of the frontal sinus. In the practical brain-function measurements, the amplitude of the NIRS signal reflects the influence of the frontal sinus. The influence of the frontal sinus on the partial optical path length in the brain, i.e. the sensitivity of the NIRS signal to the brain activation, is more significant than that on the mean optical path length in the head. The change in partial optical path length caused by the influence of the frontal sinus cannot be directly deduced from the mean optical path length in the head obtained from the time-resolved experiments. In the experimental analysis, the influence of the frontal sinus on the mean optical path length varies between individuals. Although the difference might be caused by the depth of the frontal sinus, the TPSF measurements in this study were made in two volunteers. It is difficult to draw any conclusions about the influence of the frontal sinus on the TPSF from the experimental results and further TPSF measurements are needed for systematic discussion.

Acknowledgments This work was partly supported by Japan Society for the Promotion of Science, Grant-in-Aid for Scientific Research (B) (19360035) and by a Grant-in-Aid for the Global Center of Excellence for High-Level Global Cooperation for Leading-Edge Platform on Access Spaces from the Ministry of Education, Culture, Sport, Science, and Technology in Japan.

References

1. E. Okada and D. T. Delpy, "Near-infrared light propagation in an adult head model. I Modeling of low-level scattering in the cerebrospinal fluid layer," Appl. Opt. 42(16), 2906–2914 (2003).
2. C. R. Simpson, M. Kohl, M. Essenpreis, and M. Cope, "Nearinfrared optical properties of ex vivo human skin and subcutaneous tissues measured using the Monte Carlo inversion technique," Phys. Med. Biol. 43, 2465–2478 (1998).
3. M. Firbank, M. Hiraoka, M. Essenpreis, and D. T. Delpy, "Measurement of the optical properties of the skull in the wavelength range 650–950 nm," Phys. Med. Biol. 38, 503–510 (1993).
4. P. van der Zee, M. Essenpreis, and D. T. Delpy, "Optical properties of brain tissue," in Photon Migration and Imaging in Random Media and Tissues, B. Chance and R. R. Alfano, eds., Proceedings of SPIE 1888, 454–465 (1993).
5. E. Okada and D. T.Delpy, "Near-infrared light propagation in an adult head model. II Effect of superficial tissue thickness on the sensitivity of the near-infrared spectroscopy signal," Appl. Opt. 42(16), 2915–2922 (2003).

Functional Optical Topography Analysis Using Statistical Parametric Mapping (SPM) Methodology with and without Physiological Confounds

Ilias Tachtsidis, Peck H. Koh, Charlotte Stubbs, and Clare E. Elwell

Abstract Functional optical topography (OT) measures the changes in oxygenated and deoxygenated hemoglobin (HbO_2, HHb) across multiple brain sites which occur in response to neuronal activation of the cerebral cortex. However, identification of areas of cortical activation is a complex task due to intrinsic physiological noise and systemic interference and careful statistical analysis is therefore required. A total of 10 young healthy adults were studied. The activation paradigm comprised of anagrams followed by finger tapping. 12 channels of the OT system were positioned over the frontal cortex and 12 channels over the motor cortex while the systemic physiology (mean blood pressure (MBP), heart rate (HR), scalp flux) was simultaneously monitored. Analysis was done using the functional Optical Signal Analysis (fOSA) software and Statistical Parametric Mapping (SPM), where we utilized two approaches: (i) using only HbO_2 as a regressor in the general linear model (GLM) and (ii) using all of the explanatory variables (HbO_2, MBP, HR and scalp flux) as regressors. Group analysis using SPM showed significant correlation in a large number of OT channels between HbO_2 and systemic regressors; however no differences in activation areas were seen between the two approaches.

1 Introduction

Optical topography (OT) techniques to map functional brain activation rely on making simultaneous near-infrared spectroscopy (NIRS) measurements of changes in oxygenated and deoxygenated hemoglobin (HbO_2, HHb) concentration at multiple brain sites. The generated spatial maps of the hemoglobin concentration changes correspond to specific regions of the cerebral cortex. However, identification of areas of cortical activation require statistical analysis with researchers using classical statistical approaches such as "Student's *t*-test"

I. Tachtsidis (✉)
Biomedical Optics Research Laboratory, Department of Medical Physics and Bioengineering, University College London, Gower Street, London, WC1E 6BT, UK
e-mail: iliastac@medphys.ucl.ac.uk

E. Takahashi, D.F. Bruley (eds.), *Oxygen Transport to Tissue XXXI*, Advances in Experimental Medicine and Biology 662,
DOI 10.1007/978-1-4419-1241-1_34, © Springer Science+Business Media, LLC 2010

and/or more complex tools such as Principal Component Analysis, Independent Component Analysis, and more recently Statistical Parametric Mapping (SPM) [1–5]. Interpretation of the optical functional activation remains a complex task due to the intrinsic physiological noise and systemic interference [6–8]. The aim of this study is to investigate the use of SPM analysis for interpretation of functional optical topography hemoglobin changes during frontal lobe anagram activation and motor cortex finger tapping activation with and without accounting for physiological and systemic changes.

2 Methods

We studied 10 subjects (5 male and 5 female), all had English as their first language and were right handed (this study was approved by the UCL Research Ethics Committee). The age range was between 19 and 27 years with a mean age of 22 years.

NIRS measurements were conducted with the ETG-100 Optical Topography System (Hitachi Medical Co., Japan) using two 12-channel arrays. Each optode array consisted of 5 source optodes (each delivering light at 780 and 830 nm) and 4 detector optodes. The source-detector interoptode spacing was 30 mm and data were acquired at 10 Hz. The optodes were placed over the subject's left frontal cortex and positioned according to the International 10–20 system of electrode placement such that channels 1–12 were centered approximately over the frontopolar region (Fp) and channels 13–24 were centered approximately over the left primary motor cortex (C3) (see Fig. 1). The Cartesian coordinates of the NIRS optodes placement were measured – in relation to known fiducial landmarks (nasion, inion, left and right ear and top of the head), using the Polhemus tracking device (Isotrak II, USA) and the inter-subject variability were calculated. For this study the x, y and z coordinates of each of the optodes did not vary between subjects by more than ±2 cm of the mean position of each probe.

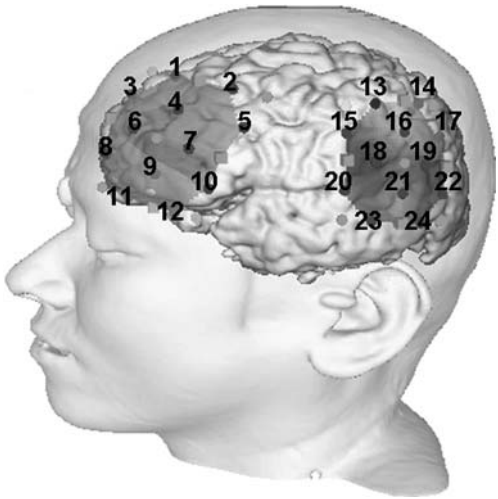

Fig. 1 A picture illustrating the approximate positions of the OT light sources, detectors and locations of corresponding measuring positions/channels co-registered with brain MRI using the Pholemus information (numbers represent OT channels)

A Portapres® system (TNO Institute of Applied Physics) was used to continuously and non-invasively measure mean blood pressure (MBP) and heart rate (HR) from the finger. A laser Doppler probe (FloLab, Moore Instruments) was placed over the forehead to monitor the changes in scalp blood flow (flux).

Data were recorded during 1 min of the subject at rest (baseline), followed by 45 s of the subject solving anagrams (a mixture of 4-letter, 6-letter and 8-letter anagrams), followed by 30 s of rest, followed by 30 s of finger-tapping. In this study solving an anagram was defined as producing one coherent word using only the letters from another word (e.g. icon – coin). Each anagram-solving and finger-tapping period was repeated a total of eight times, with the study ending after a 60 s rest period (total study time 19.5 min). During this functional paradigm the participants were asked to be still and silent; and no response to anagram solving was requested.

All data were subjected to an identical preprocessing procedure using the functional Optical Signal Analysis program (fOSA) [5] (University College London, UK) to convert the relative changes in light intensities to concentration changes in HbO_2 and HHb using a differential pathlength factor correction of 6.26. All the signals including MBP, HR and flux, were linear detrended, then decimated from 10 to 1 Hz and smoothed using a 3-second moving average.

Before performing the statistical analysis using the SPM, image processing of the HbO_2 data was performed using fOSA as described by Koh et al. [5]. In brief, it involves the spatial conversion of the OT maps of each measurement channel to its corresponding pixel location for each of the 24 channels. A series of two-dimensional SPM-OT maps were generated with each SPM-OT map representing a 1-second time point. To improve on the sensitivity and facilitate inter-subject comparisons, an interpolation process using nearest neighbors is used to produce a more realistic data grid.

In our SPM analysis we utilized two approaches to model the OT data; in the first approach we used only the HbO_2 signal in the General Linear Model (GLM) and in the second approach we incorporated the physiological measures (MBP, HR and flux) in addition to the HbO_2 signal as additional regressors in our statistical model. To treat the variability of the haemodynamic response (HbO_2) arising from different events between different brain pixels, we modeled both latency and dispersion derivatives as additional regressors to the canonical Haemodynamic Response Function (HRF) (see Fig. 2) in the two approaches. The design matrix is shown in Fig. 3.

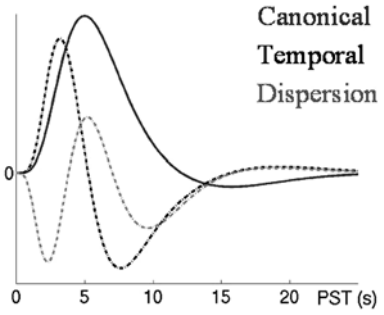

Fig. 2 Canonical HRF (2 gamma functions) plus Multivariate Taylor expansion in time (Temporal Derivative) and width (Dispersion Derivative) [9]

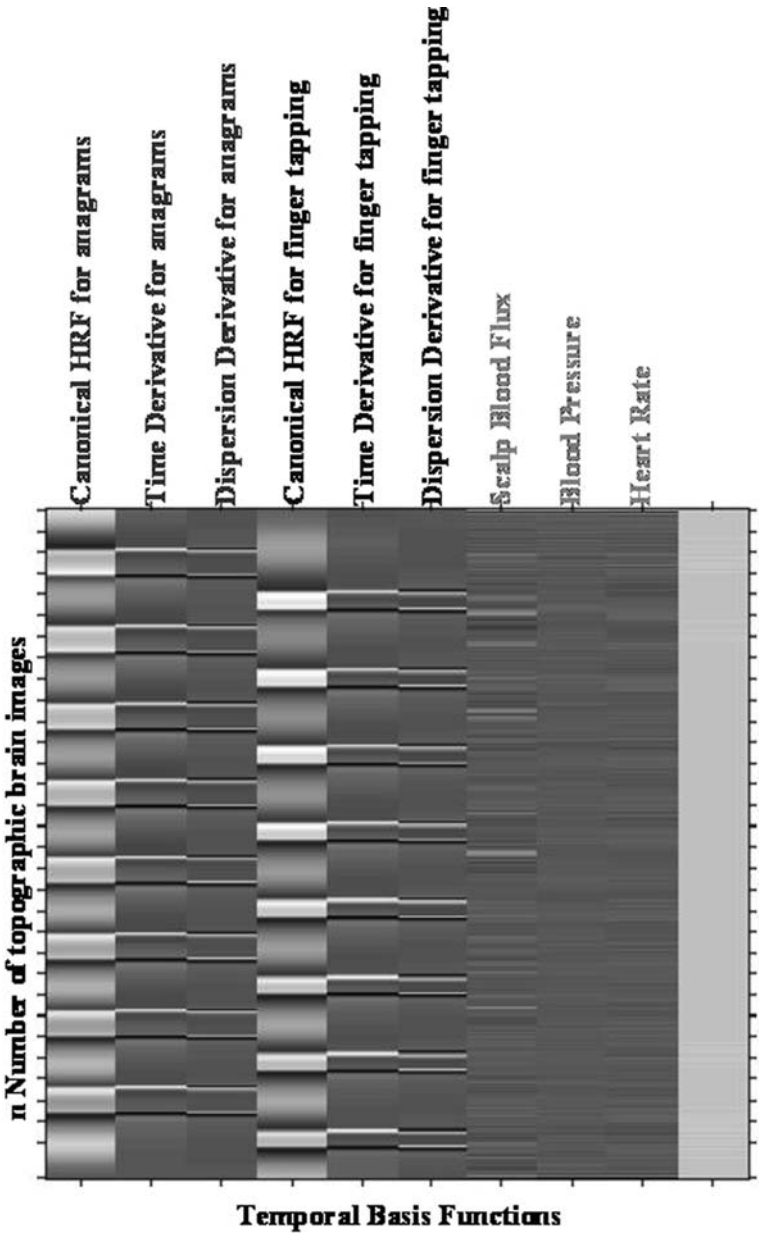

Fig. 3 Design matrix for the oxyhaemoglobin model for the anagrams (first three columns), finger tapping (next three columns) tasks followed by the three regressors (physiological confounds) and a constant error term for the design matrix. Each row represents a time slice of the topographic brain map

The resulting statistical maps were family-wise error corrected to account for the spatial correlation between neighboring pixels in OT measurements. An F-contrast was defined in the SPM test for each subject to infer on any interaction (canonical HRF, its temporal and dispersion derivatives) in each of the two tasks. A group t-statistic was then conducted in SPM to infer on its population level.

3 Results

Figure 4 shows the SPM group t-results, without physiological confounds, for (a) the anagram task and (b) the finger tapping for the HbO_2 signal. Figure 5 hows the SPM group t-results, with physiological confounds, for (a) the anagram and (b) the finger tapping task for the HbO_2 signal. Darker pixels correspond to higher t-values, with positive t scores for HbO_2 signal indicating a significant task related increase in HbO_2. Figure 5(c) shows the SPM group t-results for the physiological confounds; in this map darker pixels correspond to significant correlations of one or a combination of the regressors MBP, HR and flux, with the HbO_2 haemodynamic response.

Results from the group level analysis in the current study have demonstrated that the most significant channels (dark regions) during anagram activation are between 19, 21, 22 and 24 which are on the lower site of the temporal lobe; and during finger tapping are channels 2 and 18 which are on the upper part of the temporal lobe.

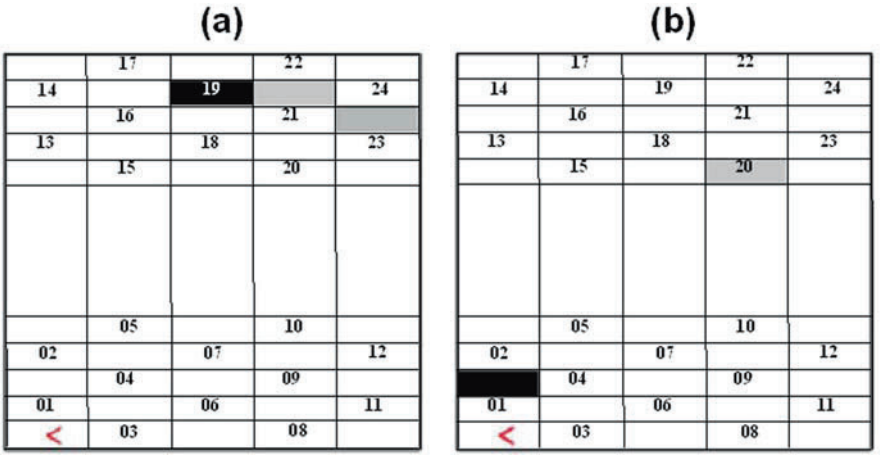

Fig. 4 The SPM group t-results without physiological confounds with a threshold of t = 4.29 and significance of $p = 0.05$; *darker* pixels correspond to higher significant t-values

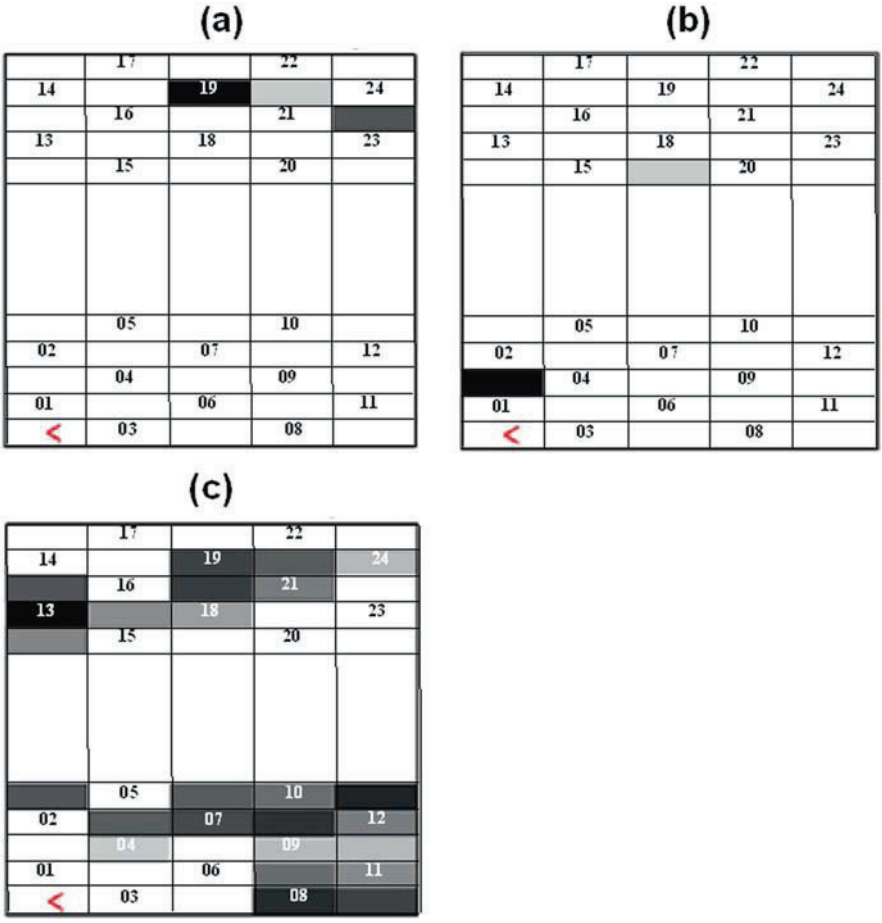

Fig. 5 The SPM group t-results with physiological confounds and a threshold of $t = 4.29$ and significance of $p = 0.05$; *darker* pixels correspond to higher significant t-values

4 Discussion

There were no differences in the activation responses in the SPM group analysis with and without physiological confounds in this functional paradigm. Group level analysis on the systemic regressors shows highly significant correlation of the systemic variables in most channels in the study; however this did not make a difference in the interpretation of the task related HbO_2 response.

Interpretation of the optical data during functional activation remains a complex task as there are many confounds due to different degrees of physiological noise and systemic interference both at the intra and inter subject level. A unified approach of statistical investigation for inference analysis of functional

activation with optical topography is needed. We have previously compared "Student's *t*-test" with SPM methods and found the SPM to be a better analysis tool [8]. Here we detail the SPM method for OT data. However further work is needed to refine the Optical SPM analysis, especially for the development of an optical response function similar to the haemodynamic response function (used in this study).

Acknowledgments The authors would like to acknowledge the EPSRC (Grant No EP/D060982/1).

References

1. Hirosaka R, Katura T, Kawaguchi H et al. (2004) Noisy time-delayed decorrelation and its application to extraction of neural activity from single optical recordings in guinea pigs. Physica D 320–332.
2. Yoshida T, Sakagami M, Yamazaki K et al. (2007) Extraction of neural activity from in vivo optical recordings using multiple independent component analysis. IEEJ Trans EIS 127(10):1642–1650.
3. Zhang X, Toronov V, Webb A (2005) Simultaneous integrated diffuse optical tomography and functional magnetic resonance imaging of the human brain. Opt Express 13(14):5513–5521.
4. Schiessl I, Stetter M, Mayhew JEW et al. (2000) Blind signal separation from optical imaging recordings with extended spatial decorrelation. IEEE Trans Biomed Eng 47(5):573–577.
5. Koh PH, Glaser DE, Flandin G et al. (2007) Functional optical signal analysis (fOSA): a software tool for NIRS data processing incorporating statistical parametric mapping (SPM). JBO 12(6):064010.
6. Tachtsidis I, Leung TS, Devoto L et al. (2008) Measurement of frontal lobe functional activation and related systemic effects: a near-infrared spectroscopy investigation. Adv Exp Med Biol 614:397–403.
7. Tachtsidis I, Leung TS, Tisdall MM et al. (2008) Investigation of frontal cortex, motor cortex and systemic haemodynamic changes during anagram solving. Adv Exp Med Biol 614:21–28.
8. Tachtsidis I, Leung TS, Chopra A et al. (2009) False positives in functional near-infrared topography. Adv Exp Med Biol 645:307–314.
9. Friston KJ, Holmes AP, Poline JB et al. (1995) Analysis of fMRI time-series revisited. NeuroImage 2(1):45–53.

Comparison of Somatosensory Evoked Potentials and Cerebral Blood Oxygenation Changes in the Sensorimotor Cortex During Activation in the Rat

Yuko Kondo, Kaoru Sakatani, Takahiro Igarashi, Tatsuya Hoshino, Yoshihiro Murata, Emiri Tejima, Tsuneo Kano, and Yoichi Katayama

Abstract The relationship between changes in cerebral blood oxygenation and neuronal activity remains to be fully established. We compared somatosensory evoked potentials (SEP) and evoked cerebral blood oxygenation (CBO) changes in the sensorimotor cortex of the rat. In rats anesthetized with urethane and alpha-chloralose, we measured SEP and CBO using visible light spectroscopy (VLS) during neuronal activity. Increase of stimulus frequency caused a decrease of SEP amplitude, but an increase in concentration changes of deoxy-Hb and oxygen satu-ration. The difference in frequency responses between SEP and CBO might be caused by activation of inhibitory neurons, which could suppress excitatory neu-rons at high stimulus frequencies; activation of inhibitory neurons could reduce SEP amplitude, and increase oxygen saturation due to an increase of evoked cere-bral blood flow.

1 Introduction

Increases in neuronal activity in the adult normal brain are accompanied by increases in regional cerebral blood flow (rCBF) that exceeds the changes in oxygen consumption, leading to a decrease in concentration of deoxyhemoglobin (deoxy-Hb) in the veins [1]. NIRS studies have revealed that neuronal activation generally causes a decrease of deoxy-Hb with increases of oxy-Hb and total-Hb in the activation cortical area of normal adults [2, 3]. However, the relationship between changes in cerebral blood oxygenation (CBO) and neuronal activity remains to be fully established. In the present study, we compared somatosensory evoked potentials (SEP) and evoked CBO changes in the sensorimotor cortex of the rat under various stimulus conditions.

Y. Kondo (✉)
Division of Neurological Surgery, Department of Neurological Surgery, Nihon University School of Medicine, Tokyo, Japan
e-mail: yk-mikan@d8.dion.ne.jp

E. Takahashi, D.F. Bruley (eds.), *Oxygen Transport to Tissue XXXI*, Advances in Experimental Medicine and Biology 662,
DOI 10.1007/978-1-4419-1241-1_35, © Springer Science+Business Media, LLC 2010

2 Method

Male Fischer 344 rats ($n = 7$) weighing between 240 and 270 g were anesthetized with urethane (0.7 g/kg) and alpha-chloralose (0.06 g/kg). The right femoral artery was exposed and cannulated for the recording of arterial blood pressure and for sampling of blood gases. The right femoral vein was cannulated for drug administration. The rats were tracheotomized, paralyzed with pancuronium chloride (2 mg/kg/h), and mechanically ventilated with a mixture of air and oxygen to achieve physiological arterial blood levels of pH (7.33–7.50), PaO_2 (150–210 mmHg), and $PaCO_2$ (24–40 mmHg); arterial blood pressure had a range of 90–150 mmHg, and body temperature had a range of 36.2 to 36.8°C. The animals were secured in a stereotaxic frame.

The right parietal bone was thinned over the sensorimotor cortex. Bipolar needle electrodes were inserted beneath the skin in the contralateral forepaw, and the median nerve was stimulated for 10 s with pulses of 8.0 mA intensity and 100 μs duration, at frequencies between 1 and 50 Hz. We recorded SEP and VLS positioned on the forepaw projection area of the somatosensory cortex. We measured SEP amplitude (P1 + N1 amplitude), and calculated ΣSEP amplitude (= SEP amplitude × stimulus frequency) [4].

We evaluated evoked CBO changes in the sensorimotor cortex using visible light spectroscopy (VLS) (C-9183, Hamamatsu Photonics, Japan) during median nerve stimulation with the same stimulus conditions as for SEP. VLS measures the changes of oxy-Hb and deoxy-Hb concentrations in the cerebral vessels based on the characteristic absorption spectra of hemoglobin in the visible light range [5]. White light from the LED was directed at the tissue through a fiber optic bundle, and reflected light was transmitted to a cooled charge-coupled-device spectrome-ter. The relative concentration changes of oxy-Hb and deoxy-Hb were calculated by least-squares error curve-fitting based on the differential spectrum: the ana-lyzed wavelength range was 520–580 nm. The VLS parameters were oxy-Hb, de-oxy-Hb, total-Hb (= oxy-Hb + deoxy-Hb) and oxygen saturation; total-Hb reflects cerebral blood volume (CBV). The sampling rate was 0.5 s.

The data were expressed as means ± SD. Statistical significance of differences was determined by analysis of variance (ANOVA) followed by Dunnet's test, us-ing StatView (Abacus Concepts, USA). P values less than 0.05 were considered as indicating statistical significance.

3 Results

The evoked CBO changes appeared approximately 1.5 s after the stimulus onset. We observed increases of oxy-Hb and oxygen saturation associated with a decrease of deoxy-Hb during activation. Fig. 1a,b, showed examples of changes in oxygen saturation and deoxy-Hb caused by rat forepaw stimuli using VLS. Increases of stimulus frequency caused increases of oxy-Hb and oxygen saturation associated with a decrease of deoxy-Hb; however, total-Hb

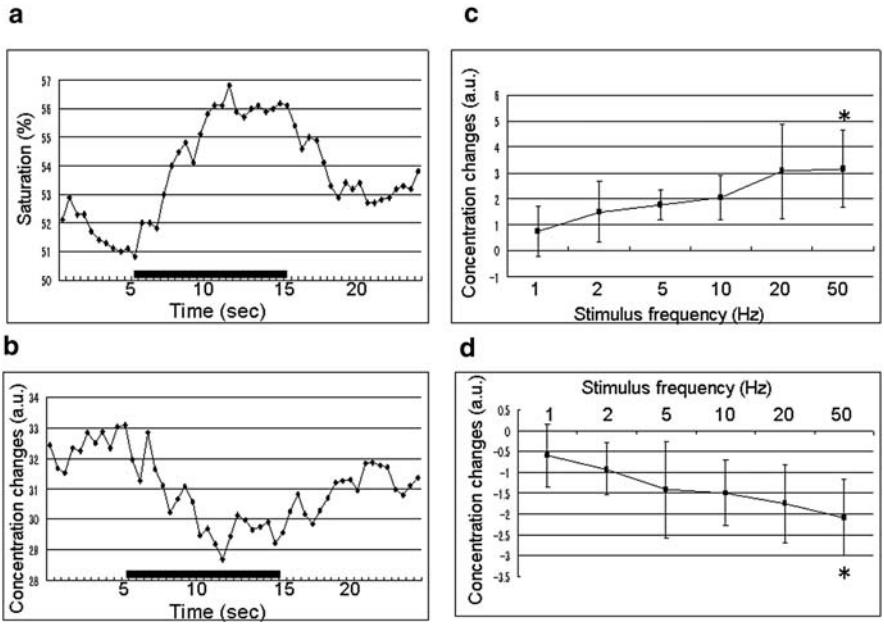

Fig. 1 (**a, b**) Examples of changes in oxygen saturation (**a**) and deoxy-Hb (**b**) caused by rat forepaw stimuli using VLS. The *horizontal thick bars* indicate stimulus periods. (**c, d**) Effect of stimulus frequency on oxygen saturation (**c**) and deoxy-Hb (**d**). Data expressed as means ± SD. There were significant differences in oxygen saturation and deoxy-Hb between 1 and 50 Hz ($P<0.05$)

did not change with increase of the stimulus frequency. The CBO change reached maximum at 50 Hz. There were significant differences in oxygen saturation and deoxy-Hb between 1 and 50 Hz ($p < 0.05$) (Fig. 1c,d).

The SEP amplitude declined with increase of the stimulus frequency (Fig. 2a). In contrast to evoked CBO changes, the maximum ΣSEP amplitude was observed at 2 Hz (Fig. 2b).

4 Discussion

We observed that an increase of stimulus frequency caused increases of oxy-Hb and oxygen saturation with a concomitant decrease of deoxy-Hb. This CBO change is consistent with the evoked CBO change observed during a focal increase of neuronal activity [2, 3]. Positron emission tomography demonstrated that increases of neuronal activity are accompanied by increases of rCBF that exceed the changes in oxygen consumption, leading to a decrease of deoxy-Hb in the veins [1].

Increase of stimulus frequency caused an increase of oxygen saturation with a decrease of deoxy-Hb, which reached the maximum levels at 50 Hz. In

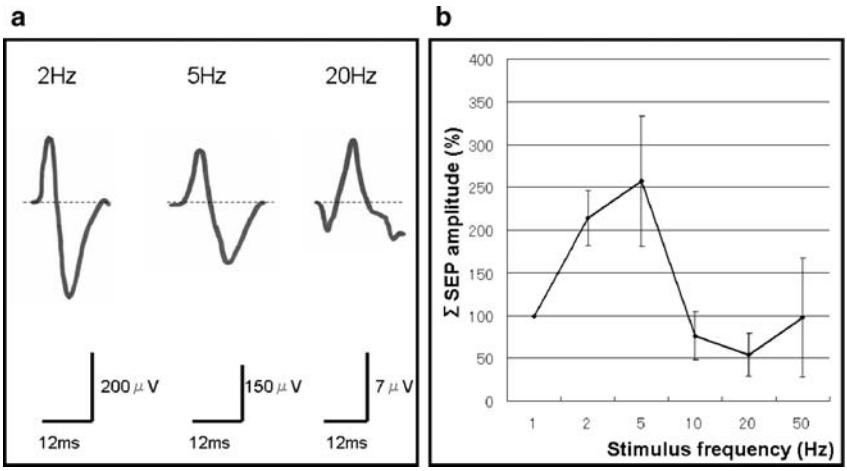

Fig. 2 (**a**) Stimultaneous recordings of somatosensory evoked potentials from one experiment. (**b**) Effect of stimulus frequency on the ΣSEP during rat forepaw stimuli. The maximum ΣSEP amplitude was observed at 5 Hz

contrast, the maximum ΣSEP amplitude was observed at 5 Hz. Ngai et al., employing the same equation for ΣSEP amplitude, evaluated the frequency response of ΣSEP amplitude (1∼20 Hz), and observed the maximum ΣSEP amplitude at 5 Hz [4]. While it is possible that the reductions of SEP are due to either inhibitory mechanisms, habituation of the peripheral nerve, or limitations of transmission of the sensory input, several studies have suggested that inhibitory mechanisms play the most important role in the reduction of SEP at high stimulus frequency [6, 7]. This might explain the physiological mechanism of the difference in frequency responses between SEP and evoked CBO responses. That is, activation of inhibitory neurons at high stimulus frequencies causes an increase of neuronal oxidative metabolism, resulting in an increase of CBO response at high stimulus frequencies. Indeed, Igarashi et al. evaluated the frequency response of the evoked changes in autofluorescence of flavoproteins, which reflect neuronal oxidative metabolism, and observed that the fluorescence attained maximal intensity at 50 Hz [8].

5 Conclusion

We compared SEP and evoked CBO changes in the sensorimotor cortex of the rat. Increases of stimulus frequency caused a decrease of SEP amplitude, but an increase of oxygen saturation with a decrease of deoxy-Hb; however, changes of stimulus frequency did not affect total-Hb concentration. Activation of inhibitory neurons at high stimulus frequencies could decrease the SEP amplitude, but in-crease evoked CBO changes.

References

1. Fox P, Raichle ME, (1986) Focal physiological uncoupling of cerebral blood flow and oxidative metabolism during somatosensory stimulation in human subjects. Proc Natl Acad Sci USA 83:1140–1144.
2. Murata Y, Sakatani K, Hoshino T, et al. (2006) Effect of cerebral ischemia on evoked cerebral blood oxygenation responses and BOLD contrast func-tional MRI in stroke patients, Stroke 37:2514–2520.
3. Sakatani K, Murata Y, Fujiwara N, et al. (2007) Comparison of blood-oxygen-level–dependent functional magnetic resonance imaging and near-infrared spectroscopy recording during functional brain activation in patients with stroke and brain tumors. J Biomed Opt 12:062110.
4. Ngai AC, Jolley MA, Ambrosio RD, et al. (1999) Frequency-dependent changes in cerebral blood flow and evoked potentials during somatosensory stimulation in the rat. Brain Research 837:221–228.
5. Hoshino T, Sakatani K, Kano T, et al. (2006) Cerebral blood oxygenation changes induced by bypass blood flow in moyamoya disease and non-moyamoya cerebral is-chaemic disease, Acta Neurochir. 148:551–557.
6. Matsuura T, Fujita H, Seki C, et al. (1999) CBF change evoked by somatosensory activation measured by laser-Doppler flowmetry: independent evaluation of RBC velocity and RBC concentration. Jpn J Physiol 49:289-296.
7. Ibáñez V, Deiber MP, Sadato N, et al. (1995) Effects of stimulus rate on regional cerebral blood flow after median nerve stimulation. Brain 118:1339–1351.
8. Igarashi T, Sakatani K, Hoshino T, et al. (this volume) Effect of transient forebrain ischemia on flavoprotein autofluorescence and the somatosensory evoked potential in the rat. Advances in Experimental Medicine and Biology.

Individual Differences in Blood Volume and Oxygenation in the Brain during a Cognitive Task based on Time-Resolved Spectroscopic Measurements

Tadashi Niioka, Soichiro Ohnuki, and Yoshifumi Miyazaki

Abstract Although a time-resolved near-infrared spectroscopy (TRS) system is difficult to make a measurement into 10 s or less at the moment, the system has a great advantage that it measures absolute values of hemoglobin concentrations. In the present study, using a device equipped with a TRS system, we examined individual differences in changes in cerebral oxygenated, deoxygenated, and total hemoglobin concentrations during two repetitive executions of a cognitive task, and compared these with data from our previous studies performed with a CWS system. As a result, large individual differences were also observed in changes in the cerebral hemoglobin concentrations during a cognitive task in this study using a TRS system. We therefore conclude that large individual differences observed in changes in the cerebral hemoglobin concentrations during a cognitive task in our previous studies using a continuous wave near-infrared spectroscopy (CWS) system would probably be universal, although a CWS system includes the limitation that the absolute value is unable to be measured in the system.

1 Introduction

For more than three decades, lots of investigations have been performed on cerebral hemodynamic changes to achieve a better understanding of oxygen transport to the cerebral cortex and to elucidate the prefrontal cortex activation during a mental activity [1–8]. Individual differences, however, in those changes in responses involved in mental activities have been left to be investigated in detail.

We have so far reported changes in cerebral blood volume and oxygenation during a cognitive task by non-invasive measurements using a continuous wave

T. Niioka (✉)
Graduate School of Environmental Earth Science, Hokkaido University, Sapporo, 060-0810, Japan
e-mail: niioka@ees.hokudai.ac.jp

E. Takahashi, D.F. Bruley (eds.), *Oxygen Transport to Tissue XXXI*, Advances in Experimental Medicine and Biology 662,
DOI 10.1007/978-1-4419-1241-1_36, © Springer Science+Business Media, LLC 2010

near-infrared spectroscopy (CWS) system [9–12]. Although a CWS system made up of relatively simple parts proved useful and is employed for optical topography, a device equipped with the system is unable to measure absolute values, letting us hesitate to make comparisons among experiments and among subjects. On the other hand, a time-resolved near-infrared spectroscopy (TRS) system [13] is difficult to make a measurement into 10 s or less at the moment, because the system requires the integration time of photons, resulting in inadequate detection of a rapid change in hemodynamics. However, the system has a great advantage that it measures absolute values of blood volume and oxygenation. In the present study, using a device equipped with a TRS system, we examined individual differences in changes in the cerebral blood volume and oxygenation during two repetitive executions of a cognitive task, and compared it with our previous studies performed with a CWS system.

2 Methods

Eighteen healthy, young, male volunteers with a mean age of 24.5 years participated in this study. All the subjects were right-handed normotensive nonsmokers. Informed consent was obtained from all the subjects before participation in the experiment. Subjects were instructed to refrain from taking alcohol and caffeine at the night before the experiment and on the day of the experiment.

Cerebral blood volume and oxygenation were measured using a TRS system. A device [14] equipped with the TRS system consists of a light source of three-wavelength (760, 795, and 830 nm) laser light pulses and a light detector of a photomultiplier tube (TRS-20, Hamamatsu Photonics K. K., Hamamatsu, Japan). The TRS system allows the determination of relative light intensity, mean optical path length, scattering coefficient, and absorption coefficient, enabling measurements of absolute concentrations of oxygenated hemoglobin ([oxy-Hb]), deoxygenated hemoglobin ([deoxy-Hb]), and total hemoglobin ([total-Hb] = [oxy-Hb] + [deoxy-Hb]). TRS-optodes with a source-detector distance of 4 cm were positioned on the left side of the frontal region of a subject's head. Subjects were instructed to sit back in a comfortable chair with a headrest to avoid movements of subjects' heads and measurement cables, which may cause movement artifacts. To eliminate light interference, the measurements were performed in a dark room with an illuminance of about 8 l×.

A five-color, computer-controlled version of a modified Stroop color-word task we developed was used as a cognitive task, and was partially described elsewhere [11]. Briefly, a subject is instructed to select one of five colored disks presented simultaneously with one color word on a computer screen, according to the instruction (i.e., "color" or "meaning"). The color of the presented word on the screen is discordant with the meaning of the word. The order of appearance of the instructions and color words is randomized. Subjects must

overcome cognitive interference to respond properly. The original Stroop color-word task [15] has been shown to actually activate the prefrontal cortex in a recent functional magnetic resonance imaging study [16].

Two repetitive task-performing sessions (the first and the second) were administered as an experimental procedure. After a resting period, subjects participated in a 4-min performing session – the first session. After a 15-min break following the first task, subjects participated again in the second performing session – the second session. Each session consisted of the baseline (the last 2-min average of the resting period), the anticipation (2-min average), and the performance (4-min average). Baseline values and changes, namely alteration of the 4-min averaged value during the performing session from the baseline, in each cerebral hemoglobin concentration were analyzed in this study.

Subjects were encouraged to do their best in the task to earn money prizes awarded to those according to the number of correct answers.

3 Results and Discussion

Baseline values of [oxy-Hb], [deoxy-Hb], and [total-Hb] were 56.4 ± 6.4 μM (mean ± SD), 22.0 ± 3.3 μM, and 78.4 ± 8.8 μM in the first performing session, respectively; furthermore, they were highly reproducible between the two repetitive performing sessions. These results indicate that the baseline values include relatively small individual differences and are stable.

On the other hand, for the change in hemoglobin concentration from the baseline as a time-averaged value during the performing session, individual differences were large as shown in Fig. 1, and subjects showed on the whole all combinations of an increase and decrease in [oxy-Hb] and [deoxy-Hb], such as, in the first session, a typical change of increase in [oxy-Hb] and decrease in [deoxy-Hb] (in 8 subjects out of 18 ones), an atypical change of decrease in [oxy-Hb] and increase in [deoxy-Hb] (in 3 subjects out of 18 ones), a change of both increases in [oxy-Hb] and [deoxy-Hb] (in 2 subjects out of 18 ones), a change of both decreases in [oxy-Hb] and [deoxy-Hb] (in 4 subjects out of 18 ones), and a very small change or almost constant in [oxy-Hb] and [deoxy-Hb] (in 1 subjects out of 18 ones), proving that cerebral hemodynamic response to the cognitive task includes large individual differences, which was similar to our previous findings observed using a CWS system (Niioka et al., unpublished data).

In addition, the means of changes in hemoglobin concentrations were decreased in terms of the amplitude in the two repetitive performing sessions; from 0.42 μM in the first session to 0.07 μM in the second session in [oxy-Hb] and from −0.22 μM in the first session to −0.20 μM in the second session in [deoxy-Hb]. This result was also similar to changes in cerebral hemoglobin concentrations in two repetitive cognitive tasks observed in our previous studies with a CWS system.

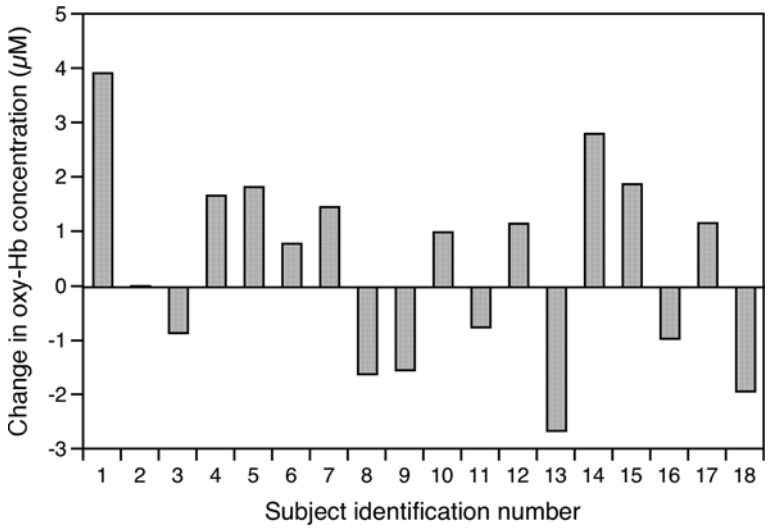

Fig. 1 Individual difference in change in oxy-Hb concentration derived from the left side of the forehead during the first performing session in all the subjects. Subject identification numbers are in order of experiments performed

In conclusion, the results obtained in the present study indicate that individual differences in changes in cerebral hemoglobin concentrations during two repetitive cognitive tasks observed in our previous studies using a CWS system would probably be universal, although a CWS system includes the limitation that the absolute value is unable to be measured in the system.

Acknowledgment This work was supported in part by Grant-in-Aid for Scientific Research (19570232).

References

1. Jöbsis FF (1977) Noninvasive, infrared monitoring of cerebral and myocardial oxygen sufficiency and circulatory parameters. Science 198:1264–1267.
2. Wyatt JS, Cope M, Delpy DT et al. (1986) Quantification of cerebral oxygenation and haemodynamics in sick newborn infants by near infrared spectrophotometry. Lancet ii:1063–1066.
3. Chance B, Leigh JS, Miyake H et al. (1988) Comparison of time-resolved and -unresolved measurements of deoxyhemoglobin in brain. Proc Natl Acad Sci USA 85:4971–4975.
4. Hoshi Y, Tamura M (1993) Detection of dynamic changes in cerebral oxygenation coupled to neuronal function during mental work in man. Neurosci Lett 150:5–8 .
5. Kato T, Kamei A, Takashima S et al. (1993) Human visual cortical function during photic stimulation monitoring by means of nearinfrared spectroscopy. J Cereb Blood Flow Metab 13:516–520.

6. Villringer A et al. (1993) Near infrared spectroscopy (NIRS): a new tool to study hemodynamic changes during activation of brain function in human adults. Neurosci Lett 154:101–104.
7. Niioka T, Chance B (1997) Relative changes in optical path length of near infrared light during a mental task. In: Chance B, Tamura M, Zuo H and Sakatani K (eds.) Non-invasive optical diagnosis: basic science and its clinical application, pp. 3–6. Magazine Office of China-Japan Friendship Hospital, Beijing.
8. Koizumi H, Yamamoto T, Maki A et al. (2003) Optical topography: practical problems and new applications. Appl Opt 42:3054–3062.
9. Shiraiwa M, Hasegawa K, Niioka T (2000) Changes in the blood volume and oxygenation in the brain during a mental arithmetic task and their relationships to cardiovascular responses. Ther Res 21:1516–1519.
10. Niioka T, Shiraiwa M, Hasegawa K (2001) Changes in the regional cerebral blood volume and oxygenation during a mental arithmetic task and their relationships to personality and stress coping traits. Ther Res 22:2004–2007.
11. Niioka T, Sasaki M (2003) Individual cerebral hemodynamic response to caffeine was related to performance on a newly developed Stroop color-word task. Opt Rev 10:607–608.
12. Niioka T, Sasaki M (2004) Changes in cerebral hemodynamics during a cognitive task after caffeine ingestion. In: Nakagawa M, Hirata K, Koga Y and Nagata K (ed.) Frontiers in Human Brain Topography, Elsevier B.V., Amsterdam.
13. Patterson MS, Chance B, Wilson BC (1989) Time resolved reflectance and transmittance for the noninvasive measurement of tissue optical properties. Appl Opt 28:2332–2336.
14. Oda M, Nakano T, Suzuki A et al. (2000) Near-infrared time-resolved spectroscopy system for tissue oxygenation monitor. Proc SPIE 4160:204–210.
15. Stroop JR (1935) Studies of interference in serial verbal reactions. J Exp Psychol 18:643–662.
16. Adleman NE, Menon V, Blasey CM et al. (2002) A developmental fMRI study of the Stroop color-word task. NeuroImage 16:61–75.

Cerebral Oxygenation in the Frontal Lobe Cortex during Incremental Exercise Tests: The Regional Changes Influenced by Volitional Exhaustion

Mikio Hiura, Tetsuya Mizuno, and Tsukasa Fujimoto

Abstract The present study examined the regional differences of cortical oxygenation in the frontal lobe by near-infrared spectroscopy (NIRS) during incremental exercise tests and the precise location of NIRS was examined by brain magnetic resonance imaging (MRI). Pulmonary gas exchange and NIRS measurement during incremental cycling ergometry tests were investigated in 14 men. In 7 of these subjects, the right middle cerebral artery mean velocity (MCA Vmean) was simultaneously measured by transcranial Doppler (TCD). In the right medial of the frontal lobe cortex, Tissue Oxygenation Index (TOI) increased by 8.8% with its peak value at respiratory compensation threshold (RCT) and Normalized Tissue Hemoglobin Index (nTHI) increased until endpoint by 16.2%. During incremental exercise tests, the changing pattern of TOI was different according to the distribution of the probes. Volitional exhaustion by exercise induced the deteriorated TOI and MCA Vmean, whereas nTHI increased.

1 Introduction

Cerebral perfusion is affected by the mental effort to exercise which seems to be indicated by RPE (ratings of perceived exertion: Borg's scales) [1]. During exercise the mental effort is associated with the increase in cerebral oxygenation [2, 3]. Near-infrared spectroscopy can monitor tissue or capillary oxygenation of the brain non-invasively in real-time and thus has advantage for monitoring of the strenuous whole body exercise [4, 5]. Considering that the mental effort to exercise would enhance the cerebral activity which affects the regional cerebral blood flow (rCBF) or metabolic substrate such as glucose [6], the rCBF of the

M. Hiura (✉)
Faculty of Humanity and Environment, Hosei University, Tokyo, Japan; Department of Neurosurgery, Showa University School of Medicine Fujigaoka Hospital, Yokohama, Japan
e-mail: phmikmd@hosei.ac.jp

E. Takahashi, D.F. Bruley (eds.), *Oxygen Transport to Tissue XXXI*, Advances in Experimental Medicine and Biology 662,
DOI 10.1007/978-1-4419-1241-1_37, © Springer Science+Business Media, LLC 2010

responsible areas for the mental effort to exercise would change in response to the work intensity or duration. Accordingly the cerebral oxygenation would be influenced by volitional exhaustion.

In the present study, we arranged the probes of NIRS in the forehead in tow ways. Purpose of this study was to (1) investigate dynamics of cerebral oxygenation and blood flow with respect to exercise intensity that was indicated by changes of cardiopulmonary variables during incremental exercise tests, (2) examine the regional differences for cortical oxygenation in the frontal lobe during exercise especially at volitional exhaustion.

2 Methods

Fourteen healthy male volunteers (Age = 20.5 ± 0.9 yr, height = 172.9 ± 3.5 cm, weight = 63.3 ± 7.4 kg) were recruited. The study was consistent with the Helsinki declaration and approved by the ethical committee of Tokyo Medical and Dental University. Subjects were divided in two groups by the distributions of the NIRS probes which were localized in 1) the right medial and the left medial regions (*group A*) and 2) the right medial and the right lateral regions (*group B*). Two groups were matched by age, height and weight. The probes were placed on the scalp over the right frontal lobe or the left frontal lobe (Fig. 1). Each subject performed an incremental exercise test on a cycle ergometer (Power Max, Combi) to volitional exhaustion. The subjects work rate was increased by 20 W every 1 min beginning from 20 W in *group A* (ramp

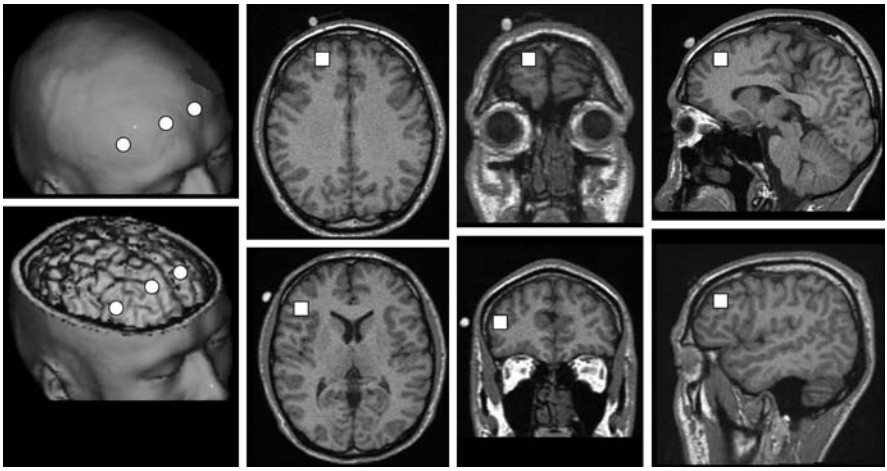

Fig. 1 Estimation of the localized portions of NIRS by MRI. *White circle*; the *center* of probe. *White square*; the estimated region in the *right* frontal lobe detected by NIRS. High intensity on the scalp showed the Vitamine E capsules as the marker of the probes

protocol) and by 30 W every 2 min beginning with 30 W in *group B* (stepwise protocol). RPE was recorded at every 2 min.

Metabolic CO_2 production (VCO_2), O_2 uptake (VO_2), and end-tidal CO_2 partial pressure ($P_{ET}CO_2$) were determined using cardiopulmonary exercise test systems (CPET, Cosmed or Mi-300, Minato). For each test, anaerobic threshold (AT) was determined by the V-slope method and respiratory compensation threshold (RCT) was determined based on the pulmonary gas exchange variables ($P_{ET}CO_2$, VE/VCO_2, and $\%FECO_2$) [7].

During exercise, cerebral blood oxygenation in the frontal lobe cortex was determined by NIRS (NIRO 200, Hamamatsu photonics). Variables of Tissue Oxygenation Index (TOI) and normalized Tissue Hemoglobin Index (nTHI) that are based on the spatially-resolved spectroscopy (SRS) method were used. Since the absolute value of TOI is dependent on the underlying tissue [8], relative change from the baseline (rest) (%) was induced. In seven subjects (*group B*), the right middle cerebral artery mean velocity (MCA Vmean) was measured simultaneously by transcranial Doppler (TCD) (Companion III, Nicolet Vascular).

In one subject, magnet resonance imaging (MRI) of the brain was obtained for the precise localization of NIRS probe positions with respect to the cortex anatomy (MAGNETOM Avanto, SIEMENS). In addition to 2D imaging, 3D reconstruction of scalp and brain surface was performed using the auto-mated software for fusion imaging (Dr.View, AJS).

The pulmonary gas exchange and NIRS measurements were time aligned and averaged over a 20 s interval for subsequent analysis. The MCA Vmean measurements were averaged over a 5 s interval at every one minute. Data are presented as mean $\pm$ SD and Pearson's correlation analysis was used to evaluate associations between variables. One-way repeated-measures ANOVA followed by Bonferroni post hoc evaluation for multiple comparisons were used to identify differences across exercise intensity. Relative changes in the NIRS variables over exercise intensity were compared between the regions by two-way repeated measures ANOVA. A P-value of 0.05 was considered statistically significant.

3 Results

The variables of at rest and at exercise intensity of 2 min, AT, RCT and endpoint are described in Table 1. In *group B* VO_2 and REP were higher at endpoint. RPE was different between the groups at 2 min due to the work rate inequality. VCO_2/VO_2 increased after RCT similarly between the groups. Between AT and RCT, VO_2 and VCO_2/VO_2 were differed but the others were similar. In the right medial frontal lobe cortex, TOI increased by $8.8 \pm 5.3\%$ from rest to maximum as nTHI ranged from 0.96 ± 0.09 to 1.15 ± 0.14. MCA Vmean ranged from 59.6 ± 16.2 cm/s to 79.8 ± 20.1 cm/s. $P_{ET}CO_2$ in *group A*

Table 1 Physiological responses, NIRS variables and MCAV mean at 2 min, anaerobic threshold, respiration threshold and endpoint

		Rest	2 min	AT	RCT	Endpoint
Exercise time (min) [§]	group A	–	120	266 ± 81	500 ± 135	581 ± 118
	group B	–	120	282 ± 35	508 ± 65	734 ± 121[††]
Work rate (W)	group A	–	60	109 ± 27	187 ± 45	213 ± 39
	group B	–	30	81 ± 15	154 ± 20	201 ± 33
VO_2 (ml / min / kg) [§]	group A	9.7 ± 0.9	13.4 ± 1.2	20.0 ± 2.6	31.0 ± 5.1[‡‡‡]	36.2 ± 3.8
	group B	8.1 ± 1.9	13.8 ± 1.5	23.1 ± 3.6[†]	33.6 ± 4.2[‡‡]	42.4 ± 6.5[†††]
VCO_2 / VO_2	group A	0.85 ± 0.05	0.85 ± 0.06	0.88 ± 0.06	1.01 ± 0.04 ***,[‡‡]	1.10 ± 0.08 ***
	group B	0.79 ± 0.07	0.79 ± 0.07	0.88 ± 0.04	1.03 ± 0.04 ***,[‡‡]	1.13 ± 0.07 ***
$P_{ET}CO_2$ (mmHg)	group A	42.4 ± 1.5	44.2 ± 2.8	48.6 ± 2.7 **	50.1 ± 2.4 ***	47.7 ± 3.6 **
	group B	38.3 ± 3.3	42.1 ± 3.1	46.4 ± 5.0 *	46.1 ± 5.4 *	42.7 ± 6.2
RPE[§§§]	group A	6	9.6 ± 1.0	12.1 ± 0.9	14.9 ± 2.0	16.9 ± 0.9
	group B	6	6.9 ± 0.7[††]	10.6 ± 2.4	14.9 ± 1.9	18.8 ± 0.8[†]
ΔTOI (%)	Rt medial [a, b]	0	2.2 ± 3.0	4.2 ± 3.8	8.8 ± 5.3 ***	6.8 ± 5.9 ***
	Lt medial [a]	0	1.3 ± 1.1	2.9 ± 2.2	5.5 ± 2.8 ***	4.3 ± 3.0
	Rt lateral [b]	0	–0.8 ± 2.2	–0.5 ± 2.2	1.4 ± 5.3	4.0 ± 8.4
nTHI	Rt medial [a, b]	0.99 ± 0.08	1.01 ± 0.09	1.04 ± 0.10	1.11 ± 0.11 *	1.15 ± 0.14 **
	Lt medial [a]	0.97 ± 0.09	0.96 ± 0.10	0.98 ± 0.11	1.06 ± 0.13	1.12 ± 0.10
	Rt lateral [b]	1.02 ± 0.04	1.02 ± 0.04	1.00 ± 0.04	1.03 ± 0.05	1.13 ± 0.16
MCA Vmean (cm /sec)		59.6 ± 16.2	68.4 ± 18.4 *	78.7 ± 21.1 ***	79.8 ± 20.1 ***	71.3 ± 18.6 **

Values are mean ± SD derived from group A ($n = 7$) and B ($n = 7$).

[a] From group A ($n = 7$), [b] group B and [a, b] the both group combined ($n = 14$).

AT = anaerobic threshold; RCT = respiratory compensation threshold; $P_{ET}CO_2$ = end-tidal CO_2 partial pressure; RPE = ratings of perceived exertion (Borg's scale : 6–20); ΔTOI = Relative changes from resting conditions of Tissue Oxygenation Index (%); nTHI = normalized Tissue hemoglobin Index (relative value); MCA Vmean = mean velocity of the right middle cerebral artery.

*, **, and *** Significantly different versus rest, $P < 0.05$, 0.01 and 0.001, respectively.

[‡‡] and [‡‡‡] Significantly different versus AT, $P < 0.01$ and 0.001, respectively.

[§] and [§§§] Significant interaction (group * exercise), $P < 0.05$ and 0.001, respectively.

[†] ,[††] and [†††] Significantly different from group A at this point, $P < 0.05$, 0.01 and 0.001, respectively.

ranged from 42.4 ± 1.5 mmHg to 50.1 ± 2.4 mmHg and $P_{ET}CO_2$ in *group B* from 38.3 ± 3.3 mmHg to 46.4 ± 5.0 mmHg. In 6 of 7 subjects, the relative change of MCA Vmean correlated with $P_{ET}CO_2$ ($r^2 = 0.47$ to 0.85). In 11 of 14 subjects, TOI and nTHI of the right medial correlated with $P_{ET}CO_2$ ($r^2 = 0.09$ to 0.81 and $r^2 = 0.13$ to 0.67, respectively). In the lateral region, TOI and nTHI did not correlated well with $P_{ET}CO_2$. As shown in Fig. 1, the medial and the lateral region of the NIRS probe correspond to the superior frontal gyrus (SFG) and the inferior frontal gyrus (IFG), respectively.

The relative changes from the baseline (rest) (%) of NIRS variables are shown in Fig. 2. In the regions of right medial and lateral frontal lobe (*group B*), there was a significant interaction (region * intensity) for TOI with difference at endpoint. TOI of the right medial increased significantly at RCT with tendency of the decline at endpoint, whereas nTHI, except for the right lateral, increased significantly at RCT and endpoint with their peaks at endpoint.

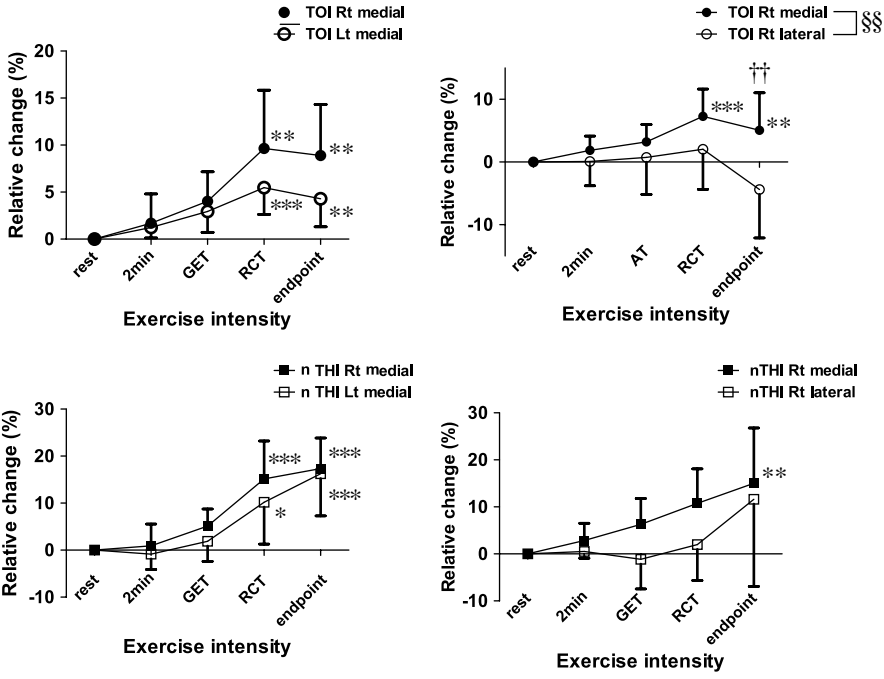

Fig. 2 Changes in NIRS variables at rest, 2 min, AT, RCT and endpoint for the region of the *right* medial (Rt medial) and the *left* medial (Lt medial) of the frontal lobe (group A, *left* side) and the *right* medial (Rt medial) and lateral (Rt lateral) (group B, *right* side). Values are mean ± SD. **, and ***Significantly higher than rest values, $P < 0.05$, 0.01 and 0.0001, respectively. §§Significantly different from TOI Rt medial at this point, $P < 0.01$

4 Discussion

We described the dynamic change of the cerebral oxygenation in the frontal lobe during exercise. VO_2 and RPE differed at endpoint, suggesting that exercise capacity of subjects was higher in *group B*. Despite the difference of the exercise protocols, exercise intensity based on gas exchange [7] was similar between two groups and this was reflected in the similar VCO_2/VO_2. Between AT and RCT, variables from brain were similar with VO_2 and VCO_2/VO_2 differed. The changing pattern of the two groups TOI in the right medial was similar ($F = 0.003$, $P = 0.42$). Cerebral oxygenation derived from NIRS has relationship with rCBF [9, 10], however neither TOI nor nTHI reflected rCBF directly. Since the arterial saturation, artery to venous ratio and oxygen consumption are required to obtain rCBF from TOI [11], rCBF could be speculated by changes of other factors. When exercise intensity exceeded RCT, a finding that TOI and nTHI in the right SFG increased implies increases of rCBF if nTHI had derived from arterial fraction. If not, with rCBF stable, we could speculate that decreases of oxygen consumption affected increases of TOI. When exercise intensity below RCT, a small increase in $P_{ET}CO_2$ would support the increase in CBF and MCA Vmean [12]. Our data were concomitant with this association of $P_{ET}CO_2$ and MCAV mean, whereas $P_{ET}CO_2$ correlated to some extent with TOI and nTHI in the SFG and did not well in the IFG. Considering the possible association of TOI and nTHI with rCBF, it implies that $P_{ET}CO_2$ would affect rCBF differently among the MCA perfusion areas and the frontal lobe regions.

Major finding of this study is the regional difference between the SFG and the IFG. Matching MRI with NIRS makes it possible to relate results to regional gyral anatomy on an individual basis [13]. With regard to the mental effort to exercise, activation of anterior cingulate cortex was demonstrated [14, 15]. Considering that the SFG in the present study was close to the region of interest defined as the anterior cingulated cortex in the previous studies, the SFG would be activated due to the mental effort exercise. The difference in the oxygenation between the SFG and the IFG at volitional exhaustion suggested that the SFG was activated related to sense of effort or central command and the IFG was not activated.

In conclusion, we described that the cerebral oxygenation changed with exercise intensity during incremental exercise tests and that the changing patterns of the cerebral oxygenation between two gyri in the frontal lobe were different.

References

1. Borg G (1970) Perceived exertion as an indicator of somatic stress. Scand J Rehab Med 23:92–98.
2. Secher N, Seifert T, Van Lieshout J (2008) Cerebral blood flow and metabolisms determining during exercise: implication for fatigue J Appl Physiol 104:306–314.

3. Ide K, Horn A, Secher N (1999) Cerebral metabolic response to submaximal exercise. J Appl Physiol 87:1604–1608.
4. Nielsen H, Boesen M, Secher N (2001) Near-infrared spectroscopy determined brain and mus-cle oxygenation during exercise with normal and resistive breathing. Acta Physiol Scand 171:63–70.
5. Nybo L, Rasmussen P (2007) Inadequate delivery of oxygen to the brain as a factor influenc-ing fatigue during strenuous exercise. Rev Sports Exerc Sci 35:110–118.
6. Dalsgaard M (2006) Fuelling cerebral activity in exercising man. J Cereb Blood Flow Metab 26:731–750.
7. Beaver W, Wasserman K, Whipp B (1986) A new method for detecting anaerobic threshold by gas exchange. J Appl Physiol 60:2020–2027.
8. Greisen G (2003) Is near-infrared spectroscopy living up to its promises? Semin Fetal Neonatal Med 11:498–502.
9. Madsen P, Secher N (1999) Near-infrared oximetry of the brain. Prog Neurobiol 58:541–545.
10. Villringer A (1997) Functional neuroimaging: optical approaches. In: Villringer A and Dirnagl U (ed.) Optical Imagings of Brain Function and Metabolism 2, Plenum Press, New York .
11. Tachtsidis I, Tisdall M, Delpy DT et al. (2008) Measurement of cerebral tissue oxygenation in young healthy volunteers during acetazolamide provocation: a transcranial Doppler and near-infrared spectroscopy investigation. Adv Exp Med Biol 614:389–396.
12. Jorgensen L, Perko M, Secher N (1992) Regional cerebral artery mean flow velocity and blood flow during dynamic exercise in humans. J Appl Physiol 73:1825–1830.
13. Hirth C Villringer K, Thiel A et al. (1997) Towards brain mapping, near-infrared spectroscopy and high resolution 3D MRI. In: Villringer A and Dirnagl U (ed.) Optical Imagings of Brain Function and Metabolism 2, Plenum Press, New York .
14. Williamson JW, McColl R Mathews D (2003) Evidence for central command activation of the human cortex during exercise. J Appl Physiol 94:1726–1734.
15. Critchley HD, Corfield DR, Chancler MP et al. (2000) Cerebral correlates of autonomic cardiovascular arousal: a functional neuroimaging investigation in humans. J Physiol 523: 259–270.

Implantable Resonators – A Technique for Repeated Measurement of Oxygen at Multiple Deep Sites with In Vivo EPR

Hongbin Li, Huagang Hou, Artur Sucheta, Benjamin B. Williams, Jean P. Lariviere, Md. Nadeem Khan, Piotr N. Lesniewski, Bernard Gallez, and Harold M. Swartz

Abstract EPR oximetry using implantable resonators allows measurements at much deeper sites than are possible with surface resonators (> 80 vs. 10 mm) and achieves greater sensitivity at any depth. We report here the development of an improved technique that enables us to obtain the information from multiple sites and at a variety of depths. The measurements from the various sites are resolved using a simple magnetic field gradient. In the rat brain multi-probe implanted resonators measured pO_2 at several sites simultaneously for over 6 months under normoxic, hypoxic, and hyperoxic conditions. This technique also facilitates measurements in moving parts of the animal such as the heart, because the orientation of the paramagnetic material relative to the sensing loop is not altered by the motion. The measured response is fast, enabling measurements in real time of physiological and pathological changes such as experimental cardiac ischemia in the mouse heart. The technique also is quite useful for following changes in tumor pO_2, including applications with simultaneous measurements in tumors and adjacent normal tissues.

1 Introduction

EPR has been developed for over several decades and applied successfully for detecting and monitoring radical levels in chemical and biological materials [1–3]. L-band EPR, in particular, has been used for measuring and monitoring tissue pO_2 in rodents and in patients with subcutaneous tumors and skin cancer [4–5]. In spite of these successful applications, L-band EPR has some limitations such as being limited to measure at tissue depths of no more than 10 mm and considerable noise when measurements are made in organs that may move during the measurement, such as the beating heart. We have developed the

H.M. Swartz (✉)
EPR Center for Viable Systems, Department of Radiology, Dartmouth Medical School, 703, Vail, Hanover, NH 03755, USA
e-mail: harold.m.swartz@dartmouth.edu

E. Takahashi, D.F. Bruley (eds.), *Oxygen Transport to Tissue XXXI*, Advances in Experimental Medicine and Biology 662,
DOI 10.1007/978-1-4419-1241-1_38, © Springer Science+Business Media, LLC 2010

implantable resonators for EPR to overcome these limitations, to enhance detection, and to measure pO_2 in diverse tissues/organs. The techniques also have applicability for other types of measurements by EPR, including biophysical parameters, free radicals, redox state, and dosimetry.

2 Materials and Methods

The implantable resonator has two sets of loops, a larger loop on one end and one or more small loops on the other end. The large loop is used to couple inductively to the L-band EPR spectrometer. The small loop contains lithium phthalocyanine (LiPc) or other oxygen sensitive paramagnetic materials and is coated with a highly gas permeable, biocompatible material (in the studies we used Teflon) [6]. The small loops are implanted in the sites of interest.

All animal procedures were conducted in accordance with the NIH Guide and approved by the Institutional Animal Care and Use Committee of Dartmouth Medical School. The implantable resonators were placed surgically into regions based on the experimental designs. To measure pO_2 in the heart, a short single probe resonator was used. The large coupling loop was placed under the skin close to the chest, while the small tip was inserted into the myocardial muscle near the coronary artery of the mouse. After surgery, the animal was allowed to recover for a 2 days before the EPR measurements. To create temporary cardiac ischemia, a fine ligature was placed around the artery that could be tightened remotely to temporarily occlude the blood flow.

For brain pO_2, either a single or a multi-probe resonator was inserted into the targeted sites, while the large loop was placed on the scalp. Rats were allowed to recover for at least 1 day before hypoxic, normoxic, hyperoxic studies of brain tissue or measurements in tumors. The tumors were established by injection of a suspension of F98 glioma cells (500,000 cells/10μl, 7μl/site) intracranially at a depth of 5$\sim$6 mm from the skull into the vicinity of the sensing tip. To qualitatively assess the tumor growth and size, we used MRI to acquire images 1 day before and 19 days after the injection of F98 cells. MRI images were acquired on a 7T Varian console interfaced to a Magnex horizontal bore magnet using a birdcage coil in transmit/receive mode. T1-weighted images were acquired using a spin-echo sequence (repetition time, 0.7 s; excitation time, 9 ms; slice thickness, 1 mm; field of view, 4 $\times$ 4 cm; number of signal averages, 2; and matrix size, 128 $\times$ 128). The total data acquisition time was 3 min, 12 s for each image set.

EPR measurements were carried out using an L-band EPR spectrometer. Rats or mice were anesthetized with $\sim$2% isoflurane/air and were placed in the magnet with the resonator sensing tip in the center of the magnet. The loop of the external resonator was placed over the coupling loop of the implantable resonator. For multi-probe resonators, a single dimensional magnetic gradient was applied to separate the EPR signals from each probe. For normoxia, the

inhaled gas was 30% O_2; to induce mild hypoxia the gas was lowered to 15% O_2, and for hyperoxia we used carbogen (95% O_2/5% CO_2).

3 Results

Figure 1 shows the myocardial pO_2 during baseline and ischemic conditions. Under normoxia, the mouse had a very stable pO_2 of about 40 mmHg. With occlusion, the pO_2 immediately decreased to 15 mmHg. Upon reperfusion, the pO_2 increased but did not reach the baseline level. For repeated brain pO_2 measurements, a 3-probe resonator was placed into a rat brain with the following coordinates: Left, 3.5 mm with depth at 3.5, 1.5 mm with depth at 2.5 mm to the midline; right 1.5 mm with depth at 2.5 mm to the midline. The pO_2 measurement was started the second day after the resonator implantation and continued for up to 180 days, Fig. 2. In the first several days, tissue pO_2 showed

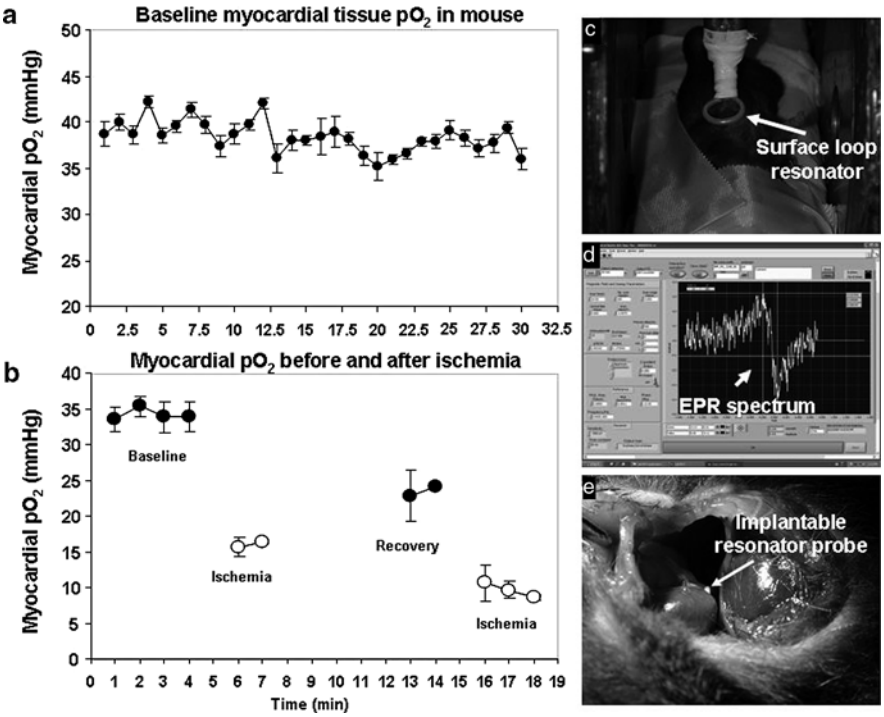

Fig. 1 Measurement of myocardial pO_2 using a short single probe resonator. **a**: baseline pO_2 of a mouse heart. **b**: pO_2 under several different conditions: baseline, ischemia and reperfusion. **c**: positioning of the external resonator over the large loop of the implantable resonator that was under the skin. **d**: a typical EPR spectrum (baseline pO_2). **e**: location of the resonator probe

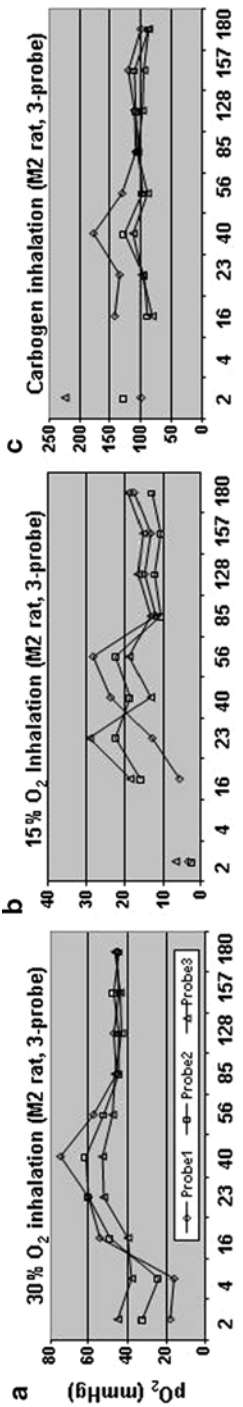

Fig. 2 Repeated, long term pO_2 measurements with a 3-probe resonator implanted in a rat brain. The measurements were started the second day after implantation and continued for up to 180 days. **a**: 30% O_2 for baseline, **b**: 15% O_2 for hypoxia and **c**: carbogen for hyperoxia

a large variation, which is likely due to the trauma associated with the insertion of the probes.

After 2 weeks, the tissue pO_2 stabilized and could be measured with a good signal to noise ratio in all measurements. The tissue pO_2 of a rat breathing 30% O_2 was 45 mmHg (Fig. 2a). Under 15% O_2, the rat had a pO_2 of 15 mmHg (Fig. 2b). When the rats breathed carbogen, the pO_2 increased to around 100 mmHg, (Fig. 2c). Importantly, there was no large variation in brain tissue pO_2 while breathing 30% O_2 from day 56 to 180. These results demonstrate the ability of this technique to monitor brain tissue oxygenation in both normal and pathologic conditions for prolonged periods of time.

For measuring the brain pO_2 dynamic changes, we used a 4-probe resonator implanted as indicated in Fig. 3. When the oxygen concentration was changed from 30% to room air, the brain pO_2 decreased gradually and reached a stable level after 10 minutes. Although all four sites did not have exactly the same pO_2 values, the dynamic patterns were very similar. When the oxygen level was changed from room air to 15% O_2, the tissue pO_2 in all sites reduced to much lower values (17∼22 mmHg). During a carbogen challenge, the two lateral sites had a much larger pO_2 response, compared to the two medial sites.

We inserted one-probe implantable resonators into the rat brain, at a depth of 5∼6 mm from the brain surface, for monitoring the pO_2 during tumor growth. Figure 4a shows the MRI images of a sham injected rat 7 days before and 19 days after an equal volume of culture media injection. There was no obvious morphological change in the MRI images. The pO_2 stayed at a very similar level (40∼55 mmHg) across the measurements (Fig. 4b). The changes in the MRI for the rats with tumors are shown in Fig. 4a, the tumor grew around the resonator tip. There was a decrease of the pO_2 in the tumor sites; the pattern of the decrease differed in different rats and showed different pO_2 decline rates (Fig. 4b). On day 25 after cell inoculation, all rats received carbogen. The brains in the sham injected rats had a robust response to the carbogen while the tumors had almost no response.

4 Discussion

We have successfully used implantable resonators to measure tissue pO_2 in the heart and the brain under diverse conditions. The use of the implantable resonators in the beating heart enabled us to overcome the problems usually encountered when trying to make measurements of pO_2 in a moving organ. Previously, to measure myocardial pO_2, we had to carry out a large amount of data averaging to reduce the noise induced by the relative motion between the paramagnetic material and the probe. This precluded measuring dynamic changes such as those associated with the acute induction of ischemia. Using a single or multi-probe resonator for long-term brain pO_2 measurements confirmed the very stable pO_2 in the targeted sites, and we were able to measure this

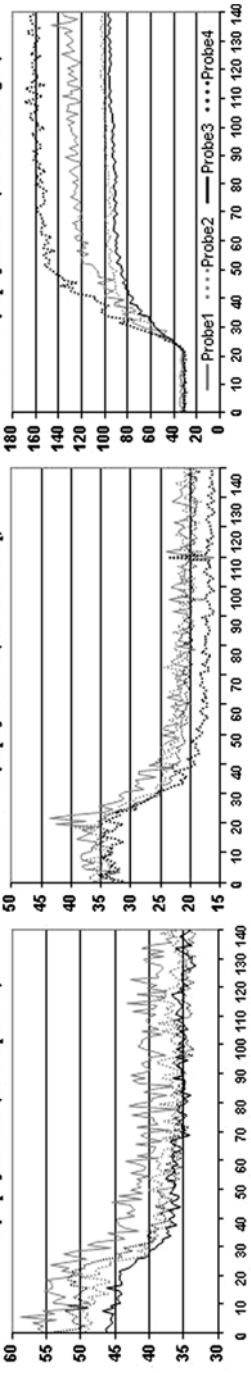

Fig. 3 A four-probe implantable resonator used to measure dynamic responses in the rat brain to changes in inhaled oxygen levels. The resonator was inserted at the following coordinates: AP, 0 mm; ML, 2.0 mm and 3.5 mm, DV, 5.5 mm. Oxygen was delivered through a nose cone to the rat. Plots from *left* to *right*: brain pO_2 during change from 30% O_2 to air, from air to 15% O_2, and from air to carbogen

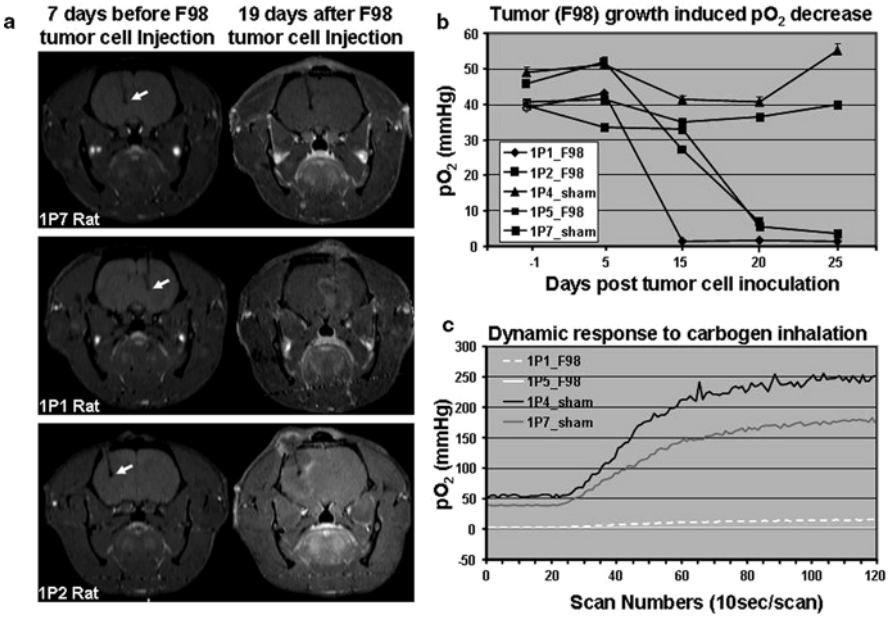

Fig. 4 pO_2 in rat F98 brain tumor measured with a single probe resonator. **a**: MRI images before and 19 days after F98 inoculation. *Arrows* indicate the probe locations in the brain. **b**: pO_2 measured the day before, 5, 15, 20 and 25 days after F98 inoculation in 3 rats with tumors and 2 sham rats. **c**: Carbogen challenge at day 25 after baseline pO_2

for days and months. Such measurements would be very difficult to do with polarographic electrodes or the OxyLite system.

Another very important advantage of this technique is the feasibility of carrying out oximetry at any depth. This extends the advantages of EPR oximetry to almost any site where the resonator can be implanted. The implantable resonators, once inserted, allow repeated pO_2 measurements with excellent time resolution and can be repeated across days or weeks.

Acknowledgments This work was supported by NIH grant PO1EB2180 and a Dartmouth NCCC Prouty Pilot Grant, and used the facilities of the EPR Center for Viable Systems (P41EB002032).

References

1. Swartz, H.M. and T. Walczak (1998) Developing in vivo EPR oximetry for clinical use. Adv Exp Med Biol 454:243–252.
2. Swartz, H.M. and B.A. Reichling (1978) The safety of X-ray examination of radioisotope scan. JAMA 239:2031–2032.

3. Hou, H., et al. (2007) The effect of oxygen therapy on brain damage and cerebral pO_2 in transient focal cerebral ischemia in the rat. Physiol Meas 28:963–976.
4. Som, S., et al. (2008) EPR oximetry in three spatial dimensions using sparse spin distribution. J Magn Reson 193(2):210–217.
5. Matsumoto, S., et al. (2008) Low-field paramagnetic resonance imaging of tumor oxygenation and glycolytic activity in mice. J Clin Invest 118:1965–1973.
6. Dinguizli, M., et al. (2006) Development and evaluation of biocompatible films of polytetrafluoroethylene polymers holding lithium phthalocyanine crystals for their use in EPR oximetry. Biosens Bioelectron 21:1015–1022.

Use of Visible Spectrophotometry to Assess Tissue Oxygenation in the Colostomy Stoma

Daya B. Singh, Iain Bain, and David K. Harrison

Abstract The aims of this study were to determine the normal range of tissue oxygenation (SO_2) in the "mature" colostomy stoma and to investigate whether there were any diurnal variations in the SO_2 values. Ten patients with an end colostomy for a minimum duration of three months and using conventional colostomy bags were included in this study. Tissue SO_2 was measured on the stoma using visible wavelength spectroscopy (Whitland RM 200, Whitland Research, Whitland, UK) The measurements were carried out on each patient on three occasions: the first early in the morning (designated "baseline"), a second after 6 h and the third on the next day at 24 h. The results showed that the mean baseline SO_2 in the colostomy stoma was 77.6 ± 6.8 and there were no differences in the SO_2 measurements between the baseline, 6 h and the 24 h values. There were also no differences in the SO_2 values between the four quadrants of the stomas. In conclusion, visible wavelength spectrophotometry can reliably measure stomal SO_2 in a non-invasive way. No significant diurnal variations in the stomal SO_2 values were detected.

1 Introduction

A colostomy is a surgical procedure in which the colon is transected and diverted through the abdominal wall to create an artificial opening or "stoma". Colostomies are common following colorectal surgery and may be temporary or permanent. In spite of recent advances in surgical techniques the complication rate for colostomies remains high (30–60%) [2, 8]. Some of these complications such as ischaemia, necrosis and stenosis of the stoma are related to the vascularity in the early post operative period. Stomal blood flow and

D.K. Harrison (✉)
Department of Medical Physics and General Surgery, University Hospital of North Durham, Durham, DH1 5TW, UK
e-mail: d.k.harrison@ncl.ac.uk

E. Takahashi, D.F. Bruley (eds.), *Oxygen Transport to Tissue XXXI*, Advances in Experimental Medicine and Biology 662,
DOI 10.1007/978-1-4419-1241-1_39, © Springer Science+Business Media, LLC 2010

oxygenation are normally not monitored in the post operative period and the diagnosis of stomal ischaemia and necrosis is based on clinical examination.

Tissue oxygen saturation (SO_2) is a functional measure of the perfusion of the tissue and is particularly sensitive to low flow states. Visible spectrophotometry (VS) can be used to measure stomal tissue oxygenation and thus would be a useful non invasive technique to monitor the stoma in the post operative period. The aims of this study, which was sponsored by ConvaTec, were to determine the range of SO_2 values in the stoma of patients who are using conventional colostomy devices and to investigate the presence of any diurnal variations in the SO_2 values. The study was also aimed at providing baseline data for the use of VS for monitoring perfusion in colostomies peri-operatively.

2 Methods

The study was carried out with prior approval from County Durham and Darlington NHS Foundation Trust Research Review Board and the Local Research Ethics Committee. Ten patients with end colostomies carried out at least 3 months previously and using conventional colostomy devices were recruited for the study. The exclusion criteria for the study were active inflammation/infection or any bleeding from the stoma. All the measurements were performed in the patients' homes.

5 males and 5 females were recruited for the study. Their median age was 63 years with a range from 43 to 77 years. The participants had had their stomas for a median of 6.3 years ranging from 10 months to 9 years. There were 2 smokers in the cohort and two participants had parastomal hernias.

Tissue SO_2 was measured circumferentially around the surface of the stoma using visible light spectrophotometry. The instrument used for the measurements was a Whitland RM 200 SO_2 monitor (Whitland Research, Whitland, UK) using a hand-held "pencil" probe (Fig. 1) incorporating a white LED and a

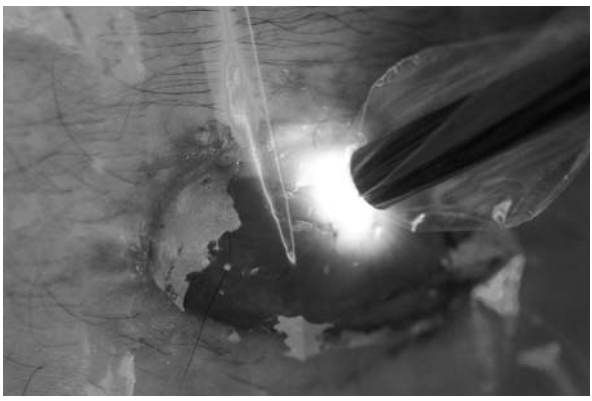

Fig. 1 The probe is covered with a transparent sheath and the stoma is covered with a transparent sheet to provide dual protection against cross infection

100 μm receiving lightguide that transmitted the reflected light to the spectrophotometer. Computer software is used to analyse the resulting absorption spectrum to obtain a value of haemoglobin oxygen saturation [6].

The measurements were carried out on 3 occasions on each patient: the first early in the morning (designated "baseline"), a second after 6 h and the third on the next day at 24 h.

In order to avoid chances of cross infection, the probe was completely wrapped in a transparent sheath and the measurements were taken through another layer of transparent sheath covering the stoma (Fig. 1). Both sheaths were disposed of after each set of measurements. The probe was disinfected using an alcohol swab before and after each set of measurements.

On each occasion, 10 SO_2 measurements were made in each quadrant around the stoma, starting and ending at the most proximal point on the stoma, giving a total of 40 SO_2 values. In this way, as well as obtaining a histogram of values, it could be observed whether a particular region of the stoma is consistently hypoxic.

3 Results

The SO_2 values at baseline, 6 and 24 h were normally distributed (Shapiro-Wilk tests) but failed the normality test when all the values were combined ($P = 0.024$). Non-parametric tests were used for data analysis.

The mean SO_2 (%) ($\pm$ SD) for each patient are given in Table 1. There were no significant differences in the SO_2 values in the colostomy stoma between baseline (74.9 ± 7.7) and 6 h (79.5 ± 6.5, $P = 0.114$), between baseline and 24 h (78.4 ± 5.8, $P = 0.059$) and between 6 and 24 h ($P = 0.386$). Overall mean SO_2 in the stoma was 77.6 ($\pm$6.8)%. There were also no significant differences in the

Table 1 Mean SO_2 values with SD at baseline, 6 and 24 h

Subject	Baseline Mean SO_2 (%)	Baseline SD (%)	6 h Mean SO_2 (%)	6 h SD (%)	24 h Mean SO_2 (%)	24 h SD (%)
1	59.5	16	82.7	3.1	80.6	6.7
2	76.9	5.7	88.4	2.8	82.9	7
3	71.9	3.5	74.8	2.1	73.8	2
4	64.6	6.3	65.5	3.6	65.3	4.9
5	75.6	2.1	86.8	2.4	81.7	3.5
6	84.6	2	82.9	3.5	83.8	3.5
7	78.1	5.4	78.3	4.5	78.9	5.3
8	78.2	4.9	79.1	3.7	74.4	2.3
9	76.9	4.2	78.4	3.2	78.9	4.8
10	82.2	2.8	78.2	3.6	84.1	2.3
Mean	74.9	7.7	79.5	6.5	78.4	5.8

Table 2 Stomal SO_2 in different quadrants of the stoma. Q1–4 represents the four quadrants in a clockwise pattern starting from 12 o'clock position

Time	Q1 SO_2 (%)	Q2 SO_2 (%)	Q3 SO_2 (%)	Q4 SO_2 (%)
Baseline	73.9 (± 9.8)	74.9 (± 8.8)	74.4 (± 8.9)	76.3 (± 6.5)
6 h	79.5 (± 6.5)	80.1 (± 6.8)	79.3 (± 6.5)	79.1 (± 6.7)
24 h	76.3 (± 5.1)	79.5 (± 7.5)	79.9 (± 5.9)	78.2 (± 6.9)

Table 3 Mean SO_2 (± SD) in male and female patients at different times of the day

Time	Male (n = 5)Mean SO_2 (± SD)%	Female (n = 5)Mean SO_2 (± SD)%	Significance (Mann –Whitney U Statistics)
Baseline	72.7 (±10.3)	77.0 (±3.8)	P = 0.675
6 h	77.5 (± 7.1)	81.5 (± 5.9)	P = 0.602
24 h	77.5 (± 7.1)	79.4 (± 4.9)	P = 0.602

SO_2 values between the four quadrants of the stoma. The SO_2 values from different quadrants are presented in Table 2

The mean SO_2 values in the female patients were higher than those in the males at all times but the differences were not statistically significant (Mann – Whitney U test, Table 3)

4 Discussion

This study showed that the mean SO_2 (± SD) in the colostomy stomas was 77.6 (±6.8)%, which is very similar to the mucosal SO_2 in the normal colon as reported in the literature [1, 5]. There was no significant difference in the stomal SO_2 between 0, 6 and 24 h. The SO_2 at 24 h was higher than the values at 0 h and it was almost significantly different (P = 0.059). It may be concluded that there is a tendency for the SO_2 values to be different at different times of the day but all these variations are within 5%, which is unlikely to have any clinical implication. There was no significant difference in the stomal SO_2 values between male and female at any time.

In one patient the morning SO_2 (0 h) was low (59.5%) but it returned to higher values during subsequent measurements at 6 h (82.7%) and 24 h (80.6%). This patient had a parastomal hernia during the first set of measurements (baseline) and this may have influenced the SO_2 values by causing pressure around the stoma. The hernia had reduced spontaneously during the subsequent two measurements and the SO_2 values showed marked improvement. Interestingly, another patient (subject 4) with a recurrent parastomal hernia also had lower SO_2 values and these values were the lowest in the group (Table 1). This patient had also had an operation about ten months previously for his parastomal hernia and the stoma was resited at the time. There is a

possibility of interference with the blood supply of the stoma during the operation which may explain the lower SO_2 values in this patient. His parastomal hernia was reduced during all the measurements so the possibility of a pressure effect was minimal in this case.

Smoking is known to affect the microcirculation in the colon [4, 9] and thus may have an affect on the oxygenation but it was not possible to evaluate the effect of smoking on colostomy SO_2 as there were only two smokers in the group and one of them (subject 4) also had a parastomal hernia.

A promising future clinical application for this non-invasive technique may be to monitor the stoma in the post-operative period when currently the diagnosis of stomal ischaemia and necrosis are based on clinical examination. The latter may not be able to diagnose early ischaemia when the clinical signs are very subtle. There are conflicting reports in the literature regarding the association of anastomotic stricture with ischaemia [3, 7] but there are no studies to correlate the ischaemic changes in the stoma and later development of stomal stenosis.

The present study has demonstrated that measurement of tissue SO_2 in the stoma is reproducible and may be useful for monitoring oxygenation in the post-operative period and thus help in the early detection of stomal ischaemia. This may prevent some of the complications of stoma operation which are due to compromised blood flow and ischaemia.

5 Conclusions

The results of this study demonstrate that measurements of stomal tissue SO_2 are reproducible and do not differ significantly from quadrant to quadrant around the circumference nor between males and females. The stomal SO_2 values in patients who are using conventional colostomy devices display minimal diurnal variations, which are of no relevance clinically.

The results of the study may pave the way for monitoring stomal SO_2 in the post-operative period.

Acknowledgments This study was sponsored by ConvaTec, a division of E.R. Squibb & Sons, L.L.C. Skillman, NJ 08534, USA. The authors are grateful to the volunteers for their willing participation.

References

1. Benaron DA, Parachikov IH, Friedland S et al. (2004) Continuous, noninvasive, and localized microvascular tissue oximetry using visible light spectroscopy. Anesthesiology 100:1469–1475.
2. Caricato M, Ausania F, et al. (2007) Retrospective analysis of long-term defunctioning stoma complications after colorectal surgery. Colorectal Dis 9:559–561.

3. Chung RS (1987) Blood flow in colonic anastomoses. Effect of stapling and suturing. Ann Surg 206:335–339.
4. Fawcett A, Shembekar M, Church JS et al. (1996) Smoking, hypertension, and colonic anastomotic healing; a combined clinical and histopathological study. Gut 38:714–718.
5. Friedland S, Benaron D, Parachikov I et al. (2003) Measurement of mucosal capillary hemoglobin oxygen saturation in the colon by reflectance spectrophotometry. Gastrointest Endosc 57:492–497.
6. Harrison DK, Hawthorn IE (2005) Amputation level viability in critical limb ischaemia: setting new standards. Adv Exp Med Biol 566:325–332.
7. Orsay CP, Bass EM, Firfer B et al. (1995) Blood flow in colon anastomotic stricture formation. Dis Colon Rectum 38:202–206.
8. Park JJ, Del Pino A, et al. (1999). Stoma complications: the cook county hospital experience. Dis Colon Rectum 42:1575–1580.
9. Sorensen LT, Jorgensen T, Kirkeby LT et al. (1999) Smoking and alcohol abuse are major risk factors for anastomotic leakage in colorectal surgery. Br J Surg 86:927–931.

Automatic Detection of Motion Artifacts in Infant Functional Optical Topography Studies

Anna Blasi, Derrick Phillips, Sarah Lloyd-Fox, Peck Hui Koh, and Clare E. Elwell

Abstract A key advantage of optical topography (OT) for cognitive neurodevelopmental studies over other imaging techniques such as magnetic resonance (MRI) or positron emission tomography (PET) is that it is less intrusive in the experimental set up. This is, in part, because in OT there is no need to impose strict movement constraints on the participants. However, large head movements can cause signal disruption, thus there is a need to (i) detect artifacts caused by movement and (ii) implement strategies to remove the noise component from the optical data. We have developed a motion sensor compatible with our in-house OT system and suitable for infant studies. With the data collected we have adjusted the thresholds that were used in the past to automatically discard data affected by movement artifacts. We have also compared the performance of two different head probe designs by measuring the amount of signal disruption present in recordings with each design. Finally, we have studied the feasibility of using the sensor data as external input of an adaptive filter to reduce the movement component of the optical data.

1 Introduction

Optical topography (OT) uses near infrared light to produce maps of haemoglobin oxygenation and concentration changes associated with neural activation. OT is becoming an essential neurodevelopmental tool thanks to its capability to image the functioning brain noninvasively with a high temporal resolution [1]. It is particularly well suited for infant studies because measurements can be made in a natural and comfortable setting. However, as the participants are allowed a relative freedom of movement, motion artifacts can be a problem. Various methods can be used to minimize their effect on the data

A. Blasi (✉)
Biomedical Optics Research Laboratory, Department of Medical Physics and Bioengineering, University College London, Gower Street, London, WC1E 6BT, UK
e-mail: ablasi@medphys.ucl.ac.uk

E. Takahashi, D.F. Bruley (eds.), *Oxygen Transport to Tissue XXXI*, Advances in Experimental Medicine and Biology 662,
DOI 10.1007/978-1-4419-1241-1_40, © Springer Science+Business Media, LLC 2010

analysis [2]. A simple approach is to detect changes that are clearly out of physiological range [3, 4] with a set of thresholds, but these are usually arbitrary and may vary from one data set to another. We have developed a motion sensor compatible with the head probe of our OT system [5] and suitable for infant studies. The information provided by the sensor has allowed us to adjust the tolerance thresholds to remove unacceptable oxy-haemoglobin changes (ΔHbO_2) and to establish possible correlation between head movement and the severity of disruption caused on the optical data.

In the past [2, 6], adaptive filtering has proved effective in removing movement artifacts from the optical data. Here we assess the feasibility of using the data provided by the motion sensor as an input to an adaptive filter with the aim of minimizing the noise contribution to the optical data.

2 Methods

2.1 Data Recording

Data was recorded from 24 five month-old infants with our in-house multichannel OT system [5]. The infants looked at visual stimuli presented in a block design. Each block (or trial) was defined starting 4 s prior to the stimulus onset and lasting until the end of the following rest period. *Task* (or stimulus on) and *rest* periods lasted 16 s (both, in 4 infants [7]) or 6 s *task* and 12 s *rest* (in the remaining 20 [8]). An average of 11.6 ($\pm$ 2.6) blocks were recorded for the 24 infants.

Two pads holding the optodes were placed over the infants' temporal lobes, and the distance between each source-detector pair was 2 cm. Two different sets of optical fibres and optodes were used in the studies, both with the same source and detector layout [7, 8], which produced a total of 20 measurement points (channels). In *design 1*, plastic fibres approached the head parallel to the scalp. Glass prisms were used to produce a 90-degree bend in the light path. The prisms were encapsulated in prism holders, which were held in position with a silicone-based rubber mould. An elastic velcro band over the pad held it firmly on the infants' head (Fig. 1a). In *design 2*, glass fibres

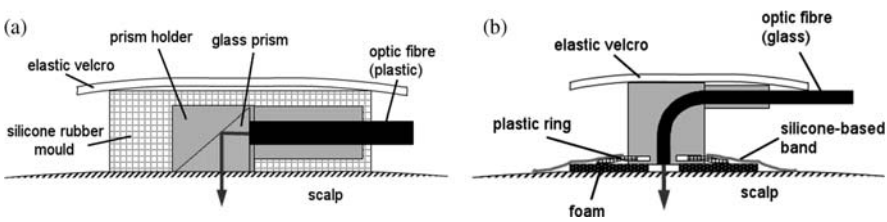

Fig. 1 Design of the pads that hold the optodes on the infant head: (**a**) design 1 with prism-ended plastic fibres; (**b**) design 2 with glass fibres curved 90 degrees

(LOPTEK GmbH & Co. KG) were guided to a 90-degree curve inside the optode. The optodes sat on a 1 mm-thick black foam with holes to allow the light through, and were held on the foam with plastic rings glued to the foam. Two bands held the pad firmly on the infant head: a silicone-based band at the base (blue line in Fig. 1b), and the same velcro as in design 1 from the top of the optodes.

The motion sensor was built with a uniaxial MTN/1800 piezoelectric accelerometer, a lightweight (9 g) accelerometer with a 1 V/g output. It was attached to the helmet with coban. Acquisition, storage and playback of the accelerometer data was collected with software developed with Labwindows/CVI.

2.2 Data Analysis

After recording, the quality of the NIRS data was assessed and channels that did not meet the criteria were eliminated from the study. Data in the remaining channels was low-pass filtered (cutoff frequency 1.8 Hz), and a linear fit was applied to each trial between the first and the last 4 s of the block [4] to remove slow drifts. The intensity data was then converted into oxy-haemoglobin (HbO_2) changes with the Beer-Lambert law and automatically inspected with a threshold-based algorithm to detect abnormal signal changes exceeding physiologically feasible values. Our thresholds were initially set to a signal change of 5 μmolar for *rest* and a signal change of 15 μmolar for *task* periods [7].

Processing of the motion sensor data started with the search for the 15-s window with the smallest standard deviation (SD), which was then used as a reference standard deviation (reference SD). Motion detection was defined as a voltage change of more than 5 times the reference SD and lasting for a minimum duration of 2 s. It was noted that the motion sensor tends to overestimate the presence of movement artefacts in the data as not all head movements cause disruption in the NIRS data. We defined *agreement* between motion sensor and the thresholding algorithm as:

$$\text{agreement} = \frac{\{N_{ms} \,\&\, N_{HbO2}\}}{\{N_{HbO2}\}} \tag{1}$$

where $\{N_{ms}\}$ are the number of trials where the motion sensor detected movement (therefore, they would be eliminated by the motion sensor), $\{N_{HbO2}\}$ are the number of trials eliminated by the thresholding algorithm described above, and $\{N_{ms}$ & $N_{HbO2}\}$ are the number of trials eliminated by both methods simultaneously.

To reduce the movement component of the optical data we implemented an adaptive filter with an external input (the data from the motion sensor) which updates the filter weights using the recursive least squares algorithm (RLS, [9], see Fig. 2) as implemented in Matlab (Matlab Mathworks, 6.5) with a forgetting factor of 0.98.

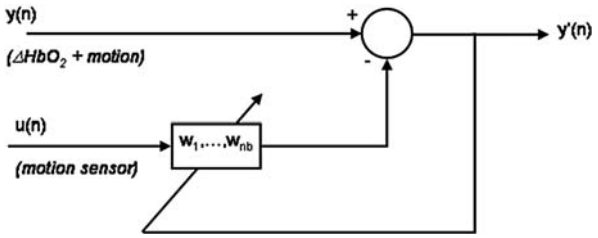

Fig. 2 Block diagram representing the adaptive filter for the removal of the noise contribution (u(n)) from the contaminated signal (the NIRS data, y(n)) by adjusting the filter weights (w1, w2, . . ., wnb) recursively to most effectively remove the noise component (u(n)) from the input signal (y(n)) to obtain a resulting signal (y'(n)) with a minimal noise component [9]

In order to evaluate the feasibility of using this technique with the accelerometer data we calculated the change in signal to noise ratio between the un-filtered (SNR) and the filtered (SNR_f) HbO_2 signal for those trials that were eliminated with the movement detection algorithm. We defined change in SNR as $\Delta SNR = SNR_f – SNR$, $SNR = 10 \log_{10}((\sigma_y)^2/(\sigma_n)^2)$, where $\sigma_y{}^2$ is the variance of the signal without movement, and $\sigma_n{}^2$ is the variance of the data with noise. Additionally, we counted the number of trials that would only pass the thresholding criteria after filtering.

3 Results and Discussion

We calculated the agreement between motion sensor and NIRS trial rejection across a range of thresholds for task and rest periods using data obtained from 6 infants with pad *design 1*. Maximum agreement of 93% was reached for rejection thresholds of 3.5 μmolar for *rest* and 8 μmolar for *task* periods (Fig. 3a).

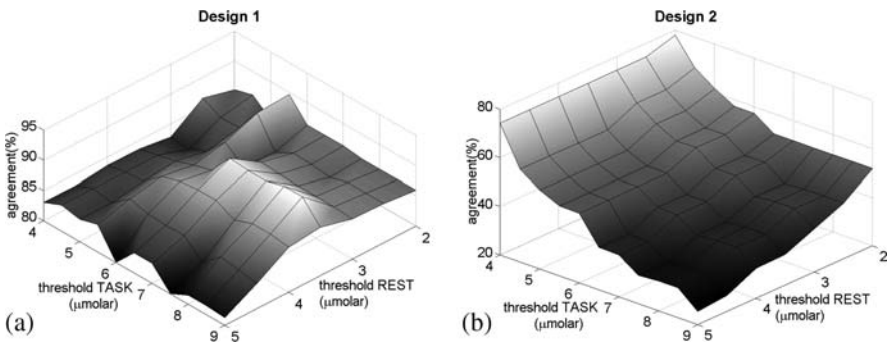

Fig. 3 Percentage of agreement between motion sensor and NIRS trial rejection over a range of thresholds for *task* and *rest* periods. (**a**) Data collected with *design 1*, average agreement across 6 infants. (**b**) Data collected with *design 2*, average agreement across 18 infants. The higher number of participants included in the average did not change the shape of (**b**)

These thresholds are lower than the more conservative ones used with the current algorithm (5 and 15 μmolar for *rest* and *task* periods respectively, [7]).

We repeated the agreement calculations for the range of thresholds using data recorded from 18 infants with pad *design 2*. Agreement between motion sensor and NIRS block rejection reached similar percentage of agreement as with design 1 only when thresholds were set so low that true physiological change was classified as movement, suggesting that, with design 2, there is a smaller disruption of the NIRS data for the same amount of head movement (Fig. 3b).

The average increase in SNR after applying the adaptive filter to remove the movement contribution to the HbO_2 signal, across data collected from 6 infants with design 1, was $\Delta SNR = 0.535$ dB (only trials where adaptive filtering increased SNR were included).

When considering data from the same 6 infants, the percentage of trials initially eliminated by the thresholding algorithm that would pass the criteria after filtering is 16%. One of these infants presented an above average number of invalid trials (29 trials) compared with the remaining 5 (average $\pm$ SD, 6 ± 2 trials). When considering only infants with a similar number of invalid trials, the percentage of trials that would pass the criteria after filtering increased to 29%.

The small improvement in SNR (a 0.535 dB increase in SNR is equivalent to a reduction of the noise variance of 0.03 μmolar) and the reduced number of recovered trials (29%) may be in part due to the inclusion of all eliminated trials in the tests, regardless of the type of motion artefact affecting the signal. However, adaptive filtering works best when the artefacts are caused by medium or slow head movement [10]. Our filter configuration, with a relative small number of coefficients (upto 5), but a rather large forgetting factor (0.98), would make it suitable for filtering these types of movement artefacts. Limitations of our motion sensor such as the use of a uniaxial accelerometer or its placement on the helmet may have further hampered the performance of the system, reducing the effectiveness of the adaptive filter.

4 Conclusions

We have successfully implemented a motion sensor for our OT studies and we have used it in infant studies without compromising either the performance of the helmet design or the infants' comfort, as recordings with and without the use of the motion sensor contain the same total amount of data per infant. We have defined the optimal threshold levels for detecting movement artefacts from the NIRS data, allowing more accurate criteria for data rejection to be established. The motion sensor has additionally been used to evaluate the amount of signal disruption due to movement in data acquired with two different pad designs and from this we conclude that design 2 is more robust to movement than

design 1. However, it is only feasible to use the data from the current sensor to inform of the presence of movement rather than quantitatively reduce the noise contribution to the NIRS data. Further developments will include the use of a tri-axial accelerometer to improve the present results.

References

1. Hoshi Y (2007) Functional near-infrared spectroscopy: current status and future prospects. J Biomed Opt doi: 10.1117/1.2804911
2. Matthews F, Pearlmutter BA, Ward TE, Soraghan C, Markham C (2008) Hemodynamics for Brain-Computer Interfaces (Optical correlates of control signals). IEEE Signal Processing Magazine. doi: 10.1109/MSP.2007.909011
3. Pena M, Maki A, Kovacic D, Dehaene-Lambertz G, Koizumi H, Bouquet F, Mehler J (2003) Sounds and silence: an optical topography study of language recognition at birth. Proc Natl Acad Sci 100:11702–11075
4. Blasi A, Fox S, Everdell N, Volein A, Tucker L, Csibra G, Gibson AP, Hebden JC, Johnson MH, Elwell CE (2007) Investigation of depth dependent changes in cerebral haemodynamics during face perception in infants. Phys Med Biol 52:6849–6864
5. Everdell NL, Gibson AP, Tullis IDC, Vaithianathan T, Hebden JC, Delpy DT (2005) A frequency multiplexed near-infrared topography system for imaging functional activation in the brain. Rev Sci Instrum doi: 10.1063/1.2038567
6. Izzetoglu M, Izzetoglu K, Bunce S, Onaral B (2003) Motion Artifact Removal in fNIR Signals Using Adaptive Filtering. Proc. of IEEE BMES 2003
7. Lloyd-Fox S, Blasi A, Volein A, Everdell N, Elwell CE, Johnson MH (2009) Social perception in infancy: a near infrared spectroscopy study. Accepted in Child Development. Child Dev 80:986–999
8. Grossman T, Johnson MH, Lloyd-Fox S, Blasi A, Deligianni F, Elwell C, Csibra G (2008) Early cortical specialization for face-to-face communication in human infants. Proc R Soc B doi:10.1098
9. Haykin S (1996) Recursive Least-Squares Algorithm. In: Kailath T (ed.) Adaptive Filter Theory, 3rd edn. Upper Saddle River, New Jersey:Prentice Hall
10. Izzetoglu M, Devaraj A, Bunce S, Onaral B (2005) Motion artifact cancellation in NIR spectroscopy using Wiener Filtering, IEEE Trans Biomed Eng 52:934–938

Modelling of Mitochondrial Oxygen Consumption and NIRS Detection of Cytochrome Oxidase Redox State

Murad Banaji, Alfred Mallet, Clare E. Elwell, Peter Nicholls, Ilias Tachtsidis, Martin Smith, and Chris E. Cooper

Abstract In recent years there has been widespread use of near infrared spectroscopy (NIRS) to monitor the brain. The signals of interest include changes in the levels of oxygenated and deoxygenated haemoglobin and tissue oxygen saturation. In addition to oxy- and deoxy-haemoglobin, the Cu_A centre in cytochrome-*c*-oxidase (CCO) is a significant NIR absorber, giving rise to another signal termed the ΔoxCCO signal. This signal has great potential as a marker of cellular oxygen metabolism, but is also the hardest to interpret. Here we use a recently constructed model to predict NIRS signal changes, and compare the model output to data from an in vivo hypoxia study in healthy adults. Our findings indicate strongly that the ΔoxCCO signal contains useful information despite the noise, and has responses consistent with the known physiology.

1 Introduction: NIRS and Brain Monitoring

Near infrared spectroscopy has been used extensively to monitor brain oxygenation, haemodynamics and metabolism [1, 2]. The chromophores of interest include oxyhaemoglobin (HbO_2) and deoxy-haemoglobin (HHb), with changes ΔHbO_2 and ΔHHb being measured using differential spectroscopy systems [3, 4, 5]. Also measured are absolute tissue oxygen saturation (TOS), the mean level of haemoglobin oxygen saturation across all vascular compartments in the tissue of interest, and changes in the level of oxidation of the Cu_A centre in cytochrome-*c*-oxidase, a signal termed the ΔoxCCO signal.

The usefulness of the ΔoxCCO signal has been the subject of much debate for two reasons: Firstly it is hard to interpret as a number of different causes may give rise to the same signal changes; Secondly the high signal-to-noise ratio raises the question of whether it contains sufficient information to be of clinical

C.E. Cooper (✉)
Department of Biological Sciences, Centre for Sports and Exercise Science, University of Essex, Wivenhoe Park, Colchester, Essex, CO4 3SQ, UK
e-mail: ccooper@essex.ac.uk

E. Takahashi, D.F. Bruley (eds.), *Oxygen Transport to Tissue XXXI*,
Advances in Experimental Medicine and Biology 662,
DOI 10.1007/978-1-4419-1241-1_41, © Springer Science+Business Media, LLC 2010

interest. However, as we will show, combining measurement with modelling allows useful information to be extracted from the signal, giving it the potential to make a significant contribution in a clinical setting.

2 The Model

A model capable of predicting behaviour of all the NIRS signals was constructed. The mathematical description is presented in [6], and the model itself is available for download at [7]. The model was designed to respond to four input stimuli, chosen both for their physiological importance, and because there is considerable data on the response of NIRS signals to these inputs:

(1) Changes in mean arterial blood pressure (ABP) [8];
(2) Changes in arterial O_2 levels (SaO_2) [9];
(3) Changes in arterial CO_2 levels ($PaCO_2$) [10] and
(4) Functional activation [5].

The most important model outputs are the NIRS signals TOS and ΔoxCCO, along with cerebral blood flow (CBF) and oxygen consumption rate ($CMRO_2$). A schematic of the structure of the model is presented in Fig. 1

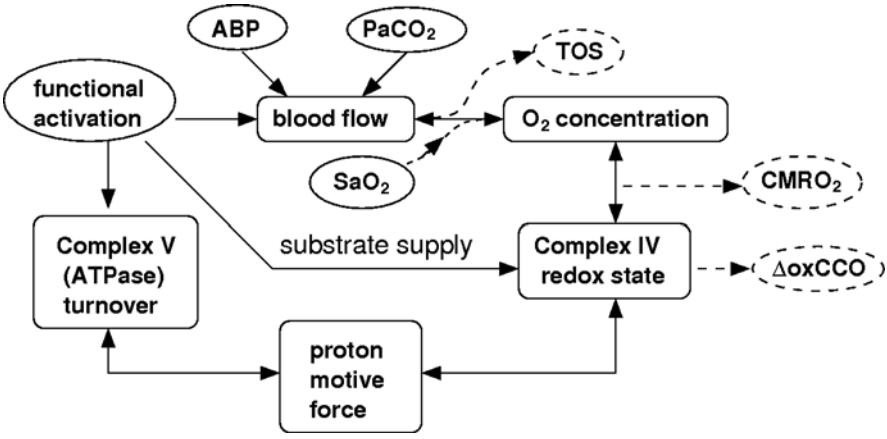

Fig.1 Summary of the main inputs, variables and processes in the model. Model inputs are enclosed in solid ovals, while outputs are enclosed in dashed ovals

The model consists essentially of two components: A submodel of the cerebral circulation, which is known to respond in complicated ways to a variety of stimuli, and a submodel of mitochondrial metabolism related to the models presented in [11] and [12]. The two components of the model are linked via

oxygen transport and consumption. In addition to the full model designed to represent an in vivo situation, a simplified model representing an in vitro situation was also constructed, in order to allow model parameter setting from in vitro data. Model parameters were chosen to be consistent with thermodynamic principles.

Parameter setting and model validation are described extensively in [6]. Examples of model behaviour are presented in Figs. 2 and 3 below. In Fig. 2 steady state behaviour of cerebral blood flow (CBF) in response to changes in arterial blood pressure and $PaCO_2$ is shown to be consistent with published in vivo experimental data. In Fig. 3, experimentally measured cytochrome *c* redox state and modelled Cu_A redox state (which for theoretical reasons can be assumed to be similar) are compared. The data suggest that the redox states are sensitive to arterial O_2 levels at physiological values.

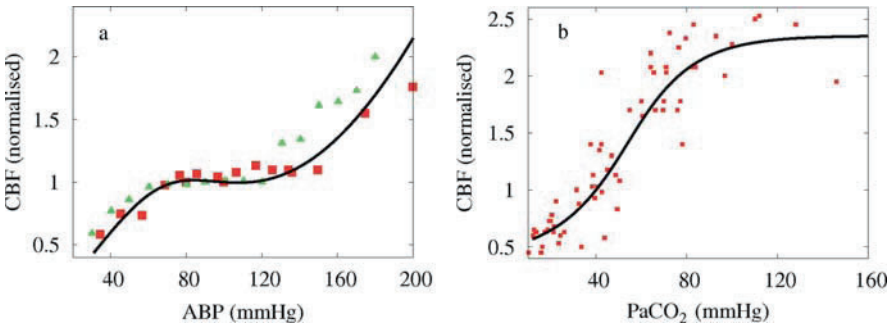

Fig. 2 (**a**) The modelled response (*solid line*) of CBF to changes in blood pressure, with data from [13] (squares) and [14] (triangles). (**b**) The modelled response (*solid line*) of CBF to changes in $PaCO_2$ with data from [15] (normal resting CBF set at 40 ml/min/100 g)

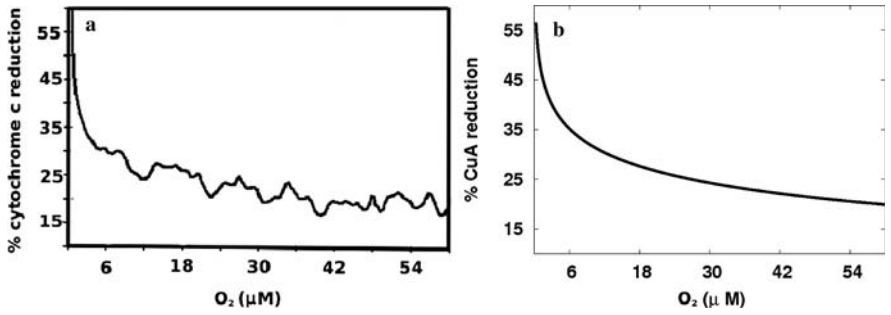

Fig. 3 (**a**) The variation in measured cytochrome *c* redox state during hypoxia, redrawn from Fig. 5a of [16]. (**b**) Modelled Cu_A redox state during hypoxia for simplified in vitro model

3 Comparison with Data from a Hypoxia Study

A study of nine healthy volunteers undergoing a hypoxic challenge (SaO_2 slowly reduced to about 80% three times) was carried out [17]. During this process both TOS (TOI, Hamamatsu NIRO300) and ΔoxCCO (multiwavelength CCD spectrometer) were measured, along with systemic data on SaO_2, $PaCO_2$ and ABP. The systemic data were used as input into the model, in order to compare modelled and measured signals. An example of such a comparison for one subject is presented in Fig. 4

In Fig. 5 modelled and measured ΔoxCCO are compared for a further eight subjects from the same study. No attempt at model fitting has been carried out – in each case the model was run at default parameter values. It is clear that in some cases model behaviour is both qualitatively and quantitatively consistent with the data. Where this fails to be the case, there appears to be some systematic drift in the measured data, with the magnitude of this drift suggesting experimental artefact. It is also interesting that where the measured data appears to lack information (e.g. panel 4 of Fig. 5) the model suggests that this may have been the physiological response, *not* measurement artefact. At this stage, the comparison is promising.

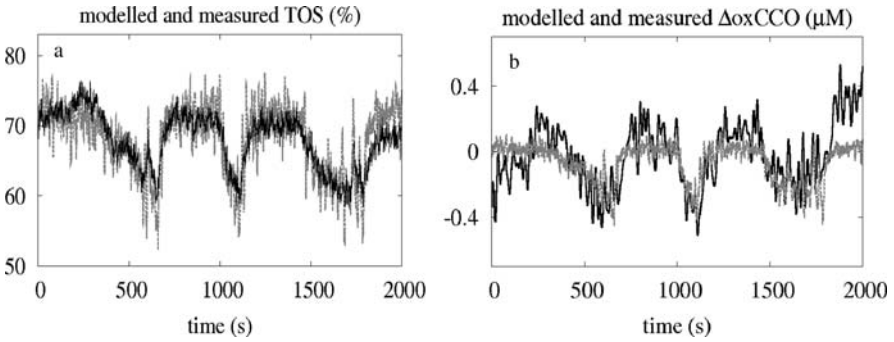

Fig. 4 The modelled (*light line*) and measured (*dark line*) responses of (**a**) TOS and (**b**) ΔoxCCO for a subject undergoing a series of three hypoxic swings. Further details are in [17]

4 Estimating ΔoxCCO Using the BRAINCIRC Model

Finally, we wished to find out if our recent model provided any improvement over a previous model, BRAINCIRC, described in [18]. Although the BRAINCIRC model cannot directly predict Cu_A redox state, ΔoxCCO can be estimated using indirect calculation from NAD/NADH levels and phosphorylation potential, based on the assumption that the electron transport chain is near

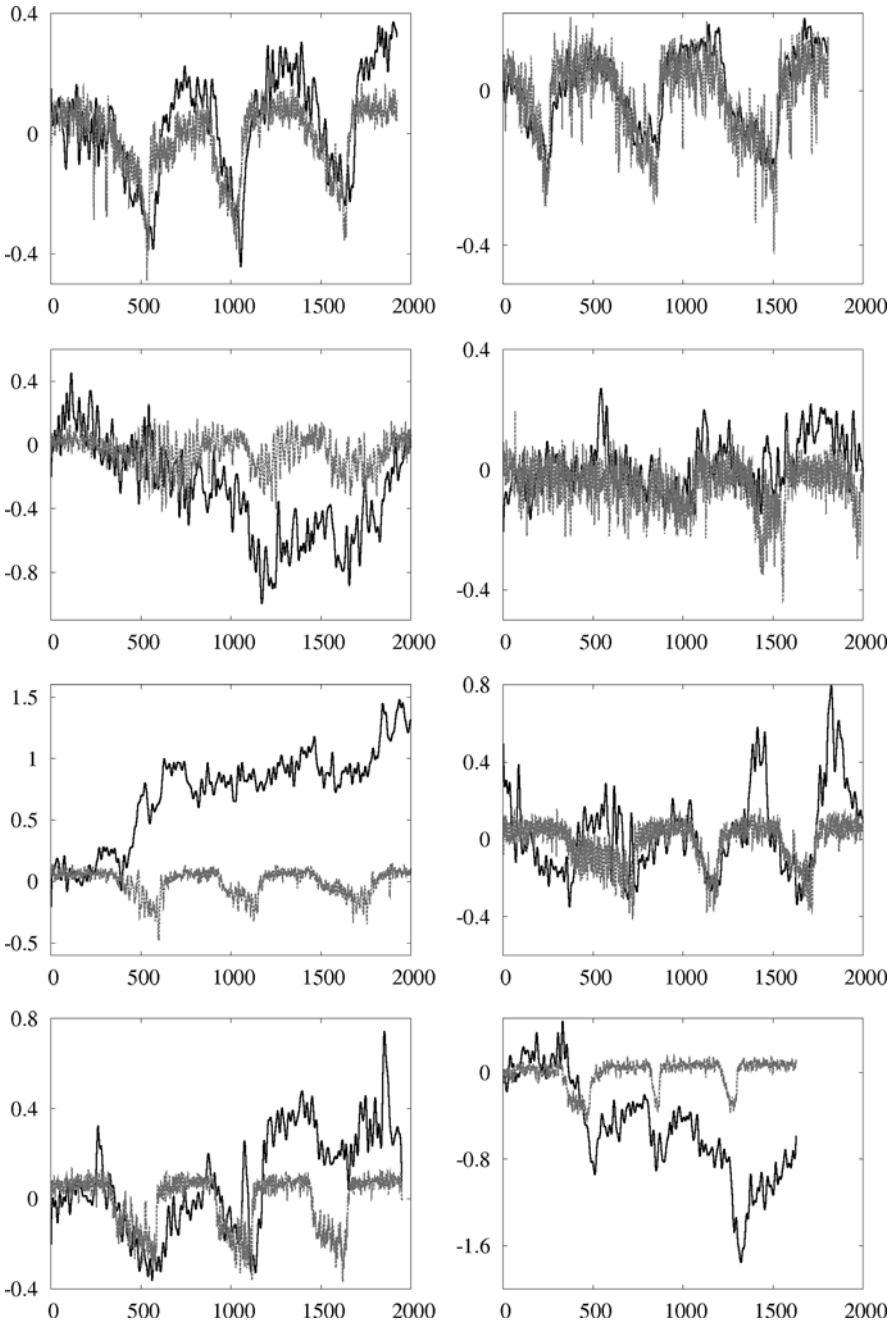

Fig. 5 The modelled (*light line*) and measured (*dark line*) responses of ΔoxCCO for eight further subjects undergoing a series of hypoxic swings

thermodynamic equilibrium [19], and that Cu_A redox changes are identical to those of cytochrome *c*.

In Fig. 6a comparison between predictions of version 2 of the BRAINCIRC model (available at [7]) and experimental data is presented for the first two subjects whose data are shown in Fig. 5. Although the estimates from the BRAINCIRC model were qualitatively reasonable, the comparison suggests that direct modelling of Cu_A using the new model yields more accurate results. It should be mentioned however that no attempt was made to optimise the BRAINCIRC model or adapt it to the current situation.

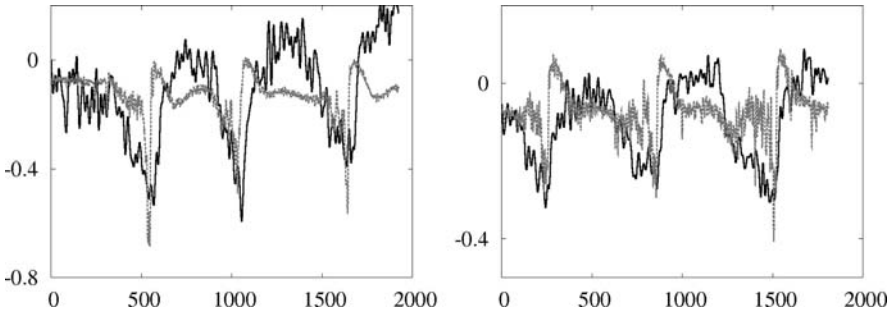

Fig. 6 The modelled (*light line*) and measured (*dark line*) responses of ΔoxCCO for the first two subjects (top two panels) presented in Fig. 5. This time the model used is the BRAINCIRC model, and ΔoxCCO was estimated using indirect calculations (see text)

5 Conclusions

Despite the low signal-to-noise ratio, the ΔoxCCO signal contains physiological information of potential clinical importance. The model we have constructed is able to reproduce the behaviour of this signal both qualitatively and sometimes quantitatively during hypoxia. It appears to give more accurate results than estimates using previous modelling work Once the model has been more extensively validated against further in vivo data, it has the potential to be used to identify artefactual trends in the measured ΔoxCCO traces, and importantly for clinical studies, to make predictions about blood flow and $CMRO_2$.

References

1. Obrig H and Villringer A (2003) Beyond the visible – imaging the human brain with light. Cereb Blood Flow Metab 23:1–18.
2. Ferrari M, Mottola L and Quaresima V (2004) Principles, techniques and limitations of near infrared spectroscopy. Can J Appl Physiol 29:463–487.
3. Hoshi Y (2003) Functional near-infrared optical imaging: Utility and limitations in human brain mapping. Psychophysiology 40:511–520.

4. Elwell CE, Cope M, Edwards A et al. (1994) Quantification of adult cerebral haemodynamics by near infrared spectroscopy. J Appl Phys 77:2753–2760.
5. Villringer A and Chance B (1997) Non-invasive optical spectroscopy and imaging of human brain function. Trends Neurosci 20:435–442.
6. Banaji M, Mallet A, Elwell C et al. (2008) A model of brain circulation and metabolism: NIRS signal changes during physiological challenges. PLoS Comput Biol 4(11):e1000212
7. Model repository at http://www.medphys.ucl.ac.uk/braincirc/download/repos/repos.html
8. Hunt K, Tachtsidis I, Bleasdale-Barr K et al. (2006) Changes in cerebral oxygenation and haemodynamics during postural blood pressure changes in patients with autonomic failure. Physiol Meas 27:777–785.
9. Hampson NB, Camporesi EM, Stolp BW et al. (1990) Cerebral oxygen availability by NIR spectroscopy during transient hypoxia in humans. J Appl Physiol 69:907–913.
10. Klaessens JHGM, Kolkman RGM et al. (2003) Monitoring cerebral perfusion using near-infrared spectroscopy and laser Doppler flowmetry. Physiol Meas 24:N35–N40.
11. Korzeniewski B and Zoladz JA (2001) A model of oxidative phosphorylation in mammalian skeletal muscle. Biophys Chem 92:17–34
12. Beard D (2005) A biophysical model of the mitochondrial respiratory system and oxidative phosphorylation. PLoS Comp Bio 1(4):e36
13. Gao E, Young WL, Pile-Spellman J, Ornstein E and Ma Q (1998) Mathematical considerations for modelling cerebral blood flow autoregulation to systemic arterial pressure. Am J Physiol Heart Circ Physiol 274:H1023–H1031.
14. Harper SL, Bohlen HG, and Rubin MJ (1984) Arterial and microvascular contributions to cerebral cortical autoregulation in rats. Am J Physiol Heart Circ Physiol 246:H17–H24
15. Reivich M (1964) Arterial P_{CO2} and cerebral hemodynamics Am J Physiol 206:25–35.
16. Wilson DF, Rumsey WL, Green TJ and Vanderkooi JM (1988) The oxygen dependence of mitochondrial oxidative phosphorylation measured by a new optical method for measuring oxygen concentration. J Biol Chem 263:2712–2718.
17. Tisdall M, Tachtsidis I, Elwell CE and Smith M (2006) changes in concentration of oxidised cytochrome oxidase measured using both broadband and four wavelength near infrared spectroscopy reflect changes in oxygen delivery during hypoxaemia in healthy volunteers. Optical Society of America, Biomedical Optics 2006 Technical Digest ME66
18. Banaji M, Tachtsidis I, Delpy D and Baigent S (2005) A physiological model of cerebral blood flow control. Math Biosci 194:125–173.
19. Wilson DF, Stubbs M, Veech RL et al. (1974) Equilibrium relations between the oxidation-reduction reactions and the adenosine triphosphate synthesis in suspensions of isolated liver cells. Biochem J 140:57–64

Forced Oscillation Technique as a Non-Invasive Assessment for Lung Transplant Recipients

Hiroshi Hamakawa, Hiroaki Sakai, Ayuko Takahashi, Jintian Zhang, Toshihiro Okamoto, Naoki Satoda, Akihiro Aoyama, Fengshi Chen, Takuji Fujinaga, Tsuyoshi Shoji, Toru Bando, Michiaki Mishima, Hiromi Wada, and Hiroshi Date

Abstract We usually use spirometry for the medical follow-up of respiratory mechanics after lung transplantation. However, especially in the first few post-operative weeks, it is easily affected by postoperative pain and the patient's co-operation during forced breathing effort. To avoid missing out on assessing pulmonary function, we perform non-invasive forced oscillation techniques on the patients who cannot perform forced breathing maneuvers. In this paper, we discuss the application of forced oscillation techniques on a patient with suspicion of acute lung rejection, whose spirometry could not be correctly performed and seemed to be unreliable. The respiratory impedance measurements had good correlation with the patient's clinical symptoms before and after steroid therapy. Thus, postoperative pulmonary function follow-up using forced oscillation technique was useful in assessing peripheral airway condition in critically ill patients, and may be able to detect acute rejection.

1 Introduction

Lung transplantation is a recent therapeutic option for the patients with end-stage lung disease [1]. Patients after lung transplantation may suffer graft dysfunction because of reperfusion injury, infection and/or rejection, and these events contribute to late allograft failure because of the development of bronchiolitis obliterans [2, 3]. Therefore, early detection of these problems is essential to determine correct therapeutic strategy.

The clinical presentation of acute lung rejection (AR) may include fever, dyspnea, pleuritic pain, or radiological appearance of infiltrates and pleural effusion. Such patients develop modest leukocytosis, a fall of arterial oxygen

H. Sakai (✉)
Departments of Thoracic Surgery, Institute for Frontier Medical Sciences,
Kyoto University, Kyoto, 606-8507, Japan
e-mail: hsakai@kuhp.kyoto-u.ac.jp

E. Takahashi, D.F. Bruley (eds.), *Oxygen Transport to Tissue XXXI*,
Advances in Experimental Medicine and Biology 662,
DOI 10.1007/978-1-4419-1241-1_42, © Springer Science+Business Media, LLC 2010

tension and decreased forced expiratory volume in one second. However, physical examination, chest radiography, spirometry and blood gas analysis are non-specific for identifying AR, which is pathologically characterized by perivascular and sub-endothelial lymphocytic infiltration. The gold standard for a correct diagnosis is histological examination of lung parenchyma acquired with multiple transbronchial biopsies [1, 4]. However, it is often difficult to repeat these invasive investigations, which have a variety of risks [5]. Therefore, on occasions, clinicians diagnose AR clinically.

The forced oscillation technique (FOT) is a method for noninvasive assessment of respiratory mechanics [6]. This technique is applicable for veterinary, preschool and senile subjects because of its noninvasiveness and less necessity for subject cooperation. In other words, assessment of respiratory mechanics by FOT can be performed on those who cannot perform spirometry [7].

The aim of this study is to ascertain whether the patient who is in early post-operative period after lung transplantation can be assessed using FOT, and to monitor how the clinical symptoms are associated with the alteration of impedance parameters.

2 Theoretical Background and Measurement Protocol

Respiratory impedance (Z_{rs}) is represented as a function of angular frequency in radians/s (ω) and consists of the in-phase and out-of-phase components: respiratory resistance (R_{rs}) and reactance (X_{rs}), where $Z_{rs}(\omega) = R_{rs}(\omega) + jX_{rs}(\omega) = R_{aw} + j(\omega I - 1/\omega C)$, where j is the imaginary unit, R_{aw} is airway resistance, I is inertia, and C is capacitance.

Master Screen Impulse Oscillometry (Erich Jaeger GmbH, Hoechberg, Germany) is used for obtaining respiratory input impedance [8, 9, 10]. In the present study, R5 (R_{rs} at 5 Hz), R20 (R_{rs} at 20 Hz) and X5 (X_{rs} at 5 Hz) were used. R5, R20 and X5 represent total respiratory resistance, proximal airway resistance and capacitive reactance, respectively. Then, R5–R20, that subtracted R20 from R5, indicates peripheral airway resistance.

Each observation consisted of at least 3 tests, which did not have artifacts caused by air leakage from the mouth or the tracheostomy, coughing, breath holding, swallowing and so on. The data set with optimum coherence values, in which $\gamma 2(f) \geq$ both 0.6 at 5 Hz and 0.9 at 20 Hz were the ideal threshold, was adopted [11, 10].

3 Case Report

A 38-year-old male with juvenile pulmonary emphysema underwent clamshell thoracotomy with transverse sternotomy at the level of 4th intercostals space, and bilateral lung transplantation from a certified brain-dead donor. On the 14th post-operative day (POD), the progress of general fatigue and minute

decrease of PaO_2/FiO_2 without asthmatic symptoms were recognized. Around 11th POD, chest radiographs revealed right pleural effusion which decreased by 14th POD. Radiographs contributed little to the diagnosis of AR because of day-by-day variation. Airway infections were excluded by microbiological examinations from broncho-alveolar lavage specimens, as well as the modest changes of serological examinations. In addition, because of the patient's tracheostomised condition, spirometry could not be performed until 12th POD. A cuff-less tracheostomy tube with a hole, which enabled vocal training, had been inserted until 12th POD (Fig. 1).

Z_{rs} could be measured after the second POD, and changes in Z_{rs} were also assessed (Fig. 2). Between 11th and 14th POD, X5 decreased from -0.10 to -0.22 kPa.s.L^{-1}, and R5-R20 increased from 0.05 to 0.12 kPa.s.L^{-1}. In the department of thoracic surgery in Kyoto University, mean values (expressed as mean $\pm$ SD) of X5 and R5–R20 of male subjects with lung tumor ($n = 79$, 64.5 ± 12.0 years of age) were -0.109 ± 0.047 and 0.039 ± 0.042 kPa.s.L^{-1}, respectively (unpublished data).

The findings suggested that peripheral airway condition had already deteriorated around 11th POD. Even without transbronchial biopsy, we considered

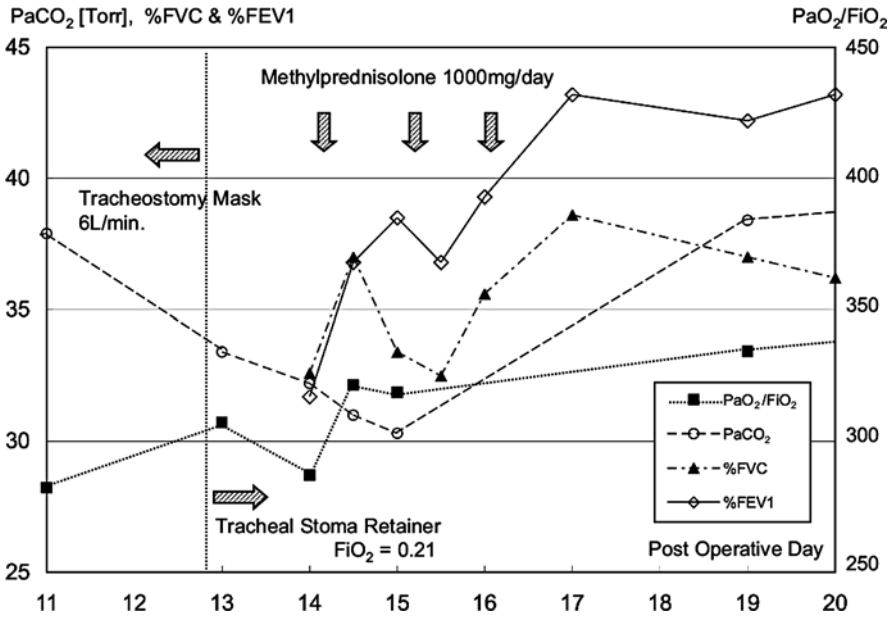

Fig. 1 Spirometry could not be performed until 12th POD because of the patient's tracheostomised condition. On 13th POD, tracheal stoma retainer was inserted instead of tracheostomy tube. After the steroid administration, FEV1 and PaO_2 were improved gradually. %FEV1 was 31.7, 36.8 and 38.5 % at pre, 12 and 24 h, respectively. PaO_2/FiO_2 was 287.1, 321.4 and 318.6 at pre, 12 and 24 h, respectively. $PaCO_2$ had decreased when AR was suspected, and increased after steroid therapy

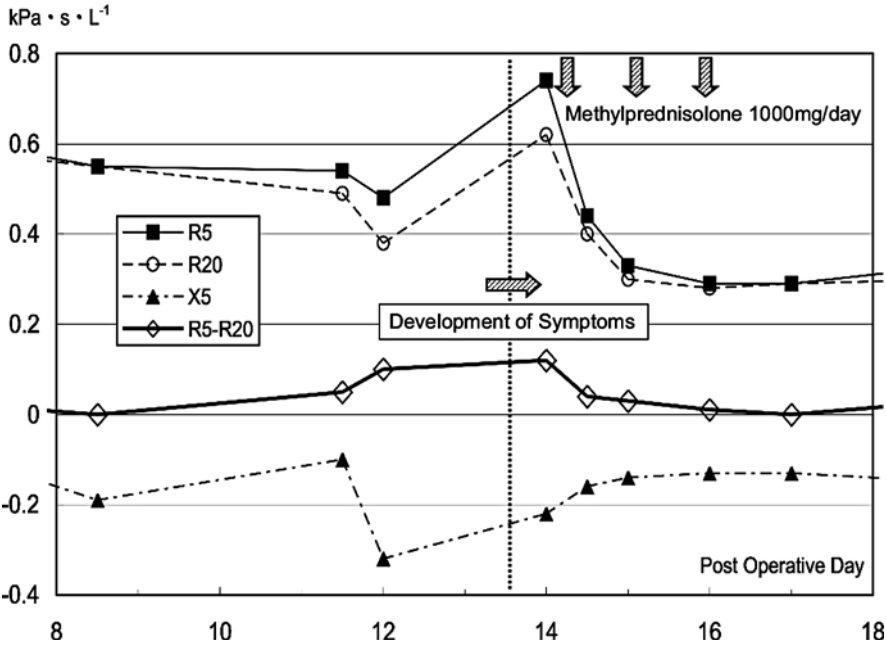

Fig. 2 Each parameter of FOT exhibited clear change before and after the steroid administration. R5 was 0.74, 0.44 and 0.33 kPa.s.L^{-1} at pre, 12 and 24 h, respectively. R20 was 0.62, 0.40 and 0.30 kPa.s.L^{-1} at pre, 12 and 24 h, respectively. X5 was −0.22, −0.16 and −0.14 kPa.s.L^{-1} at pre, 12 and 24 h, respectively. R5–R20 was 0.12, 0.04 and 0.03 kPa.s.L^{-1} at pre, 12 and 24 h, respectively. The alteration of respiratory impedance was accompanied with that of CRP, $PaCO_2$ and clinical symptoms

the symptoms as possible consequences of AR. Methylprednisolone (1000 mg/body/day) was administered intravenously daily for 3 days. Each parameter of Z_{rs} clearly changed before and after the steroid administration (Fig. 2). FEV1 and PaO_2/FiO_2 gradually improved. In contrast, $PaCO_2$ had decreased when AR was suspected and increased after steroid therapy (Fig. 1).

4 Discussion

Acute lung rejection is characterized by perivascular and subendothelial mononuclear infiltrates, and by lymphocytic bronchitis and bronchiolitis [4]. Physical examination, chest radiography, spirometry and blood gas analysis are nonspecific and unreliable in identifying AR, especially during the first few weeks post-operatively. The gold standard for diagnosing AR is histological examination of lung parenchyma acquired by multiple transbronchial biopsies [1, 4]. However, the repeated performance of these invasive investigations [5] carries a high risk for secondary complications. Recently, Jones HA et al. reported that ^{18}F-fluorodeoxyglucose uptake measured by positron emission tomography

(^{18}FDG-PET) discriminated between airway infection and rejection in lung transplant recipients with no radiological abnormalities and it was suggested that a high ^{18}FDG-PET signal was indicative of infection, but not rejection, in lung transplant recipients [12]. However, the subjects must be transported to perform the procedure, and it is impossible to check them continuously and repeatedly. An ideal marker should be obtainable non-invasively; measurable repeatedly; easy, and quick; sensitive and specific; and inexpensive. Assessment of respiratory mechanics is also non-specific for that purpose.

FOT, due to its simplicity for assessing respiratory mechanics, should complement clinical features for rapid recognition of AR and infection. In the present case, changes in R5, R5–R20 and X5 indicated the changes of peripheral airway conditions, which might have been related to the early phase of AR. Furthermore, changes of X5 and R5–R20 were detected 2 days before the patient's demonstrated clear symptomatology. These could have been consistent with the pathological features of AR.

This is only a single case report and statistical differences in the FOT parameters between pre and post steroid administration cannot therefore be demonstrated. Furthermore the relationship between histopathology and respiratory impedance spectra has not been well studied. Further studies are necessary to evaluate the sensitivity and specificity of the Z_{rs} parameters for identifying the relation between histopathology and lung mechanics. However, due to its non-invasive and minimal cooperative characters, this technique has been established as a tool for assessment of airway narrowing and peripheral capacitive behavior, especially in clinical research in infants, young children and senile subjects [7, 13, 14, 15]. This less invasiveness can also allow us to investigate the respiratory impedance both in paralyzed and non-paralyzed subjects [16]. In addition, the observation of respiratory impedance might be more relevant when combined with another investigation like ^{18}FDG-PET.

In conclusion, the FOT has potential for monitoring and evaluating lung mechanical properties in critically ill patients, such as lung transplant recipients, who cannot perform forced breathing maneuvers.

Acknowledgments The authors would like to thank Dr. Tatsuo Fukuse and Dr. Takayuki Nakamura, Department of Thoracic Surgery, Kyoto University, for their essential and critical advice during preparation of this paper. Portions of this work were presented at the 6th International Congress on Lung Transplantation Paris, September 16–17, 2004.

References

1. Stewart KC, Patterson GA. Current trends in lung transplantation. Am J Transplant 2001 Sep;1(3):204–210.
2. Bando K, Paradis IL, Komatsu K et al. Analysis of time-dependent risks for infection, rejection, and death after pulmonary transplantation. J Thorac Cardiovasc Surg 1995 Jan;109(1):49–57; discussion 57–59.
3. Girgis RE, Tu I, Berry GJ et al. Risk factors for the development of obliterative bronchiolitis after lung transplantation. J Heart Lung Transplant 1996 Dec;15(12):1200–1208.

4. Yousem SA, Berry GJ, Cagle PT et al. Revision of the 1990 working formulation for the classification of pulmonary allograft rejection: Lung rejection study group. J Heart Lung Transplant 1996 Jan;15(1 Pt 1):1–15.
5. Dark JH. Diagnosis of lung rejection. Lancet. 2004 May 8;363(9420):1487–1488.
6. DuBois AB, Brody AW, Lewis DH et al. Oscillation mechanics of lung and chest in man. J Appl Physiol 1956;8:587–594
7. Oostveen E, MacLeod D, Lorino H et al. The forced oscillation technique in clinical practice: methodology, recommendations and future developments. Eur Respir J 2003 Dec;22(6):1026–1041.
8. Michaelson ED, Grassman DE, Peters WR. Pulmonary mechanics by spectral analysis of forced random nois. J Clin Invest 1975 Nov;56:1210–1230.
9. Landser FJ, Nagels J, Demedts M et al. A new method to determine frequency characteristics of the respiratory system. J Appl Physiol 1976 Jul;41(1):101–106.
10. Miller TK, Pimmel RL. Standard errors on respiratory mechanical parameters obtained by forced random excitation. IEEE Trans Biomed Eng 1983 Dec;30(12):826–832.
11. Smith HJ, Reinhold P, Goldman MD. Forced oscillation technique and impulse oscillometry. Eur Respir Mon 2005;31(5):72–105.
12. Jones HA, Donovan T, Goddard MJ et al. Use of ^{18}FDG-PET to discriminate between infection and rejection in lung transplant recipients. Transplantation 2004 May 15;77(9):1462–1464.
13. Vink GR, Arets HG, van der Laag J et al. Impulse oscillometry: a measure for airway obstruction. Pediatr Pulmonol 2003 Mar;35(3):214–219.
14. Marotta A, Klinnert MD, Price MR et al. Impulse oscillometry provides an effective measure of lung dysfunction in 4-year-old children at risk for persistent asthma. J Allergy Clin Immunol 2003 Aug;112(2):317–22.
15. Beydon N, Davis SD, Lombardi E et al. An official American Thoracic Society/European Respiratory Society statement: pulmonary function testing in preschool children. Am J Respir Crit Care Med 2007 Jun 15;175(12):1304–1345.
16. Navajas D, Farré R, Canet J et al. Respiratory input impedance in anesthetized paralyzed patients. J Appl Physiol 1990 Oct;69(4):1372–1379

Part III
Exercise and O_2 Transport

Muscle Microcirculatory O_2 Exchange in Health and Disease

David C. Poole and Timothy I. Musch

Abstract Much of our understanding of blood-muscle O_2 and substrate exchange is predicated on the presumption that, in resting muscle, a substantial proportion of the capillary bed does not sustain red blood cell (RBC) or plasma flux. According to this notion, with contractions, more capillaries are "recruited" (i.e., begin flowing) and increased metabolic demands are supported by blood-myocyte O_2 and substrate flux in these newly recruited capillaries. This scenario is attractive because additional exchange vessels are added, and radial intercapillary diffusion distances reduced, as demands increase – but is it correct? The compelling weight of evidence gathered over the last 3 decades using intravital microscopy, phosphorescence quenching and near infrared spectroscopy (NIRS) techniques challenges conventional "wisdom" and indicates that the majority of capillaries support RBC flux at rest. Thus, at the onset of contractions blood-myocyte O_2 and substrate flux must increase in vessels that were already flowing at rest. This concept forces a radical revision of the control of blood-myocyte O_2 and substrate flux. This revision is essential if we are to understand the control of microcirculatory O_2 and substrate flux in health and resolve the mechanistic bases by which these processes are compromised in diseases such as chronic heart failure.

1 Introduction

From rest-to-exercise skeletal muscle metabolic rate may increase upto two orders of magnitude [1]. As rhythmic contractions are sustained primarily through oxidative metabolism the ability to distribute blood flow and deliver O_2 and substrates [glucose and free fatty acids (FFA)] within and among active skeletal muscles is of paramount importance. Since the seminal microscopy

D.C. Poole (✉)
Departments of Anatomy, Physiology and Kinesiology, Kansas State University, Manhattan, Kansas 66506, USA; School of Sports and Health Sciences, University of Exeter, Exeter, Devon, UK
e-mail: poole@vet.ksu.edu

E. Takahashi, D.F. Bruley (eds.), *Oxygen Transport to Tissue XXXI*, Advances in Experimental Medicine and Biology 662,
DOI 10.1007/978-1-4419-1241-1_43, © Springer Science+Business Media, LLC 2010

studies of August Krogh nearly a century ago the notion of "capillary recruitment" has been invoked to explain increased blood-muscle O_2 flux at the onset of contractions [2]. This notion is founded on the tacit presumption that many capillaries in resting muscle do not sustain red blood cell (RBC) flux and that these capillaries then initiate RBC flux with contractions.

Krogh used high pressure India ink perfusions of resting and contracting muscle to demonstrate that many more capillaries contained ink after contractions [2]. Obvious limitations of this procedure, which were acknowledged by Krogh, included vascular and myocyte distortion and the clumping together of India ink particles which may have preferentially blocked terminal arterioles in the resting condition when their caliber was the smallest. Despite these shortcomings, textbook authors [e.g., 3, 4] and contemporary researchers [e.g., 5–8] use these observations, and Krogh's O_2 diffusion model developed from them, to explain fundamental physiological phenomenon in resting and contracting muscles including: (1) Recruitment of additional capillary surface area. (2) Increased blood-muscle O_2, glucose and FFA fluxes. (3) Decreased capillary-mitochondrial diffusion distances.

It is certainly logical that, if there were a substantial reserve capacity for blood-myocyte flux at rest, during exercise when the muscles' energetic demands increased, that reserve would be recruited. However, evidence is presented herein that conflicts with the existent dogma that, in exercising muscle(s), increased blood-myocyte flux results solely or primarily from the initiation of RBC and plasma flow in previously non-flowing capillaries. Rather, the position is taken that, if RBC and plasma flow already exist in most capillaries in resting muscle (and much recent evidence indicates that this is so), increased blood-myocyte flux (i.e., phenomena 1–3 above) during exercise must occur within already-recruited capillaries. This position forces consideration of new models for blood-myocyte exchange in exercising muscle and reveals important clues into the mechanistic bases for microvascular dysfunction in chronic disease(s) (Fig. 1)

Notwithstanding the above, the motto of The Royal Society "*Nullius in Verba*" (Take nobody's word for it, see it for yourself) exhorts the scientist to challenge dogmatic adherence to ideologies especially when they conflict with rigorous scientific observations. It is pertinent that the most ardent supporters of "capillary recruitment" do not actually observe capillaries in their experiments [8] – a practice that has drawn acerbic criticism from eminent microscopists such as Eugene Renkin [9]. Instead, their conclusions are based upon assumptions that often regard a capillary as a simple switch that is either on or off [e.g., 6, 7].

It is the purpose of this review to present: (1) compelling direct evidence for RBC flux in the majority of capillaries in resting muscle – which precludes the possibility of substantial recruitment of previously non-flowing capillaries during exercise. (2) Recent NIRS evidence that supports little *de novo* capillary recruitment from rest-to-exercise. (3) Quantitative support that maintenance of RBC flux in the majority of resting muscle is feasible. (4) Putative explanations

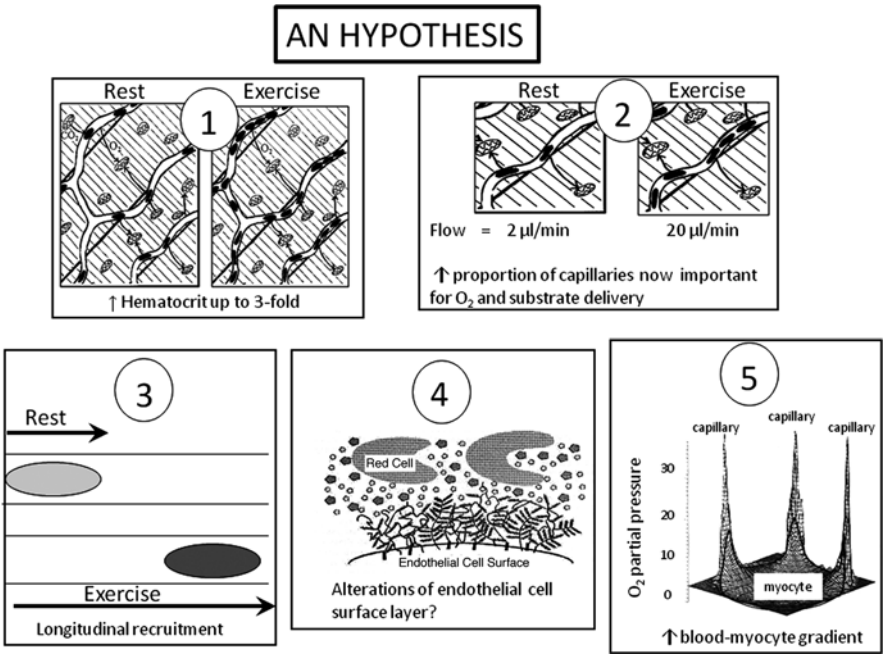

Fig. 1 Putative mechanisms that can account for the increase of blood-myocyte O_2 (and substrate) flux, from rest-exercise, within existent RBC flowing capillaries without the necessity for "recruitment" of previously non-flowing capillaries. (1) Elevation of RBC numbers (hematocrit) within capillaries. (2) Substantial elevation of blood flow (RBC flux) within originally very low flow capillaries means that capillaries that were unimportant for blood-myocyte flux at rest become important during exercise. (3) Increased RBC velocity and greater fractional O_2 extraction mean that additional capillary surface area along the length of the capillary becomes important for blood-myocyte flux. (4) There is the possibility that the endothelial cell surface layer (thought to be crucial in lowering capillary hematocrit below systemic) is modified under high flow conditions. (5) The precipitous fall in intracellular PO_2 increases the blood-myocyte gradient and also desaturates myoglobin potentially elevating its ability to transport O_2 and therefore intracellular diffusing capacity for O_2

for apparently contrary evidence. (5) A novel model that accounts for increased blood-myocyte flux without the necessity for de novo capillary recruitment (Fig. 1).

2 RBC Flux in the Majority of Capillaries in Resting Muscle

In conscious rats at rest systemic indicator infusions reveal that almost all capillaries in the muscles examined (diaphragm, soleus, vastus lateralis) evidenced perfusion within 7 s [i.e., < 1 circulation, ref. 10]. This observation is supported by an extensive array of intravital microscopy studies of rat extensor

digitorum longus [11], diaphragm [12] and spinotrapezius [13, 14] as well as hamster sartorius and cremaster [15], rabbit tenuissimus [16] and cat sartorius [17] muscles which demonstrate that > 80% of capillaries support RBC flux under resting conditions.

Intravital microscopy techniques have been criticized based upon the surgery required to visualize the muscle of interest, whether all capillaries within the optical field are visible and the necessity for anesthesia. Each of these concerns has been systematically countered as follows: Careful measurements in vasodilated [18] and contracting [14] muscles demonstrated that no more capillaries became visible under hyperemic conditions when additionally "recruited" capillaries would be obvious. Bailey et al. [19] showed that surgical preparation of the spinotrapezius muscle requisite for intravital microscopy did not alter blood flow (radiolabelled microspheres) or the precise matching of blood flow to metabolic rate (microvascular PO_2) at rest or during contractions. Regarding anesthesia, the similarity of findings between conscious and anesthetized animals suggests that the majority of the capillaries in resting muscle support RBC flux [10–15, 17]. Additional evidence that smooth muscle function is preserved under anesthesia – which counters the argument that it is a loss of vasomotor tone which accounts for > 80% of capillaries supporting RBC flux – is that muscles of anesthetized animals preserve their blood flow to metabolism (O_2 uptake) ratio of ~6:1 [20] as found in animals and humans performing voluntary exercise [1].

3 NIRS Evidence Supports Little De novo Capillary Recruitment from Rest-Exercise

If one were to accept the notion of substantial capillary recruitment at exercise onset, for example from 15 to 90%, muscle hemoglobin concentration [Hb] would be expected to increase a minimum of 6-fold (and probably much more due to augmented capillary hematocrit). Near infrared spectroscopy (NIRS) interrogation of the exercising human quadriceps reveals that the actual increase of [Hb] is a very modest <30% [21] which may be achieved via augmented capillary hematocrit within capillaries that support RBC flux at rest [22] without de novo recruitment of capillaries.

4 RBC Flux in Most Resting Muscle Capillaries is Mathematically Feasible

The exemplar 70 kg human in whom 45% of body mass (31.5 kg) is muscle has an estimated muscle blood flow of ~1 L/min (corresponding to 5.4 trillion RBC/min) [3, 4]. Accepting that capillary length and density vary among muscles 1,000 μm and 300/mm^2 are reasonable mean values. If we consider

that 80% [as in the rat, refs. 13, 14, 23] of these 8.9 billion muscle capillaries sustain RBC flux ~12 RBC/capillary/s is calculated. This value compares very closely to that actually measured in the rat spinotrapezius muscle [i.e., 15–20 RBC/capillary/s, ref. 14] and suggests that maintenance of RBC flux in the majority of muscle capillaries at rest is not quantitatively unreasonable in humans.

5 Putative Explanations for Apparently Contrary Findings

Experimental evidence for "capillary recruitment" has largely avoided critical examination because of the overall belief in the concept. Although there are serious problems with the interpretation of histological studies [e.g., 8, 24] in the interests of brevity only intravital microscopy studies are dealt with here. Paramount among many important considerations are: (A) Anesthetized animals may be hypovolemic and hypotensive which invokes a reflex vasoconstriction in muscle. This arteriolar vasoconstiction can be extreme and reduce the proportion of flowing capillaries. When relieved by superfusion of vasodilatory substances there is the appearance of capillaries being recruited. (B) If surgical exteriorization is not performed extremely carefully, so as to avoid blunt trauma or stretching, the delicate capillaries can be damaged and RBC flux ceases [23]. (C) Mean O_2 pressures within resting muscle are maintained at extremely low levels (< 20 mmHg). Experimental conditions that are hyperoxic relative to this cause reflex vasoconstriction which stops RBC flux in capillaries that would otherwise be flowing at rest. Subsequent lowering of the hyperoxic PO_2 into the normal range (or below) then gives the appearance of capillary "recruitment"[5, 8].

6 Conclusions

In physiologically well-controlled, stable preparations that are not damaged, overly stretched or hyperoxic the vast majority of capillaries support RBC flux. Thus, in response to elevations of metabolic rate that occur with contractions the increased blood flow presents primarily as an elevated RBC flux (and hematocrit) within already flowing capillaries (i.e., the concept of longitudinal recruitment as shown in Fig. 1) [14, 25, 26]. In healthy muscle(s) of young individuals this process elevates convective and diffusive O_2 delivery so rapidly that microvascular O_2 pressures are maintained close to (or above) resting values for the first few seconds of contractions despite immediate and rapid increase in muscle O_2 utilization [27]. This is crucial because if muscle O_2 delivery is adequate, it places the site of limitation for O_2 uptake dynamics within the mitochondrial respiratory chain [28]. In marked contrast to the situation in healthy muscles, chronic disease such as heart failure (and also

diabetes) severely reduce the proportion of capillaries supporting RBC flux in muscle at rest and during contractions [29]. This scenario reduces both convective and diffusive O_2 delivery and microvascular O_2 pressures fall transiently far below those in healthy muscles [30]. As the speed of muscle O_2 delivery becomes limiting both muscle and pulmonary gas exchange and their kinetics are impaired [28]. Without an appreciation of in vivo capillary hemodynamics, and the realization that recruitment of previously non-RBC flowing capillaries is not fundamental to increasing blood-myocyte O_2 and substrate flux from rest-exercise, resolution of the mechanistic bases for microvascular/muscle dysfunction in disease is severely compromised.

Acknowledgments Supported, in part, by grants from NIH HLBI 50306 and the American Heart Association, Heartland Affiliate.

References

1. Poole DC (1997) Influence of exercise training on skeletal muscle oxygen delivery and utilization. In: R.G. Crystal, J.B. West, E.R. Weibel, P.J. Barnes (eds.) *The Lung: Scientific Foundations*. New York: Raven Press, pp. 1957–1967.
2. Krogh A (1919) The number and distribution of capillaries in muscles with calculations of the oxygen pressure head necessary for supplying the tissue. *J Physiol Lond* 52:409–415.
3. Astrand P-O, Rodahl K (1986) *Textbook of Work Physiology: Physiological Basis of Exercise*. 3rd edition. New York: McGraw-Hill Book Company.
4. McArdle WD, Katch FI, Katch VL (2007) *Exercise Physiology: Energy, Nutrition and Human Performance*. 6th edition. London: Lippincott Williams & Wilkins.
5. Parthasarathi K, Lipowsky HH (1999) Capillary recruitment in response to tissue hypoxia and its dependence on red blood cell deformability. *Am J Physiol Heart Circ Physiol* 277:H2145–H2157.
6. Baron AD, Tarshoby M, Hook G, Lazaridis EN, Cronin J, Johnson A, Steinberg HO (2000) Interaction between insulin sensitivity and muscle perfusion on glucose uptake in human skeletal muscle: Evidence for capillary recruitment. *Diabetes* 49:768–774.
7. Wheatley CM, Rattigan S, Richards SM, Barrett EJ, Clark MG (2004) Skeletal muscle contraction stimulates capillary recruitment and glucose uptake in insulin-resistant obese Zucker rats. *Am J Physiol Endocrinol Metab* 287:E804–E809.
8. Clark MG, Rattigan S, Vincent MA, Poole DC, Brown MD, Hudlicka O (2008) Point: Counterpoint: There is/is not capillary recruitment in active skeletal muscle during exercise. *J Appl Physiol* 104:889–894.
9. Renkin EM (2002) Evaluation of capillary perfusion. *Am J Physiol Heart Circ Physiol* 282:H1172–H1173.
10. Snyder GK, Farrelly C, Coelho JR (1992) Capillary perfusion in skeletal muscle. *Am J Physiol Heart Circ Physiol* 262:H828-H832.
11. Anderson SI, Hudlicka O, Brown MD (1997) Capillary red blood cell flow and activation of white blood cells in chronic muscle ischemia in the rat. *Am J Physiol Heart Circ Physiol* 272:H2757–H2764.
12. Kindig CA, Poole DC (1998) A comparison of the microcirculation in the rat spinotrapezius and diaphragm muscles. *Microvasc Res* 55:249–259.
13. Hudlicka O, Zweifach BW, Tyler KR (1982) Capillary recruitment and flow velocity in skeletal muscle after contractions. *Microvasc Res* 23:201–213.

14. Kindig CA, Richardson TE, Poole DC (2002) Skeletal muscle capillary hemodynamics from rest to contractions: implications for oxygen transfer. *J Appl Physiol* 92:2513–2520.
15. Damon DH, Duling BR (1984) Distribution of capillary blood flow in the microcirculation of the hamster: An in vivo study using epifluorescent microscopy. *Microvasc Res* 27:81–95.
16. Vrielink HH, Slaaf DW, Tangelder GJ, Reneman RS (1987) Does capillary recruitment exist in young rabbit skeletal muscle? *Int J Microcirc Clin Exp* 6:321–332.
17. Burton KS, Johnson PC (1972) Reactive hyperemia in individual capillaries of skeletal muscle. *Am J Physiol* 223:517–524.
18. Kindig CA, Poole DC (2001) Sarcomere length-induced alterations of capillary hemodynamics in rat spinotrapezius muscle: Vasoactive vs passive control. *Microvasc Res* 61:64–74.
19. Bailey JK, Kindig CA, Behnke BJ, Musch TI, Schmid-Schoenbein GW, Poole DC (2000) Spinotrapezius muscle microcirculatory function: Effects of surgical exteriorization. *Am J Physiol* 279:H1331–H1337.
20. Ferreira LF, McDonough P, Behnke BJ, Musch TI, Poole DC (2006) Blood flow and O_2 extraction as a function of O_2 uptake in muscles composed of different fiber type. *Respir Physiol Neurobiol* 153:237–249.
21. Lutjemeier BJ, Ferreira LF, Poole DC, Townsend DK, Barstow TJ (2008) Muscle microvascular hemoglobin concentration and oxygenation within the contraction-relaxation cycle. *Resp Physiol Neurobiol* 160(2):131–138.
22. Klitzman B, Duling BR (1979) Microvascular hematocrit and red cell flow in resting and contracting striated muscle. *Am J Physiol* 237:H481–H490.
23. Poole DC, Musch TI, Kindig CA (1997) In vivo microvascular structural and functional consequences of muscle length changes. *Am J Physiol Heart Circ Physiol* 272: H2107–H2114.
24. Honig CR, Odoroff CL, Frierson JL (1980) Capillary recruitment in exercise: rate, extent, uniformity, and relation to blood flow. *Am J Physiol Heart Circ Physiol* 238:H31–H42.
25. Brown MD, Kelsall CJ, Milkiewicz M, Anderson S, Hudlicka O (2005) A new model of peripheral arterial disease: Sustained impairment of nutritive microcirculation and its recovery by chronic electrical stimulation. *Microcirculation* 12:373–381.
26. Hargreaves D, Egginton S, Hudlicka O (1990) Changes in capillary perfusion induced by different patterns of activity in rat skeletal muscles. *Microvasc Res* 40:14–28.
27. Behnke BJ, Barstow TJ, Kindig CA, McDonough P, Musch TI, Poole DC (2002) Dynamics of oxygen uptake following exercise onset in rat skeletal muscle. *Respir Physiol Neurobiol* 133:229–239.
28. Jones, A.M., and D.C. Poole (2005) *Oxygen Uptake Kinetics in Sport, Exercise and Medicine*. Routledge: London.
29. Richardson TS, Kindig CA, Musch I, Poole DC (2003) Effects of chronic heart failure on skeletal muscle capillary hemodynamics at rest and during contractions. *J Appl Physiol* 95(3):1055–1062.
30. Diederich ER, Behnke BJ, McDonough P, Kindig CA, Barstow TJ, Poole DC, Musch TI (2002) Effects of chronic heart failure on microvascular PO_2 dynamics in contracting muscle. *Cardiovasc Res* 56:479–486.

Arteriolar Vasomotor Control and Contractile Performance During Fatiguing Tetanic Contractions in Rat Skeletal Muscle: Role of Sympathetic System

Tadakatsu Inagaki, Takashi Sonobe, David C. Poole, and Yutaka Kano

Abstract Using a fatiguing stimulation protocol designed specifically to enhance sympathetically-mediated vasoconstrictor tone, we explored the temporal profile of the evoked vasoconstrictor response, evaluated the presence of sympatholysis, and assessed the role of α1-adrenergic receptor-mediated vasoconstriction on muscle performance. Spinotrapezius muscles of Wistar rats were exteriorized and stimulated tetanically (100 Hz, 4–7 V, stimulus duration 700 ms) every 3 s for 2.5 min under control and prazosin (1 μM) superfused conditions. The extent and time course of diameter changes in arterioles (2A) and venules (2V) were determined after each of 10 discrete sets of muscle stimulation at 5-min intervals. A significant decrease of luminal diameter was observed in arterioles after tetanic contractions at 8–10 sets (8 sets: −34.4%, 9 sets: −39.4%, 10 sets: −38.6% vs pre-contraction at each set, $p < 0.01$). Prazosin significantly reduced but did not abolish the contraction-induced vasoconstriction. In both conditions, there was no reduction of venules diameter observed. Tetanic contractions force at the final 10th set was significantly decreased to 29.3 ± 11.9% from pre-fatigue conditions, while tetanic contractions with prazosin force production was maintained at 70.4 ± 14.2% at the 10th set. We conclude that in sequential bouts of contractions there was a progressively greater degree of arteriolar (but not venular) vasoconstriction which was attenuated substantially by prazosin.

1 Introduction

Blood flow to the tissue is determined by the interaction of perfusion pressure and vascular tone. The immediate rise in blood flow at onset of muscle contraction is attributed to the muscle pump function [1] and rapid vasodilation [2].

T. Inagaki (✉)
Departments of Applied Physics and Chemistry, University of Electro-Communications, Chohu, Tokyo, Japan
e-mail: inagaki@ecc.pc.uec.ac.jp

E. Takahashi, D.F. Bruley (eds.), *Oxygen Transport to Tissue XXXI*, Advances in Experimental Medicine and Biology 662,
DOI 10.1007/978-1-4419-1241-1_44, © Springer Science+Business Media, LLC 2010

During and after exercise, vascular tone in the skeletal muscle microcirculation represents a dynamic balance between sympathetic vasoconstriction and locally released vasodilator substances [3]. Although muscle blood flow increases in an exercise intensity-dependent manner, muscle sympathetic nerve activity also increases in the same manner [4]. It is believed that local vasodilator responses, at least to some degree, override the sympathetic vasoconstrictor activity [5]. Despite this functional sympatholysis sympathetic vasoconstriction may constrain the increase of muscle blood flow during exercise [6, 7]. However, it has not been established whether such increases of sympathetic nerve activity or alternatively reduced functional sympatholysis mediates the attenuated vasodilator response observed during muscle fatigue evoked by repeated bouts of tetanic contractions. Therefore, the purpose of the present study was to explore the role of functional sympatholysis on vasomotor control during and following isometric tetanic contractions in the rat spinotrapezius muscle. Specifically, using a stimulation protocol designed to increase sympathetically-mediated vasoconstrictor tone in combination with α1-adrenergic blockade (prazosin), we tested the hypothesis that fatiguing contractions would alter the vasoconstriction-vasodilation balance towards vasoconstriction. Further, removal of this vasoconstriction would increase arteriolar diameter and reduce fatigue in this preparation.

2 Methods

Male Wistar rats (9–13 week of age, Japan SLC) were used in this study. All procedures were approved by the University of Electro-Communications Institutional Animal Care and Use Committee. Animals were anaesthetized with sodium pentbarbital (70 mg/kg i.p.) during surgery. The right carotid artery was cannulated (PE50) for the subsequent monitoring of blood pressure. The right spinotrapezius muscle was prepared for in vivo microscopic observation as previously described [8]. During all procedures, the exposed muscle surface was kept moist by superfusing with Krebs-Henseleit buffer solution at 37°C. For the contraction protocols, two partially insulated fine silver electrodes were placed at proximal and distal end of the spinotrapezius muscle, and connected to an electrical stimulator (model-3F46, NEC). After the surgical preparations, the rat was placed on a 37°C glass hotplate. Then, the anesthesia was changed to urethane (4 g; α-chloralose, 25 g; Urethane, 100 ml; Polyethylene Glycol 200, 2 ml/kg, i.p.) from pentobarbital. Arterial pressure was monitored throughout the experiment using a pressure transducer (Nihon Koden). To measure muscle force during contractions, the wire horseshoe attached to the spinotrapezius muscle was connected by fine wire to a strain gauge. Mean arterial pressure and Torque (0–10 mN·m, scale) measurements were recorded using a Chart5 via Mac Lab/8s (A/D Instruments). The microcirculation of the spinotrapezius muscle was transilluminated and observed under an intravital microscope

using a ×10 objective lens. The microscopic images were captured by a high-sensitivity charge-coupled device digital camera (DP70, Olympus).

Animals were allowed to stabilize for 15–30 min after completion of the surgical procedure. Each spinotrapezius muscle was subjected to 10 discrete sets of isometric muscle stimulation in a similar manner to that described previously [8]. Stimulations (rectangular pulses of 6–8 V intensity, 4 ms pulse width) were delivered by electro-stimulator via stimulus isolation units. This stimulation condition activates the sympathetic nerve [9]. Each set consisted of the muscle being stimulated tetanically at resting sarcomere length (100 Hz, stimulus duration 700 ms, 2.6- to 2.7-μm sarcomere length) every 3 s for 2.5 min (i.e., 50 contractions) under (1) control ($n = 7$) and (2) prazosin superfused conditions ($n = 6$).

Vasculature images of first- or second-order arterioles and venules were obtained in the resting muscles and every 5 s for the first minute, every 30 s for the next 4 min and at 5 min intervals after each of 10 discrete sets of muscle contractions. Captured images were analyzed after the experiments using ImageJ software (National Institutes of Health). Microvascular diameter measurements were reproducible to within 1 μm. The captured area included the branch of each vessel, and mean vessel diameters reported represent the average diameter at 0, 50, 100 μm distance from each branch. To investigate the role of sympathetic nerve activity during muscle fatigue, the selective α1-adrenergic receptor antagonist prazosin (1 μM, dissolved in KHB), was added to the superfusion solution.

A two-way repeated-measures ANOVA and Bonferroni post hoc test was used for arteriole vs. venule and control vs. prazosin superfused conditions. A one-way repeated-measures ANOVA and Bonferroni post-hoc test was used for relative force comparison. Measured values are presented as means ± SE. Significance was established at $p < 0.05$.

3 Results

Mean arterial pressure during the resting period was 111 ± 4 mmHg and did not change during muscle contractions in either the control or prazosin condition. Figure 1 shows the changes of relative tetanic force. In the control condition, tetanic force decreased 20–40% within a set, and at the final 10th set it was significantly decreased to 29.3 ± 11.9% of initial force. While the prazosin superfused condition also indicates decreasing tetanic force within a set, there was a marked reduction in the attenuation of tetanic force production throughout 10 sets of contractions (70. 4 ± 14.2% of pre-fatigue conditions at the final 10th set).

The time courses of change in arteriolar and venular inner diameter for each condition during recovery are shown Fig. 2. In the control condition, arteriolar vasoconstriction immediately after muscle contractions was observed at the

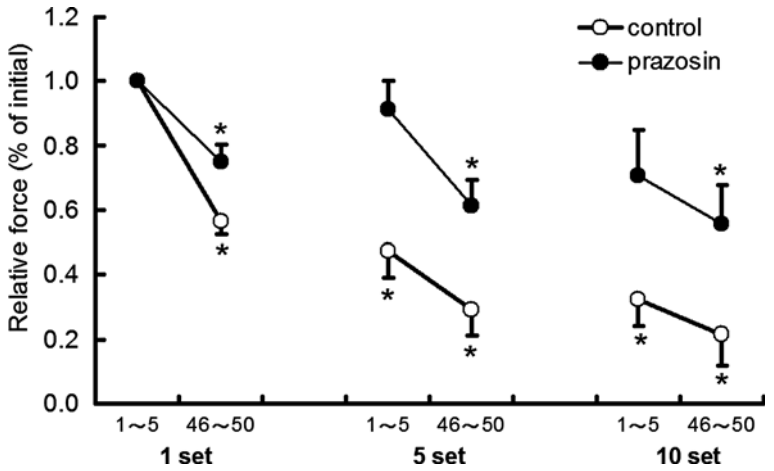

Fig. 1 Change of relative tetanic force during contraction protocols. Force normalized to initial denotes the average of first and last 5 contractions of sets 1, 5, and 10 from control and prazosin conditions. Values are means ± SE (control: $n = 4$, prazosin: $n = 5$). Significance compared with initial value for each condition: $*p < 0.01$

10th sets (−38.6% vs. pre contraction at each set, $p < 0.01$). Also, a significant decrease of luminal diameter was observed in arterioles after 8th set (−34.4%) and 9th set (−39.4%). The time constant (τ) of diameter recovery at the 5th and 10th sets was 25 ± 7 s and 46 ± 13 s, respectively. On the other hand, in the prazosin condition during contractions (time "0" in Fig. 2), arteriolar diameter did not decrease progressively as seen in control. In neither control nor prazosin conditions, did venular inner diameter change significantly.

4 Discussion

The principal finding of this investigation was that repetitive, fatiguing muscle contractions evoke a progressive vasoconstrictor response that is blocked by the selective α1-adrenergic receptor antagonist prazosin. Specifically, significant decreases of arteriolar luminal diameter were observed in arterioles after 8–10 sets of contractions under control conditions, presumably reflecting a diminishing sympatholysis, which was largely abolished by prazosin. Moreover, α1-adrenergic receptor blockade significantly reduced muscle fatigue suggesting an important role for sympathetically-mediated vasoconstriction in impairing muscle performance in this preparation (Fig. 1). It has long been recognized that studying the interaction between functional vasodilation and sympathetic vasoconstriction is fundamental to understanding blood flow control during exercise. Although the local vasodilator responses to a certain degree override the sympathetic vasoconstrictor activity (functional sympatholysis) during

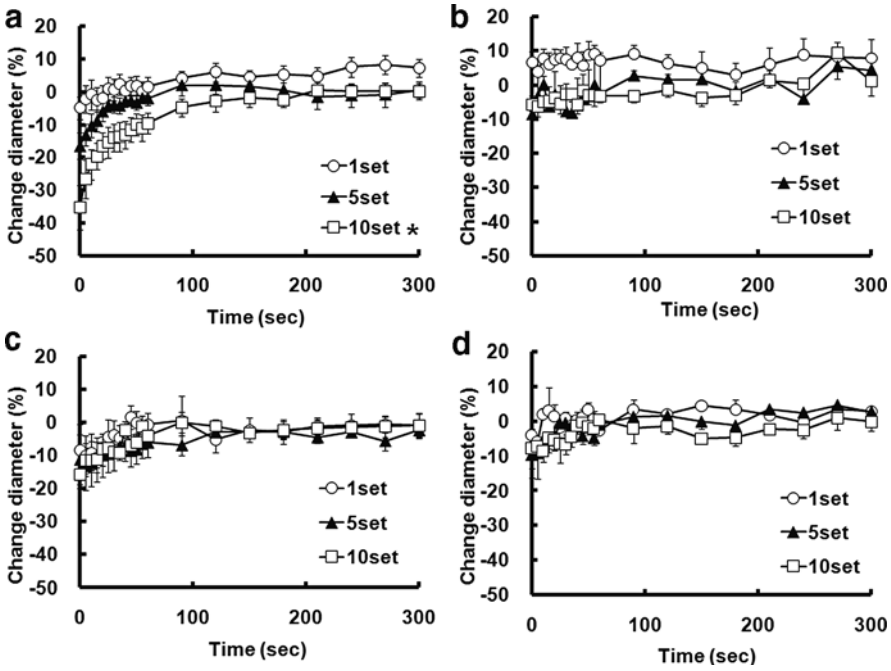

Fig. 2 Time course of arteriolar and venular inner diameter changes during recovery after 1, 5, and 10 sets of contractions under control and prazosin superfused condition. Values of vessel inner diameter are normalized to each pre-contracting baseline diameter. In the control condition and prazosin-superfused condition, relative arteriolar and venular diameter changes are shown in **a**, **b** and **c**, **d** respectively. Values are means ± SE (control: $n = 7$, prazosin: $n = 6$). Significant decrease of luminal diameter immediately after muscle contractions compared with pre-contraction diameter: $^{*}p < 0.01$

exercise, as fatigue increases, sympathetic vasoconstriction may become more pronounced and thus sympathetic receptor blockade may attenuate the associated vasoconstriction and also the muscle fatigue. Saito et al. [7] showed that muscle sympathetic nerve activity enhanced during fatigue induced with more than 25% of maximal voluntary contraction. Jacobs and Segal [10] reported that post-contraction vasodilation was attenuated with muscle fatigue in the feed artery and proximal arterioles. These previous findings and the results of the present investigation suggest that the competing balances of local vasodilator responses and sympathetic vasoconstriction shift in favor of vasoconstriction with muscle fatigue.

In the prazosin condition, the vasoconstriction was attenuated but not abolished completely. Sympathetic vasoconstriction is mediated by activation of both postjunctional α1- and α2-adrenergic receptors [11]. Recently, it was suggested that α1- and α2-adrenergic receptor responsiveness to infusion of selective α1- and α2-adrenergic receptor agonists does not decline during

prolonged mild-intensity exercise [12]. Furthermore, muscle contraction-induced impairment of α2-vasoconstriction can augment muscle blood flow [13]. Thus, further investigation will be required to identify any sympathetic vasoconstriction during muscle fatigue that arises from the α2-adrenergic receptor.

The protocol of this study did not affect venous vessel diameter following muscle contractions and this finding is consistent with previous reports that venous vessels are not under sympathetic control [14]. Also, this observation suggests that there was little or no change of muscle internal pressure, and any associated mechanical alterations of the vasculature, after contractions.

In summary, using a fatiguing stimulation protocol designed specifically to enhance sympathetically-mediated vasoconstrictor tone, we explored the temporal profile of the evoked vasoconstrictor response, evaluated the presence of sympatholysis, and assessed the role of α1-adrenergic receptor-mediated vasoconstriction on muscle performance. The principal findings were as follows: (1) muscle fatigue was reduced significantly by α1- adrenergic receptor blockade with prazosin, (2) in sequential bouts of contractions there was a progressively greater degree of arteriolar (but not venular) vasoconstriction which was attenuated substantially by prazosin. These results demonstrate that, in this preparation, as muscle fatigue becomes more pronounced there is a greater sympathetically-mediated vasoconstriction (i.e., partial attenuation of sympatholysis) relief of which can improve muscle performance.

References

1. Sheriff DD, Rowell LB, Scher AM (1993) Is rapid rise in vascular conductance at onset of dynamic exercise due to muscle pump? Am J Physiol 265:H1227–H1234
2. Tschakovsky ME, Shoemaker JK, Hughson RL (1996) Vasodilation and muscle pump contribution to immediate exercise hyperemia. Am J Physiol 271:H1697–H1701
3. Thomas GD, Segal SS (2004) Neural control of muscle blood flow during exercise. J Appl Physiol 97:731–738
4. DiCarlo SE, Chen CY, Collins HL (1996) Onset of exercise increases lumbar sympathetic nerve activity in rats. Med Sci Sports Exerc 28:677–684
5. Remensnyder JP, Mitchell JH, Sarnoff SJ (1962) Functional sympatholysis during muscular activity. Observations on influence of carotid sinus on oxygen uptake. Circ Res 11:370–380
6. Hamann JJ, Buckwalter JB, Valic Z, Clifford PS (2002) Sympathetic restraint of muscle blood flow at the onset of dynamic exercise. J Appl Physiol 92:2452–2456
7. Saito M, Mano T, Iwase S (1989) Sympathetic nerve activity related to local fatigue sensation during static contraction. J Appl Physiol 67:980–984
8. Sonobe T, Inagaki T, Poole DC, Kano Y (2008) Intracellular calcium accumulation following eccentric contractions in rat skeletal muscle in vivo: role of stretch-activated channels. Am J Physiol Regul Integr Comp Physiol 294:R1329–R1337
9. Honig CR (1979) Contributions of nerves and metabolites to exercise vasodilation: a unifying hypothesis. Am J Physiol 236:H705–H719
10. Jacobs TL, Segal SS (2000) Attenuation of vasodilatation with skeletal muscle fatigue in hamster retractor. J Physiol 524(Pt 3):929–941

11. Ohyanagi M, Faber JE, Nishigaki K (1991) Differential activation of alpha 1- and alpha 2-adrenoceptors on microvascular smooth muscle during sympathetic nerve stimulation. Circ Res 68:232–244
12. DeLorey DS, Hamann JJ, Valic Z, Kluess HA, Clifford PS, Buckwalter JB (2007) Alpha-Adrenergic receptor responsiveness is preserved during prolonged exercise. Am J Physiol Heart Circ Physiol 292:H392–H398
13. Anderson KM, Faber JE (1991) Differential sensitivity of arteriolar alpha 1- and alpha 2-adrenoceptor constriction to metabolic inhibition during rat skeletal muscle contraction. Circ Res 69:174–184
14. Marshall JM (1982) The influence of the sympathetic nervous system on individual vessels of the microcirculation of skeletal muscle of the rat. J Physiol 332:169–186

The Influence of Passive Stretch on Muscle Oxygen Saturation

Kevin K. McCully

Abstract Previous studies have suggested that chronic stretch might be able to produce skeletal muscle hypertrophy. However, stretching might also restrict blood flow, which could in turn influence any stretch-training program. This study evaluated the influence of muscle stretch on muscle oxygen saturation using near infrared spectroscopy (NIRS). A 16 channel NIRS probes were placed on the medial gastrocnemius, quadriceps, and hamstring muscles of young healthy adults. Oxygen saturation during maximal tolerated stretch was measured and normalized with cuff-induced ischemia and reperfusion. Oxygen saturation decreased in the gastrocnemius and quadriceps in a position dependent fashion, but did not change in the hamstring muscles. Passive stretching may also have a significant hypoxic component in some muscles but not others.

1 Introduction

Near infrared spectroscopy (NIRS) has been used to evaluate changes in oxygen saturation to skeletal muscle [1]. Recently, regional differences in oxygen saturation in skeletal muscle have been reported using NIRS devices with multiple source detector pairs [2, 3]. During plantar flexion exercise the more distal portion of the gastrocnemius muscles demonstrates a more rapid desaturation, potentially related to greater changes in pennation angle [4]. These studies show that for the gastrocnemius muscle, muscle action results in a regionally dependent change in oxygen saturation.

Chronic stretch to maintain an increased length has been shown to have dramatic effects on skeletal muscle [5]. Of potential clinical significance, chronic stretch has been shown to reduce much of the atrophy associated with

K.K. McCully (✉)
Department of Kinesiology, University of Georgia, 330 River Road, Athens, GA 30602, USA
e-mail: mccully@uga.edu

E. Takahashi, D.F. Bruley (eds.), *Oxygen Transport to Tissue XXXI*, Advances in Experimental Medicine and Biology 662,
DOI 10.1007/978-1-4419-1241-1_45, © Springer Science+Business Media, LLC 2010

immobilization [6]. Furthermore, stretch combined with electrical stimulation has been shown to produce greater hypertrophy than electrical stimulation alone [5]. If chronic stretched induced ischemia, this might be another mechanism for enhancing muscle hypertrophy [7–9]. The purpose of this study was to characterize the degree of muscle desaturation with continuous stretch, and to determine whether there were regional differences in the effect of stretch on muscle oxygen saturation in the gastrocnemius muscle.

2 Methods

This study was approved by the University Committee on Studies Involving Human Beings at the University of Georgia and all subjects gave informed consent. Young healthy subjects who were moderately active by self report were included in this study.

The subjects were placed in a supine position for 10 min prior to data collection. The NIRS device was placed on either the medial gastrocnemius, vastus lateralis, or biceps femoris and the occlusion cuff was placed on the subject above the NIRS probes.

Muscle oxygen saturation during 3 min at a neutral position (90 degrees) was followed by at least 10 min with the muscle stretched to the subjects' self-reported maximum stretch. The subjects reported pain ratings of 5 on a scale of 0–10 as a result of the maximum tolerated stretch.

For the gastrocnemius muscle, short isometric contractions were performed during the stretch to mimic a training protocol that included ischemic and muscle contractions. The contractions did not appear to have any noticeable effect on oxygen saturation values during the stretching period. At the conclusion of the stretch, the leg was returned to the neutral position. Five minutes of cuff ischemia followed by reactive hyperemia was used to produce minimum and maximum oxygen saturation values for normalization of the signals. Cuff ischemia was produced by inflating the cuff to approximately 100 mmHg over systolic pressure (DE Hokkansen Inc.). The cuff pressure was then released and NIRS signals collected for an additional 3 min to capture the peak reactive hyperemic response.

The NIRS measurements used a continuous light source, dual-wavelength spectrophotometer (Cogniscope; NIM, Inc.). Two light sources and six photo detectors were arranged to produce 8 different signals. The separation distance between the light sources and detector pairs was 3 cm. The source detector pairs were located in two rows covering a distance of 9.5 cm along the calf, and 5 cm wide. Light photons migrate through the tissue and were collected by the detectors with optical filters set at 760, 805, and 850 nm. The difference in signal between 760 and 850 nm was used to indicate changes in oxygen saturation. Voltage signals were converted to optical density using the Beer-Lambert Law, and used to calculated oxygen saturation (ratio of HbO_2/Hb signal). Total

blood volume measured as the Hb + HbO_2 signal was also recorded but not presented. Oxygen saturation values were calibrated as a percentage of the physiological range using 0% as the lowest value at the end of cuff ischemia, and 100% as the peak value after releasing the cuff. The average response of each gastrocnemius and biceps femoris muscles included all eight channels, and regional differences were determined by averaging the two source detector pairs at each longitudinal position (presented as proximal, mid proximal, mid distal, and distal). For the vastus lateralis muscle, 16 channels were used producing 8 locations.

Data are presented as means (standard deviations). ANOVA was used to test for a difference in oxygen saturation between baseline and stretch for the different positions.

3 Results

Nine subjects performed the gastrocnemius stretch protocol, while 5 subjects performed the quadriceps and hamstring stretch protocols. Figure 1 shows an individual response to the gastrocemius stretching protocol at two locations, proximal and distal. The short duration isometric contractions produced small motion artifacts, but did not appear to significantly influence oxygen saturation values. Gastrocnemius stretching resulted in a decline in the average oxygen saturation values relative to the baseline condition (Fig. 2). This decline in oxygen saturation with stretch was statistically significant ($F = 18.1$, $p < 0.001$).

There was a marked difference in the magnitude of change in oxygen saturation with stretch among the four positions in the gastrocnemius (Fig. 2). There was no difference in the oxygen saturation at the neutral position prior to stretch in the different locations ($F = 0.131$, $p = 0.941$). Individual comparisons showed that while the proximal position during the stretch was not

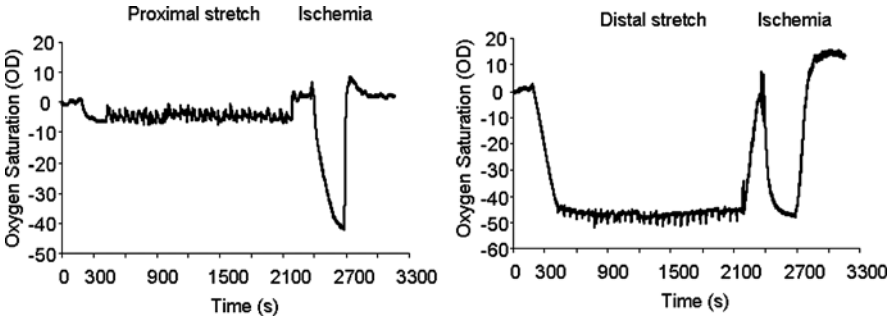

Fig. 1 Representative data for oxygen saturation at the most proximal and distal positions in one subject during continuous stretch. Note that the distal portion appears to desaturate to a greater extent relative to the desaturation during cuff ischemia

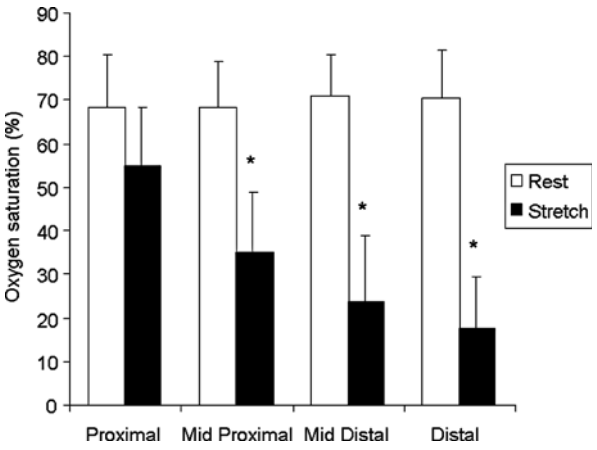

Fig. 2 Oxygen saturation values for the different locations in the gastrocnemius muscle during stretch. Rest indicates values at 90o prior to stretch, Stretch indicates the values reached after 10 min. Data are presented as means and SD. * indicates statistically different from baseline rest values ($p < 0.05$)

different from rest, oxygen saturation values at the other three positions were statistically different ($p < 0.02$ for all comparisons).

Maximum tolerated stretch produced a position-dependent decrease in oxygen saturation in the vastus lateralis, with the most distal portions decreasing oxygen saturation 36 (20) % and the proximal portions being not different from rest. However, no changes were seen in the oxygen saturation in the biceps femoris muscle with maximum tolerated stretch, despite similar pain ratings for the gastrocnemius and vastus lateralis muscles.

4 Discussion

An important finding from this study is that continuous passive stretch of the gastrocnemius muscle caused large decreases in oxygen saturation, often approaching levels comparable to complete ischemia. The magnitude of the decrease in oxygen saturation was highly dependent on the location (proximal vs. distal) within the muscle. These results to the greater distal oxygen desaturation that was seen by Miura et al. during plantar flexion exercise [2]. Miura et al. [2] suggested that during plantar flexion exercise the distal portion of the gastrocnemius muscle generates higher intramuscular pressures related to greater pennation angles [4]. It is the higher intramuscular pressures that are suspected of reducing blood flow. Intramuscular pressures were not measured in this study and it is not clear if intramuscular pressures during passive stretch reach the same levels as those during active muscle contraction. Previous studies in animals have suggested that muscle contractions involving shortening can close blood vessels due to a shearing effect. However, it is not clear if shearing could account for changes in blood flow with stretch. Poole and colleagues [10] have suggested that stretch reduces the size of capillary diameters, which increases resistance and reduces blood flow.

A number of factors could have influenced oxygen saturation during stretch. It is possible that passive stretch increases metabolic rate. We found no evidence that passive stretch increased muscle activation measured with surface EMG (data not shown). Changes in the pathlength of light with stretch might also alter the oxygen saturation results. However, absorption changes with pathlength would be expected to occur rapidly, on the same time course as the time to make the stretch movements, and this was clearly not seen in the data (see Fig. 1, for example).

It is not clear how to compare the magnitude of changes in oxygen saturation in this study to changes in muscle blood flow and diameter in previous studies. The change in fiber length in our study might have been as high as 130% of optimal length, based on a displacement of the heel of 2.5 cm at the smallest angle used (61 degrees), fascile lengths of 6.6 cm and pennation angles of 24 degrees [4]. This is within the range of length changes produced in many microvascular studies [10, 11]. Interestingly, none of the animal studies reported complete cessation of blood flow [10, 11]. However, in at least some of our subjects the magnitude of decline in oxygen saturation was similar to complete ischemia. Therefore, it is possible that passive muscle stretch in humans produces greater reductions in blood flow than predicted in animal models of stretch.

This study also found that stretching of the quadriceps (vastus lateralis) produced a similar response to the gastrocnemius in that the distal portion of the muscle desaturated while the proximal portion did not. This response was variable between subjects and 2 of the 5 subjects showed no desaturation while 3 showed a very pronounced desaturation. The hamstring (biceps femoris) muscle groups did not produce decreases in muscle oxygen saturation. This was not due to different magnitudes of stretch, at least judged by the level of discomfort caused by the stretch. The most likely explanation for this finding is that the medial gastrocnemius is more pennated than the biceps femoris, and the greater pennation angles induce great shear pressure on the blood vessels. The vastus lateralis has pennation angles that are in-between. We have also noticed that the level of muscle pressure needed to occlude blood flow is muscle lower in the forearm ($\sim$10% of maximum contractions) compared to the biceps ($\sim$50% of maximum contraction), data not shown. This is also consistent with known differences in pennation angle in these muscles.

A number of different studies have suggested that muscle ischemia, both with and without muscle contraction can enhance muscle hypertrophy [7–9]. Thus it might be important to evaluate potential changes in oxygen saturation which might occur in a stretching intervention. This study suggests that passive stretching can have a component of muscle ischemia, and the variability in the level of ischemia implies that it will be hard to predict how much ischemia will occur with passive stretch.

In conclusion, this study found that passive stretch reduced oxygen saturation in the gastrocemius and vastus lateralis muscles, but not the biceps femoris muscles. The magnitude of the reduction in oxygen saturation was highly

dependent on the location within the muscle. Thus, in order to predict the change in oxygen saturation that occurs in the skeletal muscle with stretch, it is necessary to make the actual measurements, and to make measurements in more than one location.

Acknowledgements Michele King, Richard Marks, Aaron McPherson and Katherine Scheidler assisted with data collection.

References

1. Hamaoka T, McCully KK, Quaresima V, Yamamoto K, and Chance B. (2007) Near-infrared spectroscopy/imaging for monitoring muscle oxygenation and oxidative metabolism in healthy and diseased humans. J Biomed Opt 12: 062105
2. Miura H, McCully K, Hong L, Nioka S, and Chance B. (2001) Regional difference of muscle oxygen saturation and blood volume during exercise determined by near infrared imaging device. Jpn J Physiol 51: 599–606
3. Quaresima V, Colier WN, van der Sluijs M, and Ferrari M. (2001) Nonuniform quadriceps O_2 consumption revealed by near infrared multipoint measurements. Biochem Biophys Res Commun 285: 1034–1039
4. Miura H, McCully K, Nioka S, and Chance B. (2004) Relationship between muscle architectural features and oxygenation status determined by near infrared device. Eur J Appl Physiol 91: 273–278
5. Goldspink DF, Cox VM, Smith SK, Eaves LA, Osbaldeston NJ, Lee DM, and Mantle D. (1995) Muscle growth in response to mechanical stimuli. Am J Physiol 268: E288–E297
6. Spector SA, Simard CP, Fournier M, Sternlicht E, and Edgerton VR. (1982) Architectural alterations of rat hind-limb skeletal muscles immobilized at different lengths. Exp Neurol 76: 94–110
7. Takarada Y, Nakamura Y, Aruga S, Onda T, Miyazaki S, and Ishii N. (2000) Rapid increase in plasma growth hormone after low-intensity resistance exercise with vascular occlusion. J Appl Physiol 88: 61–65
8. Takarada Y, Takazawa H, and Ishii N. (2000) Applications of vascular occlusion diminish disuse atrophy of knee extensor muscles. Med Sci Sports Exerc 32: 2035–2039
9. Takarada Y, Takazawa H, Sato Y, Takebayashi S, Tanaka Y, and Ishii N. (2000) Effects of resistance exercise combined with moderate vascular occlusion on muscular function in humans. J Appl Physiol 88: 2097–2106
10. Poole DC, Musch TI, and Kindig CA. (1997) In vivo microvascular structural and functional consequences of muscle length changes. Am J Physiol 272: H2107–H2114
11. Welsh DG and Segal SS. (1996) Muscle length directs sympathetic nerve activity and vasomotor tone in resistance vessels of hamster retractor. Circ Res 79: 551–559

NIRS Measurement of O_2 Dynamics in Contracting Blood and Buffer Perfused Hindlimb Muscle

Kazumi Masuda, Hisashi Takakura, Yasuro Furuichi, Satoshi Iwase, and Thomas Jue

Abstract In order to obtain evidence that Mb releases O_2 during muscle contraction, we have set up a buffer-perfused hindlimb rat model and applied NIRS to detect the dynamics of tissue deoxygenation during contraction. The NIRS signal was monitored on hindlimb muscle during twitch contractions at 1 Hz, evoked via electrostimulator at different submaximal levels. The hindlimb perfusion was carried out by perfusion of Krebs Bicarbonate buffer. The NIRS still detected a strong signal even under Hb-free contractions. The deoxygenation signal (Δ[deoxy]) was progressively increased at onset of the contraction and reached the plateau under both blood- and buffer-perfused conditions. However, the amplitude of Δ[deoxy] during steady state continued to significantly increase as tension increased. The tension-matched comparison of the Δ[deoxy] level under buffer-perfused and blood perfused conditions indicate that Mb can contribute approximately 50% to the NIRS signal. These results clarify the Mb contribution to the NIRS signal and show a falling intracellular PO_2 as workload increases.

1 Introduction

The transport of O_2 into myocytes and the regulation of respiration depend upon an extensive series of mechanisms and influences [1]. To clarify these mechanisms in vivo, researchers have developed non-invasive magnetic resonance spectroscopy (^{1}H-MRS) and near infrared spectroscopy (NIRS) techniques [2–4]. Indeed, these non-invasive methods have shed unique insights but have also raised controversial questions: Does the intracellular oxygen continue to decline or plateau as workload increases? Does the NIRS signal detect Hb or Mb desaturation? The near infrared spectroscopy (NIRS) is a powerful tool for detecting O_2 dynamics in contracting muscle in vivo, because it can detect O_2

K. Masuda (✉)
Faculty of Human Sciences, Kanazawa University, Kanazawa, 920-1192, Japan
e-mail: masuda@ed.kanazawa-u.ac.jp

E. Takahashi, D.F. Bruley (eds.), *Oxygen Transport to Tissue XXXI*,
Advances in Experimental Medicine and Biology 662,
DOI 10.1007/978-1-4419-1241-1_46, © Springer Science+Business Media, LLC 2010

changes with high sensitivity and time resolution. However, NIRS cannot distinguish the contribution from Mb and Hb. Currently, most researchers believe that the NIRS signal derives mainly from blood (Hb) [5–6]. In contrast, recent NMR experiments have suggested that Mb contributes significantly to NIRS signal [7].

To address these questions, we have conducted an NIRS study with buffer perfused hindlimb. Buffer-perfused muscle avoids any Hb interference. The NIRS signals reflect only the intracellular O_2 dynamics during muscle contraction. The results indicate that NIRS detects a significant contribution from Mb and that Mb desaturation does not reach a plateau with increased workload.

2 Materials and Methods

2.1 Experimental Animals and Protocol

Male Wistar rats (9 weeks old, 242–280 g, $n = 3$) were used for the present experiment. All procedures performed in the present study were approved by the ethics committee on Animal Experimentation of Kanazawa University.

The present experiment was consisted of two conditions: (1) under evoked twitch contractions without buffer perfusion (normal blood-perfused condition), and (2) under evoked twitch contractions with buffer-perfusion (without Hb interference). First of all, the rats were subjected to twitch contractions in vivo. The evoked tension via the sciatic nerve was set at several levels of the maximal tension (25∼100%), and a constant tension was maintained during a 2-min contraction. A 10-min recovery period between series of 2-min contractions to eliminated muscle fatigue. The NIRS signal returned to its control level, before the next set of stimulation began.

After the in vivo stimulations, the rats were prepared for hindlimb perfusion. Under buffer-perfused condition, the hindlimb muscle was stimulated via the sciatic nerve as same as the condition of in vivo stimulation.

Under anesthesia with pentobarbital sodium (45 mg/kg i.p.), the sciatic nerve of the left hindlimb was connected to two parallel stainless steel wire electrodes. The Achilles' tendon was connected to a strain gauge with a string (MLT500/D, ADInstrument, Australia). At the muscle's optimum length, where the muscle generated peak tension, the electric stimuli on the sciatic nerve elicited a series of isometric twitch contractions. The stimulation consisted of a single square wave (delay 10 μs, interval: 2 ms, duration: 1 ms) was controlled by the electrostimulator system (Model RU-72, Nihon Koden, Japan). The stimulation was 1 Hz of frequency for 120 s. The target tension was controlled by changing stimuli voltage to obtain 25∼75% of peak tension (4–8 volts). The twitch tension was recorded via data acquisition system (PowerLab 8SP, ADInstrument, Australia).

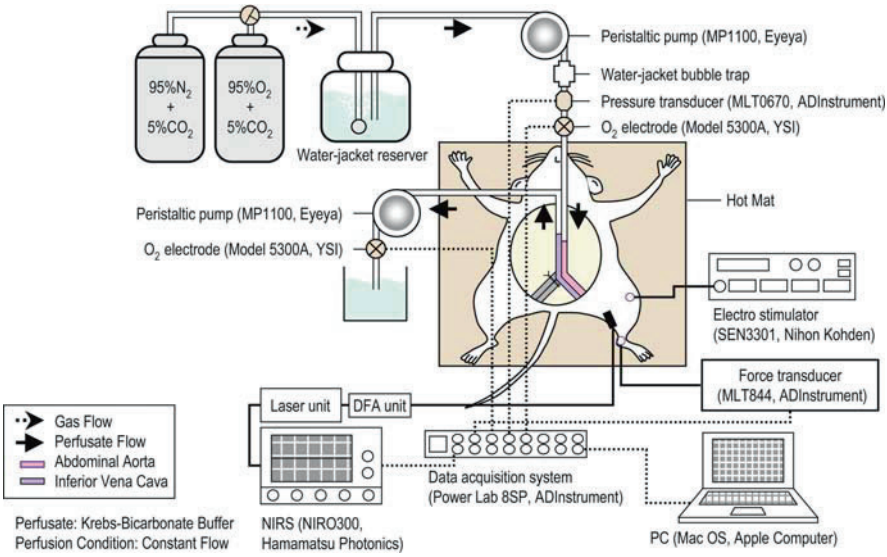

Fig. 1 The illustration of buffer perfused hindquarter system

Preparation of the isolated rat hindlimb and the perfusion apparatus were described in the previous reports [8–10]. Figure 1 shows the system. Surgery was modified from those in previous reports [11–13]. The inflow catheter was placed in the descending aorta with its tip 4–5 mm proximal to the aorta bifurcation. Initially the hypogastric trunk was occluded to evaluate whether blood flow to the trunk region could be eliminated. Subsequently ligature was placed around the contralateral (right hindlimb) common iliac artery. Blood flow to the tail was eliminated by ligation at its base. Venous effluents were collected separately from the vena cava.

Regular Krebs-Henseleit buffer contained 15 mM glucose was equilibrated with 95% O_2 + 5% CO_2. A circulating water bath and temperature jacketed reservoir and tubings maintained at 37°C. A peristaltic pump maintained a constant, non-recirculating perfusate flow. After the cannulation of the abdominal aorta, the Krebs-Henseleit buffer containing heparin (2000 U/l) was perfused into hindlimb for 30-min to prevent clotting blood and to wash out blood from hindlimb. Buffer was continued to perfuse the hindlimb until the end of experiment.

The NIRS instrument (NIRO-300 + Detection Fiber Adapter Kit, Hamamatsu Photonics, Japan) provided separate measurements of changes in deoxygenated Hb and Mb concentrations (Δ[deoxy]), changes in oxygenated Hb and Mb concentrations (Δ[oxy]), and changes in the sum of these two variables as total Hb and Mb concentrations (Δ[total]). Since previous study suggested that the Δ[oxy] was affected by the variation of blood flow compared with Δ[deoxy] signal [14], the Δ[deoxy] signal was used as the muscle oxygenation index in the present study.

The distance between the photodiode and the LED was fixed at 10 mm on the skin of m. gastrocnemius. The kinetics of Δ[deoxy] during evoked contraction was mathematically evaluated by fitting the data to the single exponential function to determine amplitude (the amplitude between baseline and the steady-state value during the exponential component, μMcm).

2.2 Statistical Analysis

All data are expressed as means ± SD. To compare measurements between tension levels or between conditions, repeated measurement of one-way analysis of variance (ANOVA) was used. Scheffé's post-hoc test was conducted if ANOVA indicated a significant difference. The level of significance was set at $p < 0.05$.

3 Results

Buffer-perfused muscle contained no Hb. Yet, NIRS still detected a very strong signal. The evoked twitch tension under buffer-perfusion remained constant during stimulation but reached half the maximal tension observed under blood-perfusion. Estimated contributions of Mb and Hb on the NIRS Δ[deoxy] amplitude during contraction is shown in Table 1 At 50% of maximal twitch tension (71.05 ± 28.47 g), the amplitude of the Δ[deoxy] signal contains about 50% contribution from Mb (Table 1). The Mb deoxygenation (at steady state) at 50%, 75% and 100% of maximal twitch tension obtained under buffer-perfusion was 6.10 ± 3.57, 10.35 ± 6.90, 15.57 ± 6.60 (μMcm) respectively, and progressively amplified as tension level increased ($p < 0.01 \sim 0.05$). Preliminary calibration experiments with anoxic buffer have yielded an estimate of total Mb desaturation at maximal exercise under buffer perfused condition to be about 50% ($S_{mb}O_2$). Since blood perfused muscle reaches a higher tension and shows almost a 50% increased in amplitude, Mb should desaturate even lower than 50%.

Table 1 Estimated Mb and Hb contribution on the NIRS Δ[deoxy] amplitude during contraction at a given tension level

	Hb + Mb	Mb	Hb
Amplitude	26 ± 11	13 ± 6*	12 ± 5*

Unit: μMcm, means ± SD, $n = 3$, *: $p < 0.05$ vs. Hb + Mb. The "Hb + Mb" denotes the amplitude under blood-perfused condition. "Mb" corresponds to the amplitude under buffer perfusion. The "Hb" was obtained by subtracting the amplitude of "Mb" from "Hb + Mb".

4 Discussion

According to the traditional assumption, Mb serves merely as an O_2 store in myocytes [15]. Mb releases O_2 only under extremely hypoxic condition. Based on this assumption, many researchers have attributed the NIRS signal from muscle to Hb rather than intracellular Mb. However, NMR experiments have raised questions about the predominant Hb contribution in the NIRS experiments. ^{1}H-NMR can detect the signals from the His F8 NH of deoxy Mb and Hb in human skeletal muscle and can monitor directly Mb and Hb desaturation during contraction [16, 17]. Based on a comparative measurement of NMR and NIRS, Mb contributes significantly to the NIRS signal [7].

Mb deoxygenation has an influence on the optical measurement such as NIRS. Surprisingly, the Mb contributes nearly 50% to the NIRS deoxy signal (Table 1). Researchers usually ignore the Mb contribution in human muscle experiments [14, 18]. Previous rat hindlimb experiments that applied chemical infusion to modify the muscle O_2 uptake have suggested that 90% of the NIRS signal comes from Hb [9]. In contrast, the present study shows a parallel change in Mb and Hb desaturation and suggests that Mb contributes equally to the Δ[deoxy] signal [7].

The present study also provides a preliminary answer to the controversial question if Mb plays a role as an O_2 store and if the O_2 gradient continues to widen as energy demand increases. Mb surely releases O_2 at the onset of the contraction, and the Mb release of O_2 depends upon the O_2 demand of mitochondria. The present result shows a progressive increase in the amplitude of the Δ[deoxy] signal for both blood- and buffer-perfused conditions. The trend does not appear to reach any plateau, and Mb desaturation increases as O_2 demand rises with muscle contraction. In essence, the O_2 gradient continues to widen with increased work. The present result supports the observation that Mb desaturation continues to deoxygenate with increasing muscle activity and does not reach any plateau [17, 19].

Physiological significance of Mb desaturation at the onset of contraction remains unclear. However, it is obvious that the gradient from extracellular layer to intracellular layer must expand once Mb desaturates. The gradient would improve the efficiency of diffusion conductance (DO_2) in the muscle tissue [20]. Even though further experiments are still required to clarify these changes in cellular O_2 during muscle contraction, our results indicate that Mb continues to deoxygenate as work increases and contributes significantly to the NIRS signal in exercising skeletal muscle.

Acknowledgments This research was supported by a Grant-in-Aid for Scientific Research from the Japanese Ministry of Education, Science, Sports and Culture (grant #: 18700527, KM), and by the Uehara Memorial Foundation.

References

1. Popel AS. Theory of oxygen transport to tissue. Crit Rev Biomed Engin 1989; 17: 257–321.
2. Bank W, Chance B. An oxidative defect in metabolic myopathies: diagnosis by noninvasive tissue oxymetry. Ann Neurol 1995; 27: 512–519.
3. Jue T. Measuring tissue oxygenation with the ^{1}H NMR signals of myoglobin. In: RJ Gillies (ed.) NMR in Physiology and Biomedicine, 1994, pp. 199–207. USA: Academic Press.
4. McCully KK, Hamaoka T. Near-infrared spectroscopy: what can it tell us about oxygen saturation skeletal muscle? Exerc Sport Sci Rev 2000; 28: 123–127.
5. Costes F, Barthelemy JC, Feasson L, Busso T, Geyssant A, Denis C. Comparison of muscle near-infrared spectroscopy and femoral blood gases during steady-state exercise in humans. J Appl Physiol 1996; 80: 1345–1350.
6. Wilson JR, Mancini DM, McCully K, Ferraro N, Lanoce V, Chance B. Noninvasive detection of skeletal muscle under perfusion with near-infrared spectroscopy in patients with heart failure. Circulation 1989; 80: 1668–1674.
7. Tran TK, Sailasuta N, Kreutzer U, Hurd R, Chung Y, Molé PA, Kuno S, Jue T. Comparative analysis of NMR and NIRS measurements of intracellular PO_2 in human skeletal muscle. Am J Physiol 1999; 176: R1682–R1690.
8. Lewis SB, Schultz TA, Westbie DK, Gerich JE, Wallin JD. Insulin-glucose dynamics during flow-through perfusion of the isolated rat hindlimb. Horm Metab Res 1977; 9: 190–195.
9. Seiyama A. Virtual cooperativity in myoglobin oxygen saturation curve in skeletal muscle in vivo. Dyn Med 2006; 5: 3–11.
10. Seiyama A, Kosaka H, Maeda N, Shiga T. Effect of hypothermia on skeletal muscle metabolism in perfused rat hindlimb. Cryobiology 1996; 33:338–346.
11. Ruderman NB, Houghton CRS, Hems R. Evaluation on the isolated perfused rat hindquarter for the study of muscle metabolism. Biochem J 1971; 124: 639–651.
12. Shiota M, Golden S. Katz J. Lactate metabolism in the perfused rat hindlimb. Biochem J 1984; 222: 281–291.
13. Shiota M, Sugano T. Characteristics of rat hindlimbs perfused with erythrocyte- and albumin-free medium. Am J Physiol 1986; 251: C78–C84.
14. DeBlasi RA, Ferrari M, Natali A, Conti G, Mega A, Gasparetto A. Noninvasive measurement of forearm blood flow and oxygen consumption by near-infrared spectroscopy. J Appl Physiol 1994; 76: 1388–1393.
15. Theorell H. Kristallinisches myoglobin. Biochem Z 1934; 268: 73–82.
16. Chung Y, Molé PA, Sailasuta N, Tran TK, Hurd R, Jue T. Control of respiration and bioenergetics during muscle contraction. Am J Physiol Cell Physiol 2005; 288: C730–C738.
17. Molé PA, Chung Y, Tran TK, Sailasuta N, Hurd R, Jue T. Myoglobin desaturation with exercise intensity in human gastrocnemius muscle. Am J Physiol 1999; 277: R173–R180.
18. MacDonald MJ, Tarnopolsky MA, Green HE, Hughson RL. Comparison of femoral blood gases and muscle near infrared spectroscopy at exercise onset in humans. J Appl Physiol 1999: 86; 687–693.
19. Richardson RS, Noyszewski EA, Kendrick KF, Leigh JS, Wagner PD. Myoglobin O_2 desaturation during exercise. Evidence of limited O_2 transport. J Clin Invest 1995; 96: 1916–1926.
20. Groebe, K. An easy-to-use model for O_2 supply to red muscle. Validity of assumptions, sensitivity to errors in data. Biophy J 1995; 68: 1246–1269.

Muscle Reoxygenation Difference Between Superficial and Deep Regions of the Muscles During Static Knee Extension

Chihoko Ueda and Atsuko Kagaya

Abstract The purpose of this study was to test the hypothesis that differences in vertical spatial difference in reoxygenation after exercise exists, reflecting heterogeneity of muscle oxygenation during exercise might be due to the difference in dominantly recruited muscle fiber type. Methods: Ten healthy female subjects performed 1 min static knee extension exercise at low (30%) and high (60%) fraction of maximal voluntary contraction (MVC). Muscle oxygenation in the vastus lateralis (VL) was monitored using multi channel near-infrared spectroscopy. Half time reoxygenation ($T_{1/2}$reoxy) after exercise was calculated from oxygenated hemoglobin in the eight channels which changed the distance between light source and detector distances at 2,3,4,5 cm. Blood flow (BF) in the femoral artery was measured by Doppler ultrasound. Mean arterial blood pressure (BP) at the end of the exercise was assessed by a Finometer device. Results: BF during exercise did not differ significantly during exercise at low and high intensity, whereas BP was elevated at high intensity. $T_{1/2}$reoxy tended to be prolonged at high intensity. It would be due to a transition of muscle fiber recruitment from type I toward type II fiber dominance, and/or insufficient oxygen supply for increased demand in the muscle. $T_{1/2}$reoxy in different light source and detector distances was not different among them. Conclusion: This study demonstrated that the reoxygenation in the superficial region did not differ from that in the deeper region, including superficial, even when exercise intensity was high.

1 Introduction

Recent studies indicated a spatial heterogeneity in lateral direction of deoxygenation and reoxygenation in a single muscle [6, 7, 9, 10]. One of the studies demonstrated that plantar flexion resulted in more deoxygenation during

C. Ueda (✉)
Research Institute of Physical Fitness, Japan Women's College of Physical Education, Tokyo, 157-8565, Japan
e-mail: cueda@jwcpe.ac.jp

E. Takahashi, D.F. Bruley (eds.), *Oxygen Transport to Tissue XXXI*, Advances in Experimental Medicine and Biology 662,
DOI 10.1007/978-1-4419-1241-1_47, © Springer Science+Business Media, LLC 2010

exercise and an earlier reoxygenation during recovery in the distal portion compared with the proximal portion in gastrocremius muscle [9]. Another study also reported that reoxygenation in VL after cycling exercise was progressively delayed from distal sites to proximal site at the same submaximal intensities [6]. Possible reasons for such regional differences in muscle oxygenation between the proximal and distal portion are differences in muscle fiber composition, intramuscular pressure, and capillary density and so on [9]. A previous study in human demonstrated that distribution of different fiber type varied within a muscle, with a predominance to type II fibers at surface and type I fibers in deeper regions of the muscle [11]. Based upon the non-uniformity of muscle fiber composition from superficial to deeper portions of muscle, we assumed that muscle reoxygenation should be different depending on the depth of the region studied in the muscle. Additionally the difference in intramuscular pressure between the superficial and deep regions [12] should be considered, because it results in the difference in oxygen delivery and therefore reoxygenation difference.

Recently, muscle oxygenation during exercise has been measured non-invasively by near-infrared spectroscopy (NIRS). Recovery time of muscle oxygenation following the completion of exercise is used as an index of deficits of oxygen delivery to the muscle in relation to oxygen demand of working muscle [1, 2, 4, 8]. Therefore we supposed that surface regions of muscle have a prolonged recovery time of muscle oxygenation as compared with deeper regions. The purpose of this study was to test the hypothesis that vertical spatial difference in recovery time of muscle oxygenation exists, reflecting heterogeneity of muscle oxygenation during exercise is probably caused by non-uniform fiber composition distribution.

2 Methods

Ten healthy females [age: 22.0 $\pm$ 1.2 (means $\pm$ SD) yr, body height: 160.4 $\pm$ 4.6 cm, body mass: 55.3 $\pm$ 5.7 kg] participated in this study. The subjects were fully informed of the purpose, nature, and potential risks of the experiments and gave their written, informed consent to participate in this study. This study was approved by The Ethical Committee of the Japan Women's College of Physical Education.

Static knee extension was adopted in this study. Before the experiments, all subjects were familiarized with the exercise equipment and the protocol. Maximal voluntary contraction (MVC) of knee extension was measured on the right leg. The exercise was performed in upright position with the knee joint angle set at 90 degrees. The exercise comprised 1 min static contraction at low (30% MVC) and high (60% MVC) intensities. The order of the contractions was random, and separated by at least 5 min.

Femoral arterial blood velocity in the right leg was measured by Doppler ultrasound method (Vivid7 pro, GE Yokokawa Medical Systems, Japan) with a 7.5 MHz transducer. The systolic and diastolic diameters in the femoral arterial were also measured using B-mode ultrasonography. The mean diameter was calculated based on the relative time periods of the systolic (1/3) and the diastolic (2/3) phases of the cardiac cycle: ([systolic diameter value $\times$ 1/3] + [diastolic diameter value $\times$ 2/3]). Mean blood velocity (Vmean) was obtained from angle corrected, time averaged, and integrated velocity of whole consecutive cardiac cycles of Doppler signals within the approximately last 5 s of each exercise. Femoral artery blood flow (FBF) was calculated by multiplying the cross-sectional area (area $= \pi \times [\text{diameter}/2]^2$) (CSA) of the femoral artery with Vmean ; FBF (L/min) = Vmean (cm/s) $\times$ CSA (mm^2) $\times 6 \times 10^{-4}$.

Mean arterial blood pressure (BP) was measured non-invasively by photoelectric plethysmogaraphy with Finometer (Finapres Medical Systems BV, Netherlands). The beat-to-beat values were averaged over the last 5 s of exercise at each intensity.

Muscle oxygenation in the VL was monitored by near infrared continuous wave spectroscopy (NIRS, OMM-3000, Shimadzu, Japan). The NIRS probe was placed over the thickest site of VL, and 3 cm distal part from there. The distance light source and detector distances was set at 2, 3, 4, and 5 cm. Tissue thickness over this position was 8.6 $\pm$ 0.6 mm for the subcutaneous adipose tissue, 20.7 $\pm$ 0.9 mm for VL and 16.2 $\pm$ 0.8 mm for Vastus intermedius (VI) muscle. The NIRS signals at wavelengths of 780, 805, 830 nm were used for calculation of changes in the concentration of oxygenated hemoglobin (oxyHb), deoxygenated hemoglobin (deoxyHb), and total hemoglobin (totalHb). Half time reoxygenation ($T_{1/2}$reoxy) was determined as the time required to reach the value halfway between the oxyHb level immediately after exercise and that at peak hyperemia during recovery.

Values are represented as means $\pm$ SE, unless indicated otherwise. Differences in BF, BP, and $T_{1/2}$reoxy between the low and high intensities were analyzed using the t test for paired samples. One-way ANOVA for repeated measurements was used to compare $T_{1/2}$reoxy for different light source detector distances. A p-value of less than 0.05 was considered statistically significant.

3 Results

FBF at 30%MVC (0.45 $\pm$ 0.04 L/min) was not different from that at 60% MVC (0.50 $\pm$ 0.06 L/min) (Fig. 1)

BP was significantly higher at 60% MVC (95 $\pm$ 3 mmHg) compared with 30% MVC (106 $\pm$ 6 mmHg) ($p < 0.05$) (Fig. 2)

$T_{1/2}$reoxy tended to be prolonged at 60% MVC as compared with 30% MVC ($p < 0.10$). However there were no differences among $T_{1/2}$reoxy values in different light source detector distances (Fig. 3)

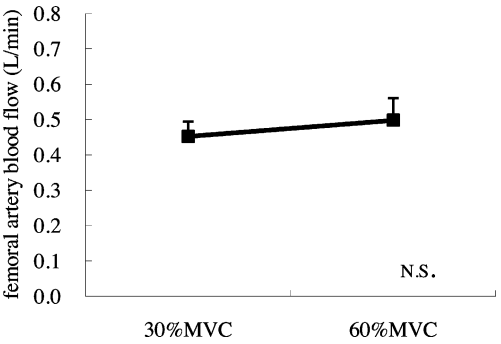

Fig. 1 Femoral artery blood flow (FBF) during knee extension exercise at low (30% MVC) and high (60% MVC) intensities. Values are mean ± SE, $n = 9$. NS

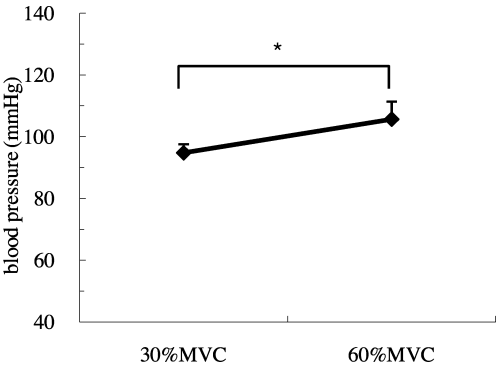

Fig. 2 Mean blood pressure (BP) during knee extension exercise at low (30% MVC) and high (60% MVC) intensities. Values are mean ± SE, $n = 9$. *Significant difference between intensities ($p < 0.05$)

4 Discussion

The present study examined muscle reoxygenation from the superficial to deep region of the VL in static knee extension exercise at low and high intensities. Results showed that $T_{1/2}$reoxy tended to be prolonged at the high-intensity exercise. This would be explained by a transition of muscle fiber recruitment from type I toward type II fiber dominance, and/or due to insufficient oxygen supply for increased demand in the muscle supposed from pre-sent result of BF. BF during exercise was constant, and means that the blood supply condition was not different between low and high intensities. This result on BF is supported by previous studies [3, 5]. The values of $T_{1/2}$reoxy in this study were smaller than that in previous references [6, 8]. It might be due to different exercise. We used static one-legged knee extension exercise and they used cycle ergometer exercise. Dynamic cycle exercise should induce recruitment of larger muscle mass and increase oxygen demand of working muscle.

We could not find differences in $T_{1/2}$reoxy among different light source and detector distances. Following three possible reasons are considered; the first is that recruited muscle fibers in this exercise are not different in proportion of

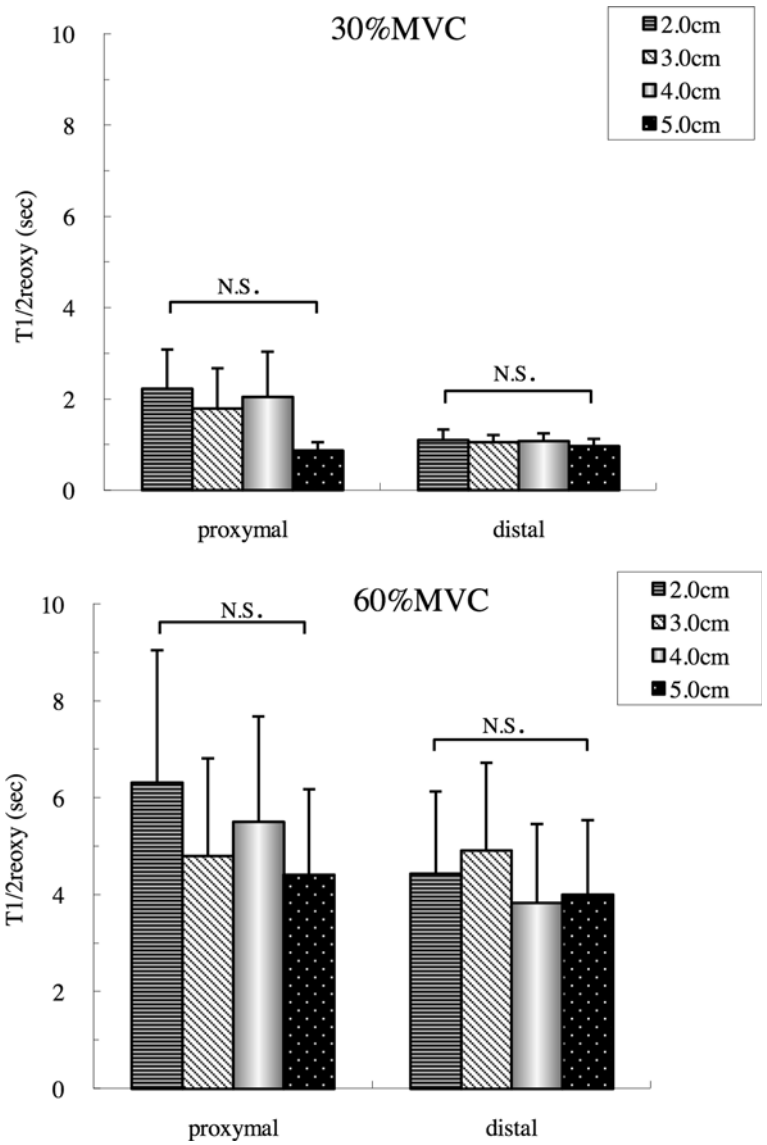

Fig. 3 Half time reoxygenation ($T_{1/2}$reoxy) during knee extension exercise at low (30% MVC) and high (60% MVC) intensities in different light source detector distances. Values are mean $\pm$ SE, $n = 10$. $p < 0.1$, 30% MVC vs. 60% MVC corresponding values

types between superficial and deep regions of the muscle. The second is that wider light source and detector distance has included not only deep region information but also superficial information of muscle oxygenation. The third is that the heterogeneity of intramuscular pressure could affect on $T_{1/2}$reoxy in

the opposite direction to the heterogeneity of muscle fiber distribution. The question remains unresolved if heterogeneity of muscle fiber composition and blood flow distribution will cause different recovery time of muscle oxygenation between superficial and deep regions of the muscle.

In conclusion, this study demonstrated that recovery time of muscle oxygena-tion in deep and superficial regions did not differ from that in the region limited to the superficial one after exercise even at high intensity.

Acknowledgments This work was supported by "Academic Frontier" Project of Japan Women's College of Physical Education. We thank Prof. T. Sadamoto, Dr. K. Sato, and Dr. K. Shibuya for their thoughtful suggestions and advice, and Ms. A. Hirasawa for her skilful assistance.

References

1. Chance B, Dait MT, Zhang C, Hamaoka T, Hagerman F. Recovery from exercise-induced desaturation in the quadriceps muscles of elite competitive rowers. Am J Physiol 1992; 262: C766–C775.
2. Hamaoka T, Albani C, Chance B, Iwane H. A new method for the evaluation of muscle aerobic capacity in relation to physical activity measured by near-infrared spectroscopy. Med Sport Sci 1992; 37: 421–429.
3. Homma S, Kagaya A. Oxygen delivery and utilization in working muscle during 1-min static handgrip exercise at varied intensity. J Exerc Sci 1998; 8: 30–37.
4. Ichimura S, Murase N, Osada T, Kime R, Homma T, Ueda C, Nagasawa T, Motobe M, Hamaoka T, Katsumura T. Age and activity status affect muscle reoxygenation time after maximal cycling exercise. Med Sci Sports Exerc 2006; 38: 1277–1281.
5. Kagaya A, Homma S. Brachial arterial blood flow during static handgrip exercise of short duration at varying intensities studied by a Doppler ultrasound method. Acta Physiol Scand 1997; 160: 257–265.
6. Kime R, Im J, Moser D, Lin Y, Nioka S, Katsumura T, Chance B. Reduced heterogeneity of muscle deoxygenation during heavy bicycle exercise. Med Sci Sports Exerc 2005; 37: 412–417.
7. Koga S, Poole DC, Ferreira LF, Whipp BJ, Kondo N, Saitoh T, Ohmae E, Barstow TJ. Spatial heterogeneity of quadriceps muscle deoxygenation kinetics during cycle exercise. J Appl Physiol. 2007; 103: 2049–2056.
8. McCully KK, Iotti S, Kendrick K, Wang Z, Posner JD, Leigh J Jr, Chance B. Simultaneous in vivo measurements of HbO_2 saturation and PCr kinetics after exercise in normal humans. J Appl Physiol 1994; 77: 5–10.
9. Miura H, McCully K, Hong L, Nioka S, Chance B. Regional difference of muscle oxygen saturation and blood volume during exercise determined by near infrared imaging device. Jpn J Physiol 2001; 51: 599–606.
10. Mizuno M, Tokizawa K, Iwakawa T, Muraoka I. Inflection points of cardiovascular responses and oxygenation are correlated in the distal but not the proximal portions of muscle during incremental exercise. J Appl Physiol. 2004; 97: 867–873.
11. Lexell J, Henriksson-Larsén K, Sjöström M. Distribution of different fibre types in human skeletal muscles. 2. A study of cross-sections of whole m. vastus lateralis. Acta Physiol Scand. 1983; 117: 115–122.
12. Sejersted OM, Hargens AR, Kardel KR, Blom P, Jensen O, Hermansen L. Intramuscular fluid pressure during isometric contraction of human skeletal muscle. J Appl Physiol 1984; 56: 287–295.

Arterial Oxygen Desaturation Response to Repeated Bouts of Sprint Exercise in Healthy Young Women

Shimpei Kuniyoshi, Yumiko Endoh, Minoru Kobayashi, and Hiroshi Endoh

Abstract The decline in arterial oxygen saturation of hemoglobin during exercise has been termed exercise-induced arterial hypoxemia (EIAH). We examined whether repeated bouts of sprint exercise (SprE) would induce EIAH in healthy young men and women. Ten men and 11 women (20.4 ± 0.3 year) performed an anaerobic power test (three bouts of 10 s cycling with 120 s intervals) using a cycle ergometer. Arterial oxygen saturation of hemoglobin measured by pulse oximeter (SpO_2), heart rate (HR), rate perceived exertion (RPE), and the blood lactate concentration ($[La]_b$) were assessed at rest, during, and 5 min after repeated bouts of SprE. Women exhibited a lower maximal anaerobic power (MAnP) compared to men (498 ± 23 vs. 759 ± 22 watts, respectively, $p < 0.01$). HR, RPE, and $[La]_b$ in women were comparable with those in men throughout the test. However, the only significant decline in SpO_2 after a single bout of SprE (95.5 ± 0.7%) from the resting value (97.9 ± 0.2%) was observed in women, and further declines occurred following heavier SprE (< 95%). In 8 of 11 women, mild to moderate EIAH developed, whereas only 2 men showed mild EIAH. Thus, these findings suggest that repeated bouts of SprE might induce mild EIAH in young women but not men.

1 Introduction

EIAH has been reported in many trained young men, some older athletes, and many habitually active women [3]. It is generally accepted that EIAH occurs at a heavy workload approximately corresponding to the maximal oxygen consumption. To our knowledge, however, most exercises to identify EIAH carried out in previous studies lasted for several min with a fast-increment, progressive, or constant heavy workload, i.e., the exercise mode did not simulate sprinting.

H. Endoh (✉)
Department of Health and Physical Education, University of the Ryukyus Graduate School of Education, Nishihara, Okinawa, 903-0213, Japan
e-mail: hiendoh@edu.u-ryukyu.ac.jp

E. Takahashi, D.F. Bruley (eds.), *Oxygen Transport to Tissue XXXI*,
Advances in Experimental Medicine and Biology 662,
DOI 10.1007/978-1-4419-1241-1_48, © Springer Science+Business Media, LLC 2010

On the other hand, some recent studies reported a high incidence of EIAH (nearly 70%) in women during the early [7] or mid [3] follicular phase of their menstrual cycle, slightly greater than the 50% value in highly fit men [2].

With this background, we examined whether repeated bouts of brief exercise with a heavy workload would induce EIAH in healthy young men and women.

2 Methods

2.1 Subjects

Twenty one (10 men and 11 women; 20.4 ± 0.3 year) healthy young subjects participants of varying fitness levels between the ages 18–24 year volunteered for this study and provided oral informed consent. In this study, we chose to collect data throughout all phases of the menstrual cycle.

One to 3 months before the present experiment, the predicted maximal oxygen consumption of all subjects was measured by the 20 m shuttle run test, which is a valid indicator of maximal aerobic capacity in various populations and may be used to predict with reasonable accuracy [6]. Subject characteristics and physical capacity data are shown in Table 1.

Table 1 Subject characteristics

	Men (n = 10)	Women (n = 11)
Age, yearr	21.0 ± 0.6	20.0 ± 0.3
Height, cm	171.0 ± 1.7	157.0 ± 1.1**
Body Weight, kg	65.5 ± 2.5	53.4 ± 2.8**
Body Fat, %	14.2 ± 1.3	25.1 ± 2.1**
BMI, $kg \cdot m^{-2}$	22.4 ± 0.6	21.7 ± 1.0
$p\dot{V}O_{2max}$, $mL \cdot min^{-1} \cdot kg^{-1}$	48.2 ± 1.4	40.9 ± 1.4**
MAnP, watts	759 ± 22	498 ± 23**

Values are means ± SE. BMI, body mass index; $p\dot{V}O_{2max}$, predicted maximal oxygen consumption; MAnP, maximal anaerobic power. Significantly different, ** $p < 0.01$ *vs*. men.

2.2 Exercise

All subjects performed the MAnP test, which comprised three bouts of SprE on an electrically braked cycle ergometer (Powermax-V II, Combi Wellness) for 10 s, with a subsequent 2 min rest interval in a thermoneutral condition (approximately 25°C ambient temperature and ~50% relative humidity) near sea level. Subjects were instructed to pedal as fast as possible during the SprE regardless of the workload. The workload on the first bout of SprE was determined based on the sex and body weight of individuals, and the following workloads were

automatically calculated by a built in computer based on the workload and pedaling rate (revolutions per min) recorded during the prior bout of SprE, as previously described [5].

2.3 Measurements

SpO_2 data were obtained by pulse oximeter with a finger probe (OX-0001, Yamagata Casio). Even though the current generation of finger probe equipped with pulse oximeters may be more accurate than ear probe equipped models [4], the sensors are subject to motion artifacts, which can interfere with signal detection during heavy exercise, such as that performed in this study. Therefore, we fixed the probe on a forefinger using elastic adhesive tape, ensuring contact between the probe and fingertip during the test. In pilot studies, we confirmed the absence of changes in SpO_2 on hand movements.

After resting measurements, SpO_2, HR (S610i, Polar), and RPE using Borg's (6–20) scale were assessed immediately after every bout of SprE and 5 min after the third bout. The blood lactate concentration ($[La]_b$) was also determined immediately after the third bout of SprE and at recovery by a portable lactate analyzer (Lactate Pro LT1710, Arklay).

2.4 EIAH

According to the proposal by Dempsey and Wagner (1999), we adopted the following criteria for EIAH: mild EIAH characterized as SpO_2 of 93–95%, moderate EIAH as 88–93%, and severe EIAH as less than 88%.

2.5 Statistics

All data are represented as the mean ± SE. The significance of differences between men and women regarding morphological and physical capacity data was assessed using Student's unpaired *t*-test. Differences between men and women for SpO_2, HR, RPE, and $[La]_b$ were assessed by a two-way analysis of variance (ANOVA) with repeated measures. When an interaction was encountered, a functional one-way ANOVA for each sex was conducted to determine differences within sex, and the Bonferroni post-hoc test was performed to determine differences between men and women in the various pairwise comparisons. Pearson's correlation coefficient was employed to determine the relationship between physical capacity data and the minimum SpO_2 on the repeated bouts of SprE. For all analyses, significance was set at $p < 0.05$.

3 Results

Mean power outputs on the first bout of SprE in men and women were 651 ± 29 and 367 ± 28 watts, respectively, which were clearly lower than those on subsequent bouts of exercise: 797 ± 24 and 490 ± 25 and 726 ± 30 and 489 ± 22 watts on the second and third bouts of SprE, respectively. Women exhibited a significantly lower MAnP compared to men (Table 1).

Table 2 summarizes the effects of repeated bouts of SprE on HR, RPE, $[La]_b$, and SpO_2. Changes in HR, RPE, and $[La]_b$ for women were comparable with those for men throughout the test, suggesting that similar relative workloads were used for each sex in this study. Although SpO_2 showed similar values in both sexes during the initial resting period, the only responding declines in SpO_2 were observed in women immediately after the first bout of SprE, and further declines occurred following heavier exercise, whereas there were no significant changes in SpO_2 in men. The differences in SpO_2 between men and women were completely abolished at recovery. It is worth noting that mild to moderate EIAH developed in 8 of 11 women ($n = 4$ in each category), whereas only 2 men were ranked as showing mild EIAH and the other 8 men were considered to be non-responders who maintained a higher SpO_2 of over 95% throughout the test.

Table 2 HR, RPE, [La]b, and SpO_2

		Rest	1st SprE	2nd SprE	3rd SprE	Recovery
HR, bpm	Men	73.2 ± 0.2	140.2 ± 0.4	149.0 ± 0.4	151.6 ± 0.5	93.8 ± 0.2
	Women	75.3 ± 0.2	133.6 ± 0.7	149.5 ± 0.8	148.8 ± 0.5	94.1 ± 0.2
RPE	Men		13.8 ± 0.6	16.1 ± 0.3	17.5 ± 0.5	
	Women		13.9 ± 0.5	15.3 ± 0.5	16.7 ± 0.5	
$[La]_b$, mM	Men	3.4 ± 0.5			12.4 ± 1.1	12.9 ± 1.1
	Women	2.8 ± 0.2			10.9 ± 0.8	10.7 ± 0.7
SpO_2, %	Men	98.2 ± 0.2	96.9 ± 0.4	97.3 ± 0.4	97.1 ± 0.5	97.6 ± 0.2
	Women	97.9 ± 0.2	95.5 ± 0.7$^{\$}$	94.7 ± 0.8$^{*,\ \$\$}$	94.9 ± 0.5$^{**,\ \$\$}$	97.5 ± 0.2

Values are means ± SE. HR, heart rate; RPE, rate perceived exertion; $[La]_b$, blood lactate concentration; SpO_2, arterial oxygen saturation of hemoglobin; SprE, sprint exercise. Significantly different, $^{*}p < 0.05$, $^{**}p < 0.01$ *vs.* men. Significantly different, $^{\$}p < 0.05$, $^{\$\$}p < 0.01$ *vs.* rest.

To demonstrate the effects of physical capacity on the arterial oxygen desaturation response to the repeated bouts of SprE, several correlation analyses were performed. We identified a significant correlation between the minimum SpO_2 and MAnP when data for both men and women were pooled ($r = -0.58$, $p = 0.006$). In contrast, the predicted maximal oxygen consumption was not correlated with the minimum SpO_2.

4 Discussion

The major finding of this study was that the repeated bouts of SprE might induce mild EIAH in young women but not in men.

SpO_2 may be reduced during heavy exercise, not only because of a reduction in the PaO_2 but also due to a pH and temperature induced rightward shift of the oxyhemoglobin (HbO_2) dissociation curve [1]. Although these factors could have some effects on our results, the increase in the $[La]_b$ response to the repeated bouts of SprE were comparable in both sexes, as well as other physiological responses, and the percentages of mean power output in MAnP during the repeated bouts of SprE were somewhat lower in both sexes (average 90% of MAnP) than in men (average 95% of MAnP), suggesting that the decrease in pH caused by the repeated bouts of SprE in women was unlikely to be greater than in men. In addition, the exercise duration (10 s) would be too brief to cause a marked elevation in the core temperature. Taken together, the repeated bouts of SprE performed by both sexes in this study might have an equal effect on the rightward shift of the HbO_2 dissociation curve.

Metabolic activities during intermittent exercise, such as repetition- or interval-mode exercise, must be maintained at a high level until the completion of the final bout of exercise, similar to the state during continuous endurance exercise. Recent studies [3, 8] suggested that a smaller vital capacity, reduced airway diameter, and a smaller diffusion surface in women compared to age and height matched men could lead to the gender based difference in the EIAH response to continuous exercise with a fast-increment, progressive workload. Thus, these anatomical and functional factors related to pulmonary limitation in women could be lead to EIAH in this study.

Although the mechanisms for EIAH represented in this study are unclear, they would necessarily include ventilation-perfusion inequality, diffusion limitation, and also the possibility that certain individuals may have had a lower breathing response (maybe due to diaphragmatic fatigue), i.e., less hyperventilation, than others in late exercise/immediate recovery. Further study is required to clarify potential mechanisms leading to the altered SpO_2 response to the repeated bouts of SprE in women.

We showed a significant negative correlation between minimum SpO_2 during the repeated bouts of SprE and MAnP. Our finding indicates that individuals with lower anaerobic capacity might be at high risk of EIAH response to repeated bouts of SprE.

Acknowledgments We thank the volunteers for participating in this study. This study was supported in part by grant-in-aids for scientific research from the Ministry of Education, Science, Sports, and culture Japan 20300221.

References

1. Dempsey JA, Wagner PD (1999) Exercise-induced arterial hypoxemia. J Appl Physiol 87(6): 1997–2006
2. Guenette JA, Diep TT, Koehle MS, Foster GE, Richards JC, Sheel AW (2004) Acute hypoxic ventilatory response and exercise-induced arterial hypoxemia in men and women. Respir Physiol Neurobiol 143(1): 17–48

3. Harms CA, McClaran SR, Nickele GA, Pegelow DF, Nelson WB, Dempsey JA (1998) Exercise-induced arterial hypoxaemia in healthy young women. J Appl Physiol 507(2): 619–628
4. Mengelkoch L, Martin D, Lawler J (1994) A review of the principles of pulse oximetry and accuracy of pulse oximeter estimates during exercise. Phys Ther 74(1): 40–49
5. Nakamura Y, Mutoh Y, Miyashita M (1984) A method for determining maximal anaerobic power using a bicycle ergometer. Jap J Sports Sci 4: 834–839
6. Paliczka VJ, Nichols AK, Boreham CA (1987) A multi-stage shuttle run as a predicator of running performance and maximal oxygen uptake in adults. Br J Sports Med 21(4): 163–165
7. Richards JC, Mckenzie DC, Warburton DR, Road JD, Sheel AW (2004) Prevalence of exercise-induced arterial hypoxemia in healthy women. Med Sci Sports Exerc 36 (9): 1514–1521
8. Walls J, Maskrey M, Wood-Baker R, Stedman W (2002) Exercise-induced oxyhaemoglobin desaturation, ventilatory limitation and lung diffusing capacity in women during and after exercise. Eur J Appl Physiol 87(2): 145–152

The Effect of Endurance Training on Resting Oxygen Stores in Muscle Evaluated by Near Infrared Continuous Wave Spectroscopy

Takayuki Sako

Abstract The purpose of this study was to examine the effects of endurance training (ET) on resting oxygen store (r-O_2mus) using near infrared continuous wave spectroscopy (NIR_{CWS}), and the validity of using this method for the evaluation of resting muscle oxygen consumption (r-VO_2mus) in a training study. Ten female subjects were tested in the following study. All subjects were physically active, but did not participate in any regular training besides this study. The subjects were fully informed of the risks and gave their consent before the start of the experiments. For ET subjects cycled for 40 min at 60–70% VO_2peak, three times a week, for 4 weeks. Before and after the period of ET, VO_2peak and r-O_2mus for the vastus lateralis muscle were measured. r-O_2mus was defined as the amount of O_2 consumed by the muscle, which was determined from r-VO_2mus measured by NIR_{CWS} (HEO200, Omron) during arterial occlusion induced by a pneumatic tourniquet. In order to verify the measurements using NIR_{CWS}, oxygen consumption for both the whole body (40%-VO_2) and vastus lateralis muscle (40%-VO_2mus) were measured at pre and post ET. 40%-VO_2mus was calculated from the ratio of the declining rates of Hb/MbO_2 immediately post-exercise and during rest (r-VO_2mus). As a result, VO_2peak significantly increased after ET. r-O_2mus also significantly increased ($p < 0.05$). Neither 40%-VO_2 nor 40%-VO_2mus changed following ET. Therefore these findings suggest the increase in r-O_2mus calculated from r-VO_2mus reflects an increase in resting oxygen stores in the trained muscle. Under the condition when resting muscle oxygen consumption is unchanged, NIR_{CWS} can be a useful non-invasive tool for measuring muscle oxygen stores.

T. Sako (✉)
Department of Food and Nutrition, Japan Women's University, Tokyo, 112-8681, Japan
e-mail: sako@fc.jwu.ac.jp

E. Takahashi, D.F. Bruley (eds.), *Oxygen Transport to Tissue XXXI*,
Advances in Experimental Medicine and Biology 662,
DOI 10.1007/978-1-4419-1241-1_49, © Springer Science+Business Media, LLC 2010

1 Introduction

Near infrared continuous wave spectroscopy (NIR_{CWS}) is widely applied to various fields, such as basic science, exercise physiology, and sports medicine, since NIR_{CWS} can evaluate the changes in Hb/MbO_2 and total Hb/Mb concentration in a non-invasive manner and at a high time resolution. The amount of Hb/MbO_2 that decreases during arterial occlusion at rest reflects the amount of oxygen consumed in muscle, and can be expressed as the oxygen store ($r\text{-}O_2mus$) [1, 2]. In other words, the oxygen store is mainly related to the number of arterioles and venules, density of capillaries which are perfused and contain HbO_2, and MbO_2 concentration at rest. Measuring these functional parameters non-invasively offers the advantage to evaluate oxygen delivery under physiological conditions, which has been typically assessed in histological studies in non physiological conditions.

Since NIR_{CWS} cannot determine the absolute value of Hb/MbO_2 content, Hamaoka et al. [2] proposed a "physiological calibration" evaluated by the difference of Hb/MbO_2 levels between the resting value and the minimum value during arterial occlusion. They also proposed a method to evaluate exercising muscle oxygen consumption from the decline rates of Hb/MbO_2 during arterial occlusion relative to the resting value [2, 3]. Using these methods, we can compare the oxygenation level and oxygen consumption at various exercise levels among different subjects.

This non-invasive method offers many benefits in human studies, but may prove difficult to apply to training studies where changes in resting muscle oxygen consumption ($r\text{-}VO_2mus$) could occur following the training period. The purpose of this study was to examine the effects of endurance training (ET) on $r\text{-}O_2mus$ using NIR_{CWS}, and the validity of using this method for the evaluation of $r\text{-}VO_2mus$ in a training study.

2 Methods

Ten female subjects (21.4 ± 1.2 years) were tested in the following study. All subjects were physically active, but did not participate in any regular training besides this study. The subjects were fully informed of the risks and gave their consent before the start of the experiments.

All exercise testing and training were performed on a cycle ergometer (AERBI-KE75XLII, COMBI, Japan), which provided work load control independently of pedaling cadence. Pulmonary gas variables were measured by a breath-by-breath method (AE-300S, Minato, Japan). Before and after the period of ET, all subjects performed a maximal aerobic test using a step method to determine VO_2peak. ET was conducted for 40 min at 60–70% VO_2peak, three times a week, for 4 weeks.

Skeletal muscle oxygen consumption at rest ($r\text{-}VO_2mus$) and during submaximum exercise ($40\%\text{-}VO_2mus$), and resting oxygen store ($r\text{-}O_2mus$) were measured using near infrared continuous wave spectrometer (HEO200, Omron, Japan)

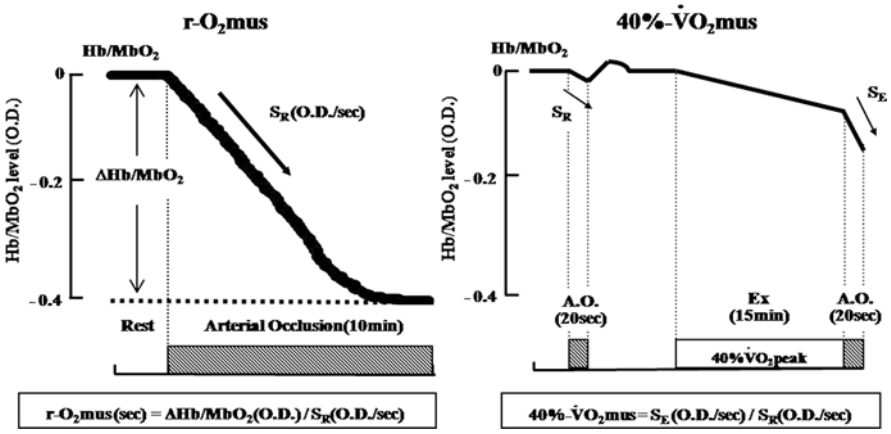

Fig. 1 Experimental protocol and calculations of resting muscle oxygen store (*left*) and muscle oxygen consumption at 40%VO_2peak (*right*). r-O_2mus, resting muscle oxygen store; $\Delta Hb/MbO_2$, the amount of change in Hb/MbO_2 level; S_R, the decline rate of Hb/MbO_2 level at rest; 40%-VO_2mus, muscle oxygen consumption at 40%VO_2peak; S_E, the decline rate of Hb/MbO_2 level; A.O., arterial occlusion; Ex, exercise with cycle ergometer

(Fig. 1). A pair of probes of NIR_{CWS} was applied to the skin 3 cm apart over the right vastus lateralis muscle. Both muscle oxygen consumption (VO_2mus) and resting muscle oxygen store (r-O_2mus) were evaluated from the changes in Hb/MbO_2 concentration during arterial occlusion by a pneumatic tourniquet attached proximal to NIR_{CWS} probes. During the measurement of NIR_{CWS} subjects were seated on a cycle ergometer with the right foot on the pedal so the thigh is positioned horizontally. r-O_2mus was measured during 10 min of arterial occlusion at rest. r-O_2mus was defined as the amount of O_2 consumed by the muscle, which was determined from the decline rate of Hb/MbO_2 reflecting r-VO_2mus and was expressed as the time for the stored oxygen to be consumed by r-VO_2mus. 40%-VO_2mus was measured during 20 s of arterial occlusion immediately after 15 min of exercise at 40%-VO_2peak, and defined as the ratio to r-VO_2mus measured during arterial occlusion 10 min before starting the exercise. Oxygen consumption for the whole body (40%-VO_2) was also measured during 15 min of exercise.

All data were expressed as means ± SE. Statistical evaluation of changes from pre-training values was done using a paired Student's *t*-test. A p value of < 0.05 was accepted as significant.

3 Results

VO_2peak significantly increased from 2147.8 ± 77.2 ml/min(mean ± SE) to 2308.5 ± 75.8 ml/min ($p < 0.01$) after ET (Fig. 2). r-O_2mus also significantly increased from 309.6 ± 17.1 s to 354.4 ± 17.5 s ($p < 0.05$) (Fig. 2). The body weight significantly decreased from 54.4 ± 2.4 kg to 53.6 ± 2.3 kg after ET

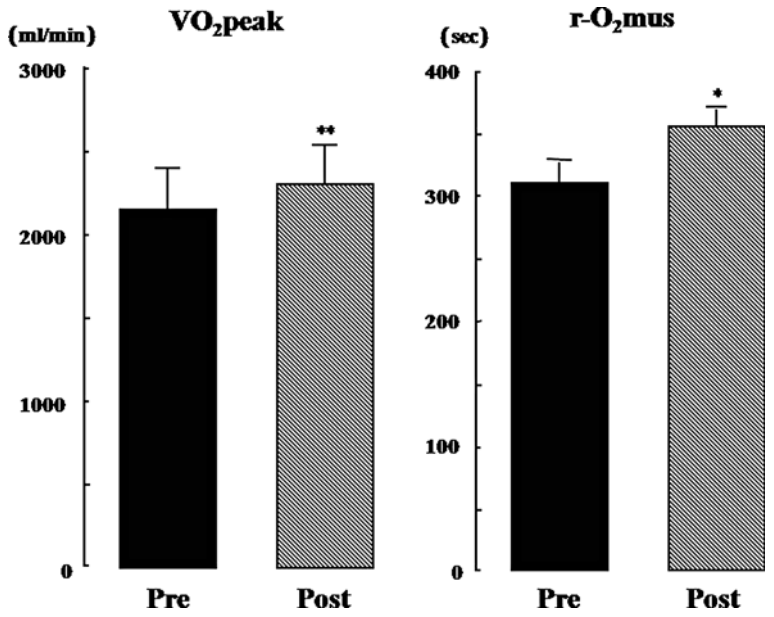

Fig. 2 The effect of endurance training on VO_2peak (*left*) and resting muscle oxygen store (r-O_2mus)(*right*). Both VO_2peak and r-O_2mus significantly increased after endurance training (ET). Values are mean±SE. Pre, value measured before ET; Post, value measured after ET. Asterisks indicate a significant difference from the pre-training value for each parameter (* $p < 0.05$, ** $p < 0.01$)

($p < 0.05$). Figure 3 shows the average changes in 40%-VO_2 and 40%-VO_2mus after ET. 40%-VO_2 did not significantly change from 898.0 ± 177.8 ml/min before ET to 880.4 ± 128.7 ml/min after ET. 40%-VO_2mus also did not vary from 20.6 ± 2.1 before ET to 20.3 ± 2.1 after ET. In order to examine the possibility of a decrease in r-VO_2mus causing an increase in r-O_2mus, 40%-VO_2mus was recalculated from the revised r-VO_2mus. Revised 40%-VO_2mus was significantly smaller than the pre-training value (17.9 ± 1.9 fold of r-VO_2mus). It was unlikely that 40%-VO_2mus would decrease after ET when compared to the pre-value, so it is reasonable to think that r-O_2mus increased after ET.

4 Discussion

The purpose of this study was to examine the effects of endurance training (ET) on r-O_2mus using NIR_{CWS}, and the validity of using this method for the evaluation of r-VO_2mus in a training study. As a result, VO_2peak significantly increased after ET. r-O_2mus also significantly increased ($p < 0.05$). Neither 40%-VO_2 nor 40%-VO_2mus changed following ET.

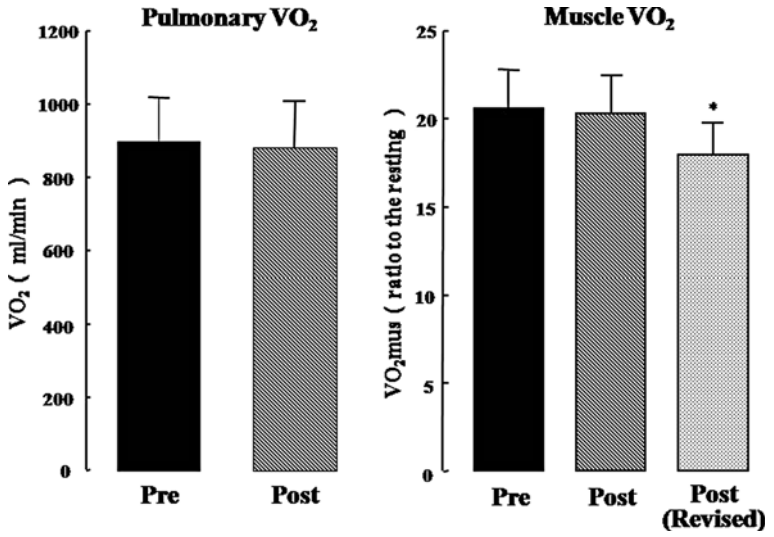

Fig. 3 The effect of endurance training on pulmonary (*left*) and muscle (*right*) oxygen consumption at 40%VO_2peak. Neither VO_2 nor VO_2mus changed following endurance training (ET). Revised VO_2mus was significantly smaller than the pre-training value. Values are mean ± SE. VO_2mus,muscle oxygen consumption; Pre, value measured before ET; Post,vale measured after ET; Post(Revised), value recalculated from revised r-VO_2mus. Asterisks indicate a significant difference from the pre-training value (* $p < 0.05$)

To the best of the author's knowledge, this is a first finding showing an increase in r-O_2mus after ET. There have been several human studies showing ET increases capillary density [4–6]. Andersen et al. [4] found a 20% increase in capillary density of muscle biopsies from the quadriceps femoris muscle after ET. Our finding of a 14.5% increase in r-O_2mus is consistent with these previous findings. In contrast to the response of capillary density on ET, there are many studies in which Mb concentration was unchanged after ET in humans [7, 8]. Based on previous studies, the increase in r-O_2mus observed in this study is likely due to an increase in capillary density. This result shows the possibility of using NIR_{CWS} to evaluate the changes in capillary density.

In this study no change in r-VO_2mus was found after ET. Most studies investigating resting metabolic rate (RMR) have focused on the whole body. Some studies found that ET increased RMR [9], but others did not show any effects [10], so the effect of ET on RMR is still unclear. Although there are a few studies that have evaluated resting muscle oxygen consumption using magnetic resonance spectroscopy [2, 3, 11], none of them evaluated the effect of ET. No change in r-VO_2mus after ET indicates the possibility of evaluating the effects of ET on VO_2mus using NIR_{CWS}.

r-O_2mus evaluated in this study may reflect the number of the capillaries perfused with blood at rest. To investigate the effect of ET on capillary density, evaluating oxygen store in maximum exercise needs to be examined.

5 Conclusion

These findings suggest the increase in r-O_2mus calculated from r-VO_2mus reflects an increase in resting oxygen stores in the trained muscle. Under the condition when resting muscle oxygen consumption is unchanged, NIR_{CWS} can be a useful non-invasive tool for measuring muscle oxygen stores.

Acknowledgments The author gratefully acknowledges the help of Kelly McGrath in writing the English manuscript.

References

1. Hampson, N.B., and Piantadosi C.A, Near infrared monitoring of human skeletal muscle oxygenation during forearm ischemia. J Appl Physiol, 1988. 64(6):2449–2457.
2. Hamaoka, T., Hisao Iwane, Teruichi Shimomitsu, Toshihito Katsumura, Norio Murase, Shinya Nishio, Takuya Osada, Yuko Kurosawa, and Britton Chance, Noninvasive measures of oxidative metabolism on working human muscles by near-infrared spectroscopy. J Appl Physiol, 1996. 81(3):1410–1417.
3. Sako, T., Hamaoka, T., Higuchi, H., Kurosawa Y., and Katsumura, T., Validity of NIR spectroscopy for quantitatively measuring muscle oxidative metabolic rate in exercise. J Appl Physiol, 2001. 90:338–344.
4. Andersen, P. and Henriksson, J., Capillary supply of the quadriceps femoris muscle of man: adaptive response to exercise. J Physiol, 1977. 270(3):677–690.
5. Ingjer, F., Effects of endurance training on muscle fibre ATP-ase activity, capillary supply and mitochondrial content in man. J Physiol, 1979. 294:419–432.
6. Hoppeler, H., et al., Endurance training in humans: aerobic capacity and structure of skeletal muscle. J Appl Physiol, 1985. 59(2): 320–327.
7. Svedenhag, J., Henriksson, J., and Sylven, C., Dissociation of training effects on skeletal muscle mitochondrial enzymes and myoglobin in man. Acta Physiol Scand, 1983. 117(2):213–218.
8. Masuda, K., et al., Endurance training under 2500-m hypoxia does not increase myoglobin content in human skeletal muscle. Eur J Appl Physiol, 2001. 85(5):486–490.
9. Van Pelt, R.E., et al., Regular exercise and the age-related decline in resting metabolic rate in women. J Clin Endocrinol Metab, 1997. 82(10):3208–3212.
10. Broeder, C.E., et al., The effects of aerobic fitness on resting metabolic rate. Am J Clin Nutr, 1992. 55(4):795–801.
11. Blei, L.M., Conley E K., and Kushmerick J M., Separate measures of ATP utilization and recovery in human skeletal muscle. J Physiol, 1993. 465:203–222.

Cerebrovascular Response During Heavy Upper Body Exercise: Effect of Mode of Ventilation on Blood Flow Velocity in the Middle Cerebral Artery

K. Sato, A. Hirasawa, N. Tsunoda, Y. Taniguchi, and T. Sadamoto

Abstract Heavy resistance exercise may be associated with a small risk of cerebral aneurysm rupture, subarachnoid hemorrhage, and symptoms of dizziness or outright weight-lifters' blackout, which may be induced by a rapid change in the cerebral blood flow. We hypothesized that these changes during heavy exercise could be associated with the mode of ventilation. The purpose of the present study was to elucidate the effect of the mode of ventilation on cerebral blood flow response during heavy upper body exercise. Subjects performed 15-s static exercises at 80% maximum voluntary contraction (MVC) under different modes of ventilation. In this study, we observed that heavy exercise with breath holding induced marked and rapid changes in the cerebral blood flow velocity in the middle cerebral artery during and after exercise as compared with that with continued normal ventilation. We also observed that hyperventilation before exercise could largely contribute to a lower cerebral blood flow velocity during exercise and which even extended to the recovery phase. Our data suggested that even during heavy upper body exercise, the mode of ventilation is very important for maintaining cerebral circulation.

1 Introduction

Heavy resistance exercise is associated with a pronounced increase in the arterial pressure and cerebral blood flow, which may occasionally result in bleeding around the brain. On the other hand, symptoms of dizziness or outright weight lifters "black out" could be linked to decrease in the cerebral blood flow during and after heavy exercise. Despite the benefits of resistance exercise on skeletal morphology and function, heavy resistance exercise may be

K. Sato (✉)
Research Institute of Physical Fitness, Japan Women's College of Physical Education, Tokyo, 157-8565, Japan
e-mail: ksato@jwcpe.ac.jp

E. Takahashi, D.F. Bruley (eds.), *Oxygen Transport to Tissue XXXI*, Advances in Experimental Medicine and Biology 662,
DOI 10.1007/978-1-4419-1241-1_50, © Springer Science+Business Media, LLC 2010

associated with a small risk of rupture of cerebral aneurysm, subarachnoid hemorrhage, and weight lifters "black out" [2, 6, 7].

Change in the cerebral blood flow during heavy exercise could be associated with the mode of ventilation, including the forced expiration against a closed glottis (breath holding induced a Valsalva-like maneuver) and hypocapnia induced by hyperventilation before and during exercise [1, 6, 7, 10]. A previous study reported marked change in the mean cerebral blood flow velocity in the middle cerebral artery (MCA V_{mean}) during heavy two legged extension with concomitant Valsalva-like maneuver [7]. More recently, Romero and Cooke [10] demonstrated that hyperventilation before exercise exacerbates the reduction in MCA V_{mean} during leg-press resistance exercise. These studies suggested that during heavy exercise the associated mode of ventilation may be of deterministic importance for cerebral circulation. However, these investigations focus on cerebral blood flow regulation during lower-body exercise involving a large muscle mass. To date, there is no information regarding the effect of the mode of ventilation on the cerebral blood flow response during upper body heavy exercise involving a small muscle mass. In addition, the individual effects of breath holding during exercise and of hyperventilation before exercise on cerebral blood flow remain unclear.

Therefore, the purpose of the present study was to elucidate the effect of the mode of ventilation on cerebral blood flow response during heavy upper body exercise. We hypothesized that hypocapnia induced by hyperventilation before exercise and by breath holding during exercise may cause greater reduction in the cerebral blood flow as compared with that during continued normal ventilation.

2 Methods

A total of 10 male field athletes (7 shot putters and 3 hammer throwers; mean age ± SD: 21.2 ± 1.2 years) volunteered to participate in this study after providing informed consent to the protocol, as approved by the ethics committee of Japan Women's College of Physical Education.

In this study, single arm elbow flexion exercise was performed with the use of a multifunctional dynamometer device. The exercise load selected was 80% of the maximal voluntary contraction (MVC) force. After a 3-min resting period, the subjects performed 15-s static exercises at 80% MVC with the following 3 different modes of ventilation (in random order): (1) continued normal ventilation (EX), (2) exercise with concomitant breath holding (EX + BH), and (3) pre-exercise hyperventilation till an end tidal partial pressure of CO_2 (P_{ET} CO_2) of 3.5% was achieved (HV). In HV, after a 2-min rest, the subjects were instructed to perform voluntary hyperventilation for 1-min in order to achieve a P_{ET} CO_2 of ~3.5% [10]. After the 1-min hyperventilation, the subjects performed 15-s static exercises with continued normal ventilation.

MCA V_{mean} measurement was performed with an ultrasound system (Vivid 7pro; GE Yokogawa Medical Systems) equipped with a 2.0 MHz sector transducer. The MCA V_{mean} was defined as the time-averaged mean velocity obtained in automatic calculation mode. Mean arterial pressure (MAP) was measured non-invasively by photoelectric plethysmography with Finometer (Finapres Medical Systems BV). Furthermore, we determined the stroke volume (SV), and cardiac output (CO), from the blood pressure wave form by using the Modelflow method. Respiratory parameters were determined with an online system for the breath-by-breath method. The ratio of MAP/ MCA V_{mean} was calculated as an index of cerebrovascular resistance (CVR).

To confirm whether the parameters had actually changed as a result of exercise as compared with the resting values, two-way analysis of variance (ANOVA) with repeated measurements and Dunnett's *t*-test were conducted.

3 Results

The MCA V_{mean} and CVR responses at rest, during, and after exercise are illustrated in Fig. 1. In EX, MCA V_{mean} decreased (not significantly) from 36.8 to 34.9 $cm \cdot s^{-1}$ and significantly ($p < 0.05$) decreased further to 32.4 $cm \cdot s^{-1}$ at 1–5s after the end of exercise. The CVR gradually increases at the onset of exercise, and returned to resting levels immediately after the end of exercise. The P_{ET} CO_2 rapidly decreased during exercise in EX.

In EX + BH, MCA V_{mean} dropped sharply to below the resting revel (from 38.2 to 31.9 $cm \cdot s^{-1}$) with a subsequent overshoot to 43.4 $cm \cdot s^{-1}$ at 1–5 s after the end of exercise. The CVR significantly ($p < 0.05$) increased at the onset of exercise, and rapidly returned to resting levels immediately after the end of exercise. The CO significantly ($p < 0.01$) decreased until just after the end of exercise (from 9.2 to 5.6 $l \cdot min^{-1}$), with a subsequent overshoot until 10 s after the end of exercise (to 10.4 $\cdot min^{-1}$).

Hyperventilation before exercise reduced the MCA V_{mean} from 35.2 $cm \cdot s^{-1}$ at rest to 28.4 $cm \cdot s^{-1}$ at 5 s before the start of exercise. In contrast to both the EX and EX + BH, the MCA V_{mean} gradually increased until the end of exercise (from 28.4 to 33.0 $cm \cdot s^{-1}$) and subsequently decreased to 30.9 $cm \cdot s^{-1}$ at 1–5 s after the end of exercise. During hyperventilation, the CVR significantly ($p < 0.05$) increased and this increase continued during and after the end of exercise. Before exercise, P_{ET} CO_2 significantly ($p < 0.05$) decreased to 27.7 mmHg with hyperventilation and was 27.5 l/min immediately before the start of exercise. P_{ET} CO_2 values during exercise were significantly ($p < 0.05$) lower than the resting values. After the end of exercise, P_{ET} CO_2 gradually returned to the baseline.

The results can be summarized as follows: (1) the magnitude of reduction in the MCA V_{mean} during exercise was larger in EX + BH than in EX, (2) EX + BH also caused a rapid overshoot of MCA V_{mean} after exercise, and (3) in HV, the hypocapnia induced by hyperventilation before exercise produced a marked reduction in the MCA V_{mean} before and during exercise, and which remained even after exercise.

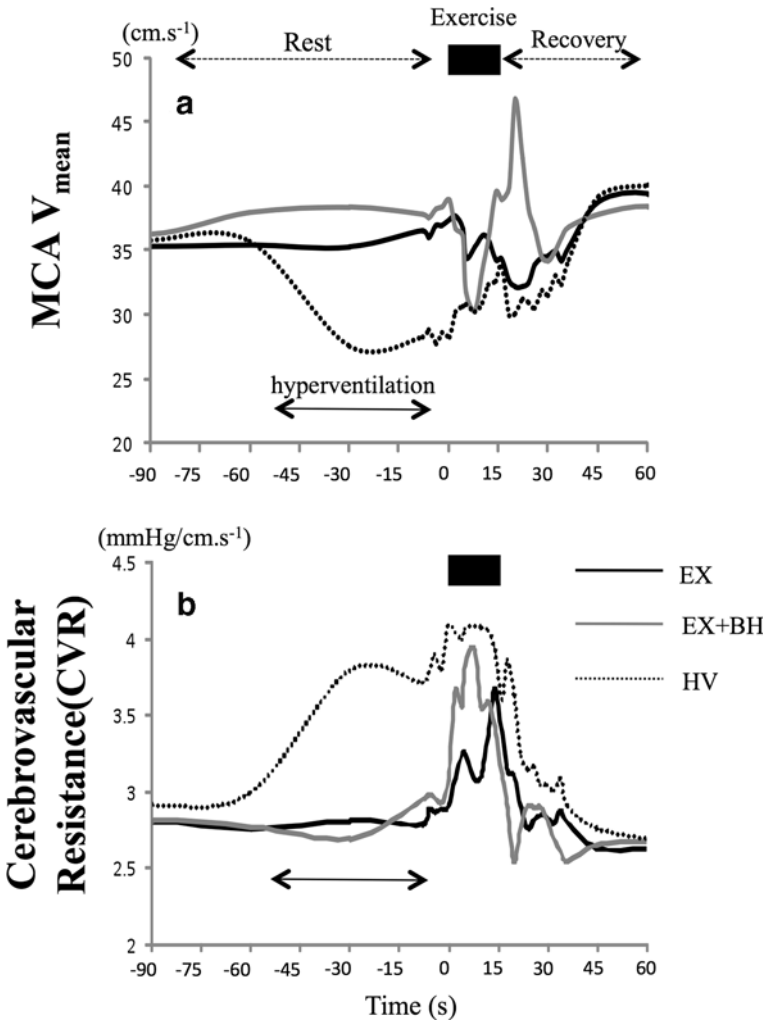

Fig. 1 Cerebrovascular responses at rest, during, and after heavy exercise. (**a**) MCA V_{mean}, Mean middle cerebral artery blood flow velocity and (**b**) CVR, Cerebrovascular resistance index

4 Discussion

It is well known that $P_a CO_2$ is important for the regulation of cerebral blood flow and CVR [4, 9, 10]. We suggested that the decrease in MCA V_{mean} during and after the end of exercise in EX might be related to $P_a CO_2$, which may reflect $P_{ET} CO_2$. The time constant for MCA V_{mean} responses to a step decrease $P_{ET} CO_2$ is ~6 s, whereas the response to a step increase in CO_2 takes ~14 s [8]. This

seems to suggest that the observed time delay between MCA V_{mean} and P_{ET} CO_2 may have contributed to the lowest MCA V_{mean} during the recovery period in the EX.

The expiratory strain during a Valsalva-like maneuver might reduce blood flow to the brain [6, 7]. Forced expiration against a closed glottis increases intrathoracic pressure and central venous pressures and marked reduces in SV and thus CO. Previous studies indicated that CO is an important determinant of cerebral blood flow during exercise [3, 5, 7, 9]. However, our data suggested relationship between CO and MCA V_{mean} was not simple under this situation. Furthermore, the rapid increase in the CVR at the onset of exercise may also contribute to the change in MCA V_{mean} and the increase in the CVR may be induced by sympathoexcitation due to heavy exercise and/or the reduction in CO and P_a CO_2. The increase in the CVR during EX + BH suggested vasoconstriction of the peripheral branches of the MCA. On the other hand, over shooting of the MCA V_{mean} immediately after the end of exercise may be induced by rapid decrease in CVR, with rapid recovery of CO and P_a CO_2.

In the HV trials, reduced MCA V_{mean} occurred in conjunction with increased CVR. This reduction in MCA V_{mean} before, during, and after exercise was attributable to the reduction in P_a CO_2. These results indicate that the increase in CVR was probably associated with vasoconstriction of the cerebral blood vessels.

In summary, our data suggested that even during upper body heavy exercise involving small muscle mass, the mode of ventilation was very important for maintaining cerebral circulation. We think that the combination of hyperventilation before heavy exercise and breath holding during exercise is the worst scenario from the perspective of cerebral circulation. It may be that continued normal ventilation during heavy upper body exercise may be safer, in that it helps to avoid rapid changes in the cerebral blood flow and CVR that may in turn cause symptoms of dizziness or outright weight lifter's "black out" and intracranial hemorrhage [7].

Acknowledgment We especially thank Hiroyuiki Yamamoto (GE Yokogawa Medical Systems, Tokyo, Japan) for his expert technical assistance. This study was supported by a research grant from the Academic Frontier Project, Japan Women's College of Physical Education, and Yamaha Motor foundation for sports.

References

1. Edwards MR, Martin DH, Hughson RL (2002) Cerebral hemodynamics and resistance exercise. Med Sci Sports Exerc 34: 1207–1211
2. Haykowsky MJ, Findlay JM, Ignaszewski AP (1996) Aneurysmal subarachnoid hemorrhage associated with weight training: three case reports. Clin J Sport Med 6: 52–55
3. Ide K, Boushel, R, Sorensen HM et al. (2000) Middle cerebral artery blood velocity during exercise with β-1 adrenergic and unilateral stellate ganglion blockade in humans. Acta Physiol Scand 170: 33–38

4. Jørgensen LG (1995) Transcranial Doppler ultrasound for cerebral perfusion. Acta Physiol Scand 625(Suppl): 1–44
5. Ogoh S, Brothers RM, Barnes Q et al. (2005) The effect of changes in cardiac output on midle cerebral artery mean blood velocity at rest and during exercise. J Physiol (Lond) 569: 697–704
6. Pott F, van Lieshout JJ, Ide K et al. (2000) Middle cerebral artery blood velocity during a Valsalva maneuver in the standing position. J Appl Physiol 88: 1545–1550
7. Pott F, Van Lieshout JJ, Ide K et al. (2003) Middle cerebral artery blood velocity during intense static exercise is dominated by a Valsalva maneuver. J Appl Physiol 94: 1335–1344
8. Poulin MJ, Liang PJ, Robbins PA (1996) Dynamics of the cerebral blood flow response to step changes in end-tidal PCO_2 and PO_2 in humans. J Appl Physiol 81: 1084–1095
9. Querido JS, Sheel AW (2007) Regulation of cerebral blood flow during exercise. Sports Med 37: 765–782
10. Romero SA, Cooke WH (2007) Hyperventilation before resistance exercise: cerebral hemodynamics and orthostasis. Med Sci Sports Exerc 39: 1302–1307

Unchanged Muscle Deoxygenation Heterogeneity During Bicycle Exercise After 6 Weeks of Endurance Training

Ryotaro Kime, Masatsugu Niwayama, Masako Fujioka, Kiyoshi Shiroishi, Takuya Osawa, Kousuke Shimomura, Takuya Osada, Norio Murase, and Toshihito Katsumura

Abstract The purpose of this study was to examine the changes in muscle oxygen saturation (SmO_2) level and its heterogeneity after 6 weeks of endurance training using multi-channel near infrared spatially resolved spectroscopy (NIR_{SRS}). Nine healthy subjects participated in this study (Male = 6, Female = 3, age: 27 ± 5 years, height: 168.7 ± 7.4 cm, weight: 62.4 ± 12.4 kg). The subjects performed a 30 W ramp incremental bicycle exercise test until exhaustion before and after endurance training. The NIR_{SRS} probe was attached to the left vastus lateralis muscle along the direction of the long axis. The subjects performed bicycle exercise for 30 min/day, 3 days/week for 6 weeks. The work rate during training was set at 60%$\dot{V}O_{2peak}$ and increased every 5%$\dot{V}O_{2peak}$ when the subjects could maintain the work rate three times consecutively. After training, $\dot{V}O_{2peak}$ was significantly increased (Pre: 42.7 ± 9.9 ml/kg/min, Post: 52.3 ± 7.2 ml/kg/min, $p < 0.001$) and the mean SmO_2 within measurement sites at $\dot{V}O_{2peak}$ was significantly decreased (Pre: 56.1 ± 1.1 %, Post: 53.3 ± 2.2 %, $p < 0.05$). Conversely, the heterogeneity of the SmO_2 during exercise was not changed by training. These results suggest that the functional heterogeneity of O_2 balance did not change due to endurance training, and the O_2 balance heterogeneity may not interfere with O_2 exchange in the activating muscle in healthy individuals.

1 Introduction

We have previously reported that muscle deoxygenation level at exhaustion was negatively correlated with peak oxygen uptake (peak VO_2), and the results suggest that O_2 availability may be enhanced in higher oxidative capacity muscles. Basically, blood flow increases in relation to local metabolic rate [1], and the O_2 balance is distributed heterogeneously in a single muscle [2, 3, 4]. The

R. Kime (✉)
Department of Sports Medicine for Health Promotion, Faculty of Medicine, Tokyo Medical University, Tokyo, 160-8402, Japan
e-mail: kime@tokyo-med.ac.jp

E. Takahashi, D.F. Bruley (eds.), *Oxygen Transport to Tissue XXXI*, Advances in Experimental Medicine and Biology 662,
DOI 10.1007/978-1-4419-1241-1_51, © Springer Science+Business Media, LLC 2010

nonuniform distribution of O_2 balance may interfere with O_2 exchange in the activating muscle [5]. We hypothesized that muscle oxygen extraction may be enhanced by endurance training, and the adaptation will lead to muscle oxygen saturation (SmO_2) distribution in the activating muscle being more homogeneous at higher work rates as nonuniform O_2 balance distribution may interfere with O_2 exchange in the activating muscle. There have been no studies reporting the changes in muscle deoxygenation heterogeneity by endurance training in an exercising muscle. Therefore, we examined the changes in muscle oxygen saturation (SmO_2) level and its heterogeneity after 6 weeks of endurance training using multi-channel near infrared spatial resolved spectroscopy (NIR_{SRS}).

2 Methods

2.1 Subjects

Nine healthy untrained volunteers (six males and three females, age: 27 ± 5 year height: 168.7 ± 7.4 cm,weight: 62.4 ± 12.4 kg) participated in this study. All subjects were briefed about the experimental protocol, and written informed consent was obtained before the experiment. The institutional review board of the Tokyo Medical University approved the research protocol.

2.2 Experimental Design

The peak oxygen uptake ($\dot{V}O_{2peak}$) and SmO_2 distribution in the vastus lateralis (VL) muscle were determined before and after 6 weeks of endurance training. As for the endurance training, the subjects performed bicycle exercise for 30 min/day, 3 days/week for 6 weeks. The work rate during training was set at 60 % $\dot{V}O_{2peak}$ and increased every 5 % $\dot{V}O_{2peak}$ when the subjects could maintain the work rate three times consecutively.

The subjects performed an incremental bicycle exercise until exhaustion to determine the $\dot{V}O_{2peak}$ and muscle deoxygenation heterogeneity in the VL muscle. During the test, pulmonary $\dot{V}O_2$ and carbon dioxide production (VCO_2) were assessed breath-by-breath with an online metabolic system (AE-300 Minato, Japan). Pedal frequency of 60 rpm was maintained by keeping time with a metronome.

2.3 Multichannel NIR_{SRS} System

We used two wavelength light-emitting diode NIR_{SRS} (ASTEM Co, Japan). The probe of the present system consisted of two light sources and one photodiode detector, and the optode distance was 20 and 30 mm, respectively. The measurement probes were attached to the left VL muscle along the direction of the long

axis. The eight measurement probes were arranged vertically and the most distal site was channel 1 and the most proximal site was channel 8. As leg length is shorter in females than in males, the seven measurement probes were used to cover the left VL muscle in the female subjects (Fig. 1). The SmO_2 was derived from the relative absorption coefficients obtained from the slope of light attenuation over a distance measured at two focal points from the light emission. The relative absorption coefficients are converted to relative concentrations of oxygenated and deoxygenated-Hb. Therefore, this device can essentially calculate tissue oxygen saturation.A previous study has reported that fat layer thickness affects SmO_2 [6]. In contrast, Niwayama et al. [7] recently reported that the SmO_2 can be quantified by the correction of fat layer thickness effects and the specifications of the NIR_{SRS} were fully described. In this study, we measured fat layer thickness on each measurement site in VL muscle to correct these effects using an ultrasound device (LogiQ3, GE-Yokokawa Medical Systems, Japan) by placing an ultrasound probe on the same sites as the NIR_{SRS} probes had been placed. The SmO_2 at rest and at VO_{2peak} were defined as the SmO_2 averaged over the last 5 s of each period.

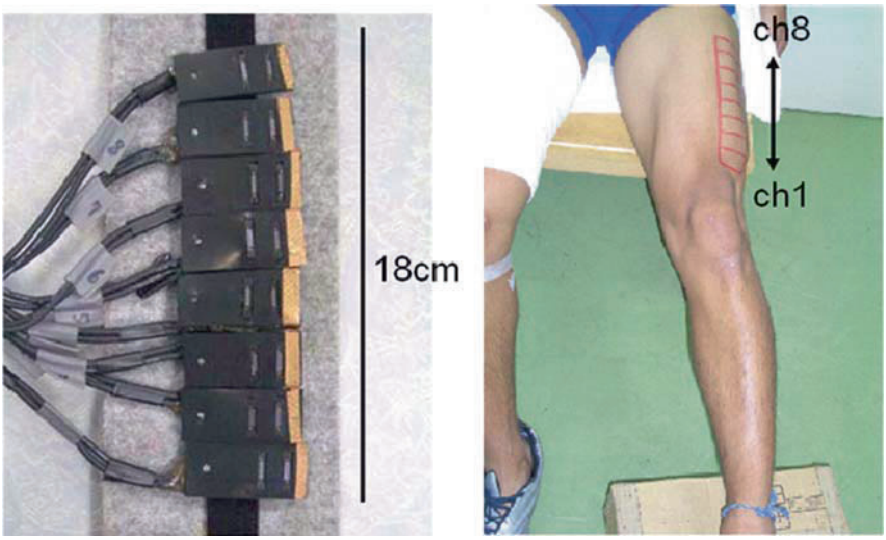

Fig. 1 NIR_{SRS} probes (*left*) and the probe position (*right*)

Relative Dispersion (RD) of StO_2 was calculated as RD = (SD/Mean) * 100 (%) as an index of heterogeneity.

2.4 Statistics

All data are expressed as means ± SD. All parameters during exercise were compared among pre- and post-endurance training by using a paired *t*-test.

Also, the RD at rest and VO_{2peak} were compared using a paired t-test. The level of significance was set at $p \pm 0.05$.

3 Results

The VO_{2peak} was significantly enhanced by 6 weeks of endurance training (Pre: 42.7 $\pm$ 9.9 ml/kg/min, Post: 52.3 $\pm$ 7.2 ml/kg/min, 22.5 % up-regulation, $p < 0.001$). At rest, the SmO_2 of each measurement site in the VL was not significantly different before or after training (Pre-T: 70.0 $\pm$ 8.2 %, Post-T: 71.5 $\pm$ 4.6 %, mean $\pm$ SD). In contrast, the SmO_2 at VO_{2peak} was significantly lower after training at increasingly proximal sites, but not at the distal sites (Fig. 2). Also, the mean SmO_2 in the VL muscle was significantly lower after training (Pre-T: 56.1 $\pm$ 9.9 %, Post-T: 52.7 $\pm$ 11.9 %, $p < 0.05$). The RD (an index of heterogeneity) was significantly lower at rest than VO_{2peak} at both pre- and post-training ($p < 0.05$). The RD was not significantly different between pre- and post-training at each rest period or VO_{2peak}, respectively (Fig. 3). Fat layer thickness was not significantly different after endurance training (Pre-T: 4.70 $\pm$ 1.78 cm, Post-T: 4.56 $\pm$ 1.65 cm, mean $\pm$ SD).

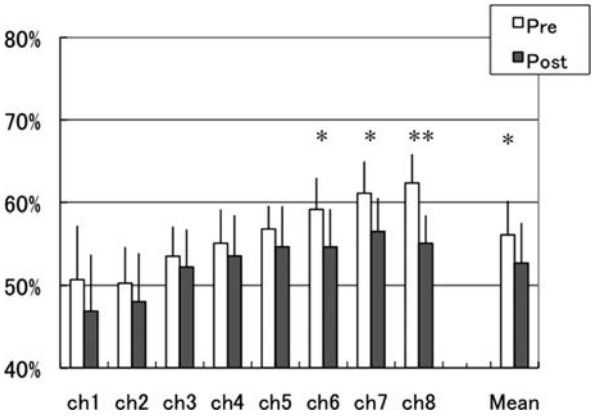

Fig. 2 SmO_2 in VL muscle at VO_{2peak} before and after endurance training. *: $p < 0.05$, **:$p < 0.01$

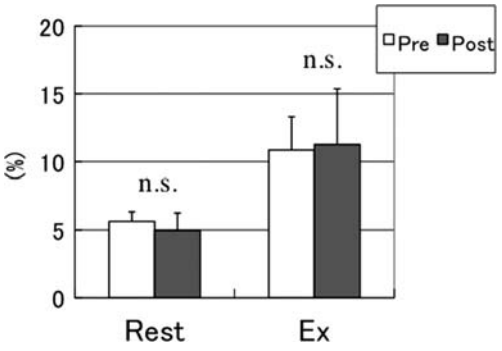

Fig. 3 Relative dispersion (RD) of SmO_2 in VL muscle before and after endurance training

4 Discussion

We investigated changes in SmO_2 and its distribution in VL muscle at rest and during bicycle exercise at VO_{2peak} by 6 weeks of endurance training using the multi-channel NIR_{SRS} system. This study reveals that muscle deoxygenation in VL was more enhanced at VO_{2peak}, but the muscle deoxygenation heterogeneity in VL was unchanged by endurance training. Recently, some PET studies have demonstrated that muscle O_2 extraction was higher and muscle blood flow heterogeneity in the exercising muscle was lower in endurance-trained men [2, 3], but not during dynamic exercise because of movement artifacts. In addition, there has been no intervention study to determine whether muscle deoxygenation heterogeneity is reduced by endurance training. This is the first study reporting unchanged muscle deoxygenation heterogeneity in a single muscle during bicycle exercise by endurance training.

Some studies have reported that muscle O_2 extraction was enhanced after endurance training as demonstrated by a lower venous femoral PO_2 during exercise [8]. Therefore, it is suggested that O_2 extraction may be improved in the activating muscle due to endurance training.

In this study, the SmO_2 in the VL muscle was significantly enhanced after 6 weeks of endurance training, especially at proximal sites, but not at distal sites. One of the reasons may be due to the small sample size. In addition, as the SmO_2 was already significantly lower at distal sites than proximal sites during exercise at pre-training, the difference in muscle deoxygenation change between distal and proximal sites post-training might be due to the inability to further deoxygenate.

The RD was significantly lower at rest than VO_{2peak} at both pre- and post-training. This implies that the dynamic O_2 balance between muscle VO_2 and O_2 supply is more uniform at rest than during bicycle exercise.

We hypothesized that SmO_2 distribution in the activating muscle would be more homogeneous at higher work rates after endurance training [9]. However, SmO_2 distribution in the VL muscle during exercise was not significantly different between pre- and post-training, even though a previous study demonstrated that the muscle blood flow heterogeneity in the exercising muscle was lower in endurance-trained men [2]. The different results in these studies may be explained by the differences of muscle group measurement, measurement depth and measurement devices. As the muscle deoxygenation heterogeneity in the activating muscle was not significantly different after endurance training, O_2 balance distribution in the activating muscle may not be related to whole body oxidative capacity in healthy individuals.

In conclusion, after 6 weeks of endurance training, the SmO_2 in VL muscle was significantly enhanced, especially at increasingly proximal sites. In contrast, the SmO_2 distribution in VL muscle during exercise was not significantly different between pre- and post-training.

Acknowledgments The authors are grateful for revision of this manuscript by Christa Colletti. We also thank Mikiko Yonemitsu and Ayaka Sato for their helpful technical

assistance. This study was supported in part by Grant-in-Aid for Young Scientists from the Japan Society for Promotion of Science 18700536 to R. K.

References

1. Knight DR, Poole DC, Schaffartzik W et al. (1992). Relationship between body and leg VO_2 during maximal cycle ergometry. J. Appl. Physiol. 73(3): 1114–1121.
2. Kalliokoski KK, Oikonen V, Takala TO et al. (2001) Enhanced oxygen extraction and reduced flow heterogeneity in exercising muscle in endurance-trained men. Am. J. Physiol. Endocrinol. Metab. 280: E1015–E1021.
3. Kalliokoski KK, Knuuti J, and Nuutila P. (2005) Relationship between muscle blood flow and oxygen uptake during exercise in endurance-trained and untrained men. J. Appl. Physiol. 98: 380–383.
4. Mizuno M, Kimura Y, and Iwakawa T et al. (2003) Regional differences in blood flow and oxygen consumption in resting muscle and their relationship during recovery from exhaustive exercise. J. Appl. Physiol. 95: 2204–2210.
5. Wagner PD. (2003) Heterogeneity of skeletal muscle perfusion and metabolism. J. Appl. Physiol. 95: 2202–2203.
6. Komiyama T, Quaresima V, Shigematsu H et al. (2001) Comparison of two spatially resolved near-infrared photometers in the detection of tissue oxygen saturation: poor reliability at very low oxygen saturation. Cli. Sci. (Lond) 101(6): 715–718.
7. Niwayama M, Sone S, Murata H et al. (2007) Errors in muscle oxygenation measurement using spatially-resolved NIRS and its correction (Abstract in English). J. Jpn. Coll. Angiol. 47(1): 17–20.
8. Roca J, Agusti AGN, Alonso et al. (1992) Effects of training on muscle O_2 transport at VO_2max. J. Appl. Physiol. 73(3): 1067–1076.
9. Kime R, Im J, Moser D et al. (2005) Reduced heterogeneity of muscle deoxygenation during heavy bicycle exercise. Med. Sci. Sports. Exer. 37(3): 412–417.

Comparison of Muscle O_2 Dynamics at Different Sites of the Forearm Flexor Muscles During Incremental Handgrip Exercise

Masako Fujioka, Ryotaro Kime, Shunsaku Koga, Takuya Osawa, Kousuke Shimomura, Takuya Osada, Norio Murase, and Toshihito Katsumura

Abstract This study investigated heterogeneity of muscle O_2 consumption (diffusive m-VO_2) and muscle oxygenation difference (m-O_2 difference) within the forearm flexor muscles using multi-optical fibers near-infrared continuous wave spectroscopy (NIRcws) during incremental exercise. Nine healthy male subjects performed incremental dynamic handgrip exercise until exhaustion. The workload was increased by 5% maximal voluntary contraction (MVC) every 1 min, starting at 10% MVC. The NIRcws probes (10 channels) were placed on the right forearm flexor muscles to monitor muscle oxygenation. The diffusive m-VO_2 and the m-O_2 difference were evaluated at each exercise stage. The diffusive m-VO_2 at the medial site was significantly greater than the lateral site at 25% MVC ($p < 0.05$). Similarly, m-O_2 difference at the medial site increased significantly over the lateral site ($p < 0.05$), whereas there were no significant differences in diffusive m-VO_2 or m-O_2 difference between the proximal and distal sites. These results in forearm muscle were different from the previous study which found that there were longitudinal differences in muscle VO_2 in the femoral muscle.

1 Introduction

Previous studies demonstrating the heterogeneity of muscle perfusion and muscle O_2 consumption (VO_2) during exercise in humans have been evaluated using positron emission tomography (PET) [1, 2]. However, the device is expensive and only produces low time resolution. In addition, the PET device cannot obtain information during dynamic exercise because of movement artifacts. On the other hand, near-infrared continuous wave spectroscopy (NIRcws) measures the balance between O_2 supply and O_2 utilization in

M. Fujioka (✉)
Department of Sports Medicine for Health Promotion, Tokyo Medical University, Tokyo, 160-8402, Japan
e-mail: m-fuji@tokyo-med.ac.jp

E. Takahashi, D.F. Bruley (eds.), *Oxygen Transport to Tissue XXXI*, Advances in Experimental Medicine and Biology 662,
DOI 10.1007/978-1-4419-1241-1_52, © Springer Science+Business Media, LLC 2010

human skeletal muscle during dynamic exercise. Recently, the NIRcws system has been developed to evaluate muscle deoxygenation distribution using multi-optical fibers NIRcws (multichannel NIRcws). There have been a number of reports of heterogeneity of muscle O_2 kinetics during exercise [3, 4]. However, no studies have examined the relationship between heterogeneity of muscle O_2 dynamics and muscle VO_2 in the forearm muscle.

Therefore, the aim of this study was to investigate the heterogeneity of muscle O_2 consumption (diffusive m-VO_2) and muscle oxygenation difference (m-O_2 difference) within the forearm flexor muscles using multichannel NIRcws during incremental exercise.

2 Methods

2.1 Subjects

Nine healthy male subjects (age: 26 ± 5 years, height: 170.9 ± 5.3 cm, weight: 64.2 ± 6.2 kg, mean ± SD) participated in this study. Written informed consent was obtained after the purpose, experimental protocol, and potential risks were explained to the subjects.

2.2 Experimental Protocol

The subjects performed incremental dynamic handgrip exercise until exhaustion. The right hand rested on a handgrip ergometer with the upper arm at heart level. The work load was increased by 5% maximal voluntary contraction (MVC) every 1 min, starting at 10% MVC, and the frequency was one contraction per 2 s. A recovery period was taken for 1 min after each exercise stage and transient arterial occlusion was performed for the initial 30 s to evaluate diffusive m-VO_2.

2.3 Multichannel NIRcws

Muscle oxygenation was measured using multichannel NIRcws (NIRO-200 with multifibers adaptor (MFA), Hamamatsu Photonics K. K.). The changes of oxygenated Hb/Mb (Δoxy-Hb/Mb), deoxygenated Hb/Mb (Δdeoxy-Hb/Mb) and Δtotal-Hb were calculated continuously from resting baseline by use of the changes in light absorbance at different wavelengths. The basic principle of this NIRcws device was reported in a previously published paper [5]. In this study, three different-wavelength laser diodes (775, 810, and 850 nm) were used as the light emitter. The NIRcws probe (10 channels, 2 emitters and 8 receivers) (Fig. 1) was placed on the right forearm flexor muscles. The distance between

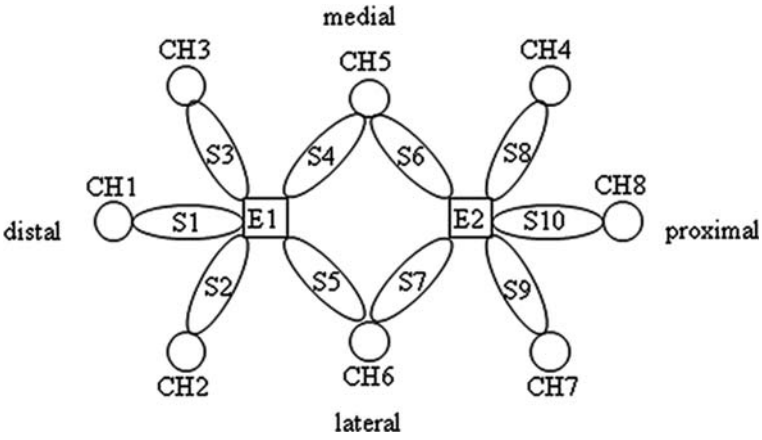

Fig. 1 The NIRcws probe (10 channels, 2 emitters and 8 receivers) was placed on the *right* forearm flexor muscle. The emitter and the receiver of the optodes, and the measurement sites were represented by E, CH and S, respectively. The sites were defined as the mean value of S6, S7, S8 and S9 for the proximal site, S2, S3, S4 and S5 for the distal site, S3, S4, S6 and S8 for the medial site, and S2, S5, S7 and S9 for the lateral site

each emitter and receiver was 3.0 cm. The E2 of the NIRcws probe was placed on the forearm flexor muscles as determined by intersection of a line extending ~30% of the length between the ulnar head and the humeral epicondylus medialis.

Because the NIRcws signal is affected by adipose tissue, it is impossible to compare the optical densities of Δoxy-Hb/Mb between individuals. Therefore, the diffusive m-VO_2 was determined by the rate of muscle deoxygenation during arterial occlusion immediately after the end of each exercise stage [6]. The rate of decrease in Hb_{diff} reflects the difference between Δoxy- and Δdeoxy-Hb/Mb ($[Hb_{diff}] = [\Delta\text{oxy-Hb/Mb}]-[\Delta\text{deoxy-Hb/Mb}]$) [7]. The diffusive m-$VO_2$ was expressed relative to that of the resting value. The m-O_2 difference was also calculated by oxygenation difference between the start and the end of each exercise stage, and was expressed relative to the resting value during arterial occlusion for 1 min. The difference in Δtotal-Hb which was reflected in blood volume was calculated between the start and the end of each exercise stage (Δtotal-Hb difference).

The fat thickness under each optode site was measured by B-mode ultrasound Doppler method (model LOGIQ3, GE-Yokogawa Medical Systems).

2.4 Statistics

All data are expressed as means ± SD. Diffusive m-VO_2 and m-O_2 difference were compared between the proximal and distal sites, and the medial and lateral

sites by using a two-way ANOVA, with site and work load as the main effects. Any significant ($p < 0.05$) interactions were further analyzed with the Bonferroni post hoc test. For Δtotal-Hb difference and fat thickness, a one-way ANOVA was used to determine significant differences. All parameters at exhaustion were compared among different sites and different exercise intensities by using a paired *t*-test. The level of significance was set at $p < 0.05$.

3 Results

The diffusive m-VO_2 during exercise at the medial site was significantly greater than the resting value ($p < 0.05$) (Fig. 2a). Also, the diffusive m-VO_2 at the medial site was significantly greater than the lateral site at 15 and 25% MVC (Fig. 2a). Similarly, m-O_2 difference at the medial site increased significantly over the lateral site ($p < 0.05$) (Fig. 2b). On the other hand, there were no significant differences in diffusive m-VO_2 or m-O_2 difference between the proximal and distal sites.

The Δtotal-Hb difference was significantly greater at the medial site than the lateral site at 10% MVC ($p < 0.05$) (Fig. 2c). Moreover, the Δtotal-Hb difference at the medial site was significantly greater at 10% MVC compared with 15 and 20% MVC ($p < 0.05$).

Fat layer thickness, which affects the absolute value of hemoglobin concentration, was not significantly different under each optode site.

4 Discussion

The main finding of this study was that the diffusive m-VO_2 and m-O_2 difference at the medial site of the forearm flexor muscles was significantly greater than the lateral site. On the other hand, there were no significant differences in diffusive m-VO_2 or m-O_2 difference between the proximal and distal sites. In previous studies, the proximal region of the vastus lateralis (VL) was better oxygenated than the distal region of VL during knee extension exercise [3]. Miura et al. [4] reported the distal portion of the medial head of the gastrocnemius showed greater deoxygenation and larger decrements in NIR-blood volume during dynamic plantar flexion compared with the proximal portion. However, these reports have not compared oxygenation between medial and lateral sites of the muscle. Although the O_2 dynamics at the forearm muscle in this study were different from the previous study which found that there were longitudinal differences in muscle VO_2 in the femoral muscle, the diffusive m-VO_2 and m-O_2 difference at the medial site was significantly greater than the lateral site.

The Δtotal-Hb at each site was not corrected by fat thickness because there were no significant differences of fat thickness between each optode site. The

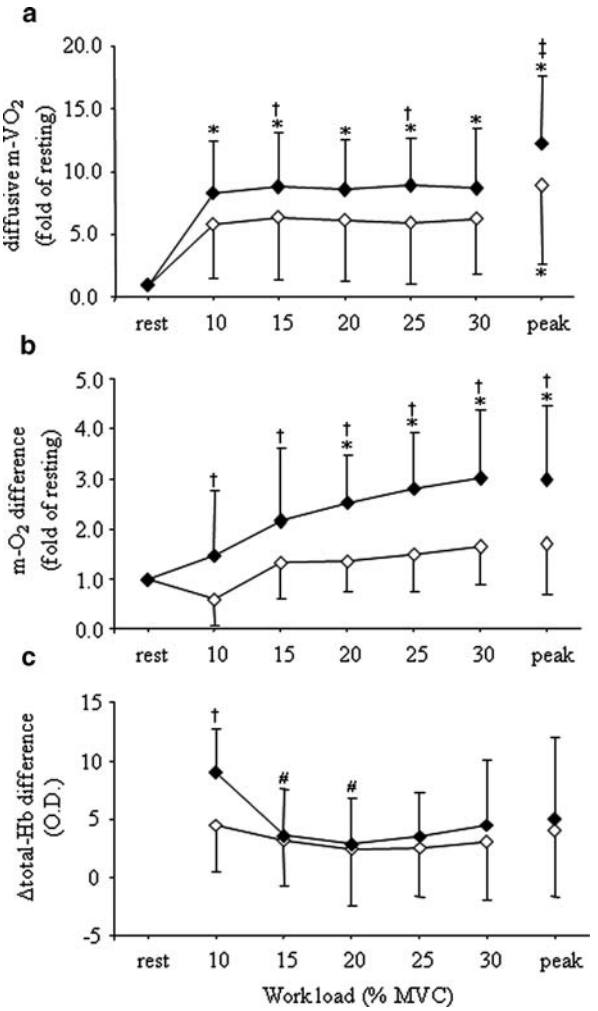

Fig. 2 Changes in diffusive m-VO_2 (**a**), m-O_2 difference (**b**), and Δtotal-Hb difference (**c**) between medial (♦) and lateral sites (◊). *Significantly different from the resting value, $p < 0.05$. †Significantly different from the lateral site, $p < 0.05$. ‡Significantly different from the prior intensity, $p < 0.05$. #Significantly different from 10% MVC at the medial site, $p < 0.05$

Δtotal-Hb difference at the medial site was significantly greater than the lateral site at 10% MVC ($p < 0.05$) (Fig. 2c). The Δtotal-Hb difference at the medial site was significantly greater at 10% MVC compared with 15 and 20% MVC ($p < 0.05$). These results suggest that the blood volume at the medial site was decreased at higher work loads. In addition, the diffusive m-VO_2 and m-O_2 difference at the medial site were significantly greater than the lateral site. Therefore, these results at the medial site suggest that the muscle VO_2 increase was greater than the muscle O_2 supply. It has been reported that intramuscular pressure has been shown to reduce muscle blood flow during exercise [8]. Moreover, Miura et al. [4] hypothesized that differences in muscle O_2 status in

this muscle would reflect regional variations in pressure or stress development that are likely a function of its complex architecture. These results imply that the muscle O_2 supply at the medial site may have been decreased due to high intramuscular pressure in this study.

In conclusion, the diffusive m-VO_2 and m-O_2 difference at the medial site of the forearm flexor muscles was significantly greater than the lateral site during the incremental handgrip exercise. These results suggest that one of the explanations for different O_2 dynamics at the different sites is due to a decrease in muscle O_2 supply.

Acknowlegments The authors thank Christa Colletti for her help in writing the English manuscript. We also thank Mikiko Yonemitsu and Ayaka Sato for their helpful technical assistance. This work was supported in part by a grant-in-aid for scientific research from the Ministry of Education, Science, and Culture of Japan (No.18207019 to S. Koga), and a grant-in-aid for Young Scientists from the Japan Society for Promotion of Science (No. 18700536 to R. Kime).

References

1. Kalliokoski KK, Oikonen V, and Takala TO et al. (2001) Enhanced oxygen extraction and reduced flow heterogeneity in exercising muscle in endurance-trained men. Am. J. Physiol. Endocrinol. Metab. 280: E1015–E1021.
2. Mizuno M, Kimura Y, Iwakawa T et al. (2003) Regional differences in blood flow and oxygen consumption in resting muscle and their relationship during recovery from exhaustive exercise. J. Appl. Physiol. 95: 2204–2210.
3. Kennedy MD, Haykowsky MJ, Boliek CA et al. (2006) Regional muscle oxygenation differences in vastus lateralis during different modes of incremental exercise. Dyn. Med. 5: 8.
4. Miura H, McCully K, Nioka S et al. (2004) Relationship between muscle architectural features and oxygenation status determined by near infrared device. Eur. J. Appl. Physiol. 91: 273–278.
5. Chance B, Dait MT, Zhang C et al. (1992) Recovery from exercise-induced desaturation in the quadriceps muscles of elite competitive rowers. Am. J. Physiol. 262: C766–C775.
6. Hamaoka T, Iwane H, Shimomitsu T et al. (1996) Noninvasive measures of oxidative metabolism on working human muscles by near-infrared spectroscopy. J. Appl. Physiol. 81: 1410–1417.
7. Van Beekvelt MC, Colier WN, and Wevers RA. (2001) Performance of near-infrared spectroscopy in measuring local O_2 consumption and blood flow in skeletal muscle. J. Appl. Physiol. 90: 511–519.
8. Gray SD, Carlsson E, and Staub NC. (1967) Site of increased vascular resistance during isometric muscle contraction. Am. J. Physiol. 213: 683–689.

Blood Flow and Arterial Vessel Diameter Change During Graded Handgrip Exercise in Dominant and Non-dominant Forearms of Tennis Players

Atsuko Kagaya, Fumiko Ohmori, Shizuyo Okuyama, Yoshiho Muraoka, and Kohei Sato

Abstract The training effect on exercise-induced maximal blood flow remains unclear. The purpose of this study was to clarify the difference of exercise-induced blood flow, blood flow velocity and vessel diameter of brachial artery in dominant and non-dominant forearms of tennis players during graded handgrip exercise. Ten female tennis players aged 20.1 ± 0.1 years. (mean ± SD) performed 30-s static handgrip exercise in the supine position with either the dominant or non-dominant hand by increasing load at 30-s intervals until exhaustion. Brachial arterial blood flow velocity (Doppler ultrasound method) did not differ between both limbs, whereas the vessel diameter (2-D method) was significantly larger in the dominant limb during diastole both at baseline ($p < 0.01$) and after exercise ($p < 0.05$), but no difference was found during systole. As a result, the blood flow was significantly higher ($p < 0.05$) in the dominant limb during post-exercise condition. Muscle thickness of the forearm muscles and maximal handgrip strength were significantly higher in the dominant limb. Thus, the effect of training on exercise-induced blood flow specific to the dominant limb was confirmed during post-exercise due to the enlarged vessel diameter during diastole of cardiac cycle. The dimensional change in the vasculature specific to the dominant side will be included in the training effects associated with the dimensional muscular changes in the dominant forearm.

1 Introduction

Maximal metabolic vasodilation capacity is enhanced due to training [2, 3, 14]. Cross-sectional study on blood flow in the dominant and non-dominant limbs of tennis players also indicated an increased blood flow in dominant limb used in tennis [7, 14]. However, it is unclear if these training effects are applicable to

A. Kagaya (✉)
Research Institute of Physical Fitness, Japan Women's College of Physical Education, Tokyo, 57-8565, Japan
e-mail: kagaya@jwcpe.ac.jp

E. Takahashi, D.F. Bruley (eds.), *Oxygen Transport to Tissue XXXI*, Advances in Experimental Medicine and Biology 662,
DOI 10.1007/978-1-4419-1241-1_53, © Springer Science+Business Media, LLC 2010

exercise-induced maximal blood flow, because the sympathetic vasoconstriction occurred during exercise and the blood flow during exercise did not reach a level of maximal metabolic vasodilation [9, 16].

Blood volume per unit time is determined by the cross-sectional area of vessel and blood flow velocity. Previous studies indicated that muscle vasculature was adjusted to training or disuse of the muscle [3, 4, 8, 13]. Despite that structural adaptation of vasculature has been reported at baseline, a training effect on vascular dimension during exercise remains to be studied.

The purpose of this study was to clarify the effects of training on blood flow and structure of the conduit artery during static exercise (muscle action). For this purpose, the blood flow velocity and vessel diameter of the brachial artery were determined in dominant and non-dominant forearms of tennis players during and after each load of graded handgrip exercise.

2 Methods

Subjects; Ten female tennis players aged 20.1 ± 0.1(mean ± SD) years old participated in the study. They were recruited from the collegiate tennis team, which won 4th place in the national inter-collegiate tennis tournament that year. The study was approved by the Ethical Committee on Human Subjects Research at the Japan Women's College of Physical Education. All subjects provided written informed consent after being informed about all experimental procedures, the exercise protocol, and possible risks associated with participation in the study.

Experimental protocol and physiological measurements; Following 3-min baseline measurements, the subject performed 30-s static handgrip exercise in a supine position with either the dominant (right side) or non-dominant hand on different days. The static handgrip exercise was repeated at 30-s intervals with increasing load by 2 kgw until exhaustion. Total work index was calculated as a sum of each work load multiplied by duration. Brachial arterial blood flow velocity (V) and diameter (D) were obtained continuously using ultrasound Doppler and 2-D methods (GE, Vivid7 Pro) and determined for 10 (baseline), 5 (during exercise) or 2–3 cardiac cycles (immediate post-exercise) each at diastole (Dd) and systole (Ds). Brachial arterial blood flow was calculated as $V*\pi(D/2)^2$ ($D = 2Dd/3 + Ds/3$). Blood pressure (BP) was measured on the contralateral finger on beat-by-beat basis throughout the experiment (Ohmeda, Finapres 2300). Maximal voluntary contraction (MVC) of forearm muscles, and radial and ulnar forearm flexor muscle thickness were measured (Aloka, SSD1000).

Data Analysis and Statistics; The group data were expressed as mean ± SE, unless otherwise indicated. Differences among the means obtained from 7 loads and 2 limbs (dominant and non-dominant) were evaluated using two-way analysis of variance (ANOVA). When significant differences (major effect, interaction) were observed, a *post hoc* comparison was performed using Tukey's HSD. A P- value less than 0.05 was accepted as significant.

3 Results

Muscle thickness of Rad and UL, MVC, highest load attained by each subject and total work index performed until exhaustion were significantly higher in the dominant limb.

The blood flow velocity during exercise and immediately after exercise increased significantly ($p < 0.01$) with loads both in dominant and non-dominant limbs. No significant differences were found between both limbs. The diastolic and systolic vessel diameters, during exercise and immediate post-exercise, gradually increased with time and increasing loads. A significant major effect on diastolic diameter was obtained only for load during ($p < 0.01$) and post ($p < 0.05$) exercise. Interaction was significant ($p < 0.01$) for the means of diastolic diameters, which were significantly larger in the dominant limb at baseline (dominant; 3.4 ± 0.1, non-dominant; 3.0 ± 0.1 mm) and after exercise at the highest load (dominant; 3.5 ± 0.1, non-dominant; 3.2 ± 0.1 mm) (Fig. 1a). In contrast, systolic diameter did not differ either during exercise or post-exercise between both limbs (Fig. 1b). The brachial arterial blood flow in both limbs increased linearly related to exercise load both during ($p < 0.01$) exercise and post-exercise ($p < 0.01$). Interaction was significant ($p < 0.05$) and higher post-exercise blood flow was obtained in the dominant limb after exercise at the highest load ($p < 0.05$) (Fig.1c).

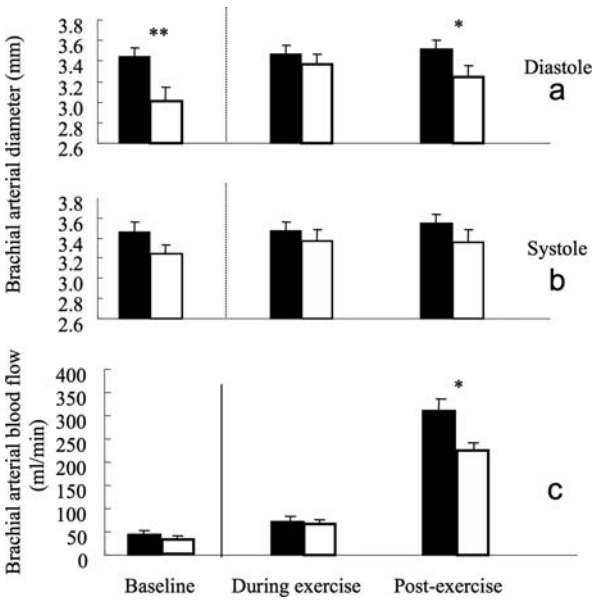

Fig. 1 Diastolic (**a**), systolic (**b**) vessel diameter and brachial arterial blood flow (**c**) at baseline, during, and after exercise at the highest loads in dominant (■) and non-dominant (□) limbs. *, **; $p < 0.05$, $p < 0.001$ between limbs

4 Discussion

The first finding of this study was that the lateral difference in blood flow in tennis players was detected post-exercise when muscle contraction was terminated, which is consistent with the study of Sinoway et al. [15] on tennis players. However, the blood flow during exercise did not differ between both arms in this study. Therefore, the exercise training will induce an increase in exercise-induced blood flow during post-exercise phase, (or relaxation phase of dynamic exercise) and metaboreceptor mediated vasodilation [7, 14, 15]. However, this functional adaptation would not increase blood flow during static muscle action, probably because an elevated intramuscular pressure due to muscle contraction [17] impedes a vasodilation in the contracting muscles.

Cross-sectional studies on vasculature demonstrated that diameters of the conduit artery were positively associated with the level of physical activity. Larger vessel size was observed in trained people of various sports, limited to the trained region of the body [8, 13], whereas smaller dimension of vessel diameter was reported in sedentary and paraplegic subjects, and in healthy people after bed-rest or limb suspension [3, 4, 8, 13]. Longitudinal study confirmed the vessel expansion due to training in various arteries [6, 12, 11]. However, those studies measured the vessel diameters at baseline, and no studies, to our knowledge, compared dimensional adaptation during exercise. Furthermore, no study except the study of Schmidt-Trucksäss et al. [13], considered the vascular size fluctuation with cardiac cycle; systole or diastole. Our second new finding, therefore, was that the luminal vessel diameter of the brachial artery during systole did not change significantly between limbs, whereas the diameter during diastole was larger in the dominant limb. The latter finding is consistent with the study of Huonker et al. [8], who studied thoracic, abdominal, subclavian and common femoral arteries in trained athletes including professional tennis players, but not with the study of Schmidt-Trucksäss et al. [13]. They demonstrated that the vessel diameters were significantly larger in athletes for both systolic and diastolic phases. The discrepancy might be due to the difference of subjects compared in the respective studies; dominant vs non-dominant (this study) limbs, or professional athletes vs sedentary and paraplegic subjects [13].

The mechanism to explain an increased blood flow with training has not yet been completely elucidated, but structural remodeling of the vasculature might be one of the most potent mechanisms [6, 11]. As the muscle thickness of the dominant forearm was significantly larger compared to that of the non-dominant one in this study, the dimensional change in muscle due to training will be considered to influence vascular remodeling. Other underlying mechanisms for the increased blood flow with training will include a change in vasoactivity because of an increased flow-mediated dilation after training [1, 5]. Considered from the role of nitric oxide (NO) in exercise hyperemia [10], one potent mechanism will be an increase in NO production or sensitivity to NO. However,

the contribution of NO to the effect of exercise training on vascular responses in human subjects remains undecided [7]. This study suggests that the training effect on NO-dependent vasodilation, if any, might be masked during muscle contraction.

In conclusion, larger brachial arterial vessel diameter and muscle thickness in tennis players will probably be included in effects training. However, the effect of training on exercise-induced blood flow specific to the dominant limb was not confirmed during exercise but was detected during post-exercise due to the enlarged vessel diameter during diastole of the cardiac cycle. The dimensional change in the vasculature specific to the dominant side will be included in the training effects associated with the dimensional muscular changes in the dominant forearm.

Acknowledgments This work was supported by the "Academic Frontier" project of Japan Women's College of Physical Education. The authors are grateful to Ms A. Mori (Graduate School of Humanities and Sciences, Ochanomizu University) for her help in analyzing data.

References

1. Allen JD, Geaghan JP, Greenway F, Welsche A. (2003) Time course of improved flow-mediated dilation after short-term exercise training. Med Sci Sports & Exerc 35:847–853.
2. Baynard T, Miller WC, Fernhall B. (2003) Effects of exercise on vasodilatory capacity in endurance- and resistance-trained men. Eur J Appl Physiol 89:69–73.
3. Bleeker MW, De Groot PC, Poelkens F, Rongen GA, Smits P, Hopman MT. (2005) Vascular adaptation to 4 week of deconditioning by unilateral lower limb suspension. Am J Physiol Heart Circ Physiol 288:H1747–H1755.
4. Bleeker MW, De Groot PC, Rongen GA, Rittweger J, Felsenberg D, Smits P, Hopman MT. (2005) Vascular adaptation to deconditioning and the effect of an exercise counter-measure: results of the Berlin Bed Rest study. J Appl Physiol 99:1293–1300.
5. Clarkson P, Montgomery HE, Mullen MJ, Donald AE, Powe AJ, Bull T, Jubb M, World M, Deanfield JE. (1999) Exercise training enhances endothelial function in young men. J Am Coll Cardiol 33:1379–1385.
6. Dinenno FA, Tanaka H, Monahan KD, Clevenger CM, Eskurza I, DeSouza CA, Seals DR. (2001) Regular endurance exercise induces expansive arterial remodelling in the trained limbs of healthy men. J Physiol 534:287–295.
7. Green DJ, Fowler DT, O'Driscoll JG, Blanksby BA, Taylor RR. (1996) Endothelium-derived nitric oxide activity in forearm vessels of tennis players. J Appl Physiol 81:943–948.
8. Huonker M, Schmid A, Schmidt-Trucksass A, Grathwohl D, Keul J. (2003) Size and blood flow of central and peripheral arteries in highly trained able-bodied and disabled athletes. J Appl Physiol 95:685–691.
9. Kagaya, A. (1994) Maximal exercise-induced vasodilation and peak pulmonary oxygen uptake during dynamic forearm and calf exercise. J Exer Sci 4:55–62.
10. Maxwell AJ, Schauble E, Bernstein D, Cooke JP. (1998) Limb blood flow during exercise is dependent on nitric oxide. Circulation 98:369–374.
11. Miyachi M, Iemitsu M, Okutsu M, Onodera S. (1998) Effects of endurance training on the size and blood flow of the arterial conductance vessels in humans. Acta Physiol Scand 163:13–16.

12. Miyachi M, Tanaka H, Yamamoto K, Yoshioka A, Takahashi K, Onodera S.(2001) Effects of one-legged endurance training on femoral arterial and venous size in healthy humans. J Appl Physiol 90:2439–2444.
13. Schmidt-Trucksäss A, Schmid A, Brunner C, Scherer N, Zäch G, Keul J, Huonker M. (2000) Arterial properties of the carotid and femoral artery in endurance-trained and paraplegic subjects. J Appl Physiol 89:1956–1963.
14. Sinoway LI, Musch TI, Minotti JR, Zelis R. (1986) Enhanced maximal metabolic vasodilatation in the dominant forearms of tennis players. J Appl Physiol 61:673–678.
15. Sinoway LI, Shenberger J, Wilson J, McLaughlin D, Musch T. (1987) A 30-day forearm work protocol increases maximal forearm blood flow. J Appl Physiol 62:1063–1067.
16. Sinoway L, Prophet S. (1990) Skeletal muscle metaboreceptor stimulation opposes peak metabolic vasodilation in humans. Circ Res 66:1576–1584.
17. Sjφgaard G, Kiens B, Jorgensen K, Saltin B.(1986) Intramuscular pressure, EMG and blood flow during low-level prolonged static contraction in man. Acta Physiol Scand 128:475–484.

Changes in Perfusion Related to Muscle Length Affect the Pressor Response to Isometric Muscle Contraction

Masaki Mizuno, Ken Tokizawa, and Isao Muraoka

Abstract To test the hypothesis that the dependence of the pressor response on muscle length is caused by changes in perfusion, we compared the cardiovascular responses to static contraction at short and long muscle lengths during free perfusion with those during circulatory arrest. Five males performed 2-min static knee extension exercise at 30% of maximal voluntary torque at each of two muscle lengths at a knee angle of 40° (short) and 90° (long). The subjects performed two trials – a free perfusion trial and a circulatory arrest trial. For circulatory arrest, an occlusion cuff placed around the proximal portion of the thigh was inflated to 250 mmHg 2 min before exercise. Mean arterial pressure (MAP), minute ventilation (V_E), and the muscle oxygenation index in the vastus lateralis muscle were measured using near-infrared spectroscopy. In the free perfusion trial, MAP and V_E were significantly greater during contractions at 90° than at 40° ($p < 0.05$). The muscle oxygenation index was significantly lower during contractions at 90° than at 40° ($p < 0.05$). Circulatory arrest diminished these differences. These results suggest that the relationship between muscle length and the pressor response can be explained by changes in perfusion, which are related to muscle length.

1 Introduction

Static muscle contraction increases mean arterial pressure (MAP) and minute ventilation (V_E). The magnitude of the pressor response is determined by exercise intensity, muscle mass [1], the exercising limb [2], and muscle fiber type [3]. The muscle length also affects the pressor response during isometric muscle contraction [4]. Ng et al. [4] showed that the pressor response during knee extension is greater at a knee angle of 90° (long muscle length) than at a

M. Mizuno (✉)
Department of Cardiovascular Dynamics, National Cardiovascular Center Research Institute, 5-7-1 Fujishirodai, Suita, 565-8565, Japan
e-mail: m-mizuno@ri.ncvc.go.jp

E. Takahashi, D.F. Bruley (eds.), *Oxygen Transport to Tissue XXXI*,
Advances in Experimental Medicine and Biology 662,
DOI 10.1007/978-1-4419-1241-1_54, © Springer Science+Business Media, LLC 2010

knee angle of 40° (short muscle length). However, the mechanisms underlying these different pressor responses associated with muscle length are not understood fully.

Muscle contraction induces changes in the muscle architecture [5], which could contribute to differences in muscle perfusion or oxygen delivery and hence modulate the pressor response at different muscle lengths. To test our hypothesis that the pressor response to static contraction at different muscle lengths is related to changes in perfusion caused by the different muscle lengths, we compared the cardiovascular responses to static contraction at short and long muscle lengths under conditions of free perfusion and circulatory arrest.

2 Methods

Five healthy active and untrained males volunteered to participate in this study (age 23.2 ± 2.6 year; height 173.0 ± 5.4 cm; weight 70.4 ± 7.5 kg; mean ± SD). Before the experiment, each subject was informed of all aspects of the study and signed an informed consent document. The study was approved by the local ethics committee and conformed to the Declaration of Helsinki.

Subjects performed 2-min static knee extensor exercise in a seated position at a knee angle of 40° and 90° at 30% of maximal voluntary contraction (MVC). The MVC torque at each exercise was assessed using the Cybex II isokinetic dynamometer (Lumex Inc., Ronkonkoma, NY, USA) before the study began. The average of three attempts was taken as the subject's MVC. The two exercises were conducted under free perfusion and circulatory arrest on different days in a random order. In the circulatory arrest trial, an occlusion cuff placed around the proximal portion of the thigh was inflated to 280 mmHg 2 min before the start of exercise, and the cuff pressure was maintained until the end of exercise.

Blood pressure was measured with a finger cuff using an optomechanical photoplethysmographic method (2300 Finapres, Ohmeda, Englewood, CO, USA). The monitoring finger cuff was placed around the middle finger of the left hand and supported at the level of the heart. Heart rate (HR) was determined using standard ECG leads (model OEC-8108, Nihon Kohden, Tokyo, Japan). V_E was monitored using a metabolic cart system (AE-280S, Minato Medical Science, Osaka, Japan).

To provide an indicator of muscle oxygenation, the change in optical density (OD) of oxygenated hemoglobin (O_2Hb) was measured at 1 Hz using a commercially available device (OM-200; Shimadzu, Kyoto, Japan) in near-infrared continuous-wave spectroscopy mode (NIRS). The NIRS probe was placed on the belly of the vastus lateralis muscle. The light emitter–detector distance of the device was 40 mm. This apparatus uses

three wavelengths of near-infrared light to measure changes in OD in O_2Hb and deoxygenated hemoglobin (HHb). The changes in the concentrations of O_2Hb and HHb were calculated according to the following equations:

$$\Delta[O_2Hb] = -1.631 \times Abs780 + 0.683 \times Abs805 + 1.605 \times Abs830$$

$$\Delta[HHb] = -1.970 \times Abs780 - 0.314 \times Abs805 - 1.195 \times Abs830$$

where Abs780, Abs805, and Abs830 are the absorbance changes at the near-infrared light wavelengths of 780, 805, and 830 nm, respectively. The equations had been determined experimentally by the manufacturer. The change in OD for total hemoglobin (total Hb) was calculated by summing the changes in OD of O_2Hb and HHb. The $\Delta[O_2Hb]$ and $\Delta[HHb]$ (where Δ represents the change and the brackets denote the concentration) were calculated with respect to an initial arbitrarily set value equal to zero and are expressed in arbitrary units. The sum of the two variables, $\Delta[O_2Hb + HHb]$, reflects the change in the "total Hb volume" in the muscle region of interest, whereas the difference between the two variables, $\Delta[O_2Hb - HHb]$, reflects an "oxygenation index."

The pennation angle of the vastus lateralis muscle was measured during contraction of the knee extensors at the two knee angles using a real-time ultrasonic apparatus (SSD-2000, 7.5 MHz, Aloka Co., Japan) on the other experimental day for four subjects. The ultrasonic transducer was placed on the skin over the muscle at position equivalent to 50% of the muscle length (i.e., halfway between the origin and insertion.

The data are expressed as means ± SE. A repeated measure two-way ANOVA was used to analyze the main effects of knee angle and time. Significance was accepted at $p < 0.05$.

3 Results

The MVC of the knee extensors was significantly greater at a knee angle of 90° than at a knee angle of 40° (90°, 220.4 ± 17.9 N • m; 40°, 153.7 ± 15.7 N • m). The pennation angles of the vastus lateralis muscle were 11.9 ± 0.8° (resting condition) and 14.1 ± 0.5° (during contraction) at a knee angle of 90°, and 16.6 ± 1.5° (resting condition) and 19.9 ± 1.1° (during contraction) at a knee angle of 40 °.

Figure 1 shows the changes from baseline of MAP, HR, V_E, and the oxygenation index during exercise under free perfusion. The absolute baseline values did not differ significantly between the 40° and 90° knee angles (MAP: 97.0 ± 9.1 vs. 94.7 ± 8.2 mmHg; HR: 73.5 ± 2.3 vs. 71.1 ± 10.1 bpm; V_E: 8.8 ± 1.0 vs. 9.2 ± 2.0 L/min, respectively). During muscle contraction, MAP, HR and V_E gradually increased more at a knee angle of 90° than at 40°, although HR did not differ statistically between the two knee angles. The mean percent changes of each parameter at 2 min of exercise were greater at a

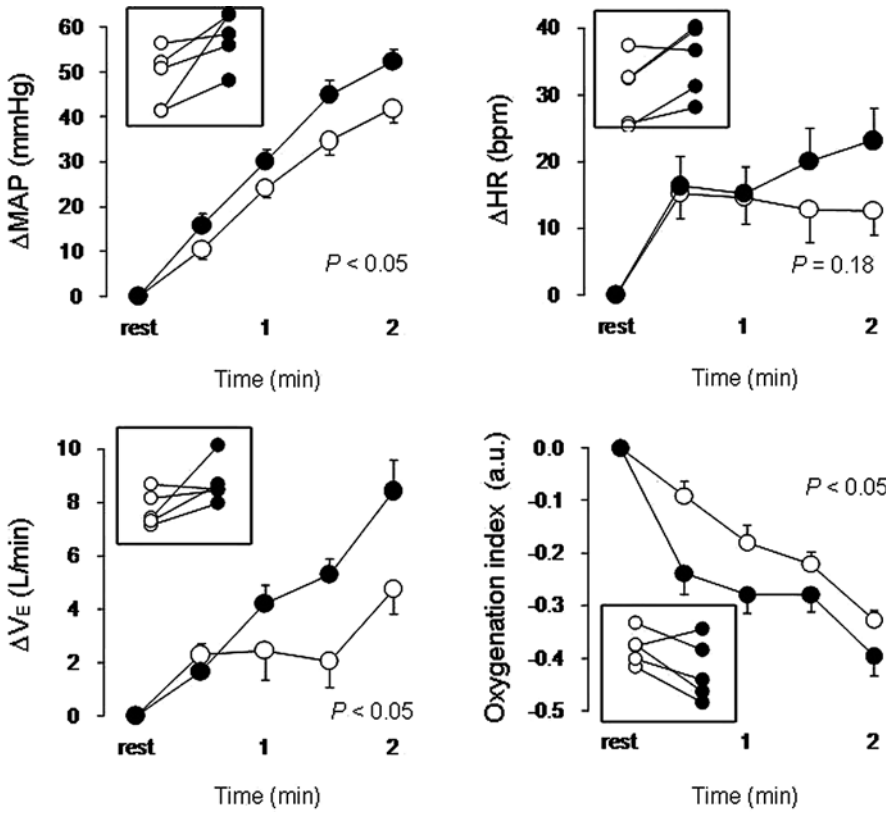

Fig. 1 The changes from baseline of mean arterial pressure (MAP), heart rate (HR), ventilation (V_E), and oxygenation index during exercise under free perfusion. The closed symbols show the responses at a knee angle of 90°, and the open symbols show the responses at a knee angle of 40°. Insets: individual data of each parameter at 2 min of exercise

knee angle of 90° than at 40° (MAP: 56.1 ± 5.0 vs. 43.4 ± 3.8 %; HR: 32.9 ± 8.1 vs. 17.1 ± 7.0%; V_E: 94.2 ± 14.8 vs. 57.0 ± 16.2%). The oxygenation index in the exercising muscle gradually decreased more at a knee angle of 90° than at 40°. Figure 2 shows the changes from baseline of MAP, HR, V_E, and the oxygenation index during exercise under circulatory arrest. The absolute baseline values did not differ significantly between exercise at a knee angle of 40° and 90° (MAP: 105.2 ± 9.8 vs. 101.1 ± 11.2 mmHg; HR: 76.7 ± 11.0 vs. 72.2 ± 9.8 bpm; V_E: 9.5 ± 0.9 vs. 9.3 ± 1.3 L/min, respectively). MAP, HR, V_E, and the oxygenation index did not differ significantly during exercise at the two knee angles. The mean percent changes of each parameter at 2 min of exercise did not differ at a knee angle of 40° and 90° (MAP: 52.5 ± 7.3 vs. 58.9 ± 4.5%; HR: 28.1 ± 7.4 vs. 36.8 ± 7.1%; V_E: 51.2 ± 2.4 vs. 55.6 ± 10.4%, respectively).

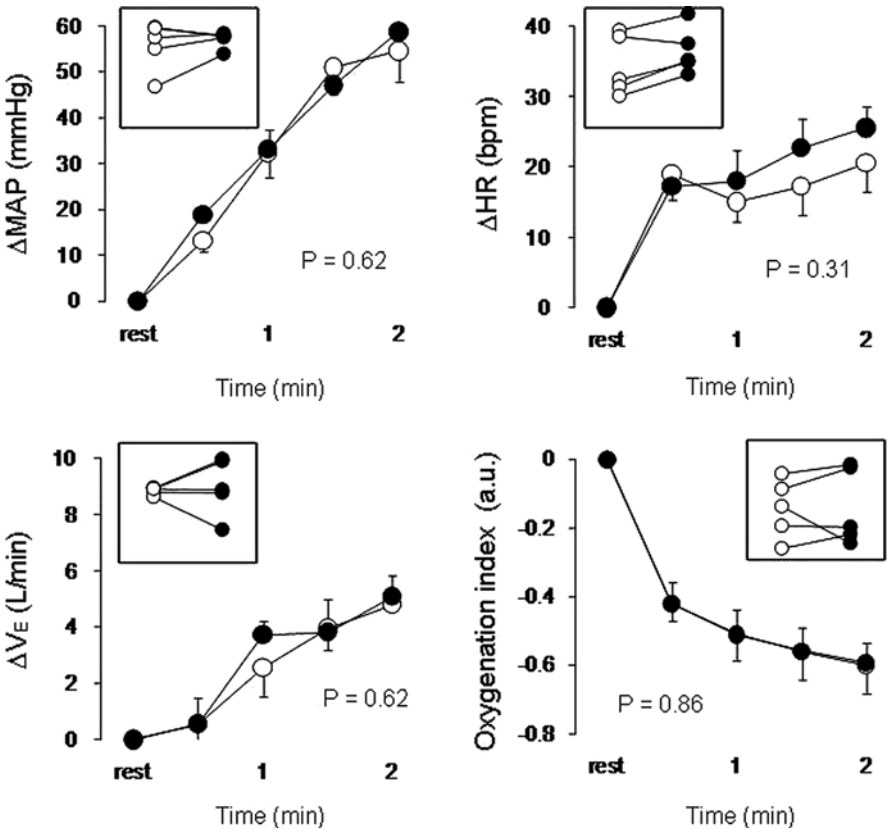

Fig. 2 The changes from baseline of mean arterial pressure (MAP), heart rate (HR), ventilation (V_E), and oxygenation index during exercise under circulatory arrest. The closed symbols show the responses at a knee angle of 90°, and the open symbols show the responses at a knee angle of 40°. Insets: individual data of each parameter at 2 min of exercise

4 Discussion

We compared the pressor response during static knee extensor contraction at two different knee angles under free perfusion with that under circulatory arrest. We found a significant difference in the pressor response between the two knee angles under free perfusion but no significant difference between the two knee angles under circulatory arrest.

Ng et al. [4] showed that the pressor response of the knee extensors is greater at a knee angle of 90° than at 40°. Our results obtained under free perfusion are consistent with the results of Ng et al. and show that the pressor response is related to the muscle length during static contraction. We showed further that the difference in the pressor response at different knee angles

disappeared under circulatory arrest. These findings shed light on the mechanisms underlying the difference in pressor response at different muscle lengths.

During physical exercise, the cardiovascular centers receive neural input from higher brain centers (central command) and contracting muscles (exercise pressor reflex). Central command refers to activation of the cardiovascular centers by the descending central neural pathways involved in the initiation of somatomotor activity [6]. HR during exercise is affected mainly by central command [7]. In the present study, HR did not differ significantly between knee angles under free perfusion, suggesting that central command contributes little to the difference in the pressor response at different knee angles.

The exercise pressor reflex, which arises from the contraction-induced stimulation of muscle afferents, is believed to be evoked by mechanical and metabolic stimuli in the exercising muscles [8]. The MVC of the knee extensors was greater at a knee angle of 90° than at 40°, indicating that greater tension in the exercising muscle was elicited at the 90° knee angle. Therefore, the muscle mechanoreflex could be the cause of the greater pressor responses at a knee angle of 90° under free perfusion. However, the pressor response did not differ between knee angles under circulatory arrest, although the MVC values under circulatory arrest were unchanged from those under free perfusion. This indicates that the muscle mechanoreflex has little effect on the pressor response at different knee angles.

The muscle metaboreflex is evoked by metabolic stimuli, which signal a mismatch between the blood and oxygen supply to and demand in the exercising muscles. The oxygenation index decreased more in the exercising muscle under free perfusion at a knee angle of 90° than at 40°. Oxygenation status reflects the balance between oxygen delivery and utilization, and the decrease in oxygenation index represents an augmentation of oxygen demand. The greater decrease in oxygenation during static contraction at a knee angle of 90° might cause greater activation of the muscle metaboreflex compared with contraction at a knee angle of 40°, which may enhance the pressor response. This is supported by the lack of significant difference in the oxygenation index and pressor response between the two knee angles under circulatory arrest. The pennation angle of the vastus lateralis muscle is greater at a knee angle of 40° than at 90°. The change in muscle architecture caused by the change in the muscle length probably causes differences in muscle perfusion.

In conclusion, the different pressor responses during static contraction between the short and long muscle length could be explained by changes in perfusion related to the muscle length.

Acknowledgments The authors gratefully acknowledge Dr. Taku Wakahara for invaluable technical support with the ultrasonic apparatus.

References

1. Mitchell JH, Payne FC, Saltin B, Schibye B. (1980) The role of muscle mass in the cardiovascular response to static contractions. J Physiol 309: 45–54.
2. Bevegard S, Freyschuss U, Strandell T. (1966) Circulatory adaptation to arm and leg exercise in supine and sitting position. J Appl Physiol 21: 37–46.
3. Fisher JP, White MJ. (2004) Muscle afferent contributions to the cardiovascular response to isometric exercise. Exp Physiol 89: 639–646.
4. Ng AV, Agre JC, Hanson P, Harrington MS, Nagle FJ. (1994) Influence of muscle length and force on endurance and pressor responses to isometric exercise. J Appl Physiol 76: 2561–2569.
5. Miura H, McCully K, Nioka S, Chance B. (2004) Relationship between muscle architectural features and oxygenation status determined by near infrared device. Eur J Appl Physiol 91: 273–.278.
6. Williamson JW, Fadel PJ Mitchell JH. (2006). New insights into central cardiovascular control during exercise in humans: a central command update. Exp Physiol 91: 51–58.
7. Williamson JW, Olesen HL, Pott F, Mitchell JH, Secher NH. (1996) Central command increases cardiac output during static exercise in humans. Acta Physiol Scand 156: 429–434.
8. Mitchell, JH, Kaufman MP, Iwamoto GA. (1983) The exercise pressor reflex: its cardiovascular effects, afferent mechanisms, and central pathways. Annu Rev Physiol 45: 229–242.

Decreased Muscle Oxygenation and Increased Arterial Blood Flow in the Non-Exercising Limb During Leg Exercise

Kiyoshi Shiroishi, Ryotaro Kime, Takuya Osada, Norio Murase, Kousuke Shimomura, and Toshihito Katsumura

Abstract We evaluated arterial blood flow, muscle tissue oxygenation and muscle metabolism in the non-exercising limb during leg cycling exercise. Ten healthy male volunteers performed a graded leg cycling exercise at 0, 40, 80, 120 and 160 watts (W) for 5 min each. Tissue oxygenation index (TOI) of the non-exercising left forearm muscle was measured using a near-infrared spatially resolved spectroscopy (NIR_{SRS}), and non-exercising forearm blood flow ($_{NONEX}FBF$) in the brachial artery was also evaluated by a Doppler ultrasound system. We also determined O_2 consumption of the non-exercising forearm muscle ($_{NONEX}\dot{V}O_{2mus}$) by the rate of decrease in O_2Hb during arterial occlusion at each work rate. TOI was significantly decreased at 160 W ($p < 0.01$) compared to the baseline. The $_{NONEX}\dot{V}O_{2mus}$ at each work rate was not significantly increased. In contrast, $_{NONEX}FBF$ was significantly increased at 120 W ($p < 0.05$) and 160 W ($p < 0.01$) compared to the baseline. These results suggest that the O_2 supply to the non-exercising muscle may be reduced, even though $_{NONEX}FBF$ increases at high work rates during leg cycling exercise.

1 Introduction

To maintain adequate O_2 supply to active muscles during exercise, nonactive tissue circulation plays an important role in the systemic blood regulation. Several investigations regarding non-exercising forearm blood flow ($_{NONEX}FBF$) during leg exercise, however, are controversial. Tanaka et al. [1] and Green et al. [2] observed an increase in $_{NONEX}FBF$ in proportion to the work rate during a graded leg cycling exercise. In contrast, Taylor et al. [3] and Bevegard et al. [4] demonstrated decreases in $_{NONEX}FBF$ during leg cycling exercise at high work

K. Shiroishi (✉)
Department of Judotherapy and Sports Medicine, Faculty of Health Science, Ryotokuji University, Chiba, 279-8567, Japan; Department of Sports Medicine for Health Promotion, Tokyo, Medical University, Tokyo, 160-8402, Japan
e-mail: cafe@foot.jp; shiroishi@ryotokuji-u.ac.jp

E. Takahashi, D.F. Bruley (eds.), *Oxygen Transport to Tissue XXXI*, Advances in Experimental Medicine and Biology 662,
DOI 10.1007/978-1-4419-1241-1_55, © Springer Science+Business Media, LLC 2010

rate for relatively short duration (5 min). These divergent findings may be due to the difference in exercise protocols such as duration and work rate.

At the muscle tissue level, a recent study demonstrated that the decrease in oxygenation in the non-exercising arm muscle during graded leg cycling exercise has been observed during high intensity exercise [5]. The study suggested that the decrease in muscle oxygenation resulted from a decrease in blood flow in the tissue. However, no study to date has determined whether the change in blood flow in the conduit artery and skeletal muscle oxygenation of non-exercising limb are similar during leg exercise. Therefore, the purpose of this study was to examine muscle saturation and blood flow of the conduit artery in non-exercising limb during graded leg cycling exercise.

2 Methods

2.1 Subjects

Ten healthy male subjects participated in this study (age; 22 ± 2, height; 169.1 ± 4.5, weight; 67.0 ± 8.6, mean $\pm$ SD). All subjects had no systemic illness, were not taking any medications, and were nonsmokers. The subjects were physically active but not conducting intense exercise. All subjects gave their informed consent.

2.2 Exercise

Each subject performed a leg cycling exercise using an electronically braked bicycle ergometer (Ergomed 903, Ergomed Inc., Sweden). The bicycle ergometer was modified for recumbent leg cycling exercise, and the non-exercising upper limb (left) was supported by an arm-rest at heart level to avoid shaking of the limb. A 2-min baseline recording followed by a graded leg cycling exercise was performed. The work rate started with 0 watt (W), and increased every 5 min by 40 W with pedaling rate at 60 rpm until volitional exhaustion. In this study, we analyzed ten subjects who were able to reach the end of the work rate at 160 W, but were not able to continue performing additional work rates (200 W) for more than 1 min.

2.3 Measurements

Heart rate (HR) from electrocardiograms, pulmonary oxygen uptake (AE-300, Minato, Japan), and arterial blood pressure (2300, Finapres, Ohmeda, Englewood, CO USA) from the middle finger (left) were continuously measured. Mean arterial blood pressure (MABP) was calculated as one-third of the pulse pressure plus diastolic pressure (Fig. 1).

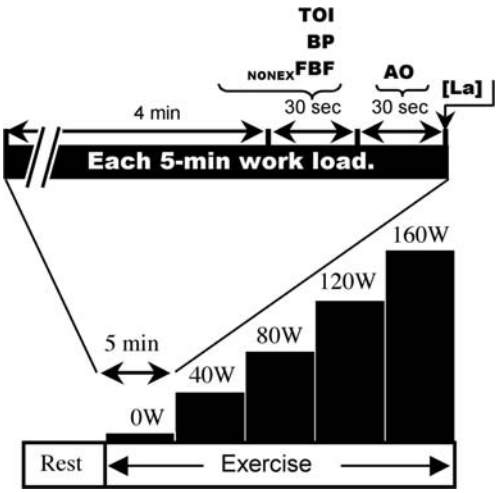

Fig. 1 Experimental protocol and measurements. Tissue oxygenation index (TOI), forearm blood flow ($_{NONEX}$FBF) in the brachial artery, and blood pressure (BP) of the *left* non-exercising limb were continuously measured at rest and during exercise. Arterial occlusion (AO) on the *upper arm* was performed over the last 30 s of each exercise work rate for evaluating muscle oxygen consumption. At the end of each work rate, blood samples were drawn from the right finger tip for lactate concentration ([La])

To determine oxygenation of the non-exercising forearm muscle, we used a near-infrared spatially resolved spectroscopy (NIR_{SRS}) (NIRO-200, Hamamatsu Photonics K. K., Hamamatsu, Japan). This oximeter has a probe of a near-infrared light emitter and the two detectors at wave lengths of 775, 810 and 850 nm. The separation distances between the emitter and the detectors are 3.5 and 4.0 cm respectively. The probe was placed over the mid-belly of the left finger flexor muscles. This oximeter enables us to measure average tissue O_2 saturation called the tissue oxygenation index (TOI, %) using a multi-distance approach. Muscle oxygen consumption of the non-exercising left finger flexor muscle (nonexVO_{2mus}, fold of resting) was estimated from the declining rate of O_2Hb volume measured by the oximeter with temporary arterial occlusion of the upper arm. We also monitored electromyography (EMG) activity to ascertain that no muscle contraction was observed in the forearm flexor muscles.

Blood samples (5 μL) for lactate concentration ([La]) were taken from the middle finger tip of the right hand and analyzed by an amperometric microvolume test strip lactate meter (Lactate Pro LT-1710, ARKRAY, USA).

The $_{NONEX}$FBF was measured on the left brachial artery using a high-frequency ultrasound machine (LogiQ3, GE-Yokokawa Medical Systems, Japan) equipped with a 7.7 MHz linear array transducer. The transducer was placed at the distal one-third of the brachial artery, 1–2 cm proximal to the

antecubital fossa at heart level. Mean blood flow velocity measurements were performed with the insonation angle of the ultrasound beam at less than 60°. The cross-sectional area of the vessel was calculated as πr^2, where r is the radius of the vessel. $_{NONEX}$FBF was calculated from the mean blood velocity and the diameter of the brachial artery. Vascular conductance of the non-exercising forearm ($_{NONEX}$VC) was calculated as $_{NONEX}$FBF/MABP.

2.4 Data Analysis and Statistics

The parameters of TOI, $_{NONEX}$FBF, blood pressure, HR and pulmonary oxygen uptake were continuously measured at rest and during exercise. These valuables were averaged for 1 min at rest and for 30 s from 1 min before the end of each exercise work rate. Arterial occlusion for non-exercising muscle oxygen consumption was performed from the last 30 s at each exercise work rate. Blood samples for lactate concentration were collected at rest and immediately after each exercise work rate.

All measured values are expressed as means ± standard deviation (SD). The statistical differences among values were tested using one-way measures ANOVA. When a significant difference was found, multiple comparisons were conducted using a Dunnett's test to compare between values at baseline and each work rate. $p < 0.05$ was regarded as significant.

3 Results

The work rates of 0, 40, 80, 120, and 160 W were equivalent to 26.5 ± 3.2, 33.2 ± 2.5, 79.7 ± 3.2, 69.0 ± 5.0, and 90.5 ± 6.1 of their peak oxygen consumption (%VO_{2peak}), respectively. HR and VO_2pul linearly increased. MABP increased with exercise work load. The results of MABP were 90.9 ± 3.5, 106.3 ± 4.9 ($p < 0.01$), 110.3 ± 4.1 ($p < 0.01$), 117.5 ± 4.2 ($p < 0.01$), 129.7 ± 5.5 ($p < 0.01$), and 132.5 ± 5.6 mmHg ($p < 0.01$) at baseline, 0, 40, 80, 120, and 160 W respectively. [La] started to accumulate at 120 W and increased significantly at 120 W ($p < 0.01$) and 160 W ($p < 0.01$).

There was no EMG activity during exercise. Figure 2 shows the changes in $_{NONEX}$TOI (A) and $_{NONEX}VO_{2mus}$ (B) during the exercise. The TOI was not changed until the work rate of 120 W but significantly deceased at 160 W from the baseline (61.4 ± 4.5% vs 51.0 ± 5.7%; $p < 0.01$). $_{NONEX}VO_{2mus}$ did not change during the exercise.

Figure 3 shows $_{NONEX}$FBF (A) and $_{NONEX}$VC (B) during the exercise. The $_{NONEX}$FBF increased on a curve and showed a significant increase at 120 W ($p < 0.05$) and 160 W ($p < 0.01$). The $_{NONEX}$VC was significantly augmented at 160 W ($p < 0.05$) from the baseline.

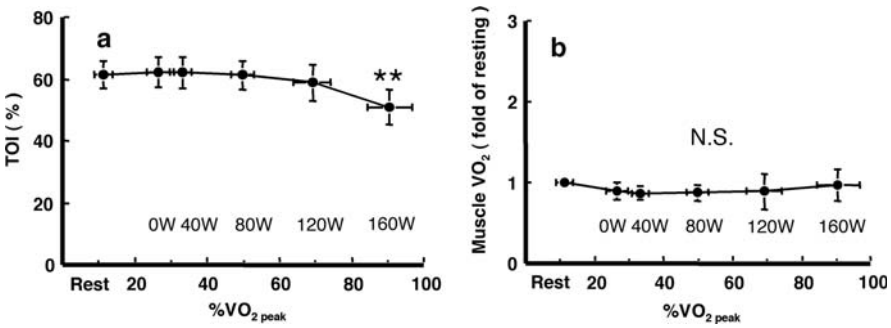

Fig. 2 Non-exercising forearm muscle tissue oxygenation index (TOI) (**a**), and oxygen consumption (**b**) during a graded leg cycling exercise. Asterisks indicate significant difference from baseline (Rest) (**$p < 0.01$)

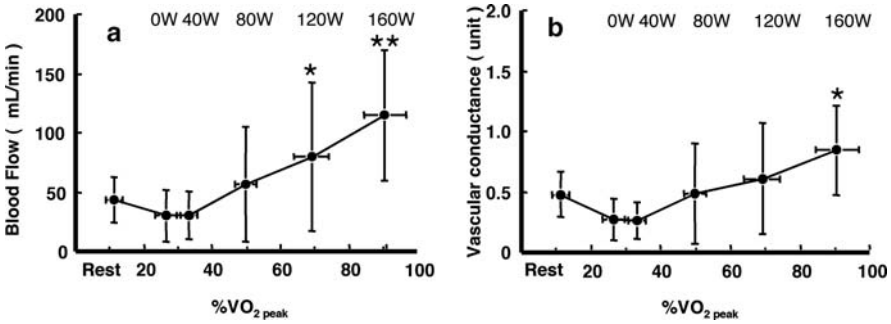

Fig. 3 Non-exercising forearm blood flow (**a**), and vascular conductance (**b**) during a graded leg cycling exercise. Asterisks indicate significant difference from baseline (Rest) (*$p < 0.05$, **$p < 0.01$)

4 Discussion

We simultaneously measured non-exercising muscle oxygenation by NIR_{SRS} and limb blood flow by Doppler ultrasound during graded leg cycling exercise. The main findings of this study were that non-exercising muscle TOI decreased significantly at the higher work rates (160 W), even though $_{NONEX}FBF$ significantly increased at higher work rates (120 and 160 W).

TOI reflects the local balance between O_2 supply and O_2 consumption. In this study, since $_{NONEX}VO_{2mus}$ at each work rate was not significantly increased from the baseline, the decreased TOI may reflect a reduction in O_2 supply to the non-exercising forearm muscles. One possible explanation is that muscle sympathetic vasoconstriction was augmented at the higher work rates. Ogata et al. [5] examined sympathetic vasoconstriction in the non-exercising forearm muscle using NIRS during ramp leg cycling, and demonstrated similar results

that oxygenated hemoglobin in the non-exercising forearm muscle began to decrease at high work rates. Muscle metaboreflex-evoked increases in muscle sympathetic activity during exercise are strongly associated with glycogenolysis and the consequent cellular accumulation of hydrogen ions in the contracting muscles [6]. We measured [La] as an indicator of the metabolic condition, and observed that the [La] increased significantly at 120 and 160 W work rates. Thus, the metabolites in active muscles could stimulate chemoreceptors and augment the consequent sympathetic vasoconstriction.

On the other hand, $_{NONEX}$FBF and the $_{NONEX}$VC showed a progressive increase during the exercise. These results were in accordance with a study by Tanaka et al. [1] that demonstrated a similar increase in $_{NONEX}$FBF and the shear stress during graded leg cycling exercise. One mechanism underlying this increase in blood flow may be due to the enhancement of nitric oxide release. Gleen et al. [2] demonstrated an endothelium-derived nitric oxide increase in $_{NONEX}$FBF during leg cycling exercise. The brachial artery is the conduit artery for O_2 supply not only to muscle but also skin, bone, and other tissue. It was reported that skin blood flow was increased in proportion to the increase in internal temperature during leg cycling exercise [7]. These results lead to another possibility that increased $_{NONEX}$FBF may be caused mainly by an increase in the skin blood flow. Considering these results, muscle O_2 delivery to the non-exercising muscle probably decreases, even though the $_{NONEX}$FBF increased at high work rate during graded leg cycle exercise.

References

1. Tanaka H, Shimizu S, Ohmori F, et al. (2006) Increases in blood flow and shear stress to nonworking limbs during incremental exercise. Med Sci Sports Exerc 38:81–85
2. Green D, Cheetham C, Mavaddat L, et al. (2002) Effect of lower limb exercise on forearm vascular function: contribution of nitric oxide. Am J Physiol Heart Circ Physiol 283:H899–H907.
3. Taylor JA, Joyner MJ, Chase PB, et al. (1989) Differential control of forearm and calf vascular resistance during one-leg exercise. J Appl Physiol 67:1791–1800.
4. Bevegård BS, Shepherd JT. (1966) Reaction in man of resistance and capacity vessels in forearm and hand to leg exercise. J Appl Physiol 21:123–132
5. Ogata H, Reyihan A, Yano T. (2004) Kinetics of oxygenation in inactive forearm muscle during ramp leg cycling. J Physiol Anthropol Appl Human Sci 23:7–17.
6. Seals DR, Victor RG. (1991) Regulation of muscle sympathetic nerve activity during exercise in humans. Exerc Sport Sci Rev 19:313–349.
7. Johnson JM, Park MK. (1981) Effect of upright exercise on threshold for cutaneous vasodilation and sweating. J Appl Physiol 50:814–818.

Effects of Acute Hypoxia on the Inflection Point of Muscle Oxygenation

Takuya Osawa, Ryotaro Kime, Toshihito Katsumura, and Masayoshi Yamamoto

Abstract The purpose of this study was to investigate the effects of acute hypoxia on the inflection point of muscle oxygenation (IPMO) using near-infrared spectroscopy during incremental bicycle exercise. Eight male subjects (age: 22 ± 2 years) performed two ramp incremental bicycle exercise tests until exhaustion under each normoxic and hypoxic (F_IO_2: 0.12) condition. Pulmonary gas exchange and locomotor muscle oxygenation were continuously measured. IPMO was determined as the attenuated point of muscle deoxygenation. Muscle oxygenation level was significantly lower in hypoxia than normoxia throughout the tests. IPMO was found in both conditions, and $\dot{V}O_2$ at IPMO was significantly decreased in hypoxia. However the percent rate of $\dot{V}O_{2peak}$ between normoxia and hypoxia was not significantly different. These results suggest that IPMO was not associated with absolute exercise intensity, but relative exercise intensity.

1 Introduction

Acute hypoxia decreases endurance performance. Some studies have reported the changes of various physiological responses [1, 2, 3]. However, the mechanism is still not fully understood, especially little is known about how acute hypoxia influences muscle responses during exercise.

One of the methods for understanding muscle responses is using near-infrared spectroscopy (NIRS). This can continuously monitor muscle oxygenation (MO) during exercise. MO decreases non-linearly during incremental exercise and has an inflection point (IPMO) at high exercise intensities [4, 5, 6]. However the effects of acute hypoxia on MO kinetics and on IPMO are unclear.

T. Osawa (✉)
Department of Sports Medicine for Health Promotion, Faculty of Medicine,
Tokyo Medical University, Tokyo, 160-8402, Japan
e-mail: osawa-t@tokyo-med.ac.jp

E. Takahashi, D.F. Bruley (eds.), *Oxygen Transport to Tissue XXXI*,
Advances in Experimental Medicine and Biology 662,
DOI 10.1007/978-1-4419-1241-1_56, © Springer Science+Business Media, LLC 2010

The purpose of this study was to investigate the effects of acute hypoxia on MO kinetics and IPMO using NIRS during incremental bicycle exercise.

2 Methods

2.1 Subjects

Eight male volunteers participated in this study [age, 22 ± 2 years; height, 173.3 ± 6.6 cm; body mass, 65.4 ± 5.8 kg, mean ± S.D.]. Before the experiment, all procedures and any potential risks were explained to each subject and an informed consent document was signed before participation. This study was approved by the local ethics committee and all work was performed in accordance with the Declaration of Helsinki.

2.2 Experiment Design

The subjects performed two ramp incremental exercise tests to exhaustion in an environmentally-simulated room (Espec engineering; Japan) under normoxic or hypoxic ($F_IO_2 = 0.12$) conditions in random order. After calibrating NIRS signals (see below) and breathing in each gas mixture at rest for at least 15 min to equilibrate body gas stores of O_2 and CO_2 [7], the subject underwent the ramp incremental exercise tests. The protocol followed a warm-up (WU) exercise at 10 W for 4 min, increased at a ramped rate of 20 W/min to exhaustion. An electro-magnetically braked cycle ergometer (75XL2, Combi, Japan) was utilized, and pedaling frequency was kept at 60 rpm.

2.3 Measurements

Pulmonary ventilation (VE) and O_2 uptake ($\dot{V}O_2$) were determined breath-by-breath by a computerized metabolic cart (model Vmax29c, Sensor Medics, USA). Expiratory flow measurements were performed by a mass flow sensor (hot wire anemometer). Ventilation threshold (VT) was calculated by V-slope methods [8]. Heart rate (HR) was determined from the ECG signal. Arterial blood O_2 saturation (SpO_2) was non-invasively, continuously monitored by pulse oximetry (OLV-3100, Nihon Kohden, Japan) from the first or second finger. To obtain accurate values, we simultaneously measured and confirmed the pulse data.

Changes in oxy-(O_2Hb) and deoxy-(HHb) hemoglobin concentrations were measured with continuous wave near-infrared spectroscopy (NIRO 200, Hamamatsu photonics, Japan). The optode was placed on the lower third of the vastus lateralis muscle (VL), and the interoptode space was 4 cm. Pen marks

were made over the skin to indicate the optode site before and after the tests to place the optode in the same location in both tests. The fat layer thickness under the optode site was 3.4 ± 0.7 mm, measured by ultrasonography (ECOCEE SSA-340A, Toshiba, Japan).

The changes in total hemoglobin (THb) were calculated by summing the changes in O_2Hb and HHb. The changes in muscle oxygenation (MO) were calculated using the difference between O_2Hb and HHb. To evaluate differences of MO between subjects, MO was expressed as relative (%MO) by arterial occlusion [9] in normoxia before exposure to each condition. 100%MO was calculated as the averaged MO value when each subject lay on a bed in normoxic conditions for 10 min. 0%MO was calculated as the minimum MO value during arterial occlusion. %MO was continuously measured until the end of each exercise test. Although NIRO 200 provides tissue oxygen index (TOI) using spatially resolved near infrared spectroscopy, we did not use TOI in this study because TOI is influenced by fat layer thickness.

An inflection point of muscle oxygenation (IPMO) was identified as a slowed decrease of MO during high intensity exercise, and was calculated by the change of MO in a previous study [6]. To establish an objective criterion, IPMO in this study was mathematically determined by computer. Piecewise linear regression analysis was automatically applied to plots of MO vs. power output, and then the intersection between two regression lines was determined as IPMO. The calculated range was from VT to exhaustion since our purpose was to estimate IPMO in high intensity. The similar analysis was used by a previous study calculating electromyographic threshold [10]. Figure 1 shows an example of the mathematical determination of IPMO in one subject.

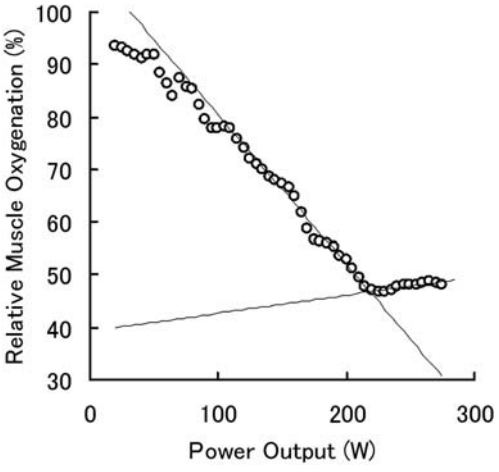

Fig. 1 Example of the mathematical determination of an inflection point of muscle oxygenation (IPMO)

2.4 Statistical Analyses

All data are averaged to 15 s, and represented as means ± S.E. Statistical analyses were performed using the statistical package SPSS for Windows (version 12.0; SPSS, Chicago, IL). For each physiological parameter, a paired *t*-test was used between normoxia and hypoxia. To compare both THb and %MO values during the same absolute and relative intensity exercise, a two-way repeated ANOVA, with F_IO_2 and power output as the main effects, was used to determine significant differences. A paired *t*-test was used when significant F_IO_2 effect was found. Values of $p < 0.05$ were considered significant.

3 Results

Peak power output, peak O_2 uptake ($\dot{V}O_{2peak}$) and peak HR were significantly reduced under hypoxia compared to normoxia. SpO_2 in hypoxia were significantly lower throughout the tests.

The averaged values of THb significantly increased from WU to VT, but did not change from VT to $\dot{V}O_{2peak}$ in either condition. There was no significant difference between either condition. %MO decreased non-linearly in both conditions as the exercise intensity increased. Significant differences between normoxic and hypoxic conditions were found at both the same absolute and relative exercise intensities (Fig. 2).

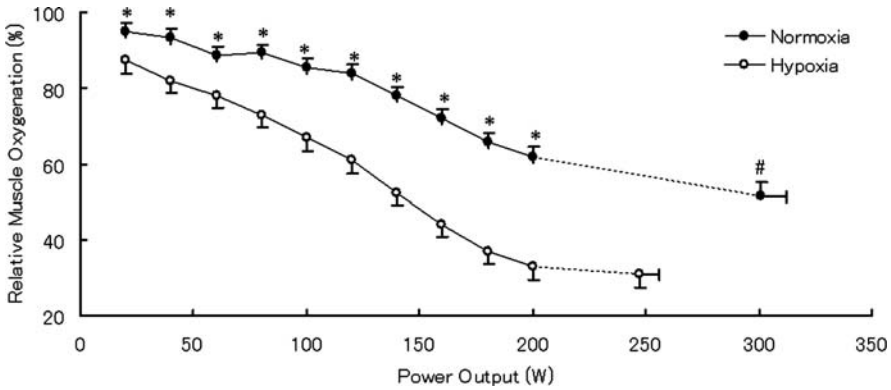

Fig. 2 Averaged relative muscle oxygenation (%MO) in normoxia and hypoxia. *Significant difference in same absolute intensity between normoxia and hypoxia, $p < 0.01$. #Significant difference at exhaustion between normoxia and hypoxia, $p < 0.01$

IPMO were found in both conditions. %MO at IPMO in hypoxia (32.6 ± 3.9%) was significantly lower than in normoxia (52.7 ± 3.8%). Also $\dot{V}O_{2peak}$ at

IPMO was significantly decreased in hypoxia (normoxia: 39.9 ± 2.3 ml/kg/min, hypoxia: 31.8 ± 1.0 ml/kg/min). However the percent rate of $\dot{V}O_{2peak}$ ($\%\dot{V}O_{2peak}$) was not significantly different in both conditions (normoxia: 75.7 ± 2.0 %, hypoxia: 78.5 ± 1.4%).

4 Discussion

MO level indicates the balance between local O_2 delivery and consumption. In the same absolute exercise intensities, since leg O_2 consumption was not influenced by hypoxia, the differences of %MO between normoxia and hypoxia were likely attributed to O_2 delivery. Similarly, as the relative exercise intensity increased, the differences of MO values between both conditions were also greater. These results were in accordance with previous studies [3, 11]. These results suggest that acute hypoxia further unbalanced the locomotor muscle oxygenation even at the same relative exercise intensity. However, there are contrasting reports to our findings about the effects of acute hypoxia on MO level [12, 13]. Some of the explanations include differences in inspiratory O_2 fraction, working muscle volume and exercise protocol.

Some authors [3, 4] have reported that IPMO indicated a slowdown or a plateau in muscle deoxygenation, but few studies have reported on the mechanism for this. One of the interpretations is to reach maximal oxygenation extraction [4]. Another is that the increased O_2 demand at the respiratory muscle limits O_2 use from the locomotor muscle [6]. Acute hypoxia decreased $\dot{V}O_2$ at IPMO, but not $\%\dot{V}O_{2peak}$. Also %MO at IPMO in hypoxia was significantly lower. These results suggest that IPMO is not associated with MO level and muscle O_2 consumption, but is associated with peripheral fatigue and aerobic capacity [2].

We have demonstrated that acute hypoxia decreased %MO during exercise and $\dot{V}O_2$ at IPMO, but did not influence $\dot{V}O_{2peak}$ at IPMO. These results imply that the MO level is influenced by both O_2 delivery and consumption, and that IPMO is associated with relative exercise intensity.

References

1. Hughson RL, Green HJ, and Sharratt MT. (1995) Gas exchange, blood lactate, and plasma catecholamines during incremental exercise in hypoxia and normoxia. J. Appl. Physiol. 79: 1134–1141.
2. Romer LM, Haverkamp HC, Amann M et al. (2007) Effect of acute severe hypoxia on peripheral fatigue and endurance capacity in healthy humans. Am. J. Physiol. Regul. Integr. Comp. Physiol. 292: R598–R606.
3. Subudhi AW, Dimmen AC, Roach RC. (2007) Effects of acute hypoxia on cerebral and muscle oxygenation during incremental exercise. J. Appl. Physiol. 103: 177–183.

4. Chance B, Dait MT, Zhang C, Hamaoka T et al. (1992) Recovery from exercise-induced desaturation in the quadriceps muscles of elite competitive rowers. Am. J. Physiol. 262: C766–C775.
5. Ferreira LF, Koga S, and Barstow TJ. (2007) Dynamics of noninvasively estimated microvascular O_2 extraction during ramp exercise. J. Appl. Physiol. 103: 1999–2004.
6. Legrand R, Marles A, Prieur F et al. (2007) Related trends in locomotor and respiratory muscle oxygenation during exercise. Med. Sci. Sports. Exerc. 39: 91–100.
7. Easton PA, Slykerman LJ, and Anthonisen NR. (1986) Ventilatory response to sustained hypoxia in normal adults. J. Appl. Physiol. 61: 906–911.
8. Beaver WL, Wasserman K, and Whipp BJ. (1986) A new method for detecting anaerobic threshold by gas exchange. J. Appl. Physiol. 60: 2020–2027.
9. Hamaoka T, Iwane H, Shimomitsu T et al. (1996) Noninvasive measures of oxidative metabolism on working human muscles by near-infrared spectroscopy. J. Appl. Physiol 81: 1410–1417.
10. Lucia A, Sanchez A, Carvajal A et al. (1999) Analysis of the aerobic-anaerobic transition in elite cyclists during incremental exercise with the use of electromyography. Br. J. Sports. Med. 33: 178–185.
11. Lorenz KA, Hom C, Lopez J et al. (2006) Effects of hypoxia on the onset of muscle deoxygenation and the lactate threshold. J. Physiol. Sci. 56: 321–323.
12. DeLorey DS, Shaw CN, Shoemaker JK et al. (2004) The effect of hypoxia on pulmonary O_2 uptake, leg blood flow and muscle deoxygenation during single-leg knee-extension exercise. Exp. Physiol. 89: 293–302.
13. Heubert RA, Quaresima V, Laffite LP et al. (2005) Acute moderate hypoxia affects the oxygen desaturation and the performance but not the oxygen uptake response. Int. J. Sports. Med. 26: 542–551.

Part IV
O_2 Microenvironment in Cancer

No Sustained Improvement in Tumor Oxygenation After Localized Mild Hyperthermia

Debra K. Kelleher and Peter Vaupel

Abstract This study has attempted to address the controversy concerning sustained increases in tumor oxygenation upon localized mild hyperthermia. While some previous studies have reported transient increases, others have reported persistent increases in tumor oxygenation, lasting for upto 2 days after application of mild hyperthermia. In order to determine changes in oxygenation at clinically relevant tumor temperatures, experimental tumors in rats underwent localized hyperthermia at either 40, 41.8°C or 43°C for 1 h using water-filtered infrared-A irradiation. Oxygenation was continuously measured before, during and upto 60 min after hyperthermia in the tumors of anesthetized rats using oxygen-sensitive catheters. The data obtained indicate that localized hyperthermia can lead, on average to an improved tumor oxygenation, although this improvement is generally transient and no longer evident 1 h after heating. Since clinically relevant increases in oxygenation enduring beyond the heating period were rarely seen, it would appear that an improvement in the efficacy of oxygen-dependent cancer therapy is unlikely to be achieved in the post-hyperthermia period.

1 Introduction

Since 1980, Vaupel and colleagues have repeatedly shown that localized hyperthermia can improve tumor oxygenation [1, 2]. In these early studies, in which 42°C hyperthermia was applied for 60 min, the mean tumor pO_2 increased transiently (upon low thermal doses) but then dropped rapidly reaching values below the baseline, with a minimum being seen during a 1 h post-hyperthermia observation period. In a further study [3], 40°C hyperthermia for 30 min led to an improvement in tumor oxygenation during the whole treatment

D.K. Kelleher (✉)
Institute of Physiology and Pathophysiology, University of Mainz, 55099 Mainz, Germany
e-mail: kelleher@uni-mainz.de

E. Takahashi, D.F. Bruley (eds.), *Oxygen Transport to Tissue XXXI*, Advances in Experimental Medicine and Biology 662,
DOI 10.1007/978-1-4419-1241-1_57, © Springer Science+Business Media, LLC 2010

period. These tumor oxygenation changes were found to reflect comparable associated alterations in tumor perfusion upon heating. Later studies by other groups reported persistent improvements in the tumor oxygenation status for upto 1–2 days following mild hyperthermia [4–7]. As a result of these conflicting reports there is some controversy concerning the role of hyperthermia in treatment schedules where hyperthermia is combined with oxygen-dependent therapies such as radiotherapy, chemotherapy or radiochemotherapy, since oxygen-related sensitizing effects of hyperthermia cannot be generally understood on the basis of the available studies.

Generally, in clinical studies in which hyperthermia enhanced the efficacy of radio-/chemotherapy, tumor temperatures could generally only be raised to 40–42°C. Application of high dose hyperthermia (> 42°C) has been seen to be hardly achievable in clinical studies, so that results seen in the available preclinical studies using higher temperatures may not be relevant to the clinical setting.

This present study has attempted to address the controversy of tumor oxygenation changes during and after hyperthermia by continuously monitoring tumor oxygenation in experimental rat tumors undergoing hyperthermia at either 40, 41.8°C or 43°C.

2 Methods

Tumors were implanted subcutaneously (0.4 ml cell suspension containing approx. 10^4 cells/μl) onto the hind foot of male Sprague-Dawley rats (body weight 200–300 g). Tumors reached a volume of 0.6–2.0 ml approx. 1 week after implantation, when treatment took place. During treatment, animals were anesthetized with sodium pentobarbital (40 mg/kg, i.p., Narcoren®, Merial, Germany), laid supine on a thermostatically controlled heating pad and the rectal temperature maintained at 37.5–38.5°C. Animals breathed room air spontaneously.

Assessment of tumor tissue oxygenation was carried out polarographically using a flexible O_2-sensitive catheter electrode (ø350 μm, LICOX pO_2, GMS, Germany). Calibration of the pO_2 electrode was carried out using room air in a constant temperature chamber, taking into account the prevalent barometric pressure. Tumor pO_2 values were monitored continuously, with data being recorded 10 min prior to hyperthermia, during hyperthermia, and for 60 min thereafter.

Localized hyperthermia was performed using an infrared-A radiation source as described previously [8]. Using a feedback control system involving measurement of temperature in the tumor centre with needle-type thermocouples (ø 250 μm; type 2ABAc, Philips, Germany), tumors were heated to the target temperature (either 40, 41.8°C or 43°C) over 20 min, and then maintained at this temperature for a further 60 min. Sham-treated tumors served as controls.

Statistical analysis of the results was carried out using the Wilcoxon test for unpaired samples. The significance level in all cases was set at $\alpha = 5\%$.

3 Results

During sham treatment, tumor oxygenation remained relatively constant, with no statistically significant changes from the initial value of approx. 20 mmHg being seen. Mean values for tumors in the control group are shown in Fig. 1 where the mean effects of hyperthermia at the three different target temperatures on oxygenation are also shown. During hyperthermia, considerable inter-tumor variability in the effects on oxygenation was evident at all temperatures assessed, a phenomenon which we have also described previously [8].

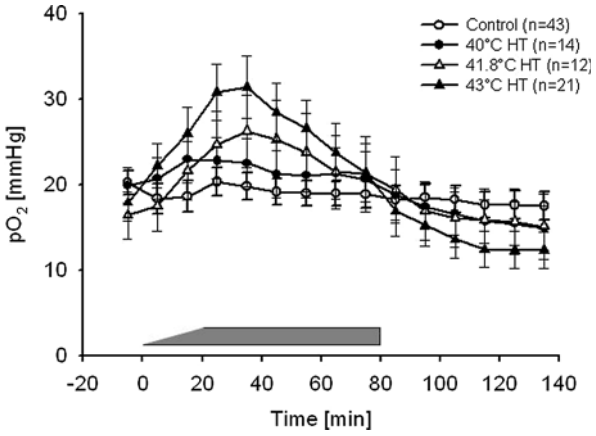

Fig. 1 Tumor pO_2 values measured continuously before, during and after 40, 41.8°C or 43°C hyperthermia. Each data point indicates the mean value (± SEM) for the number of tumors indicated. The shaded area indicates the time of heating

During the heating-up period, the mean tumor oxygenation values increased in all three temperature treatment groups. This improvement was maintained for the first 10 min of the plateau phase of the 60 min treatment period, after which the mean pO_2 value decreased slowly, returning to values comparable to those measured before commencement of the heating period by the time the heating period was completed. The extent of the increases in the tumor pO_2 is shown in Fig. 2 in which mean values before, during and after localized hyperthermia are compared and in Fig. 3 where these increases are seen to be related to the target temperature used, with the largest increases occurring at 43°C (maximum increase of approx. 16 mmHg) and progressively smaller increases at 41.8 and 40°C (maximum increases of approx. 12 and 5 mmHg, respectively). These changes in the mean oxygenation were only statistically significant during hyperthermia at 43°C. Following completion of the hyperthermia treatment, a mean temperature-dependent drop in tumor

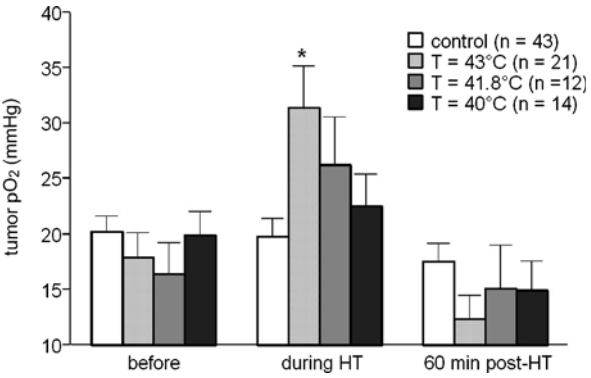

Fig. 2 Comparison of mean pO_2 values before, during (at $t = 35$ min after reaching the set temperature) and after localized hyperthermia. Each data point indicates the mean value (± SEM) for the number of tumors indicated. * = $p < 0.01$

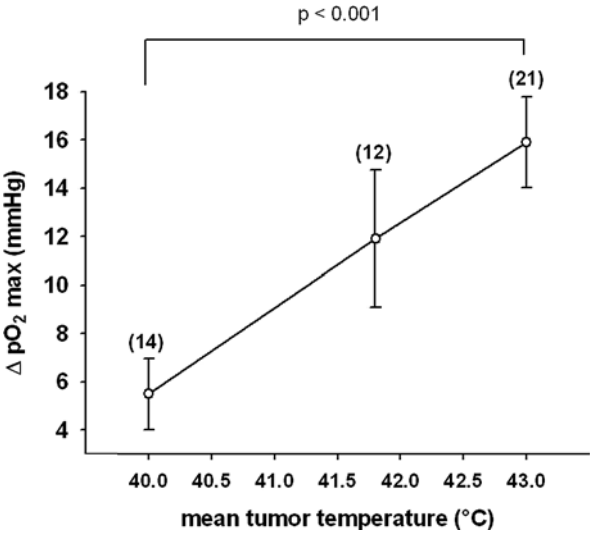

Fig. 3 Maximum pO_2 increase during hyperthermia as a function of the mean tumor temperature. Each data point indicates the mean value (± SEM) for the number of tumors indicated

oxygenation below values measured at the start of treatment was also evident, with the greatest decreases (6 mmHg) occurring in the 43°C treatment group. When oxygenation increases in individual tumors 1 h after completion of hyperthermia are considered, only 1 out of 14, 4 out of 12 and 1 out of 21 tumors undergoing hyperthermia at 40, 41.8 and 43°C respectively, were seen to show small increases in pO_2.

4 Conclusions

The investigation of changes in tumor oxygenation upon hyperthermia at three different temperatures carried out in this study showed that clinically relevant increases in pO_2 which endured beyond the actual period of heating are rarely

seen, irrespective of the tumor temperature level applied. Where improvements in tissue oxygenation were observed during hyperthermia treatment, these increases were generally transient and limited to the 60 min heating period. If these experimental results can be transferred to the clinical setting, an improvement in tumor oxygenation in the post-hyperthermia period is unlikely to be achieved and thus an improvement in the efficacy of oxygen-dependant cancer therapies, at least on the basis of an improved tumor oxygenation can not be expected. Therefore, on the basis of the results obtained in the present study, a favourable and reliable "window" for an application of a subsequent oxygen-dependent treatment modality such as radiotherapy or chemotherapy following hyperthermia does not seem to exist. Since oxygenation improvements were only – if at all – evident during the application of hyperthermia, it would appear that therapy enhancement through effects on oxygenation may only be achievable if the oxygen-dependent treatment modality is applied in the early phase of hyperthermia treatment. However, such a simultaneous treatment would be difficult to apply in the clinical setting. A similar conclusion was reached by Horsman et al. [9, 10] in studies on C3H mammary carcinomas undergoing mild hyperthermia. Improvements in oxygenation were seen, but again, only during the hyperthermia treatment period. Comparable results were obtained by Sun et al. [11] who reported improved tumor oxygenation only during and immediately after heating. In light of the decreases in oxygenation observed following 43°C hyperthermia in the present study, the application of an oxygen-dependent therapy post-hyperthermia may in fact not be advisable where high temperature hyperthermia has been applied and where decreases in oxygenation are seen. The extent of such decreases are less pronounced with hyperthermia at lower temperatures (41.8 and 40°C), so that a detrimental effect is less likely at the mild hyperthermia temperatures usually achieved in the clinical setting, but nevertheless, an improvement in the radio-/chemotherapy efficacy as a result of improved tumor oxygenation is not to be expected.

Acknowledgments This work was supported by the Dr med. h.c. Erwin Braun Foundation, Basel, Switzerland.

References

1. Vaupel P, Ostheimer K, Müller-Klieser W (1980) Circulatory and metabolic responses of malignant tumors during localized hyperthermia. J Cancer Res Clin Oncol 98:15–29
2. Vaupel P, Frinak S, Mueller-Klieser W et al. (1982) Impact of localized hyperthermia on the cellular microenvironment in solid tumors. Natl Cancer Inst Monogr 61:207–209
3. Vaupel P, Otte J, Manz R (1982) Oxygenation of malignant tumors after localized microwave hyperthermia. Radiat Environ Biophys 20:289–300
4. Song C, Park H, Griffin RJ (2001) Improvement of tumor oxygenation by mild hyperthermia. Radiat Res 155:515–528
5. Song C, Park H, Lee CK et al. (2005) Implications of increased tumor blood flow and oxygenation caused by mild temperature hyperthermia in tumor treatment. Int J Hyperthermia 21:761–767

6. Iwata K, Shakil A, Hur W-J et al. (1996) Tumour pO_2 can be increased markedly by mild hyperthermia. Br J Cancer Suppl 27:S217–S221
7. Hetzel FW, Chopp M, Dereski MO (1992) Variations in pO_2 and pH response to hyperthermia: Dependence on transplant site and duration of treatment. Radiat Res 131:152–156
8. Kelleher DK, Engel T, Vaupel PW (1995) Changes in microregional perfusion, oxygenation, ATP and lactate distribution in subcutaneous rat tumours upon water-filtered IR-A hyperthermia. Int J Hyperthermia 11:241–255
9. Horsman MR, Overgaard J (1997) Can mild hyperthermia improve tumour oxygenation? Int J Hyperthermia 13:141–147
10. Horsman MR (2006) Tissue physiology and the response to heat. Int J Hyperthermia 22:197–203
11. Sun X, Li XF, Russell J et al. (2008) Changes in tumor hypoxia induced by mild temperature hyperthermia as assessed by dual-tracer immunohistochemistry. Radiother Oncol 88:269–276

HIF-Mediated Hypoxic Response is Missing in Severely Hypoxic Uterine Leiomyomas

Arnulf Mayer, Michael Hoeckel, Angelika von Wallbrunn, Lars-Christian Horn, Alexander Wree, and Peter Vaupel

Abstract Results from our laboratory have put a question mark on the existence of a direct quantitative relationship between tumor hypoxia and HIF-mediated protein expression in cancers of the uterine cervix. In the present study, this subject has been further explored by the analysis of HIF-related marker expression in a benign tumor entity – uterine leiomyomas – using immunohistochemistry, western blotting and RT-PCR. The oxygenation status of 17 leiomyomas was assessed by means of intraoperative polarographic needle electrode measurements. Results show that these tumors are severely and uniformly hypoxic, but do not induce HIF-1α, HIF-2α, glucose transporter (GLUT)-1 or carbonic anhydrase (CA) IX. Furthermore, this downregulation of the HIF-system was not caused by an overexpression of the hypoxia-inducible prolyl hydroxylase domain proteins (PHDs) 2 and 3. Compared with normal myometrium, leiomyomas also show a poorer vascularization. Conversely, leiomyosarcomas show abundant expression of HIF-related markers despite a similar microvascular density. In conclusion, these results indicate that the strong activation of the HIF system observed in solid malignant tumors may be mechanistically linked to their transformed phenotype, rather than being a physiological reaction activated in a pathological context.

1 Introduction

Solid malignant tumors frequently contain heterogeneously distributed hypoxic tissue areas [1]. Stabilization of hypoxia-inducible factor (HIF)-1α in these microenvironments leads to the transactivation of proteins involved in angiogenesis, cell survival/proliferation, invasion and metastasis. These proteomic changes make a significant contribution to the malignant phenotype [2].

A. Mayer (✉)
Institute of Physiology and Pathophysiology, University Medical Center, Mainz, Germany
e-mail: arnmayer@uni-mainz.de

E. Takahashi, D.F. Bruley (eds.), *Oxygen Transport to Tissue XXXI*, Advances in Experimental Medicine and Biology 662,
DOI 10.1007/978-1-4419-1241-1_58, © Springer Science+Business Media, LLC 2010

However, recent data published by us and others [3, 4] disagree with a direct quantitative relationship between the extent of tumor hypoxia and hypoxia-related marker expression. This discrepancy may – at least in part – be attributable to the influence of malignancy-associated molecular changes, e.g., an inappropriate activation of growth-factor related signaling pathways. An impact of these events on the HIF-system is well-established in vitro, but their in vivo relevance is still incompletely defined. Hence, we needed to identify a benign but hypoxic tumor entity. We show here that leiomyomas, benign tumors with a very low tendency for malignant transformation, are severely and uniformly hypoxic and thus represent an ideal study system for the in vivo activity of the HIFs without the interference of malignancy-associated signaling. Although current dogma claims that activation of HIF-mediated proteome changes occur in all cell types under hypoxia, we demonstrate that the HIF-system is in fact inactive in leiomyomas.

2 Methods

Intratumoral oxygen tension (pO_2) measurements were performed with the Eppendorf histography system (Eppendorf, Hamburg, Germany) according to the standard procedure first described in 1991 [5]. This procedure was performed after informed written consent was obtained from each patient. The study was approved by the medical ethics committee of the University of Leipzig Medical Center. The pO_2 measurements in 17 premenopausal women with sporadic uterine leiomyomas were performed during surgery before any manipulation of the uterus. Furthermore, pO_2 was also assessed in the normal myometria of 6 premenopausal women who received surgery for gynecologic diseases other than leiomyoma, and in one leiomyosarcoma. Patients underwent general anesthesia, whereby the inspiratory oxygen content was reduced to 21% during the short term pO_2 measurement procedures.

Representative *tissue samples* including the electrode tracks were collected from all 17 measured leiomyomas during surgery. Expression of selected markers was also analyzed in 9 leiomyosarcomas. Among these, 8 cases were taken from archived paraffin material for which oxygenation data were not available. Both oxygenation status and marker expression were assessed in one leiomyosarcoma.

Antibodies against HIF-1α, HIF-2α, CA IX, PHD2 and PHD3 were obtained from Novus Biologicals (Littleton, CO). All other antibodies were purchased from DAKO (Glostrup, Denmark).

Immunohistochemistry (IHC) methods and *the image analysis procedure for the estimation of the intercapillary density* (ICD) have been described in detail recently [6]. PHD-2 and PHD-3 were detected using the ImmPRESS™ polymerized reporter enzyme staining system from Vector Laboratories (Burlingame, CA).

Western blotting: 25 μg of lysates of MCF-7 breast cancer cells (positive control) or cryospecimens of leiomyomas/normal myometrium were separated by SDS-PAGE and electroblotted to PVDF membranes. The primary antibody against HIF-1α was detected using a goat anti-rabbit secondary antibody conjugated to horseradish peroxidase (Santa Cruz Biotechnology, CA). Bands were developed using ECL (GE Healthcare) and images were captured with a CDD camera (LAS-3000, Fujifilm, Japan).

Real-time polymerase chain reaction was performed using SYBR green I dye with ROX according to the manufacturer's protocol (ABgene, Thermo Fisher Scientific, Hamburg, Germany) in a total volume of 25 μl. Real-time PCR was conducted on an ABI7300 system using the following parameters: denaturing at 95°C for 15 s, 40 cycles at 95°C for 15 s and at 60°C for 1 min. Beta-actin was used as an internal control and each assay included probes and calibration samples in triplicate. Data analysis was carried out using ABI data analysis software. To control the specificity of amplification products, primer inhibition plots and melting curve analyses were performed. Primer efficiencies were found to be above 90% in all cases and inspection of dissociation curves confirmed negligible levels of primer self-hybridization. Data analysis was carried out using the $2^{-\Delta\Delta Ct}$ method with ABI data analysis software. Data are presented as the n-fold change (RQ) in gene expression normalized to an endogenous reference gene (β-actin) and relative to the untreated control (normoxic MCF-7 cells). For details of the method see [7].

3 Results

In 17 leiomyomas, a grand median pO_2 of 1 mmHg (range 0–5 mmHg) was found. Individual oxygen partial pressures within each tumor varied between 1 and 50 mmHg. Fifty percent of these benign tumors had a range of pO_2 values of less than 6 mmHg. The median pO_2 of the leiomyosarcoma was 2 mmHg. For normal myometria, the grand median pO_2 was 9 mmHg (range 5–20 mmHg), which was significantly higher than that of the leiomyomas ($p < 0.0001$). A comparison of the distribution of the pO_2 values of normal myometrium ($n = 6$) and leiomyomas ($n = 17$) showed that only 4% of the measurements were found in the lowest class (0–2.5 mmHg) in the normal myometrium, whereas ≈73% of the readings in leiomyomas were in this category indicating very severe hypoxia.

Modal ICD was assessed in 15 out of 17 leiomyomas and ranged from 43 to 158 μm. Significantly higher median pO_2 values ($p = 0.006$) were found in tumors with a modal ICD below the median (86 μm). ICD values in 9 leiomyosarcomas ranged from 61 to 283 μm (median 68 μm). The median value of the modal ICD in normal myometrium was 42 μm (range 29–62 μm), i.e., significantly smaller than in the leiomyomas ($p = 0.0001$) and leiomyosarcomas ($p = 0.0001$).

Immunohistochemistry for HIF-1α/-2α, CA IX and GLUT-1 was performed in the leiomyomas, leiomyosarcomas and normal myometria. All 17 leiomyomas and all normal myometria were negative for HIF-1α and HIF-2α as well as for CA IX and GLUT-1. Additionally, PHD-2/-3 expression was assessed in 17 leiomyomas. Expression of PHD-2 was absent from the vast majority of cells. Only in some cases, a few smooth muscle cells scattered throughout the tumors were positive and a weak cytoplasmic expression was also observed in endothelial cells. PHD-3 expression in leiomyomas was limited to a weak cytoplasmic signal.

Absence of HIF-1α expression in leiomyomas was confirmed by western blotting of protein extracts from cryospecimens of 3 leiomyomas and 3 normal myometria (Fig. 1, panel a). Positive control MCF-7 cells showed low HIF-1α

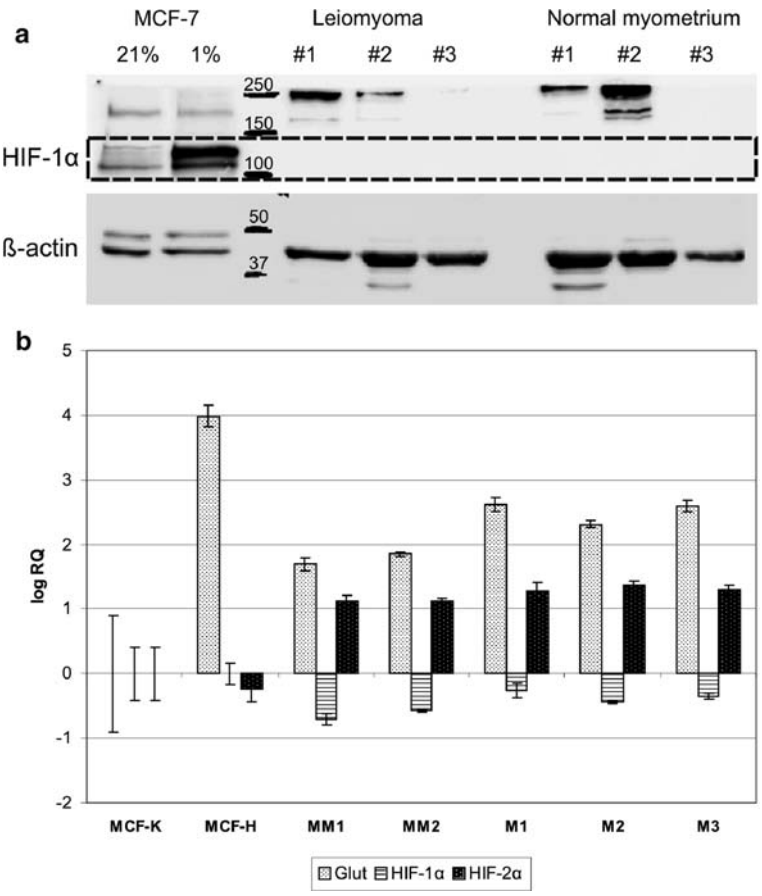

Fig. 1 (**a**) Analysis of HIF-1α expression in normoxic (21% O_2) and hypoxic (1% O_2) MCF-7 cells and cryospecimens of leiomyoma and normal myometrium by western blotting (*upper panel*). β-actin was used as a loading control (*lower panel*). (**b**) Quantification of GLUT-1, HIF-1α and HIF-2α mRNA by RT-PCR in hypoxic (MCF-H) MCF-7 cells, normal myometrium (MM) and leiomyomas (M) relative to normoxic (MCF-K) MCF-7 cells

expression under normoxia and a strong induction under hypoxic conditions (1% O_2 for 24 h). Very low levels of HIF-2α were detectable in hypoxic MCF-7 cells, while the protein was undetectable in leiomyomas and normal myometria.

RT-PCR showed similar HIF-1α levels in MCF-7 cells, leiomyomas and normal myometria. Levels of HIF-2α mRNA were slightly higher in the tissue extracts than in MCF-7 cells. As expected, a strong induction of GLUT-1 could be demonstrated in hypoxic MCF-7 cells (Fig. 1, panel b). Surprisingly, GLUT-1 expression was detected in leiomyomas and normal myometrium, conflicting with the complete absence of GLUT-1 expression at the protein level.

4 Conclusions

Benign uterine leiomyomas exhibit extremely low pO_2 values. Despite this severe hypoxia, markers of the hypoxic response (HIF-1α/HIF-2α, GLUT-1 and CA IX) were completely absent on the proteome level. Bands seen at a molecular weight = 250 kD in the HIF-1α western blot are too large to represent tissue specific isoforms. They most certainly represent unspecific binding of the primary antibody in the tissue extracts. In contrast, hypoxia-associated markers were found to be abundantly expressed in leiomyosarcomas. These findings are in agreement with those of an earlier study by Zhong et al. [8], who showed the absence of HIF-1α expression in 12 benign tumor specimens. Likewise, Younes et al. [9] assessed the expression of GLUT-1 in a wide array of normal (and cancerous) tissues and found leiomyomas, as well as several other benign tumor entities, to be negative. To our knowledge, the expression of CA IX or HIF-2α has previously not been investigated in leiomyomas. Expression of HIF-1α has, however, been demonstrated in leiomyomas from patients with the rare syndrome of hereditary leiomyoma and renal cell cancer (HLRCC, [10]). The pathogenetic basis of this disease is an inactivating mutation of the enzyme fumarate hydratase, which leads to accumulation of fumarate. This metabolite inhibits prolyl hydroxylases and consequently leads to HIF-1α stabilization secondary to decreased proteasomal degradation [11].

The RT-PCR results of our study show that the downregulation of the HIF-system in leiomyomas does not take place at the mRNA level. HIF-1α mRNA in leiomyoma tissue was only slightly lower than in MCF-7 cells. HIF-2α mRNA was even elevated in leiomyomas although the protein was clearly not detectable by western blotting or IHC. GLUT-1 mRNA abundance in leiomyomas was low compared to hypoxic MCF-7 cells but higher than in the normoxic breast cancer cells. Again, the absence of GLUT-1 protein expression, as assessed by IHC, is unequivocal.

Since prolyl hydroxylase domain-containing proteins (PHDs) -2 and -3, which initiate proteasomal HIF-degradation, are themselves hypoxia-inducible genes [12], we considered an overexpression of PHDs as a possible explanation for the absence of HIF-1α/-2α expression in chronically hypoxic leiomyomas.

According to Stiehl et al. [13], PHD-2 and PHD-3 levels may remain elevated even after downregulating endogenous HIF-1α. However, IHC showed that protein levels of PHD-2 and -3 are generally very low in leiomyomas, a finding that is not compatible with a generalized suppression of HIFs by accelerated PHD-mediated proteasomal degradation.

Oxygenation data were only available for one leiomyosarcoma, which was hypoxic. While our study found a significantly lower vascularization in leiomyomas compared with normal myometrium, no such difference existed between leiomyomas and leiomyosarcomas. These results indicate that the microenvironmental conditions in leiomyoma vs. leiomyosarcoma are too similar to explain the striking differences regarding the activity of the HIF-system. This was unexpected since the induction of HIF-1α and its target genes is generally perceived as being a physiological reaction to hypoxia, occurring independently of malignant transformation. Since our data neither support downregulation of the HIF-system at the mRNA level nor increased PHD-mediated proteasomal degradation, we may have to consider translational control as a candidate mechanism for the explanation of our findings. Indeed, a recent study pointed towards a significant impact of the mammalian target of rapamycin (mTOR) – a central regulator of mRNA translation – on the activity of the HIF-system [14]. Importantly, mTOR activity may be inhibited by hypoxia and other kinds of microenvironmental deficiencies. The inhibition of mTOR by hypoxia may be at least partially independent of HIF-1α [15]. It is conceivable – and compatible with the data presented in this study – that the HIF-system may be downregulated secondary to mTOR inhibition in certain (normal or benign) tissues. Conversely, upregulation of a variety of components of the mTOR signaling network are a hallmark of malignancy. Further studies are required to assess the relevance of these mechanisms.

Acknowledgments This work was supported by grant 106758 from Deutsche Krebshilfe. We thank Dr. Debra Kelleher for her excellent editorial assistance.

References

1. Vaupel P, Höckel M, Mayer A (2007) Detection and characterization of tumor hypoxia using pO_2 histography. Antioxid Redox Signal 9:1221–1235
2. Semenza GL (2003) Targeting HIF-1 for cancer therapy. Nat Rev Cancer 3:721–732
3. Mayer A, Wree A, Höckel M, et al. (2004) Lack of correlation between expression of HIF-1α protein and oxygenation status in identical tissue areas of squamous cell carcinomas of the uterine cervix. Cancer Res 64:5876–5881
4. Jankovic B, Aquino-Parsons C, Raleigh JA, et al. (2006) Comparison between pimonidazole binding, oxygen electrode measurements, and expression of endogenous hypoxia markers in cancer of the uterine cervix. Cytometry B Clin Cytom 70:45–55
5. Höckel M, Schlenger K, Knoop C, et al. (1991) Oxygenation of carcinomas of the uterine cervix: evaluation by computerized O_2 tension measurements. Cancer Res 51:6098–6102

6. Mayer A, Höckel M, Wree A, et al. (2008) Lack of hypoxic response in uterine leiomyomas despite severe tissue hypoxia. Cancer Res 68:4719–4726
7. Livak KJ, Schmittgen TD (2001) Analysis of relative gene expression data using real-time quantitative PCR and the $2^{-\Delta\Delta Ct}$ Method. Methods 25:402–408
8. Zhong H, De Marzo AM, Laughner E, et al. (1999) Overexpression of hypoxia-inducible factor 1a in common human cancers and their metastases. Cancer Res 59:5830–5835
9. Younes M, Lechago LV, Somoano JR, et al. (1996) Wide expression of the human erythrocyte glucose transporter Glut1 in human cancers. Cancer Res 56:1164–1167
10. Pollard PJ, Briere JJ, Alam NA, et al. (2005) Accumulation of Krebs cycle intermediates and over-expression of HIF1α in tumours which result from germline FH and SDH mutations. Hum Mol Genet 14:2231–2239
11. Isaacs JS, Jung YJ, Mole DR, et al. (2005) HIF overexpression correlates with biallelic loss of fumarate hydratase in renal cancer: novel role of fumarate in regulation of HIF stability. Cancer Cell 8:143–153
12. Marxsen JH, Stengel P, Doege K, et al. (2004) Hypoxia-inducible factor-1 (HIF-1) promotes its degradation by induction of HIF-a-prolyl-4-hydroxylases. Biochem J 381:761–767
13. Stiehl DP, Wirthner R, Koditz J, et al. (2006) Increased prolyl 4-hydroxylase domain proteins compensate for decreased oxygen levels. Evidence for an autoregulatory oxygen-sensing system. J Biol Chem 281:23482–23491
14. Land SC, Tee AR (2007) Hypoxia-inducible factor 1alpha is regulated by the mammalian target of rapamycin (mTOR) via an mTOR signaling motif. J Biol Chem 282:20534–20543
15. Arsham AM, Howell JJ, Simon MC (2003) A novel hypoxia-inducible factor-independent hypoxic response regulating mammalian target of rapamycin and its targets. J Biol Chem 278:29655–29660

FRET-Like Fluorophore-Nanoparticle Complex for Highly Specific Cancer Localization

Jianting Wang, Michael H. Nantz, Samuel Achilefu, and Kyung A. Kang

Abstract Fluorophore mediated bio-signal retrieval has been extensively used in molecular imaging. However, only a limited number of fluorophores can be used for humans and their quantum yield is usually low. Another important issue is emitting fluorescence at the disease site, with a minimal non-specific emission at any other sites. Artificial quenching and enhancing of fluorescence was found to be possible by manipulating the distance between a fluorophore and a certain type of nanometal particle. Utilizing this unique property, we have designed a novel, FRET-like, fluorophore-nanoparticle complex. The complex emits fluorescence conditionally only at a disease site at an enhanced level. As a model system, our complex is designed to target breast cancer. As an initial step for developing this cancer locator, fluorescence alteration was studied when a spacer at various lengths is placed between a nanogold particle and a safe fluorophore.

1 Introduction

Fluoropohore mediated, molecular imaging is highly beneficial for understanding mechanisms of various biomolecular functions. For in vivo bioimaging, such as cancer detection or diagnosis, the fluorohpore must be non-toxic. Fluorophores with excitation and emission in a near infrared (NIR) range have advantages over those in a visible range. They can be better differentiated from the naturally occurring fluorescence in tissue and NIR penetrates deeper into tissue [1, 2]. Fluorophores with high quantum yield is highly desirable, especially for detecting small and/or deeply seated tumors. In order for a molecular imaging to be highly effective, the fluorescence contrast should be maximized at the tumor site, with a minimal non-specific emission. A smart

J. Wang (✉)
Department of Chemical Engineering, University of Louisville,
Louisville, KY 40292, USA
e-mail: j0wang21@louisville.edu

E. Takahashi, D.F. Bruley (eds.), *Oxygen Transport to Tissue XXXI*,
Advances in Experimental Medicine and Biology 662,
DOI 10.1007/978-1-4419-1241-1_59, © Springer Science+Business Media, LLC 2010

approach is, therefore, using an entity with conditional emission, similar to Förster resonance energy transfer (FRET).

Since fluorophores emit fluorescence when their electrons are excited by photons, their fluorescence may be altered when they are placed within a strong surface plasmon polarion field (SPPF) of nano sized metal particles (NMPs). Gold, silver, and platinum are exemplary metals possessing strong SPPF [3]. When the NMP's electrons couple with excited electrons of a fluorophore, an instantaneous electron attraction occurs, altering the energy states of the electrons involved in fluorescence emission. The level of this alteration depends upon the strength of the SPPF where the fluorophore is placed, and the field strength depends upon the metal type, NMP size, and distance from the NMP surface [4, 5, 6, 7, 8]. If a fluorophore is placed within a very strong SPPF, most electrons of the fluorophore, including the ones for fluorescence emission, are attracted to the NMP, resulting in fluorescence quenching. If the fluorophore is at a particular distance from the NMP, and attracts the electrons participating in self-quenching, then the fluorescence is enhanced.

This interesting property of NMPs on a fluorophore can be effectively utilized for artificial fluorescence alternation. Utilizing nanogold particles (NGPs), we are currently developing a FRET-like, highly breast cancer specific, fluorescent contrast agent. The design of this novel agent is as follows: the NGP surface is treated with hydrophilic bio-polymer, and conjugated with cancer targeting molecules. The fluorescence of the fluorophore is manipulated by placing double spacers (one long and one short) between the fluorophore and NGP, and it is specially designed to be conditionally emitted only at a particular tumor site, at an enhanced fluorescence level.

Indocyanine Green (ICG, MW 775) is one of a few FDA-approved fluorophores. Its excitation and emission peaks are at 780 and 830 nm (both in NIR), respectively. Its quantum yield (QY) is only 0.0028 in the saline buffer and 0.012 in blood [9]. ICG does not have functional group for conjugation. Achilefu's group has developed an ICG derivative, Cypate, with two carboxylic acid groups [10].

As an initial step for developing this novel cancer locator, quenching and enhancement of Cypate fluorescence by NGPs were studied, and the result is presented here.

2 Materials, Instruments and Methods

Nanogold colloids (NGPs; 5 and 10 nm in citric and tannic acids) and Protein A conjugated NGP (NGP-PA) were from Ted Pella (Redding, CA, USA). L-glutathione (LG; Sigma/Aldrich; St. Louis, MO, USA) was immobilized on the NGP surface by the protocol developed by our research group [7, 8].

Cypate was covalently immobilized on the surface of the NGPs via LG (NGP-LG) or PA (NGP-PA) using the protocol established by our group [6].

N,N' Dicyclohexylcarbodiimide (DCC; Sigma) was used to catalyze the reaction. First, dissolve Cypate and DCC separately in a minimal amount of ethanol (< 50 μl). Mix the Cypate and DCC solutions at a molar ratio of 1:12, and immediately transfer them to NGP-LG or NGP-PA solution. Stir the mixture of Cypate and NGP-LG at room temperature for 30 min. For Cypate and NGP-PA, stir at 4°C for 5 h.

All samples (Cypate with and without NGP) were in a 0.001 M PBS, and Cypate concentration was 30 μM, at which Cypate has maxium fluorescence [11]. Fluorescence of samples was measured in 96-well EIA/RIA plate (Corning, New York, USA) using a fluorometer (Spectra Gemini XPS; Molecular Devices Corp.; Sunnyvale, CA, USA). The excitation and emission wavelengths used in our study were 780 and 830 nm, respectively.

3 Results and Discussion

3.1 Free Cypate Fluorescence by Free NGP Colloids

First, the fluorescence alteration of free Cypate by free NGPs (surfactant, tannic acid, MW = 1516) by NGPs was studied. This study result may be valuable also for fluorophore mediated biosensing [6, 7, 8] 5 and 10 nm NGPs at a weight (wt) concentration range of 0∼60 μg/ml were applied to 30 μM Cypate solution, and the fluorescence was observed (Fig. 1). It should be noted that NGP molar concentration in this range is much less than Cypate concentration (30 μM), i.e., NGP concentration is the limiting condition.

As can be seen in the figure, for both NGP sizes, at concentrations greater than 6 μg/ml, the fluorescence was quenched, and the quenching level increased with the increase in NGP concentration. At the same wt concentration, 5 nm NGPs showed greater quenching than those at 10 nm, probably because the

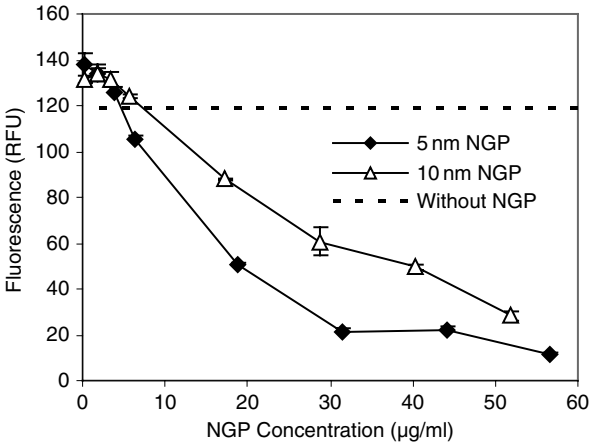

Fig. 1 Fluorescence of free Cypate with various concentrations of free NGP

number of 5 nm NGPs is 8 times greater than that of 10 nm NGP, and the total surface area is about 2 times larger. Also, due to its smaller size, 5 nm NGPs should have much great mobility than that of 10 nm, resulting in greater probability for Cypate to be near the NGP.

At very low concentrations (< 6 μg/ml), the NGPs enhanced the fluorescence. This phenomenon may be explained by Fig. 2. For free NGPs and fluorophores, when the fluorophore concentration is fixed, the distances between NGP and fluorophore is determined by NGP concentration. Cypate is negatively charged in 0.001 M PBS. NGPs are positively charged and negatively charged citric and, therefore, tannic acid ions are adsorbed on their surface. At a higher NGP concentration [Fig. 2(a)-three NGPs], the distance between NGP and Cypate is shorter and, thus, more Cypate molecules are near the NGP surface, resulting in more fluorescence quenching. When the NGP concentration is very low [Fig. 2(b)-one NGP], the average distance between Cypate and NGP is longer, and the fluorescnece is either slightly enhanced or unaffected.

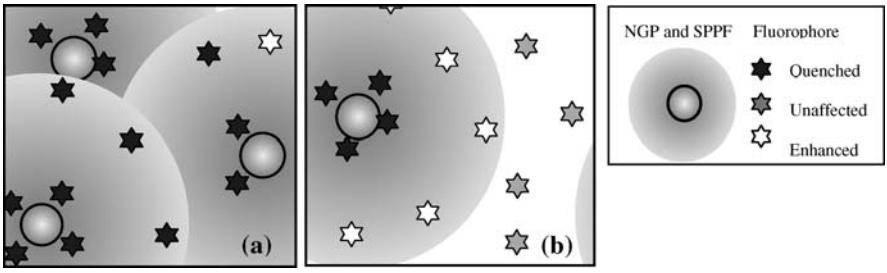

Fig. 2 Schematic diagram for fluorescence of free Cypate with (**a**) high and (**b**) low NGP concentration in solution

3.2 Fluorescence Change by NGP-Short Spacer

The next was to study the fluorescence when Cypate was conjugated onto NGP surface (e.g. in bioimaging). LG (MW = 307) was used as the short spacer, and its length was previously estimated to be 1 nm by our group [7, 8]. The fluorescence was observed when Cypate was conjugated to 5 and 10 nm NGPs via LG, at an NGP concentration range of 0∼60 μg/ml (Fig. 3).

At all concentrations, the fluorescence decreased. In general, for higher concentration of NGP, more fluorescence was quenched. At the same wt concentration, 5 nm NGPs have binding sites (LG molecule numbers) twice that of 10 nm NGPs. However, they quenched fluorescence less, probably because of the difference in SPPF strength for the different NGP size (i.e., higher field strength for a larger particle size).

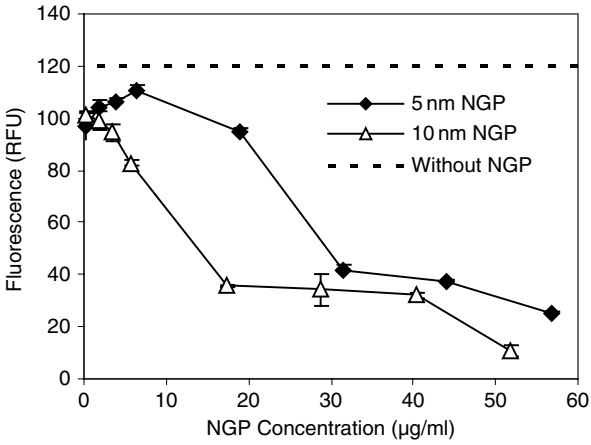

Fig. 3 Cypate fluorescence when Cypate was conjugated to NGP-LG at various concentrations

For 5 nm NGPs, at a very low concentration (< 6 μg/ml), the quenching effect did not increase with the increase in NGP concentration, probably because only a portion of Cypate was conjugated to NGPs and most of Cypate was present in a free form in the solution.

3.3 Fluorescence Change by NGP-Longer Spacer

To study the fluorescence change by NGP with a longer spacer, Protein A (PA; MW 40∼60 kD) was used as the spacer (Fig. 4). Since PA is a globular protein and we did not know how the protein is conjugated on the NGP surface, it was difficult to estimate its length as a spacer, although one of our simulation results estimates it to be approximately 5 nm (not published). The ratios of PA to NGP

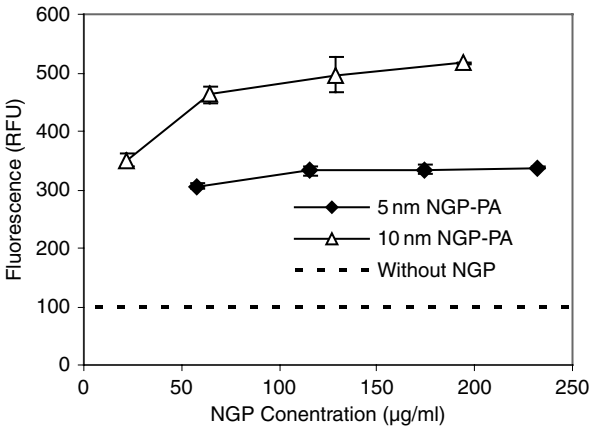

Fig. 4 Cypate fluorescence when Cypate was conjugated to NGP-PA at various concentrations

were 4:1 and 16:1 for 5 and 10 nm NGPs, respectively. NGPs at a concentration range of 20∼250 μg/ml were applied to Cypate solution (Fig. 4).

The fluorescence of Cypate was enhanced extensively by both 5 and 10 nm NGPs. The enhancement was greater for a higher NGP concentration, especially for 10 nm NGPs. At the same weight concentration range, a 5 nm NGP has binding sites (PA molecule numbers) 2 times more than a 10 nm NGP does. However, it enhances fluorescence less than 10 nm NPG does, confirming the difference in the SPPF strength for different sized particles.

4 Conclusions

Utilizing the SPPF of NMPs, artificial fluorescence alteration of Cypate (NIR fluorophore) was achieved. With manipulating the distance between an NGP and a fluorophore by placing a molecular spacer between them, upto 90% percent of fluorescence quenching and 500% of enhancement were achieved. The level of quenching and enhancement are currently being optimized to develop a novel, FRET-like, fluorophore-nanoparticle complex for higly specific breast cancer localization.

Acknowledgments Authors acknowledge U.S. Army (DoD) Breast Cancer Program (BC074387) for the financial support.

References

1. Sevick EM, Frisoli JK, Burch CL, Lakowicz JR (1997) Localization of absorbers in scattering media by the use of frequency-domain measurements of time-dependent photon migration. Acd Sci USA 94:6468–6473.
2. Natziachriostos V, Chance B (2001) Breast imaging technology: Probing physiology and molecular function using optical imaging – applications to breast cancer. Breast Cancer Res 3:41–46.
3. Hranisavljevic J, Dimitrijevic NM, Wurtz GA, Wiederrecht GP (2002) Photoinduced charge separation reactions of J-aggregates coated on silver nanoparticles. J Am Chem Soc 124:4536–4537.
4. Ruppin R (1975) Optical properties of small metal spheres. Phys Rev B 11(8):2871–2876.
5. Geddes CD, Cao H, Lakowicz JR (2003) Enhanced photostability of ICG in close proximity to gold colloids. Spectrochim Acta A: Mol Biomol Spectrosc 59:2611–2617.
6. Kang KA, Hong B (2006) Biocompatible nano-metal particle fluorescence enhancers. Crit Rev Eukaryot Gene Expr 16(1):45–60.
7. Hong B, Kang KA (2006) Fluorescence enhancers for fluorophore mediated biosensors for cardiovascular disease diagnosis. Adv Exp Med Biol 578:179–184.
8. Hong B, Kang KA (2006) Biocompatible, nanogold-particle fluorescence enhancer for fluorophore mediated, optical immunosensor. Biosens Bioelectron 21(7):1333–1338.
9. Licha K, Riefke R, Ntziachristos V, Becker A, Chance B, Semmler W (2000) Hydrophilic cyanine dyes as contrast agents for near-infrared tumor imaging: Synthesis, photophysical properties and spectroscopic in vivo characterization. Photochem Photobiol 72:392–398.

10. Achilefu S, Dorshow RB, Bugaj JE, Rajagopalan R (2000) Novel receptor-targeted fluorescent contrast agents for in vivo tumor imaging. Invest Radiol 35:479–485.
11. Hong B (2006) Nanometal particle reagents for sensitive, MEMS based fiber-optic, multi-analyte, immuno-biosensing, Dissertation, Chemical Engineering, University of Louisville, Louisville, KY, USA.

Design of Novel Hypoxia-Targeting IDO Hybrid Inhibitors Conjugated with an Unsubstituted L-TRP as an IDO Affinity Moiety

Hitomi Nakashima, Kazuhiro Ikkyu, Kouichiro Nakashima, Keiichiro Sano, Yoshihiro Uto, Eiji Nakata, Hideko Nagasawa, Hiroshi Sugimoto, Yoshitsugu Shiro, Yoshinori Nakagawa, and Hitoshi Hori

Abstract We presented here design, syntheses and inhibitory activities of novel hypoxia-targeting IDO hybrid inhibitors conjugated with an unsubstituted L-Trp as an IDO affinity moiety without inhibitor 1MT, such as L-Trp-TPZ hybrids **1** (TX-2274), **2** (UTX-3), **3** (UTX-4), and **4** (UTX-2). TPZ-monoxide hybrids **1** and **3** were good competitive IDO inhibitors, while TPZ hybrids **2** and **4** were uncompetitive IDO inhibitors. Among them TPZ-monoxide hybrid **1** have the strongest IDO inhibitory activity. It suggests that TPZ-monoxide hybrids **1** and **3** are able to bind the active site of IDO, TPZ hybrids **2** and **4** are able to bind the enzyme-substrate complex. We proposed the possible mechanism of action of TPZ hybrid **2** that may first affect as a hypoxic cytotoxin, and then metabolized to TPZ-monoxide hybrid **1**, which may do as an IDO inhibitor more effectively than its parent TPZ hybrid **2**.

1 Introduction

Indoleamine 2,3-dioxygenase (IDO) catalyzes the initial and rate limiting step of L-tryptophan (L-Trp) catabolism in the kynurenine pathway [1]. IDO is expressed in many neoplasms, and plays a role in immunosuppression [2, 3]. IDO is activated only in reductive or hypoxic conditions, because the heme iron of the active site is easily oxidized to its inactive form [4]. Hypoxic neoplastic cells indicate chemo- and radioresistances and also cause neoplasm' progression, invasion and metastasis [5]. Previously we focused on the mode of activation of IDO only in hypoxic and reductive conditions to design hypoxia-targeting IDO hybrid inhibitors, which constituted an IDO inhibitor 1-methyl-L-tryptophan (1MT) and hypoxic cytotoxin tirapazamine (TPZ) [6], such as TX-2236, TX-2235, TX-2228 and TX-2234 [7]. They were good hypoxia-targeting IDO inhibitors. 1MT-TPZ hybrids inhibited IDO uncompetitively. Thus, it suggests that

H. Hori (✉)
Department of Life System, Institute of Technology and Science, Graduate School, The University of Tokushima, Tokushima, 770-8506, Japan
e-mail: hori@bio.tokushima-u.ac.jp

E. Takahashi, D.F. Bruley (eds.), *Oxygen Transport to Tissue XXXI*, Advances in Experimental Medicine and Biology 662,
DOI 10.1007/978-1-4419-1241-1_60, © Springer Science+Business Media, LLC 2010

1MT-TPZ hybrids were able to bind the only enzyme-substrate complex, not to bind the active site. We presented here design, syntheses and inhibitory activities of novel hypoxia-targeting IDO hybrid inhibitors conjugated with an unsubstituted L-Trp as an IDO affinity moiety such as L-Trp-TPZ hybrids **1** (TX-2274), **2** (UTX-3), **3** (UTX-4), and **4** (UTX-2).

2 Materials and Methods

2.1 Syntheses of L-Trp-TPZ Hybrids

Syntheses were done in our laboratory as previously described [7]. All chemicals were of a reagent grade and commercially available. Melting points were determined on a Yanaco melting point apparatus (M.P.- J 3 model). ^{1}H NMR spectra were obtained on a JEOL JNM-EX400 spectrometer at 400 MHz. IR spectra were measured in KBr pellets on a Perkin-Elmer spectrum RX1-T1 spectrometer. Fast atom bombardment mass spectra (FABMS) and high-resolution mass spectra (FABHRMS) were measured on a JEOL JMS-DX-303 instrument. Elemental analyses were performed with a Yanaco CHN Corder (MT-5).

*[4-(1-oxido-1,2,4-benzotriazin-3-yl)aminobutyl]-(2S)-N-tert-butoxycarbonyl-2-amino-indole-3-yl-propanamide (**1**; TX-2274)*. Boc-L-Trp **6** (13 mg, 0.04 mmol) and HOBt (7 mg, 0.05 mmol) and amine **8** (10 mg, 0.04 mmol) were dried in vacuo for 30 min. After CH_2Cl_2 (3 mL) was added to the reaction mixture, DIPCDI (7 μL, 0.05 mmol) was added and the reaction mixture was stirred at room temperature for 25 h. The solvent was evaporated and the residue was purified by column chromatography by eluting with a gradient of 75% EtOAc/hexane to 10% MeOH/EtOAc gave **1** (17.4 mg, 78%) as a yellow powder: mp 181–184 °C; ^{1}H NMR ($CDCl_3$) δ 8.27 (d, J = 8.9 Hz, 1H, 8-H), 7.84 (d, J = 8.5 Hz, 1H, 7-H), 7.76 (d, J = 8.1 Hz, 1H, Ar), 7.70 (ddd, J = 8.5, 7.0, 1.4 Hz, 1H, 6-H), 7.64 (d, J = 7.8 Hz, 1H, Ar), 7.61 (d, J = 8.1 Hz, 1H, Ar), 7.15 (t, J = 7.8 Hz, 1H, 5-H), 7.06–7.10 (m, 2H, Ar), 3.07–3.37 (m, 4H, $CH_2 \times 2$), 1.42 (s, 9H, *t*-Bu), 1.27–1.32 (m, 4H, $CH_2 \times 2$), 1.29 (d, J = 6.34 Hz, 2H, CH_2); IR (KBr) 3308, 2934, 1684, 1643, 1572, 1495, 1414, 1360, 1170, 761 cm^{-1}; HRMS (FAB$^+$) calcd for $C_{27}H_{33}N_7O_4$ $(M+H)^+$ m/z 520.2665. Found 520.2673; Anal. Calcd for $C_{27}H_{33}N_7O_4$: C, 62.41; H, 6.40; N, 18.87. Found: C, 62.54; H, 6.66; N, 19.09.

*[4-(1,4-dioxido-1,2,4-benzotriazin-3-yl)aminobutyl]-(2S)-N-tert-butoxycarbonyl-2-amino-indole-3-yl-propanamide (**2**; UTX-3)*. Boc-L-Trp **6** (45 mg, 0.15 mmol) and HOBt (25 mg, 0.17 mmol) and **14** (53 mg, 0.15 mmol) were dried in vacuo for 30 min. After CH_2Cl_2 (5 mL) was added to the reaction mixture, DIPCDI (26 μL, 0.19 mmol) and DIEA (78 μL, 0.45 mmol) were added and the reaction mixture was stirred at room temperature for 24 h. The solvent was evaporated and the residue was purified by column chromatography by eluting with a gradient (0–10%) of MeOH/EtOAc gave **3** (48.8 mg, 61%) as a red powder: mp 159–162 °C; ^{1}H NMR ($CDCl_3$) δ 8.34 (d, J = 8.5 Hz, 1H, 8-H),

8.27 (d, $J = 8.0$ Hz, 1H, 5-H), 7.91 (t, $J = 7.2$ Hz, 1H, 7-H), 7.54 (d, $J = 7.4$ Hz, 1H, 6-H), 7.32–7.42 (m, 2H, Ar), 7.18 (s, 1H, Ar), 7.05–7.07 (m, 2H, Ar), 3.05–3.49 (m, 4H, $CH_2 \times 2$), 1.43 (s, 9H, *t*-Bu), 0.88–1.26 (m, 4H, $CH_2 \times 3$); IR (KBr) 3349, 2930, 1680, 1657, 1594, 1526, 1414, 1367, 1181, 768 cm^{-1}; HRMS (FAB^+) calcd for $C_{27}H_{33}N_7O_5$ $(M + H)^+$ *m/z* 536.2614. Found 536.2660.

*[5-(1-oxido-1,2,4-benzotriazin-3-yl)aminopentyl]-(2S)-N-tert-butoxycarbonyl-2-amino-indole-3-yl-propanamide (**3**; UTX-4)*. Reaction of **6** and **9** in the presence of HOBt, stirred for 3 h gave **3** (84 mg, 87%) as a yellow powder: mp 175–179°C; ^1H NMR ($CDCl_3$) δ 8.28 (d, $J = 8.5$ Hz, 1H, 8-H), 7.72 (d, $J = 7.8$ Hz, 1H, Ar), 7.68 (t, $J = 8.4$ Hz, 1H, 6-H), 7.61 (d, $J = 8.0$ Hz, 1H, 5-H), 7.41 (d, $J = 7.8$ Hz, 1H, Ar), 7.30 (t, $J = 7.2$ Hz, 1H, 7-H), 7.10–7.19 (m, 3H, Ar), 3.35–3.44 (m, 2H, CH_2), 3.23–3.35 (m, 2H, CH_2), 1.53–1.64 (m, 6H, $CH_2 \times 3$), 1.48 (s, 9H, *t*-Bu), 1.24–1.28 (m, 2H, CH_2); IR (KBr) 3342, 2934, 1683, 1656, 1572, 1496, 1419, 1358, 1170, 758 cm^{-1}; HRMS (FAB^+) calcd for $C_{28}H_{35}N_7O_4$ $(M+H)^+$ *m/z* 534.2817. Found 534.2829; Anal. Calcd for $C_{28}H_{35}N_7O_4$: C, 63.02; H, 6.61; N, 18.37. Found: C, 63.39; H, 6.71; N, 18.24.

*[5-(1,4-dioxido-1,2,4-benzotriazin-3-yl)aminopentyl]-(2S)-N-tertbutoxycarbonyl- 2-amino-indole-3-yl-propanamide (**4**; UTX-2)*. Reaction of **6** and **15** in the presence of HOBt and DIEA, stirred for 23 h gave **4** (106.6 mg, 92%) as a red powder: mp 201–203°C; ^1H NMR ($CDCl_3$) δ 8.36 (d, $J = 9.0$ Hz, 1H, 8-H), 8.33 (d, $J = 8.8$ Hz, 1H, 5-H), 7.91 (t, $J = 7.9$ Hz, 1H, 7-H), 7.69 (d, $J = 7.3$ Hz, 1H, Ar), 7.53 (t, $J = 7.7$ Hz, 1H, 6-H), 7.39 (d, $J = 7.4$ Hz, 1H, Ar), 7.07–7.19 (m, 3H, Ar), 3.49–3.51 (m, 2H, CH_2), 3.32–3.37 (m, 1H, CH), 3.06–3.17 (m, 2H, CH_2), 1.50–1.62 (m, 6H, $CH_2 \times 3$), 1.43 (s, 9H, *t*-Bu), 1.05–1.20 (m, 2H, CH_2); IR (KBr) 3346, 2934, 1678, 1657, 1600, 1498, 1415, 1367, 1181, 768 cm^{-1}; HRMS (FAB^+) calcd for $C_{28}H_{35}N_7O_5$ $(M+H)^+$ *m/z* 550.2778. Found 550.2782; Anal. Calcd for $C_{28}H_{35}N_7O_5$: C, 61.19; H, 6.42; N, 17.84. Found: C, 60.96; H, 6.30; N, 17.80.

2.2 IDO Inhibitory Activity

Purified recombinant human indoleamine 2,3-dioxygenase (rhIDO) was supplied by Dr. Sugimoto [1]. The inhibition assay was performed as previously described [7].

3 Results

3.1 Synthesis

The synthetic procedure is shown in Scheme 1. Amines **8** and **9** were conjugated to Boc-L-trp **6** to give the corresponding TPZ-monoxide hybrids **1** (TX-2274) and **3** (UTX-4). The conjugation reactions of **14** and **15** with Boc-L-Trp **6** were carried out by similar procedures to TPZ-monoxide hybrids to give the corresponding TPZ hybrids **2** (UTX-3) and **4** (UTX-2).

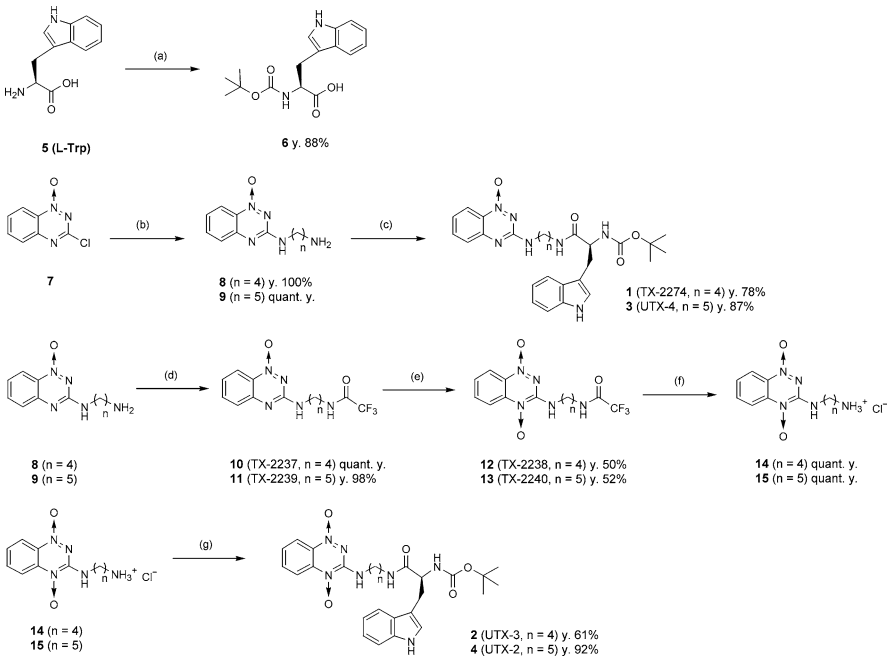

Scheme 1 Syntheses of L-Trp-TPZ hybrids. Reagents and conditions: (**a**) $(Boc)_2O$, 1 M NaOH aq., H_2O: 1,4-dioxane = 1:2, rt. (**b**) alkyldiamine, Et_3N, CH_2Cl_2, rt. (**c**) Boc-L-trp **6**, DIPCDI, HOBt, CH_2Cl_2, rt. (**d**) $(CF_3CO)_2O$, CH_2Cl_2, rt. (**e**) 35% H_2O_2, $(CF_3CO)_2O$, CH_2Cl_2, rt. (**f**) 28% NH_3 aq., MeOH, rt. (**g**) Boc-L-trp **6**, DIPCDI, HOBt, DIEA, CH_2Cl_2, rt

3.2 IDO Inhibitory Activity

IDO inhibitory activities (inhibitory constant: K_i) of L-Trp-TPZ hybrids were determined using a Lineweaver-Burk plot using rhIDO. The K_m value for L-tryptophan was 44 μM, the K_i values of all the L-Trp-TPZ hybrids tested are shown in Table 1. All L-Trp-TPZ hybrids have more or less IDO inhibitory activities: K_i values of **1**, 15.3 μM **2**, 438 μM, **3**, 267 μM, **4**, 179 μM, while their parent compounds TPZ and Boc-L-Trp **6** showed no IDO inhibitory activities.

Table 1 IDO inhibitory activity

Compounds	K_i (μM)	Inhibitory mechanism
TPZ	N. I.[a]	
6 (Boc-L-Trp)	N. I.[a]	
1 (TX-2274)	15.3	Competitive
2 (UTX-3)	438	Uncompetitive
3 (UTX-4)	267	Competitive
4 (UTX-2)	179	Uncompetitive

[a]Not Inhibited.

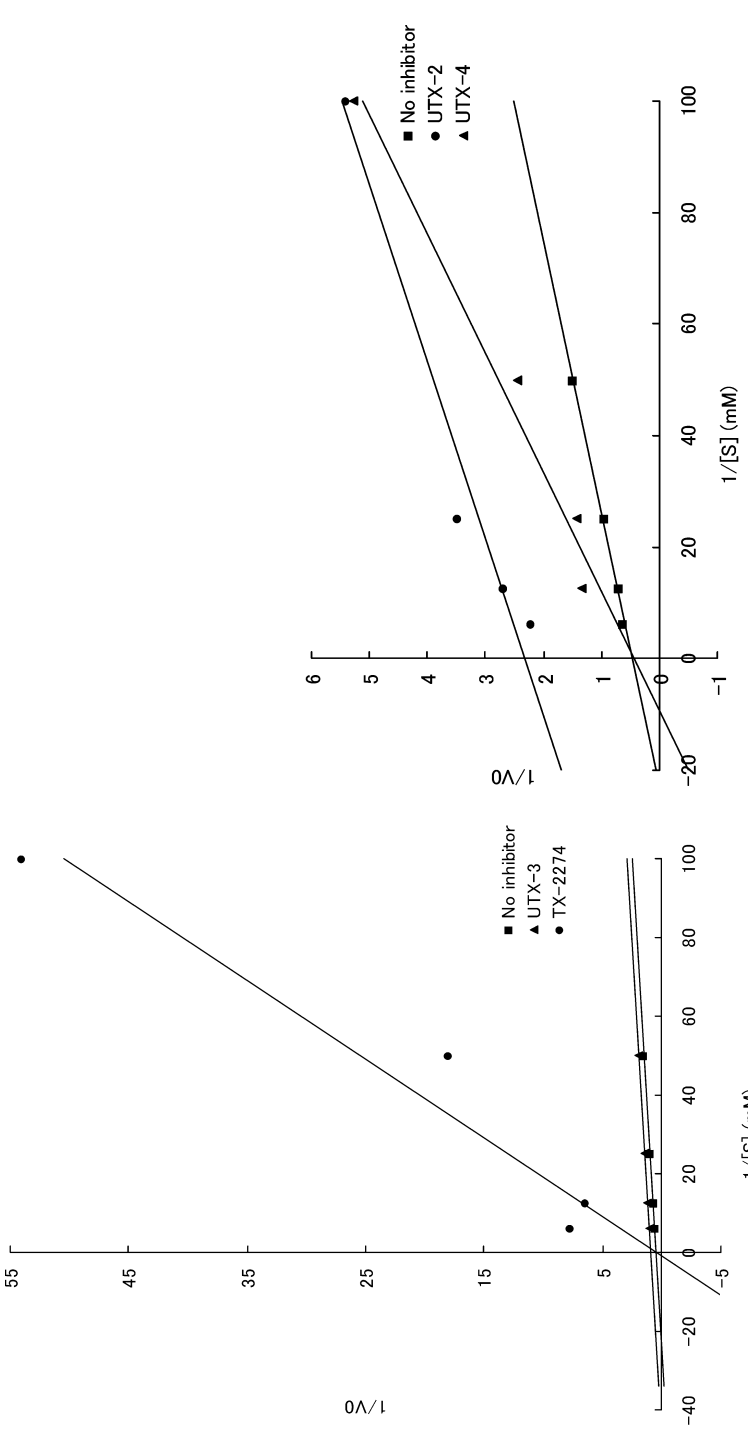

Fig. 1 Lineweaver-Burk plot of L-Trp-TPZ hybrids. (**a**) **1** (TX-2274) and **2** (UTX-3). No inhibitor (closed squares), **1** (closed circles), **2** (closed triangles). (**b**) **3** (UTX-4) and **4** (UTX-2). No inhibitor (closed squares), **3** (closed circles), **4** (closed triangles)

Among them tested, TPZ-monoxide hybrid **1** was the strongest IDO inhibitor. These TPZ hybrids **2** and **4** were uncompetitive inhibitors as well as 1MT-TPZ hybrids [7] developed previously, while TPZ-monoxide hybrids **1** and **3** were competitive inhibitors as shown in Fig. 1.

4 Discussion

We designed hypoxia-targeting novel IDO hybrid inhibitors without inhibitor 1MT, such as an unsubstituted IDO-substrate L-Trp-TPZ hybrids **1** (TX-2274), **2** (UTX-3), **3** (UTX-4) and **4** (UTX-2). Among them, L-Trp TPZ hybrid **1** showed the most potent IDO inhibitory activity. Furthermore, TPZ-monoxide hybrid **1** has stronger IDO inhibitory activities than 1MT and 1MT-TPZ hybrids. TPZ-monoxide hybrids **1** and **3** showed competitive inhibition, both were able to bind the active site of IDO. Whereas TPZ hybrids **2** and **4** showed uncompetitive inhibition, they were able to bind to the enzyme-substrate complex as well as 1MT-TPZ hybrids [7]. According to these data, to use IDO substrate L-tryptophan without modification such as *N*-methylation of indole moiety, an effective IDO inhibitor can be developed. Especially hybrid **1** is a promising example of substrate hybrid inhibitors.

We showed that 1MT-TPZ hybrids TX-2235 and TX-2234 had higher hypoxia-selective cytotoxicities than TPZ itself [7], we expect TPZ hybrids **2** and **4** also have hypoxia-selective cytotoxicities. Thus, we proposed that TPZ hybrids **2** undergo one-electron reduction to be its metabolite compound **1** which worked as an IDO inhibitor more effectively than 1MT-TPZ hybrids. We succeeded the design of novel hypoxia-targeting IDO hybrid inhibitors based on our previous report [7].

Acknowledgments The authors thank Ms. M. Nakamura, Ms. K. Yamashita, Ms. E. Okayama and the staff of our Faculty for measurement of NMR, MS and elemental analyses.

References

1. H. Sugimoto, S. Oda, T. Otsuki, T. Hino, T. Yoshida, Y. Shiro, Crystal structure of human indoleamine 2,3-dioxygenase: Catalytic mechanism of O_2 incorporation by a heme-containing dioxygenase, *Proc. Nat. Acad. Sci. USA*. **103**, 2611–2616 (2006).
2. C. Uyttenhove, L. Pilotte, I. Theate, V. Stroobant, D. Colau, N. Parmentier, T. Boon, B. Eynde, Evidence for a tumoral immune resistance mechanism based on tryptophan degradation by indoleamine 2,3-dioxygenase, *Nat. Med.* **9**, 1269–1274 (2003).
3. D. Y. Hou, A. J. Muller, M. D. Sharma, J. DuHadaway, T. Banerjee, M. Johnson, A. L. Mellor, G. C. Prendergast, D, H. Munn, Inhibition of Indoleamine 2,3-Dioxygenase in Dendritic cells by Stereoisomers of 1-Methyl-Tryptophan Correlates with Antitumor Responses, *Cancer Res.* **67**, 792–801 (2007).
4. G. J. Maghzal, S. R. Thomas, N. H. Hunt, R. Stocker, Cytochrome b_5, not superoxide anion radicals, is a major reductant of indoleamine 2,3-dioxygenase in human cells, *J. Biol. Chem.* **283**, 12014–12025 (2008).

5. M. P. Hay, K. O. Hicks, F. B. Pruijn, K. Pchalek, B. G. Siim, W. R. Willson, W. A. Denny, Pharmacokinetic/Pharmacodynamic Model-Guided Identification of Hypoxia-Selective 1,2,4-Benzotriazine 1,4-Dioxides with Antitumor Activity: The Role of Extravascular Transport, *J. Med. Chem.* **50**, 6392–6404 (2007).
6. H. Nagasawa, Y. Uto, H. Hori, Design of Hypoxia-Targeting Drugs as New Cancer Therapeutics. *Biol. Pharm. Bull.* **29**, 2335–2342 (2006).
7. H. Nakashima, Y. Uto, E. Nakata, H. Nagasawa, K. Ikkyu, N. Hiraoka, K. Nakashima, Y. Sakaki, H. Sugimoto, Y. Shiro, T. Hashimoto, Y. Okamoto, Y. Asakawa, H. Hori, Synthesis and biological activity of 1-methyl-tryptophan-tirapazamine hybrids as hypoxia-targeting indoleamine 2,3-dioxygenase inhibitors, *Bioorg. Med. Chem.* **16**, 8661–8669 (2008).

Phosphorescence-Assisted Microvascular O_2 Measurements Reveal Alterations of Oxygen Demand in Human Metastatic Colon Cancer in the Liver of Superimmunodeficient NOG Mice

Kan Handa, Mitsuyo Ohmura, Chiyoko Nishime, Takako Hishiki, Yoshiko Nagahata, Kenji Kawai, Hiroshi Suemizu, Masato Nakamura, Masatoshi Wakui, Yuko Kitagawa, Makoto Suematsu, and Kosuke Tsukada

Abstract We aimed to examine metabolism of human cancer in vivo and utilized superimmunodeficient NOG mice as an experimental model of hepatic metastasis, where human colon cancer cell line HCT116 transfected with Venus, the mutant GFP was injected intrasplenically. The mice were pretreated with Pd-porphyrin to quantify local O_2 tension through intravital phosphorescence assay. In this model, a majority of metastatic foci occurred in periportal regions but not in central regions. At 1 week after the transplantation, a PO_2 drop in periportal regions was minimal without any notable decrease in microvascular blood flow. Under these conditions, there was a negative correlation between the size of metastatic foci and the lobular O_2 consumption, suggesting that the tumor O_2 consumption is smaller than that in the residual liver. At 2 weeks, portal PO_2 was significantly smaller than controls, while the central PO_2 was not comparably decreased, indicating that metastatic foci increased the O_2 consumption, while the residual liver decreased it. These results suggest metastatic tumors derived from human colon cancer exhibit notable aerobic metabolism during their developmental process, compromising respiration of the rest of the tissue regenerated during tumor development.

1 Introduction

Liver failure caused by disseminated metastasis through portal circulation is one of the most serious clinical complications of the colon cancer, while mechanisms for derangement of the liver homeostasis of energy metabolism under the tumor-bearing conditions remain largely unknown. We established a metastasis model by injecting human colon cancer cell line (HCT116) into the spleen of superimmunodeficient NOG mice, which allows formation of

M. Suematsu (✉)
Department of Biochemistry and Integrative Medical Biology, School of Medicine, Keio University, Tokyo, 160-8582, Japan
e-mail: msuem@sc.itc.keio.ac.jp

E. Takahashi, D.F. Bruley (eds.), *Oxygen Transport to Tissue XXXI*, Advances in Experimental Medicine and Biology 662,
DOI 10.1007/978-1-4419-1241-1_61, © Springer Science+Business Media, LLC 2010

macroscopic metastasis in the liver with high reproducibility. Using this model, we attempted to examine microvascular flow velocity and O_2 concentrations in and around metastatic cancer lesions by multimodal intravital microscopy equipped with phosphorescence decay method. These results led us to suggest that metastatic tumors derived from human colon cancer exhibit notable aerobic metabolism during their developmental process, subsequently compromising respiration of the rest of the liver tissue that is regenerated during the tumor development.

2 Materials and Methods

2.1 The Model for Hepatic Metastasis of Human Colon Cancer

The experimental protocols for this study were approved by the Experimental Animal Committee of Keio University School of Medicine. NOG mice are double homozygous for severe combined immunodeficiency (scid) mutation and interleukin-2 receptor g chain (IL-2Rγ) allelic mutation (γnull). In NOG mice, most immune cells including dendritic cells as well as T, B and NK cells are depleted. NOG mice showed high engraftment rates compared to NOD/scid mice [1]. To visualize microfoci of metastasis, human colon cancer (HCT116) cells were transfected with cDNA of the fluorescent protein, Venus, a generous gift from Dr. Atsushi Miyawaki in Riken (Wako-city, Saitama, Japan) [2]. A vector containing both the green fluorescence protein, Venus and the Genetecin resistance gene were constructed. Forty-eight hours after transfection of HCT116 cells with the Venus gene, selection with the antibiotic Genetecin (1.0 mg/ml; Invitrogen) was started to select Genetecin-resistant Venus-expressing cells. HCT116/venus cells were harvested with trypsin/EDTA, and resuspended in McCoy's 5A. To generate liver metastasis, HCT116/venus cells were injected into the spleen (i.sp.). For injection, the spleen was exposed through a mini laparotomy in the left abdominal wall. After injection, splenectomy was performed for arrest of hemorrhage.

2.2 Measurement of Blood Flow and Microvascular PO_2

The portion of the liver was surgically exposed through a midline incision under isofluranate anesthesia. The surface of the liver was observed through invertedtype multimodal intravital video microscopy (IVVM). Whole blood was collected from the donor mouse and centrifuged, washed, and labeled by rhodamine 6G (Sigma). The fluorescence-labeled RBCs were diluted in as much saline. A 0.1 ml suspension of RBCs was injected into the tail vein of the mouse. The liver surface was epi-illuminated by a xenon lamp. Microscopic images of the rhodamine labeled RBCs were recorded by a high speed video

camera. On the other hand, we used the phosphorescence decay method to measure oxygen tension. The Pd-meso-tetra-(4-carboxyphenyl)-porphyrin (Pd-TCPP) used as the phosphorescence probe for the O_2-dependent quenching was dissolved (20 mg/ml) in physiological saline containing human albumin. Each mouse was administered intravenously with a bolus of Pd-TCPP. The probe in the microvessels was excited by using the second harmonic of a Q-switched Nd: YAG pulse laser (532-nm wavelength, 6-s pulse width at half maximum, 1-Hz pulse recurrence frequency, 200-nJ/pulse irradiation energy) through the objective lens of a microscope. Phosphorescence emission was detected by a photomultiplier tube through a long pass filter (> 620 nm). Since the phosphorescence lifetime which was determined through the emission decay curve becomes shorter with increasing O_2 concentrations, PO_2 values in periportal and pericentral venules were calculated as reported previously [3, 4].

3 Results

Almost all cultured HCT116/venus cells expressed strong green fluorescence in the cytoplasm. GFP fluorescence was stable for at least 8 passages in culture. Cell growth in culture was almost equal to parental cells. HCT116/venus cells forming metastatic foci indicating strong and uniform fluorescence in all mice were examined at 1 or 2 weeks after the intrasplenic injection. The incidence of metastasis formation was essentially the same between HCT116/venus and parental cells, indicating stability of metastatic potential (Fig. 1a,b). The hepatic lobule surrounded by portal venules was divided into three regions including periportal, midzone and pericentral regions. Morphometrical analysis revealed that a majority of metastatic foci occurred mainly in periportal regions rather than in midzonal or pericentral regions (Fig. 1c). To note is that the distance between portal and central venules became longer in 2 weeks than that measured in the control and 1 week groups (Fig. 1d), suggesting that the lobular size became greater at 2 weeks after the splenic tumor injection than that observed at 1 week. We recognized that metastatic tumors had a tendency to zonal heterogeneity in the liver.

Figure 2a depicted alterations in PO_2 in portal and central venules. As seen, periportal PO_2 was significantly decreased at 1 week, and further lowered at 2 weeks. To note is that PO_2 in central venules was also significantly reduced. Howevers, microvascular RBC velocity and flow were not greatly changed among the groups (Fig. 2b,c). Considering metastatic foci occurred in periportal regions, the data collected from portal regions suggest that the metastatic tumor growth appeared to stimulate O_2 consumption. On the other hand, results showing a drop of pericentral PO_2 led us to inquire if hepatocytes might change their O_2 consumption in response to metastatic development.

As shown in Fig. 3, we compared differences in the relationship between the size of individual metastatic foci and the corresponding data indicating the PO_2

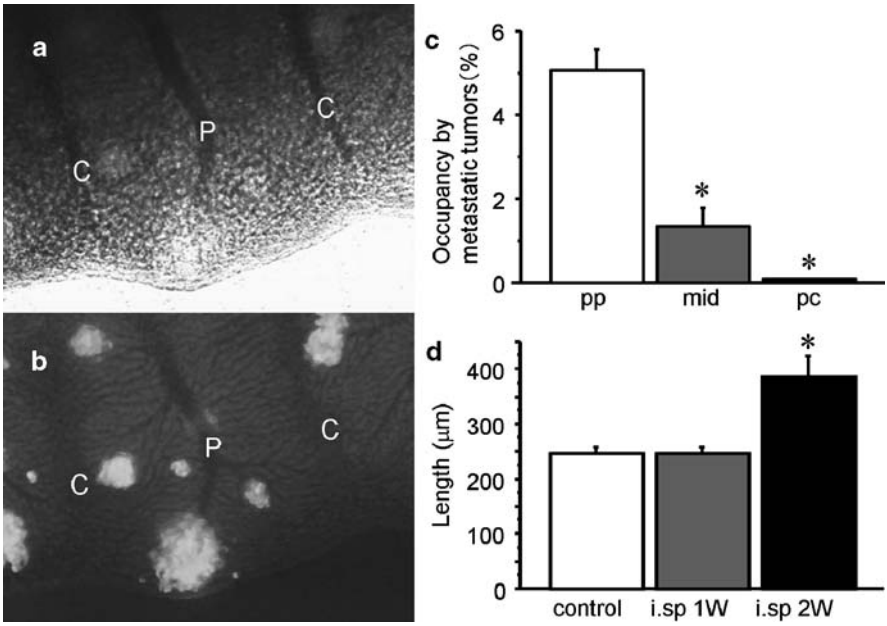

Fig. 1 Representative pictures indicating hepatic muicrometastasis of human colon cancer cell line HCT116. (**a**) transparent micrograph of liver lobules. P and C denote portal and central venules (**b**) fluorescent image in the same microscopic field. (**c**) Spatial heterogeneity of the site of metastatic foci. PP: periportal region. PC: pericetral region. (**d**) Difference in the lengths between portal and central venules. Note the enlargement of the lobules at 2 weeks. $^*p < 0.05$. mean + SE of 15 difference experiments

gradation between portal and central venules among the data collected at 1 week, 10 days and 2 weeks after the tumor transplantation. As seen, three groups indicated significant negative correlation. Considering that microvascular flow did not change greatly among the groups, the results suggested that lobules with the greater size of metastatic foci reduce their O_2 consumption.

4 Discussion

The hepatic lobules with multiple metastasis of human colon cancer down-regulated O_2 consumption. Based on the concept of Warburg's effect [5], this result might be theoretically reasonable, since the normal liver tissue consuming O_2 normally was replaced with the metastasis displaying anaerobic metabolism. However, measurements in the current study are inconsistent with such a hypothesis: At least in the current experiments, PO_2 values in periportal regions

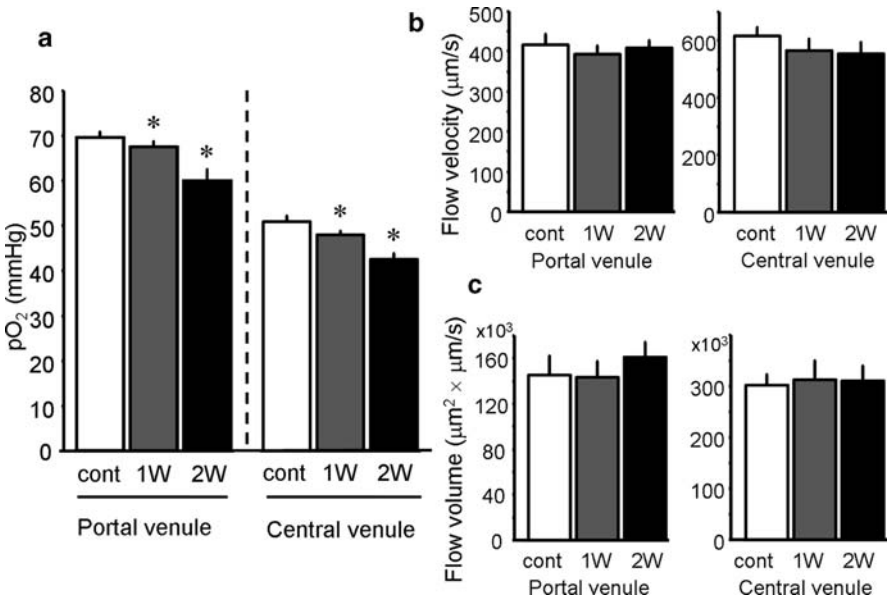

Fig. 2 Differences in PO_2 in portal and central venules after the intrasplenic injection of human colon cancer cell line HCT116. (**a**) PO_2 analysis. (Control group: 47 and 38 measurements at PP and PC in 4 mice, 1 Week group: 37 and 28 measurements at PP and PC in 4 mice, 2 Weeks group: 23 and 26 measurements at PP and PC in 4 mice) (**b**) RBC velocity in portal and central venules. (**c**): Microvascular flow velocity (For **b** and **c**: Control group: 27 and 28 measurements at PV and PV in 4 and 5 mice, respectively, 1 Week group: 40 and 27 measurements at PV and CV in 7 mice respectively, 2 Weeks group: 46 and 37 measurements at PV and CV in 8 mice, respectively). Data show mean + SE of separate experiments. $*p < 0.05$ vs. control

where metastatic foci grow first after the cancer transplantation were significantly lowered, suggesting that the foci greatly consume O_2. On the other hand, the data shown in Fig. 3 suggest that lobules with the greater size of metastatic foci reduce their O_2 consumption. Although our methodology was unable to distinguish local O_2 consumption of hepatocytes from that of the foci, it is not unreasonable to hypothesize that hepatocytes in the metastasis-bearing lobules might reduce their O_2 consumption as a function of time after the intrasplenic cancer injection. In this context, non-tumor regions of the hepatic lobules might reduce their O_2 consumption; this is consistent with the results in Fig. 2 showing that periportal and pericentral PO_2 decreases at 2 weeks were almost comparable to those in the controls. To examine such a hypothesis, further investigation to examine difference in glucose metabolism between metastatic foci and hepatocytes is now underway using metabolome analyses in our laboratory.

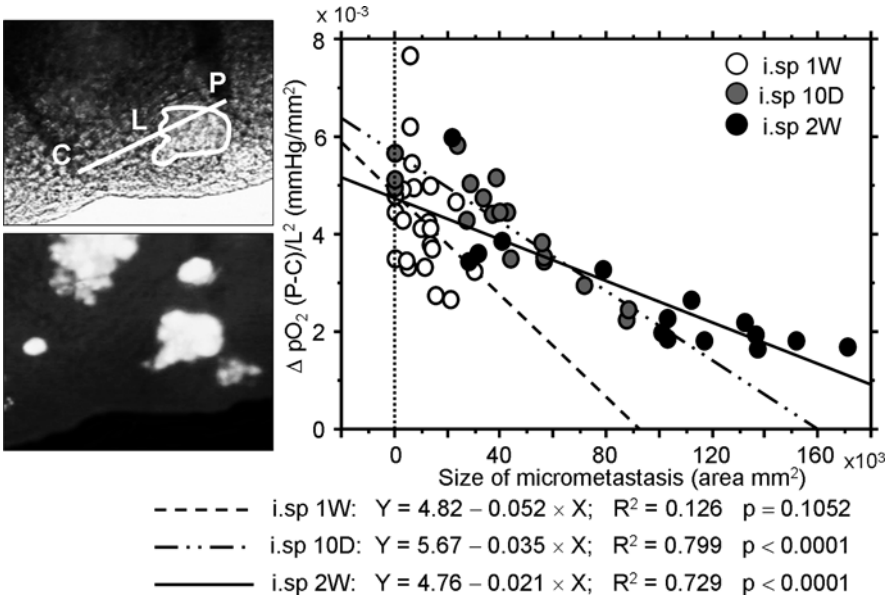

Fig. 3 Differences in the relationship between the size of individual metastatic foci and the corresponding measurements of the local PO_2 gradation normalized by the size of lobules. *Left pictures*: Transmission and fluorescent images indicate the localization of portal and central venules (P and C) and the Venus-positive metastatic foci, respectively. The values of ΔPO_2 (P-C) indicate differences in PO_2 between portal and central venules. L: Distance between the portal and central venules for individual measurements. The data were normalized by square of L. Open, shaded and closed circles indicate data collected at 1 week, 10 days and 2 weeks. Note negative correlation between the size of metastasis and ΔPO_2 (P-C)/L^2 in all groups, while statistical significance was evident in the groups at 10 days and 2 weeks ($p < 0.05$)

Acknowledgments This work was supported by RIKEN Supercomputing Science Grant by MEXT and by Grant-in-aid for Creative Scientific Research 17GS0419 from MEXT.

References

1. Ito M, Haramatsu H, Kobayashi K, Suzue K, Kawahata M, Hioki K, Ueyama Y, Koyanagi Y, Suganuma K, Tsuji K, Heike T, and Nakahata T. NOD/SCID/γ null mouse: an excellent recipient mouse model for engraftment of human cells. Blood 100(9), 3175–3182 (2002).
2. Nagai T, Ibata K, Park ES, Kubota M, Mikoshiba K, and Miyawaki A. A vari-ant of yellow fluorescent protein with fast and efficient maturation for cell-biological applications. Nat Biotechnol 20(1), 87–90 (2002).
3. Minamitani H, Tsukada K, Sekizuka E, and Oshio C. Optical bioimaging: from living tissue to a single molecule: imaging and functional analysis of blood flow in organic microcirculation. J Pharmacol Sci 93(3), 227–233 (2003).

4. Tsukada K, Sekizuka E, Oshio C, Tsujioka K, and Minamitani H. Red blood cell velocity and oxygen tension measurement in cerebral microvessels by double-wavelength photo-excitation. J Appl Physiol 96(4), 1561–1568 (2004).
5. Warburg O. On the origin of cancer cells. Science 123(3191), 309–314 (1956).

Part V
Clinical Aspects of O_2 Transport

Hemoglobin-Vesicle, a Cellular Artificial Oxygen Carrier that Fulfils the Physiological Roles of the Red Blood Cell Structure

Hiromi Sakai, Keitaro Sou, Hirohisa Horinouchi, Koichi Kobayashi, and Eishun Tsuchida

Abstract Hb-vesicles (HbV) are artificial O_2 carriers encapsulating concentrated Hb solution (35 g/dL) with a phospholipid bilayer membrane (liposome). The concentration of the HbV suspension is extremely high ([Hb] = 10 g/dL) and it has an O_2 carrying capacity that is comparable to that of blood. HbV is much smaller than RBC (250 vs. 8000 nm), but it recreates the functions of RBCs; (i) the slower rate of O_2 unloading than Hb solution; (ii) colloid osmotic pressure is zero; (iii) the viscosity of a HbV suspension is adjustable to that of blood; (iv) HbV is finally captured by and degraded in RES; (v) co-encapsulation of an allosteric effector to regulate O_2 affinity; (vi) the lipid bilayer membrane prevents direct contact of Hb and vasculature; (vii) NO-binding is retarded to some extent by an intracellular diffusion barrier, and HbV does not induce vasoconstriction. (viii) Both RBC and HbV can be a carrier of not only O_2 but also exogenous CO. However, HbV has limitations such as a shorter functional half-life when compared with RBCs. On the other hand, the advantages of HbV are that it is pathogen-free and blood-type-antigen-free; moreover, it can withstand long-term storage of a few years, none of which can be achieved by the RBC transfusion systems.

1 Introduction

Biconcave RBCs deform to a parachute-like configuration to flow through a narrower capillary. This profile is believed to be effective to increase the surface-to-volume ratio and stir the intracellular viscous Hb solution to facilitate the gas exchange. On the other hand, physicochemical analyses have revealed that O_2 unloading of Hb is significantly retarded by compartmentalization in RBC. Why has nature selected such an inefficient cellular structure for gas transport? Interestingly, some of the answers to this question have been revised by the

H. Sakai (✉)
Research Institute for Science and Engineering, Waseda University, Tokyo, Japan
e-mail: hiromi@waseda.jp

E. Takahashi, D.F. Bruley (eds.), *Oxygen Transport to Tissue XXXI*,
Advances in Experimental Medicine and Biology 662,
DOI 10.1007/978-1-4419-1241-1_62, © Springer Science+Business Media, LLC 2010

research of blood substitutes. They are, (i) retardation and targeting of O_2 unloading at microcirculation to avoid autoregulatory vasoconstriction; (ii) reduction of a high colloidal osmotic pressure, COP, of an Hb solution to zero, to increase blood Hb concentration; (iii) rheology control of blood, a RBCs dispersion, to a non-Newtonian viscous fluid; (iv) prevention of extravasation or excretion through renal glomeruli; (v) preservation of the chemical environment in cells, such as the concentrations of electrolytes and enzymes; (vi) prevention of direct contact of toxic Hbs and endothelial cell lying, and (vii) modulation of reactions with NO as an endothelium derived relaxation factor, EDRF. These observations reassure the importance of the cellular structure of RBCs to design Hb-based oxygen carriers.

Hb-vesicles (HbV) are artificial O_2 carriers encapsulating concentrated Hb solution (35 g/dL) with a phospholipid bilayer membrane [1]. Concentration of the HbV suspension is extremely high ([Hb] = 10 g/dL, [lipids] = 6 g/dL, volume fraction, ca. 40 vol%) and it has an oxygen carrying capacity that is comparable to that of blood. In this review paper, we summarize the characteristics of HbV that can fulfill some of the physiological roles of the cellular RBC structure.

2 Structural Stability and Suspension Properties

Many people think liposomes are unstable capsules. However, it depends on the lipids and the composition. In the case of RBCs, the sophisticated cytoskeleton network structure stabilizes the cellular structure. However, hypotonic hemolysis easily occurs. We confirmed that HbV are more resistant than RBCs to hypotonic shock, freezing by liquid N_2 and thawing, enzymatic attack (phospholipase A_2) [2], and a shear stress (1500 s^{-1}). Moreover, it can be stored at room temperature over 2 years [3]. In spite of such high stability, we confirmed with animal experiments that HbV are eventually captured by reticuloendothelial system (RES) and degraded promptly within 2 weeks without decomposing (hemolysis) in blood circulation [4]. Phospholipid vesicles for the encapsulation of Hb would be beneficial for heme detoxification through their preferential delivery to the RES, a physiological compartment for degradation of senescent RBCs, even at doses greater than putative clinical doses [5].

Colloid osmotic pressure (COP) is an important factor to determine blood volume in the body. Hb solution (5 g/dL) showed the COP of 16 Torr [6]. Polymerization of Hb reduces COP depending on the resulting molecular weight. PEG-conjugated Hb shows the largest COP, which is about 3 times higher than blood (ca. 25 Torr) due to the highly hydrated PEG chains [7]. On the other hand, both HbV and washed RBCs showed 0 Torr because of the suspension of large particles: the number of total particles of HbV is less than 1/100 of the number of Hb molecules at the same Hb concentration [6]. COP acts in opposition to hydrostatic pressure to balance the distribution of fluid between blood and interstitial compartments [7]. COP is a colligative property,

depending proportionally on the concentration of protein exerting the force and specifically on the macromolecular properties of that protein. Solutions with high COP cause significant transcapillary filtration of water in the direction from the interstitial space into the vascular lumen. An increase in blood volume is advantageous to increase cardiac output for resuscitation, though the composition of other components of blood and tissue will also be compromised. HbV, on the other hand, does not have an oncotic effect, and the particle should be suspended in a plasma expander (plasma substitute, water-soluble polymer). The COP of the resulting suspension is identical to that of the suspending medium. When HbV is suspended in 5% rHSA, the suspension shows 20 Torr at any Hb concentration. HbV can create a suspension of [Hb] = 10 g/dL at the physiologic COP, that cannot be attained easily by other chemically modified Hb solutions.

The HbV suspended in rHSA ([Hb] = 10 g/dL) was nearly Newtonian [8]. Other plasma substitute polymers -hydroxylethyl starch (HES), dextran (DEX), and modified fluid gelatin (MFG)- induced HbV flocculation, possibly by depletion interaction, and rendered the suspensions as non-Newtonian with a shear-thinning profile. These HbV suspensions showed a high storage modulus (G') because of the presence of flocculated HbV. However, HbV suspended in rHSA exhibited a very low G'. The viscosities of HbV suspended in DEX, MFG, and high-molecular-weight HES solutions responded quickly to rapid step changes in shear rates of $0.1-100\ s^{-1}$ and a return to $0.1\ s^{-1}$, indicating that flocculation is both rapid and reversible. The HbV suspension viscosity was influenced by the presence of plasma substitutes. The HbV suspension provides a unique opportunity to manipulate rheological properties for various clinical applications.

3 The Rate of O_2-Unloading, and NO- and CO-Bindings

The O_2-release from flowing HbVs was examined using an O_2-permeable, fluorinated ethylenepropylene copolymer tube (inner diameter, 28 μm) exposed to a deoxygenated environment [9]. Measurement of O_2 release was performed using an apparatus that consisted of an inverted microscope and a spectrophotometer, and the rate of O_2 release was determined based on the visible absorption spectrum in the Q band of Hb. HbVs and human RBCs were mixed in various volume ratios at [Hb] = 10 g/dl, and the suspension was perfused at the centerline flow velocity of 1 mm/s through the narrow tube. The mixtures of cell-free Hb solution and RBCs were also tested. Because HbVs were homogeneously dispersed, increasing the volume of the HbV suspension resulted in a thicker marginal RBC-free layer. Irrespective of the mixing ratio, the rate of O_2 release from the HbV/RBC mixtures was similar to that of RBCs alone. On the other hand, the addition of 50 vol% of acellular Hb solution to RBCs significantly enhanced the rate of deoxygenation. This difference between the HbV suspension and the acellular Hb solution should mainly be due to the difference in the particle size (250 vs. 7 nm) that affects their diffusion for the facilitated O_2

transport. It has been suggested that faster O_2 unloading from the HBOCs is advantageous for tissue oxygenation. However, this concept is controversial with regard to the recent findings, because an excess O_2 supply would cause autoregulatory vasoconstriction and microcirculatory disorders. We confirmed that HbVs do not induce vasoconstriction and hypertension. This is not only owing to the reduced inactivation of NO (see below) but also possibly due to the moderate O_2 release rate that is similar to RBCs.

One of the important roles of the RBC structure is the retardation of NO-binding. However, the mechanism has been controversial, whether, (i) an unstirred layer surrounding the cell should be the diffusion barrier, (ii) cytoskeletal cell membrane can be the diffusion barrier, or (iii) the highly concentrated Hb solution can be the barrier. To clarify the mechanism, we analyzed HbVs with different intracellular Hb concentrations, $[Hb]_{in}$, and different particle sizes using stopped-flow spectrophotometry [10]. In the case of different $[Hb]_{in}$ (1- 35 g/dl), NO-binding is retarded at a higher $[Hb]_{in}$, on the other hand, CO-binding did not show such retardation. In the case of different particle diameter of HbV at constant $[Hb]_{in}$, 35 g/dl, NO-binding is retarded with a larger particle, while the CO-binding did not show such changes. The computer simulations can recreate these tendencies. The two-dimensional concentration changes of free-NO and unbound free-hemes in one HbV at the $[Hb]_{in}$ was 1 g/dl showed that NO diffuses rapidly into HbV and the reaction proceeds quite homogeneously. On the other hand, HbV at $[Hb]_{in} = 35$ g/dl showed heterogeneous distribution. The concentration gradients of both NO and heme change from the interior surface to the core. The intrinsically fast NO-binding induces an intracellular diffusion barrier in a highly concentrated Hb solution, but not for the slow CO-binding. We can estimate the apparent binding rate constant of a particle encapsulating a 35-g/dl Hb with 8000-nm diameter, and they are similar to the reported values for RBCs. The mechanism of retardation of NO-binding is controversial, but from these data, we estimate that (i) rapid NO-binding reaction induces intracellular diffusion barrier, (ii) cellular membrane cannot be a barrier for gas diffusion, and (iii) a higher $[Hb]_{in}$ and larger size are the factors for retarding NO-binding. However, we have to admit that NO-binding of HbV is much faster than that of RBC. The absence of vasoconstriction for HbV cannot be explained with these data. We believe that small Hb would permeate across the endothelium to reach to the site where NO is produced and transferred to the smooth muscle. It was recently reported that dextran conjugated Hb permeates through the endothelium. However, much larger HbV would remain in the lumen and does not bind NO in the endothelium.

4 Resuscitation from Hemorrhagic Shock with HbV

The first attempt of HbV to restore the systemic condition after hemorrhagic shock was conducted using anesthetized Wistar rats. After 50% blood withdrawal, the rats showed hypotension and considerable metabolic acidosis and

hyperventilation. They received HbV suspended in rHSA, shed autologous blood (SAB), or rHSA alone. The HbV group restored mean arterial pressure, similar to the SAB group, which was significantly higher than the rHSA group. No remarkable difference was visible in the blood gas variables between the resuscitated groups. However, two of eight rats in the rHSA group died before 6 h [11]. After removing the catheters and awakening, the rats were housed in cages for upto 14 days. The HbV group gained body weight; the reduced Hct returned to the original level in 7 days, indicating elevated hematopoiesis. Both groups showed transient elevation of AST and ALT at 1 day. Splenomegaly was significant in the HbV group at 3 days because of the accumulation of HbV. However, it subsided within 14 days. Histopathological observation indicated that a significant amount of HbV accumulated in the spleen macrophages, and complete disappearance within 14 days. These results indicate that HbV is useful as a resuscitative fluid for hemorrhagic shock. Its performance is comparable to that of SAB. Similar experiments using beagles have shown 1-year survival after resuscitation with HbV.

The above elevations of AST and ALT after resuscitation with HbV or RBC indicate the systemic reperfusion injury. Recent reports on cytoprotective effects of exogenous CO urged us to test infusion of CO-bound HbV and RBC in hemorrhagic-shocked rats to improve tissue viability [12]. Using the similar model, hemorrhagic shocked Wistar rats received CO-HbV, CO-RBC, O_2-HbV, or O_2-RBC suspended in 5% rHSA. All groups showed prompt recovery of blood pressure and blood gas parameters, and survived for 6 h of observation period. Plasma AST, ALT and LDH levels were elevated at 6 h in the O_2-HbV and O_2-RBC groups. They were significantly lower in the CO-HbV and CO-RBC groups. Blood HbCO levels (26–39%) decreased to less than 3% at 6 h while CO was exhaled through the lung. Both HbV and RBC gradually gained the O_2 transport function. Collectively, both CO-HbV and CO-RBC showed a resuscitative effect and reduced oxidative damage to organs. Adverse and poisonous effects of CO gas were not evident for 6 h in this experimental model. Further study is necessary to clarify the neurological impact of a longer observation period, though the results suggest a possible new clinical indication.

In conclusion, HbV can mimic the functions of RBCs. However, the half-life of HbV is much shorter than that of RBCs, and limits their use. On the other hand, the advantages of HbV are that it is pathogen-free and blood-type-antigen-free; moreover, it can withstand long-term storage of a few years, none of which can be achieved by the RBC transfusion systems. We continue further development of HbV aiming at the eventual realization and contribution to the clinical medicine.

Acknowledgments This work is supported by Health and Labour Sciences Research Grants (Health Science Research Including Drug Innovation), Ministry of Health, Labour and Welfare, Japan (H.S. H.H, E.T, K.K.), and Grants in Aid for Scientific Research from the Japan Society for the Promotion of Science (B19300164) (H.S.).

References

1. Sakai H, Sou K, Horinouchi H, Kobayashi K, Tsuchida E. (2008) Haemoglobin-vesicles as artificial oxygen carriers: present situation and future visions. J Intern Med 263:4–15.
2. Sakai H, Okamoto M, Ikeda E, Horinouchi H, Kobayashi K, Tsuchida E. (2009) J Biomed Mater Res A 90:1107–1119.
3. Sakai H, Tomiyama KI, Sou K, Takeoka S, Tsuchida E. (2000) Poly(ethylene glycol)-conjugation and deoxygenation enable long-term preservation of hemoglobin-vesicles as oxygen carriers in a liquid state. Bioconjug Chem 11:425–432
4. Sakai H, Horinouchi H, Tomiyama K, Ikeda E, Takeoka S, Kobayashi K, Tsuchida E. (2001) Hemoglobin-vesicles as oxygen carriers: influence on phagocytic activity and histopathological changes in reticuloendothelial system. Am J Pathol 159:1079–1088.
5. Sakai H, Masada Y, Horinouchi H, Ikeda E, Sou K, Takeoka S, Suematsu M, Takaori M, Kobayashi K, Tsuchida E. (2004) Physiological capacity of the reticuloendothelial system for the degradation of hemoglobin vesicles (artificial oxygen carriers) after massive intravenous doses by daily repeated infusions for 14 days. J Pharmacol Exp Ther 311:874–884.
6. Sakai H, Yuasa M, Onuma H, Takeoka S, Tsuchida E. (2000) Synthesis and physicochemical characterization of a series of hemoglobin-based oxygen carriers: objective comparison between cellular and acellular types. Bioconjug Chem 11:56–64.
7. Vandegriff KD, McCarthy M, Rohlfs RJ, Winslow RM. (1997) Colloid osmotic properties of modified hemoglobins: chemically cross-linked versus polyethylene glycol surface-conjugated. Biophys Chem 69:23–30.
8. Sakai H, Sato A, Takeoka S, Tsuchida E. (2007) Rheological properties of hemoglobin vesicles (artificial oxygen carriers) suspended in a series of plasma-substitute solutions. Langmuir 23:8121–8128.
9. Sakai H, Suzuki Y, Kinoshita M, Takeoka S, Maeda N, Tsuchida E. (2003) O_2 release from Hb vesicles evaluated using an artificial, narrow O_2-permeable tube: comparison with RBCs and acellular Hbs. Am J Physiol Heart Circ Physiol 285:H2543–H2551
10. Sakai H, Sato A, Masuda K, Takeoka S, Tsuchida E. (2008) Encapsulation of concentrated hemoglobin solution in phospholipid vesicles retards the reaction with NO, but not CO, by intracellular diffusion barrier. J Biol Chem 283:1508–1517
11. Sakai H, Masada Y, Horinouchi H, Yamamoto M, Ikeda E, Takeoka S, Kobayashi K, Tsuchida E. (2004) Hemoglobin-vesicles suspended in recombinant human serum albumin for resuscitation from hemorrhagic shock in anesthetized rats. Crit Care Med 32:539–545.
12. Sakai H, Horinouchi H, Tsuchida E, Kobayashi K. (2009) Hemoglobin-vesicles and red blood cells as carriers of carbon monoxide prior to oxygen for resuscitation from hemorrhagic shock in a rat model. Shock 31(5):507–514.

Safer Surgery Using Zymogen Protein C Concentrate

Duane F. Bruley, Simon C. Mears, and Michael B. Streiff

Abstract This is the first case (November 12, 2007) of peri-operative use of zymogen protein C (ZPC) for a heterozygote Protein C deficient (50%) patient with heterozygosity for the prothrombin gene mutation. The surgery involved total left hip replacement. The patient was 74 years of age and at very high-risk for Deep Vein Thrombosis (DVT) thus possible lung emboli. He was a survivor of Venous thrombo-embolism (VTE) in 1999.

For this case the need for increased heparin to prevent a reoccurrence of thrombosis led to a further concern of internal bleeding and possible infection. As proposed by the authors in previous publications the use of a ZPC concentrate would decrease the chance of a thrombosis, with minimum or no internal bleeding. ZPC is activated at the endothelium cell surface and on the surface of the platelets where and when it is needed, therefore providing a safer procedure.

This protocol was implemented by administering ZPC concentrate 1 day prior to surgery and continuing for 10 days after. Slightly higher than normal blood loss occurred, however, a safe procedure was achieved without dangerous side effects while several additional benefits were experienced (level of PC activity as high as 235% above normal were measured during the procedure.). It is felt that positive effects were the result of increased blood flow and oxygen transport to the tissues by reducing blood sludging in the microcirculation. Further studies on Protein C dose levels will be necessary to provide economical, safe and efficacious use of Protein C products.

It is suggested that ZPC should be considered for patients with high probability of VTE which could cause thrombotic occlusion of the pulmonary and peripheral vasculature. These phenomena can result in hypoxia and hypo perfusion causing organ failure and death.

Our research includes a focused effort to optimize upstream and downstream bio-processing to produce both zymogen and activated Protein C at a lower cost

D.F. Bruley (✉)
Synthesizer, Inc., 2773 Westminster Road, Ellicott City, MD 21043, USA
e-mail: bruley@umbc.edu

E. Takahashi, D.F. Bruley (eds.), *Oxygen Transport to Tissue XXXI*,
Advances in Experimental Medicine and Biology 662,
DOI 10.1007/978-1-4419-1241-1_63, © Springer Science+Business Media, LLC 2010

and to examine the medical indications that could benefit from a more available and affordable Protein C product.

1 Introduction

The control of blood hemostasis is critical for tissue health, including its oxygenation. When there is an imbalance between coagulants and anticoagulants in the plasma, at least two major pathological conditions can develop. First, if there is a deficiency of coagulants, such as factor VIII or IX, the patient is a hemophiliac with excessive bleeding mainly in the joints. Second, if there is a deficiency of an anticoagulant, such as protein C, a hyper-coagulable situation develops and typically the patient suffers a deep vein thrombosis (DVT) and venous thrombo-embolism (VTE).

This paper focuses on the hyper-coagulable case and the resulting tissue oxygen deprivation due to blood clotting (agglutination). Dr. Melvin H. Knisely (Life Magazine, May 1948) has been credited as the first human being to observe in vivo the particulate matter of blood as it sludged to occlude the microcirculation. He accomplished this in the 1930s and 40s with his invention of the quartz rod crystal technique of illumination. He first studied normal blood flow but then applied his technology along with colleagues from the University of Chicago and University of Tennessee to observe the occlusion of the microcirculation under more than a hundred disease states. His concern about the survival of hypoxic neurons in the gray matter of the brain led to early experiments with possible anticoagulants [4].

In the last 30 years, there has been accelerated interest in the development of anticoagulant and antithrombotic drugs. Some examples of drugs being developed today are antithrombin drugs, biotechnology derived heparin-like drugs, approved antithrombin agents, anti-Xa drugs, anti-TF drugs, activated protein C, zymogen protein C (ZPC), oral heparins and GAGS, and heparinoids. Of the many anticoagulant/antithrombotic drugs being investigated, all except ZPC can create internal bleeding that can result in catastrophic problems. The safety factor of ZPC results from nature's design to activate the protein only where and when it is needed. ZPC is a multifunctional biological that has beneficial characteristics including anticoagulant, antithrombotic, anti-inflammatory, and anti-apoptotic.

Protein C (PC) is the pivotal anticoagulant and antithrombotic in the human blood coagulation cascade [12, 17]. PC is a glycoprotein with a molecular weight of 62,000 Daltons. Human PC is synthesized in the liver as a single chain precursor and circulates in the blood primarily as a two chain inactive zymogen until it is activated by proteolytic cleavage. The protein is a serine protease that requires vitamin K for normal biosynthesis. It is a member of the vitamin K-dependent (VKD) family also consisting of coagulation proteins factors VII, IX, proteins S, Z and prothrombin.

ZPC is a trace protein at a concentration of 4 ug/ml in human blood [13, 15, 16]. Patients deficient in PC are at risk of DVT [8]. Venous thrombosis is one of the most frequent complications in medical patients [3]. It is the most common cause of death in patients undergoing major orthopedic operations. In the United States it has been estimated that 300,000 hospitalizations and 50,000 deaths occur [3], and this amounts to millions and possibly billions of dollars in medical expenses annually. Previous animal testing [9, 10, 14, 23] and clinical trials indicate that PC is an effective anticoagulant/antithrombotic for many medical indications without harmful side effects.

Protein C deficiency is a hidden disease. It has been determined by Bertina [3] that one in three hundred people are hereditary deficient in protein C, while only one in sixteen thousand are symptomatic. Those who are not symptomatic, however, are highly likely to form DVTs with possible venous thrombo-embolism (VTE). To encourage an appropriate lifestyle, with minimum chances of a DVT, it is suggested that children between the ages of twelve and fourteen be tested for hereditary deficiency. In addition many people have acquired protein C deficiency that can lead to the same complications. Examples of possible acquired protein C deficient conditions [22] include pregnancy, sepsis, trauma, and other disease states.

Protein C products presently on the market for medical use include activated protein C (Xigris) produced by Eli Lilly & Company and zymogen protein C concentrate (Ceprotin) is produced by Baxter Healthcare Corporation. ZPC was approved in Europe (2002) and by the FDA in the United States (2007) for congenital protein C deficiencies. It is possible that ZPC can be considered for use in cases of acquired deficiency (i.e. pregnancy) as well as for hereditary deficiencies.

At the present time heparin and coumadin are used to treat PC deficiency and other hypercoagulable conditions. The disadvantage of these drugs is that both have dangerous side effects. Excessive internal bleeding is a major problem that can result from their use, possibly causing a stroke or major organ failure. Also, pregnant women cannot use coumadin.

Previous animal testing [9, 10, 14, 23] and clinical trials indicate that PC is an effective anticoagulant/antithrombotic for many medical indications without harmful side effects. Not only can it be used to treat genetically deficient patients, but it can also be used to treat septic shock, hip and knee replacement patients, coumadin-induced skin necrosis patients, heparin-induced thrombocytopenia, patients during fibrinolytic therapy, and patients undergoing angioplasty or suffering from unstable angina [7]. Additionally, research has shown that the use of safe anticoagulants could lower the rate of strokes in the US from 80,000 to 40,000 per year and save the medical industry an estimated $600 million per year [32].

Also, ZPC concentrate has been shown to be successful for the prevention and treatment of thrombosis in individuals with inherited and acquired PC

deficiency thus avoiding the problems associated with fresh frozen plasma administration [11, 20, 21, 31].

ZPC can be obtained from human blood plasma [18, 28, 29, 36, 35, 38, 37], cell culture and transgenic animal milk. Human blood plasma is a limited source of ZPC since only approximately 12 kg PC can be produced from the total annual blood plasma supply in the USA. Because of the difficulty of the synthesis of ZPC with the correct biological activity, few mammalian cells can be used via rDNA and the production is very expensive because of high substrate cost and low yield. Genetic engineering of animals is an alternative method to produce large quantities of human proteins. The Virginia Polytechnic Institute (VPI) and the American Red Cross (ARC) have conducted research to produce PC at concentrations as high as l mg/ml in transgenic swine milk [30].

2 The Surgery

Protein C deficiency and heterozygosity for the prothrombin gene mutation (Factor II) are inherited thrombophilic disorders that increase the risk of VTE by 5–10 fold and 2–3 fold, respectively, compared with unaffected individuals. Thrombotic occlusion of the pulmonary and peripheral vasculature can lead to hypoxia and hypoperfusion resulting in organ failure and death.

To this date, heparin and its derivatives have been the anticoagulants of choice to be used in conjunction with major surgery. This experiment involving an elderly hypercoagulable patient utilized ZPC concentrate allowing a safer surgical procedure [6, 5, 7]. The risk was especially high since the patient had previous VTE. However, total hip arthroplasty in conjunction with perioperative treatment with human protein C concentrate resulted in a successful clinical experience. No surgical complications were seen after surgery. The patient was mobilized with physical therapy. The post-operative blood loss was a little higher than average and 3 days after surgery a duplex ultrasound showed a small left peroneal deep vein thrombosis. The length of time the clot was present could not be determined and prior to discharge showed no extension with no evidence of pulmonary embolism after surgery. During the procedure the ZPC activity level increased to as high as 235% of normal. Even with this level no wound problems or infections developed after surgery and after 3 months, the patient was walking without pain in the hips and lower legs.

This surgery was the first case of peri-operative use of zymogen protein C concentrate to prevent VTE for major orthopedic surgery in a patient with heterozygous protein C deficiency and the prothrombin gene mutation and a history of previous idiopathic pulmonary embolism. The favorable results in this case demonstrate that clinicians should strongly consider prophylactic use of human protein C concentrate in highly thrombophilic patients requiring

major surgery. Further research is warranted to determine the most effective dose regime and exact dosing needed. The sited case used the manufacturers (Baxter International) recommended dosing. This led to high peak values of PC activity due to residual ZPC still in the blood stream as a result of the half-life of ZPC in vivo and the dosing interval used. It is estimated that about one-half to three-quarters of the ZPC used in this surgery would be more cost effective, with equal protection from emboli, without causing bleeds.

A predictable positive side effect that may have resulted from the use of zymogen protein C concentrate did occur. A condition unassociated with the hip osteoarthritis was present for at least a year prior to surgery. The patient complained of severe pains along the outside of the shins on both legs with no diagnosis from several medical experts. During acupuncture treatment for the pain [39], it was noticed that blood from the shin area was black in color. Immediately following the perioperative administration of the ZPC, the pains in the lower legs subsided and blood from the same points along the shin was bright red. This suggests possible blood stagnation due to sludging in the microcirculation that was flushed by the ZPC administration. If this is true, then use of ZPC might be beneficial in other cases of microcirculation occlusion.

3 Production Research

It would be beneficial to future surgical patients as well as many other heredity and acquired protein C deficient patients to develop innovative upstream and downstream bioprocessing strategies for the low-cost, high volume production of zymogen protein C. This would make ZPC available to a wider patient population.

There is ongoing research to attempt achieving this goal. The three sources of protein C that are available from upstream bioprocessing include rDNA cell culture technology, blood plasma, and transgenic animals. Our research continues to optimize the downstream processing for these raw materials via immobilized metal affinity chromatography (IMAC) [1, 2, 24–27, 33, 34]. The correct combination of ion exchange, IMAC, and absorption and elution buffers are being investigated for the optimal bio-downstream processing.

4 Conclusions

The hip surgery success is an outcome that supports the need for high volume, low cost production of ZPC. In addition, it is already established that ZPC can be used to benefit patients with other medical indications and therefore should be available for wider use.

Acknowledgments We want to thank Suzanne Bruley and Eileen Thiessen for the typing and proofing of this manuscript.

References

1. Andersson, L., 1991, Recognition of phosphate groups by immobilized aluminum (III) ions. J. Chromatogr. 539:327–334.
2. Andersson, L., Porath, J., 1986, Isolation of phosphoproteins by immobilized metal (Fe^{+++}) affinity chromatography. Anal. Biochem. 154:250–254.
3. Bertina, R.M., 1988, Protein C and Related Proteins. Churchill Livingstone, New York.
4. Bicher, H. I., Bruley, D. F., Knisely, M. H., 1973, Anti-adhesive drugs and tissue oxygenation. Adv. Exp. Med. Biol. Plenum Press, 37B:657–667.
5. Bruley, D.F, 1998, Protein C-The Ultimate Anticoagulant/Antithrombotic?, in: C.A. Thibeault and L.M. Savage (eds.). Anticoagulant, Antithrombotic, and Thrombolytic Thearapeutics II. Springer, Southborough, MA (IBC Library Series).
6. Bruley, D. F., 2009, Zymogen protein C concentrate for safer heterozygote surgery, "I am a Guinea Pig!". Adv. Exp. Med. Biol., Oxygen Transport To Tissue XXX, Springer, Vol. 645,:115–121.
7. Bruley, D.F., Drohan, W.N., 1990, Advances in Applied Biotechnology Series, Protein C and related anticoagulants, 11, Gulf Publications, Houston, TX.
8. Clouse, L.H., Comp, P.C., 1986, The regulation of hemostasis: the Protein C system. N. Engl. J. Med. 314:1298–1304.
9. Colucci, M., 1984, Influence of protein C activation on blood coagulation and fibrinolysis in squirrel monkeys. J. Clin. Invest. 74:200–204.
10. Comp, P., Esmon, C., 1981, Generation of fibrinolytic activity by infusion of activated protein C into dogs. J. Clin. Invest. 68:1221–1228.
11. Dreyfus, M., Magny, J.F. Bridey, F. et al., 1991, Treatment of homologous protein C deficiency and neonatal purpurafulminans with a purified protein C concentrate. N. Engl. J. Med. 325:1565–1568.
12. Esmon, C. T., 1989, The roles of protein C and thrombomodulin in the regulation of blood coagulation. J. Biol. Chem. 264:4743.
13. Fernlund, P., Stenflo, J., 1982, Amino acid sequence of the light chain of bovine protein C. J. Biol. Chem. 257:12170–12179.
14. Gruber, A., Griffin, J.H., Harker, L.A., Hanson, S.R., 1989, Inhibition of platelet-dependent thrombosis formation by human activated protein C in a primate model. Blood. 73:639–642.
15. Kisiel, W., 1979, Human plasma protein C: Isolation, characterization and mechanism of activation by a thrombin. J. Clin. Invest. 4:761.
16. Kisiel, W., Carnfield, W. M., Ericsson, L.H., Davie, E. W., 1977, Anticoagulant properties of bovine plasma protein C following activation by thrombin. Biochemistry. 1:5824.
17. Laemmli, U.K., 1970, Cleavage of the structural proteins during the assembly of the head of bacteriophage T4. Nature. 227:680–685.
18. Lee, J., Thiessen, E. E., and Bruley, D. F., "Anticoagulant/anti-inflammatory/antithrombotic Protein C Production-Metal Ion/Protein Intefacial Interaction in Immobilized Metal Affinity Chromatography," Proceeding of the annual ISOTT Conference.
19. Life Magazine, May 31, 1948.
20. Manco-Johnson, M., Nuss, R., 1992, Protein C concentrate prevents peripartum thrombosis. Am. J. Hematol. 40:69–70.
21. Marlar, R. A., Montgomery, R. R., Broakman, A. W., 1989, Diagnosis and treatment of homozygous protein C deficiency. Report of the working party on homozygous protein C deficiency of the subcommittee on protein C and protein S, International Committee on Thrombosis and Haemostasis. J. Paediatrics. 114:528–534.

22. Odegaard, O. R., Try, K., Anderson, T. R., 1987, Protein C: an automated activity assay. Haemostasis. 17:109–113.
23. Okajima, K., Koga, S., Kaji, M., et al., 1990, Effect of protein C and activated protein C on coagulation and fibrinolysis on normal human subjects. Thromb. Haemostas. 3:48–53.
24. Porath, J., 1992, Immobilized metal ion affinity chromatography. Prot. Express. Purif. 3:263–281.
25. Porath, J., Carlsson, J., Olsson, I., Belfrage, G., 1975, Metal chelate affinity chromatography, a new approach to protein fractionation. Nature. 258:598–599.
26. Ramadan, N., Porath, J., 1985, Fe^{3+}-hydroxamate as immobilized metal affinity-adsorbent for protein chromatography. J. Chromatogr. 321:93–104.
27. Sulkowski, E., 1988, Immobilized metal ion affinity of proteins on IDA-Fe^{3+}, Makromol. Chem. Macromol. Symp. 17:335–348.
28. Tadepalli, S. S., Bruley, D. F., Kang, K. A., Drohan, W. N., 1997, Immobilized metal affinity chromatography process identification and scale-up for protein C production. In: Harrison, D. K., Delpy, D. T. (eds.), ISOTT XIX. Advances in Experimental Medicine and Biology, Vol. 428. Plenum Press, New York, 31–43.
29. Thiessen, E. E., and D. F. Bruley, 2003 "Theoretical Studies of IMAC Interfacial Phenomena for the Production of Protein C," *Oxygen Transport to Tissue XXV* in Adv. Exp. Med. Biol. 540:183.
30. Velander, W. H., Johnson, J. L., Page, R. L., et. al., 1992, High-level expression of a heterologous protein in the milk of transgenic swine using the cDNA encoding human protein. C. Proc. Natil. Acad. Sci. 89:12003–12007.
31. Vukovich, T., Auberger, K., Weil, J., Engelmann, H., Knobl, P., Hadorn, H. B., 1988, Replacement therapy for a homozygous protein C deficiency-state using a concentrate of human protein C and S. Br. J. Haematol. 70:435–440.
32. Winslow, R., 1995, Increased use of blood-thinning drugs could prevent 40,000 strokes a year, Wall St. J. September, 8.
33. Winzerling, J. J., Patrick, B., Porath, J., 1992, How to use immobilized metal ion affinity chromatography, Methods: Compan. Methods Enzymol. 4:4–13.
34. Wong, J. W., Albright, R. L., Wang, N. H., 1991, Immobilized metal ion affinity chromatography (IMAC) chemistry and bioseparations applications. Sep. Purif. Methods. 20:49–106.
35. Wu, H., Bruley, D. F., 1999, Homologous blood protein separation using immobilized metal affinity chromatography – protein C Separation from prothrombin with application to the separation of factor IX and prothrombin. Biotechnol. Prog. 15:928–931.
36. Wu, H., Bruley, D. F., 2002, Chelator, metal ion and buffer studies for protein C separation. Comp. Biochem. Physiol., A. 132:213–220.
38. Wu, H., Bruley, D. F., Kang, K. A., 1998, Protein C separation from human blood plasma Cohn fraction IV-1 using immobilized metal affinity chromatography. in: Hudetz, A. G., Bruley, D. F. (eds.), ISOTT XX. Advances in Experimental Medicine and Biology, Vol. 454. Plenum Press, New York, 697–704.
37. Wu, H., Bruley, D. F., Kang, K. A., Drohan, W. N., 1997, Protein C separation from human plasmas Cohn fraction IV-1 using immobilized metal affinity chromatography, Topical Conference on Separation Science and Technologies – Proceedings of the 1997 Annual AIChE Meeting, 1443–1448.
39. Yu She,M.Ac.,Lic.Ac.,Dipl.Ac., yshe@umbc.edu, 2007,EllicottCity,MD,USA

Cerebral and Peripheral Tissue Oxygenation in Children Supported on ECMO for Cardio-Respiratory Failure

Maria D. Papademetriou, Ilias Tachtsidis, Terence S. Leung, Martin J. Elliott, Aparna Hoskote, and Clare E. Elwell

Abstract Extracorporeal membrane oxygenation (ECMO) is a rescue therapy for patients with cardio-respiratory failure. Establishing, maintaining and weaning from ECMO may increase the risk for intracranial injury. We used a dual channel near infrared system to monitor cerebral and peripheral tissue oxygenation in 3 venoarterial (VA) and 1 venovenous (VV) ECMO patients undergoing manipulations in the ECMO circuit flows. Spectral analysis was performed on the oxyhaemoglobin data collected from these patients with the aim of comparing oscillations at range of frequencies appearing in the two measurement sites.

1 Introduction

Extracorporeal membrane oxygenation (ECMO) is a life support system in children with intractable cardio-respiratory failure. It is aimed at supporting the heart and lungs temporarily whilst giving them a chance to recover. As ECMO is used in patients who are otherwise likely to die, the results focus on survival. However, 28–52% of these patients show abnormal neuro-imaging related both to pre-ECMO events and to the ECMO procedure itself [1]. There are 2 forms of ECMO support–venoarterial (VA) ECMO and venovenous (VV) ECMO. Establishing VA ECMO involves cannulation of major vessels in the neck–right common carotid artery (RCCA) and internal jugular vein–and supports both heart and lungs. VV ECMO involves supporting only the lungs and does not involve cannulation of the RCCA. The ECMO system can operate using 2 types of blood pumps: (1) A centrifugal pump which uses a high speed rotating device that pulls the blood into the pump and then accelerates it radially outwards and (2) a roller pump which compresses the cannula, thereby

M.D. Papademetriou (✉)
Biomedical Optics Research Laboratory, Department of Medical Physics and Bioengineering, University College London, Gower Street, London, WC1E 6BT, UK
e-mail: mpapa@medphys.ucl.ac.uk

E. Takahashi, D.F. Bruley (eds.), *Oxygen Transport to Tissue XXXI*, Advances in Experimental Medicine and Biology 662,
DOI 10.1007/978-1-4419-1241-1_64, © Springer Science+Business Media, LLC 2010

pushing the blood through the circuit. Maintaining and weaning from ECMO requires manipulation of ECMO flows, which can affect cerebral blood flow and potentially lead to neurologic complications.

Near infrared spectroscopy (NIRS) offers a continuous, non invasive means of monitoring cerebral oxygenation. Ejike et al. [2] report the use of NIRS on ECMO patients during ligation of the RCCA and during variations in the ECMO circuit flows. They concluded that regional cerebral oxygenation is not primarily affected by alterations in flows but did demonstrate a significant decrease in right sided cerebral oxygenation during ligation. Previous studies using NIRS to evaluate the effects of vessel ligation showed a decrease in oxy-(HbO_2) and increase in deoxy-(HHb) haemoglobin in the right hemisphere [3] and in both hemispheres [4].

The long-term aim is to use an optical topography system to investigate topographic cerebral oxygenation changes in patients undergoing ECMO. However initially we are monitoring regional cerebral and peripheral tissue oxygenation using a dual channel system, with the aim of investigating the relationship between brain and peripheral tissue oxygenation during changes in ECMO related variables.

2 Methods

Studies were performed on 4 ECMO patients, aged between 1 day and 5 years. The patient group in this pilot study is a rather inhomogeneous group consisting of 2 VA ECMO cases operating on centrifugal pumps, 1 VA ECMO and 1 VV ECMO operating on roller pumps.

A dual channel near infrared system (NIRO 200, Hamamatsu Photonics KK) was used to measure changes in HbO_2 and HHb haemoglobin concentrations using the modified Beer-Lambert Law, and tissue oxygenation index (TOI) using spatially resolved spectroscopy. Channel 1 was placed on the forehead (cerebral) and channel 2 on the calf (peripheral) of the patients. The optodes were held in place using elastic bandage to eliminate possible drifts in the signal arising from gradual loss in contact between the optode and the skin. For the conversion of the optical attenuation changes to chromophore concentration changes a differential pathlength factor (DPF) of 4.99 was applied [5]. Data were collected during manipulations in the ECMO circuit flow. Blood flow in the ECMO circuit was decreased or increased successively by 10% from the initial flow every 20–30 min.

The data were divided into sections for each specific flow. Power spectral density (PSD) and coherence analysis were performed on the HbO_2 signal recorded at the two measurement sites. The PSDs were obtained in order to identify the presence of any oscillations occurring in the brain and in the leg and were estimated using Welch's method [6]. The coherence function was used to characterise the frequency dependent correlation of the HbO_2 signal in the

brain with the HbO_2 signal in the leg. We defined three frequency bands (very low (VLF) 0.002–0.3 Hz, low (LF) 0.3–0.5 Hz and high (HF) 0.5–1 Hz) to extract vasomotion, respiratory and cardiac oscillations. To obtain a measure of the coherence over a specific frequency band, the coherence function was averaged over that frequency band.

3 Results and Discussion

Figure 1(a) shows the oscillatory changes in HbO_2 and (b) the corresponding PSDs during weaning for Patient 1 undergoing VA ECMO. When a patient is weaned off ECMO the blood flow in the ECMO circuit is reduced by 10% approximately every 30 min while the heart and lungs of the patient are gradually allowed to take over. In this case, the ECMO circuit operated on a roller pump.

The PSDs show the presence of a strong oscillation in the brain and leg that remains constant as the ECMO circuit flow is decreased, corresponding to the patient's respiration rate (RR). A higher frequency appears in both the brain and leg that shifts to the left with decreasing ECMO circuit flow. This frequency is twice the frequency of the pump (f_{pump}) in the ECMO circuit, which is consistent with the two headed roller pump. In addition, a very slow oscillation (~0.005 Hz) is present only in the leg. The strength of this oscillation appears to be increasing as the flow is reduced and can be clearly seen even in the time domain plots. This observation raises questions about the relationship between cerebral and systemic vascular vasomotion and whether cerebral autoregulation results in suppressing this oscillation in the brain. The coherence between the brain and leg at 90, 80 and 70% initial flow in the VLF and LF bands was significantly different ($p < 0.05$) from the coherence at initial flow in these frequency bands. Also, there was an increase in coherence in association with reduction in ECMO flows.

Figure 2 shows (a) the changes in HbO_2 data and (b) the corresponding PSDs for Patient 2, undergoing VA ECMO on a centrifugal pump. The PSDs of this patient showed the presence of two oscillations, one in the LF band corresponding to the patient's RR and the other in the HF band corresponding to the patient's heart rate (HR). There is no indication of the pump frequency in these data. However, we can identify oscillations in the VLF band. In comparison with the previous patient these oscillations occur around 0.015 Hz and appear only in the brain and not in the leg. The coherence between the brain and leg at 90 and 80% initial flow in the VLF, LF and HF bands was significantly different ($p < 0.05$) from the coherence at initial flow in these frequency bands. This is in contrast with Patient 1, who showed a decrease in coherence with reduction in ECMO flows.

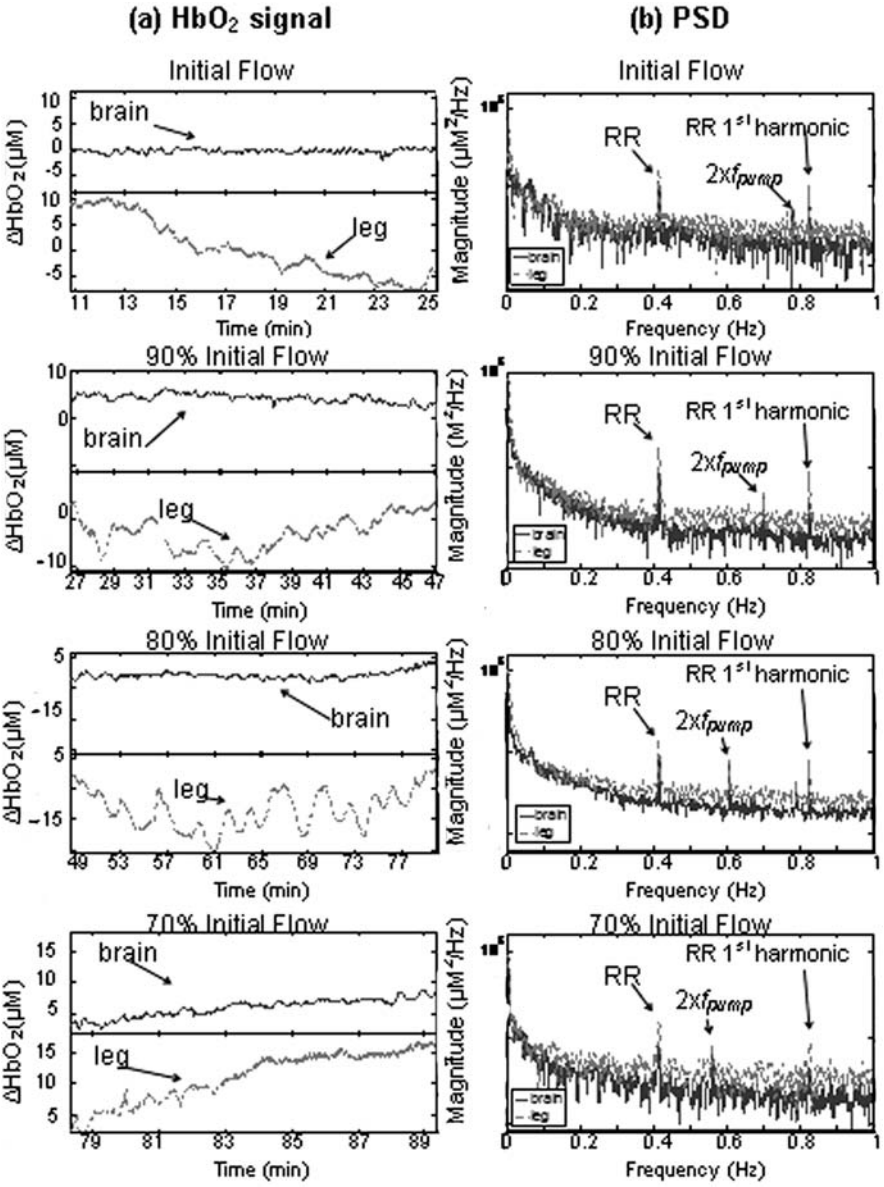

Fig. 1 (**a**) Changes in HbO_2 data in the brain and leg for Patient 1, during reduction in the ECMO circuit blood flow. (**b**) Corresponding power spectral density

Spectral analysis was performed on another patient undergoing VA ECMO with a centrifugal pump (Patient 3). The PSDs, shown in Fig. 3(b) identify the RR and the HR. Similar to the results of patient 1, the PSD of this patient showed the presence of oscillations (~0.005 Hz) in the leg and not in the brain.

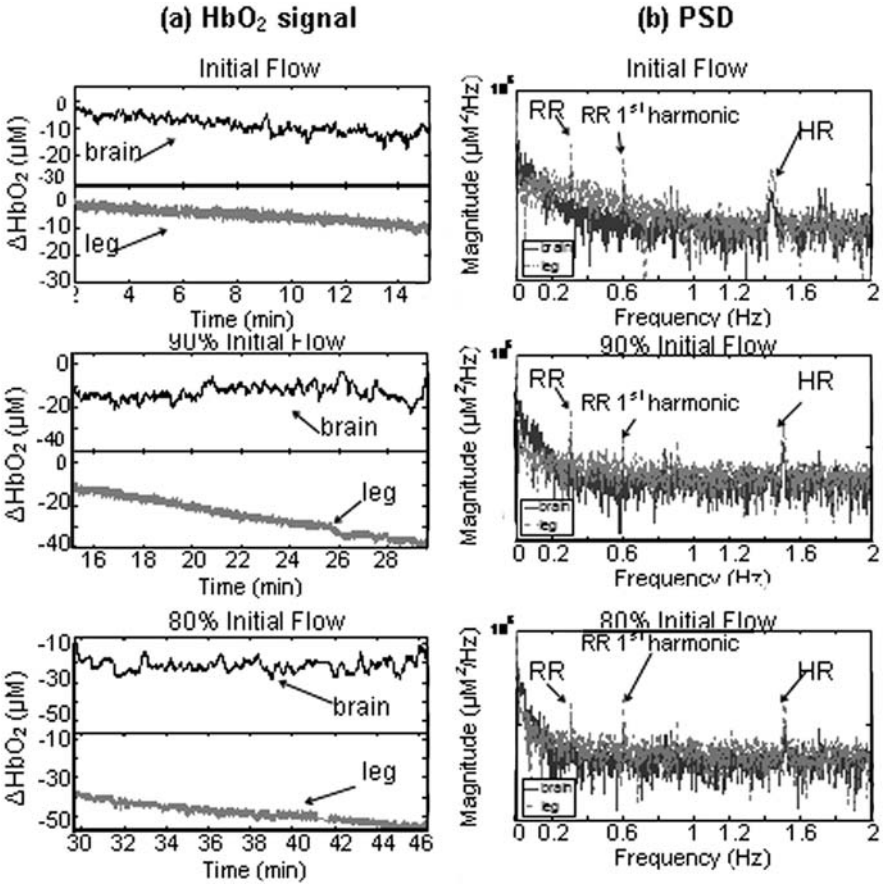

Fig. 2 (**a**) Changes in HbO_2 data in the brain and leg for Patient 2, during reduction in the ECMO circuit blood flow. (**b**) Corresponding power spectral density

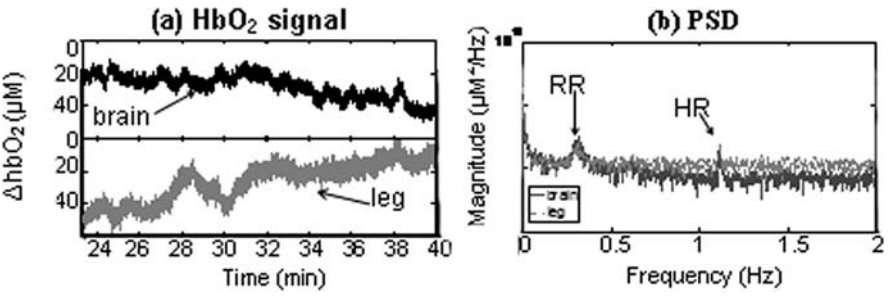

Fig. 3 (**a**) Changes in HbO_2 data in the brain and leg for Patient 3. (**b**) Corresponding power spectral density

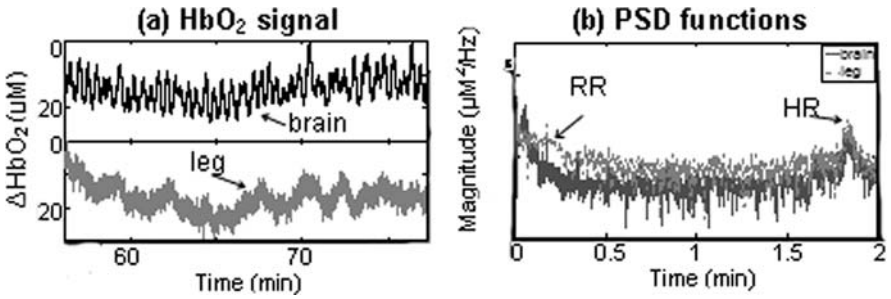

Fig. 4 (**a**) Changes in HbO_2 data in the brain and leg for Patient 4. (**b**) Corresponding power spectral density

Figure 4(a) shows the changes in HbO_2 data of a patient undergoing VV ECMO with a roller pump (Patient 4). The corresponding PSDs are shown in Fig. 4(b) with the RR and the HR present in both brain and leg. Two more oscillations were identified; ~0.005 Hz appearing in the leg only and ~0.05 Hz appearing in the brain only. The difference between the oscillations in the VLF range can be clearly seen even in the time domain plots.

4 Conclusions

NIRS is an effective technique for monitoring cerebral oxygenation in ECMO patients. We have used PSDs to identify the presence of any oscillations occurring in the brain and leg of 4 ECMO patients undergoing flow manipulations. The RR and HR can be picked up in all patients and is present in both brain and leg. In addition to these oscillations, we identified the presence of oscillations in the VLF band. It is interesting that a low frequency oscillation (0.005 Hz) was present in the leg data of 3 of the 4 patients studied (2 VA ECMO patients and 1 VV ECMO patient). Kvandal et al. report the presence of skin vasomotion oscillations in the interval 0.005–0.0095 Hz [7]. Two of the patients showed slow oscillations in the brain (~0.015 Hz in Patient 2 and ~0.05 Hz in Patient 4), similar to those described by Obrig et al. [8]. Oscillations in the HF band appearing at twice the frequency of the ECMO pump were detected in brain and leg for Patient 1 (VA ECMO on roller pump). There was not clear relationship between the origin of the oscillation and the patients' clinical condition.

Further studies are required to more fully explore the relationship between oscillations arising in specific frequency bands and the type of ECMO procedures used in different patients. These studied may elucidate cerebral autoregulation mechanisms in ECMO patients.

Acknowledgment This work is supported by Hitachi Medical Ltd.

References

1. Bulas D, Glass P (2005) Neonatal ECMO: Neuroimaging and neurodevelopmental outcome. Sem Perinatol 29: 58–65
2. Ejike JC, Schenkeman KA, Seidel K, Ramamoothy C, Roberts JS (2006) Cerebral oxygenation in neonatal and pediatric patients during veno-arterial extracorporeal life support. Pediatr Crit Care Med 7: 154–158
3. Liem KD, Hopman JCW, Oeseburg B, de Haan AFJ, Festen C, Kollee LAA (1995) Cerebral Oxygenation and hemodynamics during induction of extracorporeal membrane oxygenation as investigated by near infrared spectrophotometry. Pediatrics 95: 555–561
4. Van Heijst A, Liem D, Hopman J, Van der Stakk F, Sengers R (2004) Oxygenation and hemodynamics in left and right cerebral hemispheres during induction of veno-arterial extracorporeal membrane oxygenation. Pediatr 144: 223–228
5. Duncan A, Meek JH, Clemence M, Elwell CE, Tyszczuk L, Cope M, Delpy DT (1995) Optical pathlength measurements on adults head, calf and forearm and the head of the newborn infant using phase resolved optical spectroscopy. Phys Med Biol 40: 295–304
6. Welch, P.D. (1967) The use of fast fourier transform for the estimation of power spectra: A method based on time averaging of short, modified periodograms. IEEE Trans. Audio and Electroacoustics, AU-15(2), 70–73.
7. Kvandal P, Landsverk SA, Bernjak A, Stefanovska A, Kvernmo HD, Kirkeboen KA (2006) Low frequency oscillations of the Laser Doppler perfusion signal in human skin. Microvasc Res 72: 120–127
8. Obrig H, Neufang M, Wenzel R, Kohl M, Steinbrink J, Einhaupl K, Villringer A (2000) Spontaneous low frequency oscillations of cerebral hemodynamics and metabolism in human adults. Neuroimage 12: 623–639

Effects of Acupuncture on Autonomic Nervous Function and Prefrontal Cortex Activity

Kaoru Sakatani, Takeshi Kitagawa, Naoki Aoyama, and Mitsuyoshi Sasaki

Abstract Acupuncture is helpful in treating various diseases, including autonomic nervous system (ANS) dysfunction caused by mental stress. On the other hand, the frontal lobe is suggested to play an important role in stress responses by modulating the ANS. The aim of the study was to evaluate the effects of acupuncture on ANS and frontal lobe activities. We investigated 18 normal adults. We measured the activity of prefrontal cortex (PFC) caused by real acupuncture (WHO-LI4) and sham acupuncture, employing optical topography. To evaluate ANS function, we analyzed heart rate variability (HRV). Analysis of HRV revealed a decrease of the LF/HF ratio, and an increase of the HF power by real acupuncture, indicating a shift to parasympathetic dominancy. Acupuncture also caused cerebral blood oxygenation changes in both directions, that is, an increase and/or a decrease of oxyhemoglobin (Oxy-Hb) in the bilateral PFC. However, the Oxy-Hb change was not correlated with HRV parameters in the majority of cases. One of the possible explanations of the poor correlations might be that the PFC activity induced by acupuncture is not closely linked with ANS function.

1 Introduction

There is increasing clinical evidence that acupuncture is helpful in treating various diseases, including autonomic nervous system (ANS) dysfunction caused by mental stress. For example, acupuncture at certain points could reduce sympathetic nervous system activity associated with pain [1]. In addition, it was demonstrated that acupuncture could inhibit sympathetic activation during mental stress in patients with heart failure [2]. However, the neurobiological basis of these effects is not yet clear.

K. Sakatani (✉)
Division of Optical Brain Engineering, Department of Neurological Surgery; Division of Applied System Neuroscience, Department of Advanced Medical Science, Nihon University School of Medicine, Tokyo, 173-8610, Japan
e-mail: sakatani@med.nihon-u.ac.jp

E. Takahashi, D.F. Bruley (eds.), *Oxygen Transport to Tissue XXXI*,
Advances in Experimental Medicine and Biology 662,
DOI 10.1007/978-1-4419-1241-1_65, © Springer Science+Business Media, LLC 2010

The prefrontal cortex (PFC) plays an important role in mediating behavioral and somatic responses to stress via projections to the autonomic centers [3]. Electroencephalographic studies have shown that a greater right frontal activation is associated with increased heart rate during unpleasant emotional stimuli [4]. A functional MRI study revealed that right dominance of PFC activity during mental stress tasks correlated with changes in heart rate [5]. In addition, our near infrared spectroscopy (NIRS) studies have demonstrated that the right PFC activity predominantly modulates sympathetic effects during a mental stress task [6–8]. However, it is not yet clear whether the PFC is involved in modulation of ANS function by acupuncture, and whether the laterality of the PFC activity plays a role in regulation of the ANS by acupuncture. In order to clarify these issues, we evaluated the effect of acupuncture on ANS function and frontal lobe activity using NIRS.

2 Methods

We investigated 18 healthy male adults (20–54 years; mean 42.7 years). Seventeen of them were right-handed, and one subject was left-handed as judged by the Edinburgh Handedness Inventory. To avoid the influence of environmental stress, the subjects were seated in a comfortable chair in a regular room with good air conditioning throughout the experiments.

We measured the frontal lobe activity caused by acupuncture. Real acupuncture was performed at acupuncture point Large Intestine 4 (WHO-LI4) of the right hand (r-LI4; 18 subjects) or left hand (l-LI4; 13 subjects), and sham acupuncture was performed at skin 2–3 cm distal to the r-LI4 (18 subjects). After disinfecting the skin surface with an alcoholic cotton swab, a disposable needle was inserted quickly by an experienced acupuncturist aiming at each point, and the point was stimulated for a minute with bidirectional needle rotation, then the needle was left at the point for 1.5 min without rotation.

We employed optical topography (OMM 2001, Shimadzu, Japan) to undertake two-dimensional (2D) imaging of the changes in concentration of oxyhemoglobin (Oxy-Hb), deoxyhemoglobin (Deoxy-Hb) and total-hemoglobin (= Oxy-Hb + Deoxy-Hb; Total-Hb) in the activated cortices of the bilateral frontal lobes. The hemoglobin concentrations were expressed in arbitrary units. The optodes for the NIRS topography were placed on the skull to cover the bilateral frontal lobes, employing a holder cap to avoid motion-related artifacts; the distance between each optode was 30 mm [9]. Heart rate was simultaneously monitored with PFC activity by placing a photo-electrical sensor (Tsuyama MGF KK, Tokyo, Japan) on the subject's first finger to measure pulse waves. ANS function was evaluated by heart rate variability (HRV) analysis; the low frequency (LF) amplitude (0.04–0.15 Hz) and the high frequency (HF) amplitude (0.15–0.4 Hz) were calculated by power spectral analysis. The values of the HRV parameters were expressed as a function of the

natural logarithm (Ln). To evaluate the effects of acupuncture, the mean values of the HRV parameters for 2.5 min were compared among the prestimulus control, test stimulus and poststimulus control.

3 Results

Analysis of HRV (Table 1) revealed that real acupuncture at r-LI4 caused significant decreases of HR (A; $p = 0.0409$) and Ln LF/HF (D; $p = 0.0044$), and a significant increase of Ln HF (C; $p = 0.0087$). The significant decrease of HR could be partly attributed to the subjects with higher value of the HR at pre-stimulus condition (E). Acupuncture at contra lateral l-LI4 showed the same tendency as r-LI4 acupuncture, but there was no statistically significant change of HRV parameters during acupuncture ($p > 0.05$). Sham acupuncture caused no significant change in HR or Ln HF ($p > 0.05$).

Table 1 Effects of acupuncture on heart rate (HR) and heart rate variability

		l-L14	r-L14	Skin
HR	pre	68.0 ± 2.6	71.4 ± 2.0	67. 9 ± 2.2
	test	67.5 ± 2.8	68.5 ± 1.9 *	69.1 ± 2.7
	post	67.3 ± 2.9	70.4 ± 1.6	70.0 ± 2.6
ln LF	pre	5.80 ± 0.24	5.68 ± 0.23	5.35± 0.25
	test	5.48 ± 0.24	5.49 ± 0.21	5.56 ± 0.21
	post	5.62 ± 0.16	5.42 ± 0.19	5.19 ± 0.25
ln HF	pre	5.19 ± 0.16	5.16 ± 0.18	5.14 ± 0.19
	test	5.36 ± 0.19	5.57 ± 0.19**	5.37 ± 0.20
	post	5.31 ± 0.23	5.20 ± 0.20	5.10 ± 0.21
N LF/HF	pre	1.12 ± 0.05	1.12 ± 0.05	1.10 ± 0.05
	test	1.04 ± 0.06	1.00 ± 0.04**	1.05 ± 0.03
	post	1.08 ± 0.04	1.07 ± 0.04	1.03 ± 0.04

Each value represents mean ± S.D. pre: pre-stimulus control; stim: during stimulus; post: post-stimulus control. Asterisks indicate that the values during stimuli are statistically significantly different from the pre-stimulus control (*: $p < 0.05$, **: $p < 0.01$; two-tailed paired t-test)

Optical topography demonstrated several different patterns of NIRS parameter changes. For example, Oxy-Hb increased in the bilateral frontal lobes during real acupuncture at r-LI4 in seven subjects. A typical pattern of these subjects is the increase of Oxy-Hb in the anterior portion, as well as the lateral portion of the bilateral PFC (Fig. 1a). In contrast, one subject showed Oxy-Hb decreases in these portions during real acupuncture at r-LI4 (Figs. 1b). In the remaining 9 subjects, the directions of the Oxy-Hb changes were intermingled: an increase, a decrease or almost no change (Fig.1c) occurred with different stimuli at different portions of the PFC. Table 2 shows the mean changes of Oxy-Hb in four different regions of the PFC in 18 subjects for r-LI4 and skin, and 13 subjects for l-LI4.

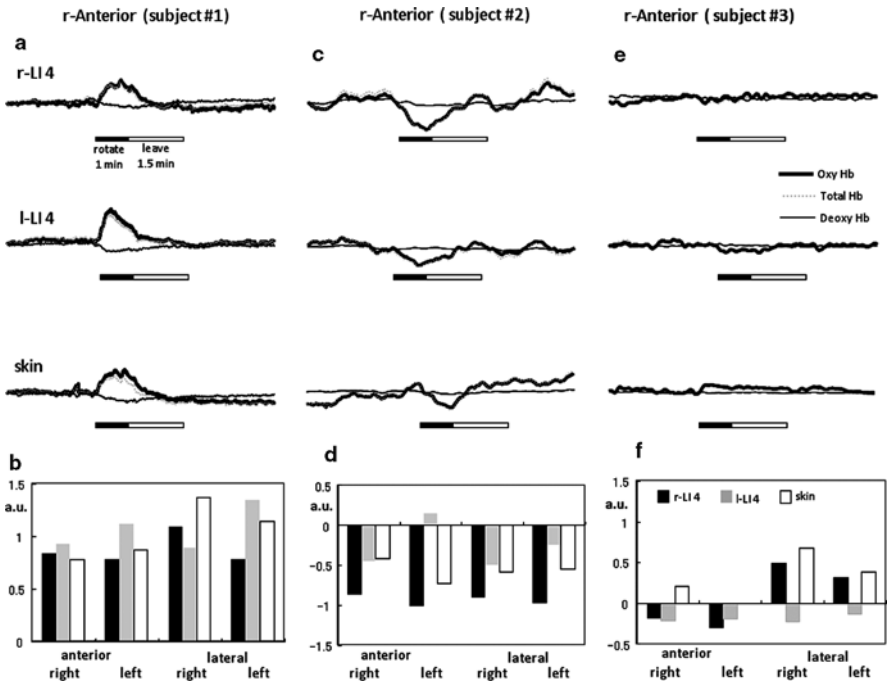

Fig. 1 Effects of acupuncture on NIRS parameters. Three typical patterns (**a**, **b**, **c**) of the concentration changes of NIRS parameters during acupuncture at r-LI4, l-LI4 and skin; traces of Oxy-Hb (*thick trace*), Deoxy-Hb (*thin trace*) and Total-Hb changes (*dotted line*) recorded on the *right anterior* PFC in three subjects (subject #1, #2, #3). Acupuncture was performed during the period indicated below each trace (*horizontal bar*); the *black* and *white bars* indicate the periods of rotation and leaving of the needle, respectively

Table 2 Effects of acupuncture on Oxy-Hb changes in the PFC

	r-APFC	l-APFC	r-LPFC	l-LPFC
r-L14	0.14 ± 0.41	-0.062 ± 0.38	0.56 ± 0.72	0.30 ± 0.64
l-L14	0.10 ± 0.37	0.25 ± 0.42	0.37 ± 0.56	0.32 ± 0.52
skin	0.19 ± 0.25	0.11 ± 0.32	0.43 ± 0.45	0.38 ± 0.45

APFC: anterior part of the prefrontal cortex, LPFC: lateral part of the prefrontal cortex. r-: right side, l-: left side. We analyzed the maximal value of Oxy-Hb changes in each region of the PFC. Each value represents mean $\pm$ S.D. Data are expressed in arbitrary units

Next we examined the relations between the changes in the HRV parameters and the Oxy-Hb change in the r-APFC, l-APFC and bilateral LPFC. In the r-APFC, a correlation was observed only between the change of Ln LF and the Oxy-Hb change during acupuncture at l-LI4 ($p = 0.009$; $r = 0.668$). In the other portions of PFC, a few positive correlations were observed. In the r-LPFC, the change of Ln HF was positively correlated with Oxy-Hb change with

acupuncture at the l-LI4 ($p = 0.0166$; $r = 0.648$). In the l-LPFC, the Ln HF was positively correlated with Oxy-Hb change with acupuncture at skin ($p = 0.0466$; $r = 0.493$). Although there was no correlation between HRV parameters and Oxy-Hb with acupuncture at the r-LI4, when combining both data of r-LI4 and l-LI4, the change of Ln HF was positively correlated with the Oxy-Hb change in the r-APFC ($p = 0.0138$; $r = 0.431$) and the l-LPFC ($p = 0.0448$; $r = 0.352$).

4 Discussion

We demonstrated that real acupuncture at r-LI4 caused a significant decrease of the HR, increase of the HF power and decrease of the LF/HF power during acupuncture, indicating that the HR was decreased by parasympathetic activation as well as sympathetic depression. A decrease in HR and an increase of HF power by acupuncture at LI4 have been reported recently [10], and these findings are consistent with the present study. They, however, reported a significant increase of the LF/HF ratio (i.e., sympathetic activation) during the first minute of stimulation. The difference between the present and the previous studies could be attributed to the difference in the methods such as manipulation of the needle.

Acupuncture caused an increase and/or a decrease of Oxy-Hb in the bilateral PFC. The increases and decreases of Oxy-Hb reflected activation and deactivation of the PFC, respectively [11]. Recently, we have demonstrated that the PFC plays an important role in regulation of ANS function [6, 7]. That is, the right PFC activity predominantly modulates sympathetic effects during mental stress tasks. In the present study, however, the degree of Oxy-Hb change was not closely associated with the ANS function. The Oxy-Hb change was correlated with HRV parameters only in a few cases. The reason why we could not find a statistical significant correlation between the PFC activity and ANS function during acupuncture might be the small number of subjects. Another possibility is that the PFC activity induced by acupuncture might not be closely linked with ANS function. Finally, it should be noted that task-related changes in systemic blood pressure may contribute to the CBO changes measured by NIRS [12]. Further studies are necessary to clarify these issues.

References

1. Arai YC, Ushida T, Osuga T et al. (2008) The effect of acupressure at the extra 1 point on subjective and autonomic responses to needle insertion. Anesth Analg 107:661–664.
2. Middlekauff HR, Hui K, Yu JL et al. (2002) Acupuncture inhibits sympathetic activation during mental stress in advanced heart failure patients. J Card Fail 8:399–406.
3. Buijs RM, van Eden CG (2000) The integration of stress by the hypothalamus, amygdale and prefrontal cortex: balance between the autonomic nervous system and the neuroendocrine system. Progress in Brain Res 126:117–132.

4. Waldstein SR, Kop WJ, Schmidt LA et al. (2000) Frontal electrocortical and cardiovascular reactivity during happiness and anger. Biol Psychol 55:3–23.
5. Wang J, Rao H, Wetmore GS et al. (2005) Perfusion functional MRI reveals cerebral blood flow pattern under psychological stress. PNAS 102:17804–17809.
6. Tanida M, Sakatani K, Takano R et al. (2004) Relation between asymmetry of prefrontal cortex activities and the autonomic nervous system during a mental arithmetic task: Near infrared spectroscopy study. Neurosci Lett 369:69–74.
7. Tanida M, Katsuyama M, Sakatani K (2007) Relation between mental stress-induced prefrontal cortex activity and skin conditions: a near infrared spectroscopy study. Brain Res 1184:210–216.
8. Tanida M, Katsuyama M, Sakatani K (2008) Effects of fragrance administration on stress-induced prefrontal cortex activity and sebum secretion in the facial skin. Neurosci Lett 432:157–161.
9. Hoshino T, Sakatani K, Katayama Y et al. (2005) Application of multi-channel near infrared spectroscopic topography to physiological monitoring of the cortex during cortical mapping: Technical case report. Surg Neurol 64:272–275
10. Streitberger K, Steppan J, Maier C, Hill H, Backs J, Plaschke K (2008) Effects of verum acupuncture compared to placebo acupuncture on quantitative EEG and heart rate variability in healthy volunteers. J Altern Complement Med 14(5):505–513.
11. Sakatani K, Katayama Y, Yamamoto T et al. (1999) Cerebral blood oxygenation changes of the frontal lobe induced by direct electrical stimulation of thalamus and globus pallidus: A near infrared spectroscopy study. J Neurol, Neurosurg Psychiatry 67:769–773.
12. Tachtsidis I, Leung TS, Devoto L, et al. (2008) Measurement of frontal lobe functional activation and related systemic effects: a near-infrared spectroscopy investigation. Adv Exp Med Biol 614:397–403.

The Effect of Glycaemia on the Cerebral Oxygenation in Very Low Birthweight Infants as Measured by Near-Infrared Spectroscopy

Joke Vanderhaegen, Sophie Vanhaesebrouck, Christine Vanhole, Paul Casaer, and Gunnar Naulaers

Abstract The cerebral tissue oxygenation index (TOI) and fractional tissue oxygen extraction (FTOE) reflect the cerebral oxygenation. We studied the effect of glycaemia on the TOI and FTOE, as measured by near-infrared-spectroscopy (NIRS). We continuously measured TOI, glycaemia, mean arterial blood pressure (MABP), saturation (SaO_2) and transcutaneous carbon dioxide pressure ($tPCO_2$) for at least 4 h during the first week of life in neonates with gestational age (GA) < 32 weeks and weight < 1500 g. FTOE was calculated. 24 measurements in 11 neonates were analyzed. We found a significant negative correlation ($r = -0.077$; $p = 0.0344$) between glycaemia and TOI, also after correction for MABP, SaO_2 and $tPCO_2$ ($r = -0.118$; $p = 0.002$) and a significant positive correlation between glycaemia and FTOE ($r = 0.147$; $p < 0.000$) which remained significant after correction for MABP and $tPCO_2$ ($r = 0.116$; $p = 0.001$). Our results indicate that in neonates during the first days of life glycaemia – even within the normal ranges and after correction for MABP, SaO_2 and $tPCO_2$ – influences the cerebral oxygenation.

1 Introduction

To ensure adequate brain development during the perinatal period, the human brain is dependent upon glucose supply and metabolism. However disturbed glycaemic control at birth is common. Hyperglycaemia is associated with an increased risk of intraventricular haemorrage (IVH), morbidities as retinopathy of prematurity (ROP) as well as with increased mortality [1]. Hypoglycaemia has been associated with poor neurodevelopmenal outcome [2] and reduced brain growth, especially in prematurely born infants, and is therefore defined as one of the most common metabolic problems in the neonatal intensive care unit [3]. The effect of glycaemia on the cerebral metabolism ($CMRO_2$) and blood

J. Vanderhaegen (✉)
UZ Gasthuisberg, Herestraat 49, B-3000 Leuven, Belgium
e-mail: joke.vanderhaegen@uz.kuleuven.ac.be

E. Takahashi, D.F. Bruley (eds.), *Oxygen Transport to Tissue XXXI*,
Advances in Experimental Medicine and Biology 662,
DOI 10.1007/978-1-4419-1241-1_66, © Springer Science+Business Media, LLC 2010

flow (CBF) has been analyzed in animal as well as in human studies, although discrepancy exists. Pryds et al. were the first to show that prematurely born infants with moderate hypoglycaemia are able to protect their immature brain by multiple processes such as a compensatory increase in CBF [4]. This was the first study describing the effect of aberrant glycaemic values on the cerebral circulation of prematurely born infants. Research on the cerebral oxygenation however is still rare. By means of near infrared spectroscopy (NIRS), cerebral oxygenation can be measured continuously and non-invasively. Spatially resolved spectroscopy (SRS) uses NIRS to measure the balance between oxygenated (HbO_2) and deoxygenated (HbR) cerebral haemoglobin: the Tissue Oxygenation Index reflects the cerebral oxygenation [5]:

$$\mathrm{TOI}(\%) = \frac{\mathrm{k\ HbO_2}}{\mathrm{k\ HbO_2 + k\ HbR}} \tag{1.1}$$

where k is a constant. The cerebral Fractional Tissue Oxygen Extraction (FTOE) reflects the ratio between oxygen delivery (OD) and consumption (VO_2) and can be calculated as

$$\mathrm{FTOE} = \frac{(\mathrm{SaO_2 - TOI})}{\mathrm{SaO_2}} \tag{1.2}$$

We analyzed the effect of glycaemia on the cerebral oxygenation, as measured by NIRS, in preterm infants during the first days of life.

2 Datasets

2.1 Patient Population

Preterm infants at the Neonatal Intensive Care Unit (NICU) of the University Hospital of Leuven, with a GA < 32 weeks, birth weight < 1500 g, arterial line and need for intensive care were included in the study. Infants with congenital malformations or cerebral complications like intraventricular hemorrage (IVH) $>$ grade I or periventricular leucomalacia (PVL) at the start of the study were excluded. The Ethics Committee of the University Hospitals Leuven approved the use of near-infrared spectroscopy. Measurements were performed after parental consent.

2.2 Clinical Data

MABP (Hewlett Packard 78353 A®) was continuously measured on an umbilical or peripheral arterial line. Simultaneously ECG, heart rate (HR), peripheral oxygen saturation (SaO_2) (Pulse Oximeter, Novametrix®), partial oxygen pressure (PaO_2) and $tPCO_2$ (TINA™ Radiometer™) were recorded in an analogous way with a sampling frequence of 100 Hz by the data acquisition system

Codas (Dataq Instruments, Akron, Ohio, USA®) and stored in a personal computer. Glycaemia values were measured (CGMS® System Gold™: Continuous Glucose Monitoring System) with average values every 5 min.

3 Methods

3.1 Monitoring Cerebral Tissue Oxygenation and Extraction

With the NIRO 300 near-infrared spectrophotometer (Hamamatsu Phototonics K.K., Tokyo, Japan®) we evaluated the cerebral oxygenation: a light detector with three emitting diodes sends near-infrared light of four different wavelengths into tissue. The light gets attenuated due to scatter loss and absorption by oxygenated (HbO_2) and deoxygenated hemoglobin (HbR). The Modified Lambert-Beer Law allows to convert changes in absorption and attenuation in changes in HbO_2 (ΔHbO_2) and HbR (ΔHbR). If the distance between the light source and the detector is more than 3 cm, scatter loss gets the same at the three sensors whereas an absolute value, the TOI, can be calculated (1.1). The optode was placed at the right frontoparietal side with the sensors at 4 cm distance and a differential pathlength factor of 1,39. ΔHbO_2, ΔHbR and total haemoglobin ($\Delta HbT = \Delta HbO_2 + \Delta HbR$) were recorded continuously and digitally with a sampling rate of 6 Hz. They were converted into analogous signals with a sample and hold function before their introduction into the Codas system.

3.2 Study Design and Statistics

Vital signs and the cerebral parameters were continuously measured for at least 4 h during the first days of life. The continuous data were imported into excel. ΔHbD ($= \Delta HbO_2 – \Delta HbR$) was calculated as a measure of CBF and also FTOE was calculated (1.2). Data are then summarized as mean values with corresponding 95% confidence interval (CI) over 5-min periods. With the Spearman rank correlation we assessed the correlations between glycaemia and TOI, FTOE and HbD for the entire group as well as for each measurement individually. We used the partial correlation to measure the correlations between glycaemia and the cerebral parameters while corecting for SaO_2, MABP and $tPCO_2$. A P value of < 0.05 was considered significant.

4 Experimental Results and Discussion

4.1 Clinical Characteristics

In total 24 measurements in 11 neonates were carried out during the first postnatal week: 2 measurements were performed on postnatal day 5 (PND) 0; 5 on PND 1; 4 on PND 2; 3 on PND 3; 3 on PND 4; 2 on PND 5; 3 on PND 6 and 2 on PND 7. The anthropometric, physiologic and cerebral variables are

Table 1 The anthropometric, physiologic and cerebral variables of our study population

	Mean (± SD)		Mean (± SD)
PMA (weeks)	27.9 (± 2.78)	PCO_2 (mmHg)	53.9 (± 10.3)
Weight (g)	946.4 (± 200.7)	SaO_2 (%)	91.7 (± 3.35)
Length (cm)	35.5 (± 2.53)	Glycaemia (mmol/l)	6.4 (± 2.48)
HC (cm)	25.4 (± 1.58)	TOI (%)	65.6 (± 7.24)
MABP (mmHg)	38.6 (± 6.56)	FTOE	0.285 (± 0.080)
		HbD (μmol/l)	7.80 (± 26.5)

shown in Table 1. All patients were mechanically ventilated. 4 of the 11 infants developed clinical signs of IVH grade I–IV and in 3 of the 11 patients PVL was diagnosed. The incidence of IVH and PVL was not related to glycaemia, $tPCO_2$, TOI, FTOE or HbD (chi-square).

4.2 The Effect of Glycaemia on TOI, FTOE and HbD

Over the entire group we found a weak but significant negative correlation ($r = -0.077$; $p = 0.0344$) between glycaemia and TOI, also after correction for MABP, SaO_2 and $tPCO_2$ ($r = -0.118$; $p = 0{,}002$) and a weak but significant positive correlation between glycaemia and FTOE ($r = 0.147$; $p < 0.000$) which remained significant after correction for MABP and $tPCO_2$ ($r = 0.116$; $p = 0.001$) (Fig. 1). A significant negative correlation between glycaemia and HbD

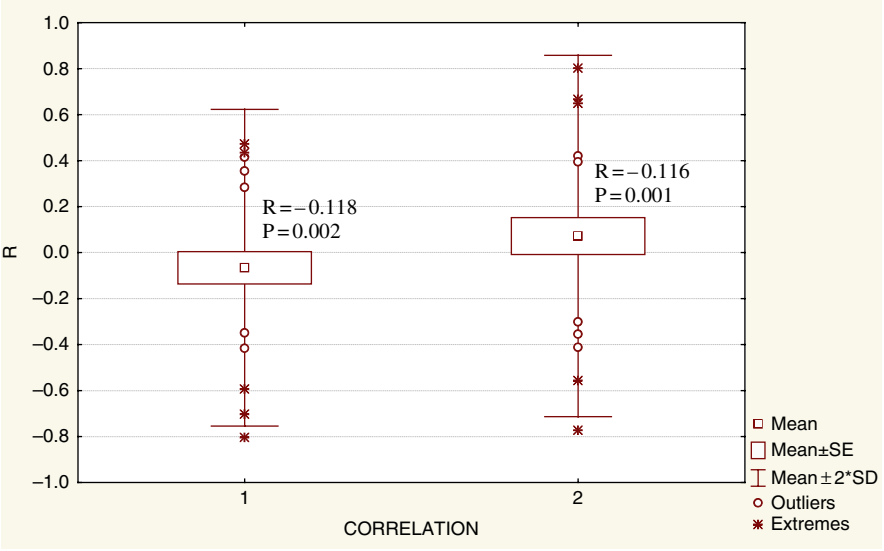

Fig. 1 The partial correlation coefficients (R) for the different measurements are plotted in (1): correlation between glycaemia and TOI; mean $R = -0.118$ and (2): correlation between glycaemia and FTOE; mean $R = 0.116$

($r = -0.0816$; $p = 0.026$) was found also after correction for MABP, SaO_2 and $tPCO_2$ ($r = -0.0893$; $p = 0.017$).

5 Discussion

Our results show that in premature infants during the first days of life glycaemia – within the normal glycaemic range and independent of changes in SaO_2, MABP and $tPCO_2$ – influences the cerebral oxygenation.

In prematurely born infants disturbed glycaemic control at birth is common and may lead to cerebral complications [2]. Research on the effect of glycaemia on the neonatal cerebral oxygenation is still rare. We therefore continuously measured glycaemia and cerebral oxygenation in preterm neonates and found a negative correlation between glycaemia and TOI and a positive correlation between glycaemia and FTOE. This can be explained as follows: a decrease in glycaemia depresses $CMRO_2$ due to a limitation of metabolizable substrate. As a compensation mechanism, CBF and cerebral oxygen delivery (OD) increase without a change in $CMRO_2$. We measured ΔHbD as a measure of CBF [6] and found a negative correlation with glycaemia which suggest that the observed changes in cerebral oxygenation we see with changes in glycaemia reflect changes in CBF. Although we should be cautious: HbD reflects CBF in case of constant SaO_2 and $CMRO_2$. SaO_2 was stable during the recording time. But we could not analyze $CMRO_2$ However since all infants were in quiet condition during the time of measurements and since temperature, ventilation,. . .were held constant, we assume that $CMRO_2$ remained constant and is unlikely to explain the observed changes in cerebral oxygenation. Hypoglycaemia is often accompanied by other conditions such as hypoxemia and hypotension, making it difficult to separate the effects of hypoglycaemia from those of concurrent pathophysiological states. With partial correlation we ruled out the effect of MABP, SaO_2 and $tPCO_2$ and still found significant correlations between glycaemia and TOI, FTOE and HbD. This indicates that glycaemia affects the cerebral oxygenation independently of MABP, SaO_2 and $tPCO_2$. With a rise in glycaemia we found a decrease in TOI and an increase in FTOE. With constant $CMRO_2$ this can be explained by the increase in glycaemia and concomitant compensatory decrease in CBF and OD. In hyperglycaemic conditions this compensatory increase in FTOE might fail and the brain can become ischaemic and hypoxic explaining the increased risk of morbidity and mortality that is seen with hyperglycaemia.

Our study has a shortcoming with regard to the data recording: in some patients only one measurement was performed whereas in other infants several recordings were made during several (consecutive) postnatal days (i.e. repeated measurements). We therefore could have missed day-effects or could have under-or overestimated our data. This probably explains why the correlations we found within our study population are rather weak

6 Conclusion

In conclusion, our results show that in premature infants during the first days of life glycaemia – even within the normal glycaemic range and independent of changes in SaO_2, MABP and $tPCO_2$ – influences the cerebral oxygenation, probably via its effect on the CBF. Thus when analyzing changes in the cerebral oxygenation parameters TOI and FTOE, not only changes in MABP, SaO_2 and $tPCO_2$ but also changes in glycaemia should be considered.

Acknowledgments This research is sponsored by the Flemish Government (FWO: Projects G.0519.06) and by the Marie-Margueritte Delacroix Foundation.

References

1. Mena P, Llanos A, Uauy R. Insulin homeostasis in the extremely low birth weight infant. *Semin Perinatol* 2001; 25:436–446
2. Lucas A, Morley R, Cole TJ. Adverse neurodevelopmental outcome of moderate neonatal hypoglycaemia. *BMJ* 1988; 297:1304–1308
3. Cornblath M. Neonatal hypoglycemia 30 years later: does it injure the brain? Historical summary and present challenges. *Acta Paediatr Jpn* 1997; 39(Suppl 1):S7–S11
4. Pryds O, Greisen G, Friis-Hansen B. Compensatory increase of CBF in preterm infants during hypoglycaemia. *Acta Paediatr Scand* 1988; 77:632–637
5. Naulaers G, Meyns B, Miserez M et al. Use of tissue oxygenation index and fractional tissue oxygen extraction as non-invasive parameters for cerebral oxygenation. A validation study in piglets. *Neonatology*. 2007; 92:120–126
6. Tsuji M, Saul JP, du PA et al. Cerebral intravascular oxygenation correlates with mean arterial pressure in critically ill premature infants. *Pediatrics*. 2000; 106:625–632.

A Novel Approach to Evaluate the Vessel Function Determined by Near Infrared Spectroscopy

Hajime Miura and Nao Okumura

Abstract The purpose of this study was to evaluate arterial function by near infrared spectroscopy (NIRS). 16 elderly subjects were studied: 8 were arteriosclerosis obliterans patients (ASO), and 8 were healthy elderly (non-ASO). A cuff around the thigh was inflated to a pressure of 20% above their ankle systolic blood pressure for 3 min. The NIRS probe was positioned over the gatrocnemius muscle to measure oxygenated hemoglobin (O_2Hb), and the recovery time and rate for ΔO_2Hb after occlusion were calculated. Compared with the non-ASO group, the ASO group had a longer recovery time ($p < 0.05$) and a shallower recovery rate gradient ($p < 0.01$). The ankle to brachial index was correlated with recovery time ($r = -0.61$, $p < 0.01$) and recovery rate ($r = 0.80$, $p < 0.001$). These data suggest that NIRS may provide an effective non-invasive method for evaluating arterial function in patients with arteriosclerosis obliterans.

1 Introduction

Several prospective studies have focused on the ability of arterial function to predict cardiovascular risk, which would allow detection of atherosclerosis status before the occurrence of critical events [1, 6, 9, 10]. The ankle to brachial index (ABI) is the gold standard for arteriosclerosis obliterans (ASO) diagnosis. ABI is determined by ankle systolic and brachial systolic blood pressure. In order to evaluate/diagnose arteriosclerosis obliterans in detail, it is necessary to measure the arterial structure and function by MRI (magnetic resonance imaging) or computed tomography. These methods involve complicated techniques and take a long time. At the clinical level, an easier screening tool is required.

H. Miura (✉)
Laboratory for Applied Physiology, Faculty of Integrated Arts and Sciences, University of Tokushima, Tokushima, Japan
e-mail: hajime-m@ias.tokushima-u.ac.jp

E. Takahashi, D.F. Bruley (eds.), *Oxygen Transport to Tissue XXXI*, Advances in Experimental Medicine and Biology 662,
DOI 10.1007/978-1-4419-1241-1_67, © Springer Science+Business Media, LLC 2010

Near infrared spectroscopy (NIRS) can monitor the balance between oxygen consumption and oxygen supply by measuring optical absorption changes in oxygenated and deoxygenated hemoglobin(Hb)/myoglobin(Mb). Previous study has suggested that oxygen status as determined by NIRS is influenced by arterial function [8]. It is therefore possible that NIRS measurements might help evaluate an individual's risk of cardiovascular disease. However, no comparisons of arterial function and NIRS results have been performed.

In order to evaluate arterial function using NIRS, we designed to determine whether NIRS could measure the severity of ASO during occlusion.

2 Methods

The subjects were 8 elderly patients who had ASO [4 male and 4 female, age:72.9 ± 9.0 years, height:156.9 ± 10.5 cm, weight:55.6 ± 9.5 kg, systolic blood pressure (SBP):176.2 ± 23.6 mmHg, diastolic blood pressure (DBP):81.7 ± 15.9 mmHg, ABI:0.51 ± 0.25 a.u.] for the ASO group, and 8 healthy subjects (3 male and 5 female, age:66.3 ± 2.3 years, height:155.4 ± 9.0 cm, weight:57.3 ± 6.3 kg, SBP:127.7 ± 10.6 mmHg, DBP:76.1 ± 9.9 mmHg, ABI:1.15 ± 0.06 a.u.) for the non-ASO group.

2.1 Protocol (OT: Occlusion Test)

All subjects remained in a sitting position with their legs extended such that their heels touched the ground at a 45 degree angle. After resting for 20 min, a cuff was positioned around the right thigh, and it was inflated to a pressure of 20% above their ankle systolic blood pressure for 3 min. The dual-wavelength (760 and 850 nm) was selected for the NIRS (COGNOSCOPE, NIM Co Ltd). The probe included 4 LED light sources and 10 detectors with 2.5 cm separation. It was positioned over the gastrocnemius muscle to measure ΔO_2Hb (μmol). Data were collected from one optical sensor positioned at patient's diseased area. The recovery time was calculated as half the time between the ΔO_2Hb at the end of occlusion and the peak ΔO_2Hb during recovery. The recovery rate was calculated as the gradient of the linear regression between the ΔO_2Hb at the end of occlusion and the ΔO_2Hb 30 s later.

2.2 Statistics

All parameters were compared between two groups using a non-paired *t*-test. Simple linear regression analysis was used to determine the relationship

between measurements. The level of significance was set at $p < 0.05$. All values are presented as the mean ± SD.

3 Results

Figure 1a shows the typical change of ΔO_2Hb during the OT. Compared with the non-ASO group, the ASO group had a slower recovery (37.4 ± 36.0 vs. 7.7 ± 2.0 s , $p < 0.05$) and a shallower recovery rate gradient (0.34 ± 0.14 vs. 1.29 ± 0.55, $p < 0.01$) (Fig. 1b, c).

There were also significant relationships between ABI and recovery time ($r = -0.61$, $p < 0.01$) and ABI and recovery rate ($r = 0.80$, $p < 0.001$).

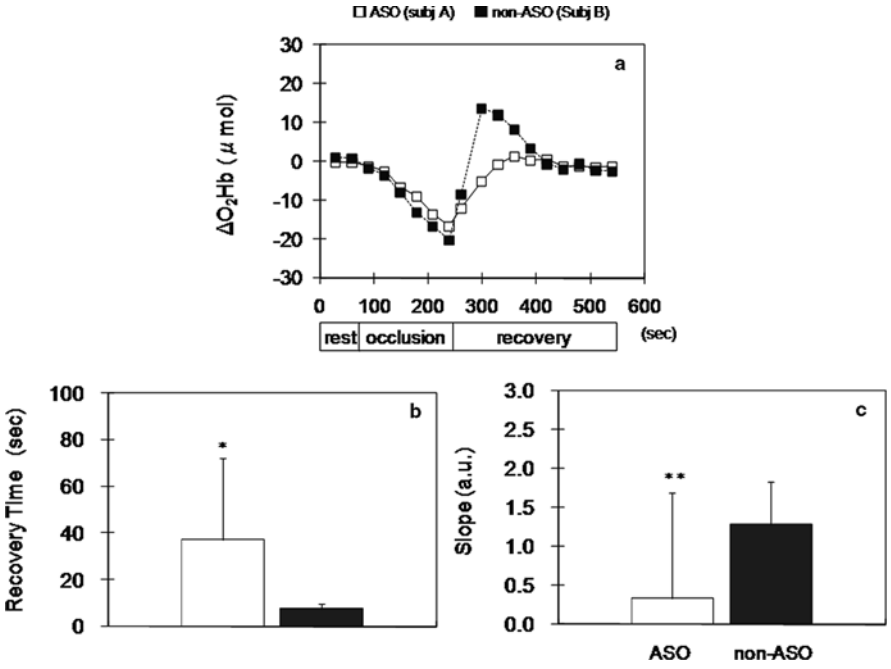

Fig. 1 Typical changes in ΔO_2H during the CPT (**a**) and comparison of recovery time (**b**) and slope (**c**) between ASO and non-ASO groups. Data are mean ± SD. *($p < 0.05$), **($p < 0.01$): significantly different from non-ASO group

4 Discussion

ASO is characterized by occlusive lesions consisting primarily of atheromas, which are often accompanied by fibrosis and calcification of the medial coat of the artery and which may be associated with thrombosis of varying extent. This

disease is now considered to be an occlusive arterial disease affecting predominantly younger to older people with diabetes mellitus.

ABI is the standard method for screening the severity of ASO [13]. To evaluate basic functions, however, rehabilitation practitioners require a method that is easy to follow and yields data critical to their patient's diagnosis. NIRS has potential for evaluating the level of oxygen supply and/or arterial function [8]. Previous studies have reported that NIRS during exercise could evaluate the severity of ASO [3, 7, 12]. These protocols cannot be applied to patients who are unable to perform the exercises, and so the quantity of intensity/work cannot be determined.

The present study adopted the OT for screening for ASO. In ASO patients, it is speculated that the slower response to hyperemia after the OT is due to their blocked vessels. The ASO patients had a longer and a slower recovery rate than the non-ASO patients (Fig. 1). An MRI study indicated that ASO patients had a slower recovery of both phosphocreatine (PCr) and pH after arterial occlusion [2]. Therefore, the slower resynthesis of PCr after occlusion might influence the recovery of O_2Hb. These data were in accordance with previous studies [3, 7, 12]. However, in the present study, the same relative pressure was applied for the occlusion test. The traditional index of ABI significantly correlates with the recovery time and recovery rate gradient. This study's protocol is performed on patients at rest, and therefore can be applied to patients regardless of their physical condition. Also despite their condition, the relative rate of pressure applied to the patient remains the same.

Measuring and analyzing arterial function using NIRS is easier and takes less time than using MRI, CT, ultrasound echo device, or others. However, there were some limitations to the present study. First, the measurements reflect the change in the concentrations of oxygenated and deoxygenated heme groups. Mb is thought to reflect less than 10% of the total heme in human tissues [5]. It has also a much higher affinity for O_2Hb and may remain fully oxygenated during the present protocol. Tran et al. [11], however, has showed that Mb oxygen saturation mirror the gradient of that of Hb. Second, O_2Hb caused changes in both intracellular oxygen consumption and small vessels/capillary oxygenation. MacDonald et al. [4] has raised the question regarding the relationship between oxygenated saturation and venous oxygen saturation. Further studies will be needed to clarify the influence of Mb and venous oxygen saturation determined by NIRS. Another key difficulty in using NIRS is the influence of subcutaneous fat. NIRS gets a signal from tissues at depths of 1/3–1/2 the separation between light source and detectors. Subjects with greater subcutaneous fat are often the most important to study for clinical perspective. Our subjects had subcutaneous fat thickness (3.1–5.4 mm) that was less than the distance from light source and detectors, but the application of NIRS to subjects with more subcutaneous fat will require modifications of current technology.

Though there are some disadvantages to using this method, it has the advantage of being non-invasive while still facilitating easy detection and

early diagnosis of arteriosclerosis obliterans. We included a small number of ASO patients as subjects. In order to confirm this method for diagnosis of ASO, a larger number of subjects should be targeted to consider a greater variety of ages, past illnesses, or severity of disease.

Acknowledgments We thank Yoshinori Takahashi and Maiko Fujisawa for their technical assistance in this study. This study was supported by a grant from Meiji Yasuda Life Foundation of Health and Welfare.

References

1. Corretti MC, Plotnick GD, Vogel RA. The effects of age and gender on brachial artery endothelium-dependent vasoactivity are stimulus-dependent. Clin Cardiol 1995; 18, 471–476.
2. Keller U, Oberhänsli R, Huber P, Widmer LK, Aue WP, Hassink RI, Muller S, Seelig J. Phosphocreatine content and intracellular pH of calf muscle measured by phosphorus NMR spectroscopy in occlusive and arterial disease of the legs. Eur J Clin Invest 1985; 15, 382–388.
3. Kooijman HM, Hopman MTE, Colier WNJM, Vliet JA, Oeseburg B. Near infrared spectroscopy for noninvasive assessment of claudication. J Surg Res 1997; 72, 1–7.
4. MacDonald MJ, Tarnopolsky MA, Green HJ, Hughson RL. Comparison of femoral blood gases and muscle near-infrared spectroscopy at exercise onset in humans. J Appl Physiol 1999; 86, 687–693.
5. Mancini DM, Bolinger L, Li H, Krndrick K, Chance B, Wilson JR. Validation of near-infrared spectroscopy in humans. J Appl Physiol 1994; 77, 2740–2747.
6. Matsui Y, Kario K, Ishikawa J, Eguchi K, Hoshide S, Shimada K. Reproducibility of arterial stiffness indices (pulse wave velocity and augmentation index) simultaneously assessed by automated pulse wave analysis and their associated risk factors in essential hypertensive patients. Hypertens Res 2004; 27, 851–857.
7. McCully KK, Halber C, Posner JD. Exercise-induced changes in oxygen saturation in the calf muscles of elderly subjects with peripheral vascular disease. J Gerontol 1994; 49, B128–B134.
8. Miura H, McCully K, Chance B. Application of multiple NIRS imaging device to the exercising muscle metabolism. Spectroscopy 2003; 17, 549–558.
9. Najjar SS, Scuteri A, Lakatta EG. Arterial aging: is it an immutable cardiovascular risk factor? Hypertension 2005; 46, 454–462.
10. Tousoulis D, Davies G, TentolourisC, Crake T, Toutouzas P. Inhibition of nitric oxide synthesis during the cold pressor test in patients with coronary artery disease. Am J Cardiol 1997; 79, 1676–1679.
11. Tran TK, Sailasuta N, Kreutzer U, Hurd R, Chung Y, Mole P, Kuno S, Jue T. Comparative analysis of NMR and NIRS measurements of intracellular PO_2 in human skeletal muscle. Am J Physiol 1999; 276, R1682–R1690.
12. Watanabe T, Matsushita M, Nishikimi N, Sakurai T, Komori K, Nimura Y. Near-infrared spectroscopy with treadmill exercise to assess lower limb ischemia in patients with atherosclerotic occlusive disease. Surg Today 2004; 34, 849–854.
13. Weitz JI, Byrne J, Clagett GP, Farkouh ME, Porter JM, Sackett DL, Strandness DE Jr, Taylor LM. Diagnosis and treatment of chronic arterial insufficiency of the lower extremities: a critical review. Circulation 1996; 94, 3026–3049.

Effects of Aging on Activity of the Prefrontal Cortex and Autonomic Nervous System during Mental Stress Task

Kaoru Sakatani, Masahiro Tanida, and Masako Katsuyama

Abstract We evaluated the effect of aging on the prefrontal cortex (PFC) activity and heart rate during the task. Employing near infrared spectroscopy (NIRS), we measured hemoglobin concentration changes in the bilateral PFC during a mental arithmetic task in young and older females. We selected the subjects who exhibited an increase in oxyhemoglobin with a decrease in deoxyhemoglobin during the task. We observed that right PFC activity predominantly modulates sympathetic effects during the task in both groups. However, the changes of oxyhemoglobin and heart rate during the task in older subjects were significantly smaller than those in young subjects. These results indicate that aging affects evoked cerebral blood oxygenation (CBO) response patterns of the PFC during a mental stress task. Aging did not affect the laterality of PFC activity in modulation of ANS function in the subjects who exhibited increases of oxyhemoglobin and deoxyhemoglobin associated with a decrease of deoxyhemoglobin during the task. However, aging reduced the heart rate increase during the task.

1 Introduction

The prefrontal cortex (PFC) plays an important role in mediating behavioral and somatic responses to stress via projections to the autonomic centers [1]. A number of studies have demonstrated that the cerebral regulations of stress responses may be differentially mediated by the right and left PFC [2]. Recently, employing near-infrared spectroscopy (NIRS), we have demonstrated that right dominant PFC activity was associated with a greater increase of heart rate during a mental arithmetic task in young females [3, 4, 5].

NIRS studies demonstrated that elderly subjects showed a significantly lower increase in oxyhemoglobin (oxy-Hb) concentrations in the frontal lobe

K. Sakatani (✉)
Division of Optical Brain Engineering, Department of Neurological Surgery; Division of Applied System Neuroscience, Department of Advanced Medical Science, Nihon University School of Medicine, Tokyo, 173-8610, Japan
e-mail: sakatani@med.nihon-u.ac.jp

E. Takahashi, D.F. Bruley (eds.), *Oxygen Transport to Tissue XXXI*, Advances in Experimental Medicine and Biology 662,
DOI 10.1007/978-1-4419-1241-1_68, © Springer Science+Business Media, LLC 2010

during cognitive tasks compared with young subjects [6]. In addition, older subjects exhibited deactivation (i.e. decreases of oxy-Hb) in the frontal lobe during cognitive tasks [7]. However, it is not yet clear how aging affects the PFC activity and the autonomic nervous system function during mental stress tasks. In the present study, employing NIRS, we measured the cerebral blood oxygenation (CBO) changes in the PFC and heart rate changes during a mental arithmetic task. We compared the CBO changes with heart rate changes in young and elderly subjects.

2 Methods

We studied young ($n = 24$, 21.3 ± 0.9 years) and elderly ($n = 11$, 56.9 ± 4.2 years) females. The subjects were all deemed right-handed according to the laterality quotient questionnaire of the Edinburgh Handedness Inventory. All subjects provided written informed consent as required by the Human Subjects Committee of the Shiseido Life Science Institute.

We employed a mental arithmetic task as a psychological stressor. The subjects were asked to consecutively subtract a two-digit number from a four-digit number (e.g. 1022–13) as quickly as possible for 60 s. In order to assess psychological stress levels, subjects were asked to fill in the State-Trait Anxiety Inventory (STAI) before and after task performance.

CBO was measured in the bilateral PFC with a NIRS monitor (NIRO-300, Hamamatsu Photonics K.K., Hamamatsu, Japan). The NIRO-300 monitor simultaneously measures the concentrations of oxy-Hb, deoxyhemoglobin (deoxy-Hb), and total hemoglobin (total-Hb; oxy-Hb + deoxy-Hb). The hemoglobin concentrations were expressed as changes from baseline concentration (arbitrary units). The NIRS probes were set symmetrically on the forehead with a flexible fixation pad so that the midpoint between the emission and detection probes was 3 cm above the centers of the upper edges of the bilateral orbital sockets; the distance between the emitter and detector was set at 4 cm. This positioning is similar to the midpoint between electrode positions Fp1/Fp3 (left) and Fp2/F4 (right) of the international electroencephalographic 10–20 system. MRI confirmed that the emitter–detector was located over the dorsolateral and frontopolar areas of the PFC.

Heart rate was simultaneously monitored with PFC activity using a photoelectrical sensor (Tsuyama MGF KK, Tokyo, Japan). Instantaneous heart rate was calculated every 10 s from a mean frequency value between 0.05 and 2 Hz by Fourier analysis. ANS function was evaluated by heart rate variability analysis; the low frequency (LF) amplitude (0.04–0.15 Hz) and the high frequency (HF) amplitude (0.15–0.4 Hz) were calculated by power spectral analysis over a 3 min-period at both the start of the task and after task performance.

To analyze PFC activity in response to psychological stress, we calculated changes in oxy-Hb during the task. In order to determine left/right asymmetry

of PFC activity, we calculated a laterality index (LI) for the oxy-Hb concentration changes ([right – left]/[right + left]); LI > 0 indicates greater activity of the right PFC, while LI < 0 indicates greater activity of the left PFC [3, 4, 5]. The relationships between PFC activity (LI of oxy-Hb), and heart rate changes were analyzed by calculating Pearson's correlation coefficient.

3 Result

We observed three different patterns of NIRS parameter changes during the task. In both groups, the most common NIRS parameter change was an increase in oxy-Hb and t-Hb associated with a decrease in deoxy-Hb. The frequency of this pattern in the older group (11/20 cases, 55.0%) was considerably lower than in the young group (24/30 cases, 80.0%). The second most common pattern was decreases of oxy-Hb and t-Hb during the task, suggesting a decrease of neuronal activity during the task. This CBO response pattern was more common in the older groups, (5/20 cases, 25%) than the younger group (2/30 cases, 6.7%). The third most common pattern was an increase of deoxy-Hb associated with decreases of oxy-Hb and t-Hb. We observed this pattern in 13.3% (4/30 cases) and 20.0% (4/20 cases) in the young and older groups, respectively. We selected the subjects who exhibited the most common pattern of NIRS parameter changes for the following analysis of the PFC activity.

We evaluated the LI of oxy-Hb concentration changes and heart rate, and found that there were significant positive correlations between heart rate changes and the LI of oxy-Hb in both young ($r = 0.64$, $p = 0.00080$) and older ($r = 0.83$, $p = 0.0016$) subjects (Fig. 1). However, there were significant

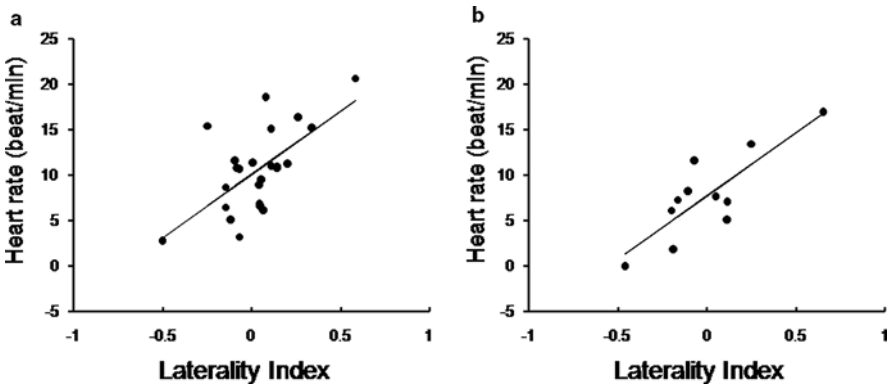

Fig. 1 Relationship between the laterality ratio scores and heart rate changes in young (**a**) and elder subjects (**b**). The *vertical and horizontal axes* denote change in heart rate (beat/min) and the laterality index (oxy-Hb), respectively. Significant positive correlations were observed in young ($r = +0.87$, $p < 0.0001$) and elder subjects ($r = +0.85$, $p < 0.0001$)

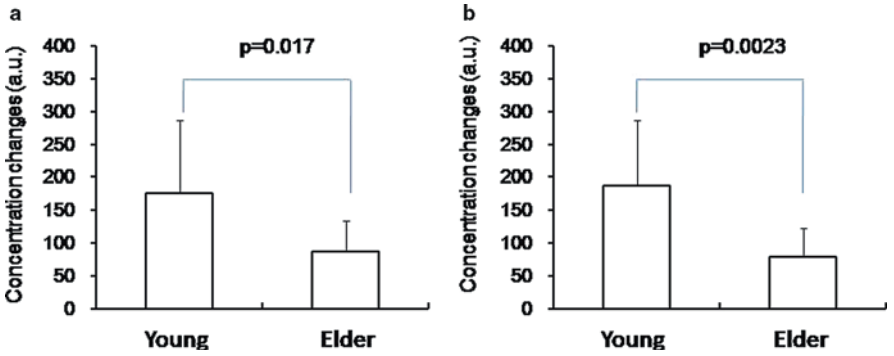

Fig. 2 Differences in oxy-Hb changes during a mental arithmetic task in the *left* (**a**) and *right* PFC. Note that the changes of oxy-Hb in older subjects were significantly smaller than those in young subjects

differences in changes of oxy-Hb, heart rate and STAI-II between young and older subjects. That is, the changes of oxy-Hb in older subjects were significantly smaller than those in young subjects (Fig. 2). The changes of heart rate in older subjects were significantly smaller than those in young subjects ($p = 0.018$), although there was no significant difference in heart rate at rest between the groups (Fig. 3a). In addition, the changes of STAI-II after the task in older subjects were significantly larger than those in young subjects (Fig. 3b).

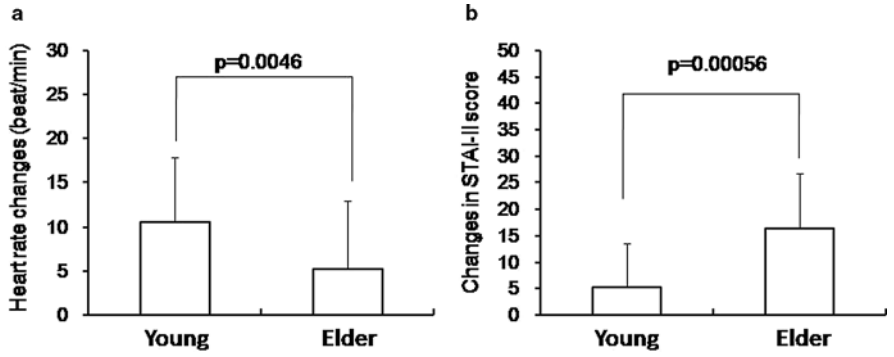

Fig. 3 Differences in changes of heart rate (**a**) and STAI-II scores (**b**) during a mental arithmetic task. Note that older subjects showed smaller changes of heart rate and larger changes in STAI-II after the task compared with young subjects

4 Discussion

In the present study, we observed several different patterns of evoked CBO response. The most common pattern of NIRS parameter change was an increase in oxy-Hb and t-Hb associated with a decrease in deoxy-Hb in both the young and older group; this pattern is consistent with the findings of a PET

study in normal adults [8]. Interestingly, the frequency of this pattern in the older group was considerably lower than in the young group. In addition, the older subjects exhibited decreases of oxy-Hb and t-Hb more frequently than the young subjects. Such differences in evoked CBO response pattern observed between young and older subjects are consistent with reported NIRS activation studies [6, 7]. These observations may reflect a possible functional reorganization during aging [9].

When we analyzed the subjects who exhibited increases of oxy-Hb and t-Hb associated with a decrease of deoxy-Hb during the task, we observed that right dominance of PFC activity was associated with an increase in heart rate during the mental stress task in both young and older subjects, indicating that the relation between left/right asymmetry of PFC activity and ANS function was not affected by aging. Interestingly, the lateralization of the PFC activity in higher-order cognitive functions tends to be reduced by aging [10]. Therefore, effects of aging on PFC activity depend on characteristics of cognitive tasks.

In the present study, aging reduced the heart rate increase during a mental arithmetic task. However, the effect of aging on ANS response to mental stress remains in dispute. A number of studies have demonstrated that sympathetic nervous system reactivity to stress increases with age in humans [11]. Ng et al., however, demonstrated that older subjects tended to show smaller increases in heart rate during cognitive tasks, including a mental arithmetic task [12]. These results indicate that sympathetic neural hyper-reactivity does not appear to be a fundamental feature of the aging process in humans.

We found that the changes of oxy-Hb in older subjects were significantly smaller than those in younger subjects However, possible changes in optical pathlength during aging could cause such differences. In our preliminary study, we compared the optical pathlength in older and young subjects using time-resolved spectroscopy; however, we found no statistically significant difference between the two groups ($p = 0.28$), which is consistent with the results obtained by Hoshi et al. [13]. These results suggest that aging reduced the neuronal activity in the PFC during a mental arithmetic task.

In summary, aging affects the evoked CBO response patterns of the PFC during a mental stress task. Aging did not affect the laterality of PFC activity in modulation of ANS function in the subjects who exhibited increases of oxy-Hb and deoxy-Hb associated with a decrease of deoxy-Hb during the task. However, aging reduced the heart rate increase during the task.

References

1. Buijs RM, van Eden CG (2000) The integration of stress by the hypothalamus, amygdala and prefrontal cortex: Balance between the autonomic nervous system and the neuroendocrine system. Prog in Brain Res 126:117–132
2. Wang J, Rao H, Wetmore GS et al. (2005) Perfusion functional MRI reveals cerebral blood flow pattern under psychological stress. PNAS 102:17804–17809

3. Tanida M, Sakatani K, Takano R et al. (2004) Relation between asymmetry of prefrontal cortex activities and the autonomic nervous system during a mental arithmetic task: Near infrared spectroscopy study. Neurosci Lett 369:69–74
4. Tanida M, Katsuyama M, Sakatani K (2007) Relation between mental stress-induced prefrontal cortex activity and skin conditions: a near infrared spectroscopy study. Brain Res 1184:210–216
5. Tanida M, Katsuyama M, Sakatani K (2008) Effects of fragrance administration on stress-induced prefrontal cortex activity and sebum secretion in the facial skin. Neurosci Lett 432:157–161
6. Hock C, Müller-Spahn F, Schuh-Hofer S et al. (1995) Age dependency of changes in cerebral hemoglobin oxygenation during brain activation: A near-infrared spectroscopy study. J Cereb Blood Flow Metab 15:1103–1108
7. Sakatani K, Lichty W, Xie Y et al. (1999b) Effects of aging on language-activated cerebral blood oxygenation changes of the left prefrontal cortex: Near infrared spectroscopy study. J Stroke Cerebrovasc Dis 8:398–403
8. Fox P, Raichle ME (1986) Focal physiological uncoupling of cerebral blood flow and oxidative metabolism during somatosensory stimulation in human subjects. Proc Natl Acad Sci USA 83:1140–1144
9. Grady CL, McIntosh AR, Horwitz B et al. (1995) Age-related reduction in human cognition memory due to impaired encoding. Science 269:218–221
10. Bellis TJ, Nicol T, Kraus N (2000) Aging affects hemispheric asymmetry in the neural representation of speech sounds. J Neurosci 20:791–797
11. Goldstein DS, Lake CR, Chernow B et al. (1983) Age-dependence of hypertensive-normotensive differences in plasma norepinephrine. Hypertension 5:100–104
12. Ng AV, Callister R, Johnson DG et al. (1994) Sympathetic neural reactivity to stress does not increase with age in healthy humans. Am J Physiol 267:H344–H353
13. Hoshi Y, Shinba T, Sato C, et al. (2006) Resting hypofrontality in schizophrenia: A study using near-infrared time-resolved spectroscopy. Schizophr Res84:411–420.

Activity in the Premotor Area Related to Bite Force Control – A Functional Near-Infrared Spectroscopy Study

Tomotaka Takeda, Mami Shibusawa, Osamu Sudal, Kazunori Nakajima, Keiichi Ishigami, and Kaoru Sakatani

Abstract The purpose of this study was to elucidate the influence of bite force control on oxygenated hemoglobin (OxyHb) levels in regional cerebral blood flow as an indicator of brain activity in the premotor area. Healthy right-handed volunteers with no subjective or objective symptoms of problems of the stomatognathic system or cervicofacial region were included. Functional near-infrared spectroscopy (fNIRS) was used to determine OxyHb levels in the premotor area during bite force control. A bite block equipped with an occlusal force sensor was prepared to measure clenching at the position where the right upper and lower canine cusps come into contact. Intensity of clenching was shown on a display and feedback was provided to the subjects. Intensity was set at 20, 50 and 80% of maximum voluntary teeth clenching force. To minimize the effect of the temporal muscle on the working side of the jaw, the fNIRS probes were positioned contralaterally, in the left region. The findings of this study are: activation of the premotor area with bite force control was noted in all subjects, and in the group analysis OxyHb in the premotor cortex was significantly increased as the clenching strengthened at 20, 50 and 80% of maximum voluntary clenching force. These results suggest there is a possibility that the premotor area is involved in bite force control.

1 Introduction

Previous positron emission tomography (PET) and functional magnetic resonance imaging (fMRI) studies have revealed the involvement of a number of different cortical areas in the execution of motor activities. These include the primary sensorimotor cortex, the premotor area, the pre-supplementary motor area (pre-SMA), the supplementary motor area (SMA), and the prefrontal area.

T. Takeda (✉)
Department of Sports Dentistry, Tokyo Dental College; Nihon University School of Medicine, Tokyo, Japan
e-mail: ttakeda@tdc.ac.jp

E. Takahashi, D.F. Bruley (eds.), *Oxygen Transport to Tissue XXXI*,
Advances in Experimental Medicine and Biology 662,
DOI 10.1007/978-1-4419-1241-1_69, © Springer Science+Business Media, LLC 2010

Studies have investigated these motor-related areas, and the influence of finger force on brain activity [1–3].

It is thought that dysfunction of the stomatognathic system is involved in reduction of learning and memory ability [4], and missing teeth are reported to be one of the risk factors for Alzheimer's disease [5]. These studies might imply that impairment of the stomatognathic system results in a decrease of brain function. Therefore, our group started research to promote brain activation through an improvement of oral function by chewing gum, eating harder food, biting force control, etc. However, investigations into the relationship between motor-related brain function and mastication are difficult, due to the undesired effect associated with jaw movement [6].

Functional near infrared spectroscopy (fNIRS) is a powerful, non-invasive imaging system. It offers many advantages, including compact size, no need of specially-equipped facilities, the potential for real-time measurement, and measurement in a natural posture and condition. Studies using fNIRS have examined the influence of wearing partial denture prosthesis on the prefrontal cortex activation [7]. Also, our recent studies have investigated the relation between biting force control and primary sensorimotor cortex activation [8]. However, the relationship between the wide area of brain activation and the strength of jaw movement, including mastication and clenching, remains to be clarified.

The premotor area is thought to be an area that has the unique function of taking part in motion control. This area is assumed to be related to not only the beginning and the accomplishment of voluntary movement, but also the preparation for the movement and the conversion of sense information into the necessary motion information. The purpose of this study was to elucidate the influence of bite force control on oxygenated hemoglobin (OxyHb) levels in regional cerebral blood flow (rCBF) as an indicator of brain activity in the premotor area using fNIRS. This study was approved by the Ethics Committee of Tokyo Dental College (No.164)

2 Methods

Subjects consisted of 13 healthy right-handed male volunteers with no subjective or objective symptoms of problems of the stomatognathic system or cervicofacial region (age 33.7 ± 9.1 years). Informed consent was obtained from all subjects in accordance with institutional guidelines.

A bite positioner equipped with an occlusal force sensor (KLC-60KA-S19, Frontier Medic Co. Ltd, Japan) (Fig. 1) was prepared to measure clenching at the position where the right upper and lower canine cusps come into contact [8]. Intensity of clenching was shown on a display and feed backed. Intensity was set at 20, 50 and 80% of maximum voluntary clenching force (20, 50 and 80%MVC) [8]. Each subject was required to perform clenching twice, at each of these three intensities. All tasks were performed using a block design

Fig. 1 Regulation and adjustment of clenching strength. A bite block equipped with an occlusal force sensor was prepared to measure clenching at the position where the *right upper* and *lower* canine cusps came into contact. Intensity of clenching was shown on a display and feedback was provided to the subjects

(20-s rest, 20-s clenching, 20-s rest). And the subjects were trained to clench without activating this muscle.

An fNIRS system (NIRStation OMM-2001, Shimazu Co. Ltd., Japan) was used. The optodes were then positioned so as to cover the areas anterior and posterior to the central sulcus. The spectroscope's 15 source and 15 detector optodes were arranged alternately in a lattice pattern, with a distance of 30 mm between them, to form 49 source-detector pairs on an adjustable surface holder for positioning on the subject's head. Two measurements were conduced in each clenching force.

OxyHb has been proposed to be the best indicator of change in rCBF in cognitive studies with NIRS [9]. Representative examples of OxyHb and deoxyHb changes were shown in color maps (Fig. 2). The OxyHb data on a channel which seemed to be corresponding to the premotor area [8] for the 10-s period commencing 5 s after commencement of clenching at each intensity were

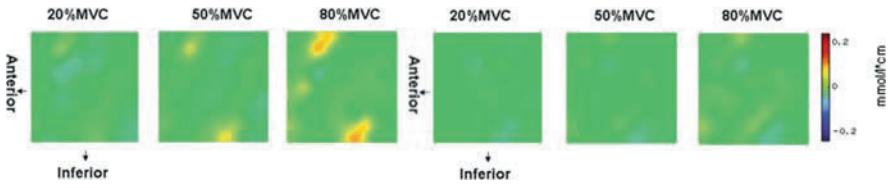

Fig. 2 Representative examples of a subject's relevant color maps of OxyHb (*left*) and DeoxyHb (*right*) at 10 s after each clenching task are shown. OxyHb increases and DeoxyHb decreases or the activations seemed to be increased as the clenching strengthened

analyzed in each subject and then averaged between all subjects as a group analysis. DeoxyHb were also analyzed to confirm general changes in blood flow. Statistical comparisons were made using a one-way analysis of variance (ANOVA) test followed by a Tukey multiple comparison tests for further comparisons among three different clenching forces ($p < 0.05$) using SPSS(r) (SPSS Japan Inc. Tokyo, Japan).

3 Results

Each color map of OxyHb and DeoxyHb represents the activated spatial distribution. Activation of the premotor area with bite force control was noted and the activations seemed to be increased as the clenching strengthened (Fig. 2).

A correlation between clenching force and OxyHb was found in the premotor cortex. In other words, OxyHb in the premotor cortex was increased as the clenching strengthened, at 20, 50 and 80%MVC. ANOVA confirmed a significant difference between the three clenching forces in OxyHb but DeoxyHb ($p < 0.05$). A significant difference was also found between 20 and 80%MVC in OxyHb (Tukey test) (Fig. 3).

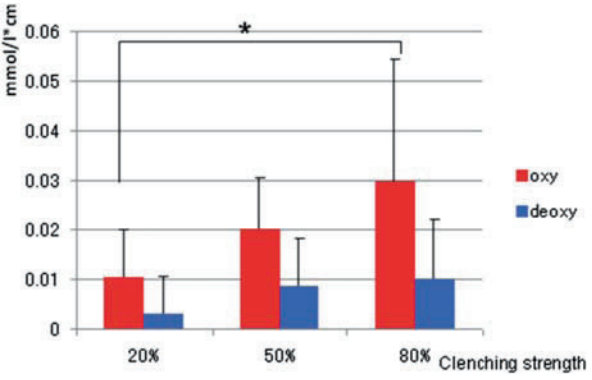

Fig. 3 Group analysis; a correlation between clenching force and OxyHb and DeoxyHb were found in the premotor cortex. One-way analysis of variance confirmed a significant difference between the three clenching forces ($p < 0.05$) not in DeoxyHb but in OxyHb. A significant difference was also found between 20 and 80%MVC (Tukey test) in OxyHb

4 Discussion

The findings of this study are: activation of the premotor area with bite force control occurred in all subjects, and in the group analysis OxyHb in the premotor cortex was significantly increased as the clenching strengthened, at 20, 50 and 80%MVC. These findings about OxyHb are similar to other studies showing that finger force is correlated with brain activity [1–3]. Although deoxyHb did not fall in the group analysis, this could be explained by the results

of a study which imply the possibility that the deoxyHb does not necessarily show a decrease in brain activity [10]. Also the slight influence of systemic artifacts related to clenching is necessarily incontrovertible.

The dorsal prefrontal cortex lies at the top of the motor hierarchy [11]. It can influence manual action indirectly by projections to the premotor area and from this area it has projections to the primary motor cortex, with other intricate connections among the prefrontal cortex, the pre-SMA and the rostal cingulated motor area, etc. [11]. The pre-SMA, the SMA, the premotor area and the prefrontal cortex are able to integrate information concerning the context and the response that is appropriate given the subject's goals [12, 13]. Motor preparation is associated with activations in the premotor cortex [14–16].

Thus, the premotor cortex does not seem to be concerned with control of the posture itself or of its adjustment, but with cognitive motion. Specifically, it is assumed that this area controls the process before the performance of an actual operation. The premotor cortex might convert sense information (mainly the visual information) into a target and body region information. In addition, the premotor cortex is assumed to participate in a process of integrating this converted information and generating operative information. It is thought that this processing starts from the ventral area in which the visual information is abundant according to the projection between the cortexes from the parietal lobe, and afterwards advances to the dorsal area [17] which has abundant input/output between this area, the prefrontal area and the first motor area.

It is possible that the premotor cortex is involved in mastication, biting preparation and control. Changes in biting strength influence not only the primary motor cortex, but also the premotor cortex (being one of the higher motor-related cortexes). These results suggest that improvement of the function of the stomatognathic system improves the wide area of brain function. Thus, dental therapy, such as reconstruction of appropriate occlusal condition for edentulous patients [18] and treatment for eating disorder patients, might improve higher cognitive functions such as memory and learning, as well as mastication quality thorough improvement of brain activation.

5 Conclusion

This study aimed to elucidate the influence of bite force control on oxygenated hemoglobin levels in regional cerebral blood flow as an indicator of brain activity in the premotor area, by means of fNIRS. The results show that: activation of the premotor area with bite force control occurred in all subjects, and in the group analysis OxyHb in the premotor cortex was significantly increased as the clenching strengthened, at 20, 50 and 80%MVC. These results suggest that there is a possibility that the premotor area is involved in bite force control.

References

1. Dettmers, C., et al., Relation between cerebral activity and force in the motor areas of the human brain. J Neurophysiol, 1995. 74(2): 802–815.
2. Nambu, I., Motor cortical activity measured with NIRS and its possible application for brain machine interface. NAIST Academic Repository, 2006: 202–204.
3. Thickbroom, G.W., et al., Isometric force-related activity in sensorimotor cortex measured with functional MRI. Exp Brain Res, 1998. 121(1): 59–64.
4. Kaku, M., et al., Influences of reduced masticatory function on learning and memory ability. Dent Jpn, 2006. 42: 82–85.
5. Kondo, K., M. Niino, and K. Shido, A case-control study of Alzheimer's disease in Japan – significance of life-styles. Dementia, 1994. 5(6): 314–326.
6. Ishikawa, T., Brain regions activated during the mandibular movement task in functional magnetic resonance imege. J Stomatol Soc, Japan 2002. 69(1): 39–48.
7. Narita N, Kamiya K, Yamaura K, Kawasaki S, Matsumoto T, et al. Chewing-related prefrontal cortex activation while wearing partial denture prosthesis: Pilot Study. J Prothodont Res. 2009; 53: 126–135.
8. Mami Shibusawa, T.T., Kazunori, and K.I. Nakajima, Kaoru Sakatani, Functional near-infrared spectroscopy study on cerebral activity response to two different levels of hardness during food mastication. Neurosci Lett, 2009. 449: 98–102.
9. Hoshi, Y., N. Kobayashi, and M. Tamura, Interpretation of near-infrared spectroscopy signals: a study with a newly developed perfused rat brain model. J Appl Physiol, 2001. 90(5): 1657–1662.
10. Watanabe, E., Functional test manual of brain :Near infrared spectroscopy. Medical Rehabilitation, (in Japanese), 2004. 40: 44–50.
11. Rushworth, M., Anatomical and functional subdivision within the primate latelal frontal cortex. Psysichobiolgy, 2000. 28: 187–196.
12. Miller, E.K. and J.D. Cohen, An integrative theory of prefrontal cortex function. Annu Rev Neurosci, 2001. 24: 167–202.
13. Passingham, R.E., I. Toni, and M.F. Rushworth, Specialisation within the prefrontal cortex: the ventral prefrontal cortex and associative learning. Exp Brain Res, 2000. 133(1): 103–113.
14. Richter, W., et al., Sequential activity in human motor areas during a delayed cued finger movement task studied by time-resolved fMRI. Neuroreport, 1997. 8(5): 1257–1261.
15. Rushworth, M.F., M. Krams, and R.E. Passingham, The attentional role of the left parietal cortex: the distinct lateralization and localization of motor attention in the human brain. J Cogn Neurosci, 2001. 13(5): 698–710.
16. Toni, I., M.F. Rushworth, and R.E. Passingham, Neural correlates of visuomotor associations. Spatial rules compared with arbitrary rules. Exp Brain Res, 2001. 141(3): 359–369.
17. Tanji, J., Recent findings on the use of premotor cortex of primates. Igakunoayumi (in Japanese), 2005. 212(10): 975–982.
18. Miyamoto, I., et al., Rehabilitation with dental prosthesis can increase cerebral regional blood volume. Clin Oral Implants Res, 2005. 16(6): 723–727.

Functional Near-Infrared Spectroscopy Study on Primary Motor and Somatosensory Cortex Response to Biting and Finger Clenching

Mami Shibusawa, Tomotaka Takeda, Kazunori Nakajima, Handa Jun, Shinichi Sekiguchi, Keiichi Ishigami, and Kaoru Sakatani

Abstract The purpose of this study was to compare the influence of biting and finger clenching intensity on the concentration of oxygenated hemoglobin (OxyHb) in regional cerebral blood flow (rCBF) as an indicator of brain activity in the primary motor (MI) and somatosensory (SI) cortices. Functional near-infrared spectroscopy (fNIRS) was used in 8 healthy subjects. Subjects were required to do biting (bite) and finger clenching (fclench) at 20, 50 and 80% of maximum force. To minimize the effect of temporal muscle activity on the working side of the jaw, the fNIRS probes were positioned contralaterally, in the left temporal region. Activation of MI and SI cortices with bite and fclench was noted in all subjects, irrespective of the intensity of bite and fclench. A significant increase was observed in OxyHb in MI and SI between 20% and both 50 and 80% intensity. In MI cortex, OxyHb showed a significant increase between 80% and both 20 and 50% fclench intensity. The results suggest that intensity of bite and fclench influences activation levels in MI and SI. Further, an activation was more obvious with bite than fclench.

1 Introduction

Previous study suggested that appropriate masticatory and occlusal forces help maintain and enhance brain function [1]. However, the underlying neurophysiological mechanism of this phenomenon remains to be clarified.

The relationship between cerebral activity and the force levels with finger stimulation has been reported in functional near infrared spectroscopy (fNIRS) studies [2], furthermore the relationship between brain activity and the stomatognathic system has been also studied using PET [3] and ffMRI [4]. However,

M. Shibusawa (✉)
Department of Sports Dentistry, Tokyo Dental College, Nihon University School of Medicine, Tokyo, Japan
e-mail: sibusawa@tdc.ac.jp

E. Takahashi, D.F. Bruley (eds.), *Oxygen Transport to Tissue XXXI*, Advances in Experimental Medicine and Biology 662,
DOI 10.1007/978-1-4419-1241-1_70, © Springer Science+Business Media, LLC 2010

few studies have carried out a detailed investigation into the relationship between temporal brain function and occlusion and mastication using NIRS.

On the other hand, fNIRS is a powerful, non-invasive imaging system. It offers many advantages, including compact size, no need of specially-equipped facilities, the potential for real-time measurement and, especially, the ability to distinguish signals, even when there is background muscular activity.

The purpose of this study was to compare the influence of biting (bite) and finger clenching (fclench) intensity in the concentration of oxygenated hemoglobin (OxyHb) in regional cerebral blood flow (rCBF) as an indicator of brain activity in the primary motor (MI) and somatosensory (SI) cortices under conditions designed to minimize the effect of associated muscle activity using fNIRS.

2 Methods

This study was approved by the Ethics Committee of Tokyo Dental College (No.164) and was conducted in accordance with the Declaration of Helsinki (Edinburgh Revision).

Subjects consisted of 8 healthy right-handed male volunteers (age, 35.6 $\pm$ 11.1 years). Informed consent was obtained from all subjects in accordance with institutional guidelines.

A bite block equipped with a force sensor (KLC-60KA-S19; Frontier Medic, Co. LTD, Japan) was prepared to measure at the position where the right upper and lower canine cusps came into contact. Furthermore, the same force sensor was used to measure fclench at the position between the right thumb and index finger. Intensity was set at 20, 50 and 80% of maximum bite and fclench force.

fNIRS (NIRStation OMM-2001, SHIMADZU Co. LTD, Japan) was used to determine rCBF in MI and SI cortices during bite and fclench. The probes were then positioned so as to cover the areas anterior and posterior to the central sulcus according to the method of Greenberg [5]. According to Hiraba et al. [6] human ipsilateral temporal muscles become active during lateral movement. Therefore, artifacts due to temporal muscle activity on the working side of the jaw can cause serious problems. The activity of left temporal muscles was monitored by an electromyograph (BioLog DL-2000, DL-141 S&ME, Inc., Japan). In order to avoid this undesirable muscle activation, the fNIRS probe helmet was positioned contralaterally, in the left temporal region. In addition, the subjects were trained to clench without activating this muscle.

Each subject was required to perform 2 blocks of tasks: the biting task block and the finger-clenching task block. Each block consisted of 6 appropriate actions (biting or finger-clenching) at the specified intensities (20%, 50 or 80%). The intensity specified was selected at random to give a final tally of two actions at each of the 3 intensities. The subject then rested for 20 s. The

subject then proceeded to the next bite or fclench task following the same 20-s rest, 20-s bite or fclench, 20-s rest pattern. This meant that each block lasted a total of 60 s.

The accuracy of the probe positions for identifying active sites in the brain was evaluated in 4 of the subjects. The probe positions were overlaid on MRI (Symphony 1.5 tesla; Simens, T1-weighted sequences, 1-mm slice) anatomical surface images of each individual using a 3-D magnetic space digitizer (FASTRAK, Polhemus, USA) and a specific software (Fusion, SHIMAZU Co. LTD, Japan).

OxyHb has been proposed as the best indicator of change in rCBF in cognitive studies with NIRS [7]. Therefore, the OxyHb data for the 10-s period commencing 10 s after commencement of bite at each intensity was averaged between all subjects. Next, a statistical analysis was performed using the paired *t*-test (SAS 9.1, SAS Institute Japan, Inc., Japan) with a level of significance $p < 0.05$.

3 Results

The portion of the probe anterior to the central sulcus was positioned over the precentral gyrus, corresponding to MI, and the portion posterior to the central sulcus was positioned over the postcentral gyrus corresponding to SI with bite and fclench. However, these activated portions during bite were superior than during fclench (Fig. 1).

A tendency toward an increase in OxyHb was observed in MI and SI with bite and fclench in all subjects, irrespective of bite intensity (Fig. 2). A significant increase was observed in OxyHb in MI and SI between 20% and both 50 and 80% bite intensity (Fig. 3. (a)). A significant increase was observed in OxyHb in MI between 80% and both 20 and 50% fclench intensity. No significant increase was observed in OxyHb in SI between all fclench intensities (Fig. 3. (b)).

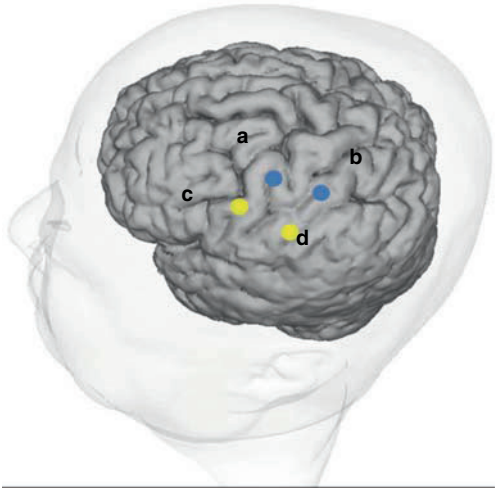

Fig. 1 Measurement positions on MRI image. (**a**) Primary motor cortex (MI) during finger clenching. (**b**) Primary somatosensory (SI) cortex during finger clenching. (**c**) MI during biting. (**d**) SI during biting

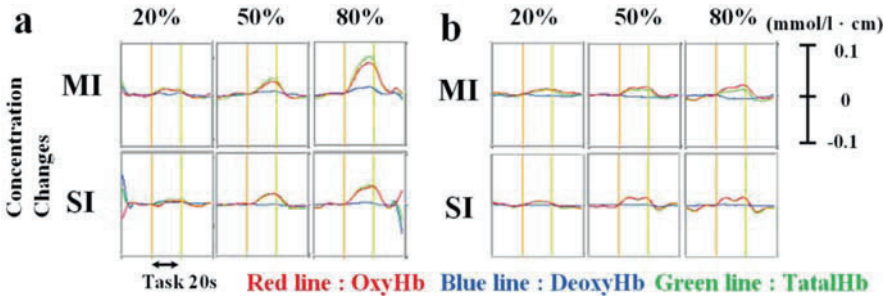

Fig. 2 rCBF changes in task. MI (*top*) and SI (*bottom*) response to biting (**a**) MI (*top*) and SI (*bottom*) response to finger clenching (**b**) A tendency toward an increase in OxyHb was observed in MI and SI with biting and finger clenching in all subjects, irrespective of intensity

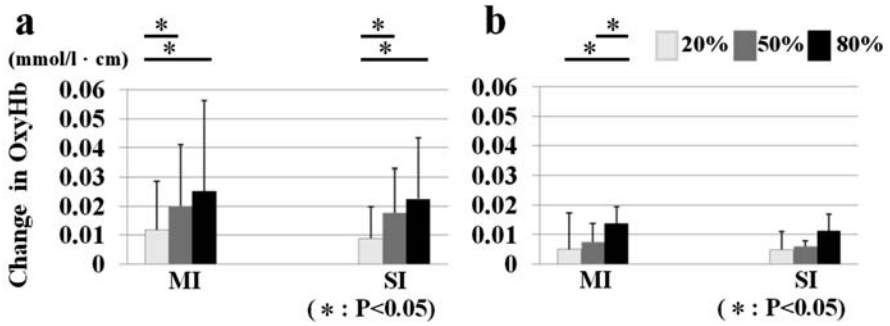

Fig. 3 Changes of OxyHb in MI and SI in response to biting. A significant increase was observed in OxyHb in the MIand SI between 20% and both 50 and 80% biting intensity (**a**) Changes of OxyHb in MI and SI in response to finger clenching. A significant increase was observed in OxyHb in the MIand SI between 80% and both 20 and 50% finger clenching intensity (**b**)

4 Discussion

The results suggest that intensity of bite and fclench influences activation levels in MI and SI. Further, an activation was more obvious with bite than fclench.

The findings of this study are consistent with those of an fMRI study by Tamura et al., in which it was found that MI and SI showed marked activation with tooth clenching and tapping. Moreover, Iwata et al. reported that the concentration chenges of totalHb at the primary hand motor area increased with the force levels [2]. This suggests that the choice of t MI and SI for measurement of brain activity in this study was appropriate.

An increased tendency toward OxyHb in the rCBF was observed contralateral to the bite side in MI and SI. This supports the findings of an fMRI study by Tamura et al. [4] which showed that the primary motor and sensory cortices exhibited remarkable activity with clenching.

Previous studies using recording of neuronal signal activity during jaw movement have suggested that many cortex neurons show movement-related activity and contribute to the control of jaw movement [8] and bite force [9]. Previous studies reported that the level of masseter muscle activity increased with hard foods [10]. Intensity of afferent-encoded information from the periodontium increases with strength of bite [11]. An increased tendency toward OxyHb in the rCBF was observed contralateral to the fclench side in the primary motor and somatosensory cortices. There are many studies using PET and fMRI clarifying a relationship between cerebral activity in the motor areas and the force levels with a tapping task [12, 13].This indicates that increase in bite intensity results in increased activity in MI.

Earlier studies on jaw movement have suggested that oral sensory information ascended into the sensory cortex, thus controlling jaw movement and discrimination of food states in monkey [14] and cat [6]. Moreover, given that there are cortico-cortical projections of the sensory cortex to the motor cortex [15, 16], it is reasonable to assume that SI information is involved in the control of biting intensity, either directly or indirectly, and that the SI region was activated in the biting task in this study. Somatosensory information not only from the periodontal ligament (predominantly via the maxillary and inferior alveolar nerve branches of the trigeminal nerve), but also from the dental pulp, gingiva, palatal mucosa, lips and skin of the jaw has been reported to increase with increase in biting intensity [17]. Therefore, with increase in bite intensity, the activity of SI increases.

Dettmers et al. found on identifiable correlation between relative rCBF and force in the primary somatosennsory cortex, and SI activation may reflect increased levels of sensory feedback with increasing peak force [12]. In addition, SI receives projections from the motor cortex. Kalaska et al. reported that SI activation highlights the intimate relationship between somatosensory and motor cortices during purposeful acts [18].

5 Conclusion

In this study, activation of MI and SI with bite and fclench was noted in all subjects, irrespective of intensity of bite and fclench. A significant increase was observed in OxyHb in MI and SI between 20% and both 50 and 80% bite intensity. In MI, OxyHb showed a significant increase between 80% and both 20 and 50% fclench intensity. The results suggest that bite elicits activation of both MI and SI and fclench elicits activation of MI. Intensity of bite and fclench influences activation levels in the brain. Further, an increasing tendency was more obvious in OxyHb with bite than fclench.

References

1. Funakoshi, M., et al., Relationship between mastication and intelligence in children. J Gifu Dent Soc, 1987. 14(1): 17–29.
2. Iwata, N.K., et al., Correlation between force and motor cortical activation measured by near infrared spectroscopy (NIRS). NeuroImage, 2001. 13(6): Part 2 of 2 Parts
3. Momose, I., et al., Effect of mastication on regional cerebral blood flow in humans examined by positron-emission tomography with 15O-labelled water and magnetic resonance imaging. Arch Oral Biol, 1997. 42(1): 57–61.
4. Tamura, T., et al., Functional magnetic resonance imaging of human jaw movements. J Oral Rehabil, 2003. 30(6): 614–622.
5. Greenberg, M.S., Handbook of Neurosurgery, fourth ed. Greenberg Graphic Inc. USA, 1997. 256(5064): 52–53.
6. Hiraba, K., Functional role of the superior and inferior heads of the human lateral ptetrygoid muscle in movements of the mandibular condyle and articular disk. J Jpn Soc Stomatognath Funct, 2003. 9(2): 141–151.
7. Hoshi, Y., N. Kobayashi, and M. Tamura, Interpretation of near-infrared spectroscopy signals: a study with a newly developed perfused rat brain model. J Appl Physiol, 2001. 90(5): 1657–1662.
8. Narita, N., K. Kamiya, K. Yamaura et al., Chewing-related prefrontal cortex activation while wearing partial denture prosthesis: Pilot Study. J. Prothodont Res. 2009; 53: 126–135.
9. Shibusawa, M., T. Takeda, K. Nakajima et al., Functional near-infrared spectroscopy study on primary motor and sensory cortex response to clenching. Neurosci Lett. 2009; 449: 98–102.
10. Weijs, W.A. and R. Dantuma, Functional anatomy of the masticatory apparatus in the rabbit (Oryctolagus cuniculus L.). Academic Press, London, 1981(359–398).
11. Yoshino, K., A. Mikami, and K. Kubota, Neuronal activities in the ventral premotor cortex during a visually guided jaw movement in monkeys. Neurosci Res, 1998. 30(4): 321–332.
12. Dettmers, C., et al., Relation between cerebral activity and force in the motor areas of the human brain. J Neurophysiol, 1995. 74(2): 802–815.
13. Thickbroom, G.W., et al., Isometric force-related activity in sensorimotor cortex measured with functional MRI. Exp Brain Res, 1998. 121(1): 59–64.
14. Lin, L.D., G.M. Murray, and B.J. Sessle, The effect of bilateral cold block of the primate face primary somatosensory cortex on the performance of trained tongue-protrusion task and biting tasks. J Neurophysiol, 1993. 70(3): 985–996.
15. Zarzecki, P., Y. Shinoda, and H. Asanuma, Projection from area 3a to the motor cortex by neurons activated from group I muscle afferents. Exp Brain Res, 1978. 33(2): 269–282.
16. Kamata, S., Reflex response of temporal muscel induced by mechanical stimulation to periodontal ligament -In the lareral jaw movement during mastication-. J Stomatological Society, Japan, 1994. 61(1): 82–97.
17. Inoue, T., A role of trigeminal sensation in the control of jaw movement. J Osaka Univ Dent Soc, 1987. 32(1): 70–90.
18. Kalaska, J.F. and D.J. Crammond, Cerebral cortical mechanisms of reaching movements. Science, 1992. 255(5051): 1517–1523.

Changes in Cerebral Blood Oxygenation and Hemodynamics After Endovascular Treatment of Vascular Malformation Measured by Time-Resolved Spectroscopy

Tatsuya Hoshino, Kaoru Sakatani, Noriaki Yokose, Takashi Awano, Sin Nakamura, Yoshihiro Murata, Tsun eo Kano, and Yoichi Katayama

Abstract Although endovascular treatment has a high success rate, it is not clear how endovascular treatment affects cerebral perfusion and hemodynamics during the perioperative period. We evaluated changes in cerebral blood oxygenation (CBO) repeatedly after endovascular treatment employing time-resolved spectroscopy (TRS). We investigated a patient (10 months old, female) who suffered cerebral arteriovenous fistula. Cerebral angiography demonstrated a pial arteriovenous fistula with three feeders (left PICA, SCA, and AICA). TRS demonstrated a decrease of oxyhemoglobin, total hemoglobin, and oxygen saturation associated with an increase of deoxyhemoglobin in all of the regions measured just after embolization, indicating that embolization improved hyperemia caused by the AV shunt. Interestingly, progressive improvement of hyperemia was observed 3 and 8 days after embolization of the feeders. The present study demonstrated that embolization of the feeders caused progressive changes in CBO and hemodynamics during the perioperative period. TRS may be a useful tool for monitoring cerebral blood perfusion changes after endovascular surgery.

1 Introduction

Intravascular surgery has been widely used for treatment of cerebrovascular diseases, including arteriovenous malformations (AVMs). Cerebral arteriovenous fistula (AVF) is a rare disease, but AVFs are not infrequently seen in neonates and infants with AVMs. Although endovascular treatment has a high success rate, it is not clear how endovascular treatment affects cerebral perfusion and hemodynamics during the perioperative period. Transcranial Doppler

T. Hoshino (✉)
Division of Neurological Surgery, Department of Neurological Surgery,
Nihon University School of Medicine, Tokyo, Japan
e-mail: hooooshino@yahoo.co.jp

E. Takahashi, D.F. Bruley (eds.), *Oxygen Transport to Tissue XXXI*,
Advances in Experimental Medicine and Biology 662,
DOI 10.1007/978-1-4419-1241-1_71, © Springer Science+Business Media, LLC 2010

was used to monitor hemodynamic changes in AVM after embolization [1]. However, it is difficult to evaluate the hemodynamic changes at various sites of the brain. A simple, non-invasive method for bed-side assessments of hemodynamic changes is required.

NIRS can measure concentration changes of oxyhemoglobin (oxy-Hb) and deoxyhemoglobin (deoxy-Hb) in the cortical vessels [2]. Various studies have shown the usefulness of NIRS for detecting cerebral ischemia during carotid endarterectomy [3]; however, it is difficult to apply NIRS to the diagnosis of vasospasm after SAH, since commercially available NIRS instruments, which employ continuous-wave light, do not provide quantitative values of the baseline Hb concentrations [4]. In contrast, time-resolved near-infrared spectroscopy (TRS) [5, 6] and frequency-domain NIRS [7] permit quantitative measurement of Hb concentrations in the resting condition. Recently, we have demonstrated the reliability of newly developed TRS by undertaking simultaneous TRS and PET measurements in normal adults [8]. In the present study, employing the TRS, we evaluated changes in cerebral blood oxygenation (CBO) and hemodynamics repeatedly after endovascular treatment.

2 Method

2.1 Case Presentation

The patient (10 months old, female) was admitted to Saitama Children Hospital due to enlargement of head circumference and convulsion on July 5th 2005. She was born by normal spontaneous vaginal delivery at gestation of 39 weeks. She showed dilatation of head circumference at 4 months after birth, and her left eye showed exophthalmus and congestion of bulbar conjunctiva. MRI revealed extra-axial mass near the sinus confluence. Digital subtraction angiography (DSA) disclosed a huge varix at the left cerebellum hemisphere and dilatation of the sinus confluence due to pial arterio-venous fistula (AVF).

At 8 months after birth, she was underwent interventional surgery via the transvenous approach. The varix was embolized with a Guglielmi detachable coil (GDC). The shunt flow was reduced remarkably; however, complete embolization was not achieved. After the embolization, exophthalmus and congestion of bulbar conjunctiva improved immediately, but these symptoms deteriorated again 3 months after the first interventional surgery. Therefore, we performed the second interventional surgery via a transarterial approach; the residual feeders were embolized via the left AICA and SCA (Fig. 1). We monitored changes in CBO and hemodynamics at various parts of the brain employing TRS before and after the second interventional surgery.

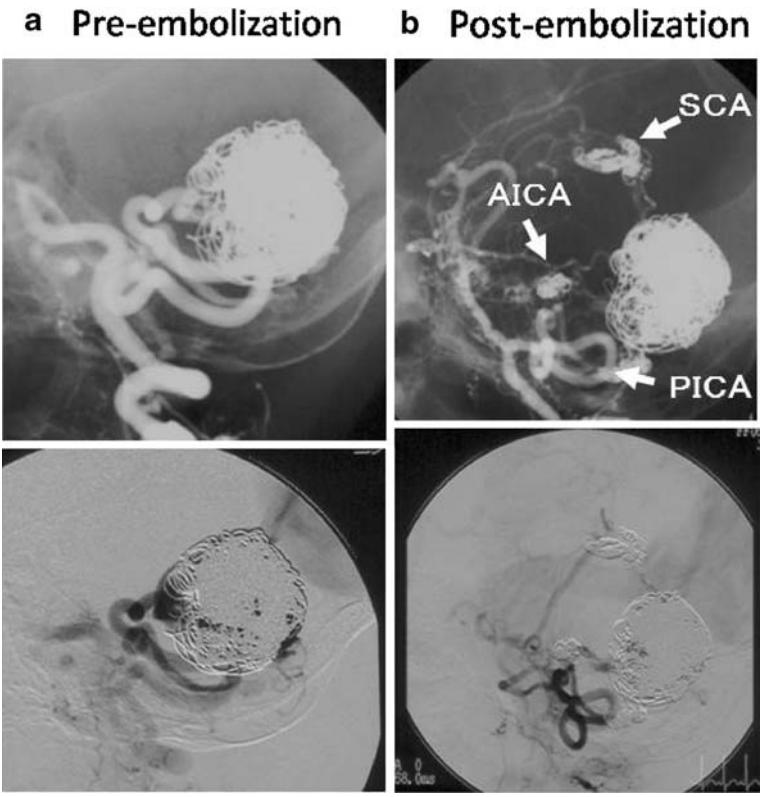

Fig. 1 Cerebral angiography before and after embolization

2.2 TRS

We measured Hb concentrations in the subject with a TRS-10 system (Hamamatsu Photonics K.K, Hamamatsu, Japan), which has been used in several studies [6, 8]. Details of this system have been described previously [6, 8]. Briefly, it consists of three pulsed laser diodes with different wavelengths (761 , 791 , and 836 nm; the pulse duration is 100 ps, with a repetition frequency of 5 Mhz), a photomultiplier tube (PMT; H6279-MOD, Hamamatsu Photonics K.K., Japan), and a circuit for time-resolved measurement based on the time-correlated single photon counting method. The observed temporal profiles were fitted to the photon diffusion equation using the non-linear least-squares fitting method. The reduced scattering (μ_s') and absorption coefficients (μ_a) for the three wavelengths were calculated. The concentrations of oxy-Hb, deoxy-Hb, total Hb (= oxy-Hb + deoxy-Hb; tHb) and oxygen saturation (StO_2) were then calculated using the least-squares method. The concentrations of Hb were expressed in μM. The distance between the emitter and receiver was 3 cm.

We measured pre- and postoperative concentration changes of hemoglobin in the second interventional surgery using the TRS. Measurements were performed before embolization, just after embolization, and at 3 and 8 days after embolization. The optodes were placed over the left frontal, temporal and occipital regions.

3 Results

Figure 2 shows the changes of oxy-Hb, deoxy-Hb, total-Hb concentrations, and StO_2 at the frontal, temporal and parietal regions on the left sides after embolization. Immediately after embolization, oxy-Hb decreased and deoxy-Hb increased, which caused reduction of StO_2, at all measurement areas.

Interestingly, the decreasing tendency of oxy-Hb and StO_2, associated with an increase of deoxy-Hb, was also observed at 3 and 8 days after embolization. In contrast, changes in t-Hb concentration were not remarkable compared with the changes in oxy-Hb and deoxy-Hb concentrations; only t-Hb on the left side, particularly at the occipital region, tended to decrease after embolization.

4 Discussion

The present study is the first demonstration of CBO changes in AVF after embolization using TRS. In contrast to standard neuroradiological techniques such as SPECT and DSA, TRS (a non-invasive optical technique) allows bed-side monitoring of CBO and hemodynamics. Employing TRS, we could evaluate the effect of embolization on CBO and hemodynamics repeatedly.

TRS yields a mixed arterial venous signal in the cortex; however, the contribution ratio of the vascular compartments is not yet clear [9]. Recently, we observed that the mean values of StO_2 in normal adults were similar to those of SjO_2 in patients with unruptured aneurysms [10], suggesting that TRS measures the blood oxygenation predominantly in the venous compartment. In addition, the Hb concentrations measured by TRS are the average concentrations within the illuminated area, including the extracranial and intracranial tissues. Simultaneous measurements of TRS and PET in normal adults suggested that the contribution ratios of the extracranial tissue were about 36.9 (830 nm), 33.2 (800 nm), and 60.3 % (760 nm) when the distance between the emitter and receiver was 3 cm [8].

In the present study, TRS demonstrated a decrease of StO_2 at all measurement areas after embolization; the reduction of StO_2 was caused by a decrease of oxy-Hb concentration and an increase of deoxy-Hb. These CBO changes indicate that embolization reduced AV shunt, since TRS measures Hb concentration mainly in venous compartments.

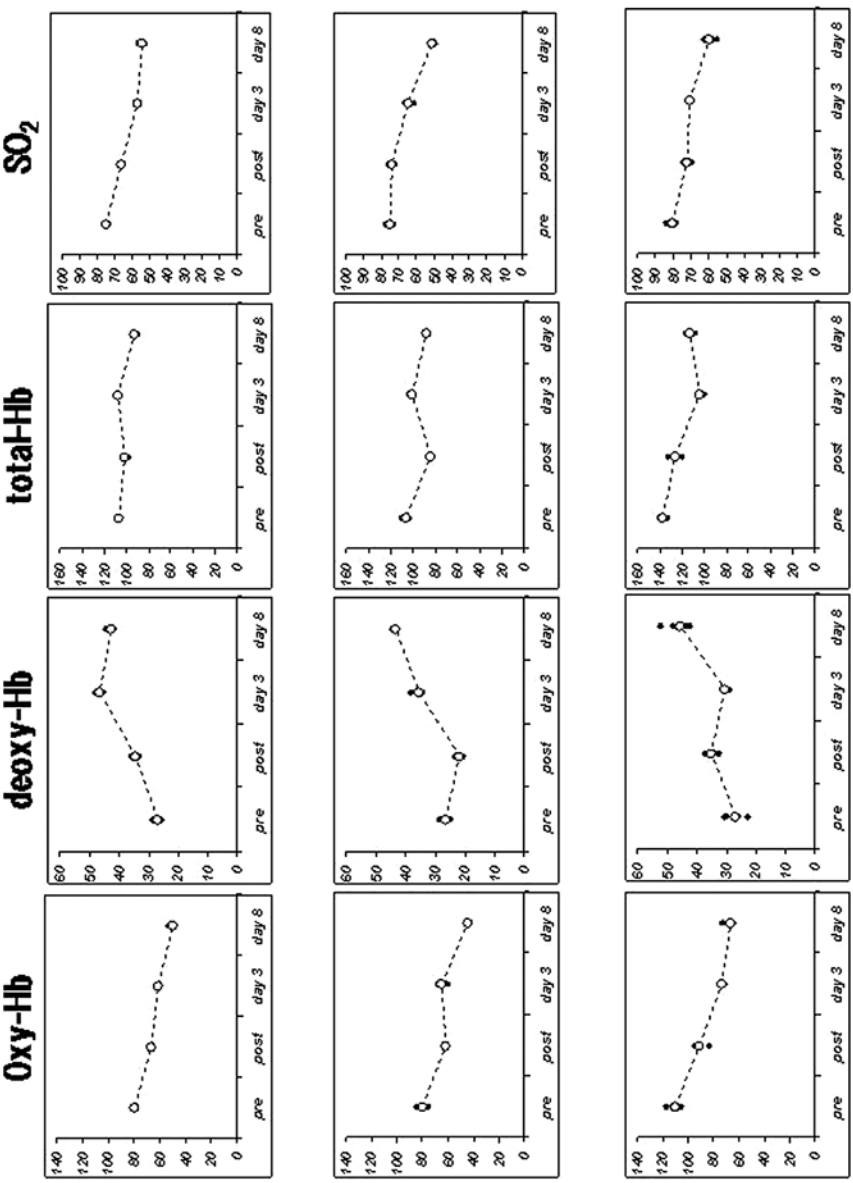

Fig. 2 Changes of oxy-Hb, deoxy-Hb, total-Hb concentrations, and StO_2 at the frontal, temporal and parietal regions on the *left sides* after embolization

In contrast to changes in oxy-Hb and deoxy-Hb, changes in total-Hb were not remarkable after embolization. In general, total-Hb, which is the sum of oxy-Hb and deoxy-Hb, reflects cerebral blood volume. Ijichi et al. measured the CBO of neonates (30–42 weeks) using TRS, and the calculated mean concentration of total-Hb was 64.7 ± 18.9 μM [6]. Thus, the concentration of total-Hb in the present case was relatively high, suggesting that venous congestion was caused by AV fistula. These results suggest that embolization did not improve venous congestion at the time of examination. In addition, improvements of venous congestion after embolization require more time compared with improvement of CBO.

5 Conclusion

TRS demonstrated that embolization of the feeders caused progressive changes in CBO and hemodynamics during the perioperative period in our patient. This indicates that the effect of embolization on the CBO and hemodynamics continued for some period after embolization. TRS, which allows repeated, non-invasive measurements of CBO, may be a useful tool for monitoring changes in CBO and hemodynamics after endovascular surgery.

References

1. Harders A, Bien S, Eggert HR et al. (1988) Haemodynamic changes in arteriovenous malformations induced by superselective embolization: transcranial Doppler evaluation. Neurol Res 10:239–245.
2. Jöbsis FF(1977) Noninvasive, infrared monitoring of cerebral and myocardial oxygen sufficiency and circulatory parameters. Science 198:1264–1267.
3. Al-Rawi P, Smielewski P, Kirkpatrick PJ (2001) Evaluation of a near infrared spectrometer (NIRO 300) for the detection of intracranial oxygenation changes in the adult head. Stroke 32:2492–2500.
4. Reynolds EO, Wyatt JS, Azzopardi D et al. (1988) New non-invasive methods for assessing brain oxygenation and hemodynamics. Br Med Bull 44:1052–1075.
5. Chance B, Leigh JS, Miyake H et al. (1988) Comparison of time-resolved and -unresolved measurements of deoxyhemoglobin in brain. Proc Natl Acad Sci USA85:4971–4975.
6. Ijichi S, Kusaka T, Isobe K et al. (2005) Developmental changes of optical properties in neonates determined by near-infrared time-resolved spectroscopy. Pediat Res 58:568–573.
7. Gatto R, Hoffman W, Mueller M, et al. (2006) Frequency domain near-infrared spectroscopy technique in the assessment of brain oxygenation: a validation study in live subjects and cadavers. J Neurosci Methods 157:274–277.
8. Ohmae E, Ouchi Y, Oda M et al. (2006) Cerebral hemodynamics evaluation by near-infrared time-resolved spectroscopy: correlation with simultaneous positron emission tomography measurements. NeuroImage 29:697–705.
9. McCormick PW, Stewart M, Goetting MG (1991) Noninvasive cerebral optical spectroscopy for monitoring cerebral oxygen delivery and hemodynamics. Crit Care Med 19:89–97.
10. Karibe H, Tominaga T, Sato K et al. (2001) Decrease in intraoperative brain surface temperature in patients with subarachnoid haemorrhage. Acta Neurochir (Wien) 143:9–14.

Development of a New Rehabilitation System Based on a Brain-Computer Interface Using Near-Infrared Spectroscopy

Takafumi Nagaoka, Kaoru Sakatani, Takayuki Awano, Noriaki Yokose, Tatsuya Hoshino, Yoshihiro Murata, Yoichi Katayama, Akihiro Ishikawa, and Hideo Eda

Abstract We describe the set-up for an electrical muscle stimulation device based on near-infrared spectroscopy (NIRS), designed for use as a brain-computer interface (BCI). Employing multi-channel NIRS, we measured evoked cerebral blood oxygenation (CBO) responses during real motor tasks and motor-imagery tasks. When a supra-threshold increase in oxyhemoglobin concentration was detected, electrical stimulation (50 Hz) of the biceps brachii muscle was applied to the side contralateral to the hand grasping task or ipsilateral to the motor-imagery task. We observed relatively stable and reproducible CBO responses during real motor tasks with an average accuracy of 100%, and during motor imagery tasks with an average accuracy of 61.5%. Flexion movement of the arm was evoked in all volunteers in association with electrical muscle stimulation and no adverse effects were noted. These findings suggest that application of the electrical muscle stimulation system based on a NIRS-BCI is non-invasive and safe, and may be useful for the physical training of disabled patients.

1 Introduction

Brain–computer interface (BCI) systems have been developed to allow control of computers or external electrical devices based on detection of brain activity alone. Previous investigations have focused on applying BCI systems as supportive tools to assist locomotion, volitional movements of the hands, and communication for disabled patients (such as those with stroke, spinal cord injury, amyotrophic lateral sclerosis, and movement disorders) [1, 2]. BCI systems may also be applicable to assist rehabilitation of chronic stroke patients [3].Current BCI systems employ surface electroencephalography (EEG) [4, 5],

T. Nagaoka (✉)
Division of Neurosurgery, Department of Neurological Surgery, Nihon University School of Medicine, Tokyo, Japan
e-mail: ntkfm@med.nihon-u.ac.jp

E. Takahashi, D.F. Bruley (eds.), *Oxygen Transport to Tissue XXXI*, Advances in Experimental Medicine and Biology 662,
DOI 10.1007/978-1-4419-1241-1_72, © Springer Science+Business Media, LLC 2010

electrocorticography (ECoG) and intracranial implanted electrodes [6], magnetoencephalography (MEG) [3, 7], blood-oxygen-level dependent functional MRI [8], and near-infrared spectroscopy (NIRS) [9, 10] as signal acquisition modalities. NIRS is a noninvasive optical technique used to measure concentration changes in oxyhemoglobin and deoxyhemoglobin in cerebral vessels based on the characteristic absorption spectra of hemoglobin in the near-infrared range [11, 12]. Recently, NIRS has been suggested to be a promising signal acquisition tool for BCI because of its handiness, portability, good spatial resolution, metabolic specificity, and suitability for continuous measurement of brain activity changes with high time resolution [9, 10]. A disadvantage, however, is that NIRS is slow to operate because of the intrinsic latency of the brain hemodynamics [10]. Therefore we considered that a NIRS-based BCI system may be more suitable for "slow operation" including rehabilitation, relaxation, treatment of pain, or bio-feedback programs, than for "fast operation" such as supporting voluntary movement or locomotion. Here, we describe the development of a new muscle stimulation system for rehabilitation as a clinical application of NIRS-based BCI technology.

2 Methods

2.1 Subjects

We studied four normal adult volunteers (4 males, mean age = 28.5), who each gave informed consent to participate. Figure 1 demonstrated the profile of our NIRS-BCI based rehabilitation system.

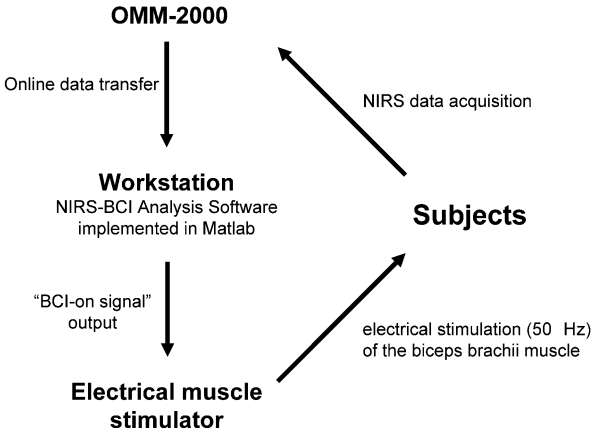

Fig. 1 Schematic illustration of NIRS-BCI-based rehabilitation system

2.2 Experimental Procedure

Hand grasping was performed as a motor task, and self-paced imagination of hand grasping was also performed as a motor-imagery task. A trial consisted of a baseline period of 10 s and a hand-grasping/motor-imagery task period of 20s. Each session consisted first of 2 trials as a preparation stage for threshold learning with data analysis software, and then the following trials as a NIRS-BCI working stage (Fig. 2). Hand-grasping and motor-imagery data were collected in separate sessions.

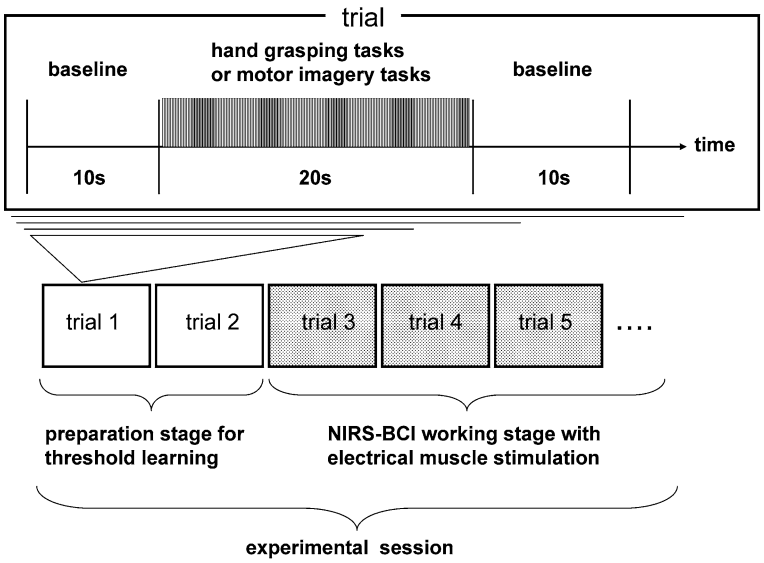

Fig. 2 Experimental protocol for hand grasping and motor imagery to elicit NIRS signals from subjects. A trial consisted of a baseline block of 10 s and a hand-grasping/motor-imagery task block of 20 s (*upper panel*). Each session consisted first of 2 trials as the preparation stage for threshold learning and then serial trials as the NIRS-BCI working stage with electrical muscle stimulation (*lower panel*). Hand-grasping and motor-imagery data were collected in separate sessions

We used a continuous-wave multi-channel NIRS instrument (OMM 2000, Shimadzu Corporation, Japan) for two-dimensional imaging of the changes in concentration of oxyhemoglobin, deoxyhemoglobin, and total hemoglobin (total hemoglobin = oxyhemoglobin + deoxyhemoglobin) in the activated cortices of the bilateral frontal lobes, as used in previous NIRS studies [13]. This system consists of 16 light-source fibers and 16 detectors, resulting in 48 source-detector pairs; each light source has 3 laser diodes with wavelengths of 780, 805, and 830 nm [14]. These probes were placed on the left and right hemispheres on the subject's head, above the motor cortex, around the C3 (left hemisphere) and

C4 (right hemisphere) areas (International 10–20 System). The distance between probes was 30 mm, and an area measuring 90×90 mm^2 was covered.

2.3 NIRS-BCI Signal Analysis

NIRS data were transferred from the OMM 2000 to a workstation via an Ethernet online connection, and NIRS data analysis was performed employing custom software for NIRS-based BCI (from Shimadzu Corporation, Japan) implemented in Matlab (Mathworks, Sherborn, MA, USA). In each subject, several (1∼3) channels in which a suitable hemodynamic response was obtained during the hand-grasping task or motor-imagery task was selected for operating decision making in NIRS-BCI. In the first two trials of each session, the changes of oxyhemoglobin were normalized in accordance with the maximum value of oxyhemoglobin, and the threshold level for "BCI-on" was determined as 0.3 (30%) of the maximum value. In the following trials in each session, the BCI-on signal command was outputted from the workstation during supra-threshold increase in cerebral regional oxyhemoglobin, and was sent to the electrical muscle stimulation device. When oxyhemoglobin fell below the threshold level, output of the BCI-on signal was interrupted.

2.4 Electrical Muscle Stimulation

This electrical muscle stimulation system based on NIRS-BCI provides a passive elbow joint movement, and assists the subject in exercising the muscle. Using a surface electrode, electrical stimulation (50 Hz) of the biceps brachii muscle was applied to the side contralateral to the grasping task or ipsilateral to the motor-imagery task. In each subject, stimulation intensity was appropriately arranged to be able to evoke flexion movement of the arm without pain.

3 Results and Discussion

We observed relatively stable and reproducible hemodynamic responses. In all subjects, NIRS showed a decrease of Deoxy-Hb associated with increases of Oxy-Hb and total Hb in the primary motor cortex contralateral to the hand-grasping (Fig. 3a) and motor-imagery task performance (Fig. 3b). Average working accuracy of the NIRS-BCI system was 100% in the hand-grasping task, and 61.5% in the motor-imagery task (Table 1). When the NIRS-BCI system sent the "on-signal" to the electrical muscle stimulator, continuous flexion movement of the forearm was evoked in all subjects in association with stimulation of the biceps brachii muscle. In the cerebral hemisphere

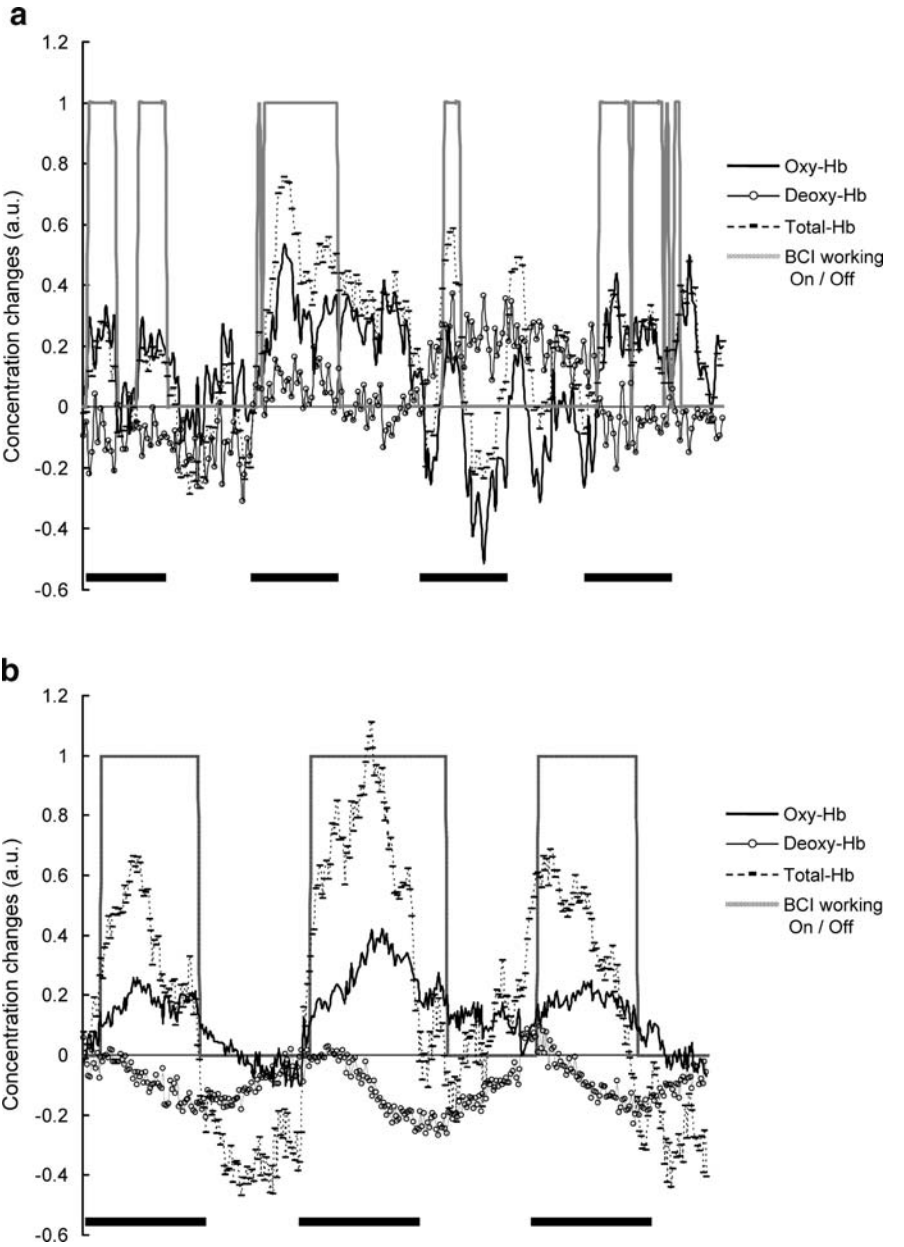

Fig. 3 Typical examples of NIRS parameter changes during hand-grasping (**a**) and motor-imagery tasks (**b**). The ordinates indicate concentration changes of oxyhemogrobin (Oxy-Hb), deoxyhemoglobin (Deoxy-Hb), and total hemoglobin (Total-Hb) in arbitrary units (a.u.). Thick horizontal bars indicate the period of hand-grasping tasks or motor-imagery tasks

Table 1 Average working accuracy of NIRS-BCI in the hand grasping tasks and the motor imagery tasks

			Accuracy(%)	
Subjects	Age	Sex	Hand grasping	Motor imagery
1	28	m	100	36.5∼68.0
2	30	m	100	80∼100
3	23	m	100	0∼3.4
4	33	m	100	40.5∼55.6
Total			100	61.5

contralateral to the motor imagery task, hemodynamic responses induced by muscle stimulation were not definitely detected. No adverse effects were noted. These findings suggest that application of an electrical muscle stimulation system based on NIRS-BCI is non-invasive and safe, and may be useful for the physical training of disabled patients.

References

1. Birbaumer N, Weber C, Neuper C, et al. (2006) Physiological regulation of thinking: brain-computer interface (BCI) research. Prog Brain Res 159: 369–391.
2. Wolpaw JR, McFarland DJ (2004) Control of a two-dimensional movement signal by a noninvasive brain-computer interface in humans. Proc Natl Acad Sci U S A 101: 17849–17854.
3. Buch E, Weber C, Cohen LG et al. (2008) Think to move: a neuromagnetic brain-computer interface (BCI) system for chronic stroke. Stroke 39: 910–917.
4. Neuper C, Müller GR, Kübler A, et al. (2003) Clinical application of an EEG-based brain-computer interface: a case study in a patient with severe motor impairment. Clin Neurophysiol 114: 399–409.
5. Pfurtscheller G, Graimann B, Huggins JE, et al. (2003) Spatiotemporal patterns of beta desynchronization and gamma synchronization in corticographic data during self-paced movement. Clin Neurophysiol 114: 1226–1236.
6. Felton EA, Wilson JA, Williams JC, et al. (2007) Electrocorticographically controlled brain-computer interfaces using motor and sensory imagery in patients with temporary subdural electrode implants. Report of four cases. J Neurosurg 106: 495–500.
7. Mellinger J, Schalk G, Braun C, et al. (2007) An MEG-based brain-computer interface (BCI). Neuroimage 36:581–593.
8. Yoo SS, Fairneny T, Chen NK, et al. (2004) Brain-computer interface using fMRI: spatial navigation by thoughts. Neuroreport 15: 1591–1595.
9. Coyle SM, Ward TE, Markham CM (2007) Brain-computer interface using a simplified functional near-infrared spectroscopy system. J Neural Eng 4: 219–226.
10. Sitaram R, Zhang H, Guan C et al. (2007) Temporal classification of multichannel near-infrared spectroscopy signals of motor imagery for developing a brain-computer interface. Neuroimage 34: 1416–1427.
11. Jöbsis FF (1977) Noninvasive, infrared monitoring of cerebral and myocardial oxygen sufficiency and circulatory parameters. Science 198: 1264–1267.
12. Reynolds EO, Wyatt JS, Azzopardi D, et al. (1988) New non-invasive methods for assessing brain oxygenation and haemodynamics. Br Med Bull 44: 1052–1075.

13. Hoshino T, Sakatani S, Katayama Y, et al. (2005) Application of multi-channel near infrared spectroscopic topography to physiological monitoring of the cortex during cortical mapping: technical case report. Surg Neurol 64:272–275.
14. Miyai I, Yagura H, Oda I, et al. (2002) Premotor cortex is involved in restoration of gait in stroke. Ann Neurol 52: 188–94.

Bedside Assessment of Cerebral Vasospasms After Subarachnoid Hemorrhage by Near Infrared Time-Resolved Spectroscopy

Noriaki Yokose, Kaoru Sakatani, Yoshihiro Murata, Takashi Awano, Takahiro Igarashi, Sin Nakamura, Tatsuya Hoshino, Tsuneo Kano, Atsuo Yoshino, Yoichi Katayama, Etsuko Ohmae, Toshihiko Suzuki, Motoki Oda, and Yutaka Yamashita

Abstract We examined the usefulness of near infrared time-resolved spectroscopy (TRS) for detection of vasospasm in subarachnoid hemorrhage (SAH). We investigated seven aneurysmal SAH patients with poor clinical conditions (WFNS grade V) who underwent endovascular coil embolization. Employing TRS, we measured the oxygen saturation (SO_2) and baseline hemoglobin concentrations in the cortices. Measurements of TRS and transcranial Doppler sonography (TCD) were performed repeatedly for 14 days after SAH. In four of the seven patients, the SO_2 and hemoglobin concentrations measured in the brain tissue of the middle cerebral artery territory remained stable after SAH. However, in three patients, TRS revealed abrupt decreases in SO_2 and total hemoglobin between 5 and 9 days after SAH. Cerebral angiography performed on the same day revealed severe vasospasms in these patients. Although TCD detected the vasospasm in two of three cases, it failed to do so in one case. TRS could detect vasospasms after SAH by evaluating the cortical blood oxygenation.

1 Introduction

Arterial vasospasm is the most common cause of delayed ischemic neurological deficits in patients with aneurysmal subarachnoid hemorrhage (SAH) [1]. Transcranial Doppler sonography (TCD) has been used to detect vasospasms after SAH [2–4], but its sensitivity is not high [3, 5–7]. In addition, TCD does not provide information about the cerebral circulation and oxygenation in the cortex. A simple, non-invasive method for bed-side assessments of cerebral ischemic status is still required. In this pilot study, we examined whether near infrared time-resolved spectroscopy (TRS), which permits quantitative measurement of the Hb concentrations [8], can detect cerebral ischemia caused by

N. Yokose (✉)
Division of Neurological Surgery, Department of Neurological Surgery,
Nihon University School of Medicine, Tokyo, Japan
e-mail: nyokose@med.nihon-u.ac.jp

E. Takahashi, D.F. Bruley (eds.), *Oxygen Transport to Tissue XXXI*,
Advances in Experimental Medicine and Biology 662,
DOI 10.1007/978-1-4419-1241-1_73, © Springer Science+Business Media, LLC 2010

vasospasm in patients with aneurysmal SAH. Initially, we measured normal values for the Hb concentrations and oxygen saturation (SO_2) in various cortical regions of normal adults. We then repeatedly measured the SO_2 and Hb concentrations in patients after SAH, and these data were compared with the results of TCD. In addition, we evaluated whether TRS measurements on day 1 after SAH can be useful for predicting the occurrence of vasospasm and clinical outcome.

2 Methods

We evaluated seven patients with poor clinical condition (e.g. WFNS grade V) who had undergone embolization of their aneurysms within 24 h after SAH using Guglielmi detachable coils. The hemorrhagic pattern on initial CT scan was assigned to Fisher group III in all patients. The systemic blood pressure, systemic oxygen saturation, Hb concentrations, and hematocrit were maintained within normal ranges during the course of the examinations; there were no significant differences in Hb concentration or hematocrit between the patients and controls. This study was approved by the Committee for Clinical Trials and Research on Humans of Nihon University School of Medicine, and the ethical committee of our university hospital approved the protocol. We measured the baseline concentrations of Hb in the subjects with a TRS-10 system (Hamamatsu Photonics K.K. Hamamatsu, Japan), which has been used in several studies on normal adults [9, 10] and newborn infants [11]. The optical probes were attached to mainly the MCA territory of the temporal lobes with an optode distance of 3 cm, since these areas are commonly affected by vasospasm after SAH. Details of this system have been described by us previously (Fig. 1) [9, 12]. To determine the reduced scattering coefficient (μ_s') and absorption coefficient (μ_a) at each wavelength first, we fit a solution of a semi-infinite homogeneous media with zero boundary condition in reflectance model [13] into the observed temporal profiles obtained from TRS using the non-linear least squares method. Based on the assumption that light absorption in the living body in this wavelength region occurs from oxy-Hb, deoxy-Hb and water, and also that there is no other background absorption in the living body [14], the concentrations of oxy-Hb, deoxy-Hb, total Hb (= oxy-Hb + deoxy-Hb; tHb) and SO_2 were calculated using the obtained μ_a each wavelength [9]. The concentrations of Hb were expressed in μM. TRS measurements were performed repeatedly for 14 days after the onset of SAH. The blood flow velocity in the MCA (M1 portion) was measured by TCD (EME Transcranial Doppler System, Nicolet Biomedical Inc., WI, USA); a 2-MHz-pulsed Doppler probe was used via the transtemporal window. TCD measurements were performed repeatedly by the same investigator (S.N.) for 14 days after SAH. Occurrence of vasospasm was considered to take place when the mean flow velocity was greater than 120 cm/s [5].

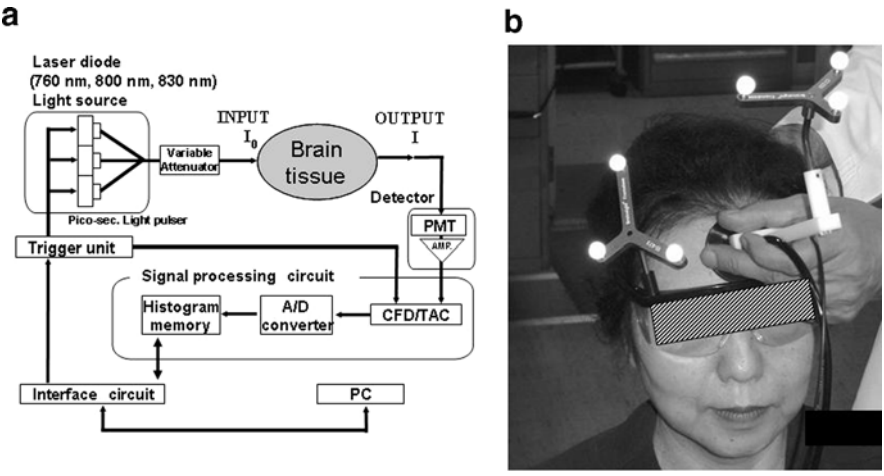

Fig. 1 (**a**) Block diagram of the TRS-10 system. (**b**) Placement of optical fibers on the head. A frameless stereotaxic system was used for identification of the TRS measurement sites on the cortex

3 Results

In four of the seven patients, TRS demonstrated only small changes in SO_2 and oxy-Hb, deoxy-Hb and t-Hb concentrations in the MCA territory during the course of the examinations (Fig. 2). Cerebral angiography performed at 7 days after SAH did not reveal vasospasms in these patients. In contrast, the three other patients (patients No.1, 2, and 7) showed abrupt decreases in SO_2 and tHb between 5 and 9 days after SAH. The cerebral angiography performed on the same day demonstrated severe vasospasms of the MCA in these patients. Figure 3 represents an example (patient No. 2) of the chronological changes in SO_2 and t-Hb. TRS showed abrupt decreases of SO_2 and tHb at 5 days after SAH. Intra-arterial injection of fasudil hydrochloride (30 mg) relieved the vasospasm and increased the SO_2 and t-Hb to the previous levels. TCD, however, failed to detect the vasospasm in this patient (flow velocity of the MCA < 100 cm/s); it revealed an acceleration of blood flow velocity indicative of vasospasm in the other two cases.

4 Discussion

The present study represents the first application of TRS to patients with SAH. Prior to this study, we have assessed the reliability of TRS measurements by undertaking simultaneous measurements of TRS and PET in normal adults [9]. We revealed significant correlations between the changes in TRS-measured

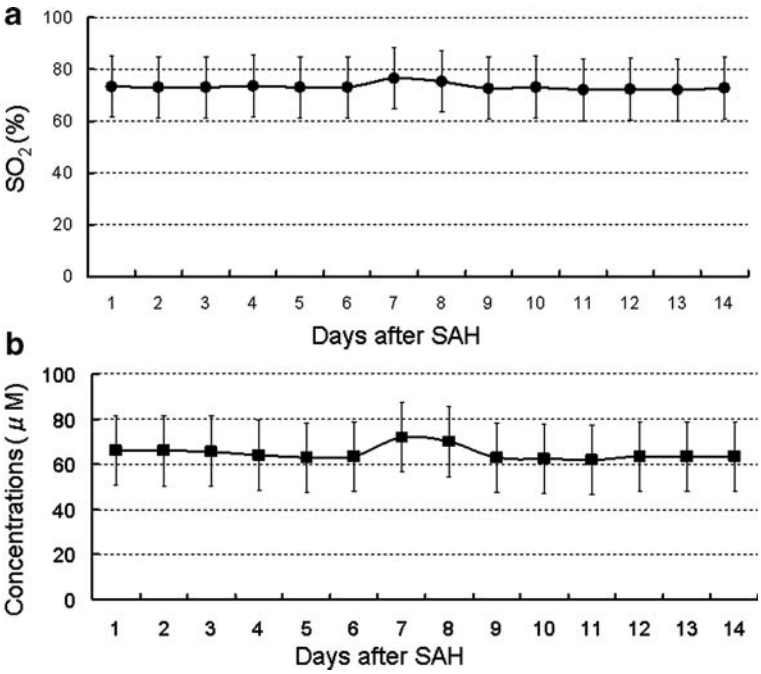

Fig. 2 Typical changes of SO_2 (**a**) and t-Hb (**b**) in the MCA territory of SAH patients without vasospasms. The ordinates in **a** and **b** indicate the oxygen saturation (%) and Hb concentrations (μM), respectively. The abscissae indicate the number of days after SAH. The error bars are standard deviation

CBV and PET-measured CBV in the corresponding cortical region during acetazolamide administration at optode spaces of 2–5 cm. These findings indicate that the present TRS measurements (3 cm of optode distance) reflected the Hb concentrations in the cortex. By means of TRS, we were able to detect the occurrence of vasospasm in all three patients with angiographical vasospasm, while TCD failed to detect vasospasm in one of them. It should be noted that TRS detects vasospasm by evaluating the ischemic status (i.e., decreases of SO_2 and t-Hb) in the cortex caused by vasospasms, and can therefore detect vasospasms regardless of the affected artery insofar as vasospasm causes cortical ischemia which decreases the SO_2 and t-Hb. In contrast, TCD could fail to detect vasospasms extending to the peripheral MCA because narrowing of the peripheral MCA increases the vascular resistance, which tends to suppress the acceleration of blood flow in the M1 segment [15]. Our results suggest that TRS is more sensitive than TCD for detecting vasospasms after SAH, although further studies are needed to clarify the differences in sensitivity and specificity between TRS and TCD. The limitations of TRS require discussion. Firstly, the Hb concentrations measured by TRS are the average concentrations within the illuminated area including the extracranial and intracranial tissues. At present,

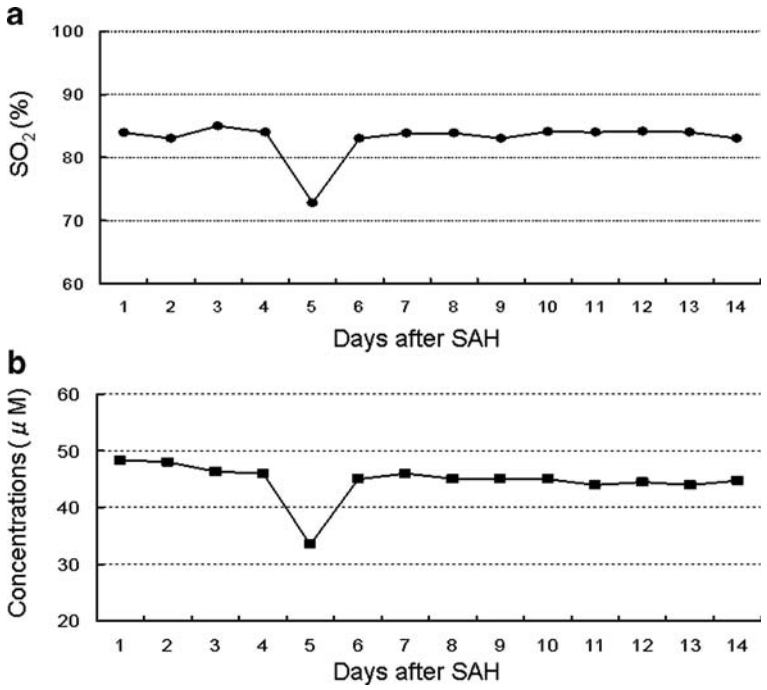

Fig. 3 Changes of SO_2 (**a**) and t-Hb (**b**) in the MCA territory of an SAH patient with vasospasm (patient No. 2). The ordinates in **a** and **b** indicate the oxygen saturation (%) and Hb concentrations (μM), respectively. The abscissa indicate the number of days after SAH

selective measurement of the Hb concentrations in the brain is difficult because the absorption coefficient (μ_a) of each compartment of the head including the brain tissue in living humans is not available. In addition, the contribution ratio of the NIRS signal of the brain tissue remains under discussion, although several studies on NIR light propagation in the human head have been performed [16, 17]. Recently, Liebert et al. have attempted to differentiate between the absorption changes occurring in the intra- and extracerebral compartments of the head by employing TRS and a bolus of indocyanine green (ICG) [18]. Secondly, TRS yields a mixed arterial venous signal in the cortex; however, the contribution ratios of the vascular compartments are not yet clear [8]. In the present study, the mean values of SO_2 in the controls were similar to those of SjO_2 in patients with unruptured aneurysms [19], suggesting that TRS measures the blood oxygenation predominantly in the venous compartment. Thirdly, NIR light propagation in the brain with SAH may differ from that in the normal brain, since the cerebrospinal fluid in the subarachnoid space exerts a significant effect on photon migration within the brain [16]. Finally, TRS may not evaluate the cerebral circulation correctly in patients whose anatomical structures of the head including the brain and skull are not normal. Further

studies such as comparisons of TRS measurements of the skin, the skull and the cortex are needed.

5 Conclusion

Although our preliminary data from a small number of patients cannot provide firm conclusions, we consider that TRS may be a useful tool for evaluating the cerebral circulatory status in SAH patients. TRS can detect vasospasm by evaluating the cortical ischemic status, and may be more sensitive than TCD, which assesses the blood flow velocity in the M1 portion. In addition, TRS performed on day 1 after SAH may be useful for predicting the occurrence of vasospasm and clinical outcome. Finally, TRS may be applicable for evaluation of the ischemic status in acute stroke patients.

References

1. Weir B, Macdonald L, Stoodley M (1999) Etiology of cerebral vasospasm. Acta Neurochir [Suppl] 72:27–46.
2. Harders AG, Gilsbach JM (1987) Time course of blood velocity changes related to vasospasm in the circle of Willis measured by transcranial Doppler ultrasound. J Neurosurg 66:718–728.
3. Creissard P, Proust F (1994) Vasospasm diagnosis: theoretical sensitivity of transcranial Doppler evaluated using 135 angiograms demonstrating vasospasm. Practical consequences. Acta Neurochir (Wien) 131:12–18.
4. Lindegaard KF (1999) The role of transcranial Doppler in the management of patients with subarachnoid hemorrhage: a review. Acta Neurochir [Suppl] 72:59–71.
5. Aaslid R, Huber P, Nornes H (1984) Evaluation of cerebrovascular spasm with transcranial Doppler ultrasound. J Neurosurg 60:37–41.
6. Sloan M, Haley E, Kassell NF et al. (1989) Sensitivity and specificity of transcranial Doppler ultrasonography in the diagnosis of vasospasm following subarachnoid hemorrhage. Neurology 39:1514–1518.
7. Lewis DH, Newell DW, Winn HR (1997) Delayed ischemia due to cerebral vasospasm occult to transcranial Doppler. An important role of cerebral perfusion SPECT. Clin Nucl Med 22:238–240.
8. Chance B, Leigh JS, Miyake H et al. (1988) Comparison of time-resolved and -unresolved measurements of deoxyhemoglobin in brain. Proc Natl Acad Sci USA 85:4971–4975.
9. Ohmae E, Ouchi Y, Oda M et al. (2006) Cerebral hemodynamics evaluation by near-infrared time-resolved spectroscopy: correlation with simultaneous positron emission tomography measurements. NeuroImage 29:697–705.
10. Hoshi Y (2003) Functional near-infrared optical imaging: utility and limitations in human brain mapping. Psychophysiology 40:511–520.
11. Ijichi S, Kusaka T, Isobe K et al. (2005) Developmental changes of optical properties in neonates determined by near-infrared time-resolved spectroscopy. Pediat Res 58:568–573.
12. Oda M, Nakano T, Suzuki A et al. (2000) Near infrared time-resolved spectroscopy system for tissue oxygenation monitor. SPIE 4160:204–210.
13. Patterson MS, Chance B, Wilson BC (1989) Time resolved reflectance and transmittance for the noninvasive measurement of tissue optical properties. Appl Opt 28:2331–2336.

14. Tromberg BJ, Coquoz O, Fishkin JB et al. (1997) Noninvasive measurements of breast tissue optical properties using frequency-domain photon migration. Philos Trans R Soc Lond B 352:661–668.
15. Okada Y, Shima T, Nishida M et al. (1999) Comparison of transcranial Doppler investigation of aneurysmal vasospasm with digital subtraction angiographic and clinical findings. Neurosurgery 43:443–449.
16. Okada E, Delpy DT (2003) Near-infrared light propagation in an adult head model. I. Modeling of low-level scattering in the cerebrospinal fluid layer. Appl Opt 42:2906–2914.
17. Boas DA, Gaudette T, Strangman G et al. (2001) The accuracy of near infrared spectroscopy and imaging during focal changes in cerebral hemodynamics. NeuroImage 13:76–90.
18. Liebert A, Wabnitz H, Steinbrink J et al. (2005) Bed-side assessment of cerebral perfusion in stroke patients based on optical monitoring of a dye bolus by time-resolved diffuse reflectance. NeuroImage 24:426–435.
19. Karibe H, Tominaga T, Sato K et al. (2001) Decrease in intraoperative brain surface temperature in patients with subarachnoid haemorrhage. Acta Neurochir (Wien) 143:9–14.

Development of an Artificial Vital Sign Generator for Pulse Oximeter

Tomoyasu Ichimura and Hiroshi Endoh

Abstract This paper presents an artificial vital sign generator that enables medical trainees to measure SpO_2 and the pulse rate of a patient simulator using a pulse oximeter. The proposed system has a biological model that possesses a structure that is the inverse of a pulse oximeter probe, and it works using the inverse procedure to that of pulse oximetry. The SpO_2 generating function has been validated using two commercially available pulse oximeters.

1 Introduction

The majority of patient simulators designed for medical training purposes do not produce pulse oximetric saturations (SpO_2) on a pulse oximeter. However, SpO_2 is one of the most important and widely used parameter in the field of emergency medicine. Therefore, medical trainees using these patient simulators may have difficulties in rigorously evaluating their skills on resuscitation procedures from the standpoint of arterial blood oxygenation. We are therefore developing a patient simulator that mimics SpO_2 changes in response to resuscitation procedures such as mechanical ventilation.

Our simulator consists of two parts: (1) software that calculates arterial blood oxygenation from the given rate and depth of mechanical ventilation and cardiac output, and (2) hardware that simulates light absorption by arterial blood according to the calculated arterial oxygen levels that may be detected by commercially available pulse oximeters attached externally to the patient simulator. In this study, we focus on the latter part, which we refer to as the artificial vital sign generator.

T. Ichimura (✉)
Department of Electronic Control Engineering, Oyama National College of Technology, Tochigi, 323-0806, Japan
e-mail: ichimura@oyama-ct.ac.jp

E. Takahashi, D.F. Bruley (eds.), *Oxygen Transport to Tissue XXXI*, Advances in Experimental Medicine and Biology 662,
DOI 10.1007/978-1-4419-1241-1_74, © Springer Science+Business Media, LLC 2010

2 Artificial Vital Sign Generator

The artificial vital sign generator consists of a biological model and a control unit; their structures are described in detail below.

2.1 Biological Model

The finger model, which is an example of a biological model, and a sectional view are shown in Figs. 1 and 2, respectively. The finger model is intended to imitate the human finger in shape and texture; this model has a photodiode under the nail to detect light and red and near-infrared LEDs on the underside to emit light, as shown in Fig. 1. This is the same as the structure of a pulse oximeter probe, but simply in reverse. Furthermore, the finger model is filled with shading materials so that the light emitted from the pulse oximeter is not received by the light-receiving device of the probe (see Fig. 2).

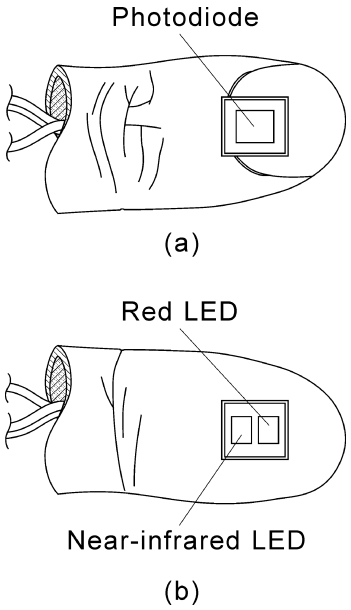

Fig. 1 Sketch of finger model. (**a**) and (**b**) are *top* and *bottom* views, respectively

2.2 Control Unit

A block diagram of a control unit along with the finger model is shown in Fig. 3. The control unit consists of a PC, an A/D converter, a D/A converter, an I/V converter, and two LED drivers.

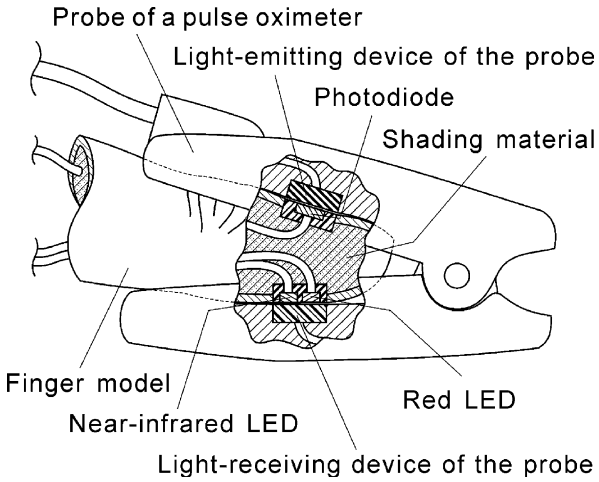

Fig. 2 Sectional view of finger model attached to the probe

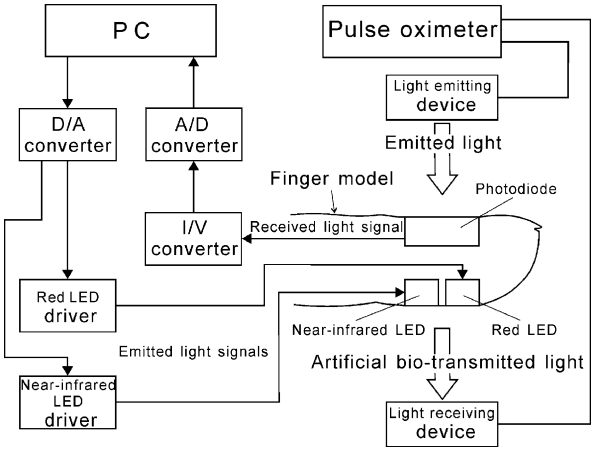

Fig. 3 Block diagram of the control unit with the finger model

The photodiode of the finger model converts the light emitted from the pulse oximeter to a received light signal. It is inputted to the PC via the I/V and A/D converters. The PC determines the time to synchronize with the light emitted from the pulse oximeter by using the received light signal. Furthermore, the PC calculates two emitted light signals that correspond to red and near-infrared lights using the target SpO_2 and pulse rate. The emitted light signals are sent to the LEDs of the finger model via the D/A converter and the two LED drivers on the above synchronized time. Thus, the finger model emits the artificial bio-transmitted light to the pulse oximeter. The above calculation of the emitted light signals is described in detail in the next section.

3 Emitted Light Signals of Artificial Vital Sign Generator

Two emitted light signals V_{F1} and V_{F2} that correspond to red and near-infrared lights, respectively, are calculated by an inverse procedure of the pulse oximetry.

3.1 Pulse Oximetry

A probe of a pulse oximeter has a light-emitting device with two LEDs and a light-receiving device with a photodiode. Red and near-infrared lights are used as lights of the LEDs because the difference in their absorption curves is large. The pulse oximeter generates these lights alternately and receives the lights transmitted through the tissue by the photodiode and converts them into signals [1–2].

Each received light signal includes a pulse wave caused by arterial beats. The pulse oximeter calculates a parameter ϕ using the pulsatile or AC component and the baseline or DC component of the received light signals, as shown in equation (1). At the same time, the pulse rate P_r is determined by the frequency of the AC component.

$$\phi = \frac{\Delta V_{b1}/V_{b1}}{\Delta V_{b2}/V_{b2}} \tag{1}$$

where ΔV_{b1} and V_{b1} are AC and DC components of the transmitted red light, respectively. ΔV_{b2} and V_{b2} are AC and DC components of the transmitted near-infrared light, respectively. The parameter ϕ represents a ratio of changes caused by arterial beats in each light's absorption.

Moreover, the pulse oximeter has the function $f(\ )$ defined by equation (2), which is the relationship between the ratio ϕ and SpO_2.

$$SpO_2 = f(\phi) \tag{2}$$

where the function $f(\ )$ depends on each model of pulse oximeters. SpO_2 is determined by equation (2).

3.2 Calculation of Emitted Light Signals

First, the parameter ϕ is calculated using the target SpO_2 from

$$\phi = g(SpO_2) \tag{3}$$

where $g(\ )$ is an inverse function of $f(\ )$ in (2). It is calculated by the least square method using the sampled ϕ and SpO_2.

Next, we determine the AC and DC components of emitted light signals V_{F1} and V_{F2}. These light signals should have a relationship similar to that as shown in (1).

$$\phi = \frac{\Delta V_{f1}/V_{f1}}{\Delta V_{f2}/V_{f2}} \tag{4}$$

where ΔV_{f1} and V_{f1} are AC and DC components of V_{F1}, respectively. ΔV_{f2} and V_{f2} are AC and DC components of V_{F2}, respectively.

Let us consider that one of the four variables (ΔV_{f1}, V_{f1}, ΔV_{f2}, and V_{f2}) is a control variable satisfying (4). V_{f1} and V_{f2} of DC components should be constants because they are related to the absorption of venous blood and tissue, excluding the arterial blood. In other words, one of the AC components (ΔV_{f1} and ΔV_{f2}) can be a control variable. Here, ΔV_{f1} is used as a control variable ΔV_{f1v} since it is proportional to ϕ. Hence, ΔV_{f1v} is calculated as follows:

$$\Delta V_{f1v} = \phi \cdot \frac{V_{f1c}\Delta V_{f2c}}{V_{f2c}} \tag{5}$$

where V_{f1c}, ΔV_{f2c}, and V_{f2c} are values in a known set (ΔV_{f1c}, V_{f1c}, ΔV_{f2c}, and V_{f2c}) that makes a pulse oximeter work normally.

Moreover, a real bio-transmitted light includes arterial beats, and thus, the pulse wave of the beats is expressed by a sine function and the pulse rate P_r is controlled by a period ($60/P_r$) of the sine function. The calculations described above are given as follows:

$$V_{F1} = \Delta V_{f1v} \sin(2\pi(P_r/60)t) + V_{f1c} \tag{6}$$

$$V_{F2} = \Delta V_{f2c} \sin(2\pi(P_r/60)t) + V_{f2c} \tag{7}$$

4 Experimental Results

The SpO_2 generating function was tested using two commercially available pulse oximeters (SAT-2100, Nihon Kohden and OX-0001, Yamagata Casio, Japan).

The experimental results are shown in Fig. 4. The reaction ranges of SpO_2 on SAT-2100 and OX-0001 were between 24 and 99% and between 31 and 98%, respectively. The differences between the target SpO_2 values and those actually measured by the external pulse oximeter were less than 2% SpO_2.

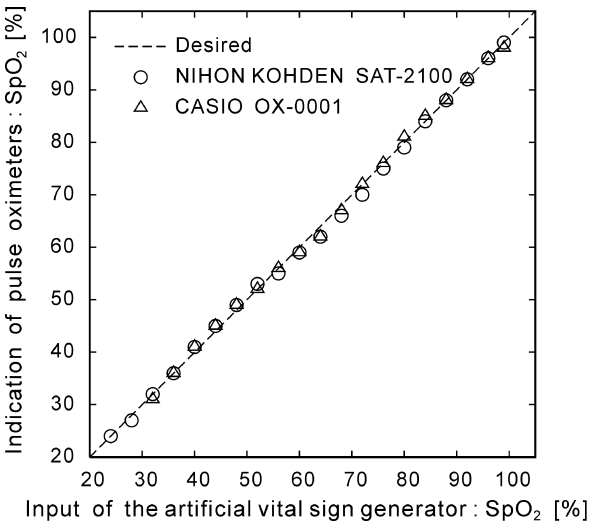

Fig. 4 Experimental results

5 Discussion and Conclusions

The reaction ranges of SpO_2 on both pulse oximeters are sufficiently wide because a pulse oximeter is normally used for SaO_2 ranges between 70 and 99%. Furthermore, the error of our system is smaller than the error of SpO_2 (2%) on the use of commercially available pulse oximeters. The changes in the errors of both pulse oximeters are very similar. The reason for these results is that the polynomial orders in the inverse function $g(\ )$ are identical to each other.

In this paper, we proposed an artificial vital sign generator that simulates the required SpO_2 and pulse rate on a pulse oximeter without using any biological tissue. The proposed system has a biological model with an inverse structure of a pulse oximeter probe, and it works using an inverse procedure of the pulse oximetry. Moreover, the suitability of the system is shown through experiments. We conclude that the present system, if included in patient simulators, may provide an opportunity for evaluating the resuscitation skills of medical trainees.

Acknowledgments We are very grateful to Dr. Eiji Takahashi for his advice.

References

1. Kelleher JF (1989) Pulse oximetry. J Clin Monit 5:37–62
2. Tremper KK, Baker SJ (1989) Pulse oximetry. Anesthesiology 70:98–108

EC-IC Bypass Function in Moyamoya Disease and Non-Moyamoya Ischemic Stroke Evaluated by Intraoperative Indocyanine Green Fluorescence Angiography

Takayuki Awano, Kaoru Sakatani, Noriaki Yokose, Tatsuya Hoshino, Norio Fujiwara, Shin Nakamura, Yoshihiro Murata, Tsuneo Kano, Yoichi Katayama, Takahiro Shikayama, and Mitsuharu Miwa

Abstract Indocyanine green (ICG) emits near-infrared fluorescence when it is excited by near-infrared light. The near infrared fluorescence of ICG was applied to the imaging of cerebral vessels during neurosurgical operations such as clipping of aneurysms. In this study, ICG angiography was applied to extracranial-intracranial (EC-IC) bypass surgery to evaluate the hemodynamic changes induced by bypass in moyamoya disease (MD) and non-moyamoya ischemic diseases (non-MD). These patients underwent superficial temporal artery-middle cerebral artery (STA-MCA) anastomosis. We compared the cortical areas where the bypass supplied blood flow between MD and non-MD. ICG angiography clearly demonstrated the bypass blood flow from the anastomosed STA to the cortical vessels including arteries, capillaries, and veins in both MD and non-MD. Interestingly, the anastomosed STA supplied blood flow to a larger cortical area in MD than non-MD. The bypass supplied greater extent of blood flow to the ischemic brain in MD than in non-MD. This difference might be caused by the fact that the perfusion pressure was lower in MD than in non-MD.

1 Introduction

Moyamoya disease is a rare occlusive cerebrovascular disease characterized by progressive stenosis of bilateral terminal portions of the internal carotid arteries (ICAs) [1]. EC-IC (extracranial-intracranial) bypass, such as superficial temporal artery-middle cerebral artery (STA-MCA) anastomosis, has become a standard surgical therapeutic option in moyamoya disease (MD) to prevent recurrent ischemic events [2, 3]. In addition, EC-IC bypass surgery has been performed to prevent stroke in patients with transient ischemic attack (TIA)

T. Awano (✉)
Division of Neurosurgery, Department of Neurological Surgery, Nihon University School of Medicine, Tokyo, Japan
e-mail: awntkyk1556@yahoo.co.jp

E. Takahashi, D.F. Bruley (eds.), *Oxygen Transport to Tissue XXXI*, Advances in Experimental Medicine and Biology 662,
DOI 10.1007/978-1-4419-1241-1_75, © Springer Science+Business Media, LLC 2010

caused by hemodynamic compromise [4, 5]. Indeed, neuroradiological studies have demonstrated beneficial effects of bypass surgery on cerebral hemodynamic status in both MD [3, 4] and non-MD ischemic diseases [4]. However, little is yet known regarding the difference in bypass function between patients with these conditions.

Indocyanine green (ICG) fluorescence angiography has been used as a technique for assessment of vascular flow. ICG emits near-infrared fluorescence when it is excited with near-infrared light [6]. Thus, ICG fluorescence is highly transmittable through biological tissue compared with visible light fluorescence. ICG fluorescence was first applied to retinal angiography [7]. In the field of neurosurgery, ICG fluorescence angiography has been used to confirm successful aneurysm clipping during surgery [7]. In addition, ICG angiography has been used for intraoperative assessment of bypass patency in EC-IC bypass surgery [10]. In the present study, employing ICG angiography, we evaluated not only patency of the bypass graft, but also blood supply via the bypass to the cortex during STA-MCA anastomosis in MD and non-MD. We compared changes in cortical perfusion by bypass blood flow between these patients.

2 Methods

We investigated 13 patients undergoing craniotomy for STA-MCA anastomosis. The subjects included 5 patients with moyamoya disease (mean age [mean ± SD], 21.8 ± 8.6 years) and 8 with non-moyamoya ischemic disease (58.1 ± 11.7 years), including 4 patients with occlusion of the ICA and 4 patients with occlusion of the MCA. In the moyamoya disease patients, cerebral angiography revealed stage 3 in 2 patients, stage 4 in 2 patients and stage 5 in 1 patient, according to the angiographical staging of moyamoya disease [1]; the principal routes of collateral circulation were mainly moyamoya vessels in these patients. In contrast, in the non-moyamoya patients, leptomeningeal anastomosis supported the collateral circulation. All moyamoya disease patients had suffered multiple episodes of TIA, while MRI did not demonstrate cerebral infarction in these patients. The present study was approved by the Committee for Clinical Trials and Research on Humans. The ethical committee of our university hospital approved the protocol of the study.

In all patients, we employed SPECT (PRISM 2000XP, Shimadzu Co., Japan) to measure the regional cerebral blood flow (rCBF) at rest and at 10 min after intravenous injection of acetazolamide (1.0 g). To evaluate the regional hemodynamics, regions of interest were designated in the cortical territory of the MCA. SPECT demonstrated a reduced rCBF at rest (< 30 ml/100 g/min) and reactivity to acetazolamide (%CVR $< 10\%$) before surgery in all of the moyamoya disease and non-moyamoya ischemic disease patients.

The parietal branch of the STA was anastomosed end-to-side to the M4 portion of the MCA. In moyamoya disease patients, encephalo-myo-synangiosis

was performed after the STA-MCA anastomosis. The physiological parameters during surgery were within the normal ranges in all patients; there were no significant differences in physiological parameters between the moyamoya disease and non-moyamoya disease groups.

Employing indocyanine green (ICG) angiography, we evaluated the hemodynamic changes in the patients during STA-MCA anastomosis. The ICG angiography system (Photodynamic Eye, C9830, Hamamatsu Photonics) consists of a light source (780 nm) and a CCD camera with optical filter (840 nm). The CCD camera is mounted on a three-legged stool, which is fitted with sterilized plastic covers. The distance between the CCD camera lens and operative field was 10 cm.

In order to image ICG fluorescence, ICG solution was injected into a branch vessel of the STA after the STA-MCA anastomosis. We analyzed the time course of ICG fluorescence intensity at ROI on the cortex. In addition, in order to analyze the ICG perfusion area quantitatively, we calculated the perfusion space when ICG fluorescence intensity reached the maximum level.

3 Results

Figure 1a shows an example of ICG fluorescence angiography after injection of ICG. We could obtain real time images of the bypass flow from the graft to the cortical vessels, and could confirm patency of the bypass graft in all cases. ICG fluorescence intensity rapidly increased to the maximum level and returned to

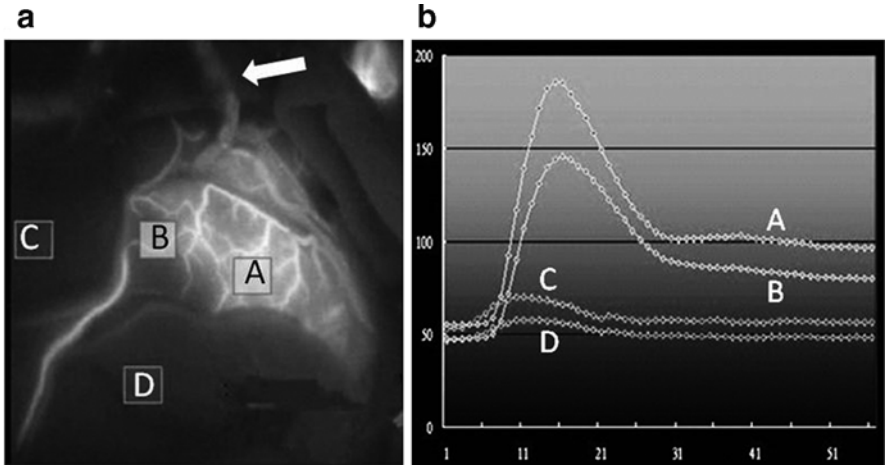

Fig. 1 Intraoperative ICG angiography during STA-MCA anastomosis. *Right*: A picture of ICG angiography at about 15 s after injection of ICG into the STA. *Left*: Time courses of ICG intensity curve. *Red* and *blue lines* correspond to *red ROI* and *blue ROI* in the *right figure*, respectively

the control level when the ROI was set at the perfusion area of ICG (Fig. 1b). In contrast, when the ROI was set outside the perfusion area, no remarkable increase of ICG fluorescence intensity was observed. Figure 2 compares the ICG perfusion areas in MD and non-MD. The STA supplied blood to a larger cortical area in MD (20.7 ± 6.6 cm^2) than non-MD (6.7 ± 4.5 cm^2, $p < 0.05$).

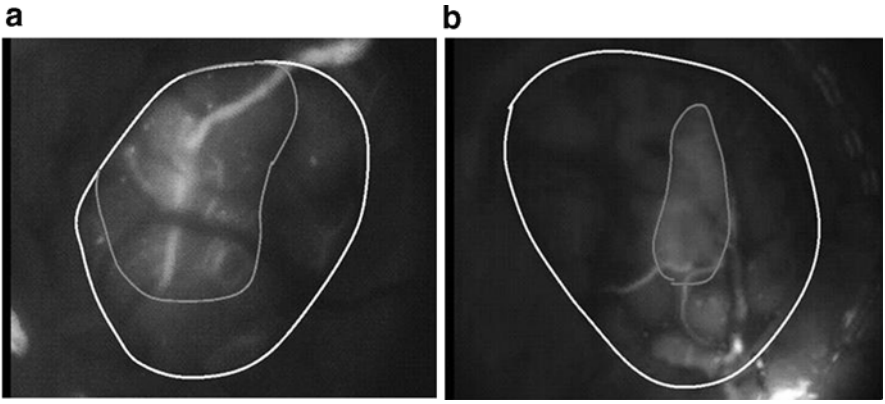

Fig. 2 Examples of cortical areas where anastomosed STA supplied blood flow between MD and non-MD. ICG angiography demonstrated that the STA supplied blood to larger cortical areas in MD (*left*) than those in non-MD (*right*)

4 Discussion

The present study demonstrated that the STA supplied blood to a larger cortical area in MD than non-MD. This finding is consistent with our previous study, which employed visual light spectroscopy to evaluate the effects of STA blood flow on the cerebral blood oxygenation (CBO) in the MCA territory during surgery in MD and non-MD [11]. We found that the STA blood flow increased the concentration of oxyhemoglobin in cortical vessels and oxygen saturation in the cortex, indicating that the bypass supplied blood flow to the ischemic brain; CBO changes were observed more frequently in MD than in non-MD. These observations suggest that the anastomosed STA supplied more blood to the ischemic brain in MD than non-MD, although the recipient artery of MD tends to be smaller and more fragile than that of non-MD. It should be noted, however, that several studies have reported the occurrence of hyperperfusion syndrome in patients with MD following STA-MCA anastomosis [11]; [13]; hyperperfusion syndrome tends to occur after carotid endarterectomy [14]or high flow bypass [15], rather than low flow bypass such as STA-MCA anastomosis.

The details of the physiological mechanisms underlying the differences in cortical perfusion induced by bypass blood flow between MD and non-MD

remain unclear; however, perfusion pressure may play a role in the STA blood supply to the ischemic brain. Our previous study using visual light spectroscopy revealed lower oxygen saturation in the cortex before anastomosis in MD than that in non-MD, suggesting that the perfusion pressure in MD was less than that in non-MD. In addition, our study on postoperative bypass function demonstrated that the bypass functioned better in cases with a lower rCBF before surgery [16]. Further studies are needed to clarify the physiological mechanism that underlies the difference in bypass blood supply between MD and non-MD.

5 Conclusion

The bypass begins to supply blood to a greater extent in MD than in non-MD, possibly because the perfusion pressure is lower in MD than in non-MD. The intraoperative ICG angiography system is considered useful for evaluating bypass function and facilitates safe and accurate bypass surgery

References

1. Suzuki J (1986) Moyamoya disease. Springer Berlin Heidelberg, New York.
2. Khan N, Schuknecht B, Boltshauser E et al. (2003) Moyamoya disease and Moyamoya syndrome: experience in Europe; choice of revascularisation procedures. Acta Neurochir (Wien) 145:1061–1071.
3. Saito N, Nakagawara J, Nakamura H, et al. (2004) Assessment of cerebral hemodynamics in childhood moyamoya disease using a quantitative and a semiquantitative IMP-SPECT study. Ann Nucl Med 18:323–331.
4. Anderson DE, McLane MP, Reichman OH et al. (1992) Improved cerebral blood flow and CO_2 reactivity after microvascular anastomosis in patients at high risk for recurrent stroke. Neurosurgery 31:26–33.
5. Ueno M, Nishizawa S, Toyoda H et al. (2001) Assessment of cerebral hemodynamics before and after revascularization in patients with occlusive cerebral revascularization by means of quantitative IMP-SPECT with double-injection protocol. Ann Nucl Med 15:209–215.
6. Benson RC, Kues HA (1978) Fluorescence properties of indocyanine green as related to angiography. Phys Med Biol 23:159–163.
7. Kogure K, David NJ, Yamanouchi U et al. (1970) Infrared absorption angiography of the fundus circulation. Arch Ophthalmol 83:209–214.
8. Bernstein M, Fleming JFR, Deck JHN (1984) Cerebral hyperperfusion after carotid endarterectomy: a cause of cerebral hemorrhage. Neurosurgery 15:50–56.
9. Raabe A, Beck J, Gerlach R, et al. (2003) Near-infrared indocyanine green video angiography: a new method for intraoperative assessment of vascular flow. Neurosurgery 52:132–139.
10. Woitzik J, Horn P, Vajkoczy P et al. (2005) Intraoperative control of extracranial-intracranial bypass patency by near-infrared indocyanine green videoangiography. J Neurosurg 102:692–698.
11. Hoshino T, Sakatani K, Kano T et al. (2006) Cerebral blood oxygenation changes induced by bypass blood flow in moyamoya disease and non-moyamoya cerebral ischaemic disease. Acta Neurochirurgica (Wien) 148:551–557.

12. Furuya K, Kawahara N, Morita A et al. (2004) Focal hyperperfusion after superficial temporal artery-middle cerebral artery anastomosis in a patient with moyamoya disease: case report. J Neurosurg 100:128–132.
13. Ogasawara K, Komoribayashi N, Kobayashi M et al. (2005) Neural damage caused by cerebral hyperperfusion after arterial bypass surgery in a patient with moyamoya disease: case report. Neurosurgery 56:E1380.
14. Piepgras DG, Morgan MK, Sundt TM et al. (1988) Intracerebral hemorrhage after carotid endarterectomy. J Neurosurg 68:532–536.
15. Stiver SI, Ogilvy CS (2002) Acute hyperperfusion syndrome complicating EC-IC bypass. J Neurol Neurosurg Psychiatry 73:88–89
16. Murata Y, Katayama Y, Sakatani K et al. (2003) Evaluation of extracranial- intracranial arterial bypass function by using near-infrared spectroscopy. J Neurosurg 99:304–310.

Effects of Revascularisation on Evoked Cerebral Blood Oxygenation Responses in Stroke Patients

Shin Nakamura, Kaoru Sakatani, Tsuneo Kano, Tetsuya Hoshino, Norio Fujiwara, Yoshihiro Murata, and Yoichi Katayama

Abstract We demonstrated that ischemic strokes exhibit an increase of deoxyhemoglobin during activation. We evaluated the effect of revascu-larization on the abnormal evoked cerebral blood oxygenation (CBO) re-sponses in these patients, employing near-infrared spectroscopy (NIRS). We selected five patients who exhibited an increase of deoxyhemoglobin associated with increases of oxyhemoglobin and total hemoglobin during activation for this study. These patients showed marked reductions of base-line regional cerebral blood flow and cerebrovascular reserve capacity, which were improved 1 week after revascularization. Postoperative NIRS demonstrated that the increase of deoxyhemoglobin during activa-tion was not observed after revascularization. This preliminary study demonstrated that the abnormal evoked-CBO response in ischemic stroke patients could be improved by revascularization.

1 Introduction

Blood oxygenation level-dependent (BOLD) contrast functional MRI (BOLD-fMRI) has been used in functional studies on stroke patients, on the assumption that these patients have normal neurovascular coupling [1–3]. Recent studies have revealed, however, that BOLD-fMRI does not correctly image activation areas in stroke patients [4–10]. It was suggested that impairments of neurovascular coupling may alter the evoked cerebral blood oxygenation (CBO) responses and hemodynamic changes in stroke patients, and this could result in failure of BOLD imag-ing. BOLD-fMRI alone, however, cannot elucidate the precise mechanisms involved, since BOLD-fMRI provides information mainly about concentration changes of deoxyhemoglobin (deoxy-Hb), which is paramagnetic [11].

S. Nakamura (✉)
Department of Neurosurgery, Nihon University School of Medicine, Tokyo, Japan
e-mail: nakashin51@ybb.ne.jp

E. Takahashi, D.F. Bruley (eds.), *Oxygen Transport to Tissue XXXI*,
Advances in Experimental Medicine and Biology 662,
DOI 10.1007/978-1-4419-1241-1_76, © Springer Science+Business Media, LLC 2010

Recently, we have evaluated evoked CBO changes in the primary sen-sorimotor cortex (PSMC) of patients with ischemic stroke [12, 13], employing near-infrared spectroscopy (NIRS) which allows measurements of concentration changes of not only deoxy-Hb, but also oxyhemoglobin (oxy-Hb) [14]. NIRS demonstrated a decrease of deoxy-Hb with in-creases of oxy-Hb and total hemoglobin (= sum of deoxy-Hb and oxy-Hb, t-Hb) in the activated PSMC on the non-lesion side, which is consistent with the physiological basis of BOLD imaging [11]. However, in the PSMC on the lesion side, the concentration of deoxy-Hb increased during the entire course of activation, concomitantly with increases of oxy-Hb and t-Hb. In addition, BOLD-fMRI showed significantly smaller activa-tion volumes in the PSMC on the lesion side. These findings suggest that the increase of paramagnetic deoxy-Hb during activation caused a reduction of BOLD signal, and this resulted in the failure of BOLD imaging in stroke patients [14].

We hypothesized that the abnormal evoked CBO response was caused by decreases of baseline CBF and cerebrovascular response (CVR) in ischemic stroke patients. In order to test this hypothesis, we evaluated the effects of revascularization on the evoked CBO changes in ischemic strokes.

2 Methods

We studied 5 patients with cerebral ischemia (four males, one female, 65.6 $\pm$ 10.6 years). All of the patients had suffered hemodynamic compromise caused by occlusion of the internal carotid artery (ICA) in four cases and stenosis of the ICA in one case. Four patients received superficial temporal artery-middle cerebral artery (STA-MCA) anastomosis, while one patient received carotid endarterectomy (CEA). The patients did not show neurological deficits at the time of examination.

We evaluated the rCBF at rest and the %CVR response to acetazolamide (1.0 g; ACZ) in the territory of the MCA, employing single photon emission tomography (SPECT) (PRISM 2000XP, Shimadzu Co., Japan): %CVR = {(rCBFACZ-rCBFrest)/rCBFrest} $\times$ 100, where rCBFACZ and rCBFrest represent the rCBF before and after the injection of ACZ, respectively.

We measured the evoked CBO responses in the PSMC contralateral to the task performance using a multi-channel NIRS (OMM 2000, Shimadzu Co., Japan). This system consists of 16 light-source fibers and 16 detectors, resulting in 48 source-detector pairs; each light source has three laser diodes with wavelengths of 780, 805, and 830 nm [15, 16]. The optodes for the NIRS topography were placed on the skull to cover the the motor cortex, employing a holder cap to avoid motion-related artifacts; the distance between each optode was 30 mm. We measured the concentration changes in oxy-Hb, deoxy-Hb, and t-Hb in the PSMC on the lesion side during contralateral hand-grasping tasks. The task paradigm consisted of 40 s of rest and 40 s of self-paced hand grasping; this task-rest cycle was repeated 6 times.

We evaluated the changes in oxy-Hb, deoxy-Hb, and t-Hb by subtracting the mean baseline values (40 s) from the mean stimulation values (40 s). Comparisons were made for each of the NIRS parameters using paired *t*-tests ($p < 0.05$ was defined as the criterion of a significant difference).

We classified NIRS responses into three patterns depending on concentration changes of deoxy-Hb during activation. That is, the deoxy-Hb concentration significantly decreased (Pattern 1), did not change (Pattern 2), or significantly increased (Pattern 3). Both oxy-Hb and t-Hb increased during the task in all subjects.

3 Results

Figure 1 shows an example of evoked CBO changes before and after revascularization. Note that revascularization reversed the direction of deoxy-Hb changes, and increased the extent of the increases in oxy-Hb and t-Hb. Preoperative NIRS demonstrated an increase of deoxy-Hb associated with increases of oxy-Hb and t-Hb (Pattern 3) during activation in all patients,

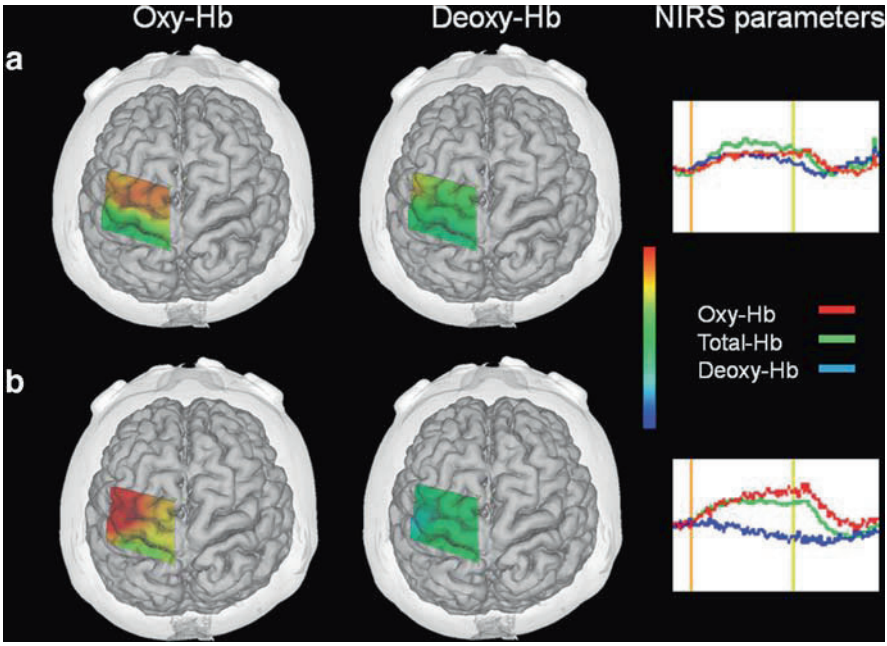

Fig. 1 NIRS topographic maps of changes in oxy-Hb and deoxy-Hb during right grasping task overlaid on anatomical MRI surface images before (**a**) and after (**b**) revascularization. The cir-cles indicate the ROI for analysis of NIRS parameter changes (*right*). Note that revascu-larization reversed the direction of deoxy-Hb changes, and increased the extent of the increases in oxy-Hb and t-Hb

while postoperative NIRS demonstrated a decrease of deoxy-Hb (Pattern 1) in three patients and no change of deoxy-Hb (Pattern 2) in two subjects.

Preoperative SPECT showed reductions of baseline rCBF and CVR in all patients; the mean rCBF and CVR were 40.9 ± 6.4 ml/100 g/min and –23.1 ± 5.6%, respectively. After revascularization, the rCBF and CVR were increased to 45.5 ± 6.1 ml/100 g/min and –5.6 ± 9.6% ($p < 0.016$), respectively.

4 Discussion

A number of studies have shown that revascularization improves the baseline rCBF and CVR in ischemic stroke patients [17–19]; however, until now, there has been no study to evaluate the effect of revascularization on the evoked CBO changes in ischemic stroke patients. The present study demonstrated that the abnormal evoked CBO response (i.e. an increase of deoxy-Hb during activation) in ischemic stroke patients could be improved by revascularization, and the improvement was associated with increases of baseline rCBF and CVR.

It should be noted that improvements of the abnormal evoked CBO response required only 1 week after revascularization. This suggests that the abnormal evoked CBO response was not caused by structural changes of cerebral vessels, such as decreases of elasticity and compliance of the vessels due to arteriosclerosis. Therefore, we considered the physiological mechanism of the deoxy-Hb increase during activation from the viewpoints of hemodynamic effects and oxygen metabolism. That is, the reduction of the rCBF and CVR under resting conditions could cause a lesser rCBF increase during activation, resulting in a decrease of the driving force to wash out deoxy-Hb in the capillaries and veins. When such an impairment of the hemodynamic response is advanced, the oxygen extraction could increase due to a decrease of oxygen delivery during activation. These alterations in the hemodynamic effects and the oxygen metabolism could lead to a lesser decrease or elevation of the deoxy-Hb concentrations in the vessels.

The increase of deoxy-Hb during activation suggests the occurrence of relative ischemia at the activation areas. Quantitative models of oxygen delivery during activation predict that disproportionately large increases of rCBF are required for small increases of the oxygen consumption [20]. Thus, a small decrease in the evoked rCBF response can cause oxygen deficiency during activation. These observations suggest that the relative ischemia during activation contributes to the occurrence of ischemic events. Further studies are necessary to investigate the relation between evoked CBO response patterns and ischemic events.

5 Conclusion

The baseline cerebral ischemic condition affects the evoked CBO response pattern in ischemic stroke patients. The abnormal CBO response in ischemic stroke patients could be normalized by revascularization. The improvements of the

abnormal evoked CBO response required only 1 week after revascularization, suggesting that the abnormal evoked CBO response was due to hemodynamic effects, rather than structural changes of cerebral vessels caused by arteriosclerosis.

References

1. Cramer SC, Nelles G, Benson RR et al. (1997) A functional MRI study of subjects recovered from hemiparetic stroke. Stroke 28:2518–2527
2. Cao Y, D'Olhaberriague L, Vikingstad EM et al. (1998) Pilot study of functional MRI to assess cerebral activation of motor function after poststroke hemiparesis. Stroke 29:112–122
3. Kato H, Izumiyama M, Koizumi H et al. (2002) Near-infrared spectroscopic topography as a tool to monitor motor reorganization after hemiparetic stroke: A comparison with functional MRI. Stroke 33:2032–2036
4. Pineiro R, Pendlebury S, Johansen-Berg H et al. (2002) Altered hemodynamic responses in patients after subcortical stroke measured by functional MRI. Stroke 33:103–109
5. Röther J, Knab R, Hamzei F et al. (2002) Negative dip in BOLD fMRI is caused by blood flow-oxygen consumption uncoupling in humans. NeuroImage 15:98–102
6. D'Esposito M, Deouell LY, Gazzaley A (2003) Alterations in the BOLD fMRI signal with aging and disease: A challenge for neuroimaging. Nature Rev Neurosci 4:863–872
7. Hamzei F, Knab R, Weiller C et al. (2003) The influence of extra- and intracranial artery disease on the BOLD signal in FMRI. NeuroImage 20:1393–1399
8. Rossini PM, Altamura C, Ferretti A et al. (2004) Does cerebrovascular disease affect the coupling between neuronal activity and local haemodynamics? Brain 127:99–110
9. Binkofski F, Seitz RJ (2004) Modulation of the BOLD-response in early recovery from sensorimotor stroke. Neurology 63:1223–1229
10. Krainik A, Hund-Georgiadis M, Zysset S et al. (2005) Regional impairment of cerebrovascular reactivity and BOLD signal in adults after stroke. Stroke 36:1146–1152
11. Ogawa S, Lee TM, Kay AR et al. (1990) Brain magnetic resonance imaging with contrast dependent on blood oxygenation. Proc Natl Acad Sci USA 87:9868–9872
12. Murata Y, Sakatani K, Hoshino T et al. (2006) Effects of cerebral ischemia on evoked cerebral blood oxygenation responses and BOLD contrast functional MRI in stroke patients. Stroke 37:2514–2520
13. Sakatani K, Murata Y, Fujiwara N et al. (2007) Comparison of blood-oxygen-level–dependent functional magnetic resonance imaging and near-infrared spectroscopy recording during functional brain activation in patients with stroke and brain tumors. J Biomed Optics 12:062110
14. Jöbsis FF (1977) Noninvasive, infrared monitoring of cerebral and myocardial oxygen sufficiency and circulatory parameters. Science 198:1264–1267
15. Hoshino T, Sakatani K, Katayama Y et al. (2005) Application of multi-channel near infrared spectroscopic topography to physiological monitoring of the cortex during cortical mapping: Technical case report. Surg Neurol 64:272–275
16. Hoshino T, Katayama Y, Sakatani K et al. (2006) Intraoperative monitoring of cerebral blood oxygenation and hemodynamics during EC-IC bypass surgery by a newly developed visual light spectroscopy system. Surg Neurol 65:569–576
17. Anderson DE, McLane MP, Reichman OH et al. (1992) Improved cerebral blood flow and CO_2 reactivity after microvascular anastomosis in patients at high risk for recurrent stroke. Neurosurgery 31:26–33
18. Gibbs JM, Wise RJ, Thomas DJ et al. (1987) Cerebral hemodynamic changes after extracranial-intracranial bypass surgery. J Neurol Neurosurg Psychiatry 50:140–150

19. Powers WJ, Martin WR, Herscovitch P et al. (1984) Extracranial-intracranial bypass surgery: hemodynamic and metabolic effects. Neurology 34:1168–1174
20. Boxerman JI, Bandettini PA, Kwong KK et al. (1995) The intravascular contribu-tion to fMRI signal change: Monte Carlo modeling and diffusion-weighted stud-ies in vivo. Magn Reson Med 34:4–10

Effects of Oral Single-Dose Administration of Sarpogrelate Hydrochloride on Saturation O_2 of Calf Muscle During Plantar Flexion Exercise

Masahiro Horiuchi, Koichi Okita, Shingo Takada, Masashi Omokawa, Tadashi Suga, Noriteru Morita, Kagami Hirabayashi, Takashi Yokota, Shintaro Kinugawa, and Hiroyuki Tsutsui

Abstract To investigate the effects of a 100-mg oral single-dose administration of sarpogrelate hydrochloride (SH) on saturation O_2 (StO_2) of calf muscle in healthy subjects experiencing simulated peripheral arterial disease (0.6 ankle brachial pressure index). Ten subjects performed three kinds of plantar flexion exercises at a work rate of 50% of maximal volunteer contraction for 4 min by using cuff occlusion ischemia,. Subjects performed a control test (C) without ischemia and SH, an ischemia test (I) without SH, and an I + SH test with ischemia. StO_2, blood pressures (BP), and heart rate (HR) were measured through all experiments. At the end of the exercise, the decrease in StO_2 from baseline in the C and I + SH tests was significantly less than that in the I test ($p < 0.05$, respectively). However, there were no significant differences in mean BP or HR in any of the exercise conditions. These results indicated that an oral single-dose administration of SH might improve peripheral circulation independent of any changes in BP and HR.

1 Introduction

Sarpogrelate hydrochloride is an effective therapeutic drug that has been widely used for peripheral arterial disease (PAD) patients in Japan [6]. Although it has been reported that long-term oral administration of sarpogrlate hydrochloride improves vascular function in PAD patients [8], investigation of the effects of a single-dose administration of sarpogrelate hydrochloride on PAD patients has been insufficient. Knowledge of these effects is important for the noninvasive, continuous, and accurate evaluation of PAD patients.

Saturation O_2 of muscle oxygenation (StO_2) derived by near-infrared spectroscopy (NIRS) is represented by the ratio of HbO_2 to total Hb. It is thought

M. Horiuchi (✉)
Department of Human Care Studies, Hokkaido University of Education, Sapporo, Japan
e-mail: horiuchi@hokusho-u.ac.jp

E. Takahashi, D.F. Bruley (eds.), *Oxygen Transport to Tissue XXXI*, Advances in Experimental Medicine and Biology 662,
DOI 10.1007/978-1-4419-1241-1_77, © Springer Science+Business Media, LLC 2010

that StO_2 would be a useful index of oxygen delivery and utilization. Therefore, this useful technique has been widely used to evaluate variation in the severity of PAD [5, 7]. However, it might be difficult to evaluate PAD patients accurately because of variation in disease severity and/or the effects and histories of administration of other medication.

The purpose of this study, therefore, was to investigate the effects of an oral single-dose administration of sarpogrelate hydrochloride on muscle oxygenation responses during plantar flexion exercise in healthy subjects who were simulated PAD patients using cuff occlusion ischemia.

2 Methods

Ten healthy male subjects with mean age 36 (5) years, height 174 (6) cm, body mass 65 (7) kg, participated in this study (values are means and standard deviation). All subjects were informed about this study and consent was obtained. This study was approved by an ethical committee of Hokusho University, Japan.

The subjects performed three kinds of unilateral planter flexion exercise with a long sitting position. The workload of all experimental exercises was set at 50% based on 1 repetition maximum. Subjects performed plantar flexion exercises for 4 min after 2 min of rest with 40 repetitions per 1 min, lifting the weight 5 cm above the ground. Exercise protocols were as follows: Control test (C) without ischemia and administration of sarpogrelate hydrochloride, Ischemia test (I) without administration of sarpogrelate hydrochloride, and ischemia test with administration of sarpogrelate hydrochloride (I + SH).

Subjects performing the I and I + SH tests had restricted blood flow caused by a pressure cuff in order to simulate PAD patients with 0.6 ankle brachial pressure index (ABI). To accomplish this, 40% pressure of systolic blood pressure (SBP) for an individual subject was carried out with a rapid inflator on the thigh muscle throughout the experiment. An oral single dose of sarpogrelate hydrochloride, 100 mg, was administered before 0.889 h of each test based on the Tmax [3].

During all tests, the responses of peripheral muscle oxygenation were measured using near-infrared spectroscopy (NIRS: BOM1-TRW, Omegawave, Japan). Optodes consisting of a transmitter and detector were placed on the right calf muscle, and the distance between the light source and the photo detector was 3 cm. This unit has continuous light source of triple wavelength (780, 810, and 830 nm) and calculates relative changes in tissue levels of muscle oxygenation (HbO_2), deoxygenation, and total Hb, according to the Beer-Lambert law. The instrument can calculate tissue blood oxygen saturation in muscle (StO_2, %) from the ratio of HbO_2 to totalHb after assuming a certain density of the red cells in the blood; here we present our results as changes in StO_2. The data were sampled by every second.

BP was monitored by the cuff occlusion method, and heart rate (HR) was monitored in synchronization with BP. Both parameters were measured at rest and 90 s after the onset of exercise at 1-min intervals. The mean BP (MBP) was calculated as diastolic pressure plus one-third of pulse pressure.

StO_2 responses in the primary decreasing phase in the first 2 min minus the first 10 s were approximated by the following equation:

$$StO_2(t) = StO_2(b) + Amp^* \left(1 - \exp^{(-(t-TD)/\tau)}\right)$$

where t is a given length of time, b is a baseline value at the onset of exercise, Amp is an amplitude between baseline value and a value at 2 min of the exercise, TD is a time delay, and τ is a time constant.

StO_2 of the calf muscle was represented as the values of a 30-s interval to minimize variability, and it represented the relative change from the value at baseline. MBP and HR were also represented as the relative change from the baseline value.

One-way ANOVA was used to compare the relative changes of StO_2, BP, and HR among three experimental conditions. Significance level was accepted at $p < 0.05$.

3 Results

Mean values of systolic BP, ABI, skinfold thickness of calf muscle, 1 RM data, resistance load of 50% 1 RM, and applied cuff pressure to simulate PAD in all subjects were 123 (7) mmHg, 1.11 (0.06), 5.3(0.7) mm, 32 (6) kg, 15 (3) kg, and 51 (2) mmHg, respectively.

The time constant in the I and I + SH tests seemed to be slower than that in the C test. In fact, the time constant in the I (19.5 ± 3.6 s) and I + SH (16.8 ± 4.2 s) tests was significantly slower than that in the C (9.3 ± 2.8 s) test ($p < 0.05$, respectively).

StO_2 changes by 30-s interval from a baseline value for all subjects are shown in Fig. 1. StO_2 decreased with a short time delay in all conditions. In the C test, StO_2 continued to decrease until about 120 s, and then it showed almost a plateau phase until the end of exercise. In the I test, it decreased rapidly until about 60 s, after which it continued to decrease gradually until the end of exercise. In the SH test, it decreased rapidly until about 60 s, after which it continued to decrease gradually until about 3 min of exercise, at which point it began to increase slightly until the end of exercise. During exercise, there were significant differences in the relative change from baseline of StO_2 at 3.5 and 4 min of exercise between the C and I tests (at 3.5 and 4 min) and between the C and I, the I and SH tests (at 4 min), ($p < 0.05$, respectively). However, there were no significant differences in StO_2 changes at 3.5 and 4 min between the C and SH tests.

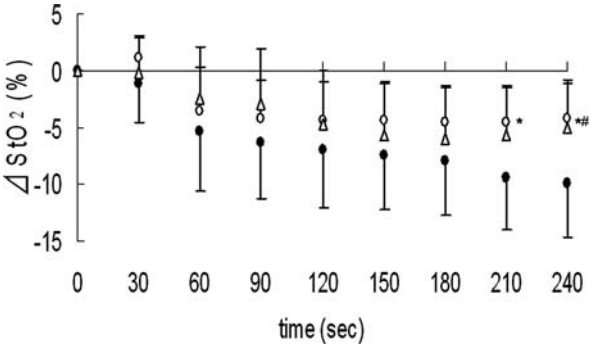

Fig. 1 Changes in StO_2 from the baseline during all experimental conditions. □; control test, •; ischemia test, ○; sarpogrelate hydrochloride test. *; $p < 0.05$ between control and ischemia test, #; $p < 0.05$ between sarpogrelate hydrochloride and ischemia test

Figure 2 shows the changing rate of MBP and HR from baseline values in all conditions, respectively. Both MBP and HR showed almost the same kinetics. MBP and HR increased temporarily after the onset of exercise, then it showed stable values during exercise. After the end of exercise, each decreased slightly and recovered toward the baseline value. There were no significant differences in MBP and HR among the experimental conditions.

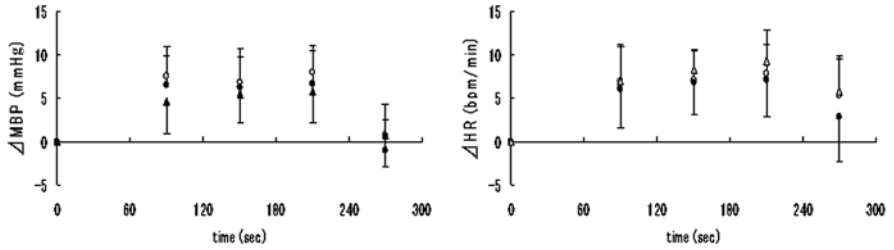

Fig. 2 Changes in mean blood pressure (MBP; *left panel*) and heart rate (HR; *right panel*) from the baseline during all experimental conditions. □; control test, •; ischemia test, ○; sarpogrelate hydrochloride test

4 Discussion

It is reasonable that StO_2 could change in either direction during exercise. That is, if StO_2 increases during exercise, it may mean that O_2 delivery to the active muscle exceeds O_2 utilization in the muscle. If StO_2 decreases during exercise, it may mean that StO_2 utilization in the muscle exceeds O_2 delivery to the active muscle. It has been reported that StO_2 kinetics of calf muscle during plantar flexion exercise at a lower work rate [1] in PAD patients was slower compared with that of healthy subjects. This slower kinetics may be associated with skeletal muscle metabolism, including muscle oxygen consumption, because of the lack of any difference in blood flow between PAD patients and healthy

subjects [1]. However, we simulated a situation of PAD patients with 0.6ABI using a cuff occlusion method by creating a relative lower pressure temporarily, and hence, muscle metabolism was not impaired. Thus, cuff occlusion ischemia might affect muscle blood flow rather than muscle metabolism. In this study, a slower time constant in the I and I + SH tests was observed compared with that in the C test. This slower response might have been caused by lower blood flow into the working muscle due to the ischemia by cuff occlusion. However, there were no differences in time constant between the I and I + SH tests.

In the decreasing phase of StO_2 during exercise, O_2 utilization was supposed to be greater than O_2 delivery due to blood flow restriction by ischemia. After 120 s of the C test, the balance between O_2 delivery and utilization may have remained constant, because StO_2 showed almost no change until the end of exercise. On the contrary, it is reasonable that O_2 utilization continued to exceed O_2 delivery until the end of the I test. Interestingly, in the latter period of the SH test, StO_2 increased slightly. As exercise continued at a same work rate in all experiments, it is unlikely that O_2 utilization decreased only in the latter phase during the SH test. Moreover, we controlled the workload that subjects could perform when lifting the weight 5 cm above the ground accurately throughout all experiments. SH is an effective medication that inhibits platelet aggregation induced by collagen and secondary aggregation by ADP or epinephrine [2]. Moreover, SH inhibits 5HT2 receptor specifically [9] with result that it can be reasonably expected to improve blood flow in tissues, because 5HT2 receptor is related to vasoconstriction [10].

To our knowledge, there has been no previous study about the effects of single-dose administration of SH on the hemodynamics of calf muscle, in particular, in simulated PAD patients of the same ABI without any effects of other factors such as cardiovascular disease, diabetes, or the action of other medication. Although we cannot compare our results with those of previous studies, we tentatively conclude, based on our results, that local muscle O_2 delivery might have increased in the latter phase of the SH test due to the effects of sarpogrelate hydrochloride.

Based on "Starling's equation", it is well known that stroke volume is affected not by arterial blood pressure but inflow in the vein. In the present study, as MBP and HR did not change during exercise in any of the test conditions, it was suggested that cardiac output did not increase during exercise. Therefore, it is unlikely that a single-dose administration of sarpogrelate hydrochloride affects the circulating blood volume from the heart.

5 Conclusion

Our results indicated that an oral single-dose administration of sarpogrelate hydrochloride improved peripheral hemodynamics in the latter period of exercise under greater demand of oxygen delivery and utilization during the exercise, independent of a lack of changes in blood pressure and heart rate.

Acknowledgments This study was supported by Tanabe-Mitsubishi Pharmaceutical Company.

References

1. Bauer TA, Brass EP, Barstow TJ, Hiatt WR (2007) Skeletal muscle StO_2 kinetics are slowed during low work rate calf muscle in peripheral arterial disease. Eur J Appl Phyisol 100: 143–151.
2. Hara H, Osakabe M, Kitajima A, Tamamo Y, Kikumoto R (1991) MCI-9042, a new antiplatelet agent is a selective S2-serotonergic receptor antagonist. Thromb Haemost 65(4): 415–420.
3. Isogai Y, Yokose T, Ikemoto T, Maeda T, Akiyama M, Hara H, Kitajima A, Izawa O (1991) Phase- 1 Study of sarpogrelate hydrochloride (MCI-9042) – single and repeated oral administration study. J Clin Therap Med 7 (6): 1177–1192.
4. Kawaguchi K, Tabusadani M, Sekikawa K, Hayashi Y, Onari K (2001) Do the kinetics of peripheral muscle oxygenation reflect systemic oxygen intake? Eur J Appl Physiol 84: 158–161.
5. Komiyama T, Shigematus H, Yasuhara H, Muto T (2000) Near-infrared spectroscopy grades the severity of the intermittent claudication in diabetics more accurately than ankle pressure measurement. Br J Surg 87(4): 459–466.
6. Matsubara J, Shiiya N, Ishida A, Miyata T, Shigematsu H, Obitsu Y, Shindo T, Hida K, Ohta T, Ando M, Nishibe T, Kawasaki T, Yasugi T, Onohara T (2007) Current status of medication therapy for arteriosclerosis obliterans (ASO) in University Hospital in Japan. J Jpn Coll Angiol 47: 153–162.
7. McCully K, Landsberg L, Suarez M, Hofman M, Posner JD (1997) Identification of peripheral vascular disease in elderly subjects using optical spectroscopy. J Gerontology 52A: B15–B165.
8. Miyazaki M, Higashi Y, Goto C, Chayama K, Yoshizumi M, Sanada H, Orihashi K, Sueda T (2007) Sarpogrelate hydrochloride, a selective 5-HT2A antagonist, improves vascular function in patients with peripheral arterial disease. J Cardiovasc Pharamacol 49(4): 221–227.
9. Tsuchihashi H, Yagi N, Kimura M, Shirota K, Kinami J, Ngatomo T (1991) Binding characteristics of 3H ketanserin for serotonin-2 receptor in the rabbit platelet. J Pharmacobiodyn 14(8): 461–466.
10. Vanhoutte PM, Houston DS (1985) Platelets, endothelium, and vasospasm. Circulation 72(4): 728–734.

Oxidative Capacity of the Skeletal Muscle and Lactic Acid Kinetics During Exercise in Healthy Subjects and Patients with COPD

Toshio Ichiwata, Gen Sasao, Tokuro Abe, Kiyokazu Kikuchi, Kenya Koyama, Hiroki Fujiwara, Asuka Nagai, Ichiro Kuwahira, and Koshu Nagao

Abstract [Background] In patients with chronic obstructive pulmonary disease (COPD), early lactic acidosis during exercise should be considered as playing a role in the limitation of exercise tolerance. It was hypothesized that the relationship between blood lactate concentrations (LA) and tissue oxygenation index (TOI) is available for the prediction of aerobic capacity of skeletal muscle. [Methods] Changes of LA and TOI in the vastus lateralis muscle were measured during incremental cycling exercise in 12 healthy subjects and 4 patients with COPD. The relationship between TOI and LA was examined in 12 healthy subjects and 4 COPD patients, and changes in the relationship were examined at an interval of several years (3.3 ± 1.0). [Results] (1) From the pattern LA as related to TOI, the healthy subjects were classified into the three groups. Group A ($n = 3$); LA increased slowly with a decrease in TOI. Group B ($n = 3$); LA increased steeply after the half point of maximal exercise. Group C ($n = 6$); LA increased steeply before the half point of maximal exercise. (2) In 3 patients with COPD, the relationship between TOI and LA shifted rightward at the second examination. [Conclusion] The steep increase in LA from the approximate resting value of TOI during exercise suggests that the aerobic capacity of working skeletal muscle decreased.

1 Introduction

In patients with moderate to severe COPD, the skeletal muscle dysfunction is characterized by a reduction in aerobic capacity and this should be considered as playing a role in the limitation of exercise tolerance [1]. In patients with COPD, the proportion of type I fibers (high oxidative capacity) are decreased as compared with age-matched controls [2] and early lactic acidosis occurs due to

T. Ichiwata (✉)
Department of Respiratory Medicine, Dokkyo Medical University Koshigaya Hospital, Koshigaya, Saitama, 343-8555, Japan
e-mail: ichiwata@dokkyomed.ac.jp

E. Takahashi, D.F. Bruley (eds.), *Oxygen Transport to Tissue XXXI*, Advances in Experimental Medicine and Biology 662,
DOI 10.1007/978-1-4419-1241-1_78, © Springer Science+Business Media, LLC 2010

the reduction in aerobic capacity during exercise. Near-infrared spectroscopy (NIRS) has recently been used to evaluate muscle oxygenation [3, 4].

2 Methods

2.1 Study Design and Subjects

With reference to the assessment of exercise intolerance and the evaluation of therapeutic interventions on clinical use, the present study performed cardiopulmonary exercise testing (CPET) comprising of the imposition of symptom-limited incremental exercise in combination with comprehensive breath-by-breath monitoring. LA and TOI of the vastus lateralis muscle were measured using NIRS. The relationship between TOI and LA was analyzed retrospectively. Twelve healthy male subjects (age, 49.0 ± 17.4 years) and 4 male outpatients with stable COPD (age, 65.3 ± 12.0 years) were examined. The 12 healthy subjects were confirmed to be free of any significant cardiopulmonary disease and represented normal exercise tolerance (Table 1). COPD patients were diagnosed as mild to moderate severity (Table 2).

Table 1 Clinical characteristics of healthy subjects

Subject No.	Age (year)	BMI (kg/m^2)	%VC (%)	FEV_1% (%)	peak VO_2 (ml/min)
1	64	25.2	112.3	84.8	1361
2	60	24.2	106.1	86.4	1170
3	57	26.3	86.7	73.7	1480
4	73	24.9	135.3	114.8	1686
5	37	20.9	107.6	89.6	1733
6	63	23.6	107.6	70.8	1338
7	36	25.6	116.3	86.8	2082
8	25	22.3	123.9	93.0	1030
9	43	23.4	111.9	84.6	1374
10	34	28.4	103.4	81.1	1870
11	45	25.3	108.6	87.6	1392
12	68	25.3	90.3	79.4	1422
Mean ± SD	49.0 ± 17.4	26.3 ± 1.8	100.8 ± 9.4	82.7 ± 4.3	1561 ± 267

2.2 Exercise Test, LA Measurement, and NIRS Monitoring

An incremental symptom-limited maximal exercise test was performed using an electromagnetically braked cycle ergometer (AEROBIKE 75XL, Combi, Tokyo, Japan). The exercise protocol consisted of 3-min rest, 3-min warm-up at 10 W of 55 revolutions per minute, and then the exercise load was increased

Table 2 Clinical characteristics of COPD patients at first and second examination

Subject No.	Exam. No.	Age (year)	BMI (kg/m^2)	VC (L)	FEV_1 (L)	DLco/VA (ml/min/mmHg/L)	Peak VO_2 (ml/min)
1	1st	75	21.8	3.81	1.86	1.17	1012
	2nd	78	21.0	3.60	1.51	1.16	684
2	1st	53	17.9	4.46	2.71	2.19	1277
	2nd	55	17.8	4.26	2.82	2.13	1527
3	1st	57	22.2	4.32	1.85	2.16	1196
	2nd	61	21.8	4.15	1.80	2.02	1081
4	1st	76	23.9	4.24	2.33	2.25	1307
	2nd	80	23.5	4.43	2.19	2.00	929

incrementally by 10 W/min. Blood samples were taken directly from the earlobe and LA was measured (Pro Analyser, Arkray of the KDK Corporation; Kyoto, Japan). Blood samples were collected at rest and during exercise testing every minute and LA was measured immediately.

Oxygenation of the vastus lateralis muscle was monitored using a commercially available NIRS system (NIRO-300: Hamamatsu Photonics KK; Hamamatsu, Japan). A probe holder containing an emission probe and detection probe was attached to the left vastus lateralis muscle along the vertical axis of the thigh approximately 15 cm from the knee joint. The NIRO-300 system also measures TOI, which can be expressed as oxyhemoglobin/(oxyhemoglobin + deoxyhemoglobin) × 100 (%). TOI was measured every 2 s from 3 min before the start of exercise until the end of exercise. The variables of NIRS were recorded and analyzed using a personal computer system (PowerLab; ADInstruments Pty Ltd; Castle Hill, Australia).

3 Results

Analysis of the relationship between TOI and LA of the vastus lateralis muscle during incremental exercise tests in the healthy subjects is shown in Fig. 1. Accordingly, the pattern of LA related to TOI in the healthy subjects was classified into the three groups. Group A ($n = 3$); LA increased slowly with a decrease in TOI and the inflection point of the steep increase in LA occurred just before stopping exercise. Group B ($n = 3$); LA increased slowly with a decrease in TOI and the inflection point of the steep increase in LA occurred above the half point of maximal exercise. Group C ($n = 6$); LA increased steeply before the half point of maximal exercise and the decrease in TOI was smaller than in Group A or B.

Changes in the relationship between TOI and LA of the vastus lateralis muscle during incremental exercise tests at intervals of 3.3 ± 1.0 years in the 4 patients with COPD is shown in Fig. 2. At the second examination, LA

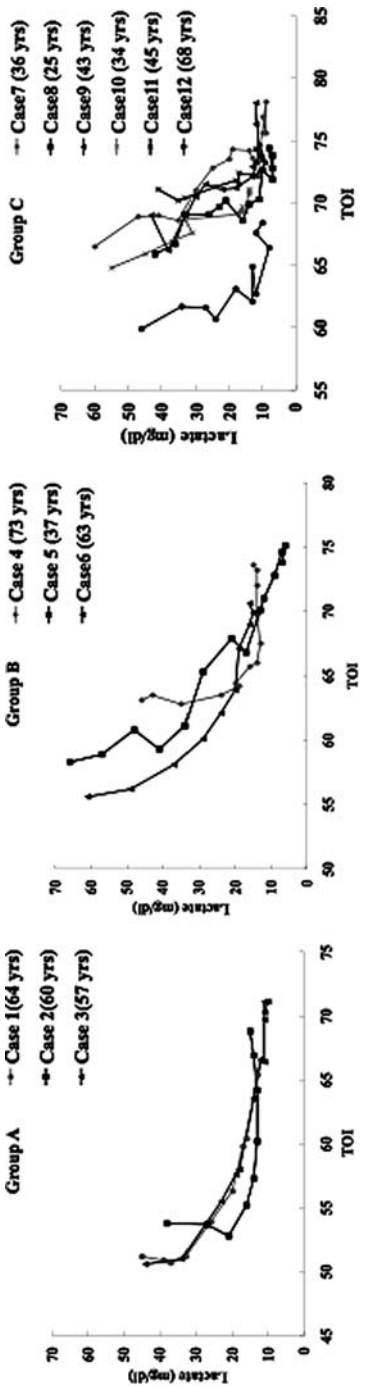

Fig. 1 Relationship between LA and TOI during incremental exercise in 12 healthy subjects

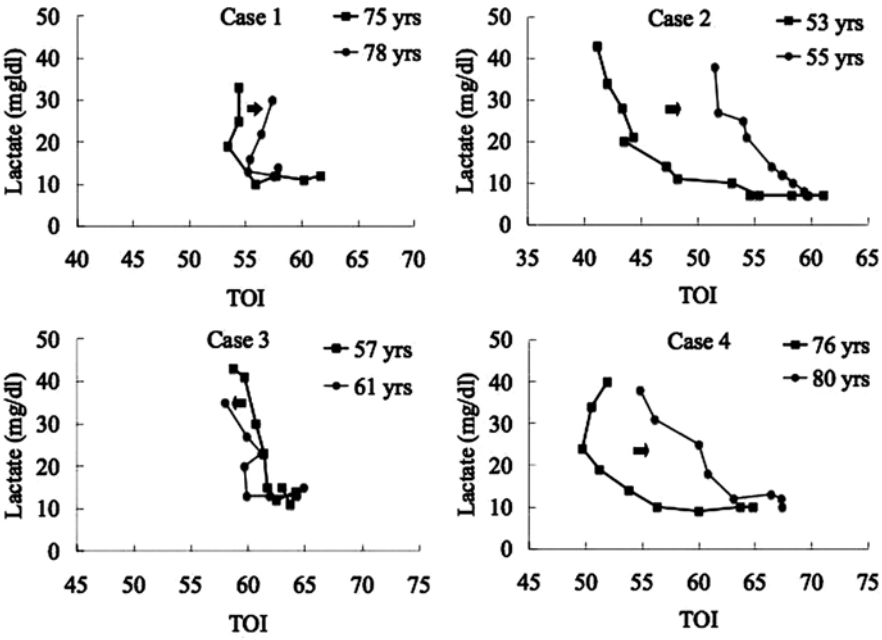

Fig. 2 Changes in relationship between LA and TOI during incremental exercise test in 4 patients with COPD

increased earlier than in the first examination, and the relationship between TOI and LA shifted rightward in 3 patients with COPD.

4 Discussion

In the present study, muscle biopsy data were not available, so the influence of muscle fiber type on oxygenation kinetics could not be determined. The kinetics of oxyhemoglobin and deoxyhemoglobin in the working skeletal muscle can be determined by the balance between O_2 utilization and muscles oxygen delivery. The NIRO-300 system also measures TOI, which is useful in the detection of muscle oxygenation changes during exercise.

We performed exercise tests using a cycle ergometer. The pedaling involves usually the vastus lateralis and the blood LA concentration reflects the production of LA in the vastus lateralis. According to the pattern of the changes in LA as related to TOI during exercise, the healthy subjects were classified into 3 groups. The subjects in Group C showed that LA increased steeply before the half point of maximal exercise and the decrease in TOI was smaller than in Groups A or B. In the healthy subjects, the increase in LA could indicate that the problem lay with skeletal muscle function rather than with O_2 delivery,

because O_2 delivery to working skeletal muscles might be adequate at the early phase from the onset of exercise.

It has been shown that muscle mass decreases and the proportion of muscle fiber types change in humans. By 60–70 years of age, muscle mass decreases by 25–30% in humans, and this is mainly due to the reduction in type II fibers. In subjects older than 70 years of age, the mean area of type II fibers decreases by approximately 15% and the percentage of type II fibers decreases by 40% [1]. Therefore, it was thought that the pattern of the change in LA as related to TOI in elderly subjects was similar to Group A, i.e. resulting from the reduction in type II fibers, but the pattern of LA as related to TOI did not relate with age. There might be two reasons why the pattern of LA as related to TOI was not related to age. Firstly, changes in muscle fiber types related to age; some loss of muscle mass and strength is almost universal in older people, but varies widely between individuals, particularly in relation to habitual levels of physical activity [5]. Secondly, the difference in muscle oxygenation within the same vastus lateralis muscle; in animal models, one of the causes of regional muscle oxygenation differences is shunting of blood flow to oxidative muscle fibers compared to non-oxidative muscle fibers within the same muscle [6]. It has also been shown that NIRS measured muscle oxygenation is variable within the same muscle [7].

Compared with matched control subjects, the reduction in the proportion of type I fibers in patients with COPD was accompanied by an increase in the proportion of type IIb fibers, and the early lactic acidosis occurred due to the reduction in aerobic energy production in the early phase from the onset of exercise [1]. Figure 2 shows the changes in the relationship between TOI and LA during incremental exercise at an interval of 3.3 ± 1.0 years in COPD patients. At the second examination, LA increased earlier than in the first examination in the same way as Group C of the healthy subjects, and the relationship between TOI and LA shifted rightward in 3 patients with COPD. This suggested that the reduction in the proportion of type I fibers accompanied the increase in the proportion of type IIb fibers due to age-related changes and advances in COPD. In addition, a shift from oxidative metabolism to glycolytic metabolism occurred in skeletal muscle of the patients with COPD at low levels of exercise.

5 Conclusion

The steep increase in LA from the approximate resting value of TOI during exercise suggests that the aerobic capacity of working skeletal muscle decreases. The relationship between TOI and LA shifted rightward at interval of several years in 3 COPD patients, suggesting that the aerobic capacity of the vastus lateralis muscle decreases. Further studies are needed to examine the relationship between TOI and LA in working skeletal muscle for the assessment of endurance training efficiency.

References

1. American Thoracic Society and European Respiratory Society. Skeletal muscle dysfunction in chronic obstructive pulmonary disease. A statement of the American Thoracic Society and European Respiratory Society. Am J Respir Crit Care Med 1999; 159: S1–S40.
2. Maltais F, Simard AA, Simard C, Jobin J, Desgagnes P, LeBlanc P. Oxidative capacity of the skeletal muscle and lactic acid kinetics during exercise in normal subjects and in patients with COPD. Am J Respir Crit Care Med 1996; 153: 288–293.
3. Grassi B, Quaresima V, Marconi C, Ferrari M, Cerretelli P. Blood lactate accumulation and muscle deoxygenation during incremental exercise. J Appl Physiol 1999: 87: 348–355.
4. Bhambhani YN. Muscle oxygenation trends during dynamic exercise measured by near infrared spectroscopy. Can J Appl Physiol 2004: 29: 504–523.
5. Steiner, MC. Sarcopaenia in chronic obstructive pulmonary disease, Thorax 2007; 62: 101–103.
6. Laughlin MH, Schrage WG. Effects of muscle contraction on skeletal muscle blood flow: when is there a muscle pump? Med Sci Sports Exerc. 1999; 31: 1027–1035.
7. Pittman RN. Oxygen supply to contracting skeletal muscle at the microcirculatory level: diffusion vs. convection. Acta Physiol Scand. 2000; 168: 593–602.

Index

A
Abe, T., 537
Absorption, 44, 143–147, 150, 170–175, 184–186, 188, 195, 201, 206, 208, 218, 225–226, 228–229, 231–232, 246, 252, 275, 321, 355, 433, 435, 463, 468, 493, 498, 506, 509, 513, 516–517
Achilefu, S., 407
Activation of prefrontal cortex, 251, 455–459, 480
Acute hypoxia, 50, 52, 125, 385–389
Acute lung rejection, 293, 296
Adachi, T., 101
Adipose, 78, 177–181, 331, 361
Aerobic capacity, 336, 339, 389, 537–538, 542
Aizawa, M., 77
Akatsu, T., 109
Alkaline phosphatase, 83–87
Altitude, 28, 127, 129–131
Alveolar macrophages, 27–30, 63
Ameye, L., 219
Anaerobic capacity, 339
Anagrams, 239–240
Angiotensin converting enzyme (ACE), 30, 42, 84, 87, 130
Anticoagulant, 34, 42, 440–442
Aoyama, A., 293
Aoyama, N., 455
Arterial blood pressure, 58–59, 84, 96, 246, 286–287, 331, 380, 535
Arterial function, 467–468, 470
Arteriosclerosis obliterans, 467, 471
Artificial oxygen carrier, 433–437
ATP release, 110–113
Autonomic nervous system (ANS), 134, 136–138, 455–456, 459, 473–477
Awano, T., 231, 491, 497, 505, 519

B
Bain, I., 273
Banaji, M., 285
Bando, T., 115, 293
Beer-Lambert law, 281, 318, 532
Beneke, R., 183
Bicycle, 353–358, 380, 386
Binzoni, T., 183
Bite force control, 479–483
Blasi, A., 279
Blood flow, 34, 42–44, 46, 80–81, 84, 87, 157, 187–188, 200–201, 229, 239, 258, 266, 273, 277, 290, 301, 303–305, 309–310, 312, 314, 320–321, 325, 334, 347–351, 353, 357, 363, 365–369, 379–384, 424–425, 440, 448–451, 486, 506, 508, 520, 522, 532, 542
Blood-muscle flux, 302
Blood substitutes, 434
BOLD-functional MRI, 214, 216, 525–526
Brachial artery, 366–369, 381–382, 384
Brain-computer interface, 497–502
Brain ischemia, 90, 95–100
Breath hold, 294, 348, 351
Broadband, 169–175
Bruley, D. F., 439

C
Cancer diagnosis, 407
Capillary density, 36, 71–72, 74–75, 83–87, 180, 330, 345
Capillary hemodynamics, 306
Capillary PO_2, 157, 161, 305
Capillary recruitment, 302–305
Carbon monoxide, 101–106, 116
Carbonyl stress, 50–51
Cardiac intensive care, 462

E. Takahashi, D.F. Bruley (eds.), *Oxygen Transport to Tissue XXXI*, Advances in Experimental Medicine and Biology 662,
DOI 10.1007/978-1-4419-1241-1, © Springer Science+Business Media, LLC 2010

Carvalho, H., 157
Casaer, P., 461
Cell respiration, 7–22
Cerebral autoregulation, 163–168, 219–224, 449, 452
Cerebral blood flow, 57, 97, 245, 257, 286–287, 347–348, 351, 448, 480, 486, 520
Cerebral blood oxygenation, 213–218, 245–248, 259, 474, 491–496, 525–529
Cerebral hemodynamics, 251, 253, 520
Cerebral microcirculation, 90
Cerebral oxygenation, 164, 206, 220, 257–262, 448, 452, 461–466
Cerebral oxygen transport, 93, 251
Cerebral tissue oxygenation index, 164, 167, 178–179, 181, 186, 219–220, 261–262, 462–463, 465, 541
Cerebral vasospasm, 505–510
Chen, F., 115, 293
Chronic obstructive pulmonary disease (COPD), 28, 115, 134, 136, 537–542
Cicco, G., 33, 41
Cicco, S., 33, 41
Circularity, 116–117
Cognitive task, 251–254, 474, 477
Coherence, 163–168, 219–224, 294, 448–449
Cold pressor test, 371–372
Colostomy stoma, 273–277
Configuration, 115–117, 145, 159–160, 170, 283, 433
Continuous-wave near-infrared spectroscopy (CW-NIRS), 143–145, 205–206
Contrast agent, 144, 408
Cooper, C. E., 169, 177, 183, 285
Coronary microvessel, 46
Cytochrome aa3, 4
Cytochrome *c* oxidase, 8, 12, 16–17, 20–22, 169, 285
Cytochrome oxidase, 191–197, 285–290

D
Dan, I., 205
Date, H., 115, 293
Depth resolution, 169
De Smet, D., 163, 219
Diastole, 366, 368–369
Dilated cardiomyopathy, 36, 41–47
Diurnal variations, 274, 277
Domain area, 83–85
Doppler ultrasound, 331, 361, 366, 383
DVT/VTE, 439–442

E
EC-IC bypass, 519–523
Eda, H., 497
EIAH, 335–339
Electrical muscle stimulation, 499–500, 502
Electron paramagnetic resonance (EPR) oximetry, 18–20, 60, 149–155, 265–271
Elliott, M. J., 447
Elwell, C. E., 169, 177, 183, 237, 279, 285, 447
Emergency medicine, 513
Emotion, 456
Endoh, H., 335, 513
Endoh, Y., 335
Endovascular treatment, 491–492
Endurance training, 342, 344–345, 354–356
Entrainment, 139
Ernstoff, M. S., 149
Eroku, B. O., 71
Erythrocyte, 110
Erythropoietin, 50, 122
Evoked cerebral blood oxygenation (CBO), 213–218, 245–247, 256, 474, 477, 492, 494, 496, 522, 525, 527–529
Exercise, 21, 128–130, 183–188, 199–200, 202, 225–230, 257–262, 301–302, 304, 310, 313–314, 317, 326, 330, 334–339, 342, 345, 347–351, 353–369, 371–376, 379–384, 386–387, 531–535, 537–542
Exercise-induced blood flow, 369
Exercise pressor reflex, 376
Extracorporeal membrane oxygenation (ECMO), 447–452

F
Fanelli, V., 41
Fat, 71, 77–81, 178–180, 184, 188, 336, 355–356, 362, 387, 470
Fatigue, 129–130, 294, 310–314, 324, 339, 389
Fatty liver, 77–81
Favale, S., 41
Finger tapping, 238–241
Flavoprotein fluorescence, 95–98
Fluorescence enhancement, 408, 410, 412
Flux analysis, 101
Forced oscillation technique, 293–297
Forearm muscle, 173, 360, 362, 366, 381, 383–384
Frequency-domain, 492
Fujimoto, T., 257
Fujinaga, T., 115, 293

Fujioka, M., 353, 359
Fujita, T., 49
Fujiwara, H., 537
Fujiwara, N., 95, 213, 519, 525
Fujiwara, T., 205
Fuku, N., 63
Functional brain imaging, 144
Functional near-infrared spectroscopy (fNIRS), 205, 479–483, 485–489
Furuichi, Y., 323

G
Gallez, B., 265
Gao, L., 169
Glucose metabolism, 50–51, 103, 105, 427
Glycaemia, 461–466
Glycolysis, 51, 101, 106, 112, 200, 202
Gnaiger, E., 7
Goda, N., 77
Golub, A. S., 157
Gonzalez, N. C., 27

H
Hamakawa, H., 115, 293
Handa, K., 423, 485
Harrison, D. K., 273
Hartford, A., 149
Hataishi, R., 133
Hattori, K., 89
Heart beat, 135–138
Heart disease, 36
Heart rate, 58, 122, 138, 147, 226, 239, 338, 372, 374–375, 380, 386, 449, 456, 457, 462, 473–477, 533–535
Heavy exercise, 226–227, 337, 339, 347–348, 350–351
Heme oxygenase, 101
Hemoglobin, 44, 46, 109–113, 122, 143, 146–147, 158, 169, 175, 180, 192, 200, 203–204, 206, 213–214, 226–227, 229, 246, 252–253, 304, 331, 338–339, 372–373, 384, 387, 433–437, 456, 463, 468, 474, 480, 486, 492, 497–498, 500–501, 526
Hemoglobin allostery, 110–112
Hemorheology, 33–38
Hepatic metastasis, 424
Heterogeneity, 13, 181, 231, 329–330, 333–334, 354–357, 359–360, 425–426
High altitude pulmonary edema (HAPE), 28, 127–131
High-intensity exercise, 225–230, 332
High resolution computed tomography (HRCT), 467
Hirabayashi, K., 531
Hirai, T., 115
Hirasawa, A., 347
Hirata, T., 115
Hirose, M., 63, 133
Hishiki, T., 109, 423
Hiura, M., 257
Hoeckel, M., 399
Hori, H., 415
Horinouchi, H., 433
Horiuchi, M., 531
Horn, L.–C., 399
Hoshino, T., 95, 205, 213, 231, 245, 491, 497, 505, 519, 525
Hoskote, A., 447
Hou, H., 265
Human, 15–17, 19, 21, 50–51, 64, 83, 109–113, 125, 138, 143–147, 150–151, 173, 205–210, 214, 226, 234, 304–305, 330, 342, 345, 359–360, 369, 417, 423–428, 435, 440–442, 461–462, 470, 474, 477, 506, 509, 514, 520, 542
Human brain circulation, 37–38, 351
Hyperbarics, 191–192, 197
Hyperoxia, 63–68, 267–268
Hypertension, 36, 50–51, 83, 86–87, 125–126, 436
Hyperthermia, 393–397
Hypertrophy, 36, 83, 86–87, 318, 321
Hyperventilation, 339, 348–349, 351, 437
Hypoxia-inducible factor (HIF)-1, 50, 72, 101
Hypoxia, 4, 7–22, 27–30, 37, 49–53, 73, 75, 89, 91–93, 101, 109–113, 121–125, 131, 150, 196, 267–268, 287–288, 385–389, 399–400, 404, 415–420, 439, 442
Hypoxic response, 399–404
Hypoxic neoplastic cells, 415

I
Iacoviello, M., 41
Ichimura, T., 513
Ichiwata, T., 127, 537
IDO hybrid inhibitors, 415–420
Igarashi, K., 205, 231
Igarashi, T., 95, 245, 505
Ikkyu, K., 415
Implantable resonator, 265–271
Inagaki, T., 309

Inagi, R., 49
Incremental exercise, 257–262, 362, 385–386, 538–539, 542
Incremental handgrip exercise, 359–364
Individual difference, 251–254
Indocyanine green, 144, 408, 509, 519–523
Indoleamine 2, 3-dioxygenase, 415, 417
Infant functional activation, 279–284
Inflammation, 27–30, 34, 50, 274
Inflection point of muscle oxygenation, 385–389
Intermittent hypoxia, 121–126
Intravital microscopy, 79–80, 303–305, 424
Ischemia, 29, 37, 50, 53, 87, 90, 95–100, 266–267, 318–321, 492, 505, 508, 526, 528, 532, 534–535
Ishigami, K., 479, 485
Ishii, M., 121
Ishikawa, A., 497
Iwamoto, T., 121, 127
Iwasaki, M., 121
Iwase, S., 323

J
Jacobs, J., 219
Joint angle, 330
Jue, T., 323
Jun, H., 485

K
K2, 127–131
Kagaya, A., 329, 365
Kajimura, M., 89
Kang, K. A., 407
Kanno, I., 57
Kano, T., 95, 231, 245, 491, 505, 519, 525
Kano, Y., 309
Katagiri, A., 205, 231
Katayama, Y., 95, 205, 213, 231, 245, 491, 497, 505, 519, 525
Katsumura, T., 353, 359, 379, 385
Katsuyama, M., 473
Kawai, K., 423
Kek, K. J., 199
Kelleher, D. K., 393
Ketogenic (KG) diet, 71–75
Khan, N., 149, 265
Kikuchi, K., 537
Kime, R., 353, 359, 379, 385
Kinugawa, S., 531
Kiryu, N., 231
Kitagawa, T., 455
Kitagawa, Y., 109, 423
Kobayashi, H., 63, 133
Kobayashi, K., 433
Kobayashi, M., 335
Koga, S., 225, 359
Kohl-Bareis, M., 169
Koh, P. H., 237, 279
Kojima, J., 95
Kokubo, K., 63, 133
Kondo, K., 77
Kondo, N., 225
Kondo, Y., 245
Koyama, K., 537
Koyama, T., 83
Kriedt, F., 191
Kriedt, C., 191
Kubota, M., 133
Kudo, N., 199
Kumagai, T., 49
Kuniyoshi, S., 335
Kuwahira, I., 3, 121, 127, 537

L
Labeled red blood cell, 58–60, 424
Lactic acid, 537–542
LaManna, J. C., 71
Lariviere, J. P., 265
L-band EPR, 265–266
LC-MS/MS, 101–106
Leiomyosarcoma, 400–404
Lemmers, P., 219
Lesniewski, P. N., 265
Leung, T. S., 169, 183, 447
Liebert, A., 143
Light propagation in head, 232–233, 235
Light propagation in tissues, 231
Li, H., 265
Lipid peroxidation, 53
Liposome, 30, 434
Liver, 15–17, 19–20, 22, 36, 77–81, 93, 161, 238, 301, 305–306, 311, 330, 342, 372, 376, 384, 389, 423–428
Lloyd-Fox, S., 279
L-Trp-TPZ hybrids, 416, 418–420
Lung function tests, 116

M
Macdonald, R., 143
Macrophage, 27–30, 63–68, 437
Mallet, A., 285

Masamoto, K., 57
Mass law, 4
Masuda, K., 323
Masuda, N., 133
Mathematical model, 157, 199–204
Mayer, A., 399
McCully, K. K., 317
Mean optical path length, 231–234, 252
Mears, S. C., 439
Microcirculation, 27–29, 33–38, 41–47, 58, 78, 80–81, 90, 157–162, 277, 310, 434, 439–440, 443
Microvascular function, 28–29, 78, 80, 157, 302, 304, 424–425
Microvascular O_2, 80, 305–306, 423–428
Mishima, M., 115, 293
Mitochondria, 7–22, 46, 52, 63–68, 81, 95, 158, 191–192, 196, 285–290, 302, 305, 327
Mitochondrial oxygen kinetics, 7–22
Mitsufuji, H., 133
Miura, H., 320, 362–363, 467
Miwa, M., 519
Miyahara, R., 115
Miyazaki, Y., 251
Mizuno, M., 371
Mizuno, T., 257
Moeller, M., 143
Molecular imaging, 407
Monte Carlo simulation, 145, 232–233
Morikawa, T., 89
Morimoto, M., 77
Morita, N., 531
Motion artifacts, 279–284, 319, 337
Motor imagery task, 499–502
Mountain climber, 131
Moyamoya disease, 519–523
MRI, 210, 213–218, 238, 258–259, 266, 269, 456, 467, 487, 492, 498, 520, 527
Mucosal SO2, 276
Multi centre study, 224
Multi-distance, 169–175
Multichannel TRS, 214
Multiple sites, 265–271
Muscle
  contractions, 188, 309, 311–314, 318, 321, 324, 327, 371–376, 381
  fiber composition, 330, 334
  length, 371–376
  metabolism, 200, 204, 534–535
  O_2 level, 357, 389
  oxygen store, 341, 343–344
  oxygenation, 177–181, 183, 199–204, 225–230, 330–331, 333–334, 360, 372, 379–389, 531–532, 538, 541–542
  VO_2, 357, 360, 362–363, 389
Muraoka, I., 371
Muraoka, Y., 365
Murase, N., 353, 359, 379
Murata, Y., 95, 213, 231, 245, 491, 497, 505, 519, 525
Muro, S., 115
Musch, T. I., 301
Mutation, 63–65, 67–68, 403, 424, 442
Myoglobin, 13, 21–22, 184–186, 188, 200, 203–204, 226–227, 229, 303, 468

N

Nagahata, Y., 423
Nagai, A., 121, 127, 537
Nagao, K., 537
Nagaoka, T., 497
Nagasawa, H., 415
Nakagawa, Y., 415
Nakajima, K., 479, 485
Nakamura, M., 423
Nakamura, S., 231, 491, 505, 519, 525
Nakano, Y., 115
Nakashima, H., 415
Nakashima, K., 415
Nakata, E., 415
Nangaku, M., 49
Nantz, M. H., 407
Naulaers, G., 163, 219, 461
Near infrared time-resolved spectroscopy (TRS), 505–510
Neonates, 163, 233, 463, 465, 491, 496
Nicholls, P., 285
Niioka, T., 251
Niizeki, K., 225
Nishigaki, Y., 63
Nishime, C., 423
Nitric oxide, 22, 34, 35–37, 81, 109–113, 368, 384, 434, 435–436
Niwayama, M., 353, 355
Normoxia, 8, 21, 64–67, 75, 110–112, 123, 193–195, 266–267, 387–389, 403

O

Obata, T., 57
Obrig, H., 143, 452

Occlusion, 89–91, 96, 98, 267, 318, 342, 343, 360–361, 372, 381–382, 387, 439–440, 442–443, 468, 470, 486, 520, 526, 532–533, 535
Oda, M., 213, 505
Ohmae, E., 505
Ohmori, F., 365
Ohmura, M., 423
Ohnuki, S., 251
Okada, E., 231
Okamoto, M., 205
Okamoto, T., 293
Okita, K., 531
Okubo, K., 115
Okumura, N., 467
Oku, Y., 115
Okuyama, S., 365
Omokawa, M., 531
Ooue, A., 225
Optical brain imaging, 144–145
Optical pathlength, 185, 205–210, 213–218, 226, 228–229, 231–235, 252, 477
Optical topography, 205, 237–243, 279–284, 448, 456–457
Osada, T., 353, 359, 379
Osawa, T., 353, 359, 385
Oxygen
  consumption, 8, 9, 11, 187, 200, 245, 285–290, 335–336, 342, 381, 468, 528, 534
  delivery, 36, 93, 330, 342, 372, 376, 462, 528, 532, 541
  gradients, 8–9, 11, 17, 19–21
  supply, 7, 21, 33–38, 78, 81, 86–87, 109, 131, 468
  uptake, 226, 353–354, 380, 382

P
PAD, 531–535
Papademetriou, M. D., 447
Parastomal hernia, 274, 276–277
Partial coherence, 219–224
Patient, 36, 42, 45, 63, 83, 121, 133–139, 151–152, 164, 167–168, 222, 224, 265, 274, 275–277, 293–294, 297, 440–441, 443, 447–448, 452, 462, 483, 492, 497, 505, 507, 509, 513, 519, 525–529, 532, 537–542
Patient simulator, 513, 518
Patterson, C., 191
Pd-porphyrin, 423
Penfold, S.-M., 177
Peripheral circulation, 531
Peripheral microcirculation, 41–47
Peripheral oxygenation, 42, 46
Peripheral vascular disease (PVD), 150, 152
Phillips, D., 279
Phosphorescence, 28, 423–428
Phosphorescence quenching, 157–162
Physiological measurement, 366
Pimonidazol, 89
Pittman, R. N., 157
PO2 cycles, 4
Polycythemia, 121–126
Poole, D. C., 301, 309, 320
Post-exercise, 341, 366–367, 369
PPARα, 78, 80–81
Pre-clinical model, 394
Prefrontal cortex, 251, 253, 455–459, 473–477, 480, 483
Premotor cortex, 482–483
Preprocessing, 167, 239
Preterm infants, 164, 219, 462
Primary motor cortex, 238, 483, 487, 500
Protein C, 439–443
Puchowicz, M. A., 71
Pulse oximeter, 337, 462, 513–518

R
Rat, 14–20, 28–30, 52–53, 57–61, 71–75, 83–87, 95–100, 121–126, 158, 161, 192, 245–248, 267, 269–271, 303, 305, 309–314, 310, 325, 327, 394, 436–437
Reactive oxygen species (ROS), 22, 28, 36, 50–53, 63–64, 93
Recovery time, 330, 334, 468–470
Red blood cells, 41, 58, 302, 433–437
Regional cerebral blood flow (rCBF), 95, 97–98, 245, 257, 480–481, 483, 486–489, 520, 523, 526, 528
Rehabilitation, 206, 470, 497–502
Renal vasoconstriction, 83–87
Renin angiotensin system, 28, 30, 84, 87
Repeated pO_2, 271
Reperfusion infury, 89–93, 293, 437
Respiration, 7–22, 49, 51, 133–135, 138, 260, 424, 449
Resting muscle oxygen consumption, 341–342, 345
Resuscitation, 191–192, 197, 435–437, 513, 518

S
Sadamoto, T., 347
Sahara, H., 115
Saitoh, T., 225
Sakai, Hiroaki, 115, 293
Sakai, Hiromi, 433
Sakatani, K., 95, 205, 213, 231, 245, 455, 473, 479, 485, 491, 497, 505, 519, 525
Sako, T., 341
Sano, K., 415
Sasaki, M., 455
Sasao, G., 121, 127, 537
Satoda, N., 293
Sato, K., 347
Sato, Kiyoshi, 115
Sato, Kohei, 365
Sato, T., 115
Scandurra, F. M., 7
Scatter, 17, 145, 170–173, 185–186, 188, 192–196, 206, 208, 210, 225–226, 228, 231–232, 252, 402, 463, 493, 506
Sekiguchi, S., 485
Severinghaus, J. W., 3
Shibusawa, M., 479, 485
Shikayama, T., 519
Shimane, M., 133
Shimazu, M., 109
Shimizu, K., 77
Shimomura, K., 353, 359, 379
Shinbo, T., 63, 133
Shiroishi, K., 353, 379
Shiro, Y., 415
Shoji, T., 115, 293
Simulation, 4, 145, 178, 201–202, 204, 232–233, 436
Singh, D. B., 273
Skeletal muscle, 15, 17, 20–22, 28, 188, 226, 301, 309–314, 317, 322, 327, 342, 360, 380, 534, 537–542
Smith, M., 285
Soeda, S., 63
Somatosensory cortex, 57–61, 246, 485–489
Somatosensory evoked potential (SEP), 95–100, 245–248
Sonobe, M., 115
Sonobe, T., 309
Sou, K., 433
Spatially resolved spectroscopy (SEP), 95–100, 245–248
Spinotrapezius muscle, 304–305, 310–311
SPM, 237–243
SpO_2, 128–130, 337–339, 386, 388, 513, 515–518
Sprint, 335–339
Static exercise, 348, 366
Steinbrink, J., 143
Stomal ischaemia, 274, 277
Streiff, M. B., 439
Stroke, 36, 45, 71, 84, 86, 93, 96, 349, 441, 497, 519–523, 525–529, 535
Stubbs, C., 237
Sucheta, A., 265
Sudal, O., 479
Suematsu, M., 77, 89, 101, 109, 423
Suemizu, H., 423
Suga-numa, K., 109
Suga, T., 531
Sugimoto, H., 415, 417
Sugioka, T., 77
Sun, X., 71, 397
Superoxide Dismutase, 63–68
Surgery, 84, 122–123, 150, 206, 266, 273, 295, 304, 310, 325, 400, 439–443, 491–492, 494, 519, 520–523
Suzuki, T., 505
Swartz, H. M., 149, 265
Sympathetic nerve, 310–311, 313
Systole, 366, 368

T
Tachtsidis, I., 169, 237, 285, 447
Taka, A., 83
Takada, S., 531
Takahashi, A., 115, 293
Takakura, H., 323
Takano, N., 101
Takeda, T., 479, 485
Takizawa, M., 77
Takubo, Y., 115
Tanabe, M., 109
Tanaka, M., 63
Tanida, M., 473
Taniguchi, Y., 347
Tejima, E., 245
Time-resolved experiment, 231–232, 234–235
Time-resolved imaging, 143–147
Time-resolved near-ingrared spectroscopy (TR-NIRS), 143–147, 213–218
Time-resolved spectroscopy (TRS), 177, 184, 207, 214, 218, 226, 228–229, 232, 252, 491–496, 505–510
Timing, 135–136, 138
Tissue oxygenation, 33, 45, 78, 80–81, 92, 150, 226, 269, 274, 394, 397, 436, 448

Tissue oxygenation index (TOI), 164, 167, 178–180, 184, 186, 188, 219–220, 224, 259, 261, 288, 381–383, 387, 448, 462–465, 538–539, 541–542
Tissue SO_2, 274, 277
Tokizawa, K., 371
Tomita, Y., 133
Tracheal index (Ti), 116–118
Training, 295, 318, 341–346, 353–357, 365–366, 368–369, 502, 513, 542
Tsipis, C. P., 71
Tsuchida, E., 433
Tsukada, K., 77, 109, 423
Tsunoda, N., 347
Tsutsui, H., 531
Tumor, 45, 52, 149–150, 152–153, 155, 206, 265–266, 269, 271, 295, 393–397, 399, 401–403, 407–408, 423–427
Tumor hypoxia, 151, 400
Tumor oxygen tension, 400
Tuzuki, D., 205

U
Ueda, C., 329
Uterine leiomyomas, 399–404
Uto, Y., 415

V
Van Bel, F., 219
Vanderhaegen, J., 163, 219, 461
Vanhaesebrouck, S., 461
Vanhole, C., 461
Van Huffel, S., 163, 219
Van Meter, K., 191
Vasomotion, 34, 449, 452
Vaupel, P., 393, 399
Ventilation, 58, 136, 138, 339, 347–351, 371, 374, 378, 386, 465, 513
Verbal fluency task, 214, 216
Visible light spectrophotometry, 274
Vital sign, 463, 513–518
Von Wallbrunn, A., 399

W
Wabnitz, H., 143
Wada, H., 293
Wakui, M., 423
Wang, J., 407
Welch averaged periodogram, 163–168
Williams, B. B., 149, 265
Wittekind, A., 183
Wolf, M., 219
Wood, J. G., 27
Women, 129, 330, 335–339, 348, 366, 400, 441
Wree, A., 399

X
Xu, K., 71

Y
Yachie-Kinoshita, A., 109
Yamaguchi, Y., 205
Yamamoto, D., 231
Yamamoto, K., 199
Yamamoto, M., 385
Yamamoto, Takamitsu, 95
Yamamoto, Takehiro, 101
Yamanaka, T., 213
Yamashita, D., 213
Yamashita, Y., 213, 505
Yokose, N., 205, 231, 491, 497, 505, 519
Yokota, T., 531
Yoshino, A., 505

Z
Zaki, B., 149
Zhang, J., 293